



UNIVERSIDADE D  
COIMBRA

António Luís Gonçalves de Aguiar

**NEW BORON-DIPYRROMETHENE (BODIPY)  
MOLECULES AS SUITABLE ELECTRON-DONORS FOR  
ORGANIC PHOTOVOLTAIC CELLS**

Tese no âmbito do Doutoramento em Química, Ramo de Especialização em Química Macromolecular, orientada pelo Professor Abílio José Fraga do Nascimento Sobral e pelo Professor Jorge Manuel Ferreira Morgado, apresentada ao Departamento de Química da Faculdade de Ciências e Tecnologia da Universidade de Coimbra.

Agosto de 2019





UNIVERSIDADE D  
COIMBRA

UNIVERSIDADE DE COIMBRA  
Faculdade de Ciências e Tecnologia da Universidade de  
Coimbra

*New boron-dipyrromethene (BODIPY)  
molecules as suitable electron-donors for  
organic photovoltaic cells*

António Luís Gonçalves de Aguiar

Tese no âmbito do Doutoramento em Química, Ramo de Especialização em Química Macromolecular, orientada pelo Professor Abílio José Fraga do Nascimento Sobral e pelo Professor Jorge Manuel Ferreira Morgado, apresentada ao Departamento de Química da Faculdade de Ciências e Tecnologia da Universidade de Coimbra.

Coimbra  
2019

This page intentionally left blank



## **Agradecimentos**

Em primeiro lugar o meu sincero agradecimento ao Professor Doutor Abílio Sobral, meu orientador, por me ter acolhido enquanto aluno de doutoramento no seu grupo de investigação. Agradeço todo o apoio científico, ensinamentos, disponibilidade, convivência pessoal e motivação, que foram fundamentais em todas as etapas do meu doutoramento.

Ao Professor Doutor Jorge Morgado, meu coorientador, agradeço por me ter acolhido no seu grupo de investigação e me ter dado a conhecer o cativante mundo das células fotovoltaicas orgânicas. Agradeço a disponibilidade e todos os ensinamentos transmitidos.

Agradeço ao grupo de Eletrónica Orgânica do Instituto de Telecomunicações pela ajuda, simpatia e boa disposição. Em especial, agradeço à Doutora Joana Farinhas pela amizade e apoio na preparação das células fotovoltaicas e obtenção das imagens de AFM. Agradeço ao Professor Doutor Luís Alcácer pelos cálculos computacionais, e à Doutora Ana Charas pelo apoio e disponibilidade para o esclarecimento de dúvidas relativas às células fotovoltaicas.

Agradeço ao Professor Doutor Christopher Brett, à Doutora Mariana Ghica e ao Mestre Wanderson da Silva por todo o apoio na obtenção e interpretação das medidas de voltametria cíclica.

À Professora Doutora Manuela Ramos agradeço pela disponibilidade e ajuda nos estudos de cristalografia por difração de raio-X.

Agradeço a todos os colegas de laboratório e de departamento, que se cruzaram comigo ao longo destes quatro anos, pela amizade, ajuda, e boa disposição. Um agradecimento especial à Maria, Wanderson, Telma, José, Krishnakumar, Santosh, Wani e Catarina pela amizade, cooperação, partilha e horas de conversas científicas e não científicas que me fizeram um cientista e uma pessoa mais rica.

A todos os meus amigos que me acompanham desde a infância e aos que fui fazendo ao longo da vida um muito obrigado.

Agradeço aos meus pais pelo apoio incondicional, sentido de ser e estar na vida e valores que me transmitiram e permitiram que eu chegasse ao final de mais uma etapa. Ao meu irmão João um muito obrigado por todos os momentos.

Agradeço à minha família por toda a motivação e apoio. Em especial, gostaria de agradecer aos meus tios João e Mila por sempre me receberem de braços abertos quando

precisei de me deslocar a Lisboa. A vossa ajuda, simpatia e alegria foram fundamentais para o meu sucesso.

Um obrigado especial à S rgia e ao Fernando por me ajudarem e aconselharem em todos os momentos. Mais uma etapa concretizada em que a vossa ajuda foi muito importante.

  Natalia agradeço toda a compreens o, motiva o, equil brio e apoio emocional. Obrigado por me ouvires, apoiares, dares foco e estares ao meu lado em todos os momentos. Tornaste este percurso mais f cil.

Finalmente, agradeço a bolsa de doutoramento ao programa doutoral ChemMat, o apoio financeiro   Funda o para a Ci ncia e Tecnologia (PD/BD/113702/2015). Ao Centro de Qu mica da Universidade de Coimbra e ao Instituto de Telecomunica es sediado no Instituto Superior T cnico agradeço o acolhimento e todas as condi es que permitiram a realiza o do meu doutoramento.

**FCT** Funda o  
para a Ci ncia  
e a Tecnologia

1 2 9 0



UNIVERSIDADE D  
COIMBRA



**ISIT** T CNICO  
LISBOA

**it** instituto de  
telecomunica es

## Articles published from this thesis

- A. Aguiar, J. Farinhas, W. da Silva, M. Susano, M. R. Silva, L. Alcácer, S. Kumar, C. M. A. Brett, J. Morgado, A. J. F. N. Sobral, **Simple BODIPY dyes as suitable electron-donors for organic bulk heterojunction photovoltaic cells**, *Dyes and Pigments*, 2020, 172, 107842.
- A. Aguiar, J. Farinhas, W. da Silva, M. E. Ghica, C. M. A. Brett, J. Morgado and A. J. F. N. Sobral, **Synthesis, characterization and application of meso-substituted fluorinated boron dipyrromethenes (BODIPYs) with different styryl groups in organic photovoltaic cells**, *Dyes and Pigments*, 2019, 168, 103-110.

## Articles published not directly related with this thesis

- B. Balakrishna, A. Aguiar, P. J. M. Sobral, M. Y. Wani, J. Almeida e Silva and A. J. F. N. Sobral, **Paal–Knorr synthesis of pyrroles: from conventional to green synthesis**, *Catalysis Reviews*, 2019, 61, 84-110.
- B. Krishnakumar, R. Hariharan, V. Pandiyan, A. Aguiar and A. J. F. N. Sobral, **Gelatin-assisted g-TiO<sub>2</sub>/BiOI heterostructure nanocomposites for azo dye degradation under visible light**, *Journal of Environmental Chemical Engineering*, 2018, 6, 4282-4288.
- S. Kumar, R. K. Yadav, K. Ram, A. Aguiar, J. Koh and A. J. F. N. Sobral, **Graphene oxide modified cobalt metallated porphyrin photocatalyst for conversion of formic acid from carbon dioxide**, *Journal of CO<sub>2</sub> Utilization*, 2018, 27, 107-114.
- B. Krishnakumar, S. Kumar, J. M. Gil, V. Pandiyan, A. Aguiar and A. J. F. N. Sobral, **Highly active P25@Pd/C nanocomposite for the degradation of Naphthol Blue Black with visible light**, *Journal of Molecular Structure*, 2018, 1153, 346-352.
- C. T. Arranja, A. Aguiar, T. Encarnação, S. M. Fonseca, L. L. G. Justino, R. A. E. Castro, A. Benniston, A. Harriman, H. D. Burrows and A. J. F. N. Sobral, **Double-tailed long chain BODIPYs - Synthesis, characterization and preliminary studies on their use as lipid fluorescence probes**, *Journal of Molecular Structure*, 2017, 1146, 62-69.

## Communications from this thesis presented by the author

- A. Aguiar, J. Farinhas, W. da Silva, M. E. Ghica, C. M. A. Brett, J. Morgado, A. J. F. N. Sobral, Oral presentation: **“Electrochemical, photophysical and photovoltaic studies of new fluorinated meso-substituted BODIPY dyes with various styryl aromatic groups”**, 4<sup>th</sup> *Green and Sustainable Chemistry*, Dresden, Germany, May 2019.

- A. Aguiar, R. Oliveira, J. Farinhas, M. E. Ghica, C. M. A. Brett, J. Morgado, A. J. F. N. Sobral, Poster presentation: “**BODIPY small molecules as highly suitable donor materials for organic photovoltaic cells: Synthesis, Characterization and OPV cells application**”, *12º Encontro Nacional de Química Orgânica*, Coimbra, Portugal, January 2018.

- A. Aguiar, M. E. Ghica, C. M. A. Brett, J. Morgado, A. J. F. N. Sobral, Poster presentation: “**Meso-substituted BODIPY small molecules as highly suitable donor materials for organic photovoltaic cells: Synthesis and Characterization**”, *Cost Action MP1307: Industry Day on Printed Electronics and Solar Cells (DaySol2017)*, Lisbon, Portugal, April 2017.

- A. Aguiar, A. Meireles, C. T. Arranja, M. M. Barsan, C. M. A. Brett, A. J. F. N. Sobral, Poster presentation: “**Synthesis and characterization of long alkyl chains BODIPYs as new donor materials for organic photovoltaic cells**”, *XXII Encontro Luso Galego*, Bragança, Portugal, November 2016.

## Abstract

Organic photovoltaic cells (OPVs) have been arising as one of the most appealing alternatives to the photovoltaic cells based on inorganic semiconductors (mainly silicon) due to their low-cost production, lightweight, mechanical flexibility and versatility for building integration.

Boron-dipyrrromethene (BODIPY) molecules are auspicious photosensitizer materials for OPV. However, the research on BODIPY-based OPVs just started 10 years ago and the number of published studies is relatively low.

This thesis comprises the synthesis, characterization and photovoltaic application of several BODIPY molecules divided into four different series. The first series is composed by simple *meso*-substituted BODIPY dyes whose molecular framework allows further derivatizations. The result of the studies of the main structural, photophysical, electrochemical properties as well as the photovoltaic results were used as standard data for performance evaluation of the subsequent series.

The other three series are made of BODIPYs obtained upon functionalization of selected molecules from the first series. The second and third series are mostly constituted by new BODIPY structures with styryl or vinyl groups, synthesised through condensation of aromatic aldehydes with some selected BODIPY structures from the first series, via Knoevenagel condensation. These new molecules presented an expansion of the  $\pi$ -system which led to absorption and emission at higher wavelengths.

The BODIPY molecules from the fourth series were obtained by changing the typical BODIPY's boron ligands (fluorine atoms) by several aryloxy or alkoxy groups.

Additionally, three BODIPY-porphyrin dyads were synthesised using both a reported pathway and a pathway developed during the PhD project. The new pathway uses porphyrins with carboxylic acid groups to synthesise the BODIPY structure directly attached to porphyrin's structure.

In addition to the standard structural characterisation (e.g. nuclear magnetic resonance spectroscopy, mass spectrometry), the synthesised compounds were characterised using a variety of techniques, namely, thermogravimetry, scanning calorimetry, absorption spectroscopy, emission spectroscopy, cyclic voltammetry and computational studies. The conjugation of all characterisation techniques allowed us to obtain a full understanding of their main properties, calculate the HOMO and LUMO energies and evaluate the suitability for application in OPVs.

All the synthesised compounds were considered suitable electron-donors (upon combination with PC<sub>61</sub>BM and PC<sub>71</sub>BM as electron-acceptors) for organic photovoltaic cells. Consequently, almost all BODIPYs were tested and the best performing BODIPY-based OPVs were optimised in several aspects related to the engineering of the devices.

In general, OPVs based on the proposed dyes presented high open-circuit voltages ( $V_{OC}$ ), and some systems reached power conversion efficiency (PCE) above 2 %. The best result was achieved by a BODIPY with two vinylnaphthalene units, with a PCE of 2.8 % and  $V_{OC}$  of 1.00 V, which is a very promising PCE result for BODIPY-based OPV and a top  $V_{OC}$  value for this sort of systems.

**Keywords:** BODIPY; organic synthesis; optoelectronic properties; organic photovoltaic cells;

## Resumo

As células fotovoltaicas orgânicas (OPVs) têm surgido como uma das alternativas mais apelativas às células fotovoltaicas baseadas em semicondutores inorgânicos (essencialmente silício), devido ao baixo custo de produção, leveza, flexibilidade dos dispositivos e versatilidade na integração em edifícios.

As moléculas de boro-dipirrometeno (BODIPY) são fotossensibilizadores muito promissores para aplicação em OPVs. Contudo, a aplicação de BODIPYs em células fotovoltaicas orgânicas começou a ser investigada há apenas 10 anos e o número de publicações é ainda relativamente baixo.

Esta tese de doutoramento abrange a síntese, caracterização e aplicação fotovoltaica de várias moléculas de BODIPY divididas em quatro séries. A primeira série é composta maioritariamente por BODIPYs *meso*-substituídos cuja estrutura permite funcionalizações adicionais. Os resultados dos estudos das principais propriedades estruturais, fotofísicas, eletroquímicas, bem como os resultados dos testes fotovoltaicos serviram como base comparativa para a avaliação das moléculas subsequentes.

As restantes três séries foram construídas a partir da funcionalização de algumas estruturas da primeira série. A segunda e terceira série são constituídas maioritariamente por novas estruturas com grupos estireno ou grupos vinílicos obtidos a partir da condensação de aldeídos aromáticos com alguns BODIPYs selecionados da primeira série, via condensação de Knoevenagel. Estes novos compostos possuem uma maior conjugação de eletrões- $\pi$  e, por isso, uma absorção e emissão deslocadas para maiores comprimentos de onda.

As moléculas de BODIPY da quarta série foram obtidas através da substituição dos ligandos típicos (átomos de flúor) por vários grupos ariloxi ou alcoxi.

Adicionalmente, foram também sintetizadas três moléculas conjugadas de BODIPY-porfirina, usando um método de síntese já conhecido e um método alternativo desenvolvido ao longo do projeto doutoral. O novo método de síntese usa porfirinas com grupos carboxílicos para sintetizar BODIPYs diretamente ligados à estrutura das porfirinas.

Além das técnicas de caracterização estrutural padrão (por exemplo, espectroscopia de ressonância magnética nuclear, espectrometria de massa), os compostos sintetizados foram estudados através de técnicas como termogravimetria, calorimetria diferencial de varredura, espectroscopia de absorção, espectroscopia de emissão, voltametria cíclica e estudos computacionais. A conjugação de todas as técnicas de caracterização permitiu obter um conhecimento abrangente das propriedades dos BODIPYs, calcular as energias das

orbitais HOMO e LUMO, e avaliar a adequabilidade dos compostos para aplicação em OPVs.

Todas as moléculas sintetizadas foram consideradas doadoras de elétrons adequadas (em combinação com os aceitadores de elétrons PC<sub>61</sub>BM e PC<sub>71</sub>BM) à aplicação em células fotovoltaicas orgânicas. Consequentemente, a maioria dos BODIPYs sintetizados foram testados e as melhores OPVs foram otimizadas em vários aspectos relativos à construção dos dispositivos.

Em geral, as OPVs baseadas nas moléculas propostas apresentaram altas tensões de circuito aberto ( $V_{OC}$ ), e alguns sistemas atingiram eficiência de conversão de energia (PCE) acima de 2 %. O melhor resultado foi alcançado por um BODIPY com duas unidades de vinilnaftaleno, com um PCE de 2.8 % e  $V_{OC}$  de 1.00 V, o que é uma eficiência muito promissora tendo em conta as OPVs baseadas em BODIPYs já publicadas, e um valor de  $V_{OC}$  alto considerando qualquer tipo de célula fotovoltaica orgânica.

**Palavras chave:** BODIPY; síntese orgânica; propriedades optoelectrónicas; células fotovoltaicas orgânicas;



## Contents

<b>CHAPTER 1. Introduction</b> .....	<b>1</b>
1.1. Photovoltaic Cells .....	2
1.1.1. Evolution of photovoltaic cells.....	5
1.1.2. Organic photovoltaic cells (OPVs).....	8
1.1.3. Operational principles of organic photovoltaic cells.....	11
1.1.4. Performance characterisation of organic photovoltaic cells.....	14
1.1.5. Polymers versus small molecules in bulk heterojunction organic photovoltaic cells.....	16
1.2. Boron dipyrromethene (BODIPY): a versatile photoactive dye .....	17
1.2.1. Background, structure and synthetic routes .....	17
1.2.2. Functionalization of the BODIPY core .....	18
1.2.2.1. Functionalization at the <i>meso</i> -position .....	20
1.2.2.2. Functionalization at the 1,3,5,7-positions.....	21
1.2.2.3. Functionalization at the 2,6-positions.....	22
1.2.2.4. Functionalization at the boron atom .....	23
1.2.3. General properties of BODIPYs.....	23
1.2.4. Applications of BODIPY dyes .....	25
1.2.5. BODIPY molecules as photoactive compounds in photovoltaic cells.....	26
1.3. Thesis objectives and outline .....	32
1.4. References for Chapter 1.....	35
<b>CHAPTER 2. <i>Meso</i>-substituted BODIPY molecules</b> .....	<b>43</b>
2.1. Synthesis of <i>meso</i> -aryl BODIPY molecules .....	44
2.1.1. Synthesis and structural characterisation of the first series of BODIPY molecules (1S-BDP).....	45
2.1.2. The <i>meso</i> -free BODIPY (58) appearance .....	51
2.1.3. BODIPY by-products 61 and 62 .....	52
2.1.4. X-ray diffraction studies.....	54
2.2. Characterisation of the first series of BODIPY molecules (1S-BDP) .....	58
2.2.1. Thermal characterisation .....	58
2.2.2. Photophysical characterisation .....	59
2.2.3. Electrochemical characterisation.....	62
2.2.4. Computational studies .....	67
2.3. BODIPY-based organic photovoltaic cells .....	70
2.3.1. Organic photovoltaic cells preparation.....	70

2.3.2. Photovoltaic studies of the first series of BODIPY molecules (1S-BDP).....	74
2.3.3. Surface morphology of the active layer .....	79
2.3.4. Photovoltaic performance evaluation of BODIPY 55 as electron-acceptor ....	81
2.4. Conclusions for Chapter 2 .....	82
2.5. References for Chapter 2 .....	83
<b>CHAPTER 3. BODIPY molecules with styryl groups .....</b>	<b>87</b>
3.1. Synthesis and structural characterisation of the second series of BODIPY molecules (2S-BDP) .....	90
3.2. Characterisation of the second series of BODIPY molecules (2S-BDP) .....	94
3.2.1. Photophysical characterisation .....	95
3.2.2. Electrochemical characterisation .....	98
3.2.3. Computational studies.....	100
3.3. Photovoltaic studies of the second series of BODIPY molecules (2S-BDP).....	102
3.3.1. Surface morphology of the active layer .....	106
3.4. Conclusions for Chapter 3 .....	107
3.5. References for Chapter 3 .....	108
<b>CHAPTER 4. <i>Meso</i>-pentafluorophenyl BODIPY molecules with different vinyl groups .....</b>	<b>111</b>
4.1. Synthesis of the third series of BODIPY molecules (3S-BDP) .....	112
4.1.1. Synthesis of a carbazole-functionalized BODIPY (78).....	114
4.2. Structural characterisation of the third series of BODIPY molecules (3S-BDP)..	115
4.2. Characterisation of the third series of BODIPY molecules (3S-BDP).....	120
4.2.1. Thermal characterisation .....	120
4.2.2. Photophysical characterisation .....	121
4.2.3. Electrochemical characterisation .....	124
4.2.4. Computational studies.....	127
4.3. Photovoltaic studies of the third series of BODIPY molecules (3S-BDP) .....	129
4.3.1. Surface morphology of the active layer .....	135
4.4. Conclusions for Chapter 4 .....	137
4.5. References for Chapter 4 .....	138
<b>CHAPTER 5. BODIPY molecules functionalized at the boron centre .....</b>	<b>139</b>
5.1. Synthesis and structural characterisation of the fourth series of BODIPY molecules (4S-BDP) .....	140
5.1.1. X-ray diffraction studies .....	149
5.2. Characterisation of the fourth series of BODIPY molecules (4S-BDP) .....	151
5.2.1. Thermal characterisation.....	152

5.2.2. Photophysical characterisation .....	152
5.2.3. Electrochemical characterisation.....	155
5.3. Photovoltaic studies of the fourth series of BODIPY molecules (4S-BDP).....	157
5.4 Functionalization of BODIPY 74 .....	158
5.4.1. Synthesis and structural characterisation of BODIPYs 92 and 93.....	158
5.4.2. Photophysical and electrochemical characterisation of BODIPYs 92 and 93 .....	161
5.4.3. Photovoltaic studies of BODIPYs 92 and 93 .....	163
5.5. Conclusions for Chapter 5.....	165
5.6. References for Chapter 5.....	166
<b>CHAPTER 6. BODIPY-porphyrin dyads .....</b>	<b>167</b>
6.1. Synthesis and structural characterisation of the BODIPY-porphyrin dyads.....	170
6.1.1. Preparation of BDP-P1 (103) .....	170
6.1.1.1. Synthesis and characterisation of BODIPY 100.....	171
6.1.1.2. Synthesis and characterisation of compound 101.....	174
6.1.1.3. Synthesis and structural characterisation of BDP-P1 (103) .....	175
6.1.2. Synthesis and structural characterisation of BDP-P2 (107) and BDP-P3 (109) ..	177
6.2. Photophysical characterisation of BDP-P1, BDP-P2 and BDP-P3 .....	181
6.3. Electrochemical characterisation of BDP-P1, BDP-P2 and BDP-P3 .....	184
6.4. Photovoltaic studies of BDP-P1 and BDP-P2 .....	186
6.4.1. Surface morphology of the active layers .....	188
6.5. Conclusions for Chapter 6.....	188
6.6. References for Chapter 6.....	189
<b>CHAPTER 7. Final remarks and future perspectives .....</b>	<b>191</b>
<b>CHAPTER 8. Experimental procedures and supplementary information.....</b>	<b>195</b>
8.1. Reagents and Solvents .....	196
8.2 Instrumentation .....	196
8.2.1. Nuclear magnetic resonance spectroscopy.....	196
8.2.2. High performance liquid chromatography .....	196
8.2.3. Mass spectrometry.....	196
8.2.4. X-ray crystallography .....	197
8.2.5. Absorption spectroscopy .....	197
8.2.6. Emission spectroscopy .....	198
8.2.7. Thermal gravimetric analysis (TGA) .....	198
8.2.8. Differential scanning calorimetry (DSC) .....	198

8.2.9. Cyclic voltammetry.....	198
8.2.10. DFT calculations.....	198
8.2.11. AFM measurements.....	199
8.3. Photovoltaic device preparation and I-V measurements.....	199
8.4. Synthetic procedures and supplementary information.....	200
8.4.1. Chapter 2.....	200
8.4.1.1. General procedures for the synthesis of the 1S-BDP.....	200
8.4.2. Chapter 3.....	209
8.4.2.1. General procedures for the synthesis of BODIPY 65 and 66.....	209
8.4.2.2. General procedures for the synthesis of BODIPY 70.....	211
8.4.2.3. General procedures for the synthesis of BODIPY 71 and 72.....	213
8.4.3. Chapter 4.....	215
8.4.3.1. General procedures for the synthesis of BODIPY 67, 74, 76, 78.....	215
8.4.3.2. General procedures for the synthesis of BODIPY 68, 75, 77.....	221
8.4.4. Chapter 5.....	226
8.4.4.1. General procedures for the synthesis of 4S-BDP.....	226
8.4.5. Chapter 6.....	236
8.4.5.1. General procedures for the synthesis of BODIPY 100 and 104.....	236
8.4.5.2. General procedures for the synthesis of porphyrin 101, 105 and 106.....	238
8.4.5.3. General procedures for the synthesis of BDP-P1 (103).....	241
8.4.5.4. General procedures for the synthesis of BDP-P2 (107).....	243
8.4.5.5. General procedures for the synthesis of BDP-P3 (109).....	244
8.5. References for chapter 8.....	246

## List of Figures

Figure 1.1. 2017's energy consumption and energy consumption trend (in million tonnes of oil equivalent (Mtoe)) over 1990-2017, adapted from Enerdata website. <sup>1</sup> .....	2
Figure 1.2. World photovoltaic (PV) cell/module production from 2005 to 2018, adapted from Jäger-Waldau's report. <sup>3</sup> .....	3
Figure 1.3. Solar irradiance (red) and corresponding photon flux curve (blue) at AM1.5 (air mass where the sun is about 41° above the horizon) as functions of light wavelength and material band gap, adapted from Sharma, Gros and co-workers. <sup>7</sup> .....	4
Figure 1.4. Timeline of highest efficiencies of various solar cell technologies, from National Renewable Energy Laboratory. <sup>23</sup> .....	7
Figure 1.5. Published articles relating to “organic photovoltaics” or “organic solar cells”, since 1998; search made at Web of Knowledge.....	8
Figure 1.6. The different OPV cell structures.....	10
Figure 1.7. The operational principle of BHJ-OPV cells. ....	12
Figure 1.8. Different device architectures of bulk heterojunction OPV cells. ....	12
Figure 1.9. Representation of a hypothetical J-V curve, under illumination, and the most used equations for photovoltaic metrics. ....	14
Figure 1.10. Best PCEs of polymer and small molecules-based OPVs since 2006. <sup>62-65</sup> ...	16
Figure 1.11. (A) BODIPY resonance structures; (B) BODIPY basic structure with the IUPAC numbering system (1 to 8) and alternative nomenclature ( $\alpha$ , $\beta$ and <i>meso</i> )......	17
Figure 1.12. Overview of the different BODIPY post-functionalization methods at their preferential site(s) of reaction; adapted from Dehaen <i>et al.</i> <sup>84</sup> .....	19
Figure 1.13. Chemical structures of various <i>meso</i> -substituted BODIPY from literature: 1 <sup>85</sup> , 2, <sup>87</sup> 3, <sup>89</sup> 4, <sup>90</sup> 5, <sup>93</sup> 6. <sup>94</sup> .....	20
Figure 1.14. Chemical structures of various BODIPYs from post-functionalizations at 1, 3, 5 and 7-position: 7, <sup>96</sup> 8, <sup>96</sup> 9, <sup>96</sup> 10, <sup>100</sup> 11, <sup>101</sup> 12, <sup>77</sup> 13, <sup>102</sup> 14. <sup>103</sup> .....	21
Figure 1.15. Influence of the BODIPY's core substitution on the spectroscopic properties, adapted from Burgess <i>et al.</i> <sup>78</sup> .....	24
Figure 1.16. Number of publications found on the Web of Science on the topics “BODIPY” or “boron dipyrromethene”.....	25
Figure 1.17. Results of the search of published articles in Web of Science using the keywords “BODIPY” or “boron dipyrromethene” with “OPV” or “organic photovoltaic cells.” ....	27
Figure 1.18. The best performing BODIPY small molecules used, as electron-donor species, in BHJ- OPVs between 2009 and 2012. <sup>153-156</sup> .....	28
Figure 1.19. BODIPY structures reported by Akkaya and co-workers, <sup>157</sup> and the dimer structures proposed by Yao and co-workers. <sup>158, 159</sup> .....	29
Figure 1.20. <i>Meso</i> -ethenylcarbazole BODIPY tested by Sharma and co-workers. <sup>161</sup> .....	29
Figure 1.21. BODIPY with the best PCE values from 3 reports of Zhao and co-workers. <sup>162-164</sup> .....	30

Figure 1.22. BODIPY small molecules reported by Bulut and co-workers <sup>163</sup> (40) and Singh and co-workers (41). <sup>166</sup> .....	30
Figure 1.23. Furan-fused BODIPYs applied in OPVs by Tian-yi Li, Zaifei Ma and co-workers. <sup>167</sup> .....	31
Figure 1.24. BODIPY based-polymers reported by Sharma and co-workers. <sup>176, 177</sup> .....	32
Figure 1.25. Best PCE values from all published BODIPY small molecules (45 different structures) tested as electron-donor species in OPVs. The data refers to BODIPY-based OPV that can have different active layer's architecture or distinct procedures (e.g. diverse electron-acceptor species, temperatures or additives).....	33
Figure 2.1. Chloroform solution of 1S-BDP (53-58) under day light (left) and under UV light (365 nm, right) irradiance. ....	46
Figure 2.2. HPLC chromatograms of the 1S-BDP obtained at 30 °C with acetonitrile : H <sub>2</sub> O (8:2) as isocratic eluent with a volume of injection of 10 μL and a flow rate of 0.8 ml/min. ....	47
Figure 2.3. <sup>1</sup> H NMR (400 MHz) spectrum of 58, in CDCl <sub>3</sub> . ....	48
Figure 2.4. Expansion of the <sup>1</sup> H NMR spectra (0.5-2.7 ppm) for compounds 53-58; star denotes trace of solvent ( <i>n</i> -hexane).....	49
Figure 2.5. <sup>19</sup> F NMR (376 MHz) spectrum of 55 in CDCl <sub>3</sub> .....	50
Figure 2.6. <sup>11</sup> B NMR spectrum of 55 in CDCl <sub>3</sub> . ....	50
Figure 2.7. HPLC chromatograms obtained at 30 °C with acetonitrile: H <sub>2</sub> O (9:1) as isocratic eluent at a flow rate of 0.8 ml/min, and fractions of the ESI-MS spectra in positive mode. . ....	52
Figure 2.8. <sup>1</sup> H NMR (400 MHz) spectra of 58, 61 and 62 compounds, in CDCl <sub>3</sub> . ....	53
Figure 2.9. <sup>19</sup> F NMR spectra of 55, 61 and 62 structures, in CDCl <sub>3</sub> .....	54
Figure 2.10. Crystallographic unit cell of structure 57. ....	55
Figure 2.11. Oak Ridge Thermal Ellipsoid Plot (ORTEP) drawing of the molecular structures of the polymorphs UNIFIG <sup>19</sup> and 56. Ellipsoids were drawn at 50% probability level; Hydrogen atoms were omitted for clarity. ....	56
Figure 2.12. Single-crystal X-ray structure of the 55 (A), 56 (B), 57 (C) and 58 (D) of a top-view (left) and side-view (right); Ellipsoids were drawn at 50 % probability level; Hydrogen atoms were omitted for clarity; The atoms numeration attributed to 55 is uniform for all structures. ....	57
Figure 2.13. (A) TGA traces of the BODIPY dyes recorded at a heating rate of 20 °C/min ); (B) DSC curve of 53 recorded at a heating and cooling rate of 20 °C/min. ....	58
Figure 2.14. Normalized absorption (A) and emission (B) spectra of the BODIPY series in chloroform solution .....	59
Figure 2.15. Emission spectra of 56 in chloroform, hexane and acetonitrile.....	61
Figure 2.16. Absorption and excitation spectra of 53 in chloroform and its film absorption spectrum .....	62
Figure 2.17. Cyclic voltammograms of 56 with and without ferrocene. ....	64

Figure 2.18. Cyclic voltammograms of 53, 55 and 58. ....	64
Figure 2.19. OPV structure used to assess the behaviour of the 1S-BDP compounds.....	70
Figure 2.20. Image of the 54:PC <sub>61</sub> BM blend, obtained with the video camera of the profilometer .....	71
Figure 2.21. Emission spectra of the films of neat 58 and 58:PC <sub>61</sub> BM blend (excitation at 545 nm).....	71
Figure 2.22. Chemical structure of PEDOT: PSS, a blend of PEDOT with PSSH (which acts as dopant and allows some “solubility” of the blended material in water). ....	72
Figure 2.23. Spin coating process and spin coater.....	73
Figure 2.24. Glove box and “sublimation chamber” (A), final photovoltaic cell (B), support measuring cell (C).....	73
Figure 2.25. Setup for solar-cell measurements and schematic illustrations of each component (solar simulator, sample cell, computer-controlled source meter unit). ....	74
Figure 2.26. BODIPY dyes from 1S-BDP tested in BHJ-OPVs .....	74
Figure 2.27. Current density-voltage characteristics of 58:PC <sub>61</sub> BM-based OPVs at different donor-acceptor ratios, under AM 1.5G illumination at 88 mW.cm <sup>-2</sup> . ....	76
Figure 2.28. Current density-voltage characteristics of BODIPY:PC <sub>61</sub> BM-based OPVs, under AM 1.5G illumination at 88 mW.cm <sup>-2</sup> . ....	76
Figure 2.29. EQE curves of the optimized 53:PC <sub>61</sub> BM, 57:PC <sub>61</sub> BM and 58:PC <sub>61</sub> BM-based OPV cells (A) and overlap of 58:PC <sub>61</sub> BM absorption film with 58:PC <sub>61</sub> BM EQE (B).....	79
Figure 2.30. AFM topography (top) and phase (bottom) images (2µm vs 2µm) of 53:PC <sub>61</sub> BM, 55:PC <sub>61</sub> BM, 56:PC <sub>61</sub> BM, 57:PC <sub>61</sub> BM and 58:PC <sub>61</sub> BM. ....	80
Figure 3.1. Hypothetical intermediate molecule from Hann-Lapworth mechanism ( $\beta$ -hydroxy intermediate (63)) and isolated aminal molecule (64) supporting the organocatalytic mechanism of the Knoevenagel reaction. ....	88
Figure 3.2. HPLC-DAD chromatograms obtained at 30 °C with acetonitrile: H <sub>2</sub> O (9:1) as isocratic eluent with a volume of injection of 10 µL and a flow rate of 0.8 cm <sup>3</sup> /min, in a C18 RP column. ....	91
Figure 3.3. HPLC chromatograms obtained at 30 °C with acetonitrile: H <sub>2</sub> O (9:1) as isocratic eluent with a volume of injection of 10 µL and a flow rate of 0.8 ml/min, in a C18 RP column. ....	92
Figure 3.4. <sup>1</sup> H-NMR (400 MHz) spectra of 70 and 72, in CDCl <sub>3</sub> .....	93
Figure 3.5. <sup>11</sup> B NMR and <sup>19</sup> F NMR spectra of 58, 71 and 72, in CDCl <sub>3</sub> .....	94
Figure 3.6. Images of 53 (A), 65 (B) and 66 (C) in chloroform under visible and under 365 nm UV light illumination. ....	95
Figure 3.7. Normalised absorption of 58 (orange), 71 (pink) and 72 (blue), in chloroform solution. ....	95

Figure 3.8. (A) Absorption spectra; (B) emission spectra (excitation at $\lambda^{\text{abs}}_{\text{max}}$ ); (C) excitation spectra; (D) spin-cast films absorption spectra of the 2S-BDP, in chloroform.....	96
Figure 3.9. Cyclic voltammograms of 53, 65, 66, 58, 71 and 72 in dichloroethane, containing 1 mM ferrocene/ferrocenium (Fc/Fc <sup>+</sup> ) as internal standard, recorded at 50 mV s <sup>-1</sup> . .....	98
Figure 3.10. BODIPY dyes from 2S-BDP tested in BHJ-OPVs.....	102
Figure 3.11. Absorption profile of 66 film and the blend films of 66: PC <sub>71</sub> BM and 66:PC <sub>71</sub> BM.....	104
Figure 3.12. Current density-voltage characteristics of OPVs based on the 67: PC <sub>61</sub> BM, 67: PC <sub>71</sub> BM, 70: PC <sub>61</sub> BM and 70:PC <sub>71</sub> BM blends. ....	104
Figure 3.13. AFM height and phase images (2 $\mu\text{m}$ vs 2 $\mu\text{m}$ ) of 65, 66, 67, 70, 71 and 72 blended with PC <sub>61</sub> BM and PC <sub>71</sub> BM.....	106
Figure 4.1. Structure of BODIPY 78 .....	115
Figure 4.2. HPLC chromatograms of 55, 67 and 68 and table with the 3S-BDP retention times. ....	115
Figure 4.3. <sup>1</sup> H NMR (400 MHz) spectra of 67 and 68, in CDCl <sub>3</sub> . ....	116
Figure 4.4. <sup>1</sup> H NMR (400MHz) spectra of 67, 74 and 76, in CDCl <sub>3</sub> . ....	117
Figure 4.5. (A) <sup>1</sup> H NMR (400MHz) spectrum; and (B) COSY NMR spectrum of 78, in CDCl <sub>3</sub> . ....	118
Figure 4.6. <sup>19</sup> F NMR (376 MHz) spectra of 55, 67 and 72, in CDCl <sub>3</sub> . ....	119
Figure 4.7. <sup>11</sup> B NMR (128 MHz) spectra of 67, 74, 76 and 78, in CDCl <sub>3</sub> .....	119
Figure 4.8. TGA curves of 3S-BDP at a heating rate of 20 °C/min under nitrogen atmosphere .....	120
Figure 4.9. Thermograms of 3S-BDP .....	121
Figure 4.10. Normalised absorption spectra of the compounds 67, 68, 74, 75, 76 and 77.....	121
Figure 4.11. The absorption spectrum regarding the molar absorption coefficient ( $\epsilon$ ) of 55, 67, 74, 76 and 78 in CHCl <sub>3</sub> .....	122
Figure 4.12. Normalised absorption (chloroform solution) and emission spectra (chloroform solution and spin-cast film) of BODIPYs 74 and 78 .....	122
Figure 4.13. Cyclic voltammograms of the 3S-BDP in dichloroethane solution in the presence of 1 mM ferrocene/ferrocenium as internal standard, recorded at a scan speed of 50 mV/s .....	124
Figure 4.14. BODIPY dyes from the 3S-BDP series tested in BHJ-OPVs.....	129
Figure 4.15. Absorption spectra of 74 obtained from solution, as deposited neat film, and annealed films of neat 74 and its blend with PC <sub>61</sub> BM .....	130
Figure 4.16. Current density-voltage characteristics of 3S-BDP:PC <sub>61</sub> BM based OPV cell ..	130



Figure 4.17. EQE spectra of the optimised 67:PC <sub>61</sub> BM, 74:PC <sub>61</sub> BM, 76:PC <sub>61</sub> BM and 78:PC <sub>61</sub> BM-based OPV cells.....	132
Figure 4.18. Current density-voltage characteristics of 67:PC <sub>71</sub> BM, 74:PC <sub>71</sub> BM 76:PC <sub>71</sub> BM and 78:PC <sub>71</sub> BM-based OPV cells , with a D/A ratio of 1:3, thermally annealed at 100 °C..	133
Figure 4.19. Current density-voltage characteristics of 74:PC <sub>71</sub> BM and 78:PC <sub>71</sub> BM-based OPV cells having three different donor:acceptor ratios. The active layers were thermally annealed at 100 °C.....	134
Figure 4.20. Absorption spectra (A and C) and EQE curves (B and D) of the optimised 74:PC <sub>61</sub> BM, 74:PC <sub>71</sub> BM and 78:PC <sub>71</sub> BM systems. ....	135
Figure 4.21. AFM height images (top) and phase images (bottom) (2µm vs 2µm) of the 3S-BDP blended with PC <sub>61</sub> BM or PC <sub>71</sub> BM.....	136
Figure 5.1. HPLC chromatograms obtained at 30 °C with acetonitrile: H <sub>2</sub> O (8:2) as isocratic eluent with a volume of injection of 10 µL and a flow rate of 0.8 ml/min. ....	142
Figure 5.2. Structure of BODIPY 91. ....	143
Figure 5.3. <sup>1</sup> H NMR spectra (400 MHz) of 84-88, 91, in CDCl <sub>3</sub> .....	145
Figure 5.4. Expansion of the <sup>1</sup> H NMR spectra (400 MHz) of 88 and 91, in CDCl <sub>3</sub> . ....	146
Figure 5.5. <sup>19</sup> F NMR spectra (376 MHz) of 84-88 and 91, in CDCl <sub>3</sub> . ....	147
Figure 5.6. <sup>11</sup> B NMR spectra (128 MHz) of 4S-BDP, obtained in CDCl <sub>3</sub> .....	148
Figure 5.7. Crystallographic unit cell and details of structure 85 and 91.....	149
Figure 5.8. Crystal packing and main intermolecular interactions of BODIPY 85 and 91...	150
Figure 5.9. TGA traces of the BODIPY dyes recorded at a heating rate of 20 °C/min and table with their melting temperatures and temperature at which 5 % of degradation occurs.	152
Figure 5.10. Normalised absorption spectra of 4S-BDP, in chloroform. ....	153
Figure 5.11. HOMO and LUMO of BODIPY 85 .....	153
Figure 5.12. Cyclic voltammograms of 63, 89 and 90 (A); 84 and 85 (B); 88 and 87 (C); 88 and 91 (D), in dichloroethane, containing 1 mM ferrocene/ferrocenium (Fc/Fc <sup>+</sup> ) as internal standard,.....	155
Figure 5.13. Current density-voltage characteristics of BODIPY:PC <sub>61</sub> BM-based OPVs, under AM 1.5G illumination at 84 mW.cm <sup>-2</sup> . ....	158
Figure 5.14. <sup>1</sup> H NMR spectra (400 MHz) of 74, 84 and 92, in CDCl <sub>3</sub> . ....	159
Figure 5.15. <sup>1</sup> H NMR and COSY spectrum (400 MHz) of compound 93, in CDCl <sub>3</sub> . ....	160
Figure 5.16. <sup>11</sup> B NMR spectrum (128 MHz) of 93, in CDCl <sub>3</sub> . ....	161
Figure 5.17. Normalised absorption and emission spectra of 92 and 93 (the insets show some photophysical parameters). ....	161

Figure 5.18. Cyclic voltammograms of 1 mM 92 and 93 in 0.1 M TBATFB in dichloroethane, using internal standard 1 mM Fc/Fc <sup>+</sup> , recorded at scan rate of 50 mV s <sup>-1</sup> ...	162
Figure 5.19. Current density-voltage characteristics of OPVs based on 67: PC <sub>61</sub> BM, 67: PC <sub>71</sub> BM, 70: PC <sub>61</sub> BM and 70:PC <sub>71</sub> BM, recorder under AM 1.5G illumination at 84 mW/cm <sup>2</sup> .....	163
Figure 5.20. AFM height and phase images (2µm vs 2µm) of the 92:PC <sub>71</sub> BM and 93:PC <sub>71</sub> BM films.....	164
Figure 6.1. Chemical structures of some BODIPY-porphyrin dyes from literature: 94, <sup>17</sup> 95, <sup>18</sup> 96, <sup>19</sup> 97. <sup>20</sup> ....	169
Figure 6.2. Chemical structures of some BODIPY-porphyrin dye 98 <sup>24</sup> and 99. <sup>25</sup> .....	170
Figure 6.3. <sup>1</sup> H NMR spectrum (400MHz) of 56, 104 and 100 in CDCl <sub>3</sub> .....	172
Figure 6.4. HPLC chromatogram obtained at 30 °C with acetonitrile: H <sub>2</sub> O (8:2) as isocratic eluent with a volume of injection of 10 µL and a flow rate of 0.8 cm <sup>3</sup> /min, in a C18 RP column and a segment of the mass spectrum showing the [M + H] <sup>+</sup> and [M+H-HF] <sup>+</sup> ion peaks.....	173
Figure 6.5. (A) Normalised absorption and emission spectra of NH <sub>2</sub> -BDP in chloroform solution; (B) comparison of emission spectra of 56 and 100 in chloroform.....	173
Figure 6.6. Structures of compound 101, 105 (TPP) and 106 (TCPP). .....	174
Figure 6.7. <sup>1</sup> H NMR spectrum (400MHz) of 101 in CDCl <sub>3</sub> and the enlargement of the 7-10 ppm region. ....	1756
Figure 6.8. (A) HPLC chromatogram of BDP-P1, obtained at 30 °C with acetonitrile: H <sub>2</sub> O (9:1) as isocratic eluent with a volume of injection of 10 µL and a flow rate of 0.8 cm <sup>3</sup> /min, in a C18 RP column; (B) Diode-array spectrum of the peak at 13.5 min; (C) Mass spectrum of the peak at 13.5 min. ....	177
Figure 6.9. <sup>1</sup> H NMR (400 MHz) spectrum of BDP-P1 in CDCl <sub>3</sub> , expansions (A and B).176	
Figure 6.10. (A) HPLC chromatogram of BDP-P2 obtained at 30 °C with acetonitrile: H <sub>2</sub> O (9:1) as isocratic eluent with a volume of injection of 10 µL and a flow rate of 0.8 cm <sup>3</sup> /min, in a C18 RP column; (B) Spectrum obtained by Diode-array peak detection (B); (C) Mass spectrum related to the HPLC peak. ....	179
Figure 6.11. <sup>1</sup> H NMR (400 MHz) and <sup>19</sup> F NMR (376 MHz) spectra of BDP-P2 in CDCl <sub>3</sub> and the identification of the BODIPY proton signals region (A), phenyl and porphyrin proton signals region (B). ....	179
Figure 6.12. HPLC chromatogram of BDP-P3, obtained at 30 °C with acetonitrile as eluent, and a flow rate of 0.8 cm <sup>3</sup> /min, in a C18 RP column.....	180
Figure 6.13. <sup>1</sup> H NMR (400 MHz) spectrum of BDP-P3 in CDCl <sub>3</sub> and corresponding expansion.....	180
Figure 6.14. <sup>19</sup> F NMR (376 MHz) spectra of BDP-P3 in CDCl <sub>3</sub> .....	181
Figure 6.15. Normalised absorption spectra of 53, 101, BDP-P1, BDP-P2 and BDP-P3, measured in toluene solution.....	182

Figure 6.16. Emission spectra of BDP-P1 (A), BDP-P2 (B) and BDP-P3 (C), excitation wavelength at 420 nm and 525nm; (D) absorption and excitation spectra (emission wavelength at 537 nm or 625 nm) of BDP-P2 (D).....	183
Figure 6.17. Cyclic voltammograms of TPP, 53, BDP-P1, BDP-P2 and BDP-P3 in dichloroethane solution, in the presence of 1 mM ferrocene/ferrocenium (Fc/Fc <sup>+</sup> ) as internal standard, recorded at 50 mV s <sup>-1</sup> in deoxygenated solution (N <sub>2</sub> ).....	184
Figure 6.18. Current density-voltage characteristics of the best case of each OPV system presented in Table 6.4.....	187
Figure 6.19. (A) Absorption spectra (films) of the best cases presented in Table 6.4; (B) EQE spectrum of the best cases presented in Table 6.4.....	187
Figure 6.20. AFM height images (top) and phase images (bottom) (2μm vs 2μm) of the BDP-P1:PC <sub>71</sub> BM (1:1) and BDP-P2: PC <sub>71</sub> BM (1:2) blends.....	188
Figure 8.1. Estimation of the λ <sub>onset</sub> through the absorption spectrum.....	197
Figure 8.2. <sup>13</sup> C NMR spectrum of 53 (100 MHz, CDCl <sub>3</sub> ).....	201
Figure 8.3. <sup>11</sup> B NMR spectrum of 53 (128 MHz, CDCl <sub>3</sub> ).....	201
Figure 8.4. <sup>19</sup> F NMR spectrum of 53 (376 MHz, CDCl <sub>3</sub> ).....	201
Figure 8.5. High resolution mass spectrum (positive mode) of 53.....	201
Figure 8.6. <sup>13</sup> C NMR spectrum of 54 (100 MHz, DCON(CD <sub>3</sub> ) <sub>2</sub> ).....	202
Figure 8.7. <sup>11</sup> B NMR spectrum of 54 (128 MHz, CDCl <sub>3</sub> ).....	202
Figure 8.8. <sup>19</sup> F NMR spectrum of 54 (376 MHz, CDCl <sub>3</sub> ).....	203
Figure 8.9. High resolution mass spectrum (positive mode) of 54.....	203
Figure 8.10. <sup>13</sup> C NMR spectrum of 55 (100 MHz, CDCl <sub>3</sub> ).....	204
Figure 8.11. High resolution mass spectrum (positive mode) of 55.....	204
Figure 8.12. <sup>13</sup> C NMR spectrum of 56 (100 MHz, CDCl <sub>3</sub> ).....	205
Figure 8.13. <sup>11</sup> B NMR spectrum of 56 (128 MHz, CDCl <sub>3</sub> ).....	205
Figure 8.14. <sup>19</sup> F NMR spectrum of 56 (376 MHz, CDCl <sub>3</sub> ).....	205
Figure 8.15. High resolution mass spectrum (positive mode) of 56.....	205
Figure 8.16. <sup>13</sup> C NMR spectrum of 57 (100 MHz, CDCl <sub>3</sub> ).....	206
Figure 8.17. <sup>19</sup> F NMR spectrum of 57 (376 MHz, CDCl <sub>3</sub> ).....	206
Figure 8.18. <sup>11</sup> B NMR spectrum of 57 (128 MHz, CDCl <sub>3</sub> ).....	207
Figure 8.19. High resolution mass spectrum (positive mode) of 57.....	207
Figure 8.20. <sup>13</sup> C NMR spectrum of 58 (100 MHz, CDCl <sub>3</sub> ).....	207
Figure 8.21. High resolution mass spectrum (positive mode) of 58.....	208
Figure 8.22. <sup>19</sup> F NMR spectrum of 65 (376 MHz, CDCl <sub>3</sub> ).....	209
Figure 8.23. <sup>1</sup> H NMR spectrum of 65 (400 MHz, CDCl <sub>3</sub> ).....	210
Figure 8.24. High resolution mass spectrum (positive mode) of 65.....	210
Figure 8.25. <sup>1</sup> H NMR spectrum of 66 (400 MHz, CDCl <sub>3</sub> ).....	211

Figure 8.26. $^{19}\text{F}$ NMR spectrum of 66 (376 MHz, $\text{CDCl}_3$ ).....	211
Figure 8.27. High resolution ESI positive mode mass spectrum of 66.....	211
Figure 8.28. $^{19}\text{F}$ NMR spectrum of 70 (376 MHz, $\text{CDCl}_3$ ).....	212
Figure 8.29. $^1\text{H}$ NMR spectrum of 70 (400 MHz, $\text{CDCl}_3$ ). ....	212
Figure 8.30. High resolution mass spectrum (positive mode) of 70. ....	213
Figure 8.31. $^1\text{H}$ NMR spectrum of 71 (400 MHz, $\text{CDCl}_3$ ). ....	214
Figure 8.32. $^{19}\text{F}$ NMR spectrum of 71 (376 MHz, $\text{CDCl}_3$ ).....	214
Figure 8.33. High resolution mass spectrum (positive mode) of 71. ....	214
Figure 8.34. $^{13}\text{C}$ NMR spectrum of 72 (100 MHz, $\text{CDCl}_3$ ). ....	215
Figure 8.35. High resolution ESI positive mode mass spectrum of 72.....	215
Figure 8.36. $^{13}\text{C}$ NMR spectrum of 67 (100 MHz, $\text{CDCl}_3$ ). ....	216
Figure 8.37. High resolution mass spectrum (positive mode) of 67. ....	217
Figure 8.38. $^{13}\text{C}$ NMR spectrum of 74 (100 MHz, $\text{CDCl}_3$ ). ....	217
Figure 8.39. $^{19}\text{F}$ NMR spectrum of 74 (376 MHz, $\text{CDCl}_3$ ).....	218
Figure 8.40. High resolution mass spectrum (positive mode) of 74. ....	218
Figure 8.41. $^{13}\text{C}$ NMR spectrum of 76 (100 MHz, $\text{CDCl}_3$ ). ....	219
Figure 8.42. $^{19}\text{F}$ NMR spectrum of 76 (376 MHz, $\text{CDCl}_3$ ).....	219
Figure 8.43. High resolution mass spectrum (positive mode) of 76. ....	219
Figure 8.44. $^{13}\text{C}$ NMR spectrum of 78 (100 MHz, $\text{CDCl}_3$ ). ....	220
Figure 8.45. $^{19}\text{F}$ NMR spectrum of 78 (376 MHz, $\text{CDCl}_3$ ).....	221
Figure 8.46. High resolution mass spectrum (positive mode) of 78. ....	221
Figure 8.47. $^{13}\text{C}$ NMR spectrum of 68 (100 MHz, $\text{CDCl}_3$ ). ....	222
Figure 8.48. $^1\text{H}$ NMR spectrum of 75 (400MHz, $\text{CDCl}_3$ ). ....	223
Figure 8.49. $^{13}\text{C}$ NMR spectrum of 75 (100 MHz, $\text{CDCl}_3$ ). ....	224
Figure 8.50. $^{19}\text{F}$ NMR spectrum of 75 (376 MHz, $\text{CDCl}_3$ ).....	224
Figure 8.51. $^1\text{H}$ NMR spectrum of 77 (400 MHz, $\text{CDCl}_3$ ). ....	225
Figure 8.52. $^{13}\text{C}$ NMR spectrum of 77 (100 MHz, $\text{CDCl}_3$ ). ....	225
Figure 8.53. $^{19}\text{F}$ NMR spectrum of 77 (376 MHz, $\text{CDCl}_3$ ).....	225
Figure 8.54. $^{13}\text{C}$ NMR spectrum of 84 (100 MHz, $\text{CDCl}_3$ ). ....	227
Figure 8.55. High resolution mass spectrum (positive mode) of 84. ....	227
Figure 8.56. $^{13}\text{C}$ NMR spectrum of 85 (100 MHz, $\text{CDCl}_3$ ). ....	228
Figure 8.57. High resolution mass spectrum (positive mode) of 85. ....	228
Figure 8.58. $^{13}\text{C}$ NMR spectrum of 86 (100 MHz, $\text{CDCl}_3$ ). ....	229
Figure 8.59. High resolution mass spectrum (positive mode) of 86. ....	229
Figure 8.60. $^{13}\text{C}$ NMR spectrum of 88 (100 MHz, $\text{CDCl}_3$ ). ....	230

Figure 8.61. $^1\text{H}$ NMR spectrum of 89 (400 MHz, $\text{CDCl}_3$ ).....	231
Figure 8.62. $^{13}\text{C}$ NMR spectrum of 89 (100 MHz, $\text{CDCl}_3$ ).....	231
Figure 8.63. $^{11}\text{B}$ NMR spectrum of 89 (128 MHz, $\text{CDCl}_3$ ).....	231
Figure 8.64. High resolution mass spectrum (positive mode) of 89.....	232
Figure 8.65. $^{13}\text{C}$ NMR spectrum of 90 (100 MHz, $\text{CDCl}_3$ ).....	232
Figure 8.66. $^1\text{H}$ NMR spectrum of 90 (400 MHz, $\text{CDCl}_3$ ).....	233
Figure 8.67. $^{11}\text{B}$ NMR spectrum of 90 (128 MHz, $\text{CDCl}_3$ ).....	233
Figure 8.68. High resolution mass spectrum (positive mode) of 90.....	233
Figure 8.69. $^{13}\text{C}$ NMR spectrum of 92 (100 MHz, $\text{CDCl}_3$ ).....	235
Figure 8.70. $^{19}\text{F}$ NMR spectrum of 92 (376 MHz, $\text{CDCl}_3$ ).....	235
Figure 8.71. High resolution mass spectrum (positive mode) of 92.....	235
Figure 8.72. $^{13}\text{C}$ NMR spectrum of 93 (100 MHz, $\text{CDCl}_3$ ).....	236
Figure 8.73. $^{19}\text{F}$ NMR spectrum of 93 (376 MHz, $\text{CDCl}_3$ ).....	236
Figure 8.74. High resolution mass spectrum (positive mode) of 93.....	236
Figure 8.75. $^{19}\text{F}$ NMR spectrum of 100 (376 MHz, $\text{CDCl}_3$ ).....	237
Figure 8.76. $^{19}\text{F}$ NMR spectrum of 104 (376 MHz, $\text{CDCl}_3$ ).....	238
Figure 8.77. High resolution mass spectrum (positive mode) of 104.....	238
Figure 8.78. High resolution mass spectrum (positive mode) of 101.....	239
Figure 8.79. $^1\text{H}$ NMR spectrum of 105 (400 MHz, $\text{CDCl}_3$ ).....	240
Figure 8.80. $^1\text{H}$ NMR spectrum of 106 (400 MHz, $\text{CDCl}_3$ ).....	241
Figure 8.81. $^{13}\text{C}$ NMR spectrum of 103 (100 MHz, $\text{CDCl}_3$ ).....	242
Figure 8.82. $^{11}\text{B}$ NMR spectrum of 103 (128 MHz, $\text{CDCl}_3$ ).....	242
Figure 8.83. $^{19}\text{F}$ NMR spectrum of 103 (376 MHz, $\text{CDCl}_3$ ).....	242
Figure 8.84. High resolution mass spectrum (positive mode) of 103.....	243
Figure 8.85. High resolution mass spectrum (positive mode) of 107.....	244

## List of Schemes

Scheme 1.1. The most used BODIPY's synthetic pathways. ....	18
Scheme 1.2. Example of a BODIPY's synthesis via pre-functionalization or post-functionalization pathways. Conditions: i) $R_2-B(OH)_2$ , $Na_2CO_3$ , cat, $Pd(PPh_3)_4$ , $80^\circ C$ ; <sup>83</sup> ii) $R_1-CHO$ , DDQ, $BF_3 \cdot OEt_2$ , rt; <sup>79</sup> iii) $R_2-N_2BF_4$ , ferrocene, acetone, room temperature. <sup>84</sup> .....	19
Scheme 1.3. i) NCS/THF, $-78^\circ C$ , 2 h. ii) DDQ room temperature, 1h; toluene, $Et_3N/BF_3 \cdot OEt_2$ , $70^\circ C$ , 2.5 h; iii) Nucleophile $Nu^-$ , $CH_3CN$ , reflux; adapted from Dehaen <i>et al.</i> <sup>84</sup> .....	21
Scheme 1.4. Synthesis of a BODIPY by cross-coupling reaction (Suzuki and Stille) or by direct C-H arylation; adapted from Yu <i>et al.</i> <sup>123</sup> .....	22
Scheme 1.5. Different pathways of BODIPY modification at the boron centre.....	23
Scheme 1.6. Applications of BODIPY frameworks. <sup>129-147</sup> .....	26
Scheme 2.1. General mechanism of the BODIPY synthesis. ....	44
Scheme 2.2. Synthesis of BODIPY 53 using $\alpha, \alpha$ -dichlorotoluene or $\alpha, \alpha$ -dibromotoluene, 3-ethyl-2,4-dimethylpyrrole, 1 eq. of DDQ, 17 eq. of boron trifluoride etherate. ....	52
Scheme 2.3. Frontier orbital energy levels of the 1S-BDP and $PC_{61}BM$ ([6,6-phenyl-C61-butric acid methyl ester). <sup>47</sup> .....	67
Scheme 2.4. Substrate patterning steps. ....	72
Scheme 3.1. Proposed mechanism for the Knoevenagel condensation of a BODIPY dye with benzaldehyde catalysed by piperidine, adapted from Thelakkatin and co-workers. <sup>25</sup> .....	89
Scheme 3.2. Synthesis of the 2S-BDP and the yield of the products.....	90
Scheme 3.3. Frontier orbital energies of some dyes of 1S-BDP (red), all 2S-BDP (blue) and the fullerenes derivatives $PC_{61}BM$ and $PC_{71}BM$ (green).....	99
Scheme 4.1. The synthesis of the third series of BODIPY dyes (3S-BDP).....	113
Scheme 4.2. Frontier orbital energy levels of the 3S-BDP, $PC_{61}BM$ and $PC_{71}BM$ .....	126
Scheme 5.1. The proposed mechanism for the formation of O-BODIPY dyes, using $AlCl_3$ as catalyst, according to Mély and co-workers. <sup>11</sup> .....	140
Scheme 5.2. General synthesis of 4S-BDP and respective yields.....	141
Scheme 5.3. Exchange of boron-ligand through treatment with methanol under acidic conditions. ....	144
Scheme 5.4. HOMO and LUMO energies of BODIPY 53, pentafluoro derivatives of the 4S-BDP series and $PC_{61}BM$ . ....	156
Scheme 5.5. Synthesis of BODIPY 92 and 93.....	159
Scheme 6.1. General steps for the preparation of BDP-P1. ....	171
Scheme 6.2. Synthesis of BODIPY 100.....	171
Scheme 6.3 Synthesis of BDP-P1 (103). ....	175
Scheme 6.4 Synthesis of BDP-P2 (A) and BDP-P3 (B)..	178

## List of Tables

Table 2.1. General procedure for the preparation of the first BODIPY series (53-58): i)TFA; ii)DDQ; iii)diisopropylethylamine, $\text{BF}_3 \cdot \text{O}(\text{C}_2\text{H}_5)_2$ and corresponding synthetic yields. ..	46
Table 2.2. Synthesis of BODIPY 58 using 5 ml of solvent, 1mmol of 3-ethyl-2,4-dimethylpyrrole, 1 eq. of DDQ, 17eq. of boron trifluoride etherate and 12 eq. diisopropylamine. ....	51
Table 2.3. Crystal data details of 55-58 structures. ....	55
Table 2.4 Conformation of the ethyl groups, length of the bond between the <i>meso</i> -carbon and the substituent (C8-C10) and the dihedral angle between the least-squares plane of the substituent and of the central core ( $\Theta_{\text{core-meso}}$ ), length of the bond between the boron and nitrogen atoms (B-N) and boron and fluorine atoms (B-F), the angles of the bonds centred at the boron g atoms ( N-B-N and F-B-F) and the torsion of the BODIPY core (boron planarity).....	56
Table 2.5. Decomposition and melting temperatures of the BODIPY compounds obtained by TGA and DSC, respectively .....	59
Table 2.6. Photophysical properties of the 1S-BDP.....	60
Table 2.7. Electrochemical properties of the 1S-BDP.....	65
Table 2.8. Optimised structures, electron distribution in HOMO and LUMO and the energies (in eV) of the BODIPY series, obtained by DFT calculations in vacuum. ....	69
Table 2.9. Photovoltaic performance parameters (short-circuit current, $J_{\text{sc}}$ , open-circuit voltage, $V_{\text{oc}}$ , fill factor, FF, and power conversion efficiency, PCE) of the optimised 58:PC <sub>61</sub> BM-based OPV under AM 1.5 G illumination at 88 mW/cm <sup>2</sup> . The blend film was prepared from a dichlorobenzene solution. ....	75
Table 2.10. Photovoltaic parameters of the optimised BODIPY:PC <sub>61</sub> BM-based OPV cells, under AM 1.5 G illumination at 88 mW/cm <sup>2</sup> . Solutions were prepared in dichlorobenzene, with a total concentration of 40 mg/ml and with a BODIPY:PC <sub>61</sub> BM weight ratio of 1:3... ..	77
Table 2.11. Photovoltaic performance parameters of the 1S-BDP OPV cells under AM 1.5 illumination at 88 mW/cm <sup>2</sup> , prepared with ratio of 1:3 BODIPY to PC <sub>61</sub> BM from a solution of chloroform at 15 mg/ml.....	78
Table 2.12. Photovoltaic parameters for blends using 55 as electron acceptor and single layer, under illumination at 88 mW/cm <sup>2</sup> , from a solution of chloroform at 15 mg/ml .....	81
Table 3.1. Photophysical properties of the 2S-BDP, measured in chloroform solution....	97
Table 3.2. Electrochemical properties of the 2S-BDP.....	97
Table 3.3. Optimised ground-state geometries, electron distribution in HOMO and LUMO and their energies (in eV) for the second series of BODIPYs, obtained by DFT calculations in vacuum.....	101
Table 3.4. Average photovoltaic performance parameters for 70:PC <sub>61</sub> BM-based OPVs, obtained under illumination at 90 mW/cm <sup>2</sup> , during the optimisation studies. Active layer films were prepared from chloroform 15mg/ml solutions.....	102

Table 3.5. Photovoltaic performance parameters of the BODIPY:PC <sub>61</sub> BM-based OPVs, under AM 1.5 G illumination at 84 mW/cm <sup>2</sup> . The donor:acceptor ratio is 1:3 by weight and the solution was prepared in chloroform at 15mg/ml. ....	103
Table 3.6. Photovoltaic performance parameters of the BODIPY:PC <sub>71</sub> BM-based OPV cells, obtained under AM 1.5 G illumination at 81 mW/cm <sup>2</sup> . The blends solutions were prepared in chloroform at 15mg/ml, with a donor:acceptor weight ratio of 1:3. ....	105
Table 4.1. Optimisation of the reaction conditions to synthesise the BODIPYs 67 and 68. . .....	114
Table 4.2. Photophysical properties of the 3S-BDP. ....	125
Table 4.3. Electrochemical properties of the 3S-BDP. ....	125
Table 4.4. Optimised ground-state structures, electron distribution in HOMO and LUMO and their energies (in eV) of the third BODIPY series, obtained by DFT calculations in vacuum. ....	125
Table 4.5. Photovoltaic performance parameters of the 67:PC <sub>61</sub> BM-based organic photovoltaic cells during the optimisation studies. Results were obtained under 84 mW/cm <sup>2</sup> illumination .....	129
Table 4.6. Photovoltaic performance parameters of the 3S-BDP:PC <sub>61</sub> BM-based OPV cells, associated to a D:A weight ratio 1:3 and thermal annealing of 100 °C. Films were prepared from a chloroform solution at 15mg/ml. ....	131
Table 4.7. Photovoltaic parameters of OPVs based on BODIPYs 67, 74, 76 and 78 blended with PC <sub>71</sub> BM. Several donor:acceptor ratios were used, and the active layers were thermally annealed at 100 °C. ....	133
Table 5.1 Conformation of the ethyl groups, selected bond lengths and angles of the crystal's structures of 85 and 91. ....	151
Table 5.2. Photophysical properties of the 4S-BDP, measured in chloroform solution ..	154
Table 5.3. Electrochemical properties of the 4S-BDP .....	154
Table 5.4. Photovoltaic performance parameters of the BODIPY:PC <sub>61</sub> BM-based OPV cells, with the active layer prepared with a BODIPY:PC <sub>61</sub> BM weight ratio of 1:3 from a solution of chloroform at 15mg/ml, under AM 1.5G illumination at 84 mW/cm <sup>2</sup> . ....	157
Table 5.5. Electrochemical properties of BODIPYs 74, 92 and 93. ....	154
Table 5.6. Photovoltaic performance parameters of the OPV cells, containing a ratio of 1:2 BODIPY to PC <sub>71</sub> BM acceptor photoactive layer prepared from a solution of chloroform at 15mg/ml, under AM 1.5G illumination at 84 mW/cm <sup>2</sup> . ....	164
Table 6.1. Photophysical properties of 56 and 100. ....	174
Table 6.2. Photophysical properties of 101, 106, 53, BDP-P1, BDP-P2 and BDP-P3, measured in toluene solutions. ....	184
Table 6.3. Electrochemical properties of TPP, 53, BDP-P1, BDP-P2 and BDP-P3.....	185
Table 6.4. Photovoltaic performance parameters of OPV from chloroform solutions at 15mg/ml under AM 1.5 G illumination at 84 mW/cm <sup>2</sup> .....	186



## List of abbreviations and symbols

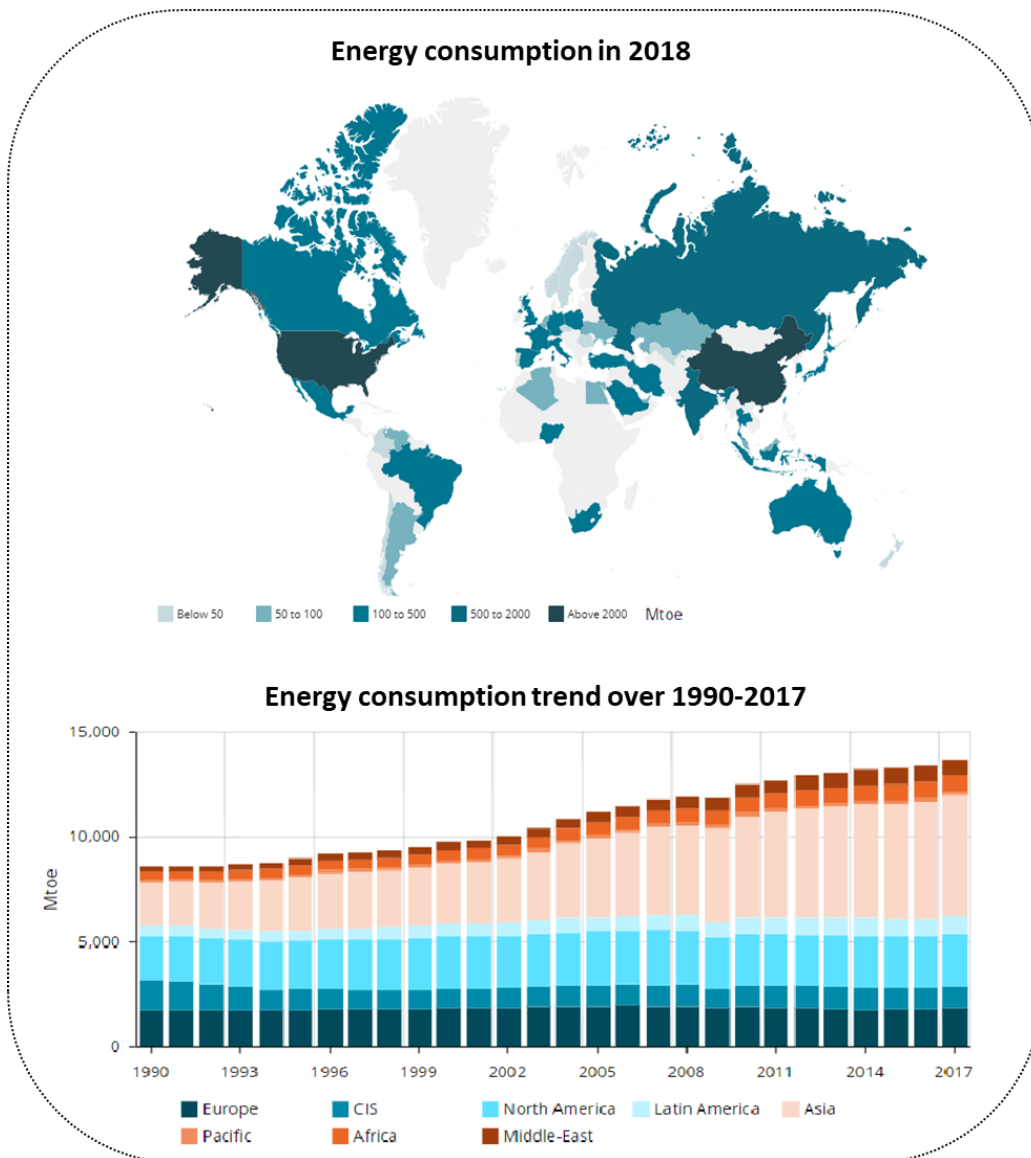
$^1\text{H}$ NMR	Proton nuclear magnetic resonance
$^{11}\text{B}$ NMR	Boron-11 nuclear magnetic resonance
$^{13}\text{C}$ NMR	Carbon-13 nuclear magnetic resonance
$^{19}\text{F}$ NMR	Fluorine-19 nuclear magnetic resonance
AFM	Atomic force microscopy
AM 1.5	Air mass 1.5
BHJ	Bulk heterojunction
BODIPY	4,4-Difluorobora-3a,4a-diaza-s-indacene
$\text{CDCl}_3$	Deuterated chloroform
COSY	Correlation spectroscopy
CV	Cyclic voltammetry
d	Doublet
dd	Double doublet
dt	Double triplet
DCM	Dichloromethane
DDQ	2,3-dichloro-5,6-dicyano-1,4-benzoquinone
DFT	Density functional theory
DMF	N,N-dimethylformamide
DMSO	Dimethyl sulfoxide
DSC	Differential scanning calorimetry
DSSC	Dye-sensitized solar cells
ETL	Electron transport layer
$E_{\text{ox}}$	Half-wave oxidation potential
$E_{\text{red}}$	Half-wave reduction potential
FF	Fill factor
HOMO	Highest occupied molecular orbital
HPLC	High-performance liquid chromatography
HTL	Hole transport layer
IC	internal conversion
I-V	Current-voltage
$I_{\text{sc}}$	Short-circuit current
ITO	Indium-tin oxide
J	Coupling constant
J-V	Current density-voltage
$J_{\text{sc}}$	Short-circuit current density
LUMO	Lowest occupied molecular orbital
m/z	Mass to charge ratio
MeOH	Methanol
MS	Mass spectrometry
NIR	Near infrared
OPV	Organic photovoltaic cell
$\text{PC}_{61}\text{BM}$	[6,6]-Phenyl-C61-butyric acid methyl ester

PC <sub>71</sub> BM	[6,6]-Phenyl-C71-butyric acid methyl ester
PCE	Power conversion efficiency
PDT	Photodynamic therapy
PEDOT-PSS	Poly(3,4-ethylenedioxythiophene) poly(styrenesulfonate)
PeT	Photoinduced electron transfer
ppm	Parts per million
q	Quartet
R <sub>S</sub>	Series resistance
R <sub>Sh</sub>	Shunt resistance
RP	Reverse Phase
rt	Room temperature
s	Singlet
SS	Stokes Shift
S <sub>0</sub>	Ground state
S <sub>1</sub>	Lowest singlet excited state
S <sub>2</sub>	Second singlet excited state
SCE	Saturated calomel electrode
t	Triplet
T <sub>1</sub>	Lowest triplet excited state
TBATFB	Tetrabutylammonium tetrafluoroborate
TFA	Trifluoroacetic acid
TLC	Thin Layer Chromatography
TCPP	<i>Meso</i> -(4-carboxyphenyl)-porphyrin
TGA	Thermogravimetric analysis
TPP	<i>Meso</i> -tetraphenylporphyrin
UV-Vis	Ultraviolet-visible
V <sub>oc</sub>	Open-circuit voltage
δ	Chemical shift
ε	Molar extinction coefficient
η	Power conversion efficiency
λ <sub>abs</sub>	Wavelength of absorption
λ <sub>em</sub>	Wavelength of emission
Φ <sub>F</sub>	Fluorescence quantum yield

## **CHAPTER 1. Introduction**

### 1.1. Photovoltaic Cells

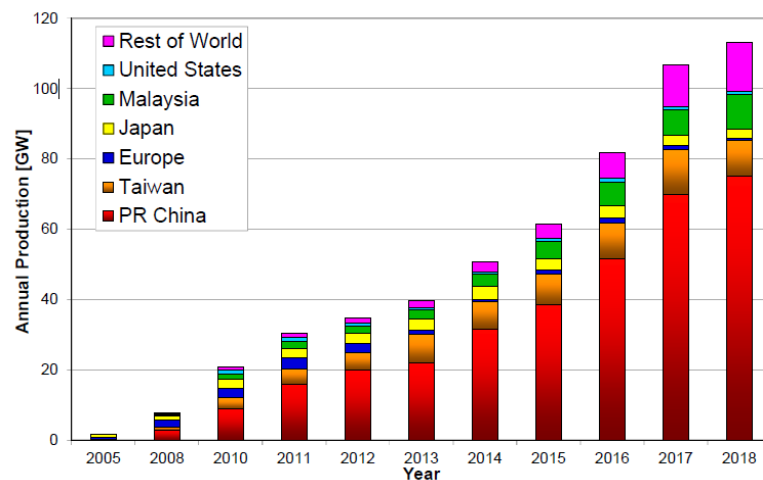
Energy is one of the biggest concerns of our society, as it has a vital role in the socioeconomic progress of all nations. Over the past years, the global energy demand has been continuously growing, and Asia is the best example to demonstrate how energy consumption has changed (Figure 1.1). China has been the energy consumer leader since 2005, with 73 % of its energy produced from coal and 8% from oil.<sup>1</sup> This path has been triggering environmental disorders and raising the hypothesis of enormous economic and social problems due to the hike in inflation rates, in the future. The word energy production has been growing but the most commonly used form of energy comes from fossil fuels like oil, coal and natural gas.



**Figure 1.1.** 2018’s energy consumption and energy consumption trend (in million tonnes of oil equivalent (Mtoe)) over 1990-2017, adapted from Enerdata website.<sup>1</sup>

The development of renewable sources has now become one of the biggest challenges of today's society. Sunlight, wind power, hydropower, geothermal, biomass, and tidal energy are some of the most relevant renewable sources of energy. Among these renewable energy sources, solar energy has received special attention over the recent decades, and its use has been growing.<sup>2</sup>

Photovoltaic cells (also known as solar cells) harvest the light from the sun and convert it into electricity via the photovoltaic effect. Photovoltaics have a huge potential to support the world's energy demand, with almost no damaging effects on the environment or population. With photovoltaic devices, everyone can generate their own energy in their homes and offices, making them energetically sustainable. Over the last 10 years, photovoltaic cells have presented a huge growth, especially in China (Figure 1.2). These developments have consequences not only in the massive market growth but also in the price pressure. Photovoltaic system hardware prices have decreased by over 80 % during the last twenty years, and the Levelized Cost of Electricity (LCoE) benchmark has decreased by over 75 %.<sup>3</sup>

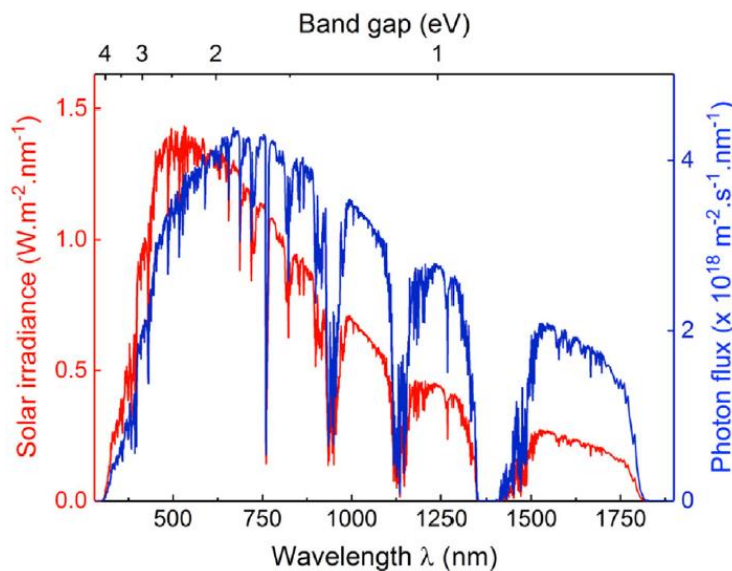


**Figure 1.2.** World photovoltaic (PV) cell/module production from 2005 to 2018, adapted from Jäger-Waldau's report.<sup>3</sup>

The production of a voltage or electric current in a material upon illumination is known as the photovoltaic effect. The photovoltaic effect was discovered in 1839 by Edmund Becquerel when he found that an electrode submerged in a conductive solution could generate an electric current when exposed to light.<sup>5</sup> Later in 1873, W. Smith discovered photoconductivity in selenium, giving rise to the photovoltaic technology.<sup>4</sup> In 1905, Einstein established the foundation for a theoretical understanding of the photoelectric effect, for which he received the Nobel prize in 1921.

The photovoltaic effect takes place in semiconductors when light, with a certain energy, induces the excitation of electrons from the valence band to the conduction band.<sup>5</sup> The electrons in the conduction band are known as photogenerated electrons, and for every photogenerated electron, there is a corresponding hole generated in the valence band. These electrons and holes need to be extracted in order to create electricity.

Light is a set of energy packets, called photons, whose energy depends on their frequency. The solar spectrum spreads over mainly three regions: ultraviolet, visible, and infrared. Around 30-40 % of incident light energy is in the visible range, while over 50 % is in the infrared range (Figure 1.3).<sup>5-7</sup> In the conventional photovoltaic systems (inorganic semiconductors), the photons in the UV and visible range have enough energy to pump electrons and effectively induce charge generation. On the other hand, infrared radiation is not able to generate electricity using conventional PV technology since the energy of incident photons is lower than the band gap of the semiconductors.



**Figure 1.3.** Solar irradiance (red) and corresponding photon flux curve (blue) at AM1.5 (air mass where the sun is about 41° above the horizon) as functions of light wavelength and material band gap, adapted from Sharma, Gros and co-workers.<sup>7</sup>

The first solid solar cell was prepared by Charles Fritts in 1883, with around 1 % of power conversion efficiency (PCE).<sup>8</sup> He coated a thin film of gold over a selenium semiconductor to create a junction. In 1953, Gerald Pearson, Daryl Chapin and Calvin Fuller at Bell Laboratories developed the first silicon photovoltaic cell with the ability to generate measurable electric current, with an efficiency of 4.5 %.<sup>9</sup> This discovery marks the beginning of modern photovoltaics and the first generation of photovoltaic cells. The space industry in

the 60s and particularly the Arab Oil Embargo during the 70s gave a great jumpstart to the development of photovoltaic technology through massive investment in research and financial support for photovoltaic panels, which led to the decrease of the photovoltaic energy costs. However, the decrease of the oil prices at the end of 70s slowed down the investment.<sup>4</sup> Since the beginning of the 90s, the photovoltaic technology investment returned, and it has become one of the most important areas of energy research. Despite their improvement in efficiency, robustness and usability, photovoltaic cells are not yet competitive towards fossil fuels. However, the environmental concerns are waking up the society for the importance of research and investment in this field.

### 1.1.1. Evolution of photovoltaic cells

Photovoltaic technology can be divided into three generations:

**First generation:** Photovoltaic cells based on silicon (monocrystalline or polycrystalline) wafers with a surface of p-n junctions, which present efficiencies around 15-25 %. Silicon-based photovoltaic cells are the most mature photovoltaic technology and currently dominate the market. Despite their great efficiency and robustness, the high production cost and the low versatility of the silicon panels are major drawbacks.

**Second generation:** Photovoltaic cells based on inorganic thin films. Amorphous silicon, CIGS (copper, indium, gadolinium and selenium), CdTe (cadmium telluride) and GaAs (gallium arsenide) are the most commonly used materials, where typical performance is above 15%.<sup>10-13</sup> This sort of photovoltaic cells have the major advantage of using smaller quantities of material, lower purity of materials and lower temperatures of processing. They also allow the construction of lightweight and flexible devices, but the manufacture costs, stability, the low abundance of some compounds and toxicity are some of the main disadvantages of this type of photovoltaic cells. A GaAs multijunction solar cell, under concentrated sunlight, achieved efficiencies around 46 %, which is a notable mark.<sup>14</sup>

**Third generation:** This generation comprises all organic materials that may or may not be coupled with inorganic materials into solar cells. This generation of solar cells includes multijunction solar cells and emerging PV technologies like dye-sensitised solar cells (DSSCs), organic photovoltaic cells (OPVs), perovskites solar cells (PSCs), and quantum dot solar cells (QDSCs).<sup>15-20</sup> The third generation aims to reduce the cost associated with photovoltaic cells with high efficiencies while maintaining the economic and environmental advantages of thin-film deposition techniques. Despite the good efficiencies of perovskite

cells (Figure 1.4), DSSCs and OPVs still are the most studied solar cells from the third generation.

DSSCs are based on a light absorbing electron donor dye deposited under a working electrode (generally  $\text{TiO}_2$ ), a redox-mediator electrolyte (commonly  $\text{I}^-/\text{I}_3^-$ ), and a counter electrode mostly based on platinum (Pt). The organic dye is the component of DSSC that harvest most of the incident light. Generally, phosphoric acid or carboxylic acid groups are inserted in the periphery of the dye to allow a covalent linkage to the working electrode. This avoids aggregation of the dye and enhancement of the electron injection.<sup>21</sup>

These thin solar cells, with low weight, can be manufactured at low temperatures on non-expensive substrates, such as plastic or glass. The low cost of the materials and manufacturing process make these cells economically attractive. In 2010, Professor Michael Grätzel was awarded the Millennium Technology Prize for making this technology an affordable way to harvest solar energy on a large scale. The efficiency of DSSC is still far from the inorganic analogues, having a maximum PCE around 14 %.<sup>22</sup>

Organic photovoltaic cells (OPVs) are based on organic thin-films combining electron-donors with electron-acceptors (typically fullerenes derivatives), often in bulk heterojunctions, which will be described in more detail in the next section. The working principle of OPVs is quite similar to the DSSC. However, in OPV the presence of a redox-mediator electrolyte is not necessary, the dye does not need an anchor group, and light can be absorbed by both components of the active layer.

Figure 1.4 presents the evolution that photovoltaics cells have been demonstrating over the last decades, in terms of different types and efficiencies.





### Best Research-Cell Efficiencies

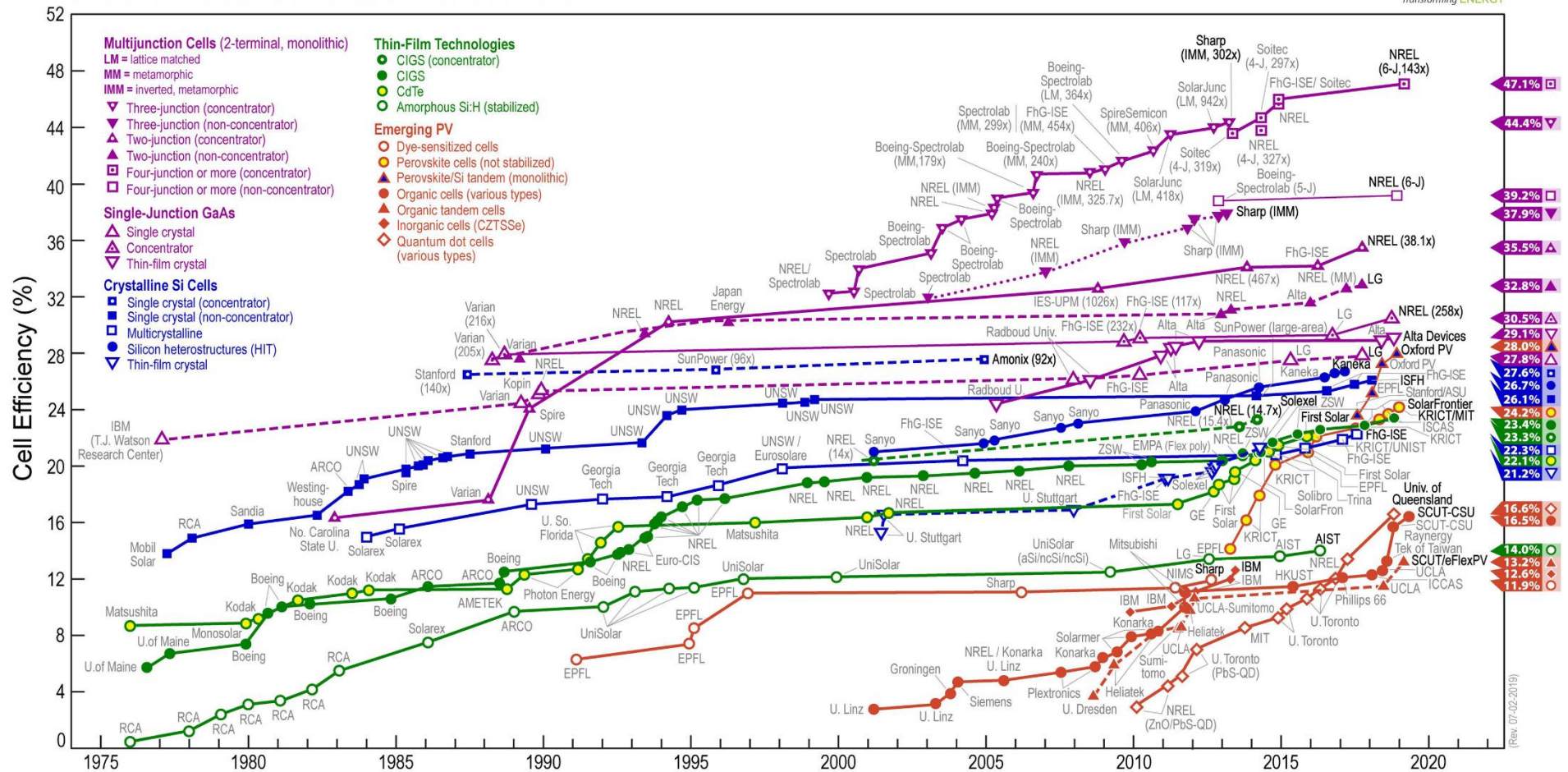
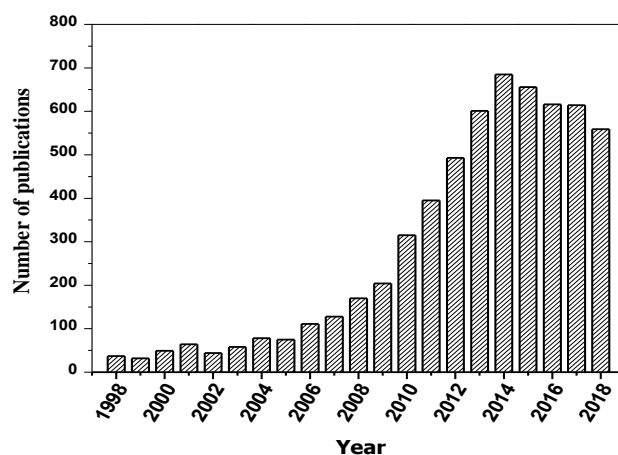


Figure 1.4. Timeline of highest efficiencies of various solar cell technologies, from National Renewable Energy Laboratory.<sup>23</sup>

### 1.1.2. Organic photovoltaic cells (OPVs)

Due to its rising popularity, OPVs have received strong scientific interest over the last 20 years, (Figure 1.5). The maximum efficiency reported to an OPV system is 15 % (laboratory cells),<sup>24</sup> and fully printed cells are arriving on the market.



**Figure 1.5.** Published articles concerning to “organic photovoltaics” or “organic solar cells”, since 1998; search made at Web of Knowledge.

The advantages of OPVs over the inorganic photovoltaic cells are:

- Significantly lower manufacturing costs;
- Continuous manufacturing process using printing protocols;
- Low weight and flexible photovoltaic devices;
- New market opportunities related to either portability or building integration;
- Low environmental impact of manufacturing;
- A large number of donor/acceptor structures that enable a vast field of research;
- Ease of optimisation of the material’s properties;

Whereas the free charges of the inorganic photovoltaic cells are directly generated when the semiconductor is irradiated, organic photovoltaic cells firstly generate excitons (strongly bounded dipole charges), and then the exciton is dissociated in two free charges ( $e^-$  and  $h^+$ ).<sup>25, 26</sup>

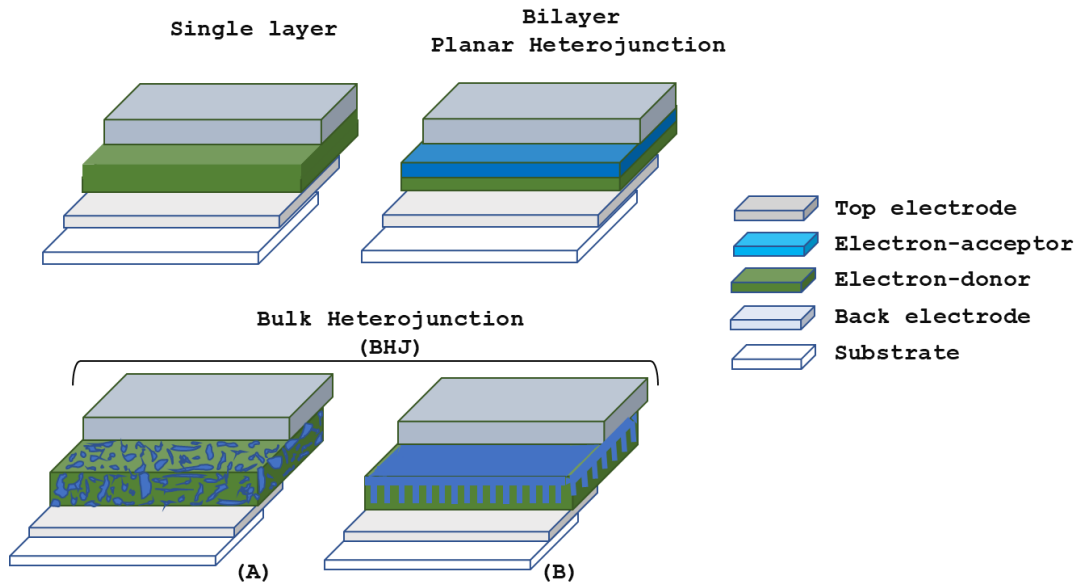
OPV architecture can be based on a single layer structure, where only one organic semiconductor is presented, or based on a bilayer structure which has a donor species and an acceptor species. The first OPV was created in 1978 by Amal Ghosh and Tom Feng.<sup>27,28</sup> It consisted of a single material (merocyanine) sandwiched between Ag and Al electrodes and it obtained very low photovoltaic efficiency.

The inorganic photovoltaic cells have a large dielectric constant (relative permittivity around 10),<sup>29</sup> which reduces the Coulomb interaction between the hole and the electron. On the other hand, the organic semiconductors have a much smaller dielectric constant (relative permittivity around 3)<sup>29</sup> causing a strong Coulombic interaction between the hole and the electron.<sup>30</sup> The smaller dielectric constant results in a small-sized exciton with high binding energy (Frenkel exciton), that prevents the exciton dissociation via thermal energy at ambient temperature. Therefore, the single layer OPV has low efficiency in general. The slow charge transport in organic semiconductors itself decreases the efficiency of the OPV, yet it also increases the charge recombination chance in the device. It was later recognised that the excitons are more efficiently dissociated at the interface between donor and acceptor, which led to the beginning of the development of the bilayer OPVs.

The bilayer OPV is characterised by a well-structured biphasic active layer, where an acceptor layer is inserted between the donor semiconducting and the cathode.<sup>19</sup> This structure was introduced by Tang in 1986, with an efficiency of around 1 %.<sup>31</sup> Among other advantages over the single layer, the bilayer suppresses more effectively the charge recombination. However, the reported efficiencies are still significantly lower than those of inorganic cells. One reason for this is the intrinsically short exciton diffusion length in organic semiconductors, which is typically around 10-20 nm. Therefore, there is a competition between exciton dissociation at the donor:acceptor interface and recombination (with no charge generation).

To overcome the low collection of free charges due to the small amounts of excitons that reach the donor-acceptor interface, the bulk heterojunction organic photovoltaic cells (BHJ-OPVs) were developed. BHJ-OPVs have an intermixed active layer and, for that reason, they have a superior interface area between donor and acceptor.<sup>32-34</sup> If the length scale of the blend is comparable to the exciton diffusion length, most of the created excitons in either material may reach the interface, where the excitons can dissociate efficiently.

The usual bulk heterojunction presents an irregular pattern of the donor or acceptor domains, Figure 1.6 (A). Generally, it is set by mixing both species (electron-donor and electron-acceptor) in a single solution for evaporation or spin-cast deposition. It was proven that columnar architecture (Figure 1.6 (B)) with highly ordered donor and acceptor domains ensure better charge transport and lead to improved performances,<sup>32,34</sup> but that morphology includes laborious and hard manufacturing procedures.



**Figure 1.6.** The different OPV cell structures (single, bilayer and bulk heterojunction) and irregular (A) and columnar (B) active layer of the bulk heterojunction.

Tandem solar cells are multilayer OPVs that involve two or more solar cells stacked directly on top of each other with a transparent electrode in the middle. The tandem cells give good perspectives regarding efficiency, but care must be taken with the deposition of the stacked layers since the deposition of a top layer can damage the bottom layer. The stability and the manufacturing limitations, particularly on a scale up perspective are the major drawbacks of this kind of architecture.

A simple approach to offer a broader absorption profile is the use of a mixture of chromophores that absorb in different wavelength regions. This method was applied in inorganic thin-film solar cells over several decades, and attempts have been made to implement it in OPVs. Similar to tandem solar cells, the use of a ternary active layer in OPVs can offer improvements in the light harvesting over the entire visible and near-infrared (NIR) spectrum. Compared to binary OPVs, the addition of a third component may increase the short-circuit current through enhancement of light harvesting, and/or can increase the open-circuit voltage through the enhancement of carrier mobility.

The ternary solar cell approach has been receiving a lot of attention, and several works have presented the improvements that this system can bring,<sup>35-39</sup> but the use of a ternary system is not so simple and requires extra optimisation procedures. The careful design of the cell's architecture and choice of the materials is required, in order to offer a suitable energy-level offset between the various components, to provide balanced electron and hole mobility, and to get good light-harvesting efficiency.<sup>40</sup> Furthermore, the addition of a third component to a binary system is likely affected to the film morphology.

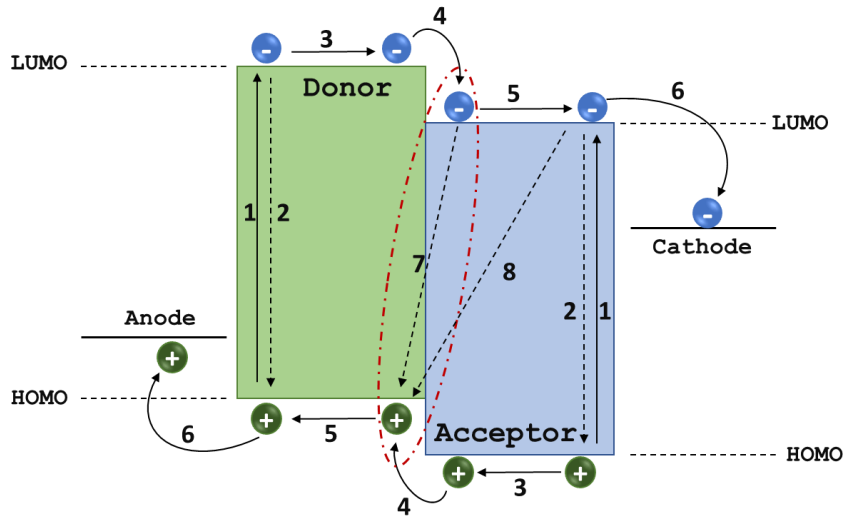
### 1.1.3. Operational principles of organic photovoltaic cells

In OPVs, the process of energy production begins when an incident photon creates an exciton in the photoactive material. In an ideal case, an electron is promoted from the highest occupied molecular orbital (HOMO) level to the lowest unoccupied molecular orbital (LUMO) level, forming the exciton.<sup>41</sup> The exciton is a neutral quasiparticle representing a bound singlet state of electron and hole, which propagates by diffusion and must dissociate into the donor-acceptor interface in order to create two free charges (electron and hole) before the recombination. The electron must then reach the electrode while the hole must reach the other electrode. In order to achieve charge migration, an electrical field is required, which is provided by the working functions of the electrodes.<sup>42</sup> The selection of the appropriate donor and acceptor material should be made very carefully since the LUMO and HOMO energy levels of the donor must be higher than the corresponding frontier orbital energy levels of the acceptor, forming a type II heterojunction. Only in this situation, there is a significant probability of charge separation.

To optimise the OPV performance, several structural and manufacturing methods have been developed. The use of an electron transport layer and a hole transport layer between the electrodes and the active layer is becoming a regular feature. Generally, the OPV's literature follows the anode/cathode definition used in OLEDs. Therefore, the electrode that receives the electrons from the active layer is considered the cathode and the electrode that collects the holes is considered the anode.

As presented in Figure 1.7, the operational principles in BHJ-OPV cells comprise the following steps:

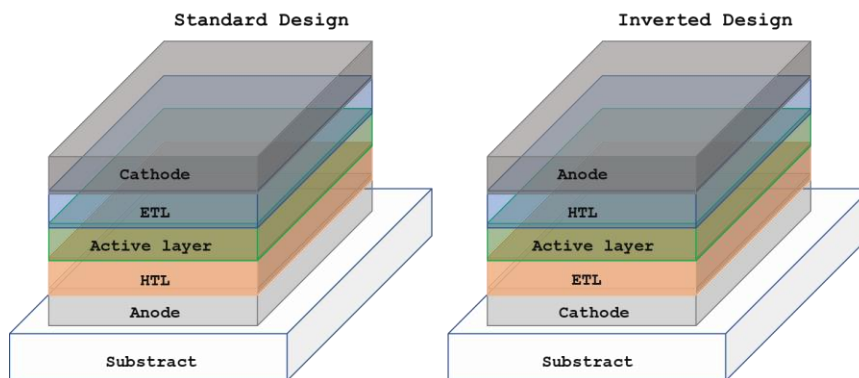
- (1) the formation of photo-induced excitons in the donor and/or in the acceptor;
- (2) intramolecular electron-hole recombination;
- (3) the excitons diffusion and dissociation at the donor/acceptor interface;
- (4) charge-transfer states generation and then dissociation into free charge carriers (electrons and holes) with an ultrafast charge transfer process;
- (5) transport of charge carriers through either donor or acceptor phase/domains;
- (6) collection of the free charges by the corresponding electrodes;
- (7) geminate recombination;
- (8) non-geminate recombination;



**Figure 1.7.** The operational principle of BHJ-OPV cells.

As shown in Figure 1.8, there are two different OPV device designs: the standard and the inverted design. The standard OPV presents an anode (generally ITO) coated with hole transport layer (HTL). Despite the application of molybdenum trioxide ( $\text{MoO}_3$ ) as a hole transport layer has been very common,<sup>19</sup> PEDOT:PSS ((poly(3,4-ethylenedioxythiophene)poly(styrenesulfonate))) is the most used thanks to its advantages in processability along with its mechanical and optical properties.<sup>19</sup> On top of the HTL, the photoactive blend layer is deposited and then it is followed by the electron transport layer (ETL) and the cathode. Ca, Ba, Mg and alkali metal compounds such as cesium carbonate ( $\text{Cs}_2\text{CO}_3$ ) and lithium fluoride (LiF) have been used to reduce the work function of the electrode (usually Al or Ag) for more efficient electron extraction.<sup>33, 43-45</sup>

In the inverted design, the cathode is near the substrate and on top of the active layer an HTL, like PEDOT:PSS, can be used. The device is completed with an air stable high work function electrode material like silver or gold.<sup>46</sup>



**Figure 1.8.** Different device architectures of bulk heterojunction OPV cells.

In addition to the structural modification, several conditions may optimise the microstructure and morphology of the active layer or the donor:acceptor interface. The active layer morphology plays a key role in the exciton dissociation and free charges collection. Aside from the individual characteristics of the organic species, the morphology is dependent on the interactions between the donor and acceptor and between these and the solvent.<sup>45</sup>

The choice of the solvent, the solution concentration, temperature and deposition rate are some of the factors that can affect the drying kinetics of the films and their morphological characteristics. The solvents should easily dissolve the donor and acceptor materials and not form complexes with them. Due to these restrictions, chloroform, tetrahydrofuran, *o*-dichlorobenzene, chlorobenzene, and dichloromethane are the most widely applied solvents.<sup>47</sup>

The use of so-called solvent additives can modify the film morphology and consequently the photovoltaic performance. The first report of solvent additives occurred in 2006 when Peet and co-workers incorporated 1-octanethiol and observed higher photocurrents from P<sub>3</sub>HT:PC<sub>61</sub>BM blend films.<sup>48</sup> Chloronaphthalene and 1,8-diiodooctane are the most common solvent additives, and their usage in small amounts (0.5-5 %) has been studied.<sup>49-51</sup> Their effect has been attributed to their ability to preferentially dissolve one of the components of the active layer, allowing this component to remain in solution for a longer time during the film formation because of their higher boiling point (compared to the solvent used to prepare the donor/acceptor components).<sup>47,52</sup> This feature is claimed to lead a higher degree of crystallinity, leading to a more efficient exciton dissociation at the donor-acceptor interface. Nevertheless, the added complexity for device fabrication and concerns about toxicity and device stability creates a disadvantage for large-scale manufacturing when such additives are involved.

Thermal annealing is a post-processing heating process, that can strongly affect the phase separation, the crystallinity and, therefore, the performance of the photovoltaic cell.<sup>47,53</sup> The effect of thermal annealing has been studied in several systems, and its influence depends on the solvent and thermal stability of the blend. Similar to thermal annealing, solvent annealing (exposure of the active layer film to a solvent vapour) can also change the phase separation and crystallinity of the film. The solvents should dissolve the sample slightly but not to a large extent, otherwise, the morphology of the film can be excessively modified.

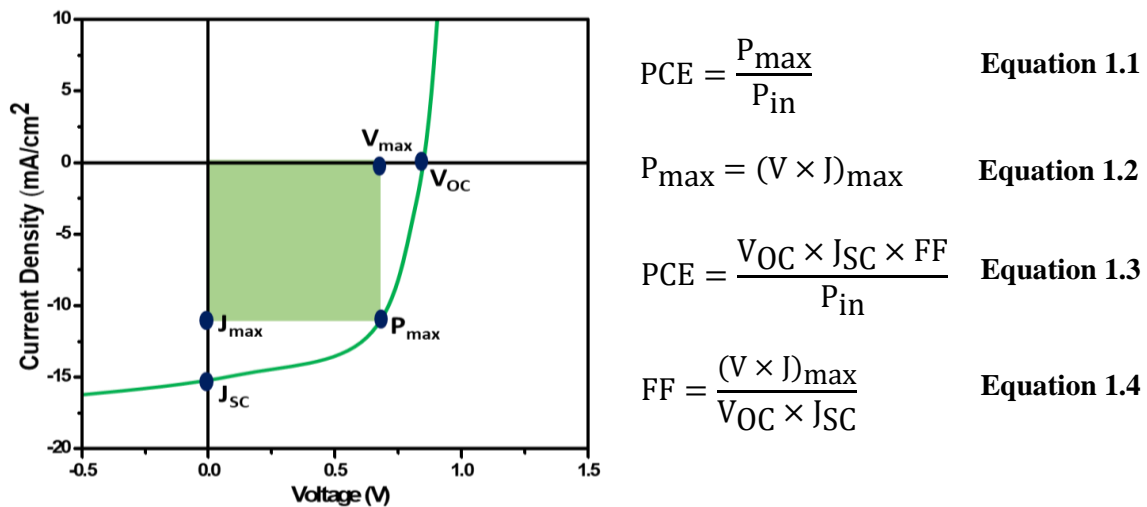


### 1.1.4. Performance characterisation of organic photovoltaic cells

When a photon is absorbed by the active layer, a bound state of an electron and a hole (exciton) is formed. This bound state can be dissociated, generating free charges that travel across the active layer to be collected by the electrodes. The collection of the photogenerated charge carriers constitutes the photocurrent.

As presented in Figure 1.9, the PCE of solar cells is calculated according to equation 1.1 and 1.3, where  $P_{\max}$  is the maximum power of the tested cell and  $P_{\text{in}}$  is the power of the total incident irradiance (from the sun or the testing lamp). The current density (J)–voltage (V) data displays a maximum power point ( $P_{\max}$ ), which corresponds to the maximum value of  $J \times V$ . The PCE is proportional to three main parameters (equation 1.3), the open-circuit voltage ( $V_{\text{OC}}$ ), the short-circuit current density ( $J_{\text{SC}}$ ), and the fill factor (FF).

$V_{\text{OC}}$  is defined as the voltage at which the current density is zero. This means that the voltage applied to the diode annihilates the photovoltage. It has been demonstrated that the value of  $V_{\text{OC}}$  is proportional to the energy difference between the HOMO of the donor and the LUMO of the acceptor. Therefore, a straight way to increase  $V_{\text{OC}}$  is the lowering of the HOMO energy of the donor and/or raising of the LUMO of the acceptor.



**Figure 1.9.** Representation of a hypothetical J-V curve, under illumination, and the most used equations for photovoltaic metrics.

Upon analysis of several reports, Sharber and co-workers established equation 1.5 relating the two parameters.<sup>54</sup> However, the real  $V_{\text{OC}}$  can also be affected by the morphology of the active layer and by the electrochemical potential (work function) of the electrodes.<sup>55-57</sup>

$$V_{\text{OC}} = \frac{1}{e} (|E_{\text{HOMO}}^{\text{donor}}| - |E_{\text{LUMO}}^{\text{acceptor}}|) - 0.3 \quad \text{Equation 1.5}$$



$J_{SC}$  is the current density passing through devices under short-circuit conditions when no external voltage is applied. This parameter is dependent on the number of absorbed photons (which is itself dependent on the absorption spectrum of the active layer and its thickness), the morphology and the loss mechanisms that reduce charge collection. The morphology of the active layer has a big impact on the generation and collection of the photogenerated charges. It is possible to enhance  $J_{SC}$  upon the increase of the layer thickness, albeit a thicker layer raises the probability of charge recombination, in view of the low charge mobility in organic materials. Therefore, it is important to achieve a compromise between all of the factors that affect the active layer morphology.

Fill factor (FF) is defined as the ratio of the maximum power from the solar cell to the product of  $V_{OC}$  and  $J_{SC}$  (Equation 1.4). FF depends on a complex combination of various parameters, such as exciton formation, diffusion, dissociation, charge carriers transport and collection.<sup>34</sup> The shape of the J-V curve shows how hardly or easily the free photogenerated charges can be collected, and an ideal J-V curve is a rectangle, which indicates an FF of 100%.<sup>58</sup> This parameter is also dependent on the electrical resistance ( $R_s$  and  $R_{sh}$ ) of the film.<sup>34</sup>

The series resistance ( $R_s$ ) arises from the intrinsic resistance morphology and thickness of the semiconductor layer and it negatively influences the FF, thereby should be minimised.

The shunt resistance ( $R_{sh}$ ) is correlated with the charge recombination and the leaks, that are closely related to the amount and character of the impurities and defects within the active layer.<sup>59, 60</sup> High  $R_{sh}$  is representative of lower shunt current and thereby represents low cell leakages. This parameter is directly associated with recombination in the interface of the electrodes. The  $R_{sh}$  and  $R_s$  values can be extracted from the J-V curve, particularly the  $R_{sh}$  is extracted from the slope at  $V = 0$  and the  $R_s$  from the slope at  $J = 0$ .

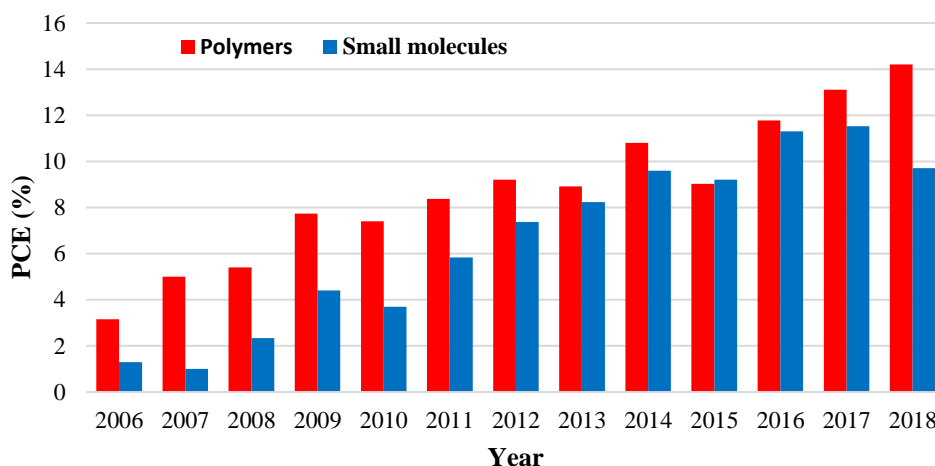
External quantum efficiency (EQE) is another important parameter in OPV characterisation. EQE is the ratio of photogenerated electrons or holes collected at the electrodes, to the number of incident photons at a certain wavelength. Equation 1.6 shows a way to calculate EQE, where  $I(\lambda)$  represents the current generated by the cell at wavelength  $\lambda$ , and  $P_{in}$  is the incoming power at wavelength  $\lambda$ .<sup>61</sup>

$$EQE = \frac{1240 \cdot I(\lambda)}{\lambda(\text{nm}) \cdot P_{in}(\lambda)} \quad \text{Equation 1.6}$$

As EQE is calculated for every wavelength, the result is a spectral distribution of the percentage of photogenerated charges per incident photon at each wavelength.

### 1.1.5. Polymers vs small molecules in bulk heterojunction organic photovoltaic cells

Organic semiconductors can either be polymers or “small molecules”. In recent times, many new polymers and small molecule-based materials have been designed and developed for organic solar cells. Initially, polymer-based OPVs showed better performance, but small molecules-based OPVs are catching up (Figure 1.10).



**Figure 1.10.** Best PCEs of polymer and small molecules-based OPVs since 2006.<sup>62-65</sup>

Polymers have been leading the OPV’s research mostly because of their low band gap and solution processability. However, recent progress has shown that small molecules can rival with polymers in OPV applications.<sup>64, 66</sup>

The main advantages of the small molecules over the polymers are:

- Well-defined chemical structure that eliminates the problems of structural variability of polymers;
- Simple purification processes;
- Relationships between chemical structure, electronic properties, and performance are more straightforward;
- Higher molecular extinction coefficients that allow thinner active layers, thus minimising problems associated with charge transport and recombination;

Different approaches have been used to gain better control over the morphology of the blends and improve their photovoltaic characteristics. Nevertheless, the discussion between the pros and cons of polymers *versus* small molecules and which could show better efficiencies and lifetimes is still under debate.

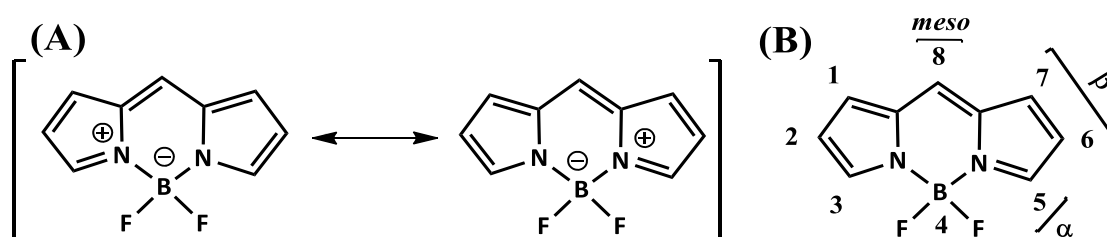
## 1.2. Boron dipyrromethene (BODIPY): a versatile photoactive dye

Pyrrole is an electron-rich, five-membered, nitrogen-containing aromatic compound that was identified by Runge in 1834 from coal tar and whose structure was correctly formulated by Baeyer in 1870.<sup>67, 68</sup> From the synthetic point of view, the feature that justifies pyrroles receiving such high attention stems from the fact they represent readily accessible and highly flexible building blocks for the construction of a variety of more complex compounds, such as polymers or macrocycles.

Among all pyrrolic structures, dipyrromethenes and tetrapyrrolic compounds are the most notorious. The dipyrromethene is a compound based on two pyrrole units bridged by a methine and is generally obtained from the oxidation of dipyrromethane. Despite the regular application of dipyrromethenes and dipyrromethanes as building blocks of tetrapyrrolic units, their research has been increasing since the discovery of the 4,4-difluoro-4-bora-3a,4a-diazas-indacene (commonly known as BODIPY).

### 1.2.1. Background, structure and synthetic routes

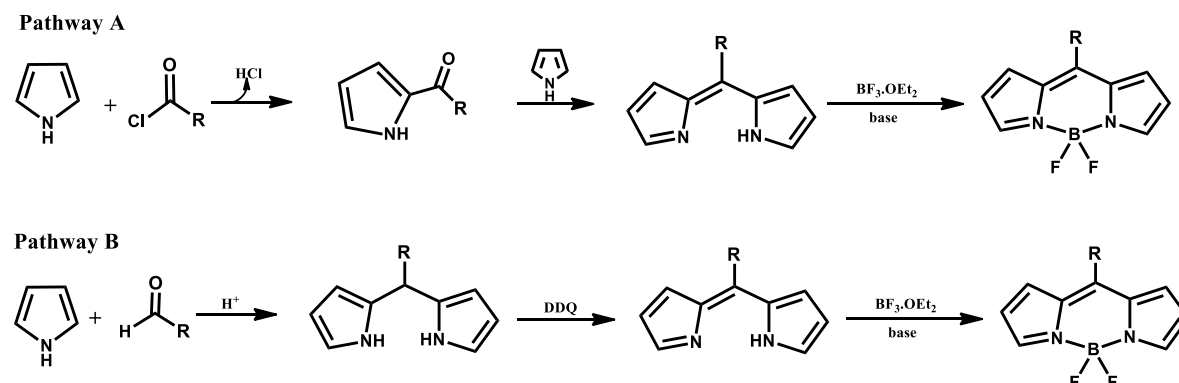
BODIPY is a boron dipyrromethene complex (Figure 1.11), first presented in 1968 by Treibs and Kreuzer.<sup>69</sup> The research on BODIPY derivatives was strongly developed in the 1990s when Boyer and co-workers realised that BODIPY dyes could be used as fluorescent probes.<sup>70, 71</sup> Since then, the research of BODIPY dyes has been consolidating mostly due to their particular photophysical properties.



**Figure 1.11.** (A) Two equivalent resonance structures (generally BODIPY dyes are represented as an uncharged structure); (B) BODIPY structure with the IUPAC numbering system (1 to 8) and alternative nomenclature ( $\alpha$ ,  $\beta$  and *meso*).

The BODIPY structure consists of two pyrrole units bridged by a methine, with coordination to a boron-difluoride centre. This family of compounds follows the numbering rule in an analogy to the tricyclic *s*-indacene, but can also have the nomenclature used for porphyrins.<sup>72</sup> Thus, the 8-methine bridge could also be designated as *meso*-position, the 1,2,6,7-positions as  $\beta$ -pyrrolic positions and the 3,5-positions as  $\alpha$ -pyrrolic positions.

Several approaches have been reported for the synthesis of BODIPY molecules, and the two most common routes are described in Scheme 1.1.



**Scheme 1.1.** The most used BODIPY's synthetic pathways.

Pathway A involves the condensation of pyrrole with an acylium equivalent (acid chloride,<sup>73,74</sup> anhydride<sup>75</sup>). It is not necessary to isolate the acylpyrrole intermediate because it reacts with the pyrrole under acidic conditions to form the dipyrromethene and then it is complexed with boron trifluoride to afford the symmetric or asymmetric BODIPY. The direct production of dipyrromethene is a great advantage of this pathway since it avoids the oxidation step.

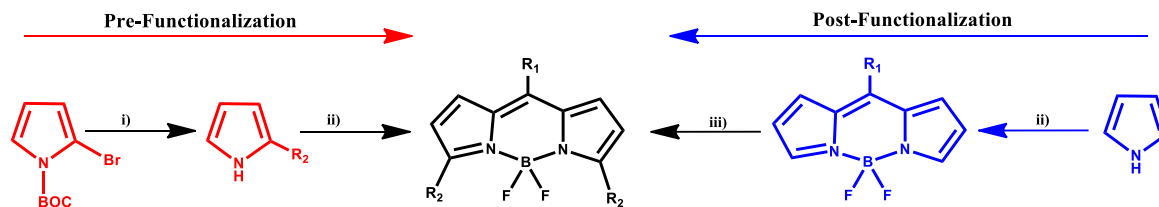
Aromatic aldehydes can be used instead of acyl chlorides when an aromatic group is intended to be at *meso*-position (pathway B). This pathway involves the formation of a dipyrromethane intermediate through condensation of pyrrole with the aromatic aldehyde in the presence of an acid catalyst.<sup>76-78</sup> The dipyrromethane intermediate is later oxidised to the corresponding dipyrromethene, followed by complexation with borontrifluoride in the presence of a base. Although this synthetic strategy involves more steps, it is the most commonly used.

Complementary synthetic procedures have been reported, such as the use of orthoesters as the electrophilic element of the condensation reaction,<sup>79</sup> or the synthesis of asymmetrical BODIPY structures, from the acid-catalysed condensation of a carbonyl-containing pyrrole and a different  $\alpha$ -free pyrrole in a very similar way to that of acid chloride condensation.<sup>80-82</sup>

### 1.2.2. Functionalization of the BODIPY core

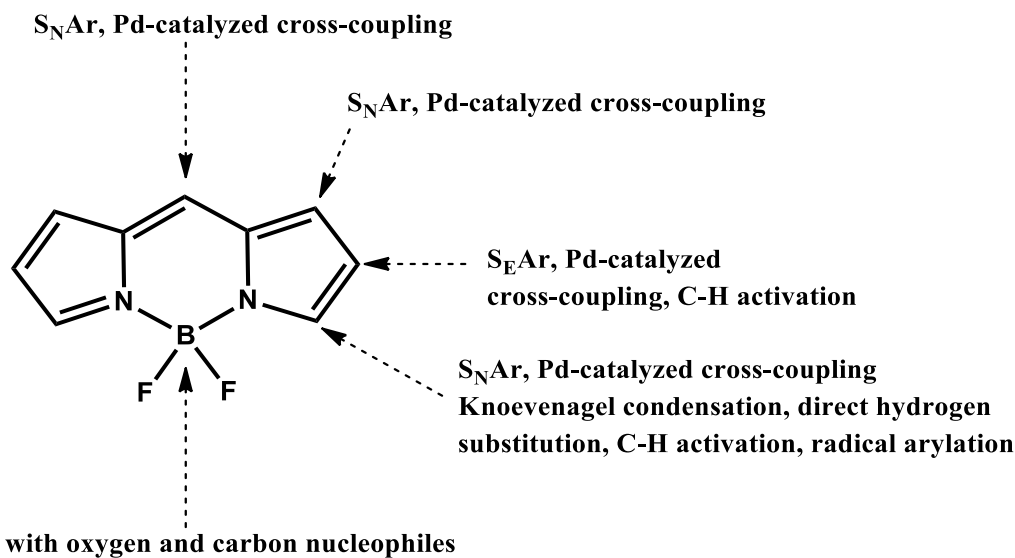
One of the most attractive motivation to work with BODIPYs is their wide scope for functionalization. The extensive number of possible functionalization methods allows a

perfect fit between the structures and the desired characteristics. There are two ways to obtain substituted BODIPY derivatives: pre-functionalization or post-functionalization (Scheme 1.2).



**Scheme 1.2.** Example of a BODIPY's synthesis via pre-functionalization or post-functionalization pathways. Conditions: i) R<sub>2</sub>-B(OH)<sub>2</sub>, Na<sub>2</sub>CO<sub>3</sub>, cat, Pd(PPh<sub>3</sub>)<sub>4</sub>, 80°C;<sup>83</sup> ii) R<sub>1</sub>-CHO, DDQ, BF<sub>3</sub>·OEt<sub>2</sub>, rt;<sup>79</sup> iii) R<sub>2</sub>-N<sub>2</sub>BF<sub>4</sub>, ferrocene, acetone, room temperature.<sup>84</sup>

Pre-functionalization is based on a suitable functionalization of the pyrroles, which are used as precursors of the desired BODIPY. On the other hand, the post-functionalization is the method used when the desired BODIPY is obtained after the final boron complexation and can result from a large variety of synthetic procedures (Figure 1.12).



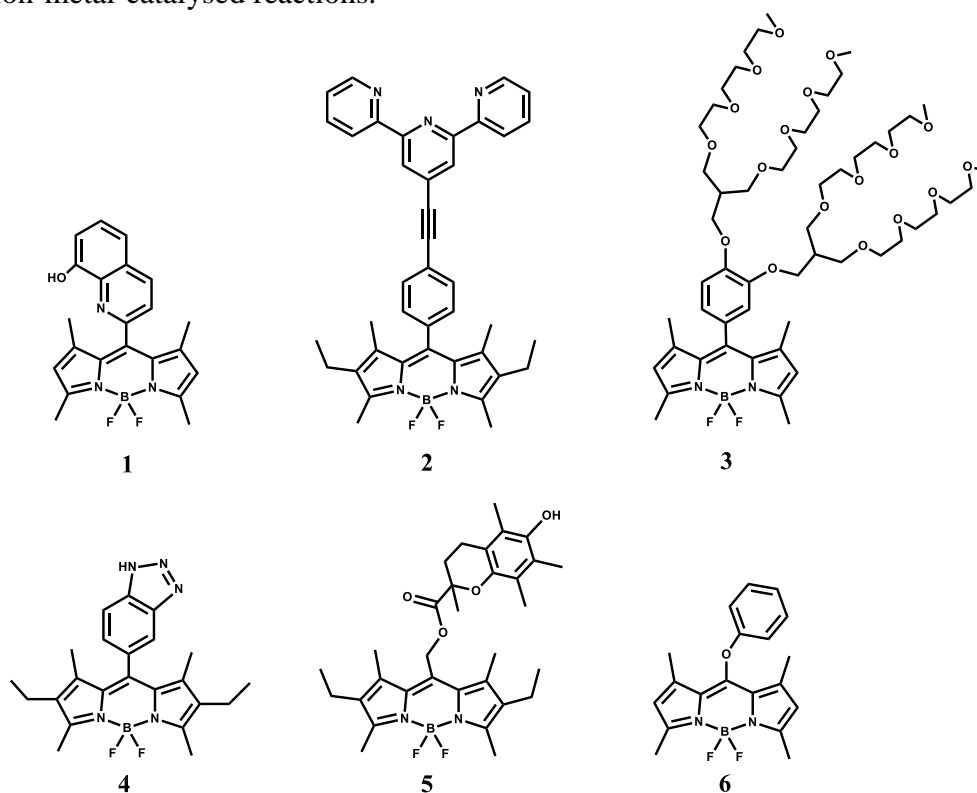
**Figure 1.12.** Overview of the different BODIPY post-functionalization methods at their preferential site(s) of reaction; adapted from Dehaen *et al.*<sup>84</sup>

The pre- and post-functionalization of the BODIPY core are rather complementary approaches. However, post-functionalization allows the introduction of a larger number of functional groups and the preparation of sophisticated compounds with diversified molecular structures.

### 1.2.2.1. Functionalization at the *meso*-position

Generally, the *meso*-substituted group is defined via pre-functionalization of the aldehyde, acyl chloride or dipyranyl intermediate. The diversity of aromatic aldehydes and acyl chlorides allows the synthesis of a large variety of BODIPY molecules, but subsequent derivatization of the substituted groups can introduce different characteristics to the BODIPY. The substituted groups at the *meso*-position can introduce several new characteristics such as metal ions detecting properties (**1** and **2**),<sup>85-87</sup> water-solubility (**3**),<sup>88, 89</sup> and selective redox or emission features (**4, 5**).<sup>90-93</sup>

The direct introduction of halogen atoms at the *meso*-position is a functionalization that can lead to interesting structures through nucleophilic aromatic substitution (**6**) or transition-metal-catalysed reactions.<sup>94</sup>

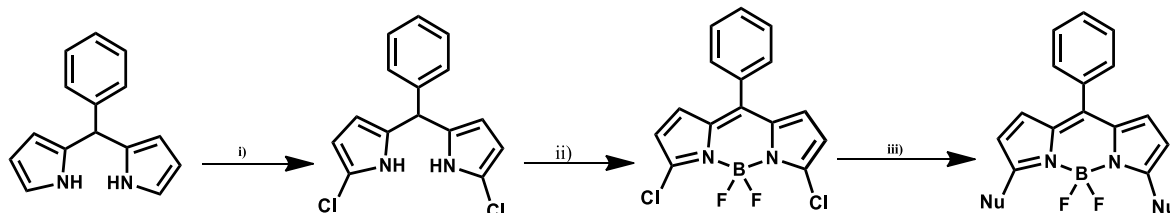


**Figure 1.13.** Chemical structures of various *meso*-substituted BODIPY derivatives from literature: **1**,<sup>85</sup> **2**,<sup>87</sup> **3**,<sup>89</sup> **4**,<sup>90</sup> **5**,<sup>93</sup> **6**.<sup>94</sup>

The halogens at the *meso*-position have a negligible effect on the absorption and emission maxima wavelength. However, their derivatives (e.g. **6**) present shifted absorption and emission spectra and larger Stokes shifts with respect to the *meso*-free BODIPY analogous.<sup>84</sup> *Meso*-halogenated BODIPYs can be prepared from dipyrrolylketones, previously synthesised from dipyrrolylthiones (obtained from the condensation of pyrroles with thiophosgene).<sup>95</sup>

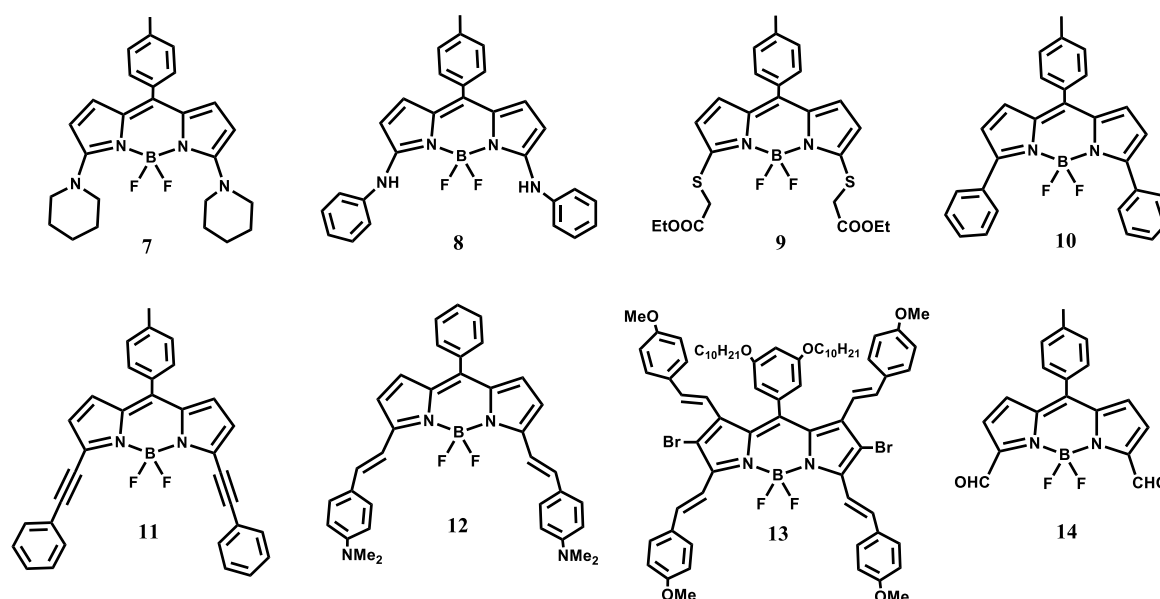
### 1.2.2.2. Functionalization at the 1,3,5,7-positions

The halogenation of the 3,5-positions makes the BODIPY even more versatile towards post-functionalization (Scheme 1.3). Halogen atoms occupying those positions allow electron-deficient BODIPYs to undergo nucleophilic substitution with amines, alkoxides, phenoxides, thiolates, or enolates, (Figure 1.14 (**7**, **8**, **9**)).<sup>84, 96, 97</sup>



**Scheme 1.3.** i) NCS/THF,  $-78^{\circ}\text{C}$ , 2 h. ii) DDQ room temperature, 1h; toluene,  $\text{Et}_3\text{N}/\text{BF}_3\cdot\text{OEt}_2$ ,  $70^{\circ}\text{C}$ , 2.5 h; iii) Nucleophile  $\text{Nu}^-$ ,  $\text{CH}_3\text{CN}$ , reflux; adapted from Dehaen *et al.*<sup>84</sup>

Furthermore, BODIPY dyes with halogen atoms are useful compounds to synthesise new carbon-substituted BODIPY molecules through palladium-catalysed C–C coupling reactions (Figure 1.14 (**10** and **11**)).<sup>77, 98-101</sup>



**Figure 1.14.** Chemical structures of various BODIPYs from post-functionalizations at 1, 3, 5 and 7-position: **7**,<sup>96</sup> **8**,<sup>96</sup> **9**,<sup>96</sup> **10**,<sup>100</sup> **11**,<sup>101</sup> **12**,<sup>77</sup> **13**,<sup>102</sup> **14**.<sup>103</sup>

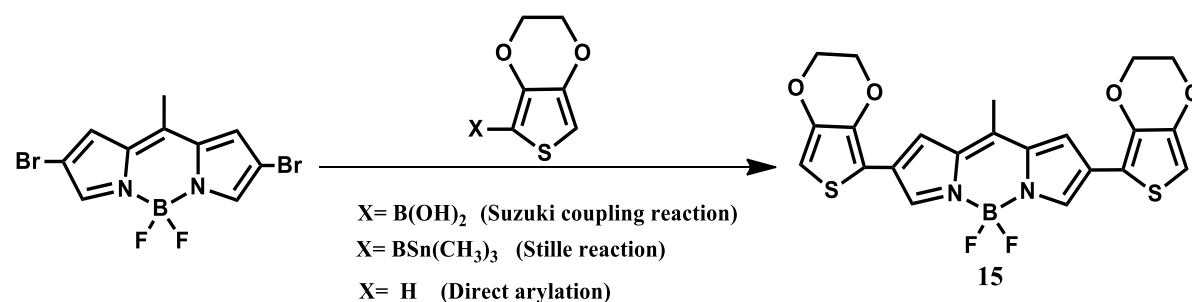
BODIPY dyes having methyl groups at the 1, 3, 5 and 7-position can be subjected to chemical modifications on the methyl carbon atoms in order to extend the degree of  $\pi$ -electron conjugation and to induce a pronounced bathochromic shift on the absorption and emission spectral maxima. The methyl groups at  $\alpha$ -position (3,5-positions) can be easily

deprotonated, and the resultant intermediate may react with an electron-rich aromatic aldehyde, originating styryl groups, and consequently extending the  $\pi$ -electron conjugation (**12**).<sup>77, 104-106</sup> The addition of halogen atoms at 2,6-positions increase even more the acidity of the hydrogens from those methyl groups and allow the introduction of vinyl groups in the 1,7-positions as well (**13**).<sup>77, 102</sup> Additionally, the intermediate carbenium ion can be oxidised *in situ*, leading to the corresponding 3-formyl derivative (**14**).<sup>107, 108</sup>

### 1.2.2.3. Functionalization at the 2,6-positions

The 2,6-positions are the most nucleophilic positions of the BODIPY core.<sup>77</sup> Consequently, electrophilic substitution reactions such as halogenation,<sup>109-111</sup> nitration,<sup>112, 113</sup> sulfonation,<sup>114, 115</sup> and formylation<sup>116, 117</sup> have been extensively studied and can cause a bathochromic shift in the absorption, fluorescence quenching and intersystem crossing to the triplet state.<sup>118</sup>

The halogenation of these position creates opportunities for several modifications through palladium-catalysed coupling reactions, including Suzuki,<sup>119, 120</sup> Stille,<sup>98, 121</sup> Sonagashira,<sup>109, 122</sup> and direct C-H arylation,<sup>123</sup> that allow the direct introduction of ethyne, ethene, or aryl groups into BODIPY core. Scheme 1.4 presents three different ways to synthesise the BODIPY **15**, starting from the same BODIPY precursor.



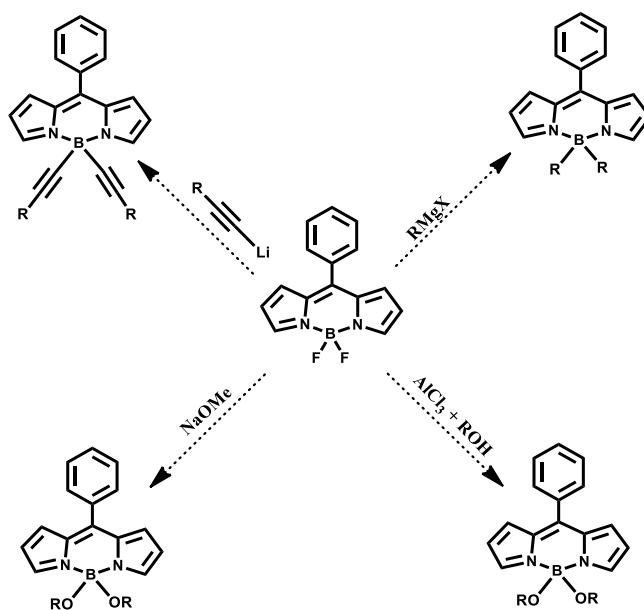
**Scheme 1.4.** Synthesis of a BODIPY by cross-coupling reaction (Suzuki and Stille) or by direct C-H arylation; adapted from Yu *et al.*<sup>123</sup>

The palladium-catalysed coupling reaction, Stille (using an organostannanes species) or Suzuki (using an organoboron species) are the most used reaction to link an aryl group to BODIPY backbone. However, the palladium-catalysed direct C-H arylation is more efficient than traditional synthesis.<sup>122</sup>



### 1.2.2.4. Functionalization at the boron atom

Boron functionalization is a convenient methodology for the introduction of additional groups into BODIPY compounds. As shown in Scheme 1.5, the functionalization at this position requires strong nucleophiles, such as Grignard reagents, organolithiums and alkoxides, or can be accomplished in the presence of a Lewis acid ( $\text{AlCl}_3$ ,  $\text{GaCl}_3$  or  $\text{SnCl}_4$ ) and milder nucleophiles.<sup>124-128</sup>



**Scheme 1.5.** Different pathways of BODIPY modification at the boron centre.

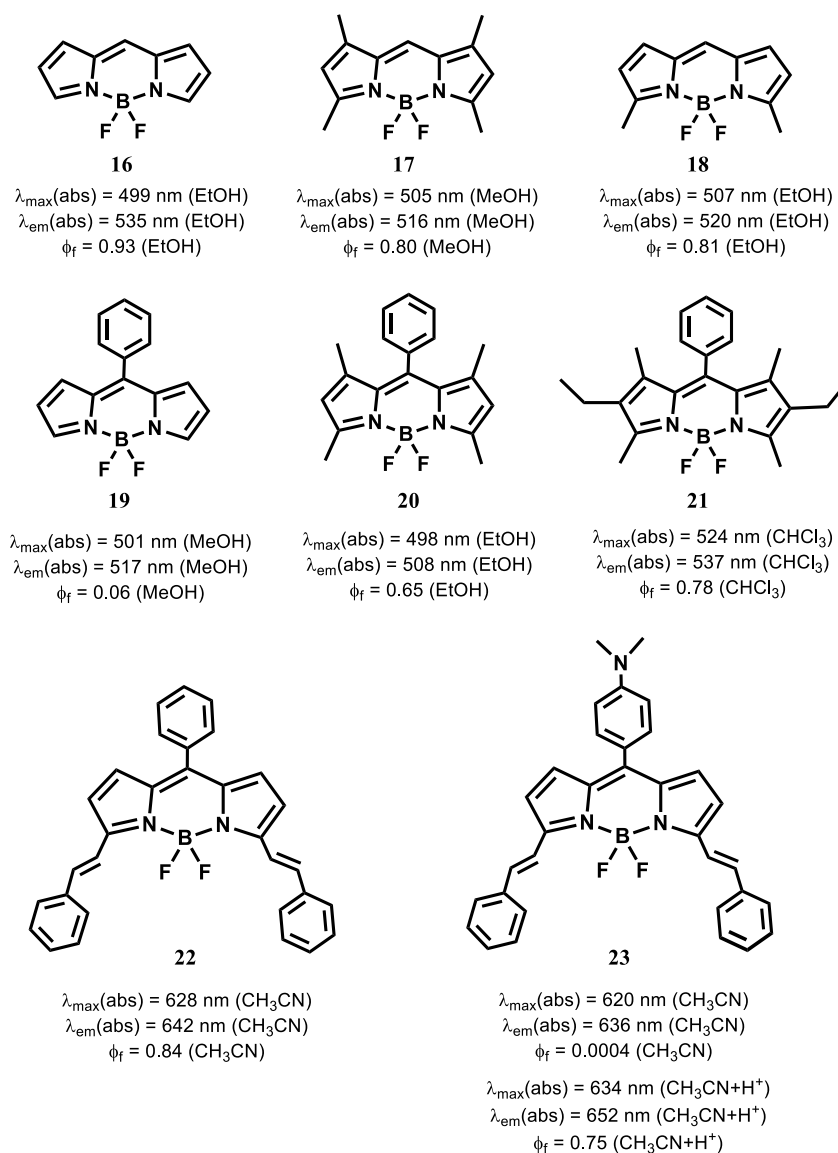
The change of fluorine atoms by ethynyl, carbon, aryloxides or alkoxides derivatives offers the opportunity to synthesize several new fluorophores. Likewise, the *meso*-substituent groups, the attachment with aryloxides or alkoxides could not affect the intrinsic photophysical properties but can lead an increased stability, solubility either in water or in organic solvents and to the insertion of new functionalized groups.<sup>125</sup>

### 1.2.3. General properties of BODIPYs

BODIPYs are generally characterized by their high molar extinction coefficients (frequently above  $50000 \text{ M}^{-1} \cdot \text{cm}^{-1}$ ), high fluorescence quantum yield, low inter-system crossing to triplet excited state and a long excited state lifetime. They are stable under physiological conditions, display low toxicity, have high photo and thermal stability and are chemically robust. They are also soluble in most organic solvents and are typically not sensitive to the solvent polarity.

The ability to design and prepare molecules with very distinctive structures is one of the most important features of BODIPY compounds since it is possible to modulate or improve their characteristics based on the final application. As an example, the introduction of alkyl groups has only a minor effect on the absorption and emission features, as can be seen in Figure 1.15 (**16**, **17**, **18**), but decreases the BODIPY aggregate formation.

However, the fluorescence of the *meso*-phenyl compound **19** (Figure 1.15) is appreciably lower than the substituted analogues **20** and **21**. Such differences are attributed to the effect of the alkyl substituents at 1,7-position, that sterically avoid free rotation of the phenyl group which reduces the loss of energy from the excited states via non-radiative molecular relaxation processes.

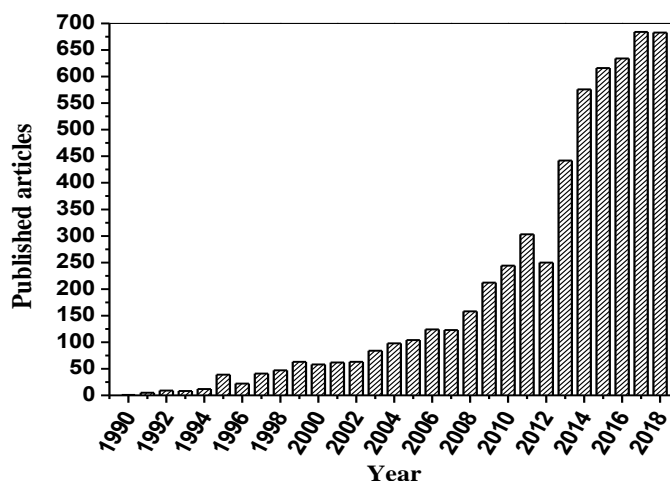


**Figure 1.15.** Influence of the BODIPY's core substitution on the spectroscopic properties, adapted from Burgess *et al.*<sup>78</sup>

By post-functionalization we can turn the BODIPY lipophilic by adding sulfonate groups,<sup>114</sup> raise the inter-system crossing via heavy atom effect or red-shift the absorbance and emission by attaching the secondary unit to enhance the  $\pi$ -electron delocalisation (**22** and **23**). The pH of the medium can also have a great impact on the photophysical properties (specially on fluorescence) if some specific substituted groups (like the dimethylaminophenyl substituted group on **23**) are attached to the BODIPY.

#### 1.2.4. Applications of BODIPY dyes

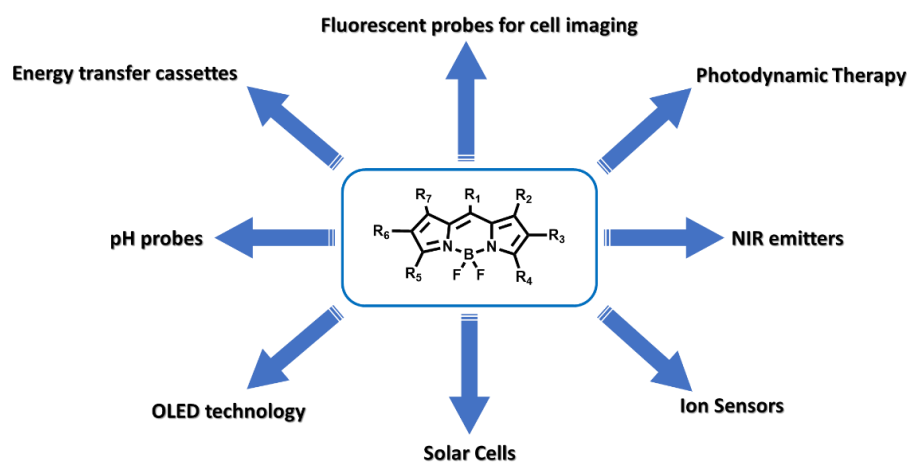
BODIPY dyes have been gaining more attention over the past 20 years, and they have been seen as molecules of interest in many research areas. In recent years, the number of published articles on BODIPY molecules has been increasing rapidly (Figure 1.16). According to the Web of Science Citation, 5957 articles were published on the topic “BODIPY” till the end of 2018.



**Figure 1.16.** Number of publications found on the Web of Science on the topics “BODIPY” or “boron dipyrromethene”.

Currently, there is a library with a few commercially available BODIPY dyes on ThermoFisherScientific® and Merck® websites, and most of them are described as a fluorescent label that can be bounded to proteins, peptides, oligonucleotides, lipids or polystyrene microspheres.<sup>129, 130</sup>

Since the first reports, BODIPYs have been studied in a wide variety of applications, such as fluorescent probes,<sup>131-134</sup> pH probes,<sup>135-138</sup> ion/molecule chelators,<sup>139-141</sup> photodynamic therapy drugs,<sup>142-144</sup> OLED active compounds,<sup>145</sup> energy transfer materials,<sup>124</sup> near-infrared emitters<sup>146, 147</sup> and active compounds for photovoltaic applications (Scheme 1.16).<sup>8, 148</sup>



**Scheme 1.16.** Applications of BODIPY frameworks.<sup>129-147</sup>

As a direct consequence of their excellent physical, chemical and biological properties, BODIPYs are among the most promising candidates for the next generation of *in vivo* fluorescent labels to target biological molecules such as amino acids, nucleotides, lipids and proteins.<sup>129-134</sup> Recently, the study of near-infrared (NIR) emitters has been developed due to their valuable ability for monitoring biological processes in living cells as a result of deep tissue penetration capability of the NIR signal and the effective elimination of tissue autofluorescence interference.<sup>142, 146, 147</sup>

Several reports have been showing the high potential of BODIPY derivatives on the detection of metal cations such as  $\text{Ni}^{2+}$ ,  $\text{K}^+$ ,  $\text{Zn}^{2+}$ ,  $\text{Hg}^{2+}$  and  $\text{Cu}^{2+}$ .<sup>89, 135, 139-141</sup> The work published by Wu and co-workers demonstrates that with the binding of  $\text{Hg}^{2+}$  the absorption band of the BODIPY chelator is blue-shifted by 29 nm due to the inhibition of the intramolecular charge transfer from the nitrogen to the BODIPY, resulting in a colour change from blue to purple and in a significant fluorescence enhancement.<sup>139</sup>

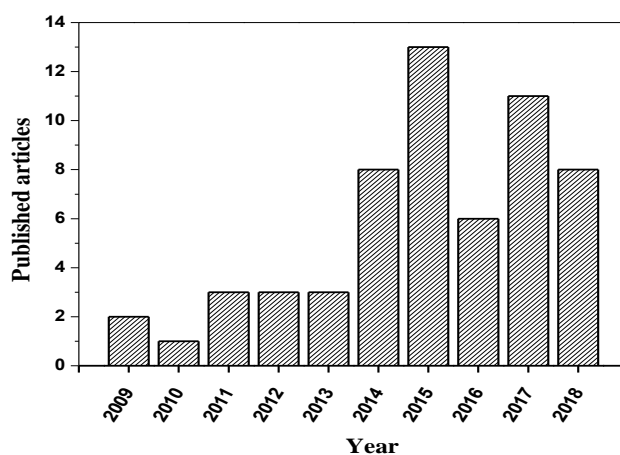
Moreover, the halogenated BODIPYs can be used to generate singlet oxygen ( $^1\text{O}_2$ ). The appropriate placing of halogens on the BODIPY core promotes spin-orbit coupling, hence intersystem crossing rate, but not energy loss from excited states.<sup>143</sup> Consequently, the studies concerning the use of BODIPYs in photodynamic therapy (PDT) are becoming more consistent.<sup>142-144</sup>

### 1.2.5. BODIPY molecules as photoactive compounds in photovoltaic cells

The research efforts on the application of BODIPY dyes in the photovoltaic area, both in dye-sensitized solar cells (DSSCs) and organic solar cells, have seen continuous

growth in the last decades. Such interest is due to their versatile structures and high absorption coefficients in the visible and NIR region. A BODIPY molecules was first used as a photosensitizer in DSSCs by Fukuzumi and co-workers in 2005, with such devices showing power conversion efficiency (PCE) values of 0.16 %.<sup>150</sup> Since then, the efficiencies of BODIPY-based DSSCs have evolved, and now the top PCE result is 6.05 %, reported by Kaneko and co-workers in 2014,<sup>151</sup> which is considered a good efficiency result when compared to all the literature of DSSCs-based solar cells.

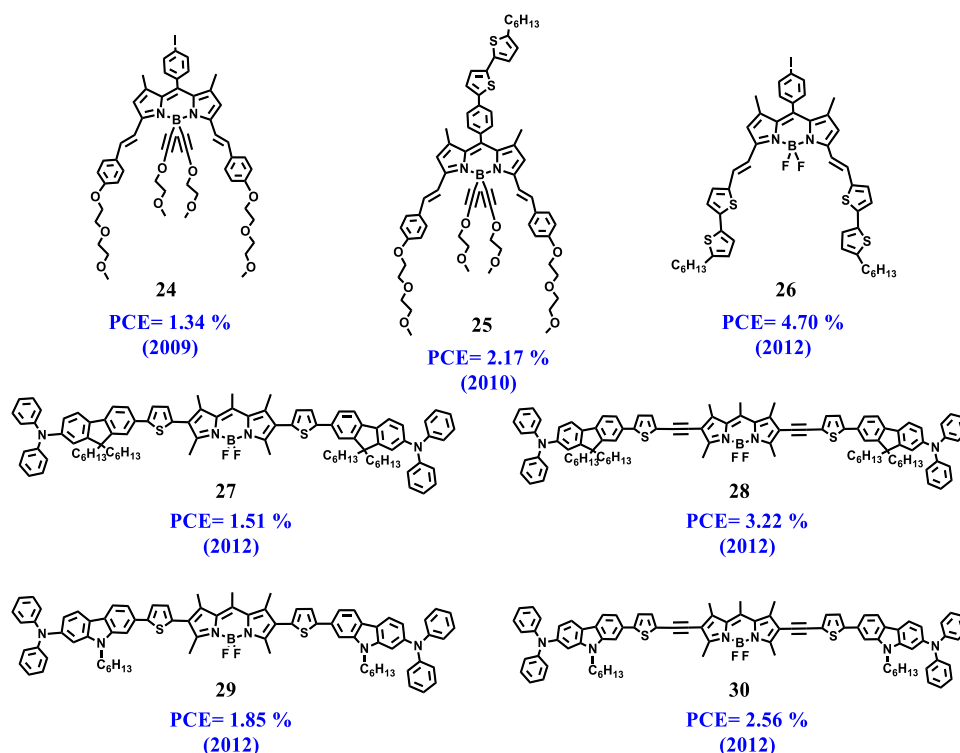
The research of BODIPY-based OPVs started in 2009, but as Figure 1.17 presents they have still not been studied with consistency, which contrasts with the other pyrrolic compounds. Although research on these compounds has increased over the last decade, it is still irregular and low. Among the 58 articles found that correlate OPVs with BODIPYs, less than a half shows a real photovoltaic application of BODIPY molecules as electron-donor or electron-acceptor materials. BODIPYs have been showing their versatility as small molecules or incorporated in polymers, and they are usually mixed with the fullerenes derivatives (PC<sub>61</sub>BM or PC<sub>71</sub>BM), where they act as excited state electron-donors.



**Figure 1.17.** Results of the search of published articles in Web of Science using the keywords “BODIPY” or “boron dipyrromethene” with “OPV” or “organic photovoltaic cells.”

The first report on BODIPY-based OPVs was published in 2009 by Roncali and co-workers.<sup>152</sup> They described the synthesis of BODIPYs having one or two styryl groups at the  $\alpha$ -position (Figure 1.18, (**24**)), with polyethylene groups to prevent aggregation in solution, and got efficiencies of 1.17 % and 1.34 %, respectively. A few months later, the authors combined both BODIPYs in a ternary blend (with PC<sub>61</sub>BM) and improved the PCE to 1.70 %, <sup>153</sup> since complementary absorptions of the BODIPY dyes increased the EQE, the J<sub>SC</sub> and the V<sub>OC</sub>. In 2010, the same group synthesised a similar structure replacing the iodide for a bithiophene group (Figure 1.18 (**25**)) and obtained OPVs with a PCE of 2.17 %.<sup>154</sup> In

the following year, the Ziesse's group published a very similar BODIPY using the bithiophene groups attached at 3,5-positions (Figure 1.18 (**26**)), and its efficiency presented a large improvement (PCE of 4.70 %).<sup>155</sup> In the same year Lin and co-workers,<sup>156</sup> with a series of four BODIPY dyes (Figure 1.18 (**27-30**)), reached efficiencies between 1.51 % and 3.22 %.

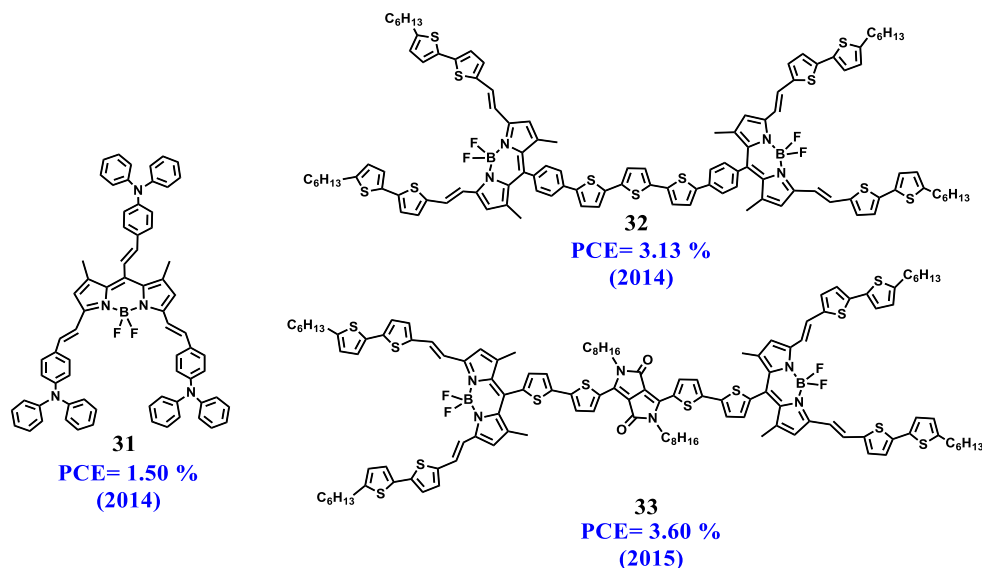


**Figure 1.18.** The best performing BODIPY small molecules used, as electron-donor species, in BHJ-OPVs between 2009 and 2012.<sup>153-156</sup>

In 2014, Akkaya and co-workers developed a BODIPY with a diphenylamino moiety linked through a styryl unit at *meso*-position (Figure 1.19 (**31**)), which allowed panchromatic sensitization by including near-IR absorption. Despite the desirable absorption features, the OPVs based on this dye obtained a maximum PCE of 1.50 %.<sup>157</sup> In the same year, Thompson and co-workers<sup>158</sup> used a lamellar architecture to obtain a power conversion efficiency up to 4.5 % with a short-circuit current ( $J_{sc}$ ) of 8.7 mA/cm<sup>2</sup> and an open-circuit voltage ( $V_{oc}$ ) of 0.8V. Each material was deposited separately during the fabrication of the devices, but spontaneous mixing of the acceptor fullerene C<sub>60</sub> and the BODIPY donor was inevitable.

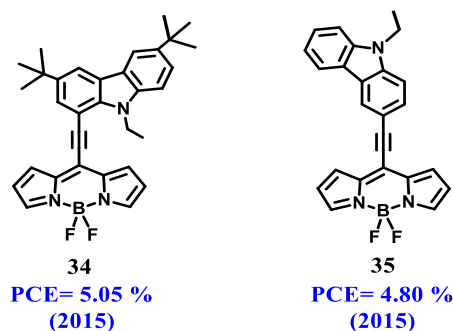
The first BODIPY dimer used in an OPV (Figure 1.19 (**32**)) was also reported in 2014 by Yao and co-workers, with a PCE of 3.13 %.<sup>159</sup> Its extended conjugation and flexible structure promote good molecular packing, allowing for a very ordered arrangement once mixed with the fullerene acceptor. In 2015 the same group used the diketopyrrolopyrrole as

linkage moiety for the BODIPY dimer (Figure 1.19 (**33**)) which led to an increase of 70 % in photocurrent and a PCE of 3.6 %.<sup>160</sup>



**Figure 1.19.** BODIPY structures reported by Akkaya and co-workers,<sup>157</sup> and the dimer structures proposed by Yao and co-workers.<sup>158, 159</sup>

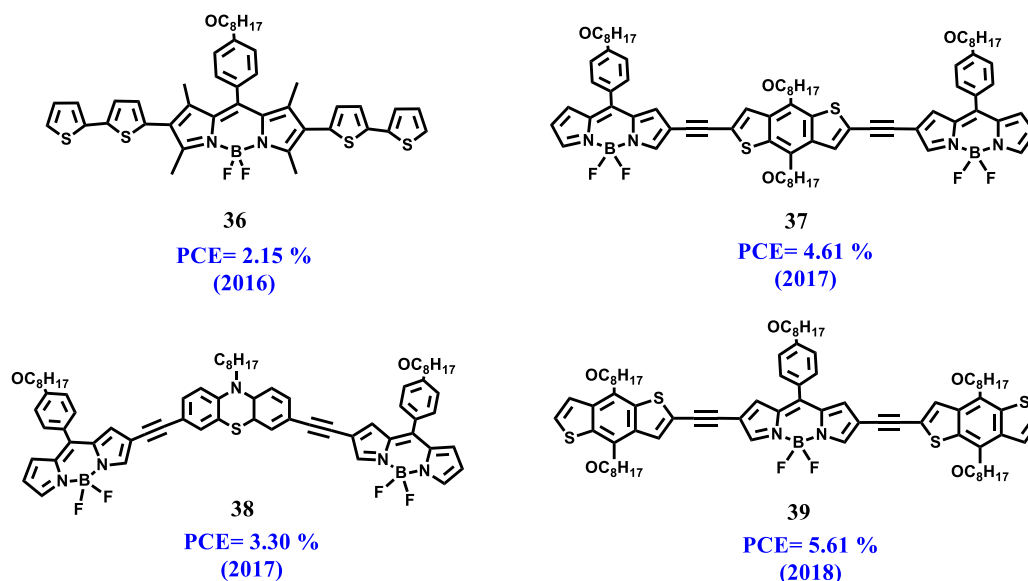
In 2015, the mark of 5 % was reached by Sharma and co-workers, with a *meso*-ethynyl BODIPYs substituted with carbazole units (Figure 1.20 (**34** and **35**)).<sup>161</sup> The molecular absorption profile led to high  $J_{SC}$  and due to their relatively low HOMO level impressive  $V_{OC}$  values (around 1 volt) were obtained. Thermal annealing and solvent annealing had a positive impact on the photovoltaic response, improving the morphology of the blends and promoting efficient charge separation and migration.



**Figure 1.20.** *Meso*-ethynylcarbazole BODIPY tested by Sharma and co-workers.<sup>161</sup>

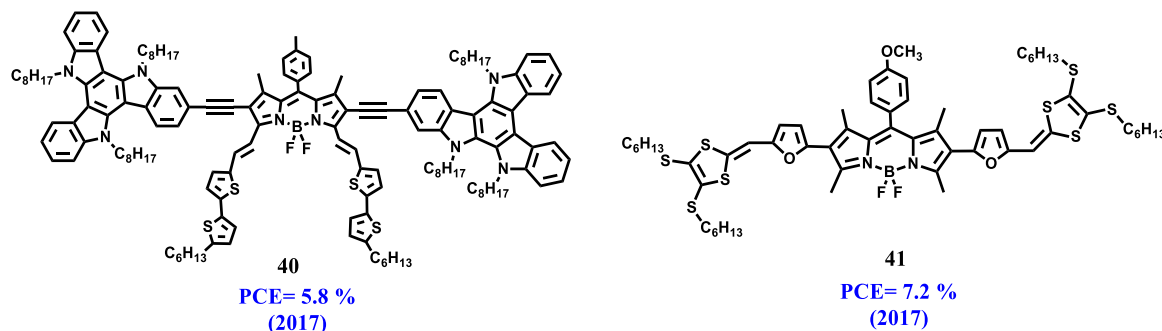
Since 2016, the research group of Zhao has been making an appreciable effort on BODIPY-based OPVs development, by using several series of novel 2,6-disubstituted BODIPY dyes.<sup>162-164</sup> The first series of BODIPY molecules, published by this group, achieved a maximum PCE of 2.15 % (Figure 1.21 (**36**)).<sup>162</sup> Then, they achieved a maximum PCE of 4.61 % with a series of  $\beta$ -alkynylated BODIPYs (Figure 1.21 (**37** and **38**)).<sup>163</sup> In

2018, the same authors went a step further reaching a 5.61 % PCE with a  $\beta$ -alkynylated BODIPY with two benzodithiophene donor moieties (Figure 1.21 (**39**)).<sup>164</sup>



**Figure 1.21.** BODIPY with the best PCE values from three reports from Zhao and co-workers.<sup>162-164</sup>

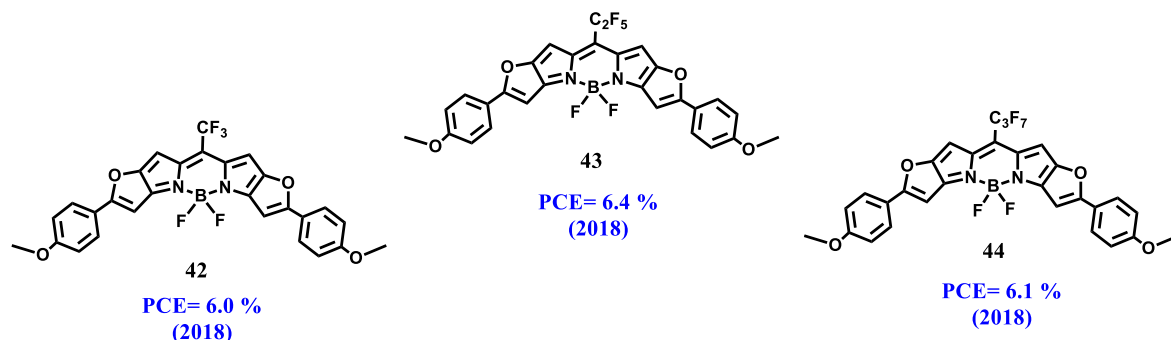
The year of 2017 brought two impressive works on BODIPY-based BHJ-OPV. Bulut and co-workers achieved 5.8 % of efficiency using the Ziesse's BODIPY scaffold with triazatruxene moieties at the 2,6-positions (Figure 1.22 (**40**)),<sup>165</sup> and Singh and co-workers established an impressive mark of 7.20 % with a new BODIPY compound with dithiafulvalene "wings" (Figure 1.22 (**41**)).<sup>166</sup> The BODIPY core acted as an electron acceptor moiety and the dithiafulvalene groups as electron-donating due to its electron-rich character and appropriate redox characteristics.<sup>166</sup> The molecule showed a broad absorption profile covering a wide range of the solar spectrum from 350 to 780 nm and extending up to NIR region. In addition to this highest efficiency (reported so far for BODIPY small molecules), this system exhibited a remarkable value of about 88.1 % of external quantum efficiency at the most favourable wavelength.



**Figure 1.22.** BODIPY small molecules reported by Bulut and co-workers<sup>165</sup> (**40**) and Singh and co-workers (**41**).<sup>166</sup>



In 2018, Tian-yi Li, Zaifei Ma and associates explored a new profile of BODIPY dyes.<sup>167</sup> Instead of using the generic *meso*-aryl-substituted, they attached perfluorinated methyl, ethyl and *n*-propyl groups at the *meso*-carbon in furan-fused BODIPYs (Figure 1.23 (42-44)). These BODIPY derivatives have a very planar structure and intense absorption in the NIR region (peak maximum at around 800 nm) with high molar extinction coefficients. The three compounds were used in OPV, by vacuum-deposition, showing PCE over 6.0 % with EQE reaching a maximum of 70 % at 790 nm.



**Figure 1.23.** Furan-fused BODIPYs applied in OPVs by Tian-yi Li, Zaifei Ma and co-workers.<sup>167</sup>

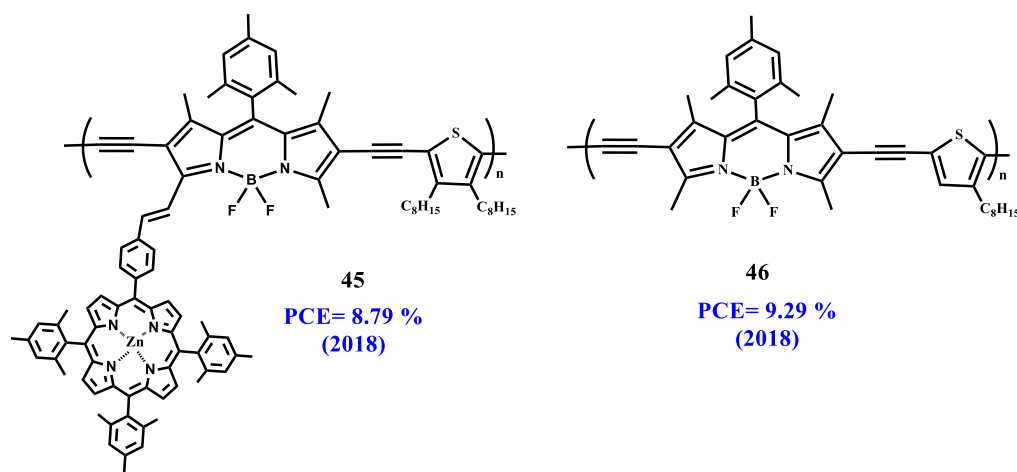
OPVs based on polymers with BODIPY moieties remain rare. In 2009, Dunuru and co-workers, prepared two NIR-emissive polymeric BODIPY dyes, by palladium-catalysed Sonogashira polymerisation of 2,6-diiodo-functionalized BODIPY monomers with 2,6-diethynyl-functionalized BODIPY monomers.<sup>168</sup> One year later, the authors applied the two polymers in OPVs blended with PC<sub>61</sub>BM.<sup>169</sup> The systems achieved PCEs of 1.3 % and 2.0 %, with a cell architecture of ITO/PEDOT:PSS/polymer:PC<sub>61</sub>BM/Al. Despite the low efficiencies, which were justified based on the poor hole transport properties of the materials, this study was very encouraging at that time since their performance was among the highest for BODIPY systems.

In 2015, Chochos and co-workers reported on a polymer with *meso*-thiophene-BODIPY and bis(thiophen-2-yl)ethene units.<sup>170</sup> When tested as a donor material in a BHJ blend with PC<sub>71</sub>BM, it led to OPVs with a very high FF (56%) but with PCE around 1%, which were justified with the ultra-low band gap (1.15 eV).

Since then, other BODIPY-based polymers were applied in OPVs exhibiting low performances,<sup>171-173</sup> but in 2018 Sharma and co-workers reported two notable works with improved photovoltaic performances.<sup>174, 175</sup> In the first, a polymer based on BODIPY dyes and thiophene units bridged by ethynyl linkers and enriched with some porphyrins units, via random formation of styryl arms on the BODIPY core (Figure 1.24 (45)), was blended with

PC<sub>71</sub>BM, leading to OPVs with 8.79 % of PCE.<sup>174</sup> The authors demonstrated that the enrichment of porphyrins units does bring advantages by comparing the photovoltaic characteristics of the polymer with and without porphyrins units. The zinc (II) porphyrin units improved the light harvesting ability of the blend and increased the J<sub>sc</sub> without affecting the V<sub>oc</sub>. The styryl functionalization was advantageous to extend the charge-separated state.

In that same year, the same research group went further, by presenting a system with a donor BODIPY-based polymer (Figure 1.24 (46)) reaching a PCE of 9.29 %. The structure of the polymer is very similar to (Figure 1.24 (45)) except for the porphyrin moiety), but instead of using the PC<sub>71</sub>BM or other typical fullerene derivative acceptor species, the authors employed a low band gap non-fullerene acceptor compound, consisting of carbazole and diketopyrrolopyrrole units linked with a tetracyanobutadiene acceptor  $\pi$ -linker.<sup>175</sup>

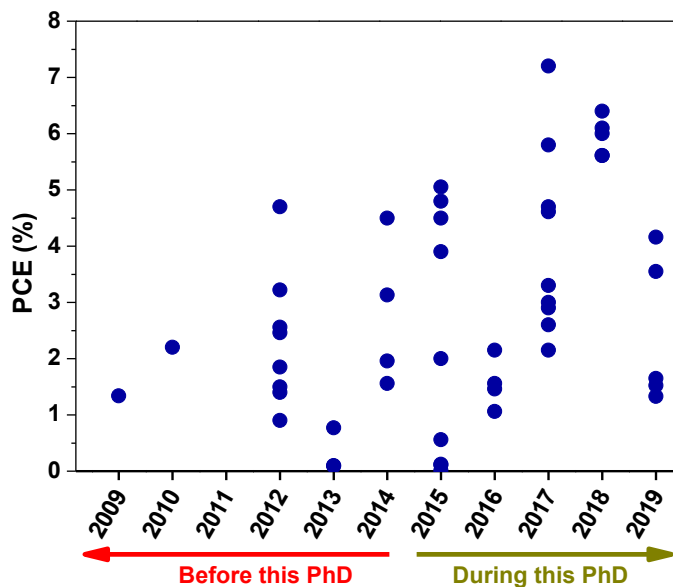


**Figure 1.24.** BODIPY based-polymers reported by Sharma and co-workers.<sup>174, 175</sup>

The authors related the outstanding PCE result with the tailoring of the BODIPY polymer where the ethynyl bridges can facilitate the intra and intermolecular interactions and the mobility of the charges, but also with the quite lower energy loss that this non-fullerene blend showed as compared to a blend with PC<sub>71</sub>BM.<sup>175</sup>

### 1.3. Thesis objectives and outline

Despite the growing interest that BODIPY derivatives have been receiving, when this PhD work began only a few articles had been published relating the use of BODIPY molecules (as small molecule, polymer or in a multichromophoric model) in OPVs, and the biggest PCE value was 5.05 % (Figure 1.25). Since then, big steps were taken concerning the photovoltaic performance, but the research effort is still low.



**Figure 1.25.** Best PCE values from all published BODIPY small molecules (49 different structures) tested as electron-donor species in OPVs. The data refers to BODIPY-based OPV that can have different active layer's architecture or distinct procedures (e.g. diverse electron-acceptor species, temperatures or additives). The results reported in this thesis are not represented in this chart.

Generally, the BODIPY small molecules applied in OPVs, are obtained through intricate reactions with several reaction steps, laborious purification processes and little yields. In view of this assessment, we conclude that the BODIPY molecules should be obtained from fast, easy and productive synthesis reactions, to preserve the economic and ecological perspective of organic solar cells. The novelty of the BODIPY structures, the understanding of their main characteristics and a thorough photovoltaic study were the main goals of this thesis, aiming to obtain new and important structure-activity correlations in order to support and contribute to the development of OPVs.

Hence, the second chapter of this PhD thesis reports a series of BODIPY dyes, which are the basis of the entire work. New features about the synthesis and characterisation are reported, and BODIPYs without pre- or post-functionalization were, for the first time, tested in OPVs.

The third and fourth chapters report the enhancement of  $\pi$ -electron delocalisation, resulting from the linkage of some donor moieties into the BODIPY core, by the Knoevenagel reaction. The two series of BODIPY dyes present some new structures that were fully characterised. This functionalization changes the main properties of BODIPY dyes, giving a significant boost in the photovoltaic performance.

The fifth chapter focuses on a new series of BODIPY functionalization at the boron atom and how the different ligands can change the chemical properties and photovoltaic response.

The sixth chapter follows the idea of using multichromophores in OPVs. This section explored the conjugation of BODIPY with porphyrin. Thus, we presented a non-explored synthetic path, three new structures and their OPV result tests, as donor species in a bulk active layer (blended with PC<sub>71</sub>BM).

This thesis describes the synthesis of more than thirty BODIPY derivatives. All are fully characterised and the assessment of their potential as electron-donor (or electron-acceptor) species was made. The majority of BODIPY derivatives were tested in OPVs with a considerable variance of efficiencies, having some of them very appreciable results.

#### 1.4. References for Chapter 1

1. Enerdate, *Global Energy Statistical Yearbook 2018*, <https://yearbook.enerdata.net/>, accessed March 2019.
2. A. Jäger-Waldau, *Green*, **2011**, 1, 277-290.
3. A. Jäger-Waldau, *Energies*, **2019**, 12, 769.
4. A. L. Fahrenbruch and R. H. Bube, in *Fundamentals of Solar Cells*, Academic Press, ISBN:9780323145381, Stanford, **1983**, 1-25.
5. B. R. Wheaton, in *Compendium of Quantum Physics*, Springer Berlin Heidelberg, ISBN:9783540706267, Berlin, **2009**, 143, 472-475.
6. A. Change McClelland, & Mankin, M., in *Optical Measurements for Scientists and Engineers: A Practical Guide*, Cambridge University Press, ISBN:9781107173019, Cambridge, **2018**, 284-286.
7. L. Bucher, N. Desbois, P. D. Harvey, G. D. Sharma and C. P. Gros, *Solar RRL*, **2017**, 1, 1700127.
8. P. Kumar, *Organic Solar Cells: Device Physics, Processing, Degradation, and Prevention*, CRS Press, ISBN:9781498723275, New York, **2017**, 233.
9. L. M. Fraas, *Low-Cost Solar Electric Power*, Springer International Publishing, ISBN:9783319075303, New York, **2014**, 1-13.
10. T. D. Lee and A. U. Ebong, *Renewable & Sustainable Energy Reviews*, **2017**, 70, 1286-1297
11. H. Heriche, Z. Rouabah and N. Bouarissa, *Optik*, **2016**, 127, 11751-11757.
12. W. A. Badawy, *Journal of Advanced Research.*, **2015**, 6, 123-132.
13. N. Asim, K. Sopian, S. Ahmadi, K. Saeedfar, M. A. Alghoul, O. Saadatian and S. H. Zaidi, *Renewable and Sustainable Energy Reviews*, **2012**, 16, 5834-5847.
14. M. A. Green, K. Emery, Y. Hishikawa, W. Warta and E. D. Dunlop, *Progress in Photovoltaics: Research and Applications*, **2013**, 21, 1-11.
15. A. J. Nozik, *Physica E*, **2002**, 14, 115-120.
16. J. P. Correa-Baena, M. Saliba, T. Buonassisi, M. Gratzel, A. Abate, W. Tress and A. Hagfeldt, *Science*, **2017**, 358, 739-744.
17. M. K. Nazeeruddin, E. Baranoff and M. Grätzel, *Solar Energy*, **2011**, 85, 1172-1178.
18. C. R. Kagan, E. Lifshitz, E. H. Sargent and D. V. Talapin, *Science*, **2016**, 353, 9.
19. O. A. Abdulrazaq, V. Saini, S. Bourdo, E. Dervishi and A. S. Biris, *Particulate Science and Technology*, **2013**, 31, 427-442.
20. G. Conibeer, *Materials Today*, **2007**, 10, 42-50.
21. K. Sharma, V. Sharma and S. S. Sharma, *Nanoscale Research Letters*, **2018**, 13, 381.
22. A. Carella, F. Borbone and R. Centore, *Frontiers in Chemistry*, **2018**, 6, 481.
23. NREL, Best Research-Cell Efficiency Chart, <https://www.nrel.gov/>, accessed March, 2019.

24. X. Che, Y. Li, Y. Qu and S. R. Forrest, *Nature Energy*, **2018**, 3, 422-427.
25. W. A. Luhman and R. J. Holmes, *Advanced Functional Materials*, **2011**, 21, 764-771.
26. D. Carsten and D. Vladimir, *Reports on Progress in Physics*, **2010**, 73, 096401.
27. A. K. Ghosh and T. Feng, *Journal of Applied Physics*, **1978**, 49, 5982-5989.
28. S. C. Ameta and R. Ameta, *Solar Energy Conversion and Storage: Photochemical Modes*, Taylor & Francis, ISBN: 9781482246308, Boca Raton, **2015**, 54-84.
29. J. Brebels, J. V. Manca, L. Lutsen, D. Vanderzande and W. Maes, *Journal of Materials Chemistry A*, **2017**, 5, 24037-24050.
30. C. Deibel, V. Dyakonov and C. J. Brabec, *Journal of Selected Topics in Quantum Electronics*, **2010**, 16, 1517-1527.
31. C. W. Tang, *Applied Physics Letters*, **1986**, 48, 183-185.
32. N. Yeh and P. Yeh, *Renewable and Sustainable Energy Reviews*, **2013**, 21, 421-431.
33. M. C. Scharber and N. S. Sariciftci, *Progress in Polymer Science*, **2013**, 38, 1929-1940.
34. M.-H. Jao, H.-C. Liao and W.-F. Su, *Journal of Materials Chemistry A*, **2016**, 4, 5784-5801.
35. S. Honda, H. Ohkita, H. Benten and S. Ito, *Chemical Communications*, **2010**, 46, 6596-6598.
36. M. M. Stylianakis, D. Konios, G. Kakavelakis, G. Charalambidis, E. Stratakis, A. G. Coutsolelos, E. Kymakis and S. H. Anastasiadis, *Nanoscale*, **2015**, 7, 17827-17835.
37. J. Farinhas, R. Oliveira, R. Hansson, L. K. E. Ericsson, E. Moons, J. Morgado and A. Charas, *Organic Electronics*, **2017**, 41, 130-136.
38. P. Cheng, J. Y. Wang, Q. Q. Zhang, W. C. Huang, J. S. Zhu, R. Wang, S. Y. Chang, P. Y. Sun, L. Meng, H. X. Zhao, H. W. Cheng, T. Y. Huang, Y. Q. Liu, C. C. Wang, C. H. Zhu, W. You, X. W. Zhan and Y. Yang, *Advanced Materials*, **2018**, 30.
39. T. M. Grant, T. Gorisse, O. Dautel, G. Wantz and B. H. Lessard, *Journal of Materials Chemistry A*, **2017**, 5, 1581-1587.
40. Y.-C. Chen, C.-Y. Hsu, R. Y.-Y. Lin, K.-C. Ho and J. T. Lin, *ChemSusChem*, **2013**, 6, 20-35.
41. M. Riede, T. Mueller, W. Tress, R. Schueppel and K. Leo, *Nanotechnology*, **2008**, 19, 424001.
42. A. K. Haghi, D. Balköse and S. Thomas, *Applied Physical Chemistry with Multidisciplinary Approaches*, Taylor & Francis, ISBN: 9781315169415, New York, **2018**, 107-135.
43. R. Steim, *The Impact of Interfaces on the Performance of Organic Photovoltaic Cells*, KIT Scientific Publishing, ISBN: 9783866445260, Karlsruhe, **2010**, 38-54.
44. H. P. Kim, A. R. b. M. Yusoff, H. J. Lee, S. J. Lee, H. M. Kim, G. J. Seo, J. H. Youn and J. Jang, *Nanoscale Research Letters*, **2014**, 9, 323.
45. T.-H. Lai, S.-W. Tsang, J. R. Manders, S. Chen and F. So, *Materials Today*, **2013**, 16, 424-432.
46. K. Wang, C. Liu, T. Meng, C. Yi and X. Gong, *Chemical Society Reviews*, **2016**, 45, 2937-2975.

47. H. Zhang, C. Wang, X. Li, J. Jing, Y. Sun and Y. liu, *Solar Energy*, **2017**, 157, 71-80.
48. J. Peet, C. Soci, R. C. Coffin, T. Q. Nguyen, A. Mikhailovsky, D. Moses and G. C. Bazan, *Applied Physics Letters*, **2006**, 89, 252105.
49. L. Li, L. Xiao, H. Qin, K. Gao, J. Peng, Y. Cao, F. Liu, T. P. Russell and X. Peng, *ACS Applied Materials & Interfaces*, **2015**, 7, 21495-21502.
50. B. Gao and J. Meng, *Journal of Electronic Materials*, **2018**, 47, 4016-4021.
51. H.-C. Liao, C.-C. Ho, C.-Y. Chang, M.-H. Jao, S. B. Darling and W.-F. Su, *Materials Today*, **2013**, 16, 326-336.
52. S. Holliday, Y. Li and C. K. Luscombe, *Progress in Polymer Science*, **2017**, 70, 34-51.
53. T. Zhang, H. Han, Y. Zou, Y.-C. Lee, H. Oshima, K.-T. Wong and R. J. Holmes, *ACS Applied Materials & Interfaces*, **2017**, 9, 25418-25425.
54. M. C. Scharber, D. Mühlbacher, M. Koppe, P. Denk, C. Waldauf, A. J. Heeger and C. J. Brabec, *Advanced Materials*, **2006**, 18, 789-794.
55. C. J. Brabec, A. Cravino, D. Meissner, N. S. Sariciftci, T. Fromherz, M. T. Rispens, L. Sanchez and J. C. Hummelen, *Advanced Functional Materials*, **2001**, 11, 374-380.
56. J. Liu, Y. Shi and Y. Yang, *Advanced Functional Materials*, **2001**, 11, 420-424.
57. H. Frohne, S. E. Shaheen, C. J. Brabec, D. C. Müller, N. S. Sariciftci and K. Meerholz, *ChemPhysChem*, **2002**, 3, 795-799.
58. S. Rafique, S. M. Abdullah, K. Sulaiman and M. Iwamoto, *Renewable and Sustainable Energy Reviews*, **2018**, 84, 43-53.
59. J. D. Servaites, M. A. Ratner and T. J. Marks, *Energy & Environmental Science*, **2011**, 4, 4410-4422.
60. B. P. Rand, J. Genoe, P. Heremans and J. Poortmans, *Progress in Photovoltaics: Research and Applications*, **2007**, 15, 659-676.
61. A. K. Kyaw, M. F. Yang, X. W. Sun, *Solar Cell asan Energy Harvesting Device*, Wiley, ISBN: 978-3527328697, **2011**, 463-569
62. R. Ilmi, A. Haque and M. S. Khan, *Organic Electronics*, **2018**, 58, 53-62.
63. S. Li, L. Ye, W. Zhao, H. Yan, B. Yang, D. Liu, W. Li, H. Ade and J. Hou, *Journal of the American Chemical Society*, **2018**, 140, 7159-7167.
64. Y. Chen, X. Wan and G. Long, *Accounts of Chemical Research*, **2013**, 46, 2645-2655.
65. J. Zhang, L. Zhu and Z. Wei, *Small Methods*, **2017**, 1, 1700258.
66. J. Roncali, *Accounts of Chemical Research*, **2009**, 42, 1719-1730.
67. F. F. Runge, *Annalen der Physik*, **1834**, 107, 65-78.
68. A. Baeyer and A. Emmerling, *Berichte chemischen Gesellschaft*, **1870**, 3, 514-517.
69. A. Treibs and F.-H. Kreuzer, *Justus Liebigs Annalen der Chemie*, **1968**, 718, 208-223.
70. M. Shah, K. Thangaraj, M.-L. Soong, L. T. Welford, J. H. Boyer, I. R. Politzer and T. G. Pavlopoulos, *Heteroatom Chemistry*, **1990**, 1, 389-399.

71. T. G. Pavlopoulos, J. H. Boyer, K. Thangaraj, G. Sathyamoorthi, M. P. Shah and M.-L. Soong, *Applied Optics.*, **1992**, 31, 7089-7094.
72. G. Ulrich, R. Ziessel and A. Harriman, *Angewandte Chemie International Edition*, **2008**, 47, 1184-1201.
73. F. Heisig, S. Gollos, S. J. Freudenthal, A. El-Tayeb, J. Iqbal and C. E. Müller, *Journal of Fluorescence*, **2014**, 24, 213-230.
74. K. Krumova and G. Cosa, *Journal of the American Chemical Society*, **2010**, 132, 17560-17569.
75. D. Wang, J. Fan, X. Gao, B. Wang, S. Sun and X. Peng, *The Journal of Organic Chemistry*, **2009**, 74, 7675-7683.
76. N. Boens, V. Leen and W. Dehaen, *Chemical Society Reviews*, **2012**, 41, 1130-1172.
77. J. H. Boyer, A. M. Haag, G. Sathyamoorthi, M.-L. Soong, K. Thangaraj and T. G. Pavlopoulos, *Heteroatom Chemistry*, **1993**, 4, 39-49.
78. A. Loudet and K. Burgess, *Chemical Reviews*, **2007**, 107, 4891-4932.
79. V. P. Yakubovskiy, M. P. Shandura and Y. P. Kovtun, *European Journal of Organic Chemistry*, **2009**, 3237-3243.
80. L. N. Sobenina, A. M. Vasil'tsov, O. V. Petrova, K. B. Petrushenko, I. A. Ushakov, G. Clavier, R. Meallet-Renault, A. I. Mikhaleva and B. A. Trofimov, *Organic Letters*, **2011**, 13, 2524-2527.
81. C. Tahtaoui, C. Thomas, F. Rohmer, P. Klotz, G. Duportail, Y. Mély, D. Bonnet and M. Hibert, *The Journal of Organic Chemistry*, **2007**, 72, 269-272.
82. J.-S. Lee, N.-y. Kang, Y. K. Kim, A. Samanta, S. Feng, H. K. Kim, M. Vendrell, J. H. Park and Y.-T. Chang, *Journal of the American Chemical Society*, **2009**, 131, 10077-10082.
83. L. A. B. Kramer G. W. , Midland M. M., *Synthesis and Reactivity in Inorganic and Metal-Organic Chemistry*, **1976**, 6, 249-250.
84. N. Boens, B. Verbelen and W. Dehaen, *European Journal of Organic Chemistry*, **2015**, 2015, 6577-6595.
85. S. Y. Moon, N. R. Cha, Y. H. Kim and S.-K. Chang, *The Journal of Organic Chemistry*, **2004**, 69, 181-183.
86. R. F. Ziessel, G. Ulrich, L. Charbonniere, D. Imbert, R. Scopelliti and J. C. G. Bunzli, *Chemistry – A European Journal*, **2006**, 12, 5060-5067.
87. M. Galletta, S. Campagna, M. Quesada, G. Ulrich and R. Ziessel, *Chemical Communications*, **2005**, 33, 4222-4224.
88. S. L. Niu, C. Massif, G. Ulrich, R. Ziessel, P.-Y. Renard and A. Romieu, *Organic & Biomolecular Chemistry*, **2011**, 9, 66-69.
89. S. Zhu, J. Zhang, G. Vegesna, F.-T. Luo, S. A. Green and H. Liu, *Organic Letters*, **2011**, 13, 438-441.
90. Y. Gabe, Y. Urano, K. Kikuchi, H. Kojima and T. Nagano, *Journal of the American Chemical Society*, **2004**, 126, 3357-3367.



91. Y. S. Marfin, M. V. Shipalova, V. O. Kurzin, K. V. Ksenofontova, A. V. Solomonov and E. V. Rumyantsev, *Journal of Fluorescence*, **2016**, 26, 2105-2112.
92. T. Ueno, Y. Urano, H. Kojima and T. Nagano, *Journal of the American Chemical Society*, **2006**, 128, 10640-10641.
93. P. Oleynik, Y. Ishihara and G. Cosa, *Journal of the American Chemical Society*, **2007**, 129, 1842-1843.
94. V. Leen, P. Yuan, L. Wang, N. Boens and W. Dehaen, *Organic Letters*, **2012**, 14, 6150-6153.
95. M. J. Plater, S. Aiken and G. Bourhill, *Tetrahedron*, **2002**, 58, 2405-2413.
96. T. Rohand, M. Baruah, W. Qin, N. Boens and W. Dehaen, *Chemical Communications*, **2006**, 266-268.
97. L. Li, B. Nguyen and K. Burgess, *Bioorganic & Medicinal Chemistry Letters*, **2008**, 18, 3112-3116.
98. Z. Feng, L. Jiao, Y. Feng, C. Yu, N. Chen, Y. Wei, X. Mu and E. Hao, *The Journal of Organic Chemistry*, **2016**, 81, 6281-6291.
99. B. Verbelen, S. Boodts, J. Hofkens, N. Boens and W. Dehaen, *Angewandte Chemie International Edition*, **2015**, 54, 4612-4616.
100. G. Duran-Sampedro, A. R. Agarrabeitia, I. Garcia-Moreno, A. Costela, J. Bañuelos, T. Arbeloa, I. López Arbeloa, J. L. Chiara and M. J. Ortiz, *European Journal of Organic Chemistry*, **2012**, 2012, 6335-6350.
101. T. Rohand, W. Qin, N. Boens and W. Dehaen, *European Journal of Organic Chemistry*, **2006**, 2006, 4658-4663.
102. O. Buyukcikir, O. A. Bozdemir, S. Kolemen, S. Erbas and E. U. Akkaya, *Organic Letters*, **2009**, 11, 4644-4647.
103. S. Madhu, M. R. Rao, M. S. Shaikh and M. Ravikanth, *Inorganic Chemistry*, **2011**, 50, 4392-4400.
104. E. Heyer and R. Ziessel, *The Journal of Organic Chemistry*, **2015**, 80, 6737-6753.
105. Z. Biyiklioglu and T. Keleş, *Inorganica Chimica Acta*, **2017**, 466, 130-138.
106. T. Arslan, T. Keleş, B. Barut, A. Özel and Z. Biyiklioglu, *Inorganica Chimica Acta*, **2018**, 471, 121-125.
107. G. Sathyamoorthi, L. T. Wolford, A. M. Haag and J. H. Boyer, *Heteroatom Chemistry*, **1994**, 5, 245-249.
108. A. Haefele, C. Zedde, P. Retailleau, G. Ulrich and R. Ziessel, *Organic Letters*, **2010**, 12, 1672-1675.
109. M. Vincent, E. Beabout, R. Bennett and P. Hewavitharanage, *Tetrahedron Letters*, **2013**, 54, 2050-2054.
110. S. Banfi, E. Caruso, S. Zaza, M. Mancini, M. B. Gariboldi and E. Monti, *Journal of Photochemistry and Photobiology B: Biology*, **2012**, 114, 52-60.
111. V. Leen, E. Braeken, K. Luckermans, C. Jackers, M. Van der Auweraer, N. Boens and W. Dehaen, *Chemical Communications*, 2009, 4515-4517.

112. T. G. Pavlopoulos, J. H. Boyer, M. Shah, K. Thangaraj and M.-L. Soong, *Applied Optics*, **1990**, 29, 3885-3886.
113. D. J. Joshi, M. Jun, L. Yang, A. J. Lough and H. Yan, *Acta crystallographica. Section E, Crystallographic communications*, **2018**, 74, 103-108.
114. A. Nierth, A. Y. Kobitski, G. U. Nienhaus and A. Jäschke, *Journal of the American Chemical Society*, **2010**, 132, 2646-2654.
115. F. Heisig, S. Gollos, S. J. Freudenthal, A. El-Tayeb, J. Iqbal and C. E. Muller, *Journal of Fluorescence*, **2014**, 24, 213-230.
116. C. Yu, L. Jiao, H. Yin, J. Zhou, W. Pang, Y. Wu, Z. Wang, G. Yang and E. Hao, *European Journal of Organic Chemistry*, **2011**, 2011, 5460-5468.
117. M. Üçüncü, E. Karakuş and M. Emrulloğlu, *New Journal of Chemistry*, **2015**, 39, 8337-8341.
118. A. Kamkaew, S. H. Lim, H. B. Lee, L. V. Kiew, L. Y. Chung and K. Burgess, *Chemical Society Reviews*, **2013**, 42, 77-88.
119. C. Bellomo, M. Chaari, J. Cabrera-González, M. Blangetti, C. Lombardi, A. Deagostino, C. Viñas, N. Gaztelumendi, C. Nogués, R. Nuñez and C. Prandi, *Chemistry – A European Journal*, **2018**, 24, 15622-15630.
120. G. Li, Y. Otsuka, T. Matsumiya, T. Suzuki, J. Li, M. Takahashi and K. Yamada, *Materials*, **2018**, 11, 1297.
121. E. Palao, T. Slanina and P. Klán, *Chemical Communications*, **2016**, 52, 11951-11954.
122. B. Sui, M. V. Bondar, D. Anderson, H. J. Rivera-Jacquez, A. E. Masunov and K. D. Belfield, *The Journal of Physical Chemistry C*, **2016**, 120, 14317-14329.
123. H. Chong, H.-A. Lin, M.-Y. Shen, C.-Y. Liu, H. Zhao and H.-h. Yu, *Organic Letters*, **2015**, 17, 3198-3201.
124. A. Harriman, G. Izzet and R. Ziessel, *Journal of the American Chemical Society*, **2006**, 128, 10868-10875.
125. E. Bodio and C. Goze, *Dyes and Pigments*, **2019**, 160, 700-710.
126. T. Lundrigan, S. M. Crawford, T. S. Cameron and A. Thompson, *Chemical Communications*, **2012**, 48, 1003-1005.
127. A. L. Nguyen, K. E. Griffin, Z. Zhou, F. R. Fronczek, K. M. Smith and M. G. H. Vicente, *New Journal of Chemistry*, **2018**, 42, 8241-8246.
128. P. Didier, G. Ulrich, Y. Mély and R. Ziessel, *Organic & Biomolecular Chemistry*, **2009**, 7, 3639-3642.
129. Search for BODIPY; <https://www.thermofisher.com>, accessed July 2019.
130. Search for BOIDIPY; <https://www.sigmaaldrich.com>, accessed July 2019.
131. C. T. Arranja, A. Aguiar, T. Encarnação, S. M. Fonseca, L. L. G. Justino, R. A. E. Castro, A. Benniston, A. Harriman, H. D. Burrows and A. J. F. N. Sobral, *Journal of Molecular Structure*, **2017**, 1146, 62-69.
132. T. Ehenschwender and H.-A. Wagenknecht, *The Journal of Organic Chemistry*, **2011**, 76, 2301-2304.

133. P. S. Deore, D. V. Soldatov and R. A. Manderville, *Scientific reports*, **2018**, 8, 16874-16874.
134. J.-J. Lee, S.-C. Lee, D. Zhai, Y.-H. Ahn, H. Y. Yeo, Y. L. Tan and Y.-T. Chang, *Chemical Communications*, **2011**, 47, 4508-4510.
135. E. Okutan, S. O. Tümay and S. Yeşilot, *Journal of Fluorescence*, **2016**, 26, 2333-2343.
136. R. Gotor, P. Ashokkumar, M. Hecht, K. Keil and K. Rurack, *Analytical Chemistry*, **2017**, 89, 8437-8444.
137. S. Hoogendoorn, A. E. M. Blom, L. I. Willems, G. A. van der Marel and H. S. Overkleeft, *Organic Letters*, **2011**, 13, 5656-5659.
138. Z. Li, L.-J. Li, T. Sun, L. Liu and Z. Xie, *Dyes and Pigments*, **2016**, 128, 165-169.
139. M. Vedamalai and S.-P. Wu, *Organic & Biomolecular Chemistry*, **2012**, 10, 5410-5416.
140. W.-J. Shi, J.-Y. Liu and D. K. P. Ng, *Chemistry – An Asian Journal*, **2012**, 7, 196-200.
141. S. C. Dodani, Q. He and C. J. Chang, *Journal of the American Chemical Society*, **2009**, 131, 18020-18021.
142. Y. Liu, Z. Li, L. Chen and Z. Xie, *Dyes and Pigments*, **2017**, 141, 5-12.
143. M. Gorbe, A. M. Costero, F. Sancenón, R. Martínez-Mañez, R. Ballesteros-Cillero, L. E. Ochando, K. Chulvi, R. Gotor and S. Gil, *Dyes and Pigments*, **2019**, 160, 198-207.
144. J. Zou, Z. Yin, K. Ding, Q. Tang, J. Li, W. Si, J. Shao, Q. Zhang, W. Huang and X. Dong, *ACS Applied Materials & Interfaces*, **2017**, 9, 32475-32481.
145. A. Zampetti, A. Minotto, B. M. Squeo, V. G. Gregoriou, S. Allard, U. Scherf, C. L. Chocho and F. Cacialli, *Scientific Reports*, **2017**, 7, 1611.
146. Y. Ni and J. Wu, *Organic & Biomolecular Chemistry*, **2014**, 12, 3774-3791.
147. L. Sansalone, S. Tang, J. Garcia-Amorós, Y. Zhang, S. Nonell, J. D. Baker, B. Captain and F. M. Raymo, *ACS Sensors*, **2018**, 3, 1347-1353.
148. S. P. Singh and T. Gayathri, *European Journal of Organic Chemistry*, **2014**, 22, 4689-4707.
149. F. Han, Y. Xu, D. Jiang, Y. Qin and H. Chen, *Analytical Biochemistry*, **2013**, 435, 106-113.
150. S. Hattori, K. Ohkubo, Y. Urano, H. Sunahara, T. Nagano, Y. Wada, N. V. Tkachenko, H. Lemmetyinen and S. Fukuzumi, *The Journal of Physical Chemistry B*, **2005**, 109, 15368-15375.
151. Y. Kubo, D. Eguchi, A. Matsumoto, R. Nishiyabu, H. Yakushiji, K. Shigaki and M. Kaneko, *Journal of Materials Chemistry A*, **2014**, 2, 5204-5211.
152. T. Rousseau, A. Cravino, T. Bura, G. Ulrich, R. Ziessel and J. Roncali, *Chemical Communications*, **2009**, 13, 1673-1675.
153. T. Rousseau, A. Cravino, T. Bura, G. Ulrich, R. Ziessel and J. Roncali, *Journal of Materials Chemistry*, **2009**, 19, 2298-2300.
154. T. Rousseau, A. Cravino, E. Ripaud, P. Leriche, S. Rihn, A. De Nicola, R. Ziessel and J. Roncali, *Chemical Communications*, **2010**, 46, 5082-5084.
155. T. Bura, N. Leclerc, S. Fall, P. Lévéque, T. Heiser, P. Retailleau, S. Rihn, A. Mirloup and R. Ziessel, *Journal of the American Chemical Society*, **2012**, 134, 17404-17407.

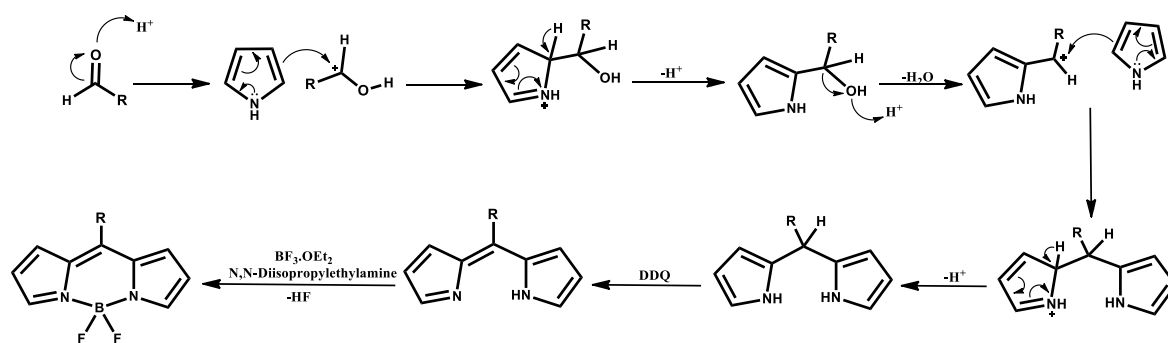
156. H.-Y. Lin, W.-C. Huang, Y.-C. Chen, H.-H. Chou, C.-Y. Hsu, J. T. Lin and H.-W. Lin, *Chemical Communications*, **2012**, 48, 8913-8915.
157. S. Kolemen, Y. Cakmak, T. Ozdemir, S. Erten-Ela, M. Buyuktemiz, Y. Dede and E. U. Akkaya, *Tetrahedron*, **2014**, 70, 6229-6234.
158. J. J. Chen, S. M. Conron, P. Erwin, M. Dimitriou, K. McAlahney and M. E. Thompson, *ACS Applied Materials & Interfaces*, **2015**, 7, 662-669.
159. W. Liu, A. Tang, J. Chen, Y. Wu, C. Zhan and J. Yao, *ACS Applied Materials & Interfaces*, **2014**, 6, 22496-22505.
160. W. Liu, J. Yao and C. Zhan, *RSC Advances*, **2015**, 5, 74238-74241.
161. T. Jadhav, R. Misra, S. Biswas and G. D. Sharma, *Physical Chemistry Chemical Physics*, **2015**, 17, 26580-26588.
162. J. Liao, H. Zhao, Y. Xu, Z. Cai, Z. Peng, W. Zhang, W. Zhou, B. Li, Q. Zong and X. Yang, *Dyes and Pigments*, **2016**, 128, 131-140.
163. J. Liao, Y. Xu, H. Zhao, Q. Zong and Y. Fang, *Organic Electronics*, **2017**, 49, 321-333.
164. J. Liao, H. Zhao, Z. Cai, Y. Xu, F. G. F. Qin, Q. Zong, F. Peng and Y. Fang, *Organic Electronics*, **2018**, 61, 215-222.
165. I. Bulut, Q. Huahlmé, A. Mirloup, P. Chávez, S. Fall, A. Hébraud, S. Méry, B. Heinrich, T. Heiser, P. Lévêque and N. Leclerc, *ChemSusChem*, **2017**, 10, 1878-1882.
166. R. Srinivasa Rao, A. Bagui, G. Hanumantha Rao, V. Gupta and S. P. Singh, *Chemical Communications*, **2017**, 53, 6953-6956.
167. T.-y. Li, J. Benduhn, Y. Li, F. Jaiser, D. Spoltore, O. Zeika, Z. Ma, D. Neher, K. Vandewal and K. Leo, *Journal of Materials Chemistry A*, **2018**, 6, 18583-18591.
168. V. R. Donuru, G. K. Vegesna, S. Velayudham, S. Green and H. Liu, *Chemistry of Materials*, **2009**, 21, 2130-2138.
169. B. Kim, B. Ma, V. R. Donuru, H. Liu and J. M. J. Fréchet, *Chemical Communications*, **2010**, 46, 4148-4150.
170. B. M. Squeo, N. Gasparini, T. Ameri, A. Palma-Cando, S. Allard, V. G. Gregoriou, C. J. Brabec, U. Scherf and C. L. Chochos, *Journal of Materials Chemistry A*, **2015**, 3, 16279-16286.
171. D. Cortizo-Lacalle, C. T. Howells, S. Gambino, F. Vilela, Z. Vobecka, N. J. Findlay, A. R. Inigo, S. A. J. Thomson, P. J. Skabara and I. D. W. Samuel, *Journal of Materials Chemistry*, **2012**, 22, 14119-14126.
172. S. P. Economopoulos, C. L. Chochos, H. A. Ioannidou, M. Neophytou, C. Charilaou, G. A. Zissimou, J. M. Frost, T. Sachtan, M. Shahid, J. Nelson, M. Heeney, D. D. C. Bradley, G. Itskos, P. A. Koutentis and S. A. Choulis, *RSC Advances*, **2013**, 3, 10221-10229.
173. X. Song, N. Gasparini and D. Baran, *Advanced Electronic Materials*, **2018**, 4, 1700358.
174. L. Bucher, N. Desbois, P. D. Harvey, C. P. Gros and G. D. Sharma, *ACS Applied Materials & Interfaces*, **2018**, 10, 992-1004.
175. L. Bucher, N. Desbois, P. D. Harvey, C. P. Gros, R. Misra and G. D. Sharma, *ACS Applied Energy Materials*, **2018**, 1, 3359-3368.

## **CHAPTER 2. *Meso*-substituted BODIPY molecules**

In general, the BODIPY molecules applied in OPVs are functionalized at  $\alpha$ - or  $\beta$ -positions, and the most used methods to prepare such derivatives are either the Sonogashira reaction or the Suzuki coupling.<sup>1-4</sup> These reactions involve several synthetic steps that increase the cost of the final product. On the other hand, “simple” BODIPY dyes (BODIPY without any pre- or post-functionalization) were never reported as electron-donors, and their photovoltaic performances have not been described yet. In this scope, we prepared a series of BODIPYs based on the condensation reaction between  $\alpha$ -free pyrrole and aryl aldehydes in the presence of a catalytic amount of acid. All the final products were fully characterised and tested as electron-donor materials in OPVs, and the performance results can be used as a standard for more complex BODIPY structures.

## 2.1. Synthesis of *meso*-aryl BODIPY molecules

BODIPY molecules can be prepared by different methods, such as acid-catalysed condensation of pyrroles with acid chlorides, condensation of pyrroles with anhydrides or reaction between pyrrole-2-carbaldehyde and an unsubstituted pyrrole. However, the most used method to attach an aryl substitute group at *meso*-position is the conventional three-step method, that uses an acid catalysed condensation of aromatic aldehydes and pyrroles, followed by the DDQ oxidation step and finished by the complexation with borontrifluoride in the presence of a base (Scheme 2.1).<sup>5, 6</sup>



**Scheme 2.1.** General mechanism of the BODIPY synthesis.

The first step for BODIPY's synthesis is the condensation of one unit of the aldehyde with two units of pyrrole, catalysed by an acid. This reaction is quite similar to the reaction typically used for other pyrrolic compounds such as porphyrins, but in BODIPY's case, the ratio of aldehyde to pyrrole is one to two.

The second step is the oxidation of the dipyrromethane to dipyrromethene, which takes place with the presence of a strong oxidising agent, such as 2,3-dichloro-5,6-dicyanoquinone (DDQ).

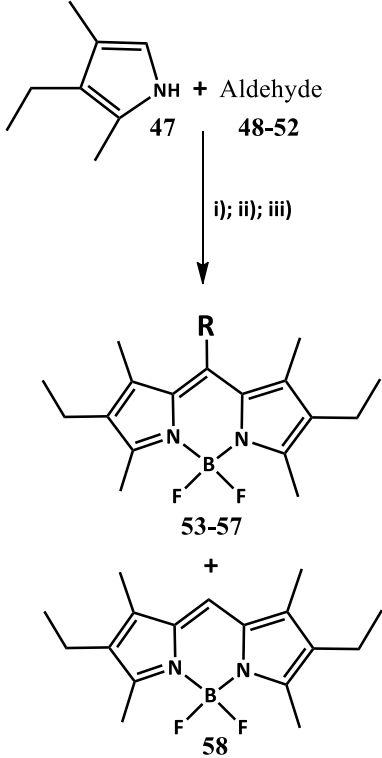
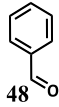

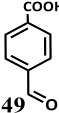
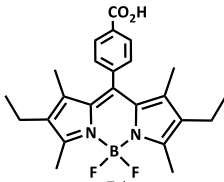
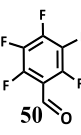
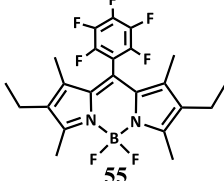
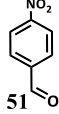
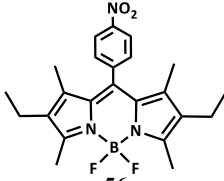
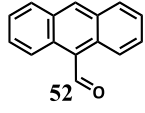
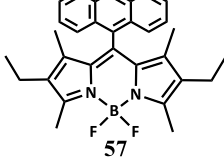
The third step is the complexation of the dipyrromethene with  $\text{BF}_3$  in a two-step progression that starts with donor-acceptor interactions between the electrons lone pair of the pyrrolenine nitrogen atom with the vacant orbital of the boron atom of  $\text{BF}_3$ . This stage converts the planar geometry of  $\text{BF}_3$  molecule into a tetrahedral geometry. Then occurs a hydrogen bond contact between the hydrogen atom of the NH group of the dipyririn and the adjacent fluorine atom from the  $\text{BF}_3$  molecule and finally the elimination of HF to complete the BODIPY core formation.<sup>7</sup>

### 2.1.1. Synthesis and structural characterisation of the first series of BODIPY molecules (1S-BDP)

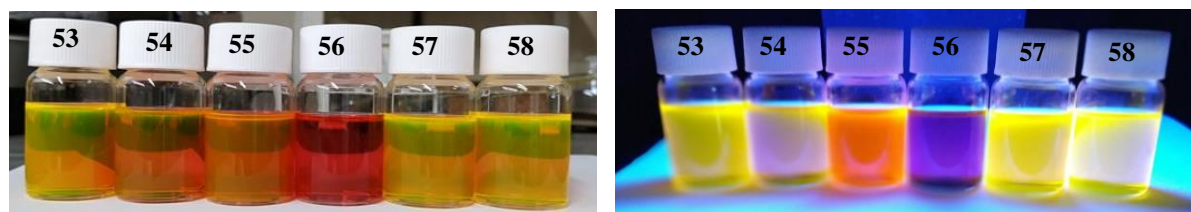
The first series of BODIPY molecules (**1S-BDP**) was planned to create a fully substituted BODIPY molecules series, due to their general good stability and ease of purification. The use of the pyrrole with alkyl groups at  $\alpha$  and  $\beta$  positions decrease the side reactions occurrence and reduce the propensity of the final BODIPY dyes to aggregate. As shown in Table 2.1, the first series of BODIPY dyes includes five different *meso*-aryl BODIPY dyes (**53-57**) and one *meso*-free BODIPY (**58**). BODIPYs with electron-withdrawing groups (carboxylic acid group, fluorine atoms, nitro group) at the *para*-position of benzaldehyde were obtained in higher yields, which indicates that withdrawing groups may enhance the activity of the aldehyde.

A considerable amount of the *meso*-unsubstituted BODIPY (**58**) was obtained along with *meso*-aryl BODIPY molecules. This contamination is particularly clear in the synthesis of **53** and **57**, and it could have a direct influence on the lower yields of these compounds due to the competition of pyrrole unit's consumption. The appearance of BODIPY **58** will be enlightened further, and its unintended preparation and isolation allow us to compare its main properties and the photovoltaic performance with those of the several *meso*-substituted molecules.

**Table 2.1.** General procedure for the preparation of the first BODIPY series (**53-58**): i)CH<sub>2</sub>Cl<sub>2</sub>, TFA; ii)DDQ; iii)diisopropylethylamine, BF<sub>3</sub>.O(C<sub>2</sub>H<sub>5</sub>)<sub>2</sub> and corresponding synthetic yields.

	Aldehyde	BODIPY	Yield (%)	Yield of <b>58</b> (%)
	 48	 53	18	5
	 49	 54	30	2
	 50	 55	25	3
	 51	 56	30	4
	 52	 57	13	6

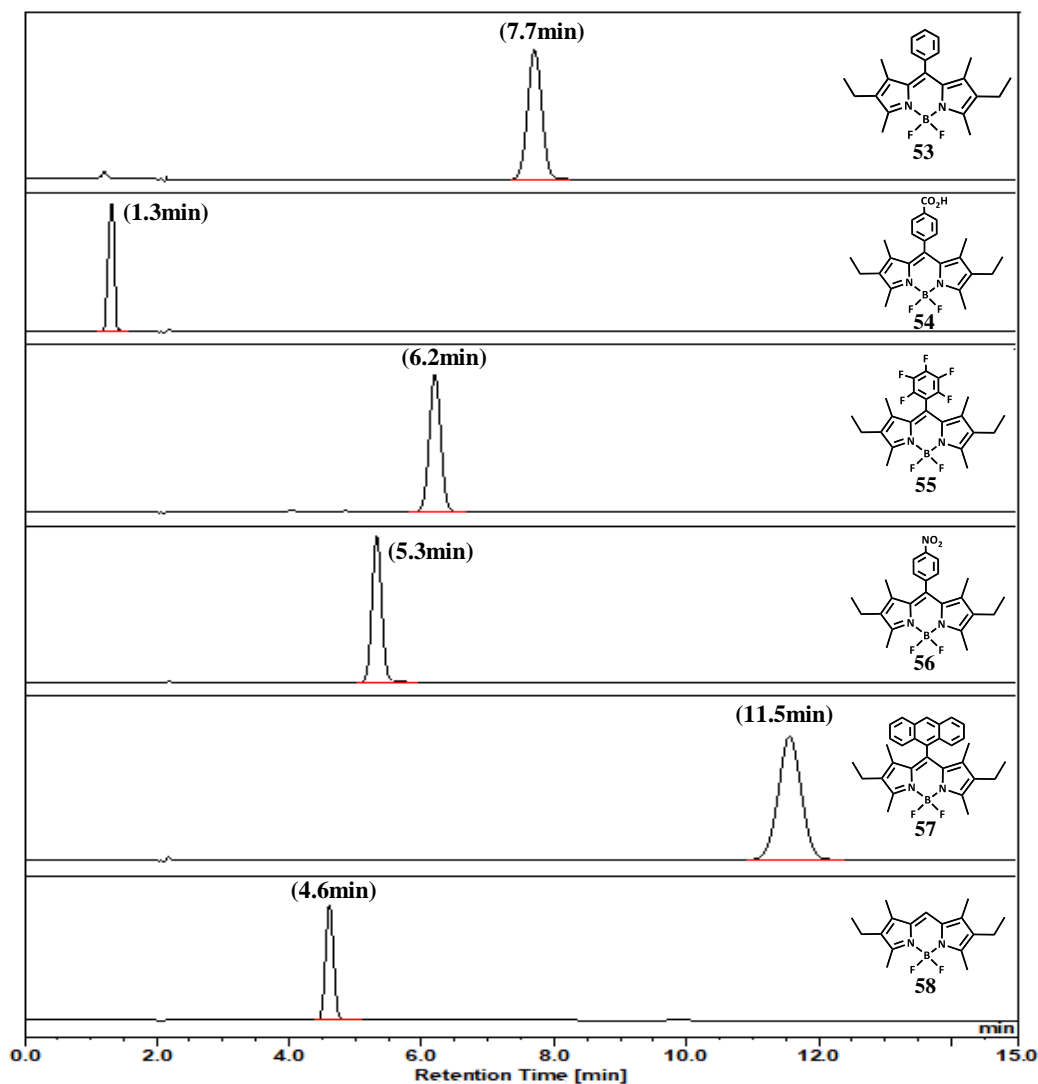
BODIPY molecules **53-58** are very soluble in organic solvents like dichloromethane, chloroform, dimethylformamide, toluene, tetrahydrofuran, but their solubility in alcohols (ethanol or methanol) is rather weak and none is soluble in water. With the exception of BODIPY with nitrophenyl group (**56**), the solutions of the BODIPY dyes present high fluorescence under UV light (Figure 2.1).

**Figure 2.1.** Chloroform solution of **1S-BDP** (**53-58**) under daylight (left) and under UV light (365 nm, right) irradiance.



All compounds were characterised by NMR and HRMS (details in Chapter 8), and the purity of the compounds was assessed by high-performance liquid chromatography (HPLC) coupled with a diode-array detector and a tandem mass spectrometer detector.

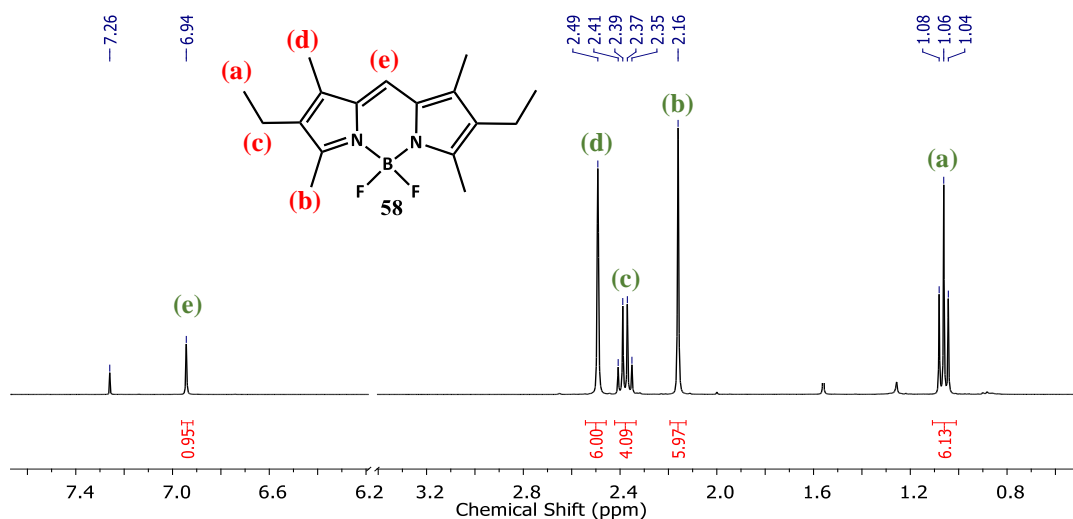
The HPLC analyses were performed on a C18 reversed phase column with an isocratic mobile phase consisting of acetonitrile and water (8:2 v/v) at a flow rate of 0.8 ml/min. As shown in Figure 2.2, every HPLC chromatogram revealed only one peak, which confirms the excellent separation of **58** from the other BODIPY dyes and the high purity level of the samples. Due to the non-polar stationary phase (RP C18 column), the most hydrophilic compound shows the lowest retention time, thereby the peak of BODIPY **54** showed up at the lowest retention time, while BODIPY **57**, due to the higher hydrophobicity of anthracene moiety, presents the highest retention time.



**Figure 2.2.** HPLC chromatograms of the **1S-BDP** obtained at 30 °C with acetonitrile : H<sub>2</sub>O (8:2) as isocratic eluent with a volume of injection of 10 µL and a flow rate of 0.8 ml/min.

All mass spectrometry analyses were made in positive mode. Besides the peak corresponding to the molecular ion  $[M + H]^+$ , the molecular ion peak corresponding to the loss of a fluorine atom was always obtainable. This peak was confirmed by the fragmentation of molecular ion  $[M + H]^+$  peak. The neutral loss of HF ( $[M+H-HF]^+$ ) is a regular feature in MS analyses of BODIPYs and can be very convenient to identify them in intricate matrices.<sup>8,9</sup>

The  $^1\text{H}$  NMR spectra of the compounds from **1S-BDP** can be analysed considering two main regions of the spectrum: up to 3 ppm ( $\alpha$  and  $\beta$ -position of BODIPY core) and at 6-9 ppm (*meso*-position). The  $^1\text{H}$  NMR spectrum of **58** (Figure 2.3) is ideal to understand the chemical environment of the BODIPY's core. The proton signals assigned to the methyl and ethyl groups directly attached to the core (a-d) can be seen from 1.06 ppm to 2.75 ppm, and the proton directly attached at *meso*-position (e) is much more deprotected (6.94 ppm) due to the acceptor effect of the core.

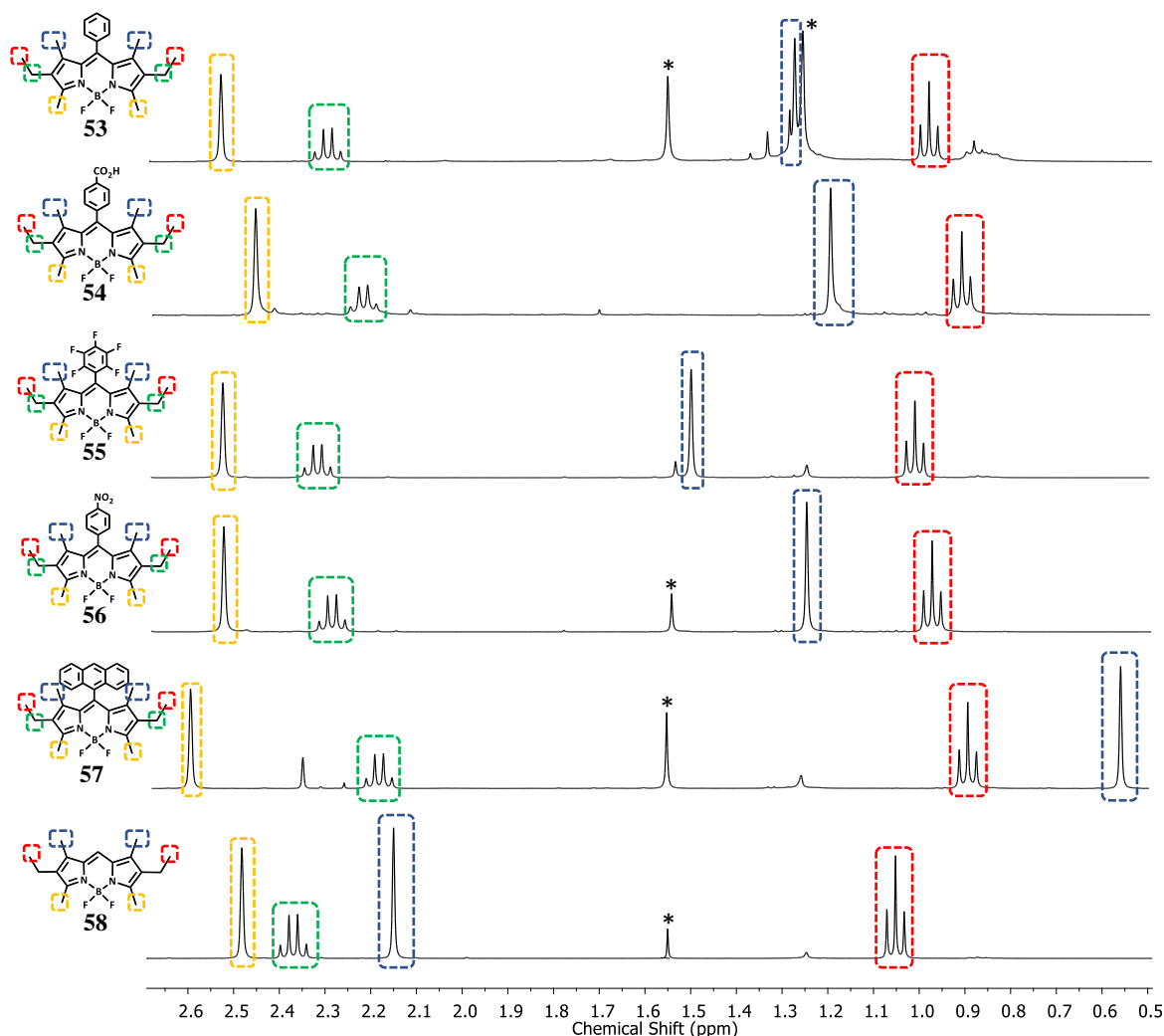


**Figure 2.3.**  $^1\text{H}$  NMR (400 MHz) spectrum of **58**, in  $\text{CDCl}_3$ .

BODIPYs **53-57** do not present the singlet at 6.94 ppm since they have aromatic substitution groups at that position. The signals from the hydrogens of phenyl, p-carboxyphenyl, p-nitrophenyl and anthracenyl groups (**53**, **54**, **56** and **57** respectively) display chemical shifts ( $\delta$ ) between 7.4 and 8.6 ppm.

All six BODIPY compounds present very similar  $^1\text{H}$  NMR spectra, particularly in the region related to the protons of BODIPY's core. In the spectra shown in Figure 2.4, the signals assigned to  $-\text{CH}_3$  group at the  $\alpha$ -pyrrolic position (yellow) and  $-\text{CH}_2$  from the ethyl group at the  $\beta$ -pyrrolic position (green) are placed between 2 ppm and 2.7 ppm. The triplet near 1 ppm is associated to  $-\text{CH}_3$  from the ethyl group at the  $\beta$ -pyrrolic position (red).

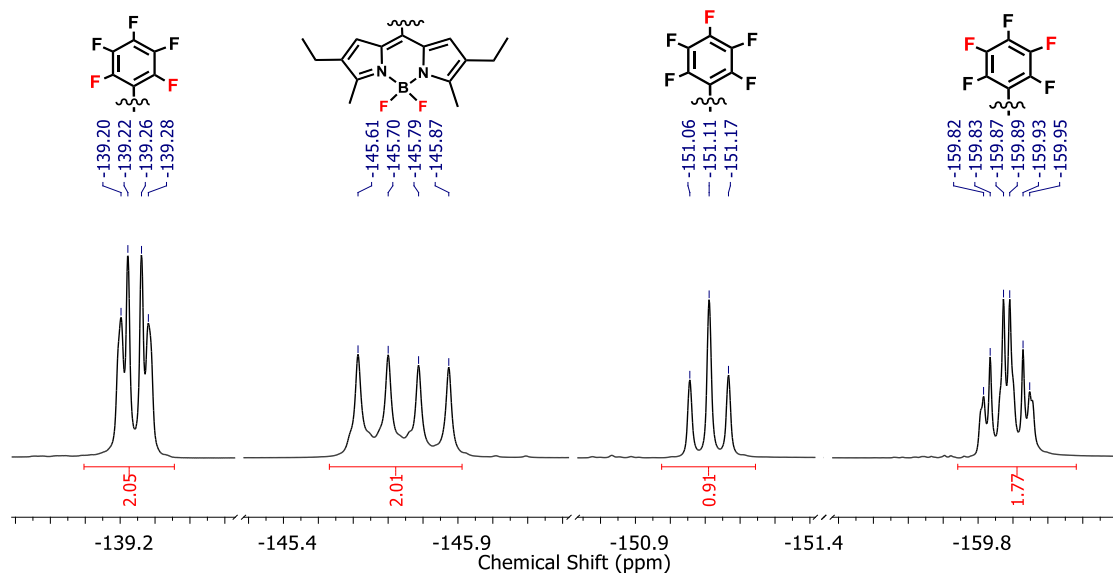
The main differentiating factor between the spectra is the position of the signal assigned to  $-CH_3$  at  $\beta$ -pyrrolic position (blue). As the different aryl-substituted groups at *meso*-position are in a perpendicular or quasi-perpendicular position with respect to the BODIPY core, the protons from the methyl group at  $\beta$ -pyrrolic position could experience shielding effects, induced by the magnetic field of the aromatic ring. This evidence is quite clear in Figure 2.4, where the methyl group experience a strong protection in **57** (0.55 ppm), less in **53** (1.26 ppm) and lesser in **58** (2.16 ppm).



**Figure 2.4.** Expansion of the  $^1\text{H}$  NMR spectra (0.5-2.7 ppm) for compounds **53-58**; star denotes trace of solvent (water and *n*-hexane).

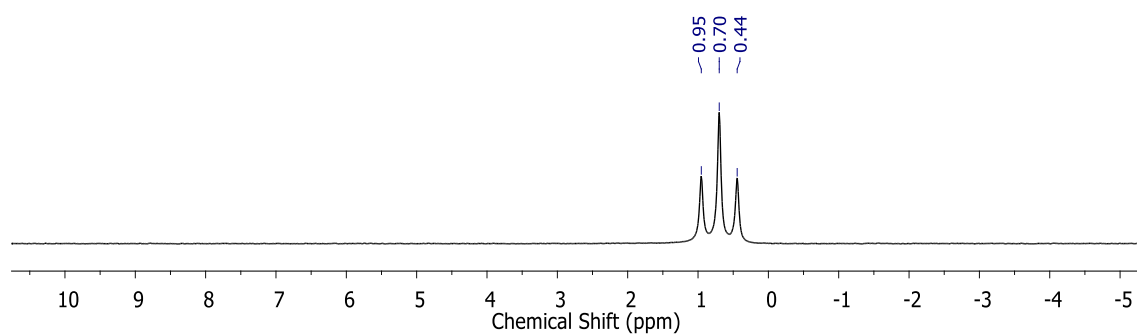
Generally,  $^{19}\text{F}$  NMR spectra of BODIPY compounds with two fluorine atoms as ligands show a non-binomial quartet (1:1:1:1 quartet) due to the coupling of fluorine with the quadrupolar  $^{11}\text{B}$  nucleus (nuclear spin is  $I = 3/2$ ). This inherent characteristic is found in all components of **1S-BDP**, where the quartet is lying around -145 ppm with coupling constants of 33-34 Hz. Figure 2.5 displays the  $^{19}\text{F}$  NMR spectrum of BODIPY **55**, which

presents three extra signals: a doublet of doublet at -139.2 ppm assigned to the fluorine atoms at *ortho*-position, a triplet at -151.1 ppm assigned to the fluorine at *para*-position and a triplet of doublets at -159.9 ppm assigned to the fluorine atoms at *meta*-position.



**Figure 2.5.**  $^{19}\text{F}$  NMR (376 MHz) spectrum of **55** in  $\text{CDCl}_3$ .

Figure 2.6 displays the  $^{11}\text{B}$  NMR spectrum of **55**. All the molecules of the **1S-BDP** have very similar spectra. The spectra present a triplet at 0.5-1.0 ppm with a 33-34 Hz coupling constant.



**Figure 2.6.**  $^{11}\text{B}$  NMR spectrum of **55** in  $\text{CDCl}_3$ .

The coupling constant is related to the quartet found in the  $^{19}\text{F}$  spectra and the similarity of the spectra of all compounds from **1S-BDP** indicates that the *meso*-substitution groups have a minor effect on the electronic density at the boron centre.

### 2.1.2. The *meso*-free BODIPY (**58**) appearance

In the synthesis of all *meso*-substituted BODIPYs, BODIPY **58** was isolated as a by-product in yields ranging from 2 % to 6 %. This peculiarity was previously reported but not explained.<sup>10, 11</sup> In fact, this BODIPY by-product can be easily masked by the main BODIPY. Using HPLC, it is possible to identify and then isolate it either by column chromatography or preparative thin layer chromatography.

To evaluate the hypothesis of the occurrence of **58** as the result of some degradation of the main BODIPY, we made a study in which 1mg of each BODIPY molecules was dissolved in 5 ml of dichloromethane in several conditions such as: room temperature, 50 °C, under direct light, under acidic conditions (1 % HCl), under basic conditions (1 % NaOH solution), oxidative conditions (1 eq of DDQ), or reductive conditions (1 eq of hydrazine). All the experiments were continuously monitored for 24 hours and under no conditions was detected the formation of **58** from the *meso*-substituted BODIPY molecules. This study indicates that there is no correlation between the formation of **58** and the degradation of *meso*-substituted BODIPY molecules.

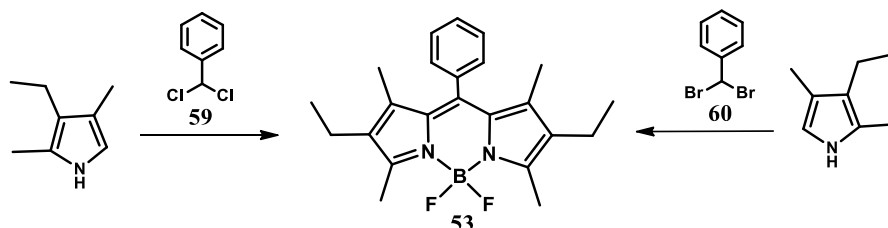
Subsequently, we assessed the influence of the solvent. Table 2.2 shows some reactions in various halogenated methane derivatives, with and without the trifluoroacetic acid (TFA) and in the absence of aldehyde.

**Table 2.2.** Synthesis of BODIPY **58** using 5 ml of solvent, 1 mmol of 3-ethyl-2,4-dimethylpyrrole, 1 eq. of DDQ, 17 eq. of boron trifluoride etherate and 12 eq. diisopropylamine.

Solvent/reagent	TFA	yield
CH <sub>2</sub> Cl <sub>2</sub>	yes	4%
CH <sub>2</sub> Cl <sub>2</sub>	no	4%
CH <sub>2</sub> I <sub>2</sub>	no	8%
CH <sub>2</sub> Br <sub>2</sub>	no	4%

It was possible to isolate **58** in the total absence of aldehyde, which shows that the solvent is the source of the *meso*-carbon. In all these reactions, compound **58** was the only BODIPY species isolated, and it was easily purified by column chromatography. We also found that the use of TFA as catalyst is not required. Based on the data from Table 2.2, we conclude that **58** is the product of the reaction of pyrrole with the electrophilic carbon of the halogenated solvent.

To further support this hypothesis, we performed a BODIPY synthesis using 3-ethyl-2,4-dimethylpyrrole with  $\alpha,\alpha$ -dichlorotoluene (**59**) or  $\alpha,\alpha$ -dibromotoluene (**60**), and in both cases the BODIPY **53** was obtained, with 6 % and 4% yield, respectively (Scheme 2.2).

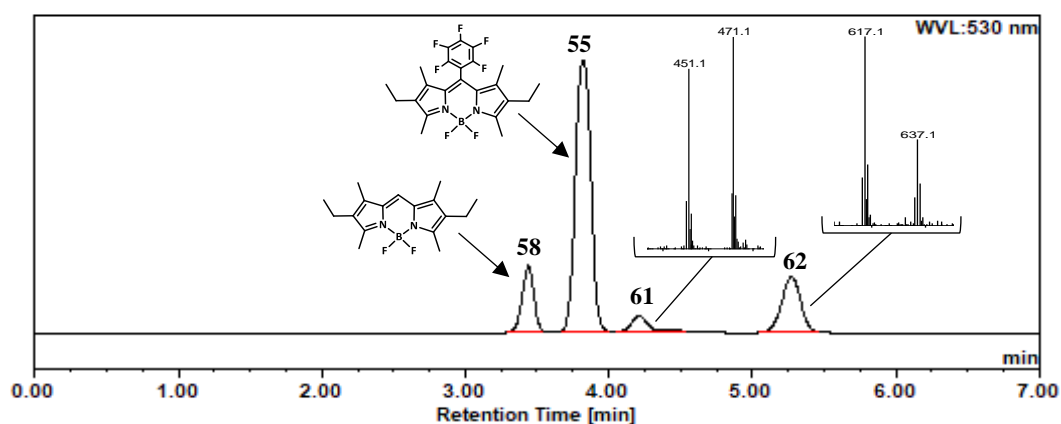


**Scheme 2.2.** Synthesis of BODIPY **53** using  $\alpha,\alpha$ -dichlorotoluene or  $\alpha,\alpha$ -dibromotoluene, 3-ethyl-2,4-dimethylpyrrole, 1 eq. of DDQ, 17 eq. of boron trifluoride etherate.

This result is consistent with previous studies, namely the reaction of pyrrole salts with dihalogenates electrophiles reported by Pictet and Rilliet,<sup>12</sup> the 2,2'-dipyrrolyl ketone synthesis by reaction of pyrrole with thiophosgene reported by Lugtenburg and co-workers,<sup>13</sup> and the reaction of pyrrole with a dihalogenated alkane to synthesise corrole derivatives by Gross and co-workers.<sup>14</sup>

### 2.1.3. BODIPY by-products **61** and **62**

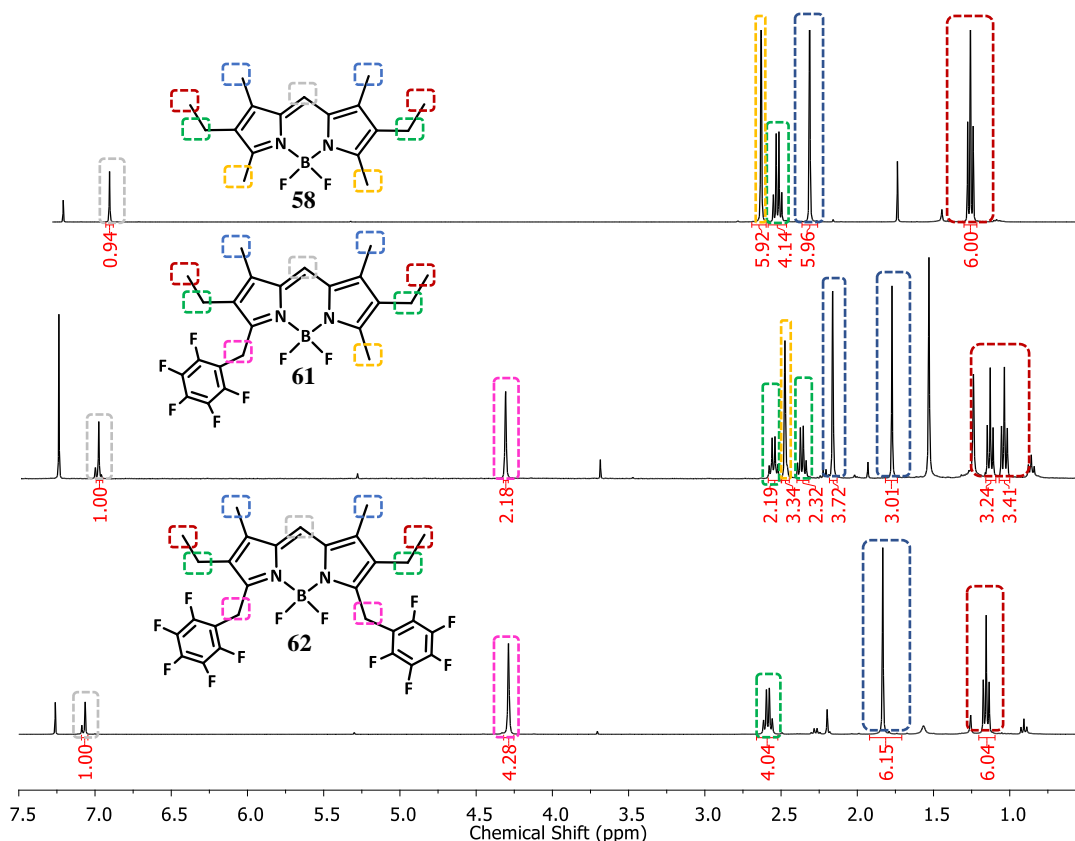
In the synthesis of **55**, it was possible to identify two other BODIPY by-products (**61** and **62**) in addition to compound **58**. By HPLC-MS analysis of the final reaction mixture, two peaks with absorption profile of BODIPY were found but with different retention times from those of **55** or **58** (Figure 2.7). The mass spectrometry analyses of these two peaks show molecular ion  $[M + H]^+$  peak at 471.1 m/z and 637.1 m/z.



**Figure 2.7.** HPLC chromatograms obtained at 30 °C with acetonitrile: H<sub>2</sub>O (9:1) as isocratic eluent at a flow rate of 0.8 ml/min, and fractions of the ESI-MS spectra in positive mode.

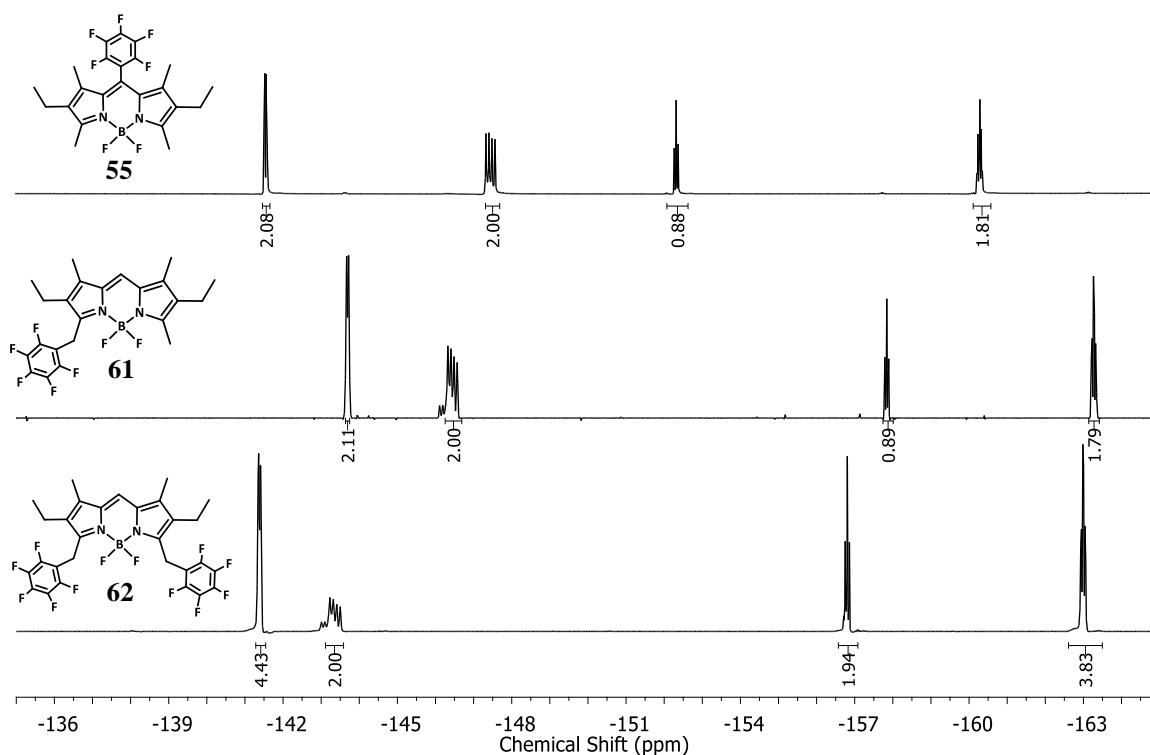
Excess of DDQ slightly increases the presence of these two by-products, which allowed us to isolate both by column chromatography. The  $^1\text{H}$  NMR and  $^{19}\text{F}$  NMR facilitated the identification of both structures (**61** and **62**) and their molecular masses are in agreement with the values obtained by HPLC-MS (Figure 2.7).

Figure 2.8 presents the  $^1\text{H}$  NMR of **58**, **61** and **62**, which allows to conclude that the three spectra are very similar. The singlet corresponding to the *meso* hydrogen (grey) appears in the three BODIPY spectra confirming that the two identified structures are *meso*-free substituted. The  $^1\text{H}$  NMR spectrum of the structure **62** shows a new singlet signal at 4.3 ppm (pink) corresponding to 4 protons and did not show the singlet related to methyl group at  $\alpha$ -pyrrolic (yellow), evidencing a di-substitution at the  $\alpha$ -pyrrolic position. The spectrum of **61** shows all the signals presented on **58** and **62** spectra but with half of the intensity for the singlet related to methyl group at  $\alpha$ -pyrrolic and for the new singlet signal at 4.3 ppm, which denotes a mono-functionalization.



**Figure 2.8.**  $^1\text{H}$  NMR (400 MHz) spectra of **58**, **61** and **62** compounds, in  $\text{CDCl}_3$ .

The  $^{19}\text{F}$  NMR spectra of **61** and **62** show the existence of fluorine atoms in addition to the two coupled with the boron. The spectra of the compounds **61** and **62** show the same signals as **55**, but with some deviations. The integration of the signals confirms the presence of one pentafluoro group on the **61** structure and two pentafluoro groups on **62**.



**Figure 2.9.**  $^{19}\text{F}$  NMR spectra of **55**, **61** and **62** structures, in  $\text{CDCl}_3$ .

The excess of DDQ facilitates the formation of both by-products and the conversion of the methyl at the  $\alpha$ -pyrrolic positions into a formyl group through DDQ activation was already reported.<sup>15-17</sup> This reaction could be the starting point for a more intricate mechanism that originates **61** and **62**, but another option such as the cleavage of the carbon-carbon bond at *meso*-position originating a pentafluorophenyl radical is also conceivable. Thus, further studies are necessary to understand the cause and mechanism of formation of these two BODIPY molecules.

#### 2.1.4. X-ray diffraction studies

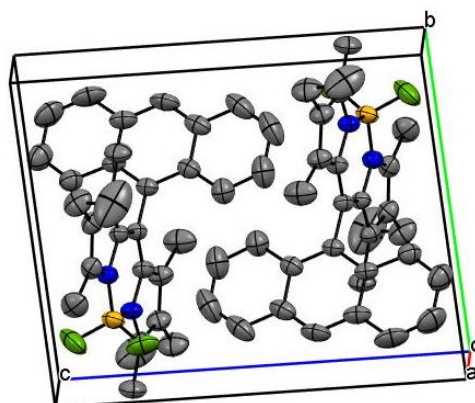
By slow evaporation from a dichloromethane/hexane solution, it was possible to produce crystals of **55**, **56**, **57** and **58**. Their molecular structures were determined by single-crystal diffraction analysis, and the crystallographic data are listed in Table 2.3. Crystals of **55** and **58** exhibit a unit cell equal to that already reported by Rurack *et al.*<sup>18</sup> and Beniston *et al.*<sup>11</sup>, but the crystal structure for compounds **56** and **57** are new.

BODIPY **57** has a triclinic unit cell (space group P-1) with two molecules per cell (Figure 2.10). It packed efficiently without any solvent accessible voids, and without significant intermolecular  $\pi$ - $\pi$  interactions. The molecules of **57** have a head-to-tail packing arrangement, facilitated by halogen short contacts for both C-F and H-F interactions.



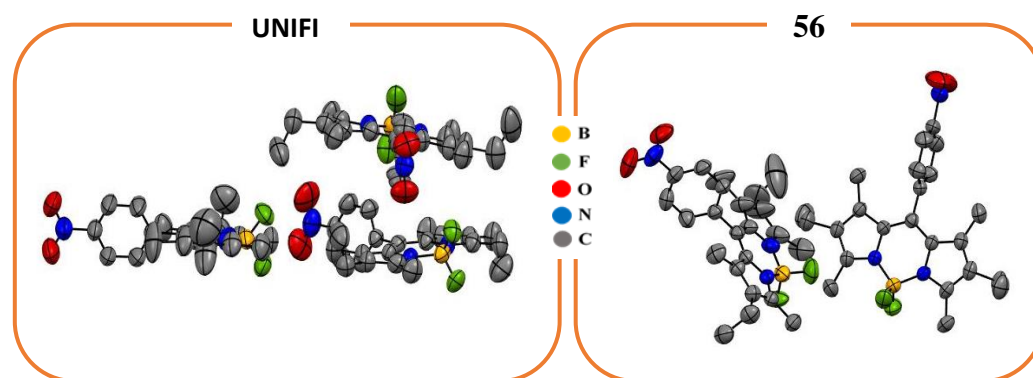
**Table 2.3.** Crystal data details of **55-58** structures.

Crystal data	<b>55</b>	<b>56</b>	<b>57</b>	<b>58</b>
<b>Chemical formula</b>	C <sub>23</sub> H <sub>22</sub> B F <sub>7</sub> N <sub>2</sub>	C <sub>23</sub> H <sub>26</sub> B F <sub>2</sub> N <sub>3</sub> O <sub>2</sub>	C <sub>31</sub> H <sub>31</sub> B F <sub>2</sub> N <sub>2</sub>	C <sub>17</sub> H <sub>23</sub> B F <sub>2</sub> N <sub>2</sub>
<i>M<sub>r</sub></i>	470.24	425.28	480.39	304.19
<b>Crystal system, space group</b>	monoclinic, P2 <sub>1</sub> /c	Triclinic, P-1	Triclinic, P-1	Triclinic, P-1
<b>Temperature (K)</b>	273	273	273	273
<i>a, b, c</i> (Å)	8.7467(4), 11.6672(1), 22.5737(7)	11.6249(3), 13.6843(4), 14.2855(3)	11.2904(4), 11.5999(4), 12.6196(4)	8.5941(12), 9.3460(15), 12.1216(16)
<i>a, β, γ</i> (°)	90.00(10), 95.630(4), 90.00	83.8040(10), 86.0120(10), 81.1080(10)	82.7320(17), 81.7817(15), 62.8494(13)	100.577(12), 103.717(9), 113.991(12)
<i>V</i> (Å <sup>3</sup> )	2294.7(2)	2228.86(10)	1452.01(9)	820.0(2)
<i>Z</i>	4	2	2	2
<b>Radiation type</b>	Mo <i>K</i> α	Mo <i>K</i> α	Mo <i>K</i> α	Mo <i>K</i> α
<i>μ</i> (mm <sup>-1</sup> )	0.119	0.092	0.072	0.087

**Figure 2.10.** Crystallographic unit cell of structure **57**.

The crystallisation of BODIPY **56** afforded crystals with a structure different from that reported previously by Diederich *et al.* (codename **UNIFIG**).<sup>19</sup> As shown in Figure 2.11, the new polymorph has two symmetry-independent molecules while in **UNIFIG** there are three symmetry-independent molecules. In the new polymorph, both molecules have the ethyl groups in a *trans*-conformation, while **UNIFIG** has two molecules with the ethyl groups in a *trans*-conformation, and a third one with the ethyl groups in a *cis*-conformation.

The crystal structures of the four BODIPY dyes are very similar and comparable to the other BODIPY crystal structures reported so far.<sup>20-24</sup> All the structures of **55-58** have a head-to-tail packing arrangement. The shortest contact in all the structures occurs in **55**, with a distance of 2.8 Å, related to an H-F interaction.

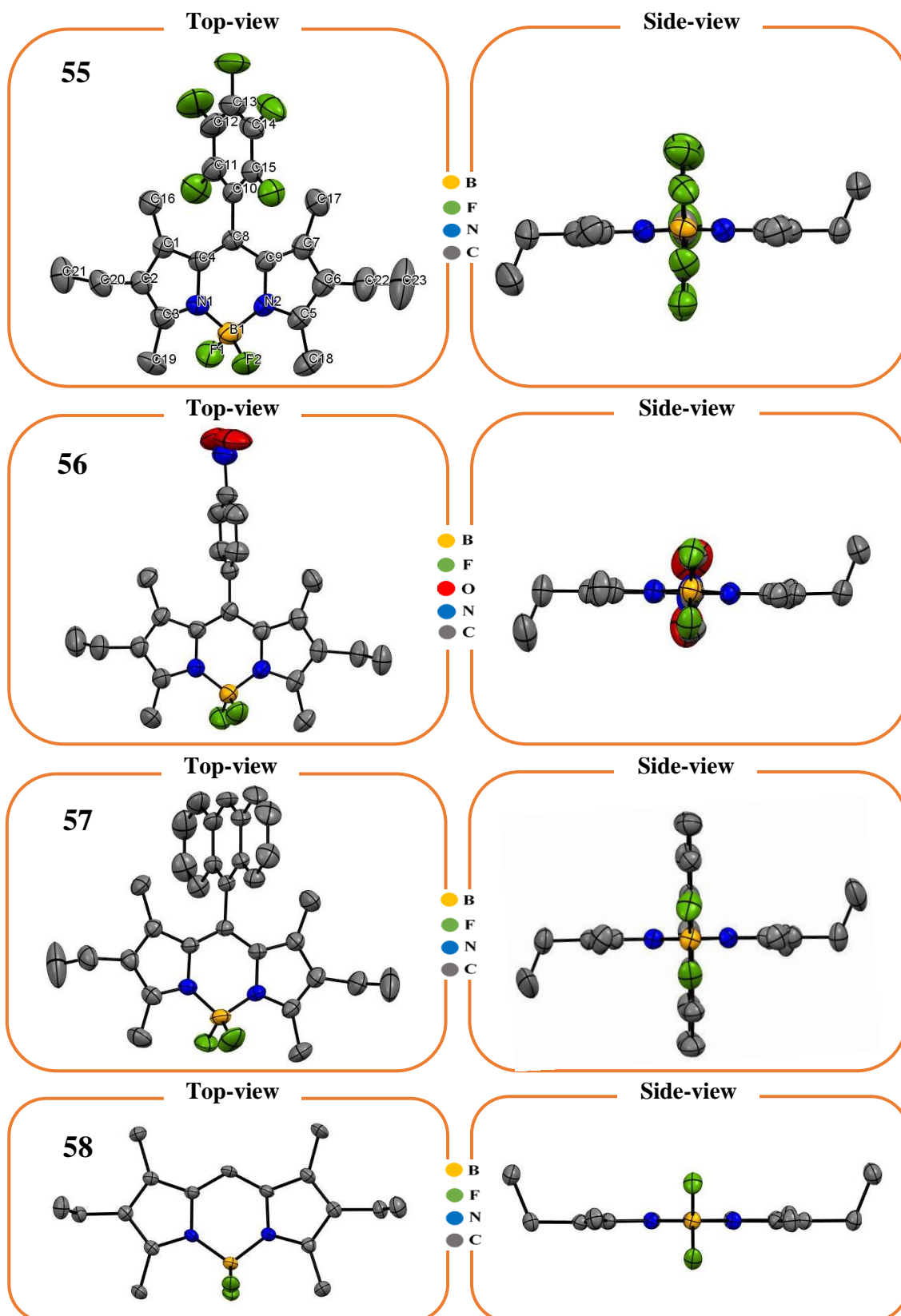


**Figure 2.11.** Oak Ridge Thermal Ellipsoid Plot (ORTEP) drawing of the molecular structures of the polymorphs **UNIFI**<sup>19</sup> and **56**. Ellipsoids were drawn at 50% probability level; Hydrogen atoms were omitted for clarity.

Details of the molecular configurations of the four BODIPY structures are shown in Table 2.4 and Figure 2.12. All structures have very similar bond lengths and angles and torsion angles within the BODIPY's core (planarity). The dihedral angle between the *meso*-substituent group and of the central core is close to 90°. The bond length of the *meso*-aryl C-C bond did not vary upon the increase of the electron withdrawing ability of the aryl substituent. The BODIPY core is almost planar, the fluorine atoms are in a plane perpendicular to it, and the boron atom has a slightly distorted tetrahedral coordination. The two B-N bond lengths are typical from single B-N bonds,<sup>18</sup> and both have similar distances, which reveals the delocalisation of the positive charge.

**Table 2.4.** Conformation of the ethyl groups, length of the bond between the *meso*-carbon and the substituent (C8-C10), the dihedral angle between the least-squares plane of the substituent and of the central core ( $\Theta_{\text{core-meso}}$ ), length of the bond between the boron and nitrogen atoms (B-N), boron and fluorine atoms (B-F), the angles of the boron bonding atoms (N-B-N and F-B-F) and the torsion of the BODIPY core (boron planarity).

Entries	55	56	57	58
<b>Conformation</b>	<i>trans</i>	<i>trans; trans</i>	<i>trans</i>	<i>cis</i>
<b>C8-C10 (Å)</b>	1.514(3)	1.486(3); 1.482(3)	1.495(2)	-
<b><math>\Theta_{\text{core-meso}}</math> (°)</b>	89.60	87.87(6); 89.89(7)	89.88	-
<b>N1-B (Å); N2-B (Å)</b>	1.544(5); 1.556(4)	1.539(3); 1.534(3) 1.542(3); 1.525(3)	1.534(3); 1.537(3)	1.560(3); 1.559(3)
<b>B-F1 (Å); B-F2 (Å)</b>	1.397(5); 1.408(5)	1.388(3); 1.378(3) 1.377(3); 1.384(3)	1.3889(2); 1.384(2)	1.398(3); 1.402(2)
<b>N-B-N (°)</b>	108.11	107.3(2)	107.3 (1)	107.12
<b>F-B-F (°)</b>	108.85	109.0(2)	109.1 (2)	109.10
<b>Boron planarity (°)</b>	178.41 (3)	178.7 (2)	177.4 (2)	179.93



**Figure 2.12.** Single-crystal X-ray structure of the **55** (A), **56** (B), **57** (C) and **58** (D) of a top-view (left) and side-view (right); Ellipsoids were drawn at 50 % probability level; Hydrogen atoms were omitted for clarity; The atoms numeration attributed to **55** is uniform for all structures.

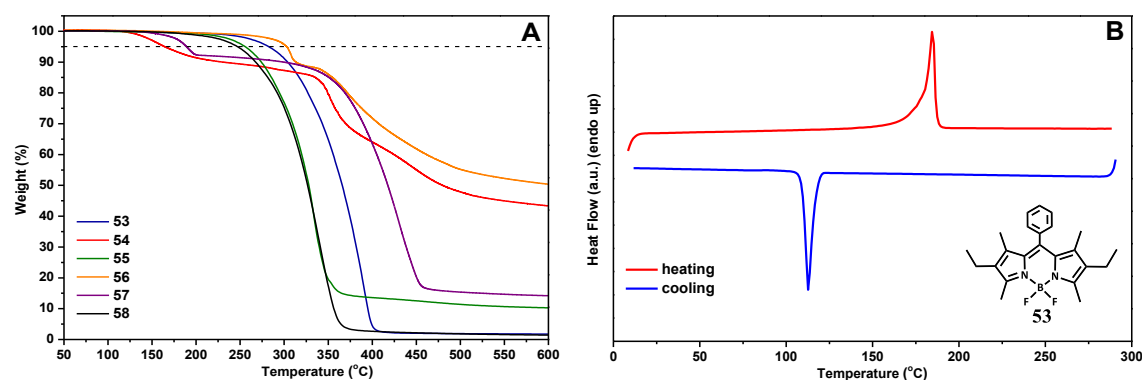
## 2.2. Characterisation of the first series of BODIPY molecules (1S-BDP)

The structures of the **1S-BDP** are already published in different works,<sup>10, 11, 18, 19, 24</sup> but some of their individual characteristics are not available as well as their comparative studies. In view of our interest in their application as photoactive materials in photovoltaic cells, we studied their thermal, photophysical and electrochemical properties. Density Functional Theory (DFT) studies were also carried out to complement the photophysical and electrochemical properties.

### 2.2.1. Thermal characterisation

Thermogravimetric analysis (TGA) and differential scanning calorimetry (DSC) provide valuable information about the thermal behaviour and thermostability of the BODIPYs.

Thermogravimetric analysis monitors the weight losses of the sample upon the increase of the temperature, evidencing the presence of solvent residues, impurities or material degradation. Only the compounds **54** and **57** present 5 % of mass loss by decomposition below 240 °C (162 °C and 189 °C, respectively).



**Figure 2.13.** (A) TGA traces of the BODIPY dyes recorded at a heating rate of 20 °C/min); (B) DSC curve of **53** recorded at a heating and cooling rate of 20 °C/min.

In DSC the energy required at each temperature to maintain the sample temperature equal to that of a reference is recorded. Any transition involving the absorption or release of energy (endothermic or exothermic processes) when occurring will require a compensation to maintain its temperature equal to that of the reference.

The DSC measurements show a sharp endothermic peak for all BODIPYs, associated with the melting. The melting temperature ( $T_m$ ), determined as the onset of the peak, was confirmed by a conventional melting-temperature measurement. Only for **53** (Figure 2.13 (B)) and **58**, a crystallisation peak was observed in the cooling cycle.

**Table 2.5.** Decomposition and melting temperatures of the BODIPY compounds obtained by TGA and DSC, respectively.

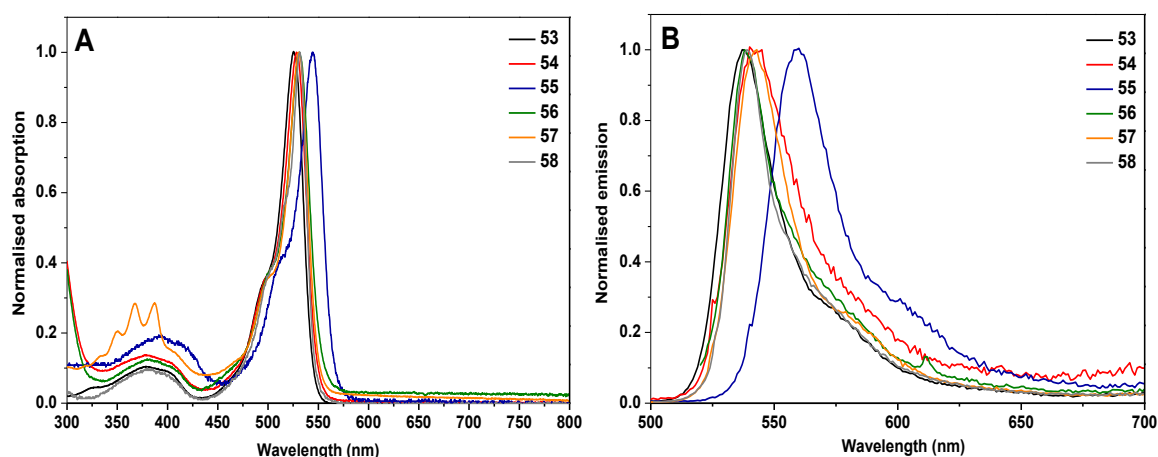
BODIPY	T <sub>d</sub> * (°C)	T <sub>m</sub> (°C)
<b>53</b>	284	176
<b>54</b>	162	271
<b>55</b>	256	190
<b>56</b>	302	186
<b>57</b>	189	315
<b>58</b>	243	179

\*Temperature at which 5% decomposition occurs

The results obtained from the thermal analysis confirm that all BODIPYs exhibit high thermal stability and high melting temperatures, as observed for similar structures previously published,<sup>18, 24</sup> these being important characteristics for OPV applications.

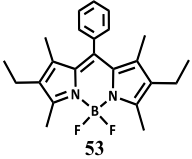
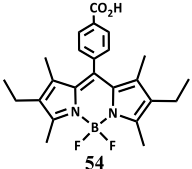
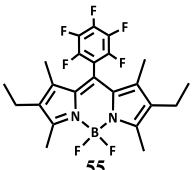
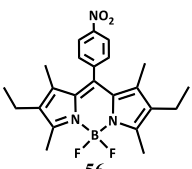

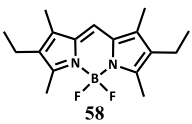
### 2.2.2. Photophysical characterisation

BODIPY dyes are widely known for having a strong absorption in visible, high extinction coefficients, sharp absorption and emission bands and low Stokes shift (SS). The absorption and emission studies of **1S-BDP** have confirmed such characteristics as shown in Figure 2.14. The optical data obtained from experiments with three different solvents (chloroform, hexane and acetonitrile) are presented in Table 2.6.

**Figure 2.14.** Normalized absorption (A) and emission (B) spectra of the BODIPY series in chloroform solution.

The absorption spectra of the BODIPY series cover a broad range of the visible spectrum. The absorption and emission studies revealed sharp absorption and emission spectra with high molar extinction coefficient, general high quantum yields of fluorescence and narrow absorption and emission bandwidths.

**Table 2.6.** Photophysical properties of the **1S-BDP**.

Dyes	Solvent	$\lambda^{abs}$ (nm)	$\epsilon$ ( $\text{cm}^{-1} \text{M}^{-1}$ )	$\lambda^{abs}_{film}$ (nm) <sup>a</sup>	$\lambda^{em}$ (nm)	$\Phi_F$ (%)	SS ( $\text{cm}^{-1}$ )	$E_g^{opt}$ (eV) (onset) <sup>b</sup>
 53	Chloroform	525	$6.8 \times 10^4$		538	98	460	2.28
	Hexane	524	$8.8 \times 10^4$	548	535	79	388	2.28
	Acetonitrile	520	$1.0 \times 10^5$		533	92	468	2.29
 54	Chloroform	530	$5.4 \times 10^4$		543	76	452	2.25
	Hexane	526	$6.4 \times 10^4$	539	539	73	459	2.26
	Acetonitrile	523	$6.9 \times 10^4$		537	71	498	2.26
 55	Chloroform	544	$5.9 \times 10^4$		558	98	461	2.19
	Hexane	543	$1.0 \times 10^5$	551	555	90	398	2.19
	Acetonitrile	539	$7.9 \times 10^4$		554	88	502	2.21
 56	Chloroform	530	$6.2 \times 10^4$		539	0.6	315	2.25
	Hexane	530	$8.6 \times 10^4$	542	549	28	645	2.25
	Acetonitrile	526	$7.8 \times 10^4$		535; 650	0.4	284	2.27
 57	Chloroform	532	$7.8 \times 10^4$		543	80	209	2.26
	Hexane	528	$9.6 \times 10^4$	545	538	77	175	2.27
	Acetonitrile	527	$5.9 \times 10^4$		537	67	284	2.27
 58	Chloroform	533	$6.2 \times 10^4$		539	84	381	2.27
	Hexane	531	$7.6 \times 10^4$	548	536	79	352	2.27
	Acetonitrile	526	$6.4 \times 10^4$		534	78	254	2.29

<sup>a</sup> absorbance of the films prepared from chloroform solution.

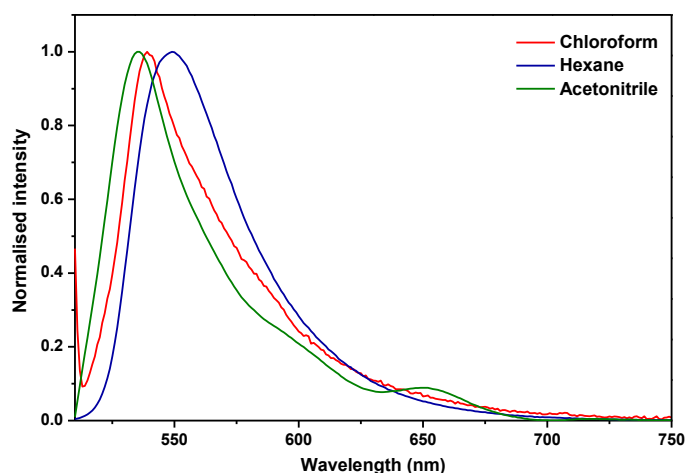
<sup>b</sup>  $E_g =$  estimated from the absorption spectra of dyes in solution,  $E_g$  (eV) =  $1240 / \lambda_{onset}$  (nm).

The six absorption spectra are characterised by a strong S0-S1 ( $\pi$ - $\pi^*$ ) transition (525-544 nm) with a higher energy shoulder at about 30 nm from the main peak and a weaker broad band (340-420nm) arising from the S0-S2 ( $\pi$ - $\pi^*$ ) transition. The S0-S2 ( $\pi$ - $\pi^*$ ) transition of **57** presents the general profile of the anthracene molecule, proving that the *meso*-substituted groups impact on this transition. All BODIPY dyes show high extinction coefficients in the different solvents (ranging from  $5.4 \times 10^4$  to  $1.0 \times 10^5 \text{ cm}^{-1} \text{M}^{-1}$ ), which confirms their excellent light-harvesting ability.

The presence of an aromatic group at the *meso*-position has a weak effect on the main absorption characteristics.<sup>15, 17, 25</sup> This is due to the negligible electronic interaction between the *meso*-aromatic ring and the BODIPY core since the two moieties are almost perpendicular to each other. However, the absorption of **55** presents a small red-shift, which can be explained by the inductive effect of the strong electron-withdrawing character of the *meso*-C<sub>6</sub>F<sub>5</sub> group.

BODIPY's fluorescence is very sensitive to the rotation of the substituents (particularly at the *meso*-position)) and electron transfer.<sup>5, 25</sup> The rotation of *meso*-position substituted groups can be controlled by substitution at positions 1 and 7 with alkyl groups. This substitution blocks or hinders the movement of the aryl-substituted group, decreasing the non-radiative processes. Apart from **56**, the different BODIPY dyes present very high fluorescence quantum yields, and there is no notable solvent effect on either the absorption or the steady-state emission spectra, which excludes the possibility of any highly polarised excited state.

The emission of **56** is significantly affected by solvent polarity. In non-polar hexane, it shows fluorescence emission at 549 nm. In chloroform, the fluorescence quantum yield becomes very weak (at 539 nm), and in a more polar solvent (acetonitrile) the fluorescence is residual, and a new band at 650 nm appears (Figure 2.15).



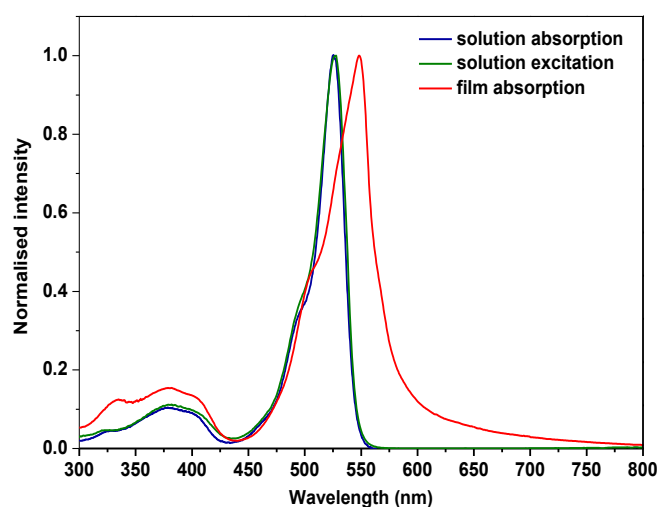
**Figure 2.15.** Emission spectra of **56** in chloroform, hexane and acetonitrile.

When electron transfer occurs within a molecule, it competes with the radiative deactivation and reduces the emission quantum yield. The electron transfer may involve an intramolecular transfer of electrons between two moieties of the fluorescent molecule upon excitation or involves intermolecular processes. Photoinduced electron transfer (PeT) can

occur by either a reductive or an oxidative process. Reductive PeT occurs when the substituent attached to the BODIPY core transfers electrons to the BODIPY core in the excited state. In contrast, if the substituent is receiving electrons from the BODIPY core, an oxidative PeT occurs. Due to the acceptor character of the nitrophenyl group, an oxidative PeT occurs in **56**.

The small Stokes shift (SS) suggests that the equilibrium nuclear configuration of the compounds experience little change between the ground ( $S_0$ ) and the first excited state ( $S_1$ ).

As Figure 2.16 shows for compound **53**, the excitation spectra of the BODIPY match with the absorption spectra.



**Figure 2.16.** Absorption and excitation spectra of **53** in chloroform solution and its film absorption spectrum.

The absorption spectra of the molecular thin films show a bathochromic shift of the absorption maximum accompanied by a broadening of the peaks, due to the interactions between adjacent molecules, possibly involving  $\pi$ -orbitals.

### 2.2.3. Electrochemical characterisation

The electrochemical properties of a compound provide valuable information about the energy of HOMO and LUMO levels and also about the reversibility of the redox processes. Cyclic voltammetry (CV) measurements require the use of three electrodes (working, reference and auxiliary electrode), which are dipped into a solution having a salt (support electrolyte). The active species is either dissolved in the electrolyte (as used here) or deposited over the working electrode, as a film. During the measurement, the compound is oxidized or reduced on the surface of the working electrode, which generates an electron



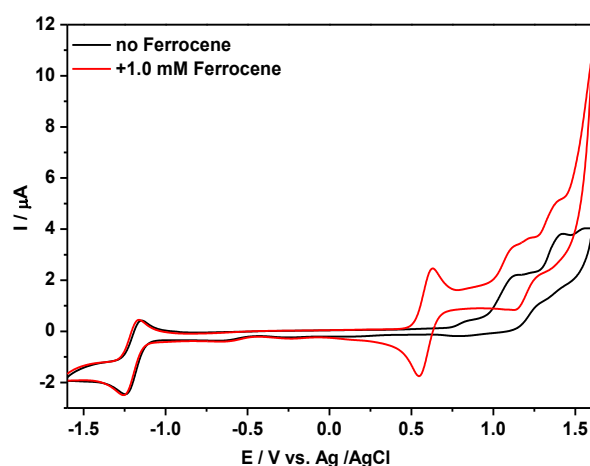
current between the working and the auxiliary electrodes. The recording of that current as a function of the potential applied between the working and the reference electrodes constitutes the cyclic voltammogram. In this technique, the electrodes are static, and the peaks obtained are diffusion controlled.

BODIPY dyes, in view of their attractive properties, have been widely characterized by cyclic voltammetry measurements. In several cases, the CVs show a one-electron oxidation at half wave potential ( $E_{1/2}$ ) around 1.0 V vs. SCE and a one-electron reduction at around -1.4 V vs. SCE, but, depending on the substitution of BODIPY, these typical values can vary by more than 500 mV.<sup>27-29</sup>

The electrochemical features of BODIPY derivatives are largely dependent on the level of substitution of BODIPY core.<sup>30-32</sup> The reduction potential is deeply affected by the *meso* substituent, where electron acceptors bring the reduction potential to more positive values.<sup>33</sup> DFT studies showed that the anionic charge of the reduced dye is localised at the *meso*-position.<sup>28</sup> The substitution at *meso*-position stabilises the radical anion, which improves the reversibility of the reduction process.<sup>33</sup> Additionally, absence of substitution in the 1-, 3-, 5- and 7-positions also conducts to irreversible reduction, because of the high reactivity of the electrogenerated radical ions.

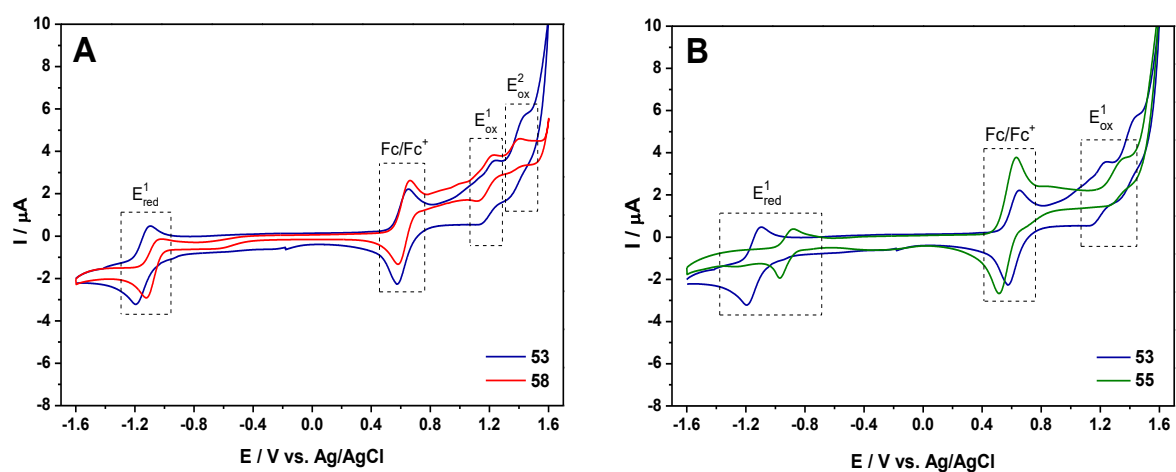
Non-substitution at the 2-, 3-, 5-, or 6-positions destabilises the radical cation produced upon oxidation.<sup>28</sup> BODIPY radical cations unsubstituted at these positions are vulnerable to nucleophilic attack and capable of dimerisation.<sup>34</sup> Thus, the substitution of BODIPY core positions with alkyl groups can significantly influence the electrochemical properties. The redox process becomes more reversible with the addition of alkyl substituents, leading to the observation of clean looking cyclic voltammograms.<sup>27</sup>

In this work, cyclic voltammetry measurements were carried out using tetrabutylammonium tetrafluoroborate (TBATFB (0.1 M)) as supporting electrolyte in dichloroethane solution with a one-compartment three electrode system consisting of a glassy carbon electrode (GCE) as working electrode, a platinum wire as counter electrode and Ag/AgCl as reference electrode. The ferrocene/ferrocenium (Fc/Fc<sup>+</sup>) couple (1mM) was used as internal reference, and it was assumed that the redox potential of Fc/Fc<sup>+</sup> has an absolute energy of -4.80 eV to vacuum.<sup>35, 36</sup> The CVs were recorded in deaerated solutions, at a scan speed of 50 mV/s, under nitrogen atmosphere. As can be observed in Figure 2.17, the addition of ferrocene into the solution does not interfere with the redox potentials of the BODIPY dyes, and its oxidation processes appear in all CVs at half-wave potential of 0.58 V - 0.62 V.



**Figure 2.17.** Cyclic voltammograms of **56** with and without ferrocene.

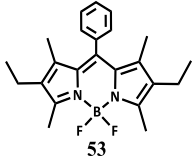
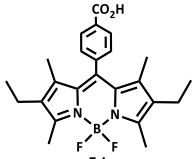
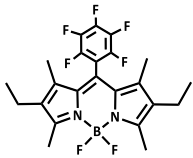
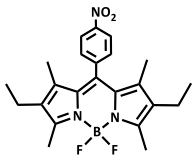
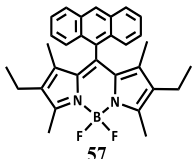
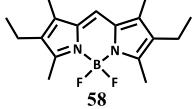
Figure 2.18 shows the cyclic voltammograms of **53**, **55** and **58**, and the corresponding electrochemical parameters of all BODIPY dyes are summarized in Table 2.7. All BODIPY molecules present very similar cyclic voltammograms, with two oxidations processes ( $E_{\text{ox}}^1$  and  $E_{\text{ox}}^2$ ) and one reduction process ( $E_{\text{red}}^1$ ). We consider that these redox processes take place in the BODIPY core, an assumption that is supported by the similarity between the electrochemical behaviour of **58** and that of the other compounds (Figure 2.18).



**Figure 2.18.** Cyclic voltammograms of **53**, **55** and **58**.

With the exception of the reduction of **54** and **58**, all BODIPY dyes show reversible redox processes with peak current ratios ( $i_{\text{pa}}/i_{\text{pc}}$  or  $i_{\text{pc}}/i_{\text{pa}}$ ) approximately to unity, which indicates the stability of the radical ions. The reduction of **58** has a peak current ratio above 1.5, and irreversible reduction wave, which reveal lower stability, attributed due to the lack of substitution on *meso*-position. Table 2.7 shows the half-wave ( $E_{\text{ox}}^1$ ,  $E_{\text{ox}}^2$  and  $E_{\text{red}}^1$ ) and the onset potentials.

**Table 2.7.** Electrochemical properties of the **1S-BDP**.

BODIPY	$E_{\text{red}}^1$ (onset) (V)	$E_{\text{ox}}^1$ (onset) (V)	$E_{\text{ox}}^2$ (V)	$E_{\text{HOMO}}^{\text{elec}}$ (eV)	$E_{\text{LUMO}}^{\text{elec}}$ (eV)	$E_{\text{g}}^{\text{elec}}$ (eV)	$E_{\text{g}}^{\text{opt}}$ (eV)	$E_{\text{LUMO}}^{\text{opt}}$ (eV)
	-1.15 (-1.07)	1.17 (1.09)	1.43	-5.28	-3.12	2.16	2.28	-3.00
	-1.18 (-1.03)	1.24 (1.12)	1.43	-5.33	-3.18	2.15	2.25	-3.08
	-0.97 (-0.87)	1.35 (1.21)	1.53	-5.44	-3.36	2.08	2.19	-3.25
	-1.25 (-1.14)	1.15 (1.01)	1.38	-5.23	-3.08	2.15	2.25	-2.98
	-1.13 (-1.04)	1.25 (1.13)	1.42	-5.34	-3.17	2.17	2.26	-3.08
	-1.13 (-1.02)	1.22 (1.08)	1.39	-5.26	-3.05	2.21	2.27	-2.99

$$E_{\text{HOMO}}^{\text{elec}} = [-(E_{\text{onset}}^{\text{ox}1} - E^{\text{Fc}/\text{Fc}^+}) - 4.8] \text{ eV.}$$

$$E_{\text{LUMO}}^{\text{elec}} = [-(E_{\text{onset}}^{\text{red}1} - E^{\text{Fc}/\text{Fc}^+}) - 4.8] \text{ eV.}$$

$$E_{\text{LUMO}}^{\text{opt}} = [E_{\text{HOMO}} + E_{\text{g}}^{\text{opt}}] \text{ eV.}$$

Table 2.7 and Figure 2.18 show a clear shift to higher potentials of the redox processes of BODIPY **55**. If compared with **53** (Figure 2.18 (B)), structure **55** ( $E_{\text{red}} = -0.97$  and  $E_{\text{ox}} = 1.35$ ) is easier to reduce than **53** ( $E_{\text{red}} = -1.21$  and  $E_{\text{ox}} = 1.22$ ) by 240 mV and it is harder to oxidise by 130 mV. These deviations are caused by the electron withdrawing effect, brought by the pentafluorophenyl group, that increases the ability to stabilise a radical anion and reduces the ability to stabilise a positive charge. The shift to negative potentials makes the compound **56** the easiest compound to oxidize among all **1S-BDP**. This feature is

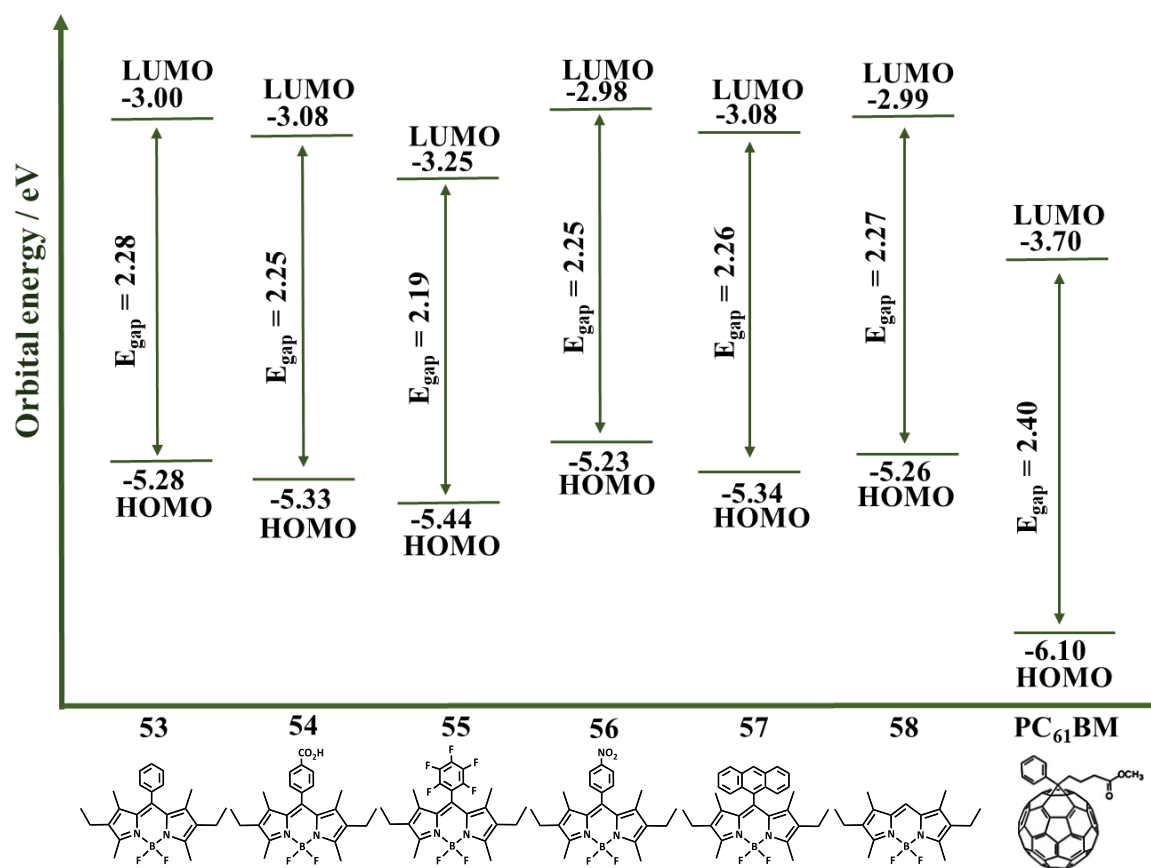
attributed to the different distribution of the electron density and to the intramolecular charge transfer already mentioned in the photophysical discussion.

Brédas and co-workers demonstrated a linear correlation between the ionisation potential (energy required to tear the least bound electron) and the oxidation potential, and the electronic affinity (energy released when an electron is added) with the reduction potential.<sup>37</sup> Thus, after  $E_{\text{onset}}^{\text{ox}}$  being referred to the vacuum level it corresponds to ionisation potential (IP) and  $E_{\text{onset}}^{\text{red}}$  to the electron affinity (EA) of the molecule.<sup>38</sup> It can also be considered that IP corresponds to the absolute energy of the HOMO ( $E_{\text{HOMO}} = -\text{IP}$ ) and EA corresponds to the absolute energy of the LUMO ( $E_{\text{LUMO}} = -\text{EA}$ ).

The data depicted in Table 2.7 show that the differences between the energy gaps obtained from cyclic voltammetry ( $Eg^{\text{elec}}$ ) and those calculated from the absorption spectra ( $Eg^{\text{opt}}$ ) are minimal. Some previous studies explained the differences between  $Eg^{\text{elec}}$  and  $Eg^{\text{opt}}$  based on their fundamental operational principles,<sup>39, 40</sup> since electrochemical experiment results are related to addition or extraction of single charges while UV-Vis spectrophotometry analysis refers to the formation of an excited state where the electron and the hole remain bounded to each other. Thus, electrochemical band gap would be expected to be higher (by the exciton binding energy) than the optical band gap.

In addition to the calculation of HOMO and LUMO energies, there is a method where LUMO energies can be calculated from -IP ( $E_{\text{HOMO}}$ ) by adding the optical gap energy. This method is widely used in the BODIPY-OPVs reports.<sup>2, 41-46</sup> From the molecular point of view, it could be argued that EA refers to the LUMO energy of the negatively charged species, which could be different from the LUMO energy of the neutral species. However, polarisation effects of the neighbour molecules in the solid state may contribute to stabilise that negative charge. Therefore, there is no agreement on the proper way to obtain LUMO energy levels. Table 2.7 presents the LUMO energies calculated by both methods ( $E_{\text{LUMO}}^{\text{elec}}$  and  $E_{\text{LUMO}}^{\text{opt}}$ ) and the difference between them is not significant.

Scheme 2.3 presents the HOMO-LUMO energy levels of all BODIPY compounds of **1S-BDP** and the electron-acceptor molecule used in the photovoltaic studies (PC<sub>61</sub>BM). The HOMO and LUMO energies lie above the corresponding levels of PC<sub>61</sub>BM. Therefore, the six BODIPYs are suitable candidates to be used as electron-donors (concerning PC<sub>61</sub>BM) in BHJ photovoltaic cells, thereby forming a type II heterojunction.



**Scheme 2.3.** Frontier orbital energies of all synthesised BODIPYs and PC<sub>61</sub>BM ([6,6]-phenyl-C61-butyric acid methyl ester).<sup>47</sup>

#### 2.2.4. Computational studies

To better understand the change of photophysical and electrochemical properties among the various BODIPYs, the energies of the frontier orbitals were calculated by Density Functional Theory (DFT) in vacuum after optimisation of the ground-state geometries (conformations). The optimised ground-state geometries and electronic distribution in HOMO and LUMO levels are shown in Table 2.8. All calculations were carried out using the B3LYP method and a 6-31 G\* basis set using the SPARTAN v.10 software package (Spartan, Wave Function Inc. USA).

The vacuum optimised geometry results corroborate the results obtained by x-ray diffraction studies in single crystals. The BODIPY core is almost planar, the two fluorine atoms are in a plane that is perpendicular to the BODIPY core, the boron atom has tetrahedral coordination, and the *meso*-substituted groups are nearly perpendicular to the plane of the BODIPY core.

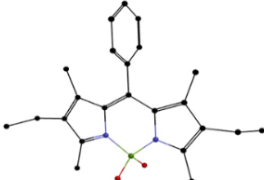
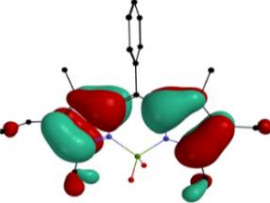
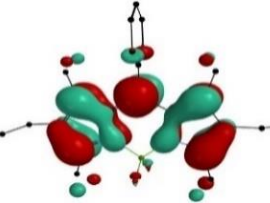
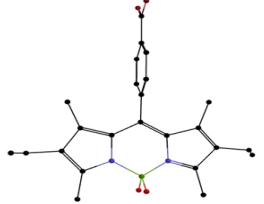
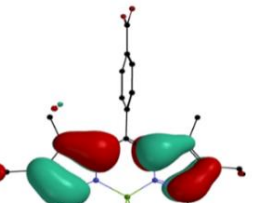
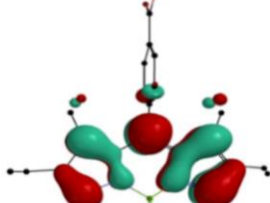
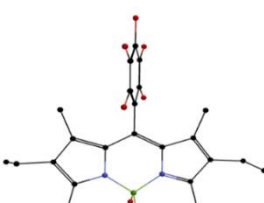
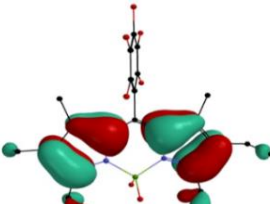
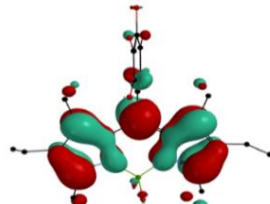

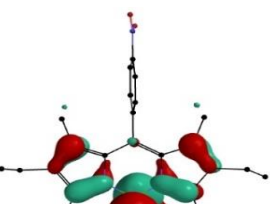
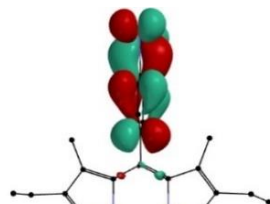
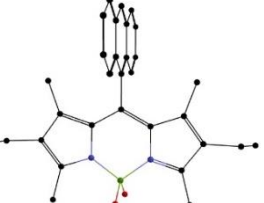
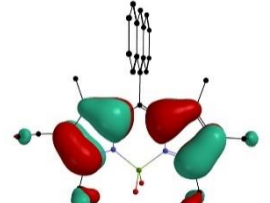
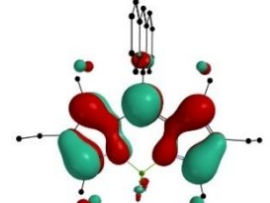
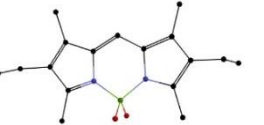
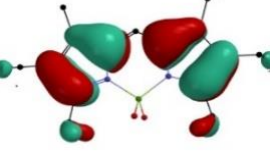
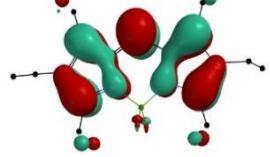
The  $\pi$ -electrons in the HOMOs are delocalised over the entire BODIPY with higher density at  $\beta$ -pyrrolic positions. In none of the compounds, we find significant electron density on the *meso* substituent group.

The LUMO orbitals are also delocalised within the BODIPY backbone, but with higher electron density at the *meso* carbon (with the exception of **56**). Neither HOMO and LUMO show significant delocalisation between the core and the *meso* substituents, as expected for their nearly perpendicular orientation.

In the case of **56**, the LUMO is entirely localised in the nitrophenyl substituent. The absence of spatial overlap between HOMO and LUMO of **56**, indicates that the HOMO – LUMO transition has a charge transfer character, which is in line with the fluorescence results discussed above.

The HOMO energies obtained from cyclic voltammetry are very similar to the calculated ones. However, a somewhat higher deviation is found for LUMO energies. The dissimilarity between the experimental LUMO energy and the calculated can be justified by the lack of solvent stabilisation effects. Nevertheless, the experimental and calculated data follows the same trend, in what concerns HOMO, LUMO and energy-gap, despite the fact that theoretical calculations considered that the molecules were in vacuum.

**Table 2.8.** Optimised structures, electron distribution in HOMO and LUMO and their energies (in eV) of the BODIPY series, obtained by DFT calculations in vacuum.

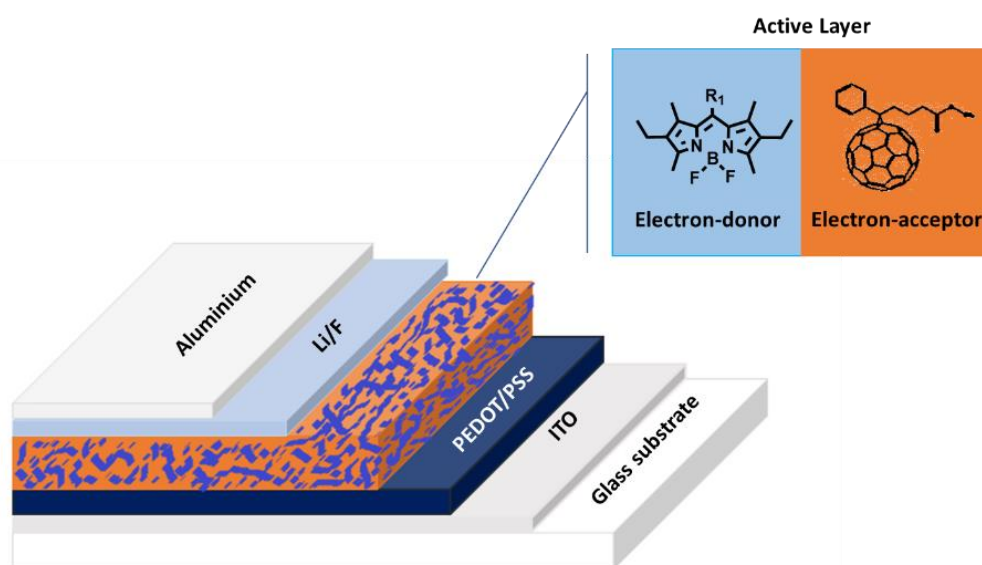
BODIPY	Optimized Geometry	HOMO	LUMO
53		 -5.16	 -2.24
54		 -5.25	 -2.29
55		 -5.42	 -2.62
56		 - 4.91	 -2.65
57		 -5.18	 -2.27
58		 -5.23	 -2.30

### 2.3. BODIPY-based organic photovoltaic cells

As mentioned above, organic photovoltaics rely on a combination of an electron-donor (D) and an electron-acceptor (A) materials with an offset of the HOMO and LUMO levels that favours excited state electron (or hole) transfer, being the energy gain high enough to overcome the exciton binding energy. Even though the free charges generation from excitons at the D/A interface are quite complex and still a matter of debate, this remains a key requirement. As shown in Scheme 2.3 all the compounds from **1S-BDP** can be combined with PC<sub>61</sub>BM when aiming to form such heterojunction. The combination of materials can be made either on bi-layer structure or in a blend, forming a bulk heterojunction (BHJ). Due to the much larger D/A interfacial area, the BHJ structure is the one that leads to the best performing OPVs.<sup>48,49</sup> Following the photophysical and electrochemical results, we assessed the photovoltaic performance of the **1S-BDP** compounds in BHJ cells, using PC<sub>61</sub>BM as electron-acceptor.

#### 2.3.1. Organic photovoltaic cells preparation

BHJ photovoltaic cells are multilayer devices as shown in Figure 2.19. Our work focus was mainly on the active layer, where the BODIPYs were mixed with fullerenes and spin-coated over the hole extraction layer (PEDOT-PSS). The efficiency of the photovoltaic cell is strongly dependent on the donor/acceptor (D/A) ratio in the photoactive layer, its thickness and the solvent used to prepare the D/A mixture.



**Figure 2.19.** OPV structure used to assess the behaviour of the **1S-BDP** compounds.



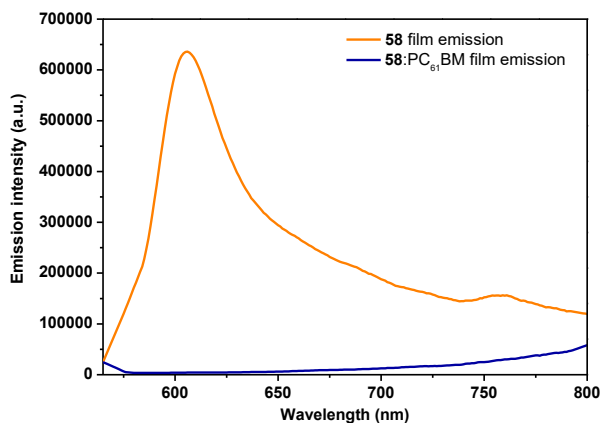
PC<sub>61</sub>BM is a soluble derivative of the buckminsterfullerene C<sub>60</sub> and one of the most commonly used electron-acceptors. It has good solubility in common solvents, contributing to a good quality of the photoactive film. It combines strong electron-accepting character, low-lying LUMO level, quick and efficient charge transfer, and high electron mobility, making it an appealing material for photovoltaic applications.<sup>50, 51</sup>

The first films of **1S-BDP**:PC<sub>61</sub>BM were produced from 20 mg of solids per 1 ml of chloroform solution, with a weight ratio of 1:1 and deposited by spin-coating at 1200 rpm on a glass substrate. Compound **54** showed low solubility in chloroform and the blend films prepared under the mentioned conditions were non uniform (see Figure 2.20), leading to devices with irregular current-voltage (J–V) response. For this reason, **54** was not included in the photovoltaic studies.



**Figure 2.20.** Image of the **54**:PC<sub>61</sub>BM blend, obtained with the video camera of the profilometer.

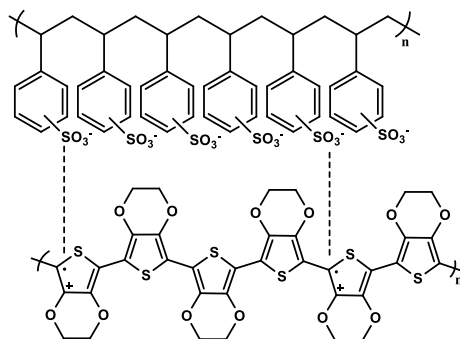
A first assessment of the efficiency of exciton dissociation by a D/A blend film is the measurement of its fluorescence intensity and comparison with that of the neat compound (BODIPY), in view of the negligible fluorescence of neat fullerenes. Efficient exciton dissociation should translate into an extensive BODIPY fluorescence quenching. Figure 2.21 reveals a complete quenching of the BODIPY **58** emission upon blending with PC<sub>61</sub>BM, which is consistent with an efficient excited state electron transfer from BODIPY to fullerene, signalling good perspectives for application in OPVs.



**Figure 2.21.** Emission spectra of the films of neat **58** and **58**:PC<sub>61</sub>BM blend (excitation at 545 nm).

In OPVs, the top and bottom of the device are defined by two selective electrodes that extract the free charges (electrons and holes). We used a transparent indium tin oxide (ITO) as back/bottom electrode (deposited on glass) and LiF/Al or Ca/Al as top electrode.

PEDOT:PSS (Figure 2.22) was used in all experiments as a hole extraction layer material. It is a conductive polymer, available as an aqueous dispersion. High-quality PEDOT:PSS films can be readily prepared by conventional solution processing techniques, such as spin coating and printing. PEDOT:PSS films have high transparency, high mechanical flexibility, and good thermal stability.<sup>52, 53</sup> Additionally, the PEDOT:PSS layer reduces the surface roughness of the ITO electrode as well as facilitates the hole injection/extraction, due to its high work function (ca. 5.1 eV).<sup>54</sup>

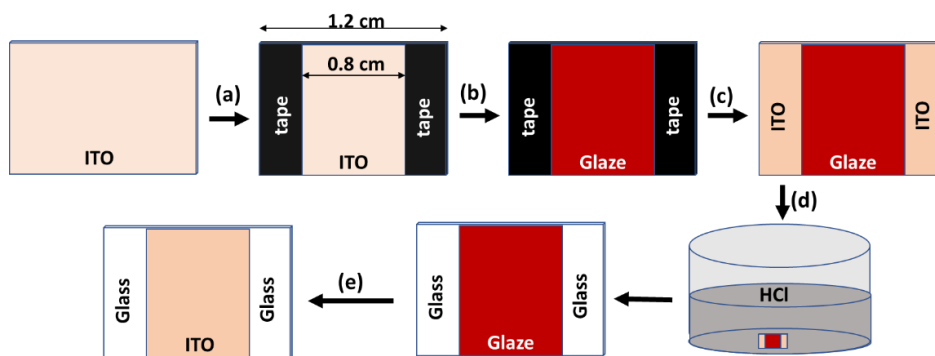


**Figure 2.22.** Chemical structure of PEDOT: PSS, a blend of PEDOT with PSSH (which acts as a dopant and allows some “solubility” of the blended material in water).

The OPV manufacture followed several steps:

(1) Active layer solution preparation: the BODIPY compound and PC<sub>61</sub>BM were weighed and mixed in the selected solvent and left stirring for up to 16 hours at 50°C.

(2) Substrate patterning: the sequence of steps involved is shown in Scheme 2.4: (a) coverage of ITO sidebands with tape; (b) coating the uncovered ITO region, with glaze; (c) removal of the tape; (d) etching (with HCl solution); (e) clearance of the glaze with acetone.

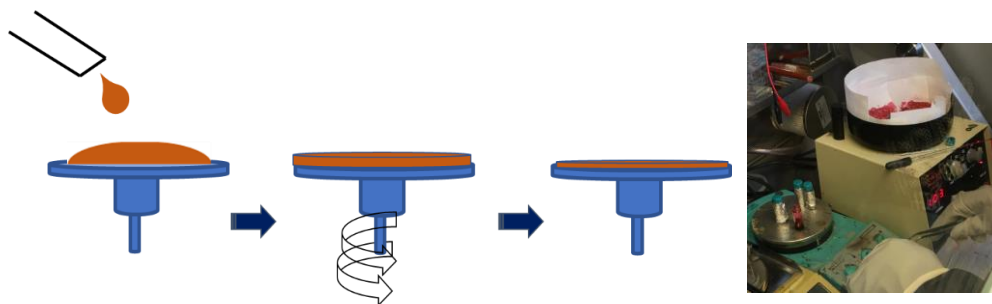


**Scheme 2.4.** Substrate patterning steps.

(3) Substrate cleaning: The patterned glass substrates were systematically cleaned in an ultrasonic bath with non-ionic detergent, distilled water, acetone, and isopropanol for 15 minutes each. Then, they were dried under nitrogen and treated with O<sub>2</sub> plasma.

(4) PEDOT:PSS layer: deposition by spin coating (1800 rpm, 60 seconds), and then dried on a hot plate at 125 °C for 10 minutes, resulting in a film thickness of 40 nm.

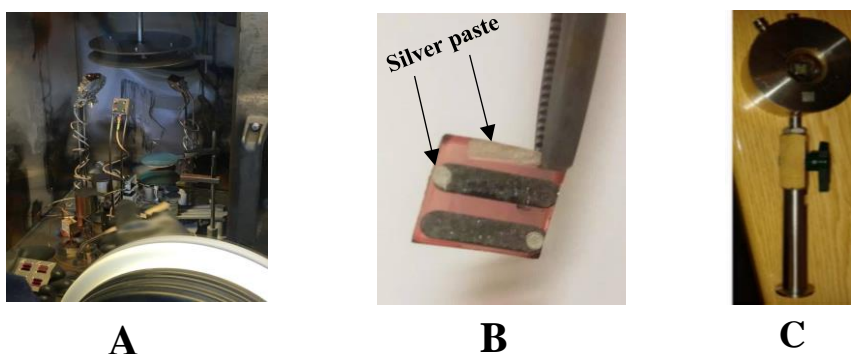
(5) Active layer: the solution of the BODIPY:PC<sub>61</sub>BM blend was spin-coated (1300 rpm, 60 seconds) on the PEDOT:PSS layer, Figure 2.23.



**Figure 2.23.** Spin coating process and spin coater.

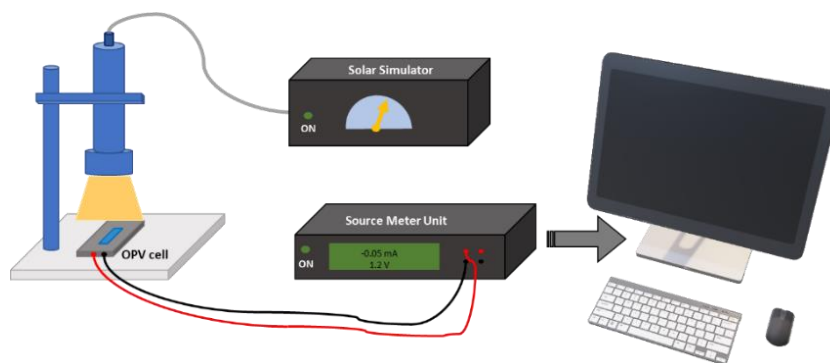
(6) Top electrodes: to obtain electrodes with very low work function, Ca (20 nm) or LiF (1.5 nm) were first deposited followed by a layer of Al (60-100nm). These films were thermally deposited on the top of active layer film, under a base pressure of 10<sup>-6</sup> mbar, defining a device area of 0.24 cm<sup>2</sup>, using a chamber inside the glove box Figure 2.24 (A).

(7) Electric contacts: electrical contacts to both electrodes were made upon placement of the photovoltaic cell inside the measuring cell, using a spring load contact and using silver paste on top of ITO and Al to improve the quality of the contact and provide higher robustness (Figure 2.21 (B)). The measuring cell is close inside the glove box and taken outside to the test setup, thereby maintain the photovoltaic cell under nitrogen atmosphere (Figure 2.21 (C)).



**Figure 2.24.** Glove box and “sublimation chamber” (A), final photovoltaic cell (B), support measuring cell (C).

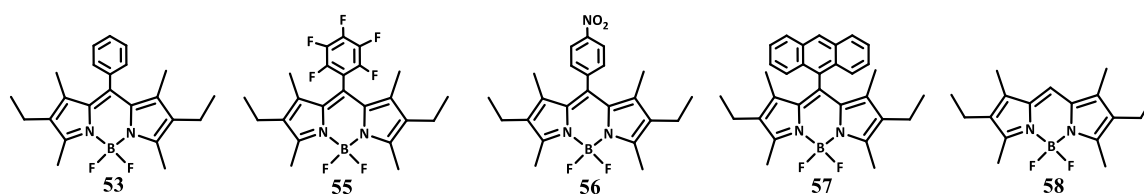
The photovoltaic characterisation was done with the help of a set of components (Figure 2.25) including a solar simulator (Oriol Sol3A, class AAA), a calibrated silicon cell, and a computer-controlled source meter (Keithley 2400 Source-Meter unit). The OPVs were characterised under room temperature, and a simulated irradiance, generated by a solar simulator consisting of a xenon lamp and an appropriate AM1.5G filter, between  $82 \text{ mW}\cdot\text{cm}^{-2}$  and  $100 \text{ mW}\cdot\text{cm}^{-2}$  at air mass (AM) 1.5G condition. The light intensity was accurately measured with a calibrated silicon solar cell after each study. External quantum efficiency (EQE) spectra were obtained under short-circuit conditions, using a homemade system with a halogen lamp as light source coupled to a monochromator. Its intensity at each wavelength was determined using a calibrated photodiode. Like in the I-V measurements, the EQE spectra were measured under inert atmosphere conditions and the short-circuit current was measured with a Keithley 2400 Source-Meter unit.



**Figure 2.25.** Setup for solar-cell measurements and schematic illustrations of each component (solar simulator, sample cell, computer-controlled source meter unit).

### 2.3.2. Photovoltaic studies of the first series of BODIPY molecules (1S-BDP)

Due to the minor solubility of compound **54** and the difficulty to obtain a uniform film of its blend with PC<sub>61</sub>BM, we did not assess the performance of OPVs based on this compound. Bulk heterojunction OPVs were manufactured with a typical multilayer structure: ITO/PEDOT:PSS/active layer/LiF or Ca/Al for the remaining compounds of the **1S-BDP** (Figure 2.6) At least eight cells of each different blend were tested, and the average results reflect the contribution of at least six of such photovoltaic cells.



**Figure 2.26.** BODIPY dyes from **1S-BDP** tested in BHJ-OPVs.

Aiming the best power conversion efficiency (PCE), various preparation conditions of the active layer film were tested. The optimisation procedures (Table 2.9) were carried out using **58**, and dichlorobenzene as solvent, and the varied parameters: donor/acceptor weight ratio, active layer solution solids concentration and the top electrode (Ca/Al or LiF/Al).

**Table 2.9.** Photovoltaic parameters (short-circuit current,  $J_{sc}$ , open-circuit voltage,  $V_{oc}$ , fill factor, FF, and power conversion efficiency, PCE) of the optimised **58**:PC<sub>61</sub>BM-based OPV under AM 1.5 G illumination at 88 mW/cm<sup>2</sup>. The blend film was prepared from a dichlorobenzene solution.

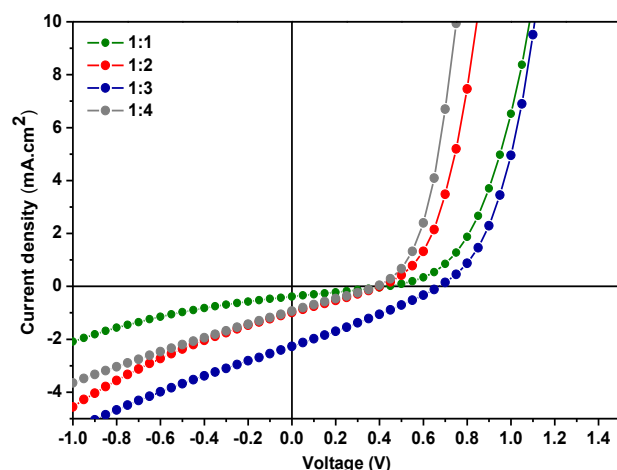
58:PC <sub>61</sub> BM ratio (m/m)	Concentration	Active layer thickness (nm)	Top electrode	Maximum				Average*			
				$J_{sc}$ (mA/cm <sup>2</sup> )	$V_{oc}$ (V)	FF	PCE (%)	$J_{sc}$ (mA/cm <sup>2</sup> )	$V_{oc}$ (V)	FF	PCE (%)
1:1	40 mg/ml	116	LiF/Al	0.38	0.44	0.27	0.05	0.33	0.40	0.27	0.04
1:2	40 mg/ml	112	LiF/Al	0.99	0.41	0.26	0.12	0.83	0.38	0.25	0.09
1:3	40 mg/ml	72	LiF/Al	2.27	0.67	0.27	0.47	1.90	0.62	0.28	0.37
1:4	40 mg/ml	69	LiF/Al	0.94	0.39	0.26	0.11	0.93	0.31	0.26	0.08
1:3	30 mg/ml	67	LiF/Al	0.97	0.45	0.26	0.13	0.75	0.39	0.26	0.09
1:3	25 mg/ml	60	LiF/Al	0.64	0.31	0.27	0.06	0.56	0.26	0.24	0.04
1:3	40 mg/ml	80	Ca/Al	1.43	0.64	0.28	0.32	1.40	0.64	0.28	0.31

\* Average values calculated from at least 6 devices.

The best OPVs based on compound **58** were prepared from a **58**:PC<sub>61</sub>BM blend with a weight ratio of 1:3, dissolved in dichlorobenzene at 40 mg/ml, deposited by spin-coating at 1300 rpm, and LiF/Al as top electrode.

Figure 2.27 compares the J-V characteristics of the **58**:PC<sub>61</sub>BM OPVs at different donor: acceptor ratios, evidencing the best performance of the cell with 1:3 ratio. It is well known that the donor:acceptor ratio has a strong impact on the bulk heterojunction OPVs performance. The ratio affects the phase separation (namely the size and distribution of the donor and acceptor domains) which, affects not only the efficiency of exciton dissociation but also the charge transport.

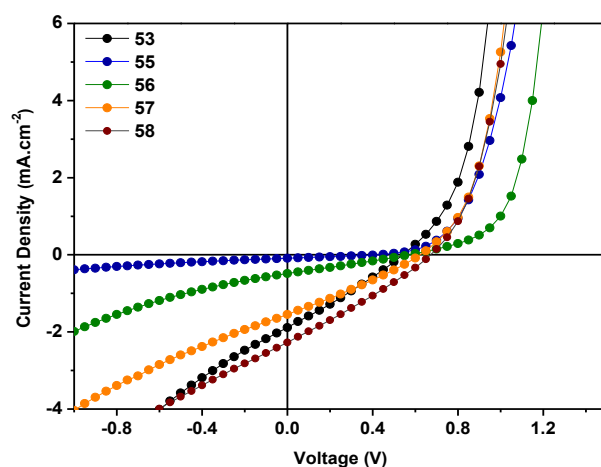
As shown in Table 2.9, while keeping the total solids concentration, the change of D:A ratio changes also the film thickness, which might also affect the OPVs performance. Thicker layers increase the photons absorption probability and consequently exciton formation, but, due to the low charge mobility in these organic systems, it also increases the probability of charge recombination. Thus, an equilibrium situation must be found for every system. The optimisation process showed that 70 nm is the most favourable thickness.



**Figure 2.27.** Current density-voltage characteristics of **58**:PC<sub>61</sub>BM-based OPVs at different donor-acceptor ratios, under AM 1.5G illumination at 88 mW.cm<sup>-2</sup>.

The top electrode should have a low work function to allow an efficient electron extraction and not to influence the open-circuit voltage. While Al alone, with a work function of ca. 4.28 eV is a poor electron extraction electrode, its combination with a low work function metal like Ca or an interlayer of LiF (with a thickness around 1nm) decrease the work function, improving electron extraction ability, improve selectivity and help to prevent Al atoms from diffusing into the active layer.<sup>55</sup> During the optimisations, the OPVs with LiF produced more current than those with Ca, which resulted in better PCE (0.47 % against 0.32 % of maximum PCE, Table 2.9).

The other four BODIPY molecules (**53**, **55**, **56** and **57**) were tested using the preparation conditions optimised for compound **58**. The results of the photovoltaic measurements are shown in Table 2.10, and the best J–V curves recorded for each BODIPY compound are shown in Figure 2.28.


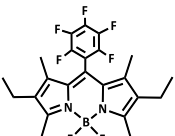
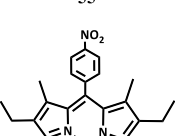
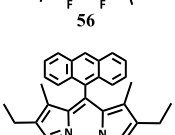
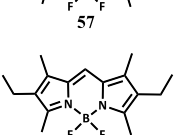


**Figure. 2.28.** Current density-voltage characteristics of BODIPY:PC<sub>61</sub>BM-based OPVs, under AM 1.5G illumination at 88 mW.cm<sup>-2</sup>.

As mentioned above, the best thickness of the active layer should be around 70 nm. However, under the optimal conditions (solution concentration of 40 mg/ml) the active layer of the **55**-based OPV has 110 nm of thickness (Table 2.10). When the thickness was reduced to 77 nm (using 35 mg/ml), the PCE remained at 0.01 %.

The OPV with the best performance was based on the BODIPY without substitution at *meso*-position (**58**), and the poorest performing compounds (**55** and **56**) are those with electron-withdrawing groups at the *meso*-position. These results indicate that the nature of the group at the *meso*-position affects the photovoltaic performance, though the explanation is not clear as many factors are involved (such as phase separation details upon blending with PC<sub>61</sub>BM and hole transporting ability).

**Table 2.10.** Photovoltaic parameters of the optimised BODIPY:PC<sub>61</sub>BM-based OPV cells, under AM 1.5 G illumination at 88 mW/cm<sup>2</sup>. Solutions were prepared in dichlorobenzene, with a total concentration of 40 mg/ml and with a BODIPY:PC<sub>61</sub>BM weight ratio of 1:3.

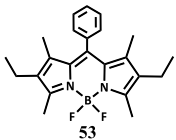
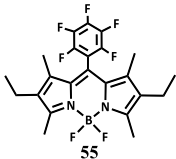
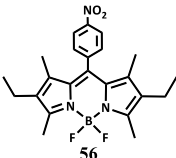
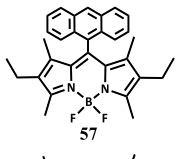
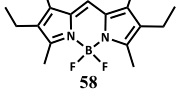
Dye	Active layer thickness (nm)	Maximum						Average*			
		J <sub>sc</sub> (mA/cm <sup>2</sup> )	V <sub>oc</sub> (V)	FF	R <sub>SH</sub> (Ω.cm <sup>2</sup> )	R <sub>s</sub> (Ω.cm <sup>2</sup> )	PCE (%)	J <sub>sc</sub> (mA/cm <sup>2</sup> )	V <sub>oc</sub> (V)	FF	PCE (%)
	63	1.93	0.54	0.26	340	230	0.31	1.67	0.51	0.25	0.24
	110	0.09	0.42	0.26	2870	1330	0.01	0.09	0.39	0.22	0.01
	70	0.49	0.53	0.30	930	740	0.09	0.51	0.51	0.27	0.08
	63	1.55	0.62	0.27	480	250	0.30	1.46	0.56	0.27	0.26
	72	2.27	0.67	0.27	350	180	0.47	1.90	0.62	0.28	0.37

\* Average values calculated from at least 6 devices.

The OPVs based on the **1S-BDP** presented high  $V_{OC}$  values which some are similar to the  $V_{OC}$  of the best BODIPY-based solar cells.<sup>56</sup>  $J_{SC}$  and FF are the main limiting factors in these photovoltaic systems. The proposed BODIPY dyes show high absorption coefficients and absorbance in a favourable range of the spectrum. Therefore, the high  $R_s$  related to a sub-optimal active layer morphology and/or poor charge transport could be the reason for the less optimum parameters.

All the former OPVs were fabricated from blends solutions prepared in dichlorobenzene with a concentration of 40 mg of solids per ml. In spite of good film formation, the high concentration of the active blend solution is a limitation since a considerable amount of materials is consumed per film, in view of the significant waste of solution that occurs during spin coating. We found that using chloroform instead of dichlorobenzene we could obtain films ca. 80 nm in thickness with 15mg/ml concentration, with the previously optimised donor-acceptor ratio. The performance results of the OPVs prepared from chloroform solution are presented in Table 2.11.

**Table 2.11.** Photovoltaic performance parameters of the **1S-BDP** OPV cells under illumination at 88 mW/cm<sup>2</sup>, with ratio of 1:3 BODIPY to PC<sub>61</sub>BM from a solution of chloroform at 15 mg/ml.

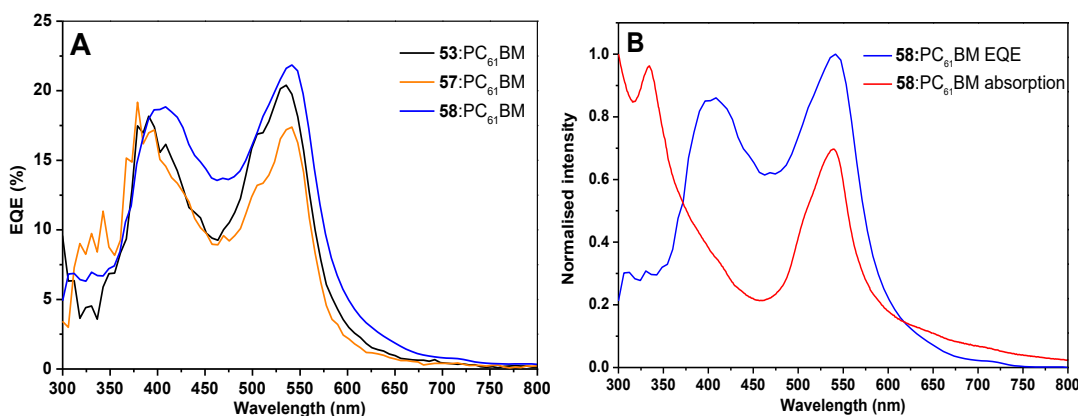
Dye	Active layer thickness (nm)	Maximum						Average			
		$J_{sc}$ (mA/cm <sup>2</sup> )	$V_{oc}$ (V)	FF	$R_{SH}$ ( $\Omega \cdot cm^2$ )	$R_s$ ( $\Omega \cdot cm^2$ )	PCE (%)	$J_{sc}$ (mA/cm <sup>2</sup> )	$V_{oc}$ (V)	FF	PCE (%)
 53	80	0.93	0.73	0.27	810	454	0.22	0.85	0.62	0.27	0.17
 55	77	0.13	0.37	0.27	2956	2321	0.02	0.11	0.37	0.27	0.01
 56	85	0.46	0.30	0.26	624	483	0.04	0.39	0.26	0.26	0.03
 57	81	0.91	0.73	0.26	804	669	0.20	0.68	0.69	0.26	0.15
 58	78	1.18	0.58	0.26	482	349	0.21	1.00	0.53	0.26	0.16

\* Average values calculated from at least 6 devices.



The change to chloroform did not bring better efficiencies to the BODIPY-based OPV in the majority of the tests. It improved the  $V_{OC}$  of **53** and **57**-based OPVs, but, with the exception of **55**,  $J_{SC}$  decreased when compared with the OPVs prepared from dichlorobenzene. These differences can be explained by changes in the morphology of the blend since the morphology of a system is strongly dependent on thermodynamic and kinetic aspects of the thin film formation during the spin-casting and drying processes.<sup>57, 58</sup>

The external quantum efficiency (EQE) is calculated from the number of electrons collected under short-circuit conditions, divided by the number of incident photons. As this parameter is calculated for every wavelength, the result is a spectral distribution plot, which indicates the percentage of radiation at each wavelength that can be successfully converted into electrical charges collected at the electrodes. The external quantum efficiency (EQE) was calculated for **53**:PC<sub>61</sub>BM, **57**: PC<sub>61</sub>BM and **58**: PC<sub>61</sub>BM OPVs fabricated from dichlorobenzene solution, and it is shown in Figure 2.29 (A).



**Figure 2.29.** EQE curves of the optimized **53**:PC<sub>61</sub>BM, **57**:PC<sub>61</sub>BM and **58**:PC<sub>61</sub>BM-based OPV cells (A) and overlap of **58**:PC<sub>61</sub>BM absorption film with **58**:PC<sub>61</sub>BM EQE (B).

The EQE profiles are similar to the corresponding absorption spectra of the blends (Figure 2.29 B), with a broad response in the 375-600 nm range. This response is mainly due to the BODIPY absorption profile, but some contribution of PC<sub>61</sub>BM at 300-400 nm is also detected. The stronger response of the **58**-based OPV is consistent with a higher short-circuit current.

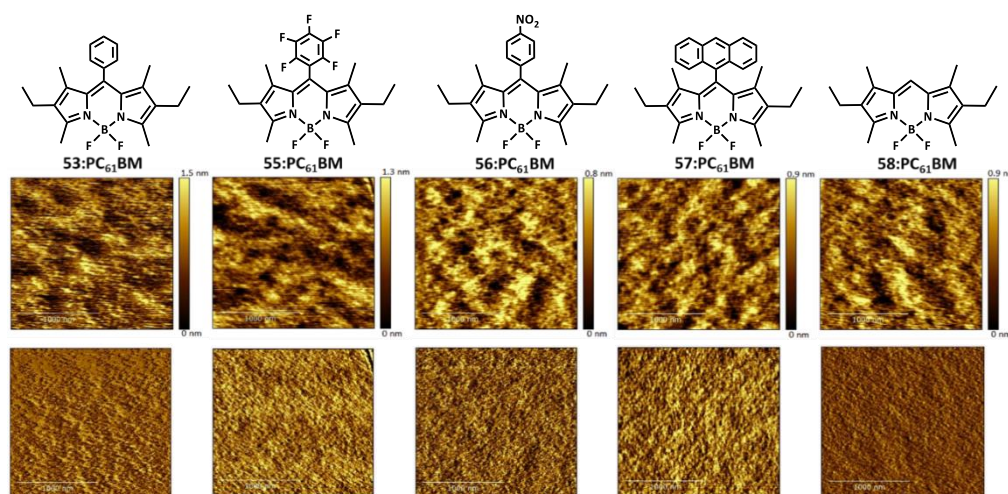
### 2.3.3. Surface morphology of the active layer

Atomic Force Microscopy (AFM) is a technique that relies on the interaction between a very sharp tip and the surface of a sample. Upon scanning of the sharp probe on a surface, the topographic images of the surfaces (height images) at a nanometre scale can be obtained.

When the measurement is carried without contact, a phase image can be acquired, which reflects the phase difference between the voltage pulse that imposes a vibration of the tip and the deflections of the tip due to the interactions with the surface. The phase image is sensitive to both the topography and the viscoelastic properties of the surface material, that can be used to identify regions of different materials of a blend.

It was mentioned above, the OPVs performance is highly sensitive to the morphology of the blend. Although AFM can only give information about the surface, this can provide indications about the details of the phase separation and, therefore, be related to the photoelectronic response. However, it should be kept in mind that the surface topography may not represent the bulk morphology, and therefore it is difficult to correlate the efficiency with the AFM results.

The films' surface of **53:PC<sub>61</sub>BM**, **55:PC<sub>61</sub>BM**, **56:PC<sub>61</sub>BM**, **57:PC<sub>61</sub>BM** and **58:PC<sub>61</sub>BM**, were characterized by AFM. Figure 2.30 presents the topography and phase images of the films. All films exhibit very similar surface topography without noticeable phase domains or aggregates.



**Figure 2.30.** AFM topography (top) and phase (bottom) images (2 $\mu$ m vs 2 $\mu$ m) of **53:PC<sub>61</sub>BM**, **55:PC<sub>61</sub>BM**, **56:PC<sub>61</sub>BM**, **57:PC<sub>61</sub>BM** and **58:PC<sub>61</sub>BM**.

The blends exhibited very flat surfaces (root mean squared (RMS) inferior to 0.40nm). Usually, low roughness and small phase domains are indicators of good miscibility between the donor and the acceptor and are associated with good photovoltaic efficiencies. These results suggest that there is good miscibility between the BODIPY dyes and the PC<sub>61</sub>BM, with a good donor:acceptor interpenetrating network within the blend films. This morphology facilitates the exciton dissociation (by virtue of a large donor/acceptor interface) but tends to limit the charge transport, as it does not allow the formation of percolation paths for the generated charges to reach the electrodes.

### 2.3.4. Photovoltaic performance evaluation of BODIPY 55 as electron-acceptor

Fullerene derivatives are by far the most used electron-acceptor materials in OPVs. However, the search for non-fullerene acceptors has gained significant attention in recent years, mainly driven by the possibility of cheaper and better light-harvesting new acceptor molecules. Perylene and diketopyrrolopyrrole compounds are examples of new electron-acceptor that have been gaining interest in the photovoltaic field.<sup>59-63</sup>

The use of BODIPYs as electron-acceptors in BHJ photovoltaic cells could be an interesting possibility due to their general deep LUMO energy levels. However, only two works relating the use of BODIPY dyes as electron-acceptor units in OPVs were found.<sup>43,64</sup>

Compound **55** shows absorption properties and frontier orbital energy levels that prompted us to study its capability to act as electron-acceptor. Table 2.12 presents the preliminary results of the study showing the photovoltaic response of **58:55** and P3HT:**55** blends and the photovoltaic measurements of the individual compounds (single layer). Poly-3-hexylthiophene-2,5-diyl (P3HT) is a well-established electron-donor compound with HOMO and LUMO energies at 5 eV and 3 eV, respectively.<sup>65-69</sup>

The results depicted in Table 2.12 demonstrate that the **58:55** and P3HT:**55** OPVs produce low current and consequently small efficiencies. Despite the weak efficiency results, the **58:55** (1:1 ratio) and the P3HT:**58** blends seem to bring a little improvement, mainly due to the enhancement of  $V_{OC}$ , if compared with the single layer devices.

**Table 2.12.** Photovoltaic parameters for blends using **55** as electron acceptor and single layer, under AM 1.5 G illumination at 88 mW/cm<sup>2</sup>, from a solution of chloroform at 15 mg/ml.

Blend	Ratio (w/w)	Active layer thickness (nm)	Average			
			$J_{SC}$ (mA/cm <sup>2</sup> )	$V_{OC}$ (V)	FF	PCE (%)
<b>58:55</b>	1:1	101	0.002	0.52	0.27	0.0003
<b>58:55</b>	1:2	85	0.0002	0.24	0.25	0.00002
<b>58:55</b>	2:1	109	0.001	0.17	0.24	0.00005
<b>P3HT:55</b>	1:1	135	0.07	0.61	0.22	0.01
<b>58</b>	-	140	0.001	0.35	0.22	0.00009
<b>55</b>	-	91	0.001	0.27	0.22	0.00007
<b>P3HT</b>	-	108	0.05	0.41	0.26	0.006

\* Average values calculated from at least 6 devices.

The weak photovoltaic response is possibly due to an inefficient exciton dissociation. BODIPY **55** has lower HOMO and LUMO energies (-5.44 eV and -3.25 eV) than **58** (-5.26 eV and -3.99 eV) and P3HT (-5.00 eV and -3.00 eV), but the difference between them is probably not large enough to overcome the exciton binding energy. This difference should be at least 0.3 eV,<sup>70</sup> but, in both cases, the differences between the LUMOs is less than 0.3 eV, which could be one of the main reasons for such low efficiencies.

## 2.4. Conclusions for Chapter 2

This chapter reports the synthesis and characterization of a series of simple *meso*-substituted BODIPY molecules (first series), as well as two new crystal structures. The proposed first series of BODIPY molecules has an accessible synthesis and characteristics that par with those BODIPY dyes having more complex structures, which makes them very interesting materials for OPV production. Despite being a series with structures already published, the comparison of some characteristics has not been done, some by-products have never been presented or explained and the application in OPVs has not been reported for this sort of BODIPYs (without post functionalization). Additionally, it was demonstrated that the synthesis of the unexpected *meso*-free-BODIPY (**58**) results from the reaction of the pyrrole with the solvent (dichloromethane). We also showed that the use of dihalogenated reagents like  $\alpha,\alpha$ -dichlorotoluene or  $\alpha,\alpha$ -dibromotoluene lead to the formation of **53**, which is a new alternative to the synthesis of BODIPY derivatives.

The best photovoltaic performance was obtained with compound **58** (BODIPY without *meso*-groups), pointing to the fact that the substitution at this position can negatively influence the photovoltaic cells efficiency. Among the *meso*-substituted BODIPY molecules, **53** (phenyl group at the *meso*-position) and **57** (anthracenyl group at *meso*-position) have a similar photovoltaic response and they are around 3 times better than **56** (*para*-nitrophenyl group at *meso*-position) and 27 times better than **55** (pentafluorophenyl group at the *meso*-position). This variation indicates that having strong electron withdrawing groups can cause a large drop in OPV performance, especially in the photogenerated current. In general, the  $V_{OC}$  of the tested BODIPY-based OPV cells are comparable to the values of some of the best OPV cells, and the AFM studies of the active layer blend indicate good miscibility between our tested BODIPY dyes and PC<sub>61</sub>BM, with the blend films showing very flat surfaces.

## 2.5. References for Chapter 2

1. J. Liao, Y. Xu, H. Zhao, Q. Zong and Y. Fang, *Organic Electronics*, **2017**, 49, 321-333.
2. J. Liao, H. Zhao, Y. Xu, Z. Cai, Z. Peng, W. Zhang, W. Zhou, B. Li, Q. Zong and X. Yang, *Dyes and Pigments*, **2016**, 128, 131-140.
3. H. Zhao, B. Wang, J. Liao, H. Wang and G. Tan, *Tetrahedron Letters*, **2013**, 54, 6019-6022.
4. R. Misra, T. Jadhav, B. Dhokale, P. Gautam, R. Sharma, R. Maragani and S. M. Mobin, *Dalton Transactions*, **2014**, 43, 13076-13086.
5. A. Loudet and K. Burgess, *Chemical Reviews*, **2007**, 107, 4891-4932.
6. A. Bessette and G. S. Hanan, *Chemical Society Reviews*, **2014**, 43, 3342-3405.
7. E. V. Rumyantsev, Y. S. Marfin and E. V. Antina, *Russian Chemical Bulletin*, **2010**, 59, 1890-1895.
8. Y. Qi, T. Geib, A.-M. Huynh, G. Jung and D. A. Volmer, *Rapid Communications in Mass Spectrometry*, **2015**, 29, 885-890.
9. A. C. Nicolescu, Q. Li, L. Brown and G. R. Thatcher, *Nitric oxide: biology and chemistry*, **2006**, 15, 163-176.
10. S. Banfi, G. Nasini, S. Zaza and E. Caruso, *Tetrahedron*, **2013**, 69, 4845-4856.
11. A. C. Benniston, G. Copley, K. J. Elliott, R. W. Harrington and W. Clegg, *European Journal of Organic Chemistry*, **2008**, 2008, 2705-2713.
12. A. Pictet and A. Rilliet, *Berichte der deutschen chemischen Gesellschaft*, **1907**, 40, 1166-1172.
13. J. A. de Groot, J. H. Koek and J. Lugtenburg, *Recueil des Travaux Chimiques des Pays-Bas*, **1981**, 100, 405-408.
14. Q.-C. Chen, M. Soll, A. Mizrahi, I. Saltsman, N. Fridman, M. Saphier and Z. Gross, *Angewandte Chemie International Edition*, **2018**, 57, 1006-1010.
15. G. Sathyamoorthi, L. T. Wolford, A. M. Haag and J. H. Boyer, *Heteroatom Chemistry*, **1994**, 5, 245-249.
16. A. Haefele, C. Zedde, P. Retailleau, G. Ulrich and R. Ziessel, *Organic Letters*, **2010**, 12, 1672-1675.
17. S. Madhu, M. R. Rao, M. S. Shaikh and M. Ravikanth, *Inorganic Chemistry*, **2011**, 50, 4392-4400.
18. M. Hecht, T. Fischer, P. Dietrich, W. Kraus, A. B. Descalzo, W. E. S. Unger and K. Rurack, *ChemistryOpen*, **2013**, 2, 25-38.
19. V. A. Azov, P. J. Skinner, Y. Yamakoshi, P. Seiler, V. Gramlich and F. Diederich, *Helvetica Chimica Acta*, **2003**, 86, 3648-3670.

20. J. A. K. Howard, V. J. Hoy, D. O'Hagan and G. T. Smith, *Tetrahedron*, **1996**, 52, 12613-12622.
21. X. Zhou, *Acta Crystallographica Section E*, **2010**, 66, o757.
22. D.-C. Wang, C. He, J.-L. Fan, W.-W. Huang and X.-J. Peng, *Acta Crystallographica Section E*, **2007**, 63, o2900-o2900.
23. H.-J. Xu, *Acta Crystallographica Section E*, **2008**, 64, o1672.
24. M. A. Filatov, S. Karuthedath, P. M. Polestshuk, S. Callaghan, K. J. Flanagan, M. Telitchko, T. Wiesner, F. Laquai and M. O. Senge, *Physical Chemistry Chemical Physics*, **2018**, 20, 8016-8031.
25. N. Boens, V. Leen and W. Dehaen, *Chemical Society Reviews*, **2012**, 41, 1130-1172.
26. M. Maus, W. Rettig, D. Bonafoux and R. Lapouyade, *The Journal of Physical Chemistry A*, **1999**, 103, 3388-3401.
27. A. C. Benniston and G. Copley, *Physical Chemistry Chemical Physics*, **2009**, 11, 4124-4131.
28. J. Bañuelos-Prieto and R. S. Llano, *BODIPY Dyes: A Privilege Molecular Scaffold with Tunable Properties*, IntechOpen, **2019**.
29. S. Xuan, N. Zhao, X. Ke, Z. Zhou, F. R. Fronczek, K. M. Kadish, K. M. Smith and M. G. H. Vicente, *The Journal of Organic Chemistry*, **2017**, 82, 2545-2557.
30. V. Lakshmi, M. S. Shaikh and M. Ravikanth, *Journal of Fluorescence*, **2013**, 23, 519-525.
31. A. B. Nepomnyashchii, S. Cho, P. J. Rossky and A. J. Bard, *Journal of the American Chemical Society*, **2010**, 132, 17550-17559.
32. R. Y. Lai and A. J. Bard, *The Journal of Physical Chemistry B*, **2003**, 107, 5036-5042.
33. N. Heiland, C. Cidarér, C. Rohr, M. Piescheck, J. Ahrens, M. Bröring and U. Schröder, *ChemSusChem*, **2017**, 10, 4215-4222.
34. A. B. Nepomnyashchii, M. Bröring, J. Ahrens and A. J. Bard, *Journal of the American Chemical Society*, **2011**, 133, 19498-19504.
35. J.-H. Kim, M. Lee, H. Yang and D.-H. Hwang, *Journal of Materials Chemistry A*, **2014**, 2, 6348-6352.
36. W.-a. Cai, J.-w. Cai, H.-j. Niu, T.-d. Xiao, X.-d. Bai, C. Wang, Y.-h. Zhang and W. Wang, *Chinese Journal of Polymer Science*, **2016**, 34, 1091-1102.
37. J. L. Bredas, R. Silbey, D. S. Boudreaux and R. R. Chance, *Journal of the American Chemical Society*, **1983**, 105, 6555-6559.
38. F. N. Crespilho, V. Zucolotto, J. R. Siqueira Junior, A. J. F. d. Carvalho, F. C. Nart and O. N. d. Oliveira Junior, *International Journal of Electrochemical Science*, **2006**, 1, 151-159.
39. J. Sworakowski, *Synthetic Metals*, **2018**, 235, 125-130.
40. K. Vandewal, J. Benduhn and V. C. Nikolis, *Sustainable Energy & Fuels*, **2018**, 2, 538-544.

41. Y. Kubo, K. Watanabe, R. Nishiyabu, R. Hata, A. Murakami, T. Shoda and H. Ota, *Organic Letters*, **2011**, 13, 4574-4577.
42. L. Zou, S. Guan, L. Li and L. Zhao, *Chemical Research in Chinese Universities*, **2015**, 31, 801-808.
43. A. M. Poe, A. M. Della Pelle, A. V. Subrahmanyam, W. White, G. Wantz and S. Thayumanavan, *Chemical Communications*, **2014**, 50, 2913-2915.
44. T. Bura, N. Leclerc, S. Fall, P. L ev eque, T. Heiser, P. Retailleau, S. Rihn, A. Mirloup and R. Ziessel, *Journal of the American Chemical Society*, **2012**, 134, 17404-17407.
45. H. Y. Lin, W. C. Huang, Y. C. Chen, H.-H. Chou, C.-Y. Hsu, J. T. Lin and H. W. Lin, *Chemical Communications*, **2012**, 48, 8913-8915.
46. M. Mao, J.-B. Wang, Z.-F. Xiao, S.-Y. Dai and Q.-H. Song, *Dyes and Pigments*, **2012**, 94, 224-232.
47. L. Li, Y. Huang, J. Peng, Y. Cao and X. Peng, *Journal of Materials Chemistry A*, **2013**, 1, 2144-2150.
48. M. C. Scharber and N. S. Sariciftci, *Progress in Polymer Science*, **2013**, 38, 1929-1940.
49. N. Yeh and P. Yeh, *Renewable and Sustainable Energy Reviews*, **2013**, 21, 421-431.
50. N. S. Sariciftci, L. Smilowitz, A. J. Heeger and F. Wudl, *Science*, **1992**, 258, 1474-1476.
51. E. von Hauff, V. Dyakonov and J. Parisi, *Solar Energy Materials and Solar Cells*, **2005**, 87, 149-156.
52. F. Zabih, Y. Xie, S. Gao and M. Eslamian, *Applied Surface Science*, **2015**, 338, 163-177.
53. M. Hokazono, H. Anno and N. Toshima, *Journal of Electronic Materials*, **2014**, 43, 2196-2201.
54. S. G unes, H. Neugebauer and N. S. Sariciftci, *Chemical Reviews*, **2007**, 107, 1324-1338.
55. R. Steim, *The Impact of Interfaces on the Performance of Organic Photovoltaic Cells*, KIT Scientific Publishing, ISBN: 9783866445260, Karlsruhe, **2010**, 38-54.
56. L. Bucher, N. Desbois, P. D. Harvey, G. D. Sharma and C. P. Gros, *Solar Rrl*, **2017**, 1.
57. H. Zhang, C. Wang, X. Li, J. Jing, Y. Sun and Y. liu, *Solar Energy*, **2017**, 157, 71-80.
58. C. McDowell, M. Abdelsamie, M. F. Toney and G. C. Bazan, *Advanced Materials*, **2018**, 30, 1707114.
59. L. Bucher, N. Desbois, P. D. Harvey, C. P. Gros, R. Misra and G. D. Sharma, *ACS Applied Energy Materials*, **2018**, 1, 3359-3368.
60. P. Sonar, G.-M. Ng, T. T. Lin, A. Dodabalapur and Z.-K. Chen, *Journal of Materials Chemistry*, **2010**, 20, 3626-3636.
61. D. Zhao, Q. Wu, Z. Cai, T. Zheng, W. Chen, J. Lu and L. Yu, *Chemistry of Materials*, **2016**, 28, 1139-1146.

62. A. Godoy, L. Cattin, J. C. Bernède, F. Díaz and M. A. del Valle, *Macromolecular Symposia*, **2011**, 304, 109-114.
63. S. A. Lopez, B. Sanchez-Lengeling, J. de Goes Soares and A. Aspuru-Guzik, *Joule*, **2017**, 1, 857-870.
64. W. Liu, J. Yao and C. Zhan, *Chinese Journal of Chemistry*, **2017**, 35, 1813-1823.
65. M. D. Irwin, D. B. Buchholz, A. W. Hains, R. P. H. Chang and T. J. Marks, *Proceedings of the National Academy of Sciences*, **2008**, 105, 2783-2787.
66. J. J. R. Arias and M. D. V. Marques, *React. Funct. Polym.*, **2017**, 113, 58-69.
67. U. Mehmood, A. Al-Ahmed and I. A. Hussein, *Renew. Sust. Energ. Rev.*, **2016**, 57, 550-561.
68. F. Laquai, D. Andrienko, R. Mauer and P. W. M. Blom, *Macromol. Rapid Commun.*, **2015**, 36, 1001-1025.
69. J. Singh, N. Prasad, K. R. Peta and P. K. Bhatnagar, *Materials Research Express*, **2017**, 4, 085101.
70. Y.-W. Su, S.-C. Lan and K.-H. Wei, *Materials Today*, **2012**, 15, 554-562.



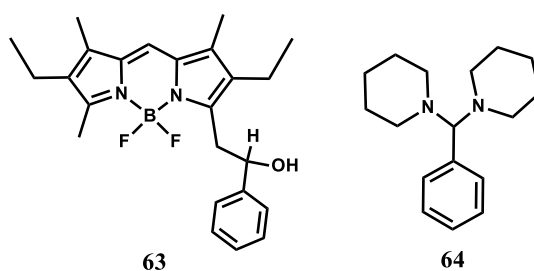
## **CHAPTER 3. BODIPY molecules with styryl groups**

There are several approaches to adjust the characteristics of BODIPY molecules, including electrophilic substitutions at the 2,6-positions,<sup>1-3</sup> nucleophilic substitution at the 3,5-positions,<sup>4-6</sup> palladium-mediated cross couplings with halogenated BODIPY derivatives,<sup>7-9</sup> attachment of styryl groups at the 1,7,3,5-positions via electrophilic methyl groups,<sup>10-13</sup> nucleophilic substitution of fluorine at the boron centre,<sup>14-17</sup> and fusion of aromatic rings in the pyrrole units.<sup>18-20</sup>

Knoevenagel condensation is a simpler, and less time consuming than the majority of functionalization methods. It has been considered one of the best strategies for obtaining BODIPYs with absorption and emission at higher wavelengths. This reaction leads to the formation of styryl or vinyl groups through the methyl groups at 2,6-positions, due to their moderate acidity. Moreover, the reaction can also occur at 1,7-positions if withdrawing groups are attached at 2,6-positions.<sup>21</sup>

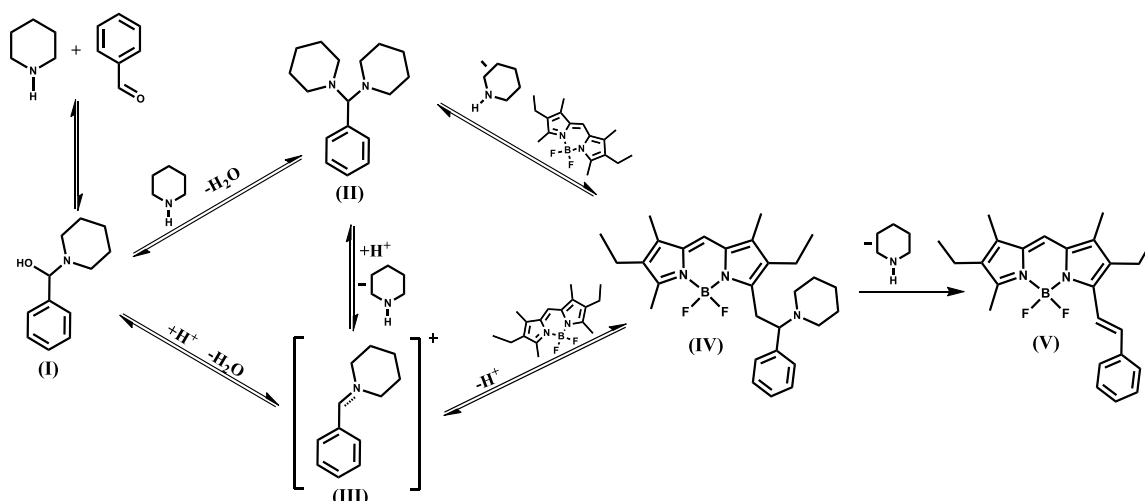
Typically, the most used path to describe the Knoevenagel condensation is based on Hann-Lapworth mechanism.<sup>22-24</sup> It includes the deprotonation of the reactive methyl compound by an amine and subsequent formation of a stabilised carbanion. Then an attack of the carbanion to the electropositive carbon atom of the aldehyde forms the new C-C bond. The resulting alkoxide group is protonated, and the resultant  $\beta$ -hydroxy compound (Figure 3.1 (**63**)) undergoes dehydration to afford the unsaturated product. The identification of the  $\beta$ -hydroxy intermediate could prove the occurrence of this mechanism.

However, Thelakkatin and co-workers when studied a Knoevenagel reaction with BODIPY scaffolds did not find any evidence of such  $\beta$ -hydroxy intermediate.<sup>25</sup> Rather, the aminal derivative (**64**) was isolated, which ruled out the Hann-Lapworth mechanism.



**Figure 3.1.** Hypothetical intermediate molecule from Hann-Lapworth mechanism ( $\beta$ -hydroxy intermediate (**63**)) and isolated aminal molecule (**64**) supporting the organocatalytic mechanism of the Knoevenagel reaction.

Scheme 3.1 shows an alternative pathway (organocatalytic mechanism) where the aminal intermediate (**64**) is formed. This mechanism has been studied to understand the condensation between malonic acid derivatives and aromatic aldehydes in the presence of secondary amines.<sup>25-27</sup>



**Scheme 3.1.** Proposed mechanism for the Knoevenagel condensation of a BODIPY dye with benzaldehyde catalysed by piperidine, adapted from Thelakkatin and co-workers.<sup>25</sup>

In the first step of the organocatalytic mechanism, the piperidine acts as a nucleophile to react with the electropositive carbonyl carbon of the aromatic aldehyde forming the hemiaminal (I). The hemiaminal can receive an additional piperidine to form the aminal (II) or can lose a molecule of H<sub>2</sub>O and originate the iminium ion intermediate (III). The same iminium intermediate can also be formed through piperidine molecule elimination from aminal (II) intermediate under acidic conditions. Then, the methyl groups of the BODIPY compound can react with the aminal (II) or with iminium ion (III) leading to the formation of the  $\beta$ -amino intermediate (IV). In the last step, there is an elimination of the piperidine molecule and formation of the mono-styryl product (V). Moreover, it is reported that the deamination of  $\beta$ -amino compound (IV) is the rate-limiting step, which can be accelerated in the presence of H<sup>+</sup>, explaining the importance of the acid (glacial acetic acid or *p*-toluenesulfonic acid) in the reaction.<sup>25, 27</sup>

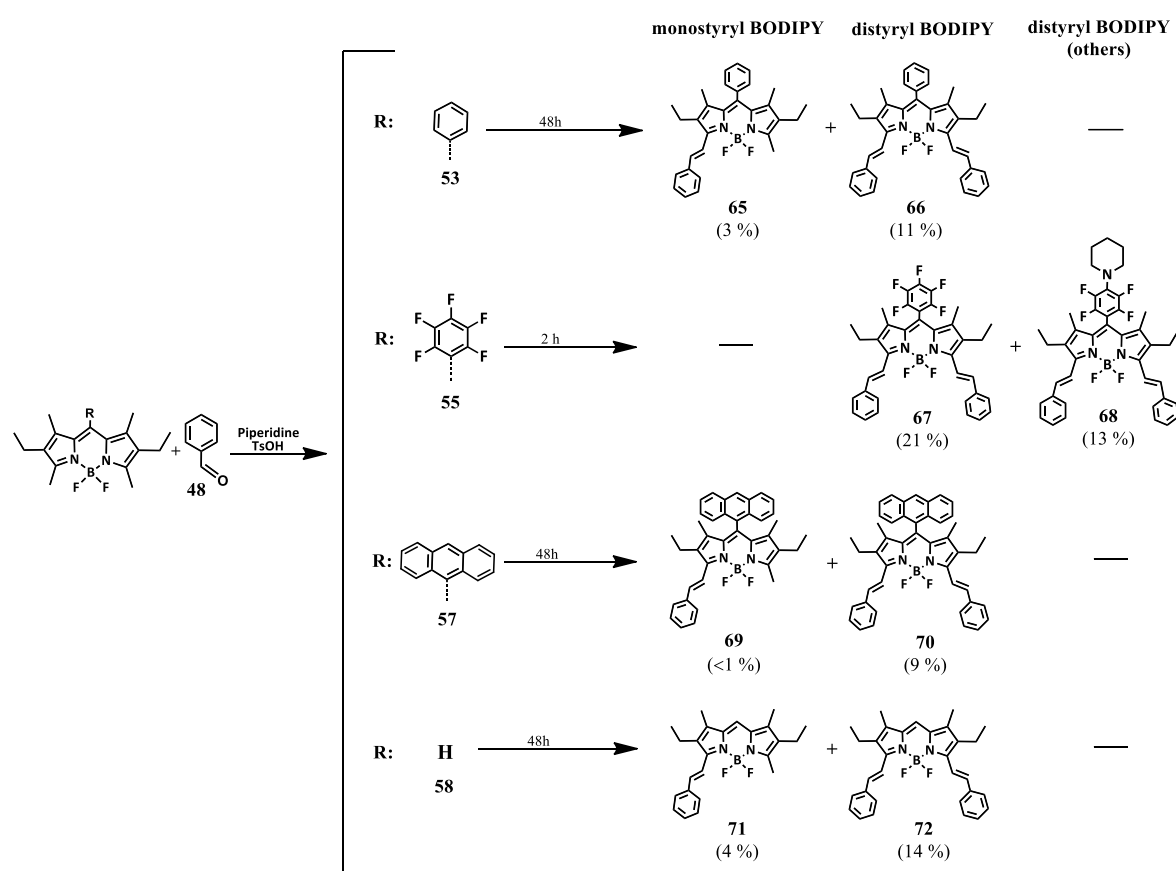
BODIPY compounds prepared by Knoevenagel condensation (distyryl-BODIPY molecules) were the first BODIPY molecules used in OPVs.<sup>28</sup> However, the most used methods to prepare BODIPY derivative for OPVs are either the Sonogashira reaction or the Suzuki coupling.<sup>29-32</sup>

In Chapter 2, it was demonstrated that simple BODIPY dyes (**1S-BDP**) fulfil the main photophysical and electrochemical requirements to be applied as electron-donor molecules in OPVs. Despite their PCE values below 0.5 %, respectable open-circuit voltages were obtained. In this context, we proposed to functionalize some of the BODIPY molecules tested in the previous chapter, by exploring the distyryl-BODIPY derivatives, to achieve new molecular structures with improved photovoltaic efficiencies.

### 3.1. Synthesis and structural characterisation of the second series of BODIPY molecules (2S-BDP)

BODIPY dyes of the second series (**2S-BDP**) were synthesised via Knoevenagel condensation of BODIPYs **53**, **55**, **57** and **58** with benzaldehyde. Compounds **53**, **57** and **58** were selected based on the preliminary OPV studies presented in Chapter 2. Despite the very low PCE values, we functionalized **55** because of its differentiated characteristics such as strong electron withdrawing *meso*-group and lower HOMO and LUMO energy levels.

Scheme 3.2 shows the synthesised products and the corresponding yields. The synthesis protocol of the **2S-BDP** BODIPYs was based on the work published by Yang and co-workers.<sup>33</sup>

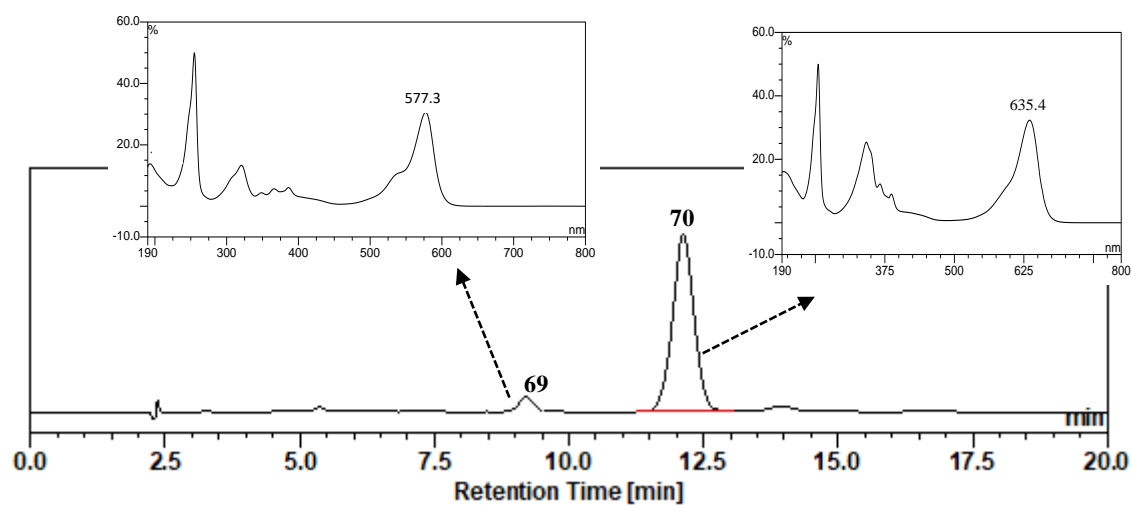


**Scheme 3.2.** Synthesis of the **2S-BDP** and the yield of the products.

The reaction between benzaldehyde and BODIPY was carried out in a solution of toluene, using piperidine, *p*-toluenesulfonic acid (as catalyst) and molecular sieves to keep the reaction mixture dehydrated. The reaction time for the functionalization of **53**, **57** and **58** was 48h at 120 °C. In order to maximise the formation of the desired distyryl products, we used 10 equivalents of benzaldehyde. Yet, some monostyryl product was still isolated in some cases.

The reaction time for BODIPY **55** did not exceed 2 hours until all the BODIPY had been consumed. This is due to the strong electron-withdrawing character of the pentafluoro fraction, which facilitates the deprotonation of the methyl groups at the  $\alpha$ -position.<sup>34</sup> There was no evidence of the mono-substituted derivative of **55**. However, a by-product (**68**) was formed since the pentafluorophenyl group is prone to undergo a highly regioselective nucleophilic aromatic substitution reaction in the presence of proper nucleophiles such as thiols, amines or alcohols.<sup>35</sup> This reaction can be controlled by its duration and by the amount of piperidine. The appearance of compound **68** is one of the main topics of the next chapter. Therefore, it is not included in the **2S-BDP** series and its properties will not be discussed in this chapter.

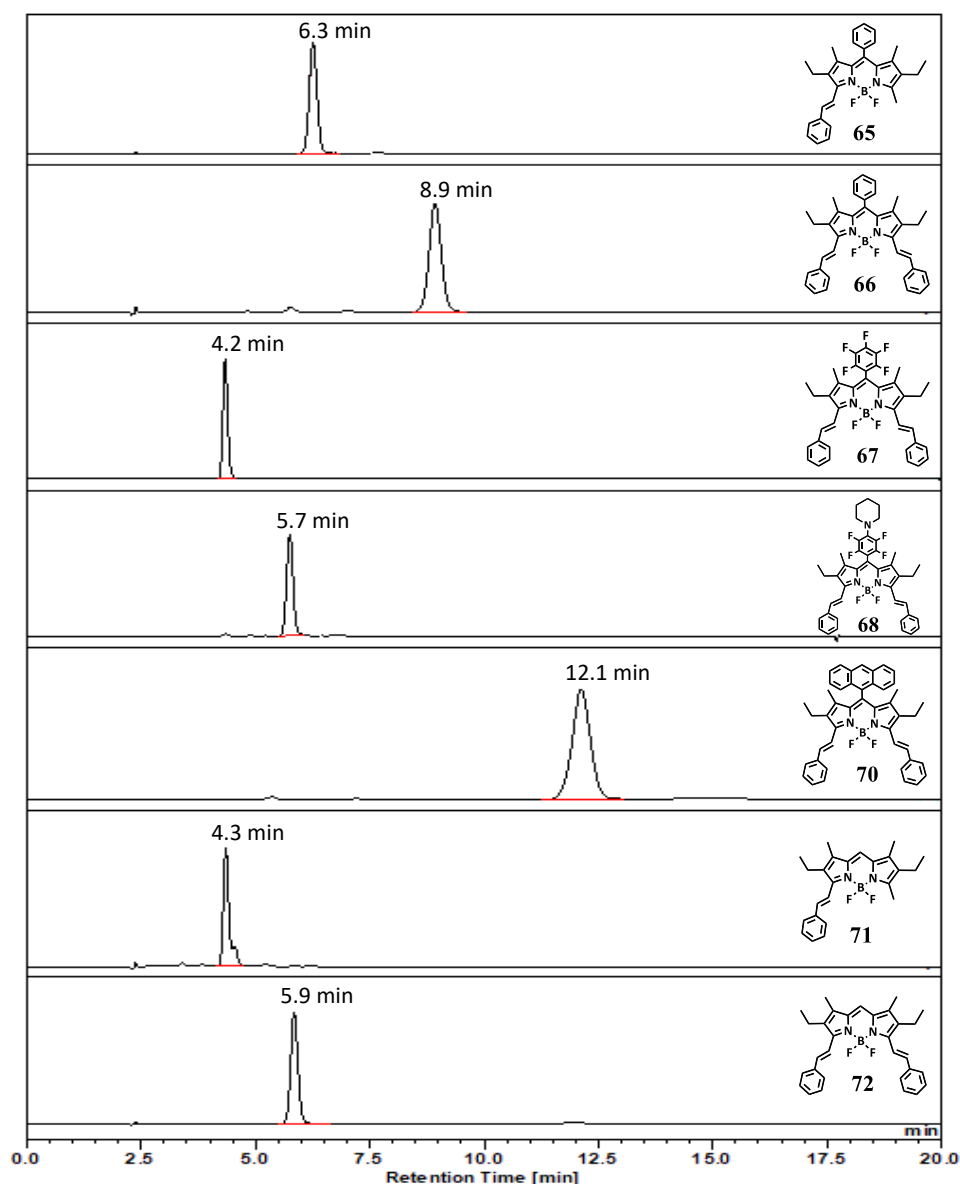
The reactions with **53** and **58** led to similar results in terms of final di/mono-substitution ratios and yields. In the reaction of **57**, only the disubstituted BODIPY was isolated (**70**), but by HPLC, as shown in Figure 3.2, it was possible to identify traces of a possible mono-styryl BODIPY (**69**) since its maximum absorption wavelength is between those obtained with **57** and **70**.



**Figure 3.2.** HPLC-DAD chromatogram with the corresponding peaks of BODIPY **69** and **70**, obtained at 30 °C with acetonitrile: H<sub>2</sub>O (9:1) as eluent and a flow rate of 0.8 ml/min.

All the prepared BODIPY derivatives exhibit good solubility in common organic solvents such as dichloromethane, chloroform, dichlorobenzene, THF, and toluene. In some cases, the purification through column chromatography or preparative thin-layer chromatography revealed some difficulty to separate the mono from the di-functionalized compound, and the separation of **67** from **68** has always deserved special attention. Thus, HPLC analysis (Figure 3.3) is of great importance to confirm the purity level of the compounds.

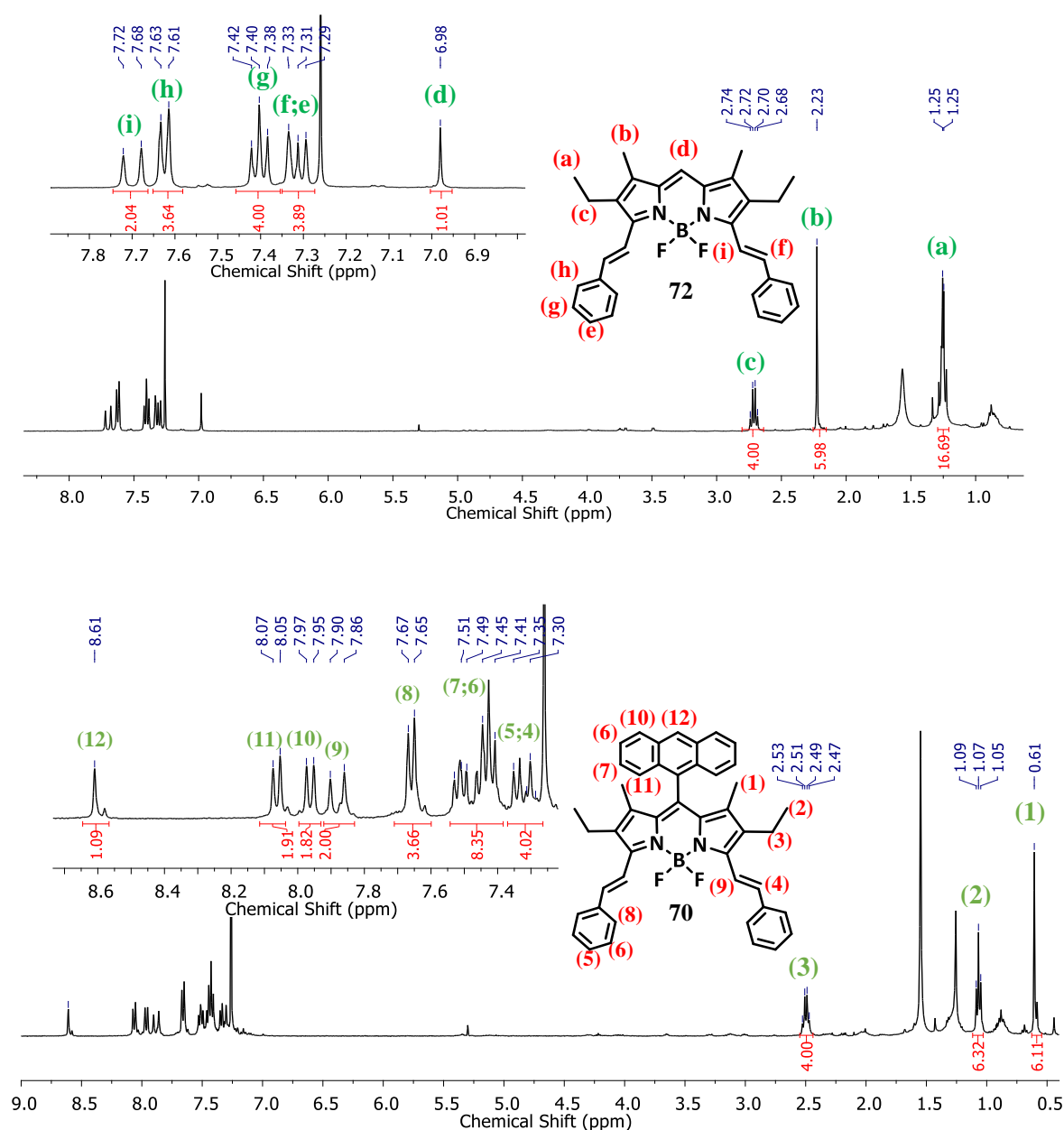
Figure 3.3 shows the chromatograms of all isolated BODIPYs from the second series and confirms their purity. Because a C18 reverse phase column (hydrophobic stationary phase) was used, the increase of aromatic units in the structure, through the attachment of phenyl rings, caused the peak to appear at higher retention times. BODIPY **70** is the one that presents the peak at higher retention time, which was nonetheless expected due to its anthracene moiety.



**Figure 3.3.** HPLC chromatograms obtained at 30 °C with acetonitrile: H<sub>2</sub>O (9:1) as isocratic eluent with a volume of injection of 10 μL and a flow rate of 0.8 ml/min, in a C18 RP column.

From analysis of Figure 3.4, it is possible to conclude that the NMR signals assigned to the hydrogens of BODIPY core did not change significantly upon functionalization. The same figure shows the disappearance of the singlet attributed to the methyl group from 3,5-position and the new signals from the new phenyl fractions. All the compounds from the

second series show the same spectroscopic feature but the new signals are more distinguishable in the **67** or **72** spectra because their structure does not have groups at *meso*-position with hydrogen atoms to mask the signals from both the new phenyl moieties and the vinylic hydrogens.

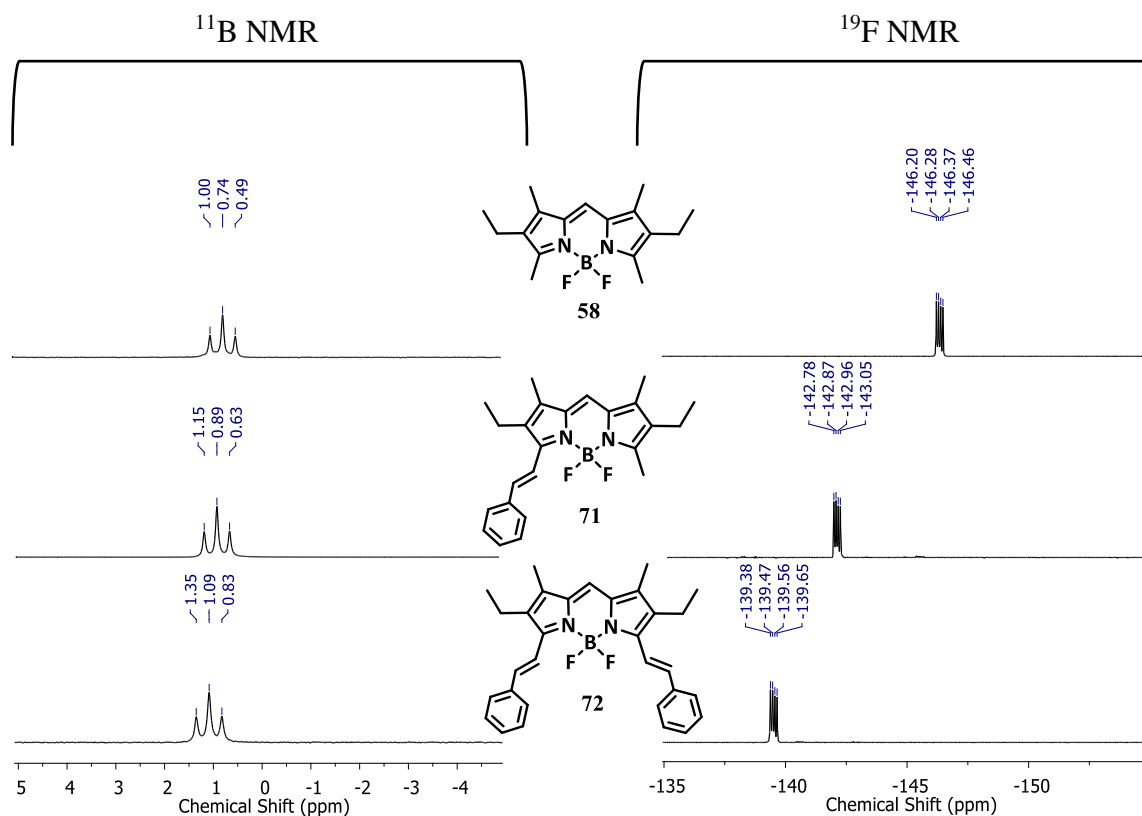


**Figure 3.4.** <sup>1</sup>H NMR (400 MHz) spectra of **70** and **72**, in CDCl<sub>3</sub>.

Based on <sup>1</sup>H-NMR spectra we can conclude that the vinyl hydrogens between the BODIPY core and the donor group are in a *trans* conformation since the values for the vicinal <sup>3</sup>J<sub>H/H</sub> couplings are on the range of 16-17 Hz for all compounds.

Figure 3.5 shows an example of how the <sup>19</sup>F NMR and <sup>11</sup>B NMR spectra evolved from **1S-BDP** (compound **58**) to **2S-BDP** (compounds **71** and **72**). If compared with the first

series, the quartet signal assigned to the fluorine atoms coupled to boron presents a small shift when BODIPY has one styryl group and a larger shift to positive chemical shifts when two styryl groups are present. On the other hand, the  $^{11}\text{B}$  NMR spectra of the new compounds are essentially equal to the spectrum of the **1S-BDP**.



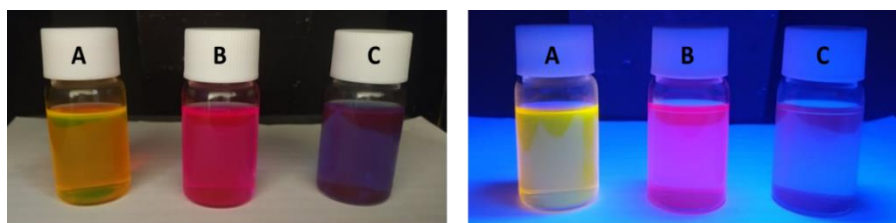
**Figure 3.5.**  $^{11}\text{B}$  NMR (128 MHz) and  $^{19}\text{F}$  NMR (376 MHz) spectra of **58**, **71** and **72**, in  $\text{CDCl}_3$ .

Additionally, all BODIPY dyes from the second series were analysed by HRMS (details in Chapter 8), which confirmed the structure through the peak of the molecular ion  $[\text{M}+\text{H}]^+$  and by the presence of the typical fragment resulting from the loss of HF.

### 3.2. Characterisation of the second series of BODIPY molecules (2S-BDP)

The attachment of distyryl groups to BODIPY backbone induces deep changes on the main characteristics of the dyes. These changes can be noticed even before any characterisation technique by visual inspection since there is a variation in the colours of the solutions and a decrease in their fluorescence. As shown in Figure 3.6, the chloroform solution of compound **58** has a yellow colour, and when one (**71**) or two styryl moieties (**72**) are attached, it changes to pink or blue, respectively. This change in colour is uniform across all BODIPYs from the second series.



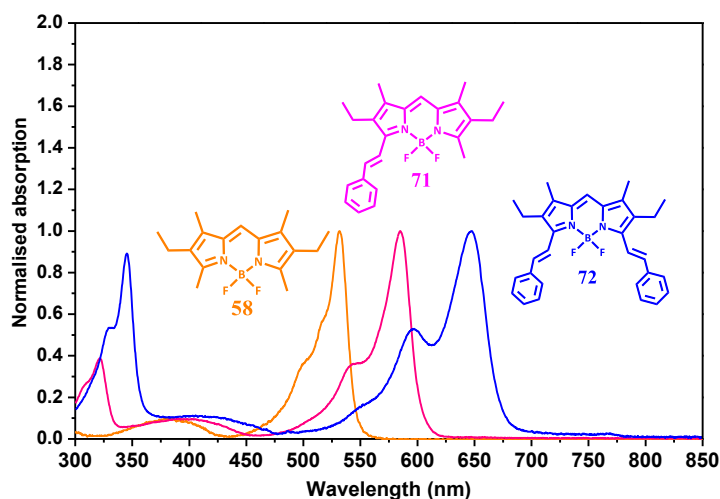


**Figure 3.6.** Images of **58** (A), **71** (B) and **72** (C) in chloroform under daylight and under 365 nm UV light illumination.

To assess the modification of properties introduced by the styryl groups and the suitability of the new compounds for OPV applications (upon blending with fullerenes) photophysical, electrochemical and DFT studies were done for all **2S-BDP** components.

### 3.2.1. Photophysical characterisation

The colour variation (yellow to blue) corresponds to a significant red-shift of the absorption spectrum, showing the effect of the stepwise expansion of the  $\pi$ -system due to the attachment of the mono and distyryl moieties. Figure 3.7 shows the normalised absorption spectra of **58**, **71** and **72** in chloroform solutions. The mono-substituted BODIPY compound has a red-shift of about 50 nm in both absorption and fluorescence spectra, while the di-substituted BODIPY molecules present a red-shift of ca.110 nm.

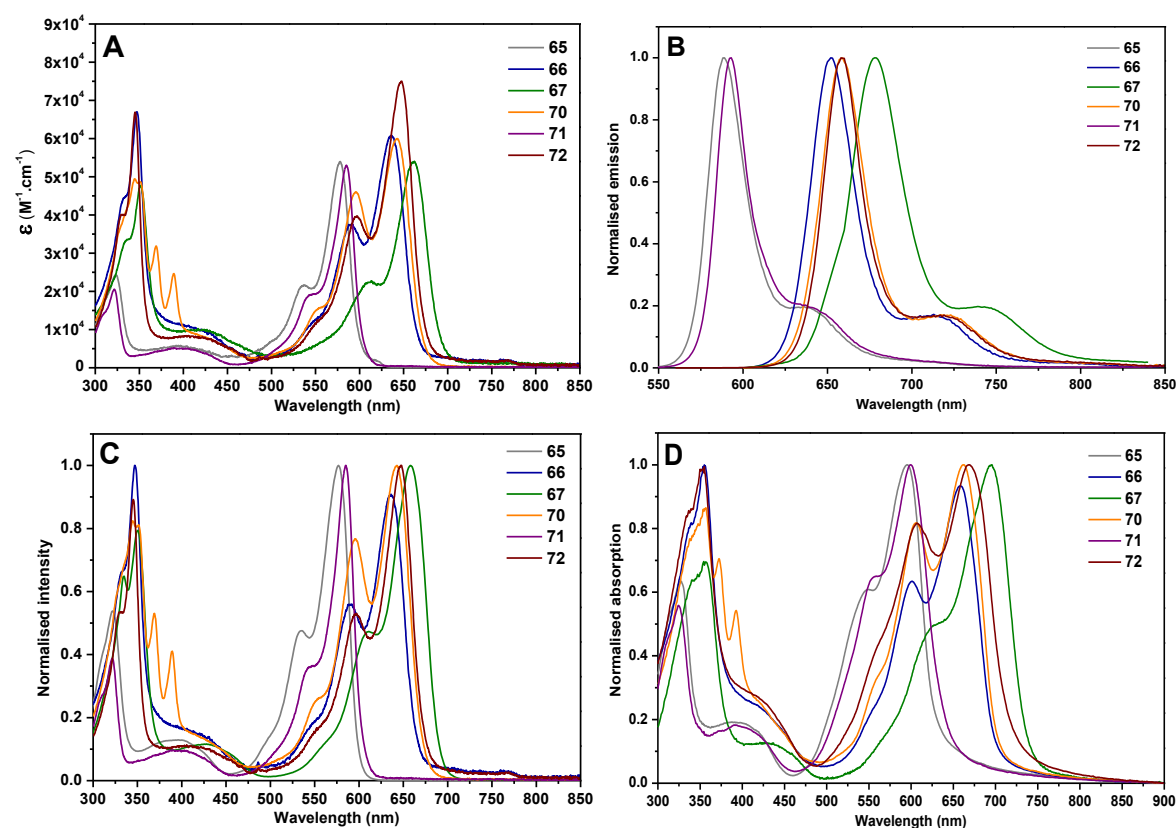


**Figure 3.7.** Normalised absorption of **58** (orange), **71** (pink) and **72** (blue), in chloroform solution.

Figure 3.8 shows the absorption spectra of all BODIPY derivatives from the second series. Absorption and emission spectra of all compounds were recorded in chloroform solution, and the photophysical data of all series are listed in Table 3.1.

Despite the shift of the maximum absorption and the maximum emission, the general characteristics of the BODIPY molecules (presented in Chapter 2) are kept in this second

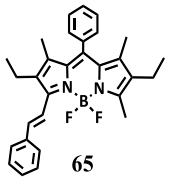
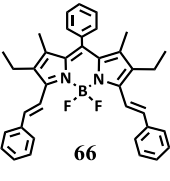
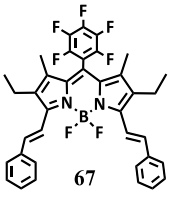
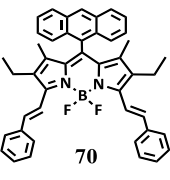
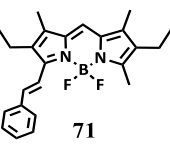
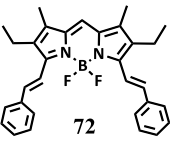
series. The absorption spectra exhibit a minor broadening of the absorption bands but the intense visible  $S_0 \rightarrow S_1$  absorption, the similarity (mirror image) between absorption and emission bands and the small Stokes shifts remained.



**Figure 3.8.** (A) Absorption spectra; (B) emission spectra (excitation at  $\lambda_{\text{max}}^{\text{abs}}$ ); (C) excitation spectra; (D) spin-cast films absorption spectra of the **2S-BDP**, in chloroform.

The absorption band at shorter wavelengths (300-450 nm) is assigned to a  $\pi\text{-}\pi^*$  transition within the new phenyl fragments. The occurrence of this new absorption bands masks the weaker absorption band attributed to the  $S_0 \rightarrow S_2$  ( $\pi\text{-}\pi^*$ ) transition of BODIPY core. The absorption bands at lower energy (500-775 nm) are attributed to the  $S_0 \rightarrow S_1$  ( $\pi\text{-}\pi^*$ ) transition. Additionally, the excitation spectra of the BODIPY molecules match the absorption spectra and all these dyes show high molar absorption coefficients in chloroform solution, ranging from  $5.3$  to  $7.4 \times 10^4 \text{ M}^{-1}\text{cm}^{-1}$ , which confirms their exceptional light harvesting ability. The film absorption spectra show a clear bathochromic shift of the absorption maximum with a considerable broadening of the peaks. The red-shift and broadening relative to solution spectra result from intermolecular interactions, possibly involving the  $\pi$  orbitals of adjacent molecules. The excitation of the compounds from **2S-BDP** at their respective three absorption bands maximum at room temperature led to the same emission spectrum.

**Table 3.1.** Photophysical properties of the **2S-BDP**, measured in chloroform solution.

BODIPY	$\lambda_{\text{max}}^{\text{abs}}$ (nm)	$\epsilon$ ( $\text{cm}^{-1} \cdot \text{M}^{-1}$ )	$\lambda_{\text{film}}^{\text{abs}}$ (nm) <sup>a</sup>	$\lambda_{\text{max}}^{\text{em}}$ (nm)	$\Phi_{\text{F}}$ (%)	$\Delta\lambda$ ( $\text{cm}^{-1}$ )	$E_{\text{g}}^{\text{opt}}$ (eV) (onset) <sup>b</sup>
 65	577	$5.4 \times 10^4$	596	588	60	325	2.08
 66	636	$6.0 \times 10^4$	658	652	44	386	1.89
 67	661	$6.4 \times 10^4$	694	678	59	380	1.80
 70	642	$6.4 \times 10^4$	662	658	73	378	1.86
 71	585	$5.3 \times 10^4$	600	592	77	202	2.06
 72	647	$7.4 \times 10^4$	669	659	50	281	1.85

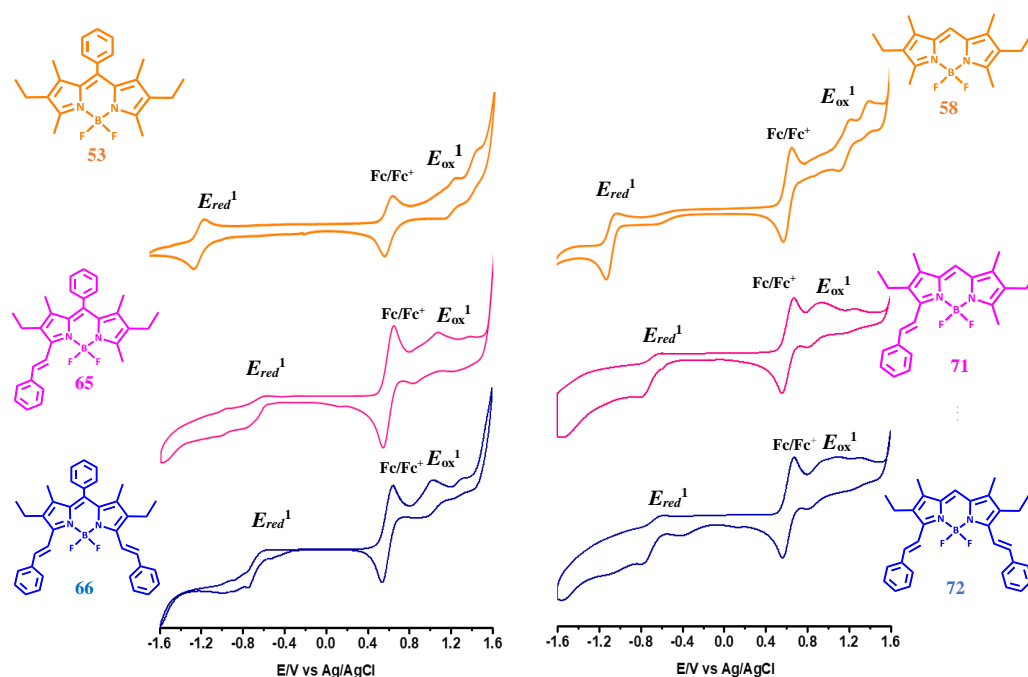
<sup>a</sup> Absorbance of the films prepared from chloroform solution.<sup>b</sup> Estimated from the absorption spectra onset of dyes in solution,  $E_{\text{g}} \text{ (eV)} = 1240 / \lambda_{\text{onset}} \text{ (nm)}$ .

When compared with the emission of **1S-BDP**, the emission spectra of the **2S-BDP** show a bathochromic shift within the same order of the absorption, keeping the Stokes Shifts small. At room temperature, the quantum yield decreases with the addition of styryl moieties, but their chloroform solutions still have a considerable fluorescence. Rigid BODIPY scaffolds result in higher quantum yields. Thereby, the introduction of flexible moieties will increase the non-radiative decay and consequently decrease the fluorescence quantum yield.

### 3.2.2. Electrochemical characterisation

Cyclic voltammetry studies were carried out under the conditions described in Chapter 2. Figure 3.9 shows the evolution of the cyclic voltammograms upon addition of phenyl moieties to BODIPYs **53** or **58**. All electrochemical data from the **2S-BDP** is summarised in Table 3.2.

The BODIPYs of the second series show two oxidation processes ( $E_{ox}^1$  and  $E_{ox}^2$ ) and a single reduction process ( $E_{red}^1$ ), as observed for their corresponding non-functionalized compounds. However, the attachment of phenyl moieties to the BODIPY core facilitates both processes, as shown by the gradual and significant decrease of the potential. As discussed in the previous chapter, the redox processes are assigned to the BODIPY core. Therefore, the changes on the redox properties are consistent with an improved electronic delocalisation brought by the addition of the styryl moieties.



**Figure 3.9.** Cyclic voltammograms of **53**, **65**, **66**, **58**, **71** and **72** in dichloroethane, containing 1 mM ferrocene/ferrocenium ( $\text{Fc}/\text{Fc}^+$ ) as internal standard, recorded at 50 mV/s.

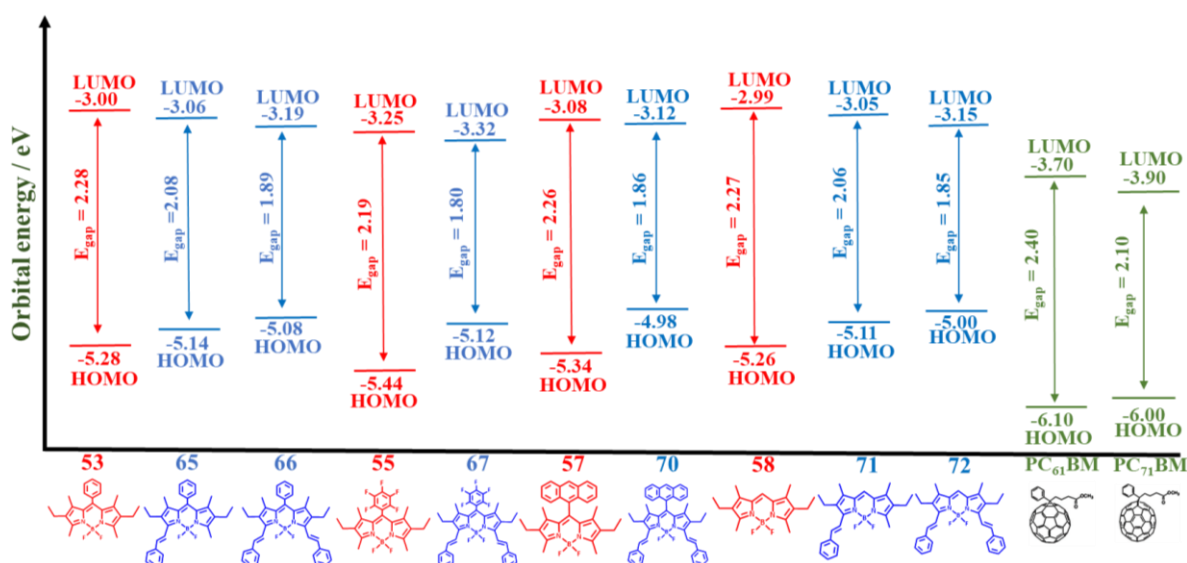
As described for **1S-BDP** (second chapter), the HOMO and LUMO energies are calculated from the onset potentials obtained from the cyclic voltammograms of the BODIPY dyes as reported by Ziessel and co-workers.<sup>36</sup> The optical band gap ( $E_g^{\text{opt}}$ ), obtained from the absorption onset, combined with the HOMO (obtained from  $E_{\text{onset}}^{\text{ox}1}$ ) allows the calculation of the  $E_{\text{LUMO}}$ .

**Table 3.2.** Electrochemical properties of the **2S-BDP**.

Dyes	$E_{\text{red}}^1$ (V)	$E_{\text{ox}}^1$ (V)	$E_{\text{ox}}^2$ (V)	$E_{\text{onset}}^{\text{ox}1}$ (V)	$E_{\text{HOMO}}^{\text{elec}}$ (eV) <sup>a</sup>	$E_{\text{g}}^{\text{opt}}$ (eV)	$E_{\text{LUMO}}$ (eV) <sup>b</sup>
<b>65</b>	-0.71	0.95	1.29	0.93	-5.14	2.08	-3.06
<b>66</b>	-0.68	0.94	1.29	0.87	-5.08	1.89	-3.19
<b>67</b>	-0.62	1.08	1.39	0.91	-5.12	1.80	-3.32
<b>70</b>	-0.71	0.84	1.27	0.80	-4.98	1.86	-3.12
<b>71</b>	-0.72	0.98	1.26	0.92	-5.11	2.06	-3.05
<b>72</b>	-0.71	0.87	1.25	0.81	-5.00	1.85	-3.15

<sup>a</sup>  $E_{\text{HOMO}} = [-(E_{\text{onset}}^{\text{ox}1} - E^{\text{Fc}/\text{Fc}^+}) - 4.8]$  eV ; <sup>b</sup>  $E_{\text{LUMO}} = [E_{\text{HOMO}} + E_{\text{g}}^{\text{opt}}]$  eV.

Scheme 3.3 shows the HOMO and LUMO energies of some dyes of **1S-BDP** and of all components of **2S-BDP**. The relation between the shift of the HOMO and LUMO energy between the two series and the level of functionalization with styryl groups is evident. The increase of the reduction potential and the decrease of the oxidation potential upon functionalization was expected since for 3,5-substituents, the enlargement of the  $\pi$ -system increases the HOMO energy and decreases the LUMO energy.<sup>37</sup> This variation translates into a reduction of the energy gap. Nevertheless, the energy levels are both above the energy levels of PC<sub>61</sub>BM and PC<sub>71</sub>BM (the selected acceptor molecules).<sup>38</sup> This means that even with the decrease of LUMO energies, the BODIPY-fullerene combination forms a type II heterojunction.



**Scheme 3.3.** Frontier orbital energies of some dyes of **1S-BDP** (red), all **2S-BDP** (blue) and the fullerenes derivatives PC<sub>61</sub>BM and PC<sub>71</sub>BM (green).

### 3.2.3. Computational studies

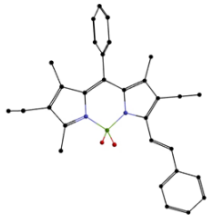
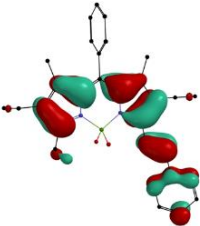
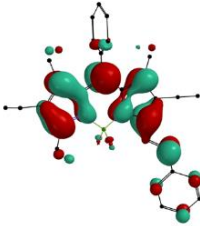
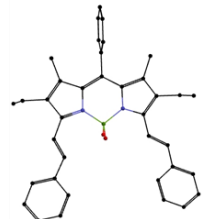
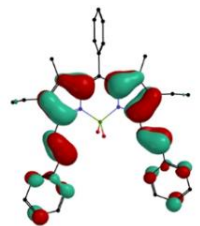
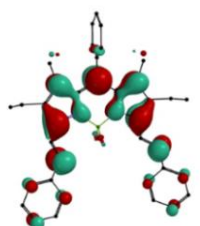
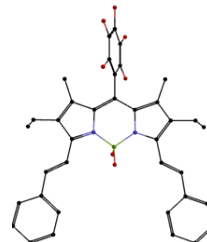
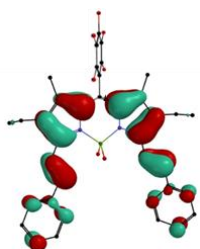
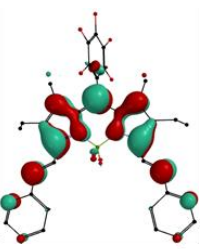
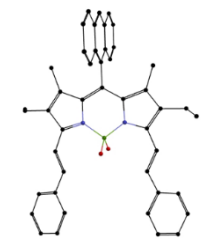
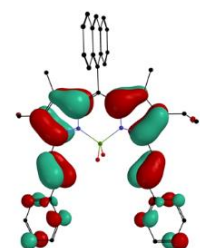
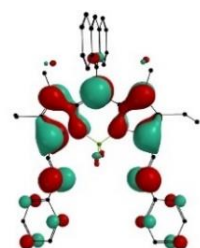
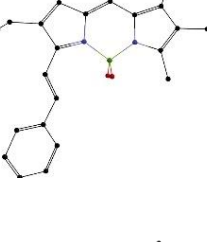
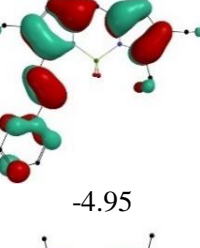
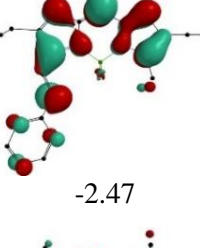
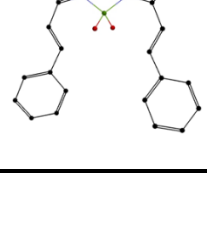
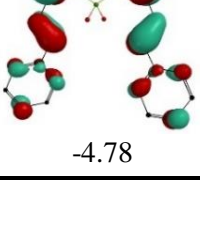
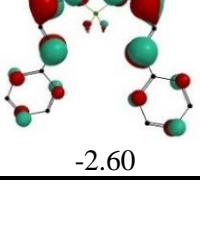
To obtain some insight on the electronic structure of this series of BODIPYs, the geometries and energies of the frontier orbitals were calculated by Density Functional Theory (DFT) in vacuum. All the geometry of the BODIPY compounds were optimized using the same method, and Table 3.3 displays the optimised ground-state geometries and electronic distribution of the HOMO and LUMO.

The main features of the first series of BODIPY molecules, such as the near orthogonal orientation of the *meso*-substitute group in relation to the plane of the core, the tetrahedral geometry of the boron centre and the orthogonality of the plane defined by the BF<sub>2</sub> moiety with respect to the BODIPY core plane are retained.

DFT calculations support the conclusion, based on the absorption and cyclic voltammetry experiments, that the conjugation of the system is extended upon functionalization with the styryl moieties. The calculated frontier molecular orbital profiles and energies show that the HOMO of the BODIPY dyes are delocalized over the pyrrole units of BODIPY core and the styryl groups, while the LUMO is mainly located on the BODIPY core, with a strong density at the *meso*-position.

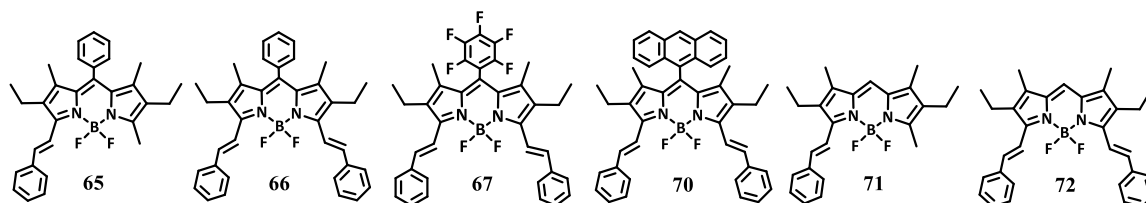
Despite the higher difference between the experimental and calculated HOMO energies, when compared with the first series, they are nonetheless similar. The BODIPY **71** has the lowest deviation with a difference of 0.17 eV, and the highest deviation is attributed to **66** with a difference of 0.29 eV. As observed in the first series of BODIPYs, the experimental and calculated LUMO energies have larger deviation (between 0.41 and 0.64 eV) which could be explained by the solvent effect on the excited state that was not considered in these computational studies.

**Table 3.3.** Optimised ground-state geometries, electron distribution in HOMO and LUMO and their energies (in eV) for the second series of BODIPYs, obtained by DFT calculations in vacuum.

BODIPY	Optimised Geometry	HOMO	LUMO
65		 -4.97	 -2.43
66		 -4.79	 -2.58
67		 -5.31	 -2.91
70		 - 4.76	 -2.57
71		 -4.95	 -2.47
72		 -4.78	 -2.60

### 3.3. Photovoltaic studies of the second series of BODIPY molecules (2S-BDP)

All BODIPYs from the second series (Figure 3.10) were tested in BHJ-OPV with the structure and preparation procedures used in Chapter 2. However, chloroform was chosen as solvent since it allows similar layer thicknesses and efficiencies as dichlorobenzene but with much more diluted solutions (15mg/ml vs 40mg/ml).



**Figure 3.10.** BODIPY dyes from **2S-BDP** tested in BHJ-OPVs.

The optimisation of the OPV conditions was carried out for **70**:PC<sub>61</sub>BM and the conditions that gave the best performance were replicated for the remaining BODIPYs. Table 3.4 shows the photovoltaic parameters obtained during the optimisation study. The best performing **70**:PC<sub>61</sub>BM blend was prepared in a weight ratio of 1:3, deposited by spin-coating at 1200-1300 rpm from a chloroform solution at 15mg/ml, and with a Ca/Al top electrode. These optimised conditions are comparable to the best conditions obtained for the first series of BODIPY compounds, in chloroform, with the only difference on the top electrode (LiF/Al was then found the best electrode).

**Table 3.4.** Average photovoltaic performance parameters for **70**:PC<sub>61</sub>BM-based OPVs, obtained under illumination at 90 mW/cm<sup>2</sup>, during the optimisation studies. Active layer films were prepared from 15mg/ml chloroform solutions. Values calculated from at least 5 devices.

Concentration (mg/ml)	Ratio (D:A)	Active layer thickness (nm)	Top electrode	J <sub>sc</sub> (mA/cm <sup>2</sup> )	V <sub>oc</sub> (V)	FF	PCE (%)
20	1:2	119	LiF/Al	0.80	0.56	0.26	0.13
20	1:3	114	LiF/Al	0.96	0.66	0.24	0.17
20	1:4	111	LiF/Al	0.69	0.40	0.24	0.07
15	1:3	94	LiF/Al	1.41	0.62	0.25	0.24
13	1:3	82	LiF/Al	1.13	0.65	0.26	0.21
15	1:3	102	Ca/Al	1.66	0.65	0.25	0.30



The photovoltaic performance parameters of the BODIPYs from first and second series, blended with PC<sub>61</sub>BM, under similar conditions are summarised in Table 3.5. The introduction of the styryl groups in BODIPY **55** led to a great improvement in the photovoltaic response since its PCE increases from 0.02 % to 0.27 %. Despite this impressive improvement, the other BODIPY dyes from the second series did not show such improvement. In the case of **66**, **71** and **72** compounds the efficiency presented a significant drop, where not only the current density decreased but also the V<sub>OC</sub>. This may indicate non ideal morphology of the active layer and poor charge transport.

**Table 3.5.** Photovoltaic performance parameters of the BODIPY:PC<sub>61</sub>BM-based OPVs, AM 1.5 G illumination at 84 mW/cm<sup>2</sup>. The donor:acceptor ratio is 1:3 by weight and the solution was prepared in chloroform at 15mg/ml.

Dye	Layer thickness (nm)	Maximum						Average**			
		J <sub>sc</sub> (mA/cm <sup>2</sup> )	V <sub>OC</sub> (V)	FF	R <sub>SH</sub> (Ω.cm <sup>2</sup> )	R <sub>s</sub> (Ω.cm <sup>2</sup> )	PCE (%)	J <sub>sc</sub> (mA/cm <sup>2</sup> )	V <sub>OC</sub> (V)	FF	PCE (%)
<b>53*</b>	80	0.93	0.73	0.27	810	454	0.22	0.85	0.62	0.27	0.17
<b>65</b>	114	1.67	0.59	0.24	340	253	0.28	1.62	0.51	0.24	0.23
<b>66</b>	100	0.28	0.29	0.24	1195	542	0.02	0.22	0.27	0.26	0.02
<b>55*</b>	77	0.13	0.37	0.27	2956	2321	0.02	0.11	0.37	0.27	0.01
<b>67</b>	99	1.40	0.67	0.24	402	370	0.27	1.23	0.64	0.24	0.22
<b>57*</b>	81	0.91	0.73	0.26	804	669	0.20	0.68	0.69	0.26	0.14
<b>70</b>	102	1.74	0.63	0.25	385	323	0.33	1.56	0.64	0.25	0.30
<b>58*</b>	78	1.18	0.58	0.26	482	349	0.21	1.00	0.53	0.26	0.16
<b>71</b>	97	0.59	0.46	0.22	606	749	0.07	0.54	0.44	0.22	0.06
<b>72</b>	82	0.38	0.31	0.29	941	444	0.04	0.35	0.28	0.28	0.03

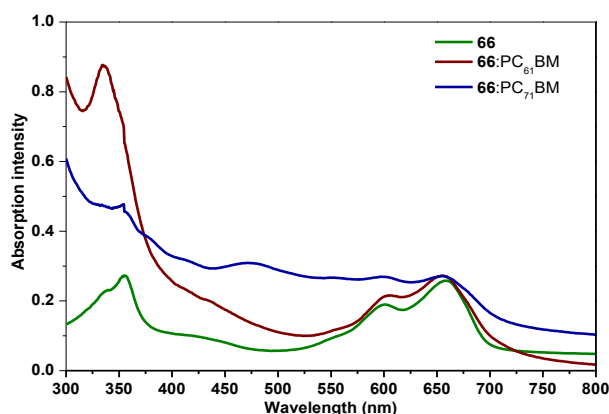
\*Data already presented in Table 2.10. It is shown here for comparison purposes.

\*\*Values calculated from at least 5 devices.

The best PCE values were obtained for **65**, **67** and **70**, but they are still lower than the average efficiency values of BODIPY-based OPVs already published. The increase in efficiency of **65** and **70**-based OPVs is attributed to the enhancement of J<sub>sc</sub>. All molecules

from the second series presented FF values below those found in the OPVs prepared with the BODIPYs of the first series, which is an indication of increased photoelectric losses.

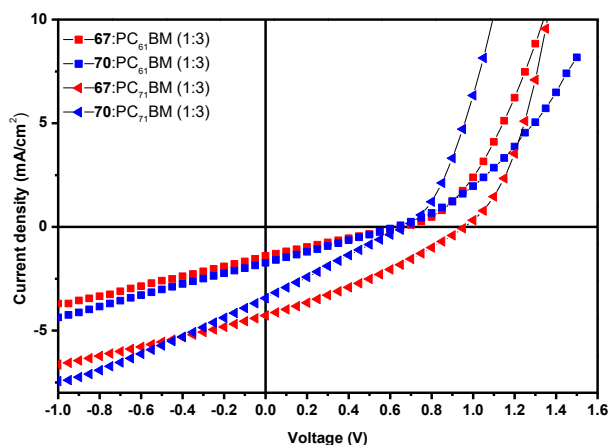
PC<sub>61</sub>BM is commonly used electron-acceptor material in OPVs, but the low absorption in the visible range is a handicap.<sup>39</sup> Hence, a possibility to improve the PCE of the photovoltaic cells is the introduction of a bigger fullerene such [6,6]-phenyl-C<sub>71</sub>-butyric acid methyl ester (PC<sub>71</sub>BM) which shows stronger absorption and, in general, enhanced solubility.<sup>40</sup> As shown in Figure 3.11, the blend of BODIPY **66** with PC<sub>71</sub>BM presents an enlarged absorption profile, due to the complementary absorption of the two compounds.



**Figure 3.11.** Absorption profile of **66** BODIPY film and the blend films of **66**: PC<sub>71</sub>BM and **66**:PC<sub>61</sub>BM.

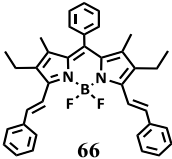
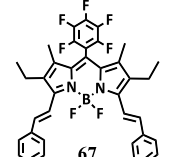
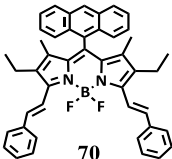
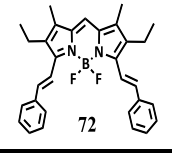
The photovoltaic performance of the distyryl-functionalized molecules **66**, **67**, **70** and **72**, blended with PC<sub>71</sub>BM, was therefore evaluated. The photovoltaic cells were fabricated using the conditions of the OPVs based on the BODIPY:PC<sub>61</sub>BM blends.

The change of fullerene had a positive effect on the photovoltaic performance parameters of **67** and **70** as is attested in Figure 3.12 and Table 3.6. However, the effect on the OPVs based on **66** and **72** BODIPYs was not significant (Table 3.6).



**Figure 3.12.** Current density-voltage characteristics of OPVs based on the **67**: PC<sub>61</sub>BM, **67**: PC<sub>71</sub>BM, **70**: PC<sub>61</sub>BM and **70**:PC<sub>71</sub>BM blends.

**Table 3.6.** Photovoltaic performance parameters of the BODIPY:PC<sub>71</sub>BM-based OPV cells, obtained under AM 1.5 G illumination at 81 mW/cm<sup>2</sup>. The blends solutions were prepared in chloroform at 15mg/ml, with a donor:acceptor weight ratio of 1:3.

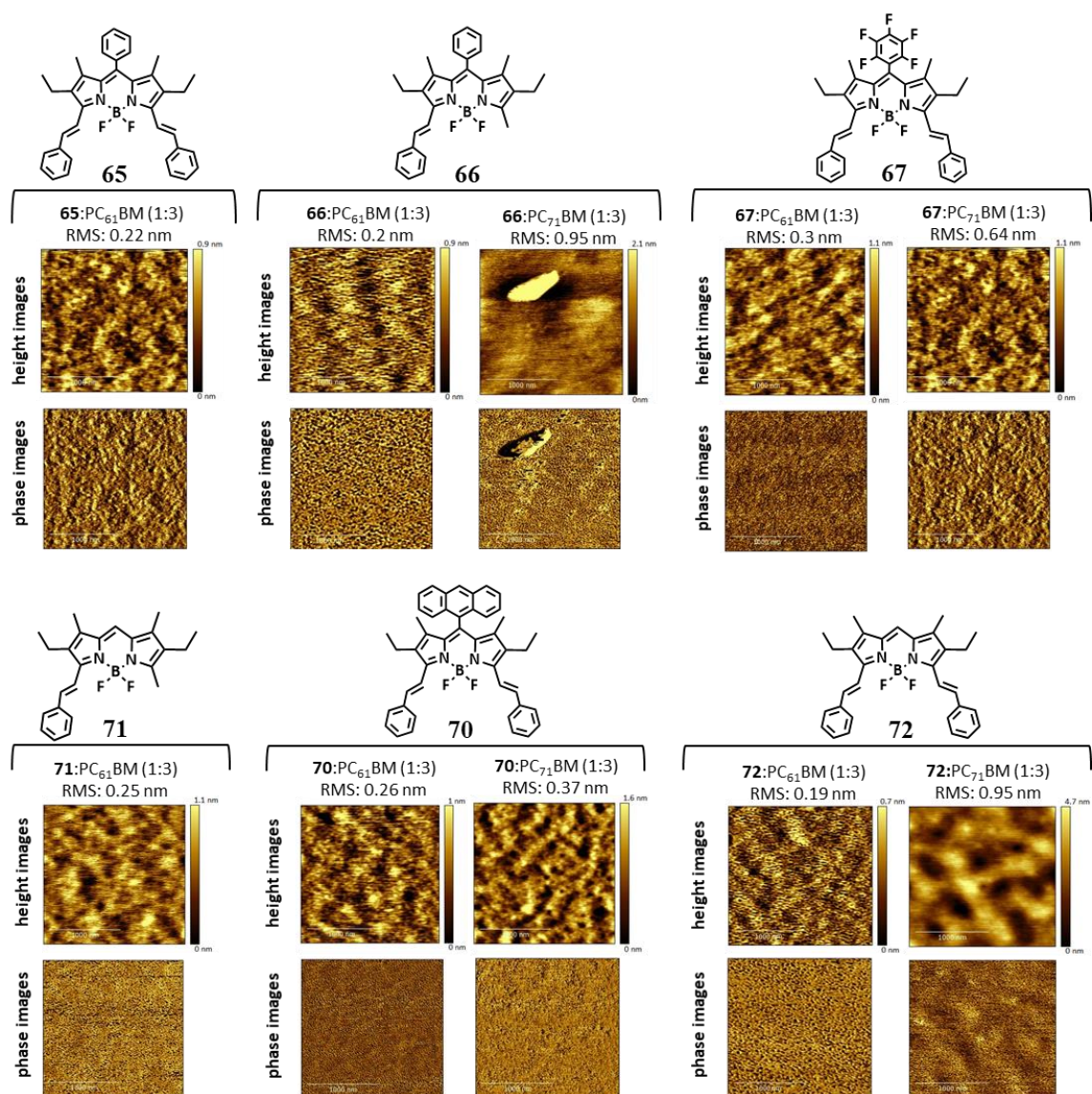
Dye	Layer thickness (nm)	Maximum						Average			
		J <sub>sc</sub> (mA/cm <sup>2</sup> )	V <sub>oc</sub> (V)	FF	R <sub>sh</sub> (Ω.cm <sup>2</sup> )	R <sub>s</sub> (Ω.cm <sup>2</sup> )	PCE (%)	J <sub>sc</sub> (mA/cm <sup>2</sup> )	V <sub>oc</sub> (V)	FF	PCE (%)
 66	98	0.34	0.36	0.26	1167	777	0.04	0.32	0.37	0.26	0.04
 67	89	4.27	0.96	0.31	345	131	1.57	3.97	0.94	0.30	1.38
 70	111	3.44	0.67	0.25	194	163	0.71	3.14	0.66	0.25	0.66
 72	112	0.18	0.28	0.29	1608	778	0.02	0.17	0.28	0.28	0.02

\* Average values calculated from at least 4 devices.

The OPV based on the **70**:PC<sub>71</sub>BM blend preserved the V<sub>oc</sub> value of the device based on PC<sub>61</sub>BM, but the near duplication of the J<sub>sc</sub> made this system much more efficient. When blended with PC<sub>71</sub>BM, the **67**-based OPVs experienced a massive improvement. The resulting photovoltaic cells delivered more than twice the current density of the PC<sub>61</sub>BM analogous system and the PCE value was improved by more than five times. The V<sub>oc</sub> of 0.96 V is very near to the highest V<sub>oc</sub> ever obtained for BODIPY-based OPVs (1.08 V)<sup>41</sup>, and it is on par with the state-of-the-art electron-donors. The high Voc is a sign of good conjugation of the frontier orbital energies offsets from the donor and acceptor materials and good morphology of the blend. With such high V<sub>oc</sub>, the main limitation remains on FF and its current density, which could be caused by poor charge carriers transport.<sup>42, 43</sup> Even so, 1.57 % of efficiency is higher than that of several BODIPY-based OPVs already published and indicates that this kind of compounds with styryl groups at α-position have potential to exhibit good photovoltaic results.

### 3.3.1. Surface morphology of the active layer

The blend morphology is of great importance in OPV field since it is essential to understand the nature of some loss, such as exciton dissociation, transport of charges or free charges collection.<sup>44, 45</sup> To gain insights about the possible contributions that differentiate and affect the studied BODIPY-based OPVs, the surface morphology of **65**, **66**, **67**, **70**, **71** and **72** blended with PC<sub>61</sub>BM and PC<sub>71</sub>BM were scrutinised by AFM, Figure 3.13.



**Figure 3.13.** AFM height and phase images (2 $\mu$ m vs 2 $\mu$ m) of **65**, **66**, **67**, **70**, **71** and **72** blended with PC<sub>61</sub>BM and PC<sub>71</sub>BM.

As can be observed in Figure 3.16, most of the blend films exhibited very smooth and uniform surfaces with root mean squared (RMS) roughness below 1 nm. The blends with PC<sub>71</sub>BM showed a small increase of roughness if compared with films of the PC<sub>61</sub>BM

blends. Apart from **66**:PC<sub>71</sub>BM, which presented some grains on the surface, all the films were very flat and do not exhibit aggregates. With the phase separated domain size decreased, the interfacial contact between the donor and acceptor increases, which facilitates exciton dissociation. However, small domains have a detrimental effect on the charge-collection efficiency. Thus, some works suggest an ideal domain size of 10–20 nm,<sup>45</sup> for copolymers, since both larger or smaller domain phase sizes may limit charge transfer and/or separation.

### 3.4. Conclusions for Chapter 3

In this chapter, the attachment of styryl groups at the 3,5-positions of the BODIPY was explored. The second series of BODIPY molecules (**2S-BDP**) includes some new BODIPY structures with absorption at high wavelengths due to the extension of the electron- $\pi$  system. The synthesised compounds present good stability and solubility. After all photophysical and electrochemical characterisation, it was proved that they could perform as excited state electron-donors in heterojunction BODIPY:fullerene systems.

The photovoltaic tests revealed a remarkable performance improvement for some BODIPYs of the **2S-BDP**. In the blend with PC<sub>61</sub>BM, the PCE of BODIPY **70** experienced a small improvement if compared with its predecessors (0.20 % to 0.33 %). However, when blended with PC<sub>71</sub>BM, its PCE more than doubled (0.71 %).

The improvements of the OPVs based on BODIPY **67** are quite impressive. In blends with PC<sub>61</sub>BM, BODIPY **67** showed an evolution of almost 14 times in its PCE (from 0.02 % to 0.28 %) with the distyryl addition, and when blended with PC<sub>71</sub>BM it achieved a maximum efficiency of 1.74 % which is an outstanding enhancement. Additionally, the **67**:PC<sub>71</sub>BM-based OPV presented very high V<sub>OC</sub> values (0.96 V) which are in line with the best published so far, since BHJ-OPV with V<sub>OC</sub> values above 1 V have rarely been described.

### 3.5. References for Chapter 3

1. G. Duran-Sampedro, A. R. Agarrabeitia, I. Garcia-Moreno, A. Costela, J. Bañuelos, T. Arbeloa, I. López Arbeloa, J. L. Chiara and M. J. Ortiz, *European Journal of Organic Chemistry*, **2012**, 2012, 6335-6350.
2. M. Vincent, E. Beabout, R. Bennett and P. Hewavitharanage, *Tetrahedron Letters*, **2013**, 54, 2050-2054.
3. M. Üçüncü, E. Karakuş and M. Emrullahoğlu, *New Journal of Chemistry*, **2015**, 39, 8337-8341.
4. T. Rohand, M. Baruah, W. Qin, N. Boens and W. Dehaen, *Chemical Communications*, **2006**, 266-268.
5. N. Boens, B. Verbelen and W. Dehaen, *European Journal of Organic Chemistry*, **2015**, 2015, 6577-6595.
6. L. Li, B. Nguyen and K. Burgess, *Bioorganic & Medicinal Chemistry Letters*, **2008**, 18, 3112-3116.
7. C. Bellomo, M. Chaari, J. Cabrera-González, M. Blangetti, C. Lombardi, A. Deagostino, C. Viñas, N. Gaztelumendi, C. Nogués, R. Nuñez and C. Prandi, *Chemistry – A European Journal*, **2018**, 24, 15622-15630.
8. G. Li, Y. Otsuka, T. Matsumiya, T. Suzuki, J. Li, M. Takahashi and K. Yamada, *Materials*, **2018**, 11, 1297.
9. B. Sui, M. V. Bondar, D. Anderson, H. J. Rivera-Jacquez, A. E. Masunov and K. D. Belfield, *The Journal of Physical Chemistry C*, **2016**, 120, 14317-14329.
10. A. Loudet and K. Burgess, *Chemical Reviews*, **2007**, 107, 4891-4932.
11. E. Heyer and R. Ziessel, *The Journal of Organic Chemistry*, **2015**, 80, 6737-6753.
12. Z. Biyiklioglu and T. Keleş, *Inorganica Chimica Acta*, **2017**, 466, 130-138.
13. T. Arslan, T. Keleş, B. Barut, A. Özel and Z. Biyiklioglu, *Inorganica Chimica Acta*, **2018**, 471, 121-125.
14. C. Tahtaoui, C. Thomas, F. Rohmer, P. Klotz, G. Duportail, Y. Mély, D. Bonnet and M. Hibert, *The Journal of Organic Chemistry*, **2007**, 72, 269-272.
15. E. Bodio and C. Goze, *Dyes and Pigments*, **2019**, 160, 700-710.
16. A. L. Nguyen, K. E. Griffin, Z. Zhou, F. R. Fronczek, K. M. Smith and M. G. H. Vicente, *New Journal of Chemistry*, **2018**, 42, 8241-8246.
17. P. Didier, G. Ulrich, Y. Mély and R. Ziessel, *Organic & Biomolecular Chemistry*, **2009**, 7, 3639-3642.
18. Y. Ni, W. Zeng, K.-W. Huang and J. Wu, *Chemical Communications*, **2013**, 49, 1217-1219.
19. A. Wakamiya, T. Murakami and S. Yamaguchi, *Chemical Science*, **2013**, 4, 1002-1007.
20. J. Wang, Q. Wu, S. Wang, C. Yu, J. Li, E. Hao, Y. Wei, X. Mu and L. Jiao, *Organic Letters*, **2015**, 17, 5360-5363.
21. O. Buyukcakir, O. A. Bozdemir, S. Kolemen, S. Erbas and E. U. Akkaya, *Organic Letters*, **2009**, 11, 4644-4647.
22. A. C. O. Hann and A. Lapworth, *Journal of the Chemical Society, Transactions*, **1904**, 85, 46-56.

23. R. P. Herrera and E. Marques-Lopez, *Multicomponent Reactions: Concepts and Applications for Design and Synthesis*, Wiley, ISBN: 9781118016008, Zaragoza, **2015**, 416-482.
24. W. li, R. Li, X. Yu, X. Xu, Z. Guo, T. Tan and S. Fedosov, *Biochemical Engineering Journal*, **2015**, 101.
25. K. Gräf, T. Körzdörfer, S. Kümmel and M. Thelakkat, *New Journal of Chemistry*, **2013**, 37, 1417-1426.
26. E. V. Dalessandro, H. P. Collin, L. G. L. Guimarães, M. S. Valle and J. R. Pliego, *The Journal of Physical Chemistry B*, **2017**, 121, 5300-5307.
27. S. Bednarz and D. Bogdal, *International Journal of Chemical Kinetics*, **2009**, 41, 589-598.
28. T. Rousseau, A. Cravino, T. Bura, G. Ulrich, R. Ziessel and J. Roncali, *Chemical Communications*, **2009**, 1673-1675.
29. J. Liao, Y. Xu, H. Zhao, B. Wang, Q. Zong and Y. Fang, *Organic Electronics*, **2017**, 49, 321-333.
30. J. Liao, H. Zhao, Y. Xu, Z. Cai, Z. Peng, W. Zhang, W. Zhou, B. Li, Q. Zong and X. Yang, *Dyes and Pigments*, **2016**, 128, 131-140.
31. H. Zhao, B. Wang, J. Liao, H. Wang and G. Tan, *Tetrahedron Letters*, **2013**, 54, 6019-6022.
32. R. Misra, T. Jadhav, B. Dhokale, P. Gautam, R. Sharma, R. Maragani and S. M. Mobin, *Dalton Transactions*, **2014**, 43, 13076-13086.
33. H. Kang, Y. Si, J. Liu, L. Chen, Y. Li, H. Chen, J. Groeper and B. Yang, *RSC Advances*, **2016**, 6, 23094-23101.
34. J. Xu, L. Zhu, Q. Wang, L. Zeng, B. Fu and Z. Sun, *Tetrahedron*, **2014**, 70, 5800-5805.
35. H. R. A. Golf, H.-U. Reissig and A. Wiehe, *Organic Letters*, **2015**, 17, 982-985.
36. D. Kumaresan, R. P. Thummel, T. Bura, G. Ulrich and R. Ziessel, *Chemistry – A European Journal*, **2009**, 15, 6335-6339.
37. N. Heiland, C. Cidarér, C. Rohr, M. Piescheck, J. Ahrens, M. Bröring and U. Schröder, *ChemSusChem*, **2017**, 10, 4215-4222.
38. L. Li, Y. Huang, J. Peng, Y. Cao and X. Peng, *Journal of Materials Chemistry A*, **2013**, 1, 2144-2150.
39. F. Zhang, Z. Zhuo, J. Zhang, X. Wang, X. Xu, Z. Wang, Y. Xin, J. Wang, J. Wang, W. Tang, Z. Xu and Y. Wang, *Solar Energy Materials and Solar Cells*, **2012**, 97, 71-77.
40. R. Ganesamoorthy, G. Sathiyam and P. Sakthivel, *Solar Energy Materials and Solar Cells*, **2017**, 161, 102-148.
41. T. Jadhav, R. Misra, S. Biswas and G. D. Sharma, *Physical Chemistry Chemical Physics*, **2015**, 17, 26580-26588.
42. H. Usta, M. D. Yilmaz, A.-J. Avestro, D. Boudinet, M. Denti, W. Zhao, J. F. Stoddart and A. Facchetti, *Advanced Materials*, **2013**, 25, 4327-4334.
43. D. Baran, S. Tuladhar, S. P. Economopoulos, M. Neophytou, A. Savva, G. Itskos, A. Othonos, D. D. C. Bradley, C. J. Brabec, J. Nelson and S. A. Choulis, *Synthetic Metals*, **2017**, 226, 25-30.
44. G. Li, V. Shrotriya, J. Huang, Y. Yao, T. Moriarty, K. Emery and Y. Yang, *Nature Materials*, **2005**, 4, 864-868.

45. M. L. Keshtov, D. V. Marochkin, V. S. Kochurov, A. R. Khokhlov, E. N. Koukaras and G. D. Sharma, *Journal of Materials Chemistry A*, **2014**, 2, 155-171.



**CHAPTER 4. *Meso*-pentafluorophenyl BODIPY  
molecules with different vinyl groups**

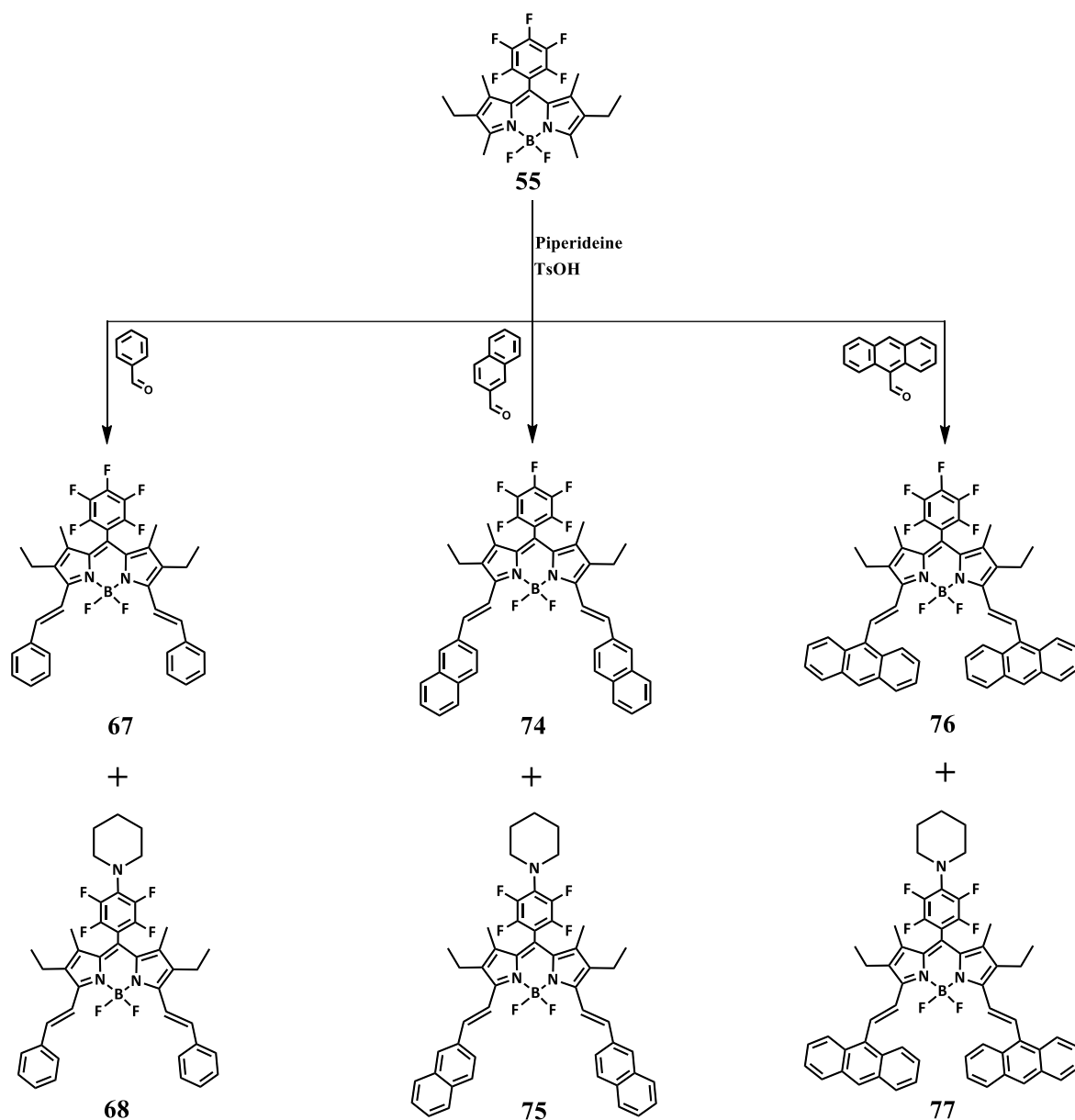
In the previous chapter, it was demonstrated that the attachment of styryl groups through the 3,5-methyls from BODIPY's  $\alpha$ -position is a simple functionalization that deeply changes the main optical and electronic properties of the BODIPY molecules. From the synthetic point of view, the BODIPY compound with the pentafluoro moiety at *meso*-position (**55**) is by far the most reactive BODIPY compound to produce the distyryl derivatives (**67** and **68**). When compound **67** was tested in OPVs, it revealed an outstanding increase in the photovoltaic performance, if compared with its predecessor (**55**), and achieved the highest PCEs of the **2S-BDP**. Therefore, this chapter is focused on a series of new BODIPY structures (third series) based on *meso*-substituted fluorinated BODIPY molecules with different donor aromatic moieties at  $\alpha$ -pyrrolic positions and with or without piperidine motifs at the *para*-position of the group at *meso* position.

#### 4.1. Synthesis of the third series of BODIPY molecules (3S-BDP)

Highly fluorinated BODIPY dyes might combine some advantageous features, such as high stability, prominent spectroscopic properties, and increased electron-accepting character.<sup>1</sup> The electron-withdrawing effect of the pentafluorophenyl moiety promotes a decrease of HOMO and LUMO energies, which could increase the open-circuit voltage ( $V_{OC}$ ) when used as electron-donor material or even provide an electron-acceptor character to the molecule.

The third series of BODIPY molecules (**3S-BDP**) was planned to include the already reported BODIPY structures with styryl moieties (**67** and **68**), and new structures with vinyl groups (naphthalenyl and anthracenyl). These groups were inserted by Knoevenagel condensation reaction, catalysed by piperidine and *p*-toluenesulfonic acid (Scheme 4.1). As explained in Chapter 3, the strong electron-withdrawing character imposed by the *meso*-pentafluorophenyl fraction speeds up the reaction and makes it much more effective. However, the pentafluorophenyl group could easily undergo a nucleophilic aromatic substitution reaction in the presence of a nucleophile like piperidine, resulting in piperidine substituted by-products at the *para*-position of the pentafluorophenyl moiety.

The Knoevenagel condensation often uses twenty equivalents of piperidine and several hours of reaction time (sometimes days), but due to the strong tendency of **55** to suffer nucleophilic substitution at the *para* position of pentafluorophenyl moiety, the amount of piperidine and the reaction time require optimisation.



**Scheme 4.1.** The synthesis of the third series of BODIPY dyes (**3S-BDP**).

To study the selectivity of the synthesis, the amount of **55**, benzaldehyde (10 eq), *p*-TsOH.H<sub>2</sub>O (0.01 eq), the volume of toluene (15 ml) and temperature of the reaction (120 °C) were kept, while the time of reaction and the amount of piperidine were varied and carefully controlled. The yields of the obtained products were calculated after careful chromatographic purification by preparative thin-layer chromatography.

As shown in Table 4.1, to reduce the amount of BODIPY by-product (**68**), the reaction time has to be short and with low quantity of piperidine. Nevertheless, even with the optimisation of the reaction time and the control of the amount of piperidine, it was impossible to prevent the *para*-nucleophilic substitution. Moreover, when 20 equivalents of piperidine and longer reaction times were used (24 hours), only **68** was found and isolated.

Therefore, for the condensation reaction with the other two aldehydes (2-naphthaldehyde and 9-anthracenecarboxaldehyde), we used 2 hours of reflux with 5 equivalents of piperidine to synthesise **74** and **76**, while to synthesise **75** and **77**, we used 24 hours of reflux and 20 equivalents of piperidine.

**Table 4.1.** Optimisation of the reaction conditions to synthesise the BODIPYs **67** and **68**.

Time (h)	Piperidine equivalents	BODIPY 67 Yield (%)*	BODIPY 68 Yield (%)*
2 h	20	21	13
4 h	20	19	18
6 h	20	19	25
24 h	20	0	34
1 h	5	17	traces
2 h	5	31	2
4 h	5	30	8

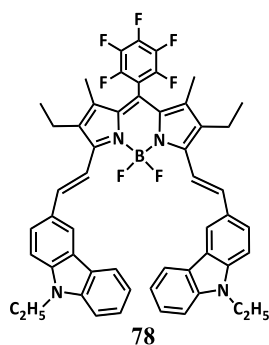
\*All the yields were calculated based on the mass of isolated BODIPY molecules.

We anticipated that the piperidine at *meso*-group should not influence the optoelectronic properties of the compounds. However, the OPVs performance is highly dependent on the morphological features of the blends, and, for that reason, compounds **68**, **75** and **77** were also tested in BHJ-OPVs.

#### 4.1.1. Synthesis of a carbazole-functionalized BODIPY (**78**)

Carbazole is a heterocyclic organic molecule with interesting properties such as ease of functionalization, strong electron-donating character, stability, low redox potential, and hole transporting properties.<sup>2-6</sup> Such properties make it attractive as photoelectrical material, and its linkage to BODIPY dyes has been published with some regularity.<sup>6-11</sup> The use of carbazole-BODIPY dyes in OPVs was first reported by Shrama and co-workers in 2015, with a *meso*-ethynyl BODIPY molecule substituted with a carbazole unit. High efficiencies (5 %) and the highest  $V_{OC}$  value reported for BODIPY-based OPVs to date (1.09 V) were obtained.<sup>12</sup> However, it is the only work relating the use of materials combining these two chromophores in OPVs.

Such considerations led us to prepare a carbazole-conjugated BODIPY compound (**78**, Figure 4.1), where two carbazolyl units are attached at positions 3 and 5 of BODIPY through Knoevenagel condensation of BODIPY **55** with N-ethylcarbazole.

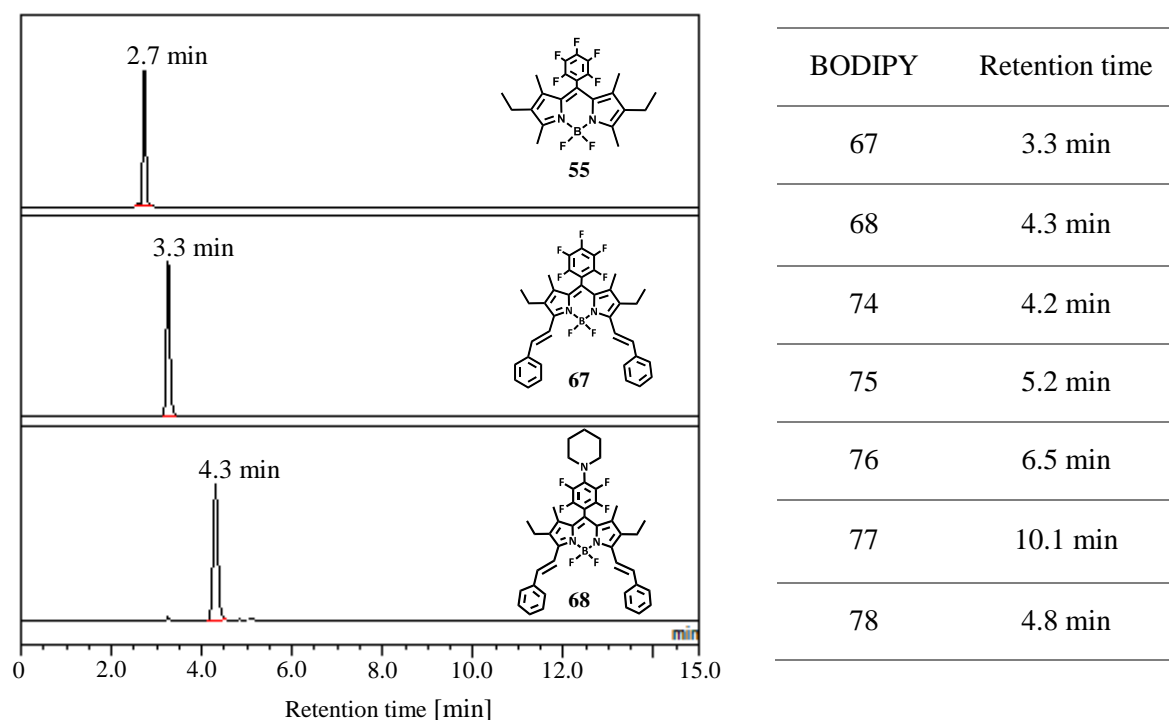


**Figure 4.1.** Structure of BODIPY **78**.

BODIPY **78** was synthesised with 72% yield, following the same protocol we used for the preparation of BODIPYs **67**, **74** or **76**, and it completes the third series of BODIPY dyes (**3S-BDP**). To the best of our knowledge, among the **3S-BDP** series of compounds, only the structure of **67** has already been reported.<sup>13</sup>

#### 4.2. Structural characterisation of the third series of BODIPY molecules (**3S-BDP**)

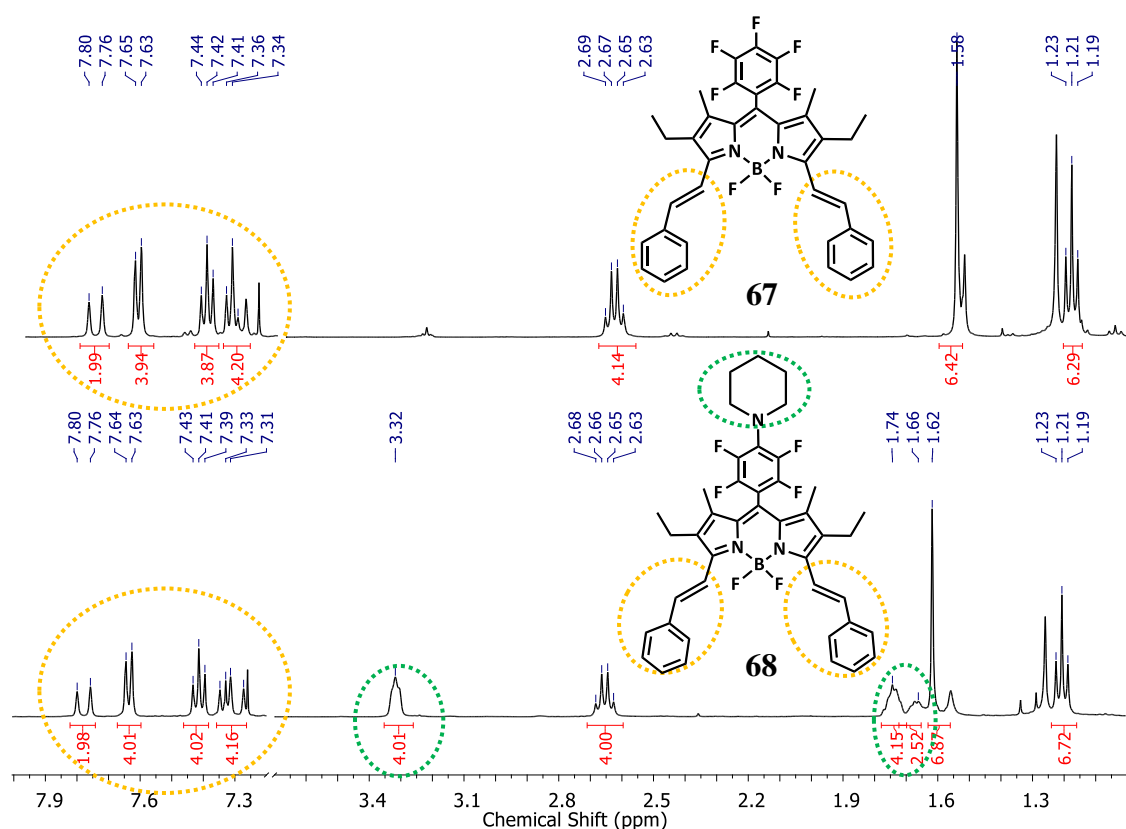
HPLC-DAD was used to check the effectiveness of the purification steps. To shorten the run times and to acquire well-defining peaks, the HPLC chromatograms were obtained at 30 °C with acetonitrile: water (98:2) as isocratic eluent in a C18 reverse phase column. Figure 4.2 displays the effect of both substitutions (styryl and piperidine) in the retention time of all structures of **3S-BDP**.



**Figure 4.2.** HPLC chromatograms of **55**, **67** and **68** and table with the **3S-BDP** retention times.

With the exception of **78** that was obtained as a dark green powder, the compounds from the third series were obtained as deep blue solids, and they all exhibit good solubility in organic solvents such as dichloromethane, chloroform, dichlorobenzene, THF or toluene.

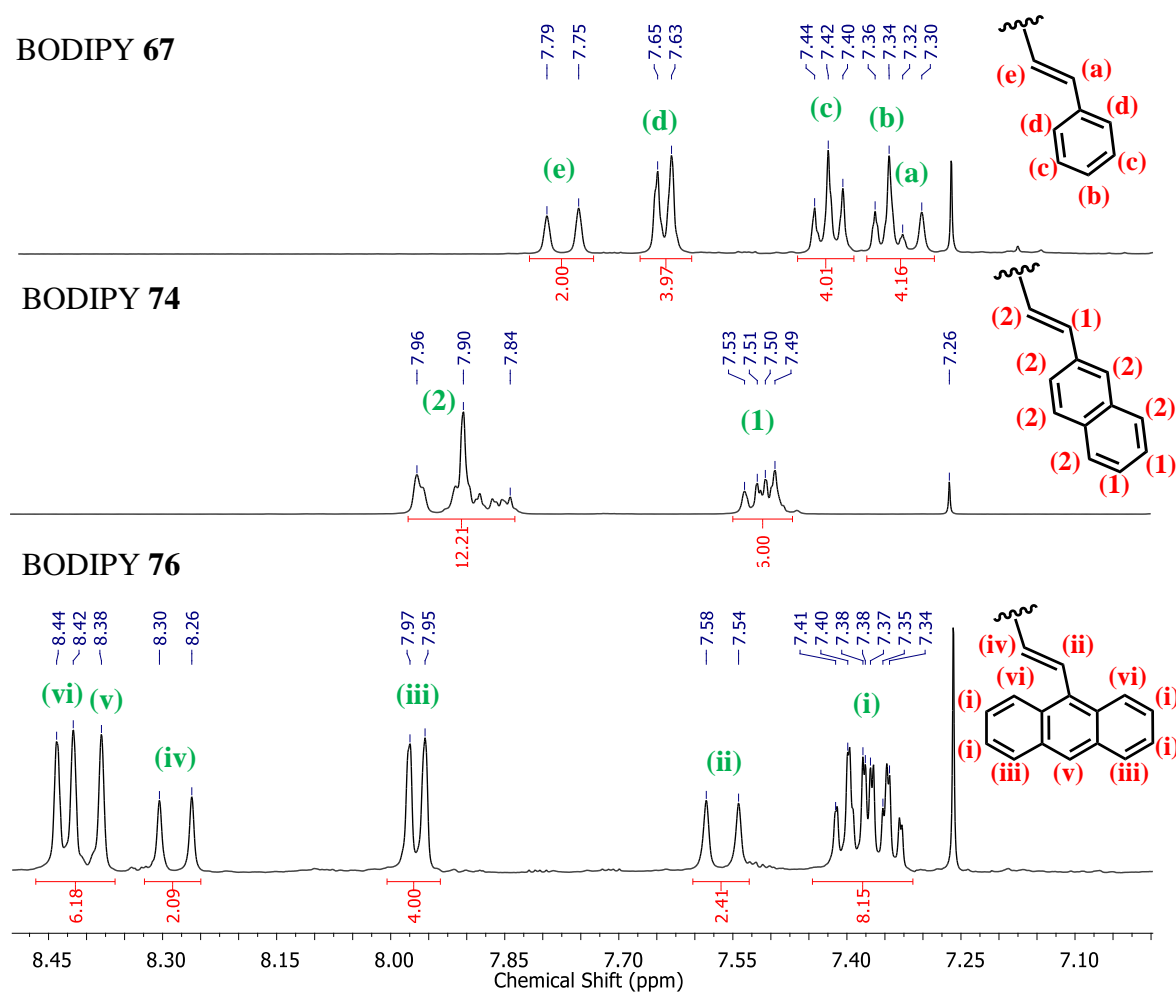
The structures of the BODIPY dyes from **3S-BDP** were confirmed by NMR ( $^1\text{H}$ ,  $^{19}\text{F}$ ,  $^{11}\text{B}$  and  $^{13}\text{C}$ ) and by HRMS, that are described in detail in the experimental section (Chapter 8). As depicted in Figure 4.3, there are not many differences between the  $^1\text{H}$  NMR spectra of a non-piperidine-substituted BODIPY (**67**) and a piperidine-substituted BODIPY (**68**).



**Figure 4.3.**  $^1\text{H}$  NMR (400 MHz) spectra of **67** and **68**, in  $\text{CDCl}_3$ .

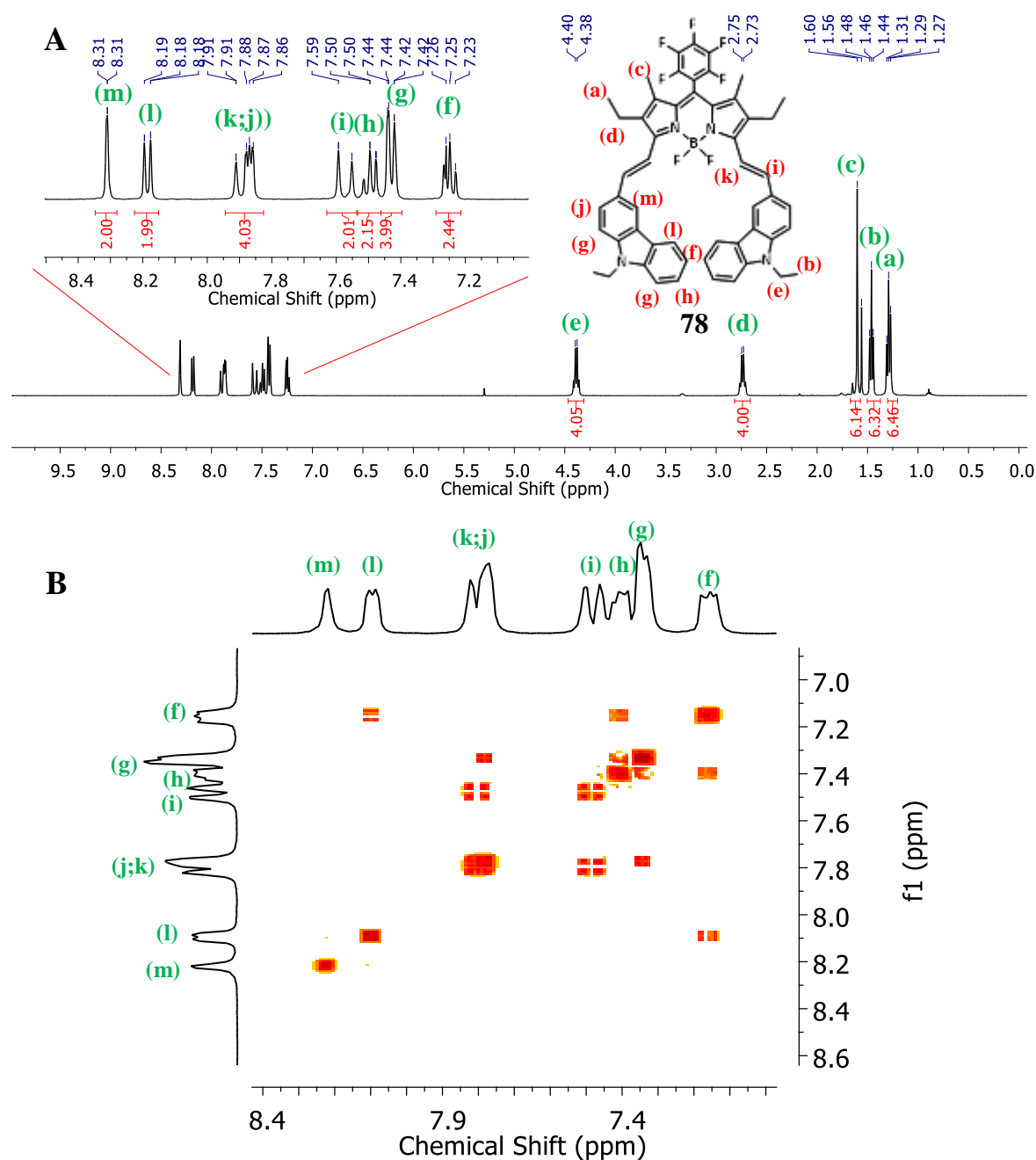
As described before, the signals from the styryl groups are found at higher chemical shifts (7.30-8.50 ppm), and the difference between the piperidine substituted or non-piperidine-substituted dyes is minimal when these signals are compared. The chemical shift and multiplicity of the proton signals from the core are constant for both structures as well. Despite the similarities, the piperidine-substituted BODIPY molecules present three extra broad signals corresponding to the piperidine protons. The signal at 3.30 ppm is assigned to the  $-\text{CH}_2$  protons next to the nitrogen atom. The other two signals appear at 1.65-1.75 ppm and correspond to the other six hydrogens of piperidine.

Apart from the appearance of the signals allocated to the piperidine group, the  $^1\text{H}$ -NMR differences between the BODIPY molecules from the third series exist at the aromatic region of the spectrum. Figure 4.4 shows the fraction of the  $^1\text{H}$  NMR spectra where the phenyl, naphthyl and anthracenyl signals appear. The coupling constants for the olefinic hydrogens is around 17 Hz, as in the **2S-BDP** compounds, which reveal a *trans* stereochemistry.



**Figure 4.4.**  $^1\text{H}$  NMR (400MHz) spectra of **67**, **74** and **76**, in  $\text{CDCl}_3$ .

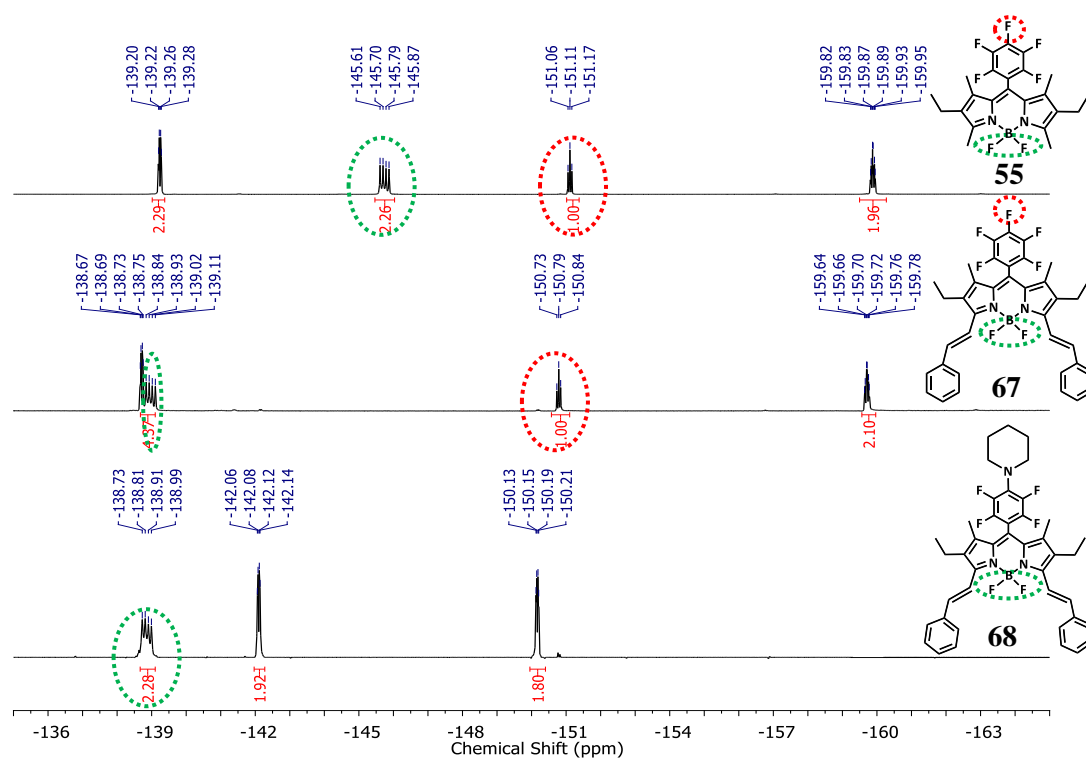
The  $^1\text{H}$  NMR spectrum of BODIPY **78** (Figure 4.5) is somewhat more complex. After COSY NMR analysis it was possible to assign all the signals and confirm that the triplet at 1.46 ppm is representative of  $-\text{CH}_3$  (b) from carbazole ethyl group and the triplet at 1.29 ppm is attributed to  $-\text{CH}_3$  from BODIPY core (a). The quartet signal related to the  $-\text{CH}_2$  from carbazole is well defined at 4.39 ppm (e) and the doublets assigned to olefinic hydrogens (i and k) although a slightly overlapped by the carbazole proton signals confirm the *trans* stereochemistry with coupling constants around 17 Hz.



**Figure 4.5.**  $^1\text{H}$  NMR (400MHz) spectrum (A) and COSY NMR spectrum (B) of **78**, in  $\text{CDCl}_3$ .

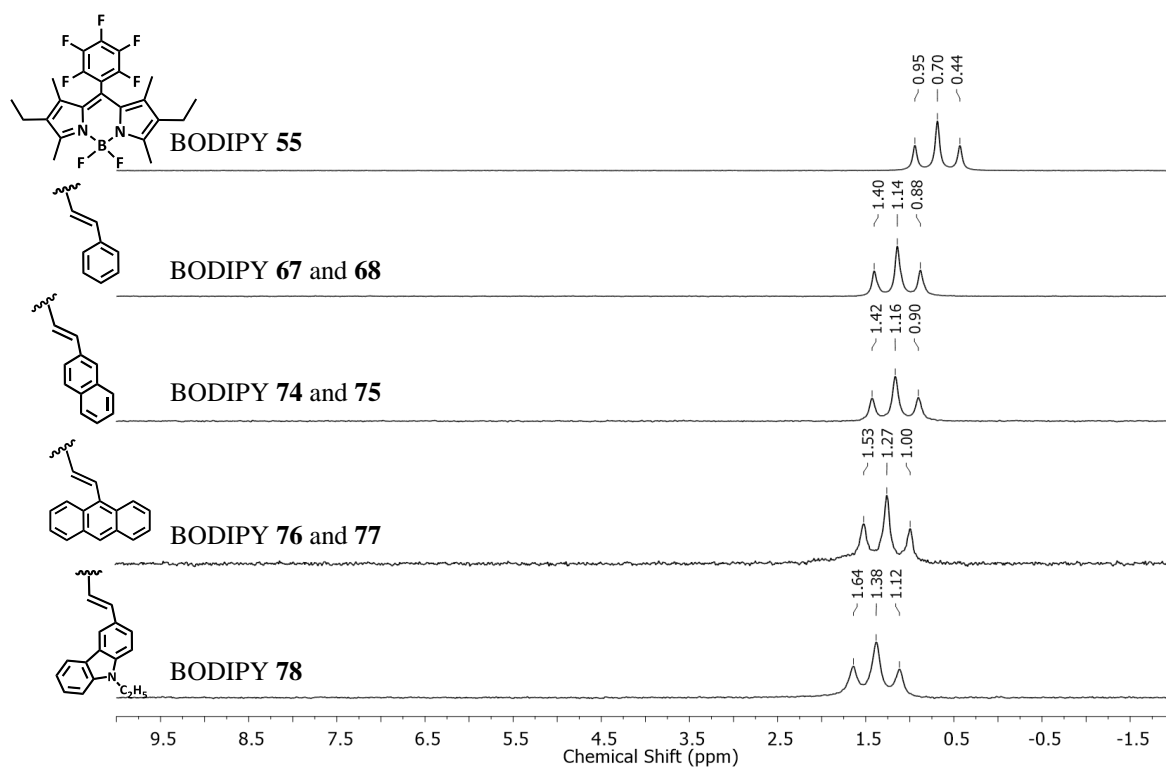
The  $^{19}\text{F}$  NMR (Figure 4.6) was a valuable tool to inquire about the piperidine substitution and purity of the compounds. Apart from the *para*-fluorine missing signal (red circle) in the spectra of **68**, **75** and **78**, the  $^{19}\text{F}$  NMR spectra of the **3S-BDP** are very similar. With the attachment of distyryl motifs, the quartet signal corresponding to the fluorine atoms coupled to boron (green circle) moves to more positive chemical shifts (-145.75 to -138.98). All the compounds from **4S-BDP** present that signal at around -138 ppm.





**Figure 4.6.**  $^{19}\text{F}$  NMR (376 MHz) spectra of **55**, **67** and **72**, in  $\text{CDCl}_3$ .

The  $^{11}\text{B}$  NMR spectra (Figure 4.7) of **3S-BDP** reveals very slight deviations to higher chemical shifts with the increase of bulkiness of the donor units and shows no differences between the non-piperidine-substituted and the piperidine-substituted structures.



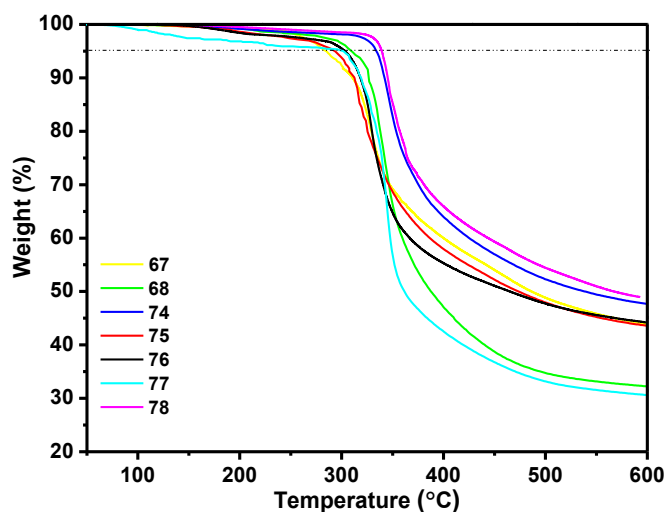
**Figure 4.7.**  $^{11}\text{B}$  NMR (128 MHz) spectra of **3S-BDP**, in  $\text{CDCl}_3$ .

## 4.2. Characterisation of the third series of BODIPY molecules (3S-BDP)

To gain better insight into the thermo-behaviour and thermostability of the BODIPY derivatives from the third series, DSC and TG analysis were made. The photophysical and electrochemical studies were once again extremely important to understand the main properties of the dyes and assess the suitability of the molecules to be applied in OPVs. DFT studies helped to better understand the experimental data.

### 4.2.1. Thermal characterisation

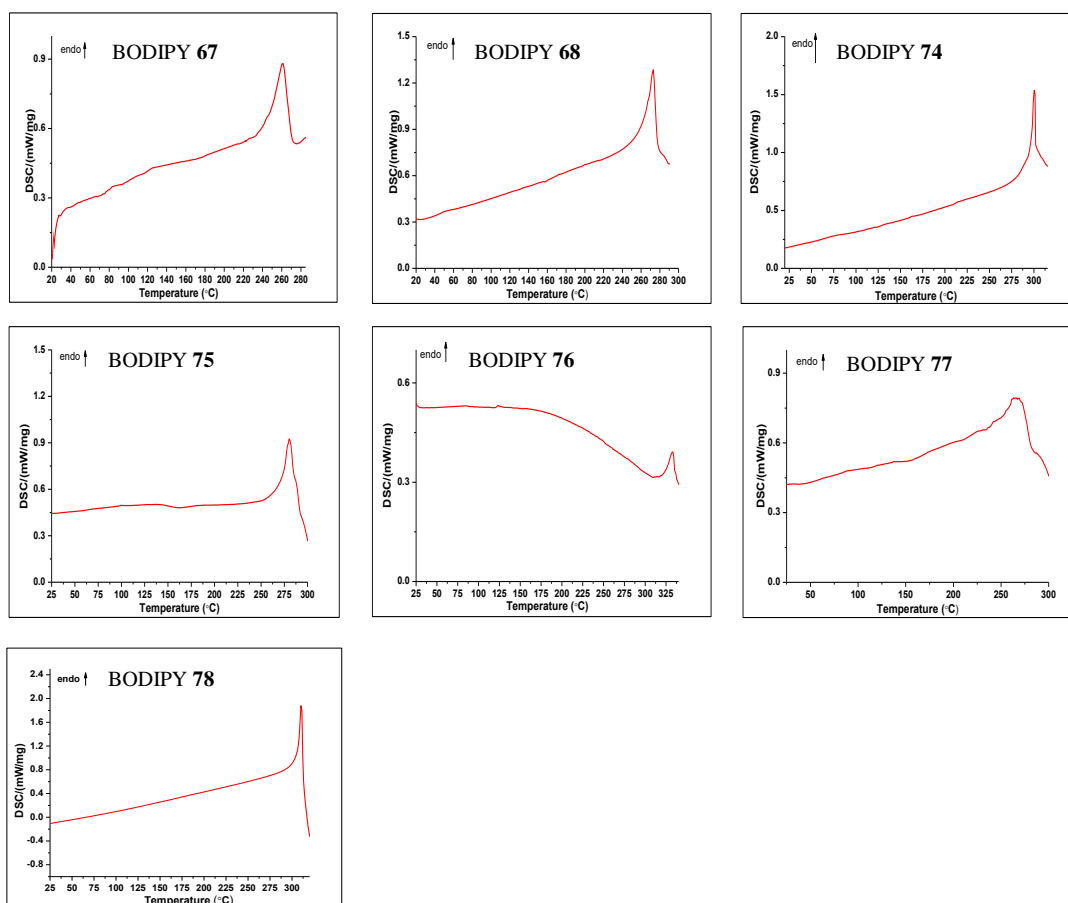
The decomposition temperatures obtained from TGA curves (Figure 4.8) of **67**, **68**, **74**, **75**, **76**, **77** and **78**, observed at 5 % weight loss are at 285 °C, 306 °C, 333 °C, 289 °C, 303 °C, 300 °C and 335 °C, respectively.



**Figure 4.8.** TGA curves of **3S-BDP** at a heating rate of 20 °C/min under nitrogen atmosphere.

In the DSC analyses (Figure 4.9), the samples were heated from 25 to 350 °C and then cooled to 25 °C, with a rate of 10 °C/min under nitrogen flow. The thermograms of **67**, **68**, **74**, **75**, **76**, **77** and **78** revealed endothermic peaks at 259 °C, 272 °C, 300 °C, 332 °C, 280 °C, 268 °C and 309 °C, respectively, which correspond to their melting temperatures. These values were similar to those obtained by a melting point meter. In two cases (**68** and **75**) the BODIPYs substituted with piperidine showed higher melting temperatures than their analogues without piperidine, but the differences are not significant. No glass transitions during the heating or exothermic peaks during the cooling process were observed.

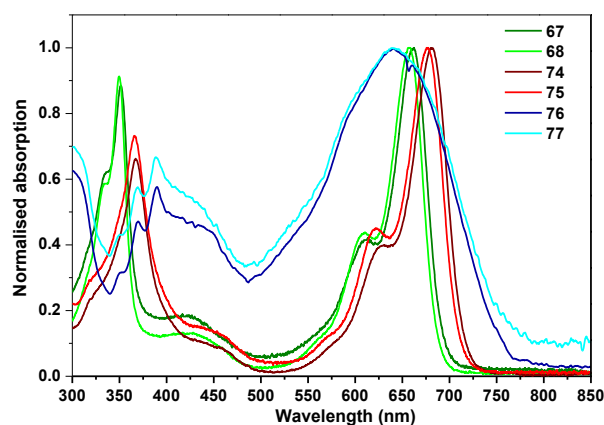
The results obtained by TG and DSC confirm that all BODIPY molecules from **3S-BDP** exhibit high thermal stability, with high melting temperatures, which is very important concerning their application in photovoltaic cells.



**Figure 4.9.** Thermograms of **3S-BDP**.

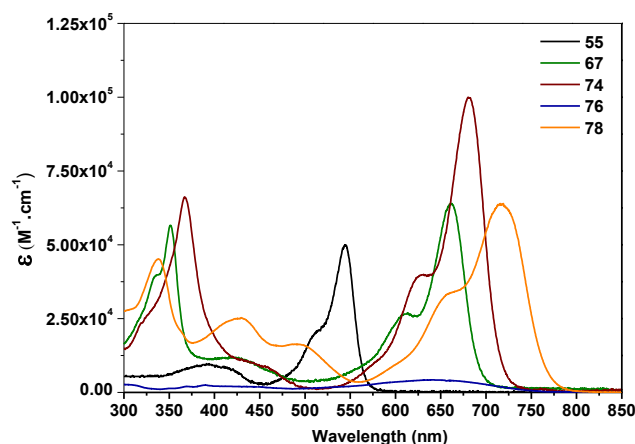
#### 4.2.2. Photophysical characterisation

As it was expected, there is not an effective influence of the piperidine moiety on the spectra of the dyes (Figure 4.10). The absorption and emission spectra of the **3S-BDP** are shown in Figures 4.10, 4.11 and 4.12, and the optical data corresponding to the experiments with three different solvents (chloroform, hexane and acetonitrile) are summarised in Table 4.2. For comparison reasons, the spectra and optical data of BODIPY **55** (BODIPY from the first series, with the pentafluorophenyl group at *meso*-position) are also presented.



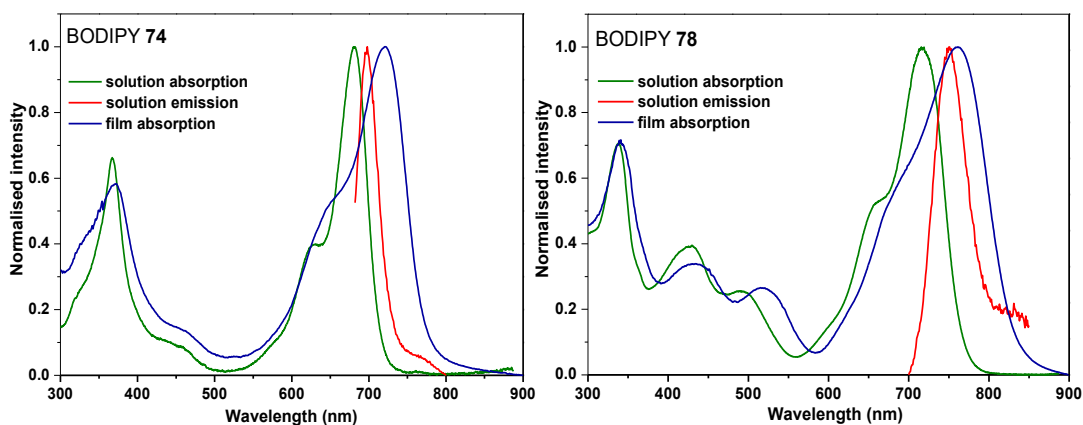
**Figure 4.10.** Normalised absorption spectra of the compounds **67**, **68**, **74**, **75**, **76** and **77**, in  $\text{CHCl}_3$ .

As Figure 4.11 evidences, the absorption spectra of the **3S-BDP** exhibit a higher broadening of the absorption bands and a significant red-shift, if compared with the absorption spectrum of **55**. This feature arose from the effect of the stepwise expansion of the  $\pi$ -system, and it is particularly pronounced in the spectrum of **78**, that holds a maximum absorption wavelength at 718 nm, in chloroform solution.



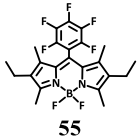
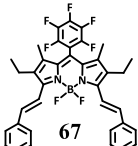
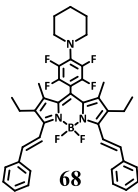
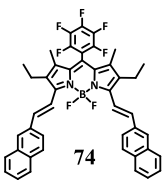
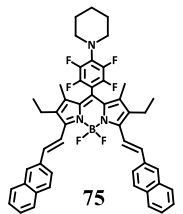
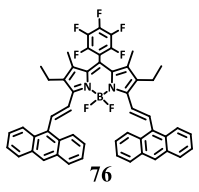
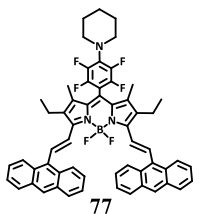
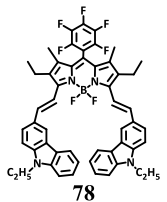
**Figure 4.11.** The absorption spectrum regarding the molar absorption coefficient ( $\epsilon$ ) of **55**, **67**, **74**, **76** and **78**, in  $\text{CHCl}_3$ .

The first band of the absorption spectrum, at around 300-450 nm, is assigned to a localised  $\pi$ - $\pi^*$  transition from the electron-donor fragments, such as phenyl, naphthalenyl, anthracenyl and N-ethyl-carbazolyl. The contribution of anthracenyl fraction (best visualised in Figure 4.10) or N-ethyl-carbazolyl is particularly obvious, and they improve the light harvesting ability of the dye. The occurrence of these new absorption bands masks the weaker absorption band attributed to the S0-S2 ( $\pi$ - $\pi^*$ ) transition of the BODIPY core. The absorption bands at lower energy (at around 500-775 nm) is attributed to an S0-S1 ( $\pi$ - $\pi^*$ ) transition.



**Figure 4.12.** Normalised absorption (chloroform solution and spin-cast film) and emission (chloroform solution) of BODIPYs **74** and **78**.

**Table 4.2.** Photophysical properties of the 3S-BDP.

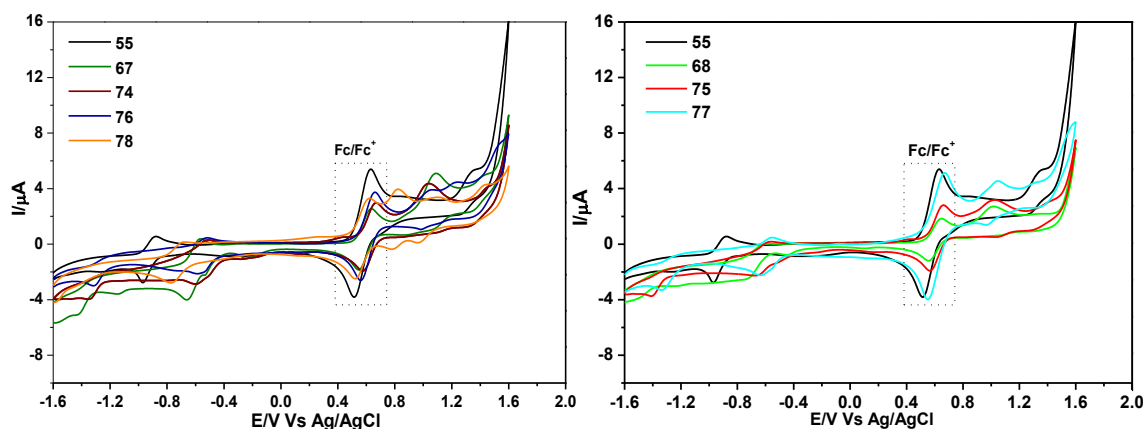
Dyes	Solvent	$\lambda^{abs}$ (nm)	$\epsilon$ ( $\text{cm}^{-1} \text{M}^{-1}$ )	$\lambda^{abs}_{film}$ (nm)	$\lambda^{em}$ (nm)	$\Phi_F$ (%)	SS ( $\text{cm}^{-1}$ )	$E_{g}^{opt}$ (eV) (onset)
 <b>55</b>	Chloroform	544	$5.9 \times 10^4$		558	98	493	2.19
	Hexane	543	$1.0 \times 10^5$	551	555	90	398	2.19
	Acetonitrile	539	$7.9 \times 10^4$		554	88	502	2.21
 <b>67</b>	Chloroform	661	$6.4 \times 10^4$		678	59	308	1.80
	Hexane	663	$7.0 \times 10^4$	694	679	47	333	1.80
	Acetonitrile	652	$7.3 \times 10^4$		670	54	412	1.82
 <b>68</b>	Chloroform	657	$7.4 \times 10^4$		670	51	295	1.80
	Hexane	649	$8.1 \times 10^4$	700	665	54	371	1.82
	Acetonitrile	650	$6.9 \times 10^4$		668	48	415	1.81
 <b>74</b>	Chloroform	681	$1.0 \times 10^5$		697	39	337	1.73
	Hexane	675	$9.6 \times 10^4$	725	688	36	413	1.74
	Acetonitrile	673	$7.8 \times 10^4$		694	32	449	1.74
 <b>75</b>	Chloroform	676	$7.4 \times 10^4$		694	40	383	1.75
	Hexane	669	$7.6 \times 10^4$	729	684	44	328	1.77
	Acetonitrile	678	$7.5 \times 10^4$		688	47	214	1.75
 <b>76</b>	Chloroform	648	$2.1 \times 10^4$	678	690	3	940	1.65
	Hexane	655	$2.6 \times 10^4$		688	3	732	1.63
 <b>77</b>	Chloroform	651	$3.9 \times 10^4$	680	685	7	762	1.65
	Hexane	645	$3.6 \times 10^4$		677	5	733	1.68
 <b>78</b>	Chloroform	718	$6.4 \times 10^4$	760	752	20	630	1.62
	Acetonitrile	714	$6.7 \times 10^4$		763	18	899	1.62

The **3S-BDP** dyes show high molar absorption coefficients ( $\epsilon$ ), ranging from  $2.1 \times 10^4$  to  $1.0 \times 10^5 \text{ M}^{-1}\text{cm}^{-1}$ , which confirms their excellent light harvesting ability. The film absorption spectra have a bathochromic shift of the absorption maximum and a broadening of the peaks, which are likely the result of interactions between the molecules, which may contribute to a planarization of the system. The small Stokes shifts indicate a reduced geometry reorganisation between S1 and S0. Excitation of each of these compounds at their respective three absorption bands at room temperature resulted in the same emission spectrum, and the different solvents do not produce a significant effect on the compound's spectra.

When compared with **55** or the majority of the BODIPYs from the **1S-BDP**, this series presents lower fluorescence intensity, that is likely related to the loss of structure rigidity, originating new non-radiative pathways from the BODIPY  $\pi$ - $\pi^*$  excited state to the ground state, and/or due to charge transfer between the donor moieties and the BODIPY core. The lower emission quantum yield, molar extinction coefficient ( $\epsilon$ ) and the lack of structure of the band attributed to the S0-S1 transition of the structures **75** and **76** (678 nm and 680 nm, respectively) could be explained by a torsional motion around an equilibrium configuration.<sup>14</sup>

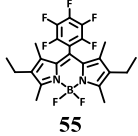
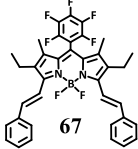
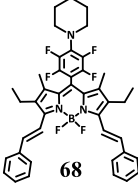
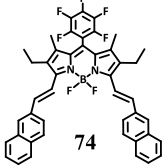
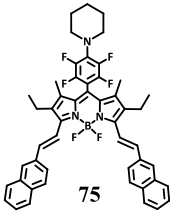
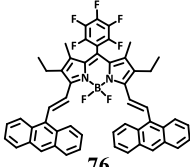
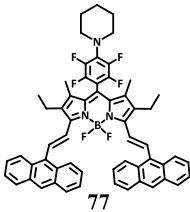
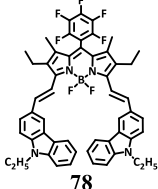
#### 4.2.3. Electrochemical characterisation

Figure 4.13 shows the cyclic voltammograms of the compounds of the **3S-BDP** and the corresponding electrochemical parameters are summarised in Table 4.3. The cyclic voltammograms of the compounds exhibit a quasi-reversible profile, and the first oxidation potential (onset oxidation potential) was used to estimate the HOMO energy in the same way as it was done in the former chapters.



**Figure 4.13.** Cyclic voltammograms of the **3S-BDP** in dichloroethane solution in the presence of 1 mM ferrocene/ferrocenium as internal standard, recorded at a scan speed of 50 mV/s.

**Table 4.3.** Electrochemical properties of the 3S-BDP.

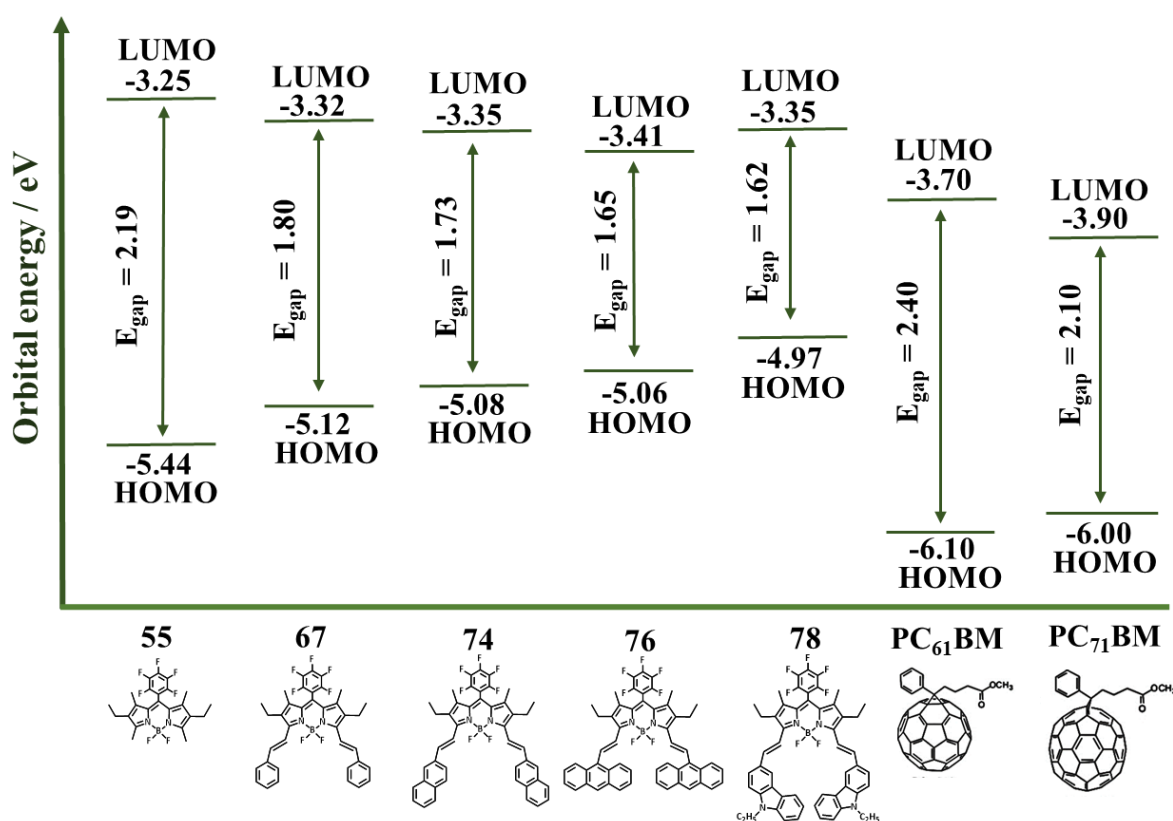
Dyes	$E_{\text{red}}^1$ (V)	$E_{\text{ox}}^1$ (V)	$E_{\text{ox}}^2$ (V)	$E_{\text{ox}}^3$ (V)	$E_{\text{onset}}^{\text{ox}1}$ (V)	$E_{\text{HOMO}}$ (eV) <sup>a</sup>	$E_{\text{g}}^{\text{opt}}$ (eV)	$E_{\text{LUMO}}$ (eV) <sup>b</sup>
 55	-0.97	1.35	1.53	-	1.21	-5.44	2.19	-3.25
 67	-0.62	1.08	1.39	-	0.91	-5.12	1.80	-3.32
 68	-0.64	1.04	1.36	-	0.88	-5.10	1.80	-3.30
 74	-0.59	1.03	1.38	-	0.89	-5.08	1.73	-3.35
 75	-0.56	1.01	1.35	-	0.89	-5.08	1.75	-3.33
 76	-0.54	1.02	1.23	1.50	0.87	-5.06	1.65	-3.41
 77	-0.59	1.01	1.28	1.46	0.88	-5.07	1.65	-3.42
 78	-0.73	0.80	1.03	1.39	0.74	-4.97	1.62	-3.35

<sup>a</sup>  $E_{\text{HOMO}} = [-(E_{\text{onset}}^{\text{ox}1} - E^{\text{Fc}/\text{Fc}^+}) - 4.8] \text{ eV}$ .<sup>b</sup>  $E_{\text{LUMO}} = [E_{\text{HOMO}} + E_{\text{g}}^{\text{opt}}] \text{ eV}$ .

As exposed in Figure 4.13 and Table 4.3, there is not a clear variance between the BODIPY dyes with the pentafluoro group and those with piperidine substitution on this group. The movement of the reduction peak to higher potentials and the oxidation peaks to lower potentials reveals a facilitated reduction and oxidation of the compounds from the third series in relation with their reference compound **55**.

Compounds **76**, **77** and **78** exhibit an additional oxidation peak that should be attributed to anthracene or carbazole electrochemical oxidation.<sup>15</sup> Comparing the redox potentials of the derivative compounds, it was observed that the different moieties (phenyl, naphthalenyl, anthracenyl) did not have a pronounced effect on the redox potentials. Compound **78** showed the redox processes at smaller potentials due to the stronger electron-donor character of the carbazole moieties.

The HOMO and LUMO energies obtained from the electrochemical and photophysical data are both above the HOMO and LUMO energies of both PC<sub>61</sub>BM and PC<sub>71</sub>BM as represented in Scheme 4.2.



**Scheme 4.2.** Frontier orbital energy levels of the **3S-BDP**, PC<sub>61</sub>BM and PC<sub>71</sub>BM.

The constant increase of the HOMO energy and the decrease of the LUMO is a strong indication that the increase of aromaticity from phenyl to anthracenyl affects the electronic properties of the compounds. As discussed for **2S-BDP**, the enlargement of the  $\pi$ -system



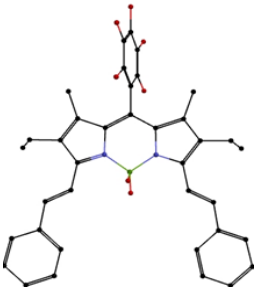
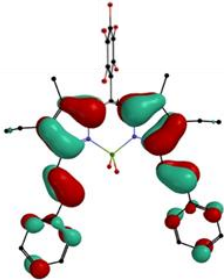
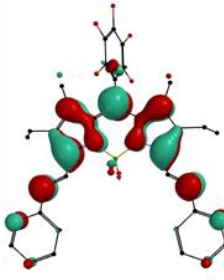
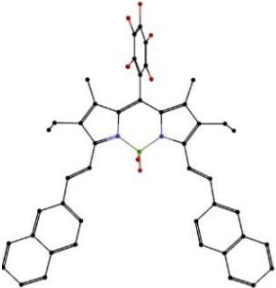
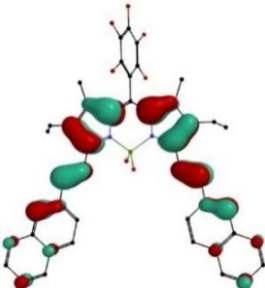
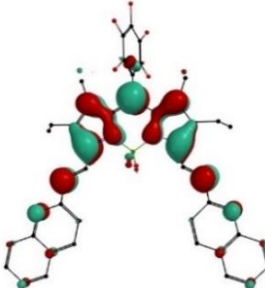
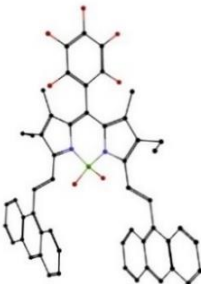
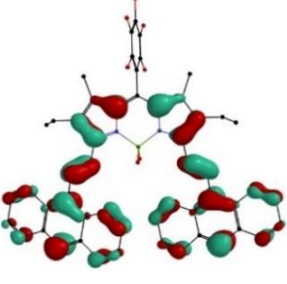
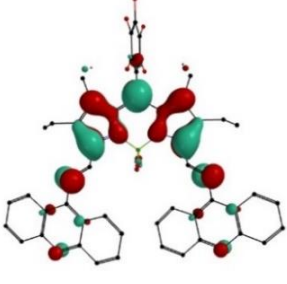
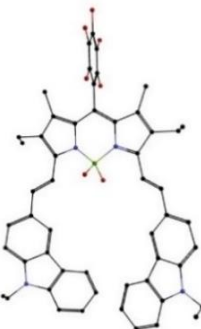
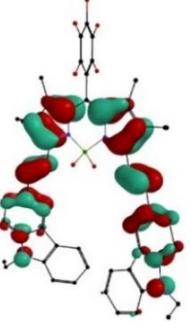
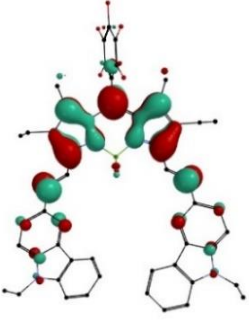
increases the HOMO energy and decreases the LUMO energy, but the electron-donating character could increase both.<sup>16</sup> Thus, the carbazolyl motif induces to the resulting BODIPY (**78**) the higher HOMO energy level but not the lower LUMO energy level, and a band gap of 1.62 eV.

#### 4.2.4. Computational studies

DFT studies (Table 4.4) confirmed that the **3S-BDP** has the same main features as those of **2S-BDP** (Chapter 3). There is not a notorious change on the ground state geometry, and the HOMO orbital is delocalised through the styryl donor groups and BODIPY's core while the LUMO is mainly located at the core. HOMO and LUMO orbitals show different spatial distribution of the electron density, pointing to some degree of intramolecular charge transfer. However, there is some spatial overlap between the two, which means that intramolecular charge transfer between the vinyl units and the BODIPY core (acting as acceptor) is not expected to be significant. The photophysical studies show higher Stokes Shifts for BODIPY dyes with anthracene or carbazole units, which could be motivated by more effective intramolecular charge transfer.

The HOMO energies obtained from the electrochemical studies are well reproduced from the computational calculations, but a larger deviation is found for the LUMO energy. This behaviour was already found for the dyes of the first and second series.

**Table 4.4.** Optimised ground-state structures, electron distribution in HOMO and LUMO and their energies (in eV) of the third BODIPY series, obtained by DFT calculations in vacuum.

BODIPY	Optimized Geometry	HOMO	LUMO
67		 -5.31	 -2.91
74		 -4.92	 -2.89
76		 -4.85	 -2.90
78		 -4.67	 -2.59

### 4.3. Photovoltaic studies of the third series of BODIPY molecules (3S-BDP)

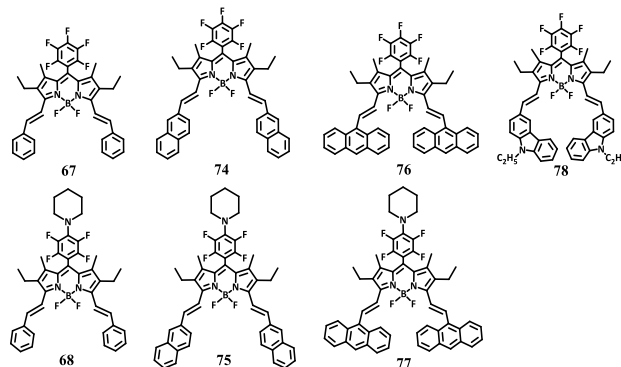
BHJ-OPVs with the usual structure (ITO/PEDOT:PSS/active layer/ Ca/ Al) were fabricated and characterised. Thermal annealing is a post-processing heating process that can strongly affect the performance of the photovoltaic cells.<sup>12, 17-19</sup> Therefore, the thermal annealing was an extra parameter that we studied during the active layer blend optimisation in this series (Table 4.5).

**Table 4.5.** Photovoltaic performance parameters of the 67:PC<sub>61</sub>BM-based organic photovoltaic cells during the optimisation studies. Results were obtained under 84 mW/cm<sup>2</sup> illumination.

Concentration (mg/ml)	Ratio (67:PC <sub>61</sub> BM)	Thermal Annealing (°C)	Active layer thickness (nm)	J <sub>SC</sub> (mA/cm <sup>2</sup> )	V <sub>OC</sub> (V)	FF	PCE (%)
20	1:2	-	118	0.80	0.56	0.25	0.13
20	1:3	-	111	0.89	0.76	0.23	0.19
20	1:4	-	115	0.69	0.40	0.24	0.08
15	1:3	-	99	1.23	0.64	0.24	0.22
13	1:3	-	82	1.13	0.62	0.24	0.20
15	1:3	60	95	1.71	0.57	0.24	0.28
15	1:3	100	97	1.65	0.61	0.24	0.29
15	1:3	125	98	1.60	0.61	0.23	0.27

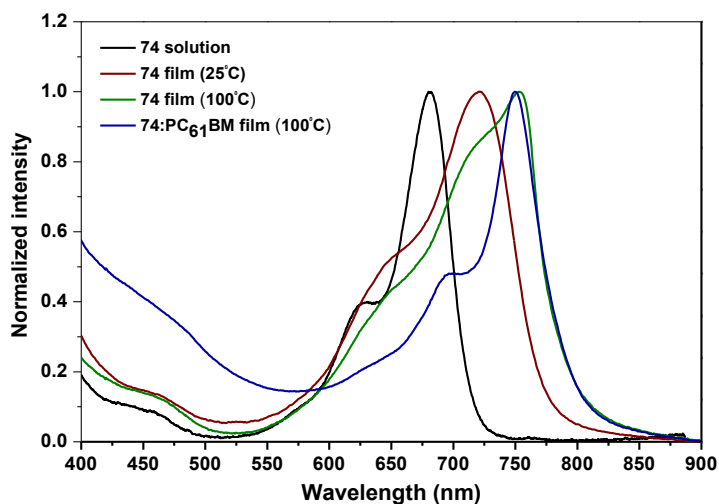
\*Average values calculated from at least 4 devices.

The blend optimisation process, carried out for the 67:PC<sub>61</sub>BM blend, showed that the best OPV was obtained with blend with a weight ratio of 1:3, deposited by spin-coating at 1200-1300 rpm from a chloroform solution at 15mg/ml, and thermally annealed at 100 °C for 10 min. These optimum conditions are similar to those established for the 2S-BDP series, which is justified by the structural similarity. Even though, thermal annealing induced a small increment of J<sub>SC</sub>. As the BODIPY dyes are stable at this temperature, thermal annealing of 100 °C for 10 min was set up for all blend's preparation (Figure 4.14).



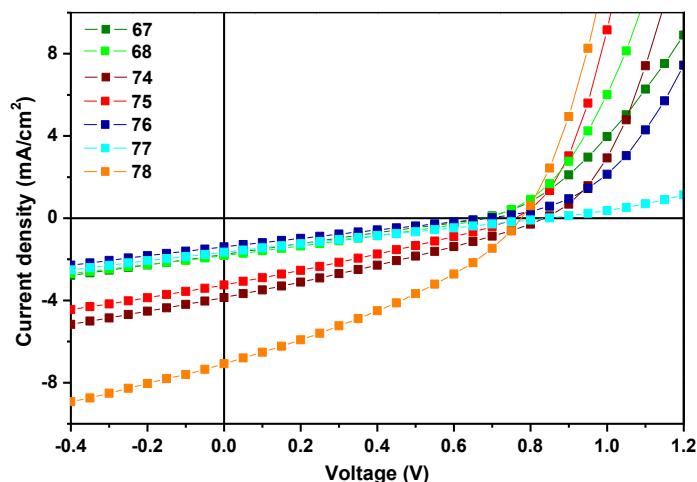
**Figure 4.14.** BODIPY dyes from the third series tested in BHJ-OPVs.

Figure 4.15 shows the differences in the absorption spectrum of **74** in solution, spin-cast film at room temperature, spin-cast films of neat **74** and the **74**:PC<sub>61</sub>BM blend after thermal annealing. As mentioned above, the film spectrum is broader and red-shifted when compared with solution, but when the film is thermally treated its spectrum becomes even more broad and red-shifted. This effect was also observed in the blend spectrum.



**Figure 4.15.** Absorption spectra of **74** obtained from solution, as deposited neat film, and annealed films of neat **74** and its blend with PC<sub>61</sub>BM.

Figure 4.16 shows the current density-voltage (*J*–*V*) characteristics of the best OPV cells, and the photovoltaic performance parameters are summarised in Table 4.6. Under the optimised conditions, the best PCE values were obtained with **78** (1.83 %) followed by **74** (1.05 %) and **75** (0.79 %). All the other BODIPY dyes presented much lower values of PCE but the components of **3S-BDP** exhibited a remarkable evolution with respect to the PCE value of **55** (0.02 %). The correlation between efficiencies and the piperidine substitution is not clear since BODIPYs **68** and **77** were better than their non-piperidine analogous, but **75** presented lower PCE than **74**.



**Figure 4.16.** Current density-voltage characteristics of **3S-BDP**:PC<sub>61</sub>BM based OPV cell.

**Table 4.6.** Photovoltaic performance parameters of the **3S-BDP**:PC<sub>61</sub>BM-based OPV cells, associated with a D:A weight ratio 1:3 and thermal annealing of 100 °C. Films were prepared from a chloroform solution at 15mg/ml.

Dye	Active layer thickness (nm)	P <sub>in</sub> (mW/cm <sup>2</sup> )	Maximum						Average*			
			J <sub>sc</sub> (mA/cm <sup>2</sup> )	V <sub>oc</sub> (V)	FF	R <sub>SH</sub> (Ω.cm <sup>2</sup> )	R <sub>s</sub> (Ω.cm <sup>2</sup> )	PCE (%)	J <sub>sc</sub> (mA/cm <sup>2</sup> )	V <sub>oc</sub> (V)	FF	PCE (%)
<b>67</b>	97	84	1.76	0.68	0.24	367	250	0.34	1.65	0.61	0.24	0.29
<b>68</b>	109	84	1.82	0.68	0.27	427	197	0.40	1.72	0.63	0.28	0.36
<b>74</b>	96	90	3.86	0.84	0.29	276	114	1.05	4.00	0.78	0.28	0.97
<b>75</b>	100	88	3.24	0.76	0.28	263	210	0.79	3.30	0.73	0.28	0.77
<b>76</b>	114	88	1.40	0.69	0.24	443	401	0.26	1.37	0.67	0.24	0.25
<b>77</b>	119	90	1.65	0.84	0.24	490	508	0.37	1.58	0.83	0.24	0.35
<b>78</b>	72	100	7.10	0.78	0.33	181	40	1.83	6.62	0.77	0.34	1.73

\*Average values calculated from at least 6 devices.

The performance results shown in Table 4.6 and in Figure 4.16 were obtained with the incident light power varying between 84 and 100 mW/cm<sup>2</sup>. It has been reported that the performance parameters vary with illumination power.<sup>20</sup> In particular, for powers well above 1 sun (100 mW/cm<sup>2</sup>) there is a decrease in PCE. In the analysis that follows, we assume that the OPVs performance does not vary significantly between 84 and 100 mW/cm<sup>2</sup>.

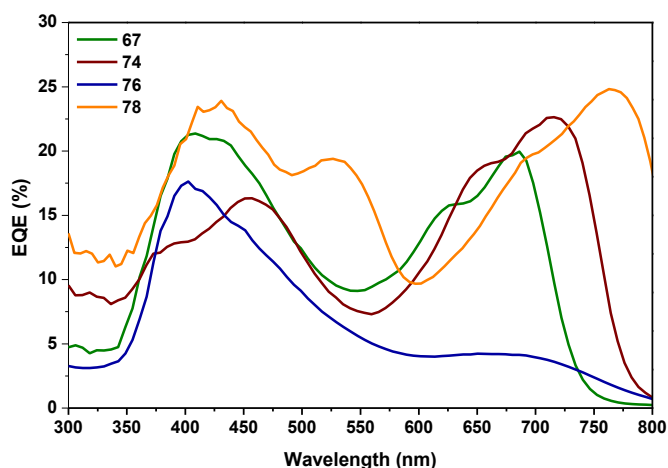
Whatever the dye from this series, the corresponding OPVs present high V<sub>oc</sub> values, with the 0.84 V achieved by OPVs based on **74** and **77** worthing a special note. The conjugation of the higher V<sub>oc</sub> with the maximum J<sub>sc</sub> of 3.86 mA/cm<sup>2</sup> and FF of 0.29 allowed the **74**-based OPV to overcome the efficiency barrier of 1 %. The higher efficiency of the cells based on BODIPY **78** is mostly due to its superior J<sub>sc</sub> (almost twice of the second best) and FF. Since BODIPY **78** has a light harvesting ability similar to the other BODIPY compounds, the higher J<sub>sc</sub> and FF of **78**-based OPVs is likely related to an improved hole transport, attributed to the presence of the carbazole motifs.<sup>2, 4, 21</sup>

The PCE increased from the phenyl to naphthalenyl substituent groups but then drops when the substituent size and π system extension increased (anthracenyl substitution groups). The better photovoltaic efficiency of **74** and **78** can be due to the highest absorption

coefficient, extended absorption to higher wavelengths, and the higher hole transporting properties brought by the presence of carbazole.

The BODIPY dyes with anthracenyl fractions are the worst performing dyes of the series. The anthracenyl is more aromatic than naphthalenyl but, its size may influence the details of the blend film morphology. Although the anthracenyl-based dyes of **76** and **77** show a broader absorption bands, their molar absorption coefficients are lower.

As displayed in Figure 4.17, the EQE profiles follow those of the blend films absorption spectra. A broad response in the 300-800 nm spectral region is observed for BODIPY:PC<sub>61</sub>BM systems, that is mainly due to the BODIPY absorption profile. However, some contribution of PC<sub>61</sub>BM at 300-400 nm is also present. The larger and stronger response of the **78**-based OPV is consistent with a higher short-circuit current.

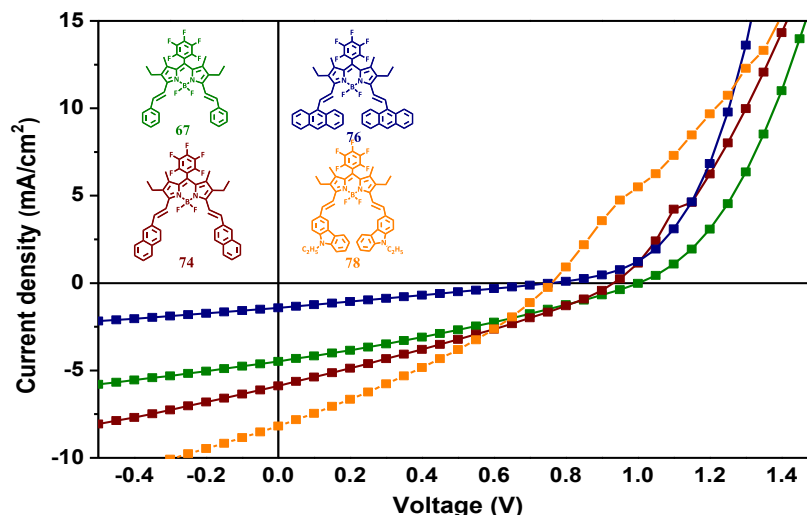


**Figure 4.17.** EQE spectra of the optimised **67**:PC<sub>61</sub>BM, **74**:PC<sub>61</sub>BM, **76**:PC<sub>61</sub>BM and **78**:PC<sub>61</sub>BM-based OPV cells.

In Chapter 3, we reported that compound **67** blended with PC<sub>71</sub>BM produced much better results than the blend with PC<sub>61</sub>BM. Therefore, the blends of compounds **67**, **74**, **76** and **78** with PC<sub>71</sub>BM were also tested (under the same preparation conditions used for the blends with PC<sub>61</sub>BM). The OPVs results are shown in Figure 4.18 and Table 4.7.

The blend of **67**:PC<sub>71</sub>BM was the one that presented the most significant improvement, but **74**:PC<sub>71</sub>BM and **78**:PC<sub>71</sub>BM showed the best PCE results and a positive increment on their photovoltaic parameters as well. On the other hand, **76**:PC<sub>71</sub>BM gave similar results to those of the **76**:PC<sub>61</sub>BM blend.

The efficiencies of the cells are largely dependent on the relative amounts of the donor and acceptor materials used in the active layer. Trying to obtain a better efficiency, we further investigated the photovoltaic parameters of the same blends with donor:acceptor ratios of 1:2 and 1:1 (Table 4.7).



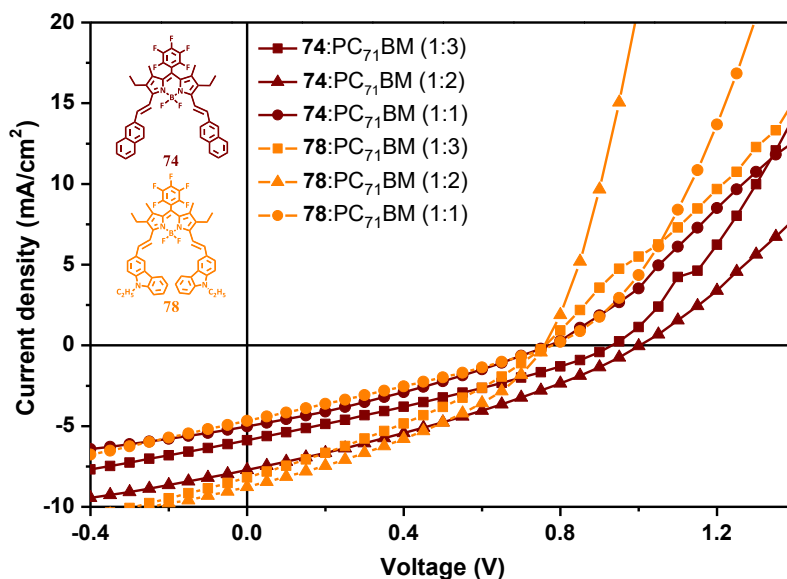
**Figure 4.18.** Current density-voltage characteristics of **67**:PC<sub>71</sub>BM, **74**:PC<sub>71</sub>BM **76**:PC<sub>71</sub>BM and **78**:PC<sub>71</sub>BM-based OPV cells, with a D/A ratio of 1:3, thermally annealed at 100 °C.

**Table 4.7.** Photovoltaic performance parameters of OPVs based on BODIPYs **67**, **74**, **76** and **78** blended with PC<sub>71</sub>BM. Several donor:acceptor ratios were used, and the active layers were thermally annealed at 100 °C.

Dye	Active layer thickness (nm)	Power (mW/cm <sup>2</sup> )	Maximum						Average*			
			J <sub>sc</sub> (mA/cm <sup>2</sup> )	V <sub>oc</sub> (V)	FF	R <sub>SH</sub> (Ω.cm <sup>2</sup> )	R <sub>s</sub> (Ω.cm <sup>2</sup> )	PCE (%)	J <sub>sc</sub> (mA/cm <sup>2</sup> )	V <sub>oc</sub> (V)	FF	PCE (%)
Ratio 1:3	<b>67</b>	81	4.58	1.00	0.31	313	126	1.74	4.46	0.94	0.30	1.55
	<b>74</b>	85	5.88	0.93	0.29	199	71	1.87	5.64	0.93	0.29	1.79
	<b>76</b>	93	1.41	0.76	0.26	559	443	0.30	1.39	0.74	0.26	0.29
	<b>78</b>	83	100	8.18	0.76	0.31	143	45	1.93	7.57	0.76	0.31
Ratio 1:2	<b>67</b>	100	4.02	0.80	0.30	268	67	0.96	3.85	0.80	0.29	0.89
	<b>74</b>	84	7.52	1.00	0.31	192	71	2.79	7.04	0.96	0.32	2.57
	<b>76</b>	84	1.33	0.80	0.23	511	645	0.29	1.16	0.80	0.24	0.27
	<b>78</b>	100	100	8.76	0.76	0.36	165	25	2.39	7.56	0.76	0.36
Ratio 1:1	<b>67</b>	81	2.85	0.81	0.30	393	205	0.86	2.28	0.91	0.30	0.77
	<b>74</b>	88	5.03	0.78	0.30	228	112	1.34	4.10	0.78	0.30	1.09
	<b>76</b>	93	1.58	0.83	0.24	490	508	0.34	1.34	0.75	0.24	0.26
	<b>78</b>	130	100	4.68	0.77	0.29	186	92	1.05	4.39	0.78	0.28

\*Average values calculated from at least 6 devices.

All cells exhibit high  $V_{OC}$  values, with those based on **67**:PC<sub>71</sub>BM and **74**:PC<sub>71</sub>BM exhibiting  $V_{OC}$  in line with the best published so far. The systems with **74** and **78** achieved efficiencies above 1 % in all the scenarios (Figure 4.19 and Table 4.7), and for the ratio of 1:2 (BODIPY:PC<sub>71</sub>BM) they presented 2.79 % and 2.39 % of maximum efficiencies, which are considered very reasonable PCE results for BODIPY-based OPVs. In most cases, the OPVs did not suffer significant changes on  $V_{OC}$  and FF upon variation of the active layer D:A composition ratio, but the discrepancies between their  $J_{SC}$  were considerable.

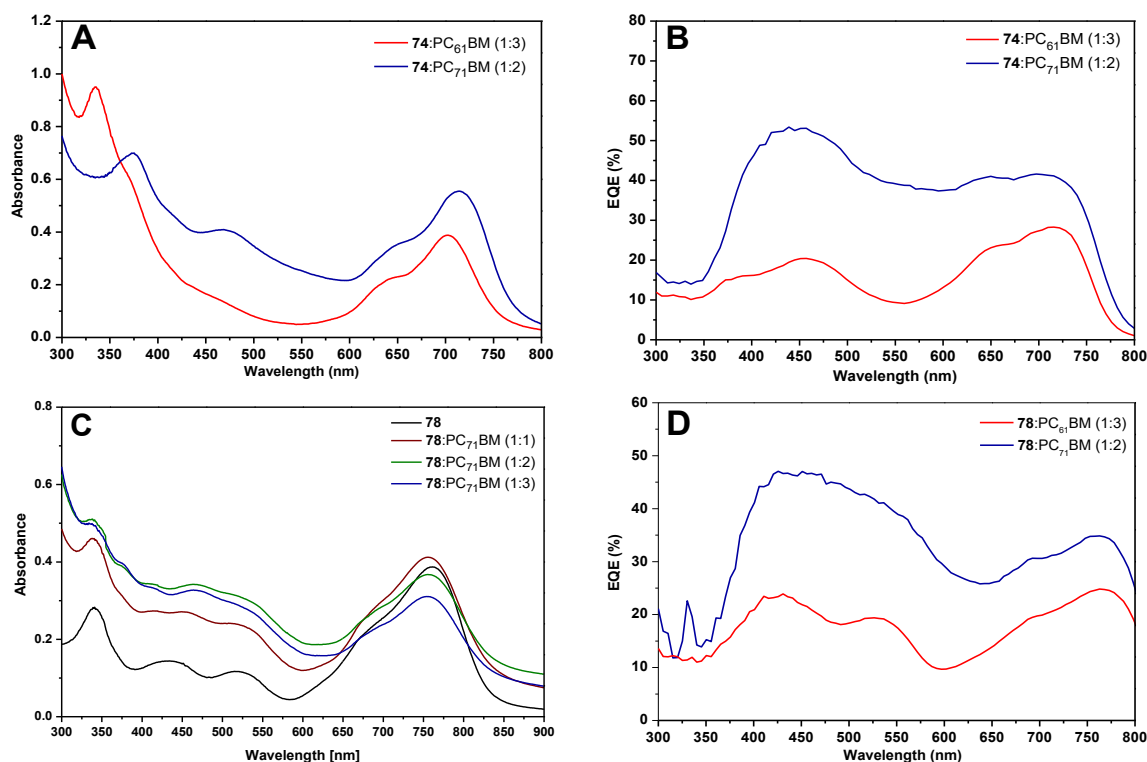


**Figure 4.19.** Current density-voltage characteristics of **74**:PC<sub>71</sub>BM and **78**:PC<sub>71</sub>BM-based OPV cells having three different donor:acceptor ratios; thermally annealed at 100 °C.

In addition to the thermal annealing and the general active layer optimisation procedures already described, the use of solvent annealing and solvent additives (1,8-diiodooctane and chloronaphthalene) were also tested. The solvent annealing did not result in an improvement of the photovoltaic response, and the use of additives led to worse PCE results. The additives contributed to the formation of thinner active layers and probably they could have a positive effect if used with a different solvent.

The EQE profiles (Figure 4.20) follow the absorption profile of the blend and demonstrate the superior performance of the blends with PC<sub>71</sub>BM over those with PC<sub>61</sub>BM. A broad response in the visible region of the spectrum is observed for both systems, but the higher EQE of the PC<sub>71</sub>BM-based cell is attributed to the larger PC<sub>71</sub>BM absorption in the visible region of the spectrum and to the higher  $J_{SC}$ . Additionally, the different donor:acceptor ratios (Figure 4.19 (C)) bring a significant variation in the absorption intensities of the several bands of the blend.





**Figure 4.20.** Absorption spectra (A and C) and EQE curves (B and D) of the optimised **74:PC<sub>61</sub>BM**, **74:PC<sub>71</sub>BM** and **78:PC<sub>71</sub>BM** systems.

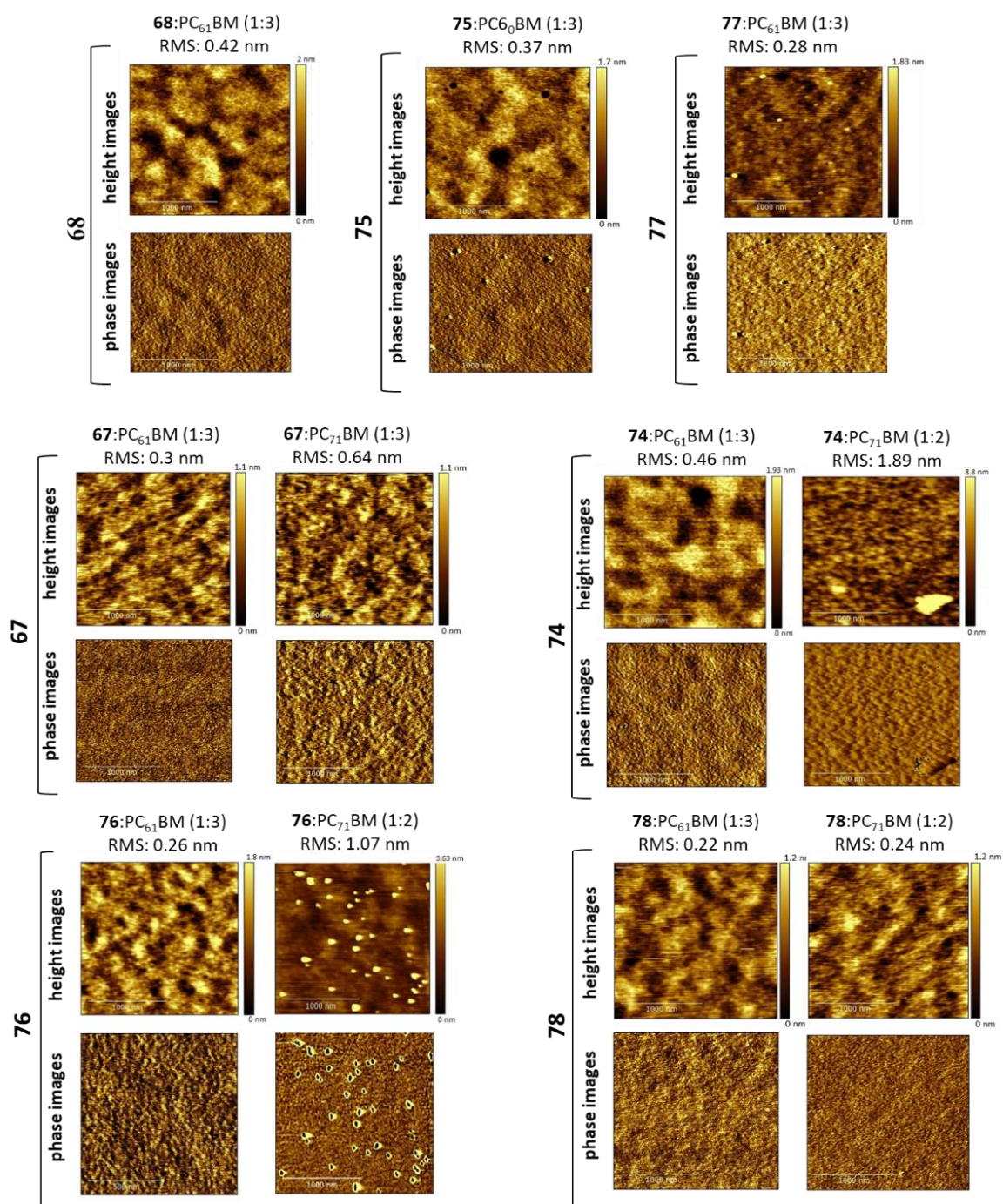
The **78:PC<sub>71</sub>BM** (1:2) OPV also showed an EQE spectrum with extensive coverage and intensities between 30 % and 45 % in almost all visible region of the spectrum. Unfortunately, it was not possible to record all the EQE profile of the **78:PC<sub>71</sub>BM** OPV because the S<sub>0</sub>-S<sub>1</sub> transition lies at wavelengths above 800 nm, which is the limit of the equipment we used to carry out the EQE measurements.

#### 4.3.1. Surface morphology of the active layer

The films of the best performing dyes of the **3S-BDP** series presented in Table 4.6 (blended with PC<sub>61</sub>BM (1:3)) and the films of the BODIPY dyes tested with PC<sub>71</sub>BM with a ratio of 1:2 were characterised by AFM. As shown in Figure 4.21, the films presented flat surfaces like the blends described in previous chapters. In addition to the low roughness, no significant phase separation was found, evidencing good miscibility between the BODIPYs and the fullerenes.

The blends of **77** and **78** with fullerenes present some dispersed aggregates in a non-uniform pattern which were more persistent when blended with PC<sub>71</sub>BM. The aggregates formation could be due to the higher aromaticity of these BODIPY dyes (with anthracene

units) and it is one of the possible reasons for the lower efficiency of the OPVs based on these molecules.



**Figure 4.21.** AFM height images (top) and phase images (bottom) ( $2\mu\text{m}$  vs  $2\mu\text{m}$ ) of the 3S-BDP blended with  $\text{PC}_{61}\text{BM}$  or  $\text{PC}_{71}\text{BM}$ .

#### 4.4. Conclusions for Chapter 4

In this chapter, we described the synthesis of a series of BODIPY dyes (**3S-BDP**), combining an electron-acceptor moiety (pentafluorophenyl) at the *meso*-position and four different electron-donor vinyl moieties linked to the backbone. The extremely fast reaction time, compared with the same kind of synthesis for other BODIPY molecules, and the photo-electrochemical properties of these BODIPYs, made them excellent candidates to be applied as electron-donor materials in BHJ photovoltaic cells.

The **3S-BDP** dyes reveal excellent thermal stability, strong spectral coverage, deep HOMO levels and good miscibility with PC<sub>61</sub>BM and PC<sub>71</sub>BM. With the increase of aromaticity of vinyl groups, a shifting of absorbance to higher wavelengths is observed, and the band gap was decreased to 1.62 eV (compound **78**).

The BODIPYs with piperidine substitution (**68**, **75** and **77**) showed the same characteristics as their pentafluorophenyl analogous (**67**, **74** and **76**), without a noticeable influence of the piperidine presence on the overall photovoltaic characteristics.

All BODIPY dyes could work as electron-donor materials in a BODIPY:PC<sub>61</sub>BM blend. With the exception of compound **78**, with a maximum PCE of 1.83 %, they presented efficiencies around 1 % or below. The higher efficiency of this BODIPY is the result of a higher short-circuit current that the carbazole motif brings to the system. Although less efficient, the other OPVs based on BODIPY:PC<sub>61</sub>BM presented high V<sub>OC</sub> (between 0.68 V and 0.84 V).

The dyes showed a large increase in their photovoltaic parameters when blended with PC<sub>71</sub>BM. The 2.39 % and 2.79 % of PCE achieved for **78**:PC<sub>71</sub>BM and **74**:PC<sub>71</sub>BM blends, respectively, are very encouraging results. The V<sub>OC</sub> of 1.00 V obtained for the cells with **67** and **74** is only 80 mV below the best V<sub>OC</sub> published so far in BODIPY based-OPVs and are amongst the best reported.

#### 4.5. References for Chapter 4

1. M. Hecht, T. Fischer, P. Dietrich, W. Kraus, A. B. Descalzo, W. E. S. Unger and K. Rurack, *ChemistryOpen*, **2013**, 2, 25-38.
2. B. Xu, E. Sheibani, P. Liu, J. Zhang, H. Tian, N. Vlachopoulos, G. Boschloo, L. Kloo, A. Hagfeldt and L. Sun, *Advanced Materials*, **2014**, 26, 6629-6634.
3. S. Das and I. Gupta, *Journal of Porphyrins and Phthalocyanines*, **2019**, 23, 367-409.
4. M. Li, Z. Wang, M. Liang, L. Liu, X. Wang, Z. Sun and S. Xue, *The Journal of Physical Chemistry C*, **2018**, 122, 24014-24024.
5. G. Reddy, N. Duvva, S. Seetharaman, F. D'Souza and L. Giribabu, *Physical Chemistry Chemical Physics*, **2018**, 20, 27418-27428.
6. I. F. Sengul, E. Okutan, E. Astarçı and B. Çoşut, *Dyes and Pigments*, **2015**, 123, 32-38.
7. H.-j. Lv, X.-t. Zhang, S. Wang and G.-w. Xing, *Analyst*, **2017**, 142, 603-607.
8. J. Xu, L. Zhu, Q. Wang, L. Zeng, X. Hu, and Z. Sun, *Tetrahedron*, **2014**, 70, 5800-5805.
9. R. Misra, T. Jadhav, B. Dhokale, P. Gautam, R. Sharma, R. Maragani and S. M. Mobin, *Dalton Transactions*, **2014**, 43, 13076-13086.
10. S. Wanwong, P. Khomein and S. Thayumanavan, *Chemistry Central Journal*, **2018**, 12, 60.
11. X. Zhang, Y. Xiao, J. Qi, J. Qu, B. Kim, X. Yue and K. D. Belfield, *The Journal of Organic Chemistry*, **2013**, 78, 9153-9160.
12. T. Jadhav, R. Misra, S. Biswas and G. D. Sharma, *Physical Chemistry Chemical Physics*, **2015**, 17, 26580-26588.
13. O. Galangau, C. Dumas-Verdes, R. Méallet-Renault and G. Clavier, *Organic & Biomolecular Chemistry*, **2010**, 8, 4546-4553.
14. G. Lanzani, M. Nisoli, S. De Silvestri and R. Tubino, *Chemical Physics Letters*, **1996**, 251, 339-345.
15. K. Karon and M. Lapkowski, *Journal of Solid State Electrochemistry*, **2015**, 19, 2601-2610.
16. N. Heiland, C. Cidarér, C. Rohr, M. Piescheck, J. Ahrens, M. Bröring and U. Schröder, *ChemSusChem*, **2017**, 10, 4215-4222.
17. T.-y. Li, J. Benduhn, Y. Li, F. Jaiser, D. Spoltore, O. Zeika, Z. Ma, D. Neher, K. Vandewal and K. Leo, *Journal of Materials Chemistry A*, **2018**, 6, 18583-18591.
18. J. X. Liao, Y. J. Xu, H. B. Zhao, Q. Zong and Y. T. Fang, *Organic Electronics*, **2017**, 49, 321-333.
19. J. X. Liao, H. B. Zhao, Y. J. Xu, Z. D. Cai, Z. X. Peng, W. T. Zhang, W. N. Zhou, B. H. Li, Q. Zong and X. X. Yang, *Dyes and Pigments*, **2016**, 128, 131-140.
20. R. Steim, T. Ameri, P. Schilinsky, C. Waldauf, G. Dennler, M. Scharber and C. J. Brabec, *Solar Energy Materials and Solar Cells*, **2011**, 95, 3256-3261
21. B. Kim, B. Ma, V. R. Donuru, H. Liu and J. M. J. Fréchet, *Chemical Communications*, **2010**, 46, 4148-4150.

## **CHAPTER 5. BODIPY molecules functionalized at the boron centre**

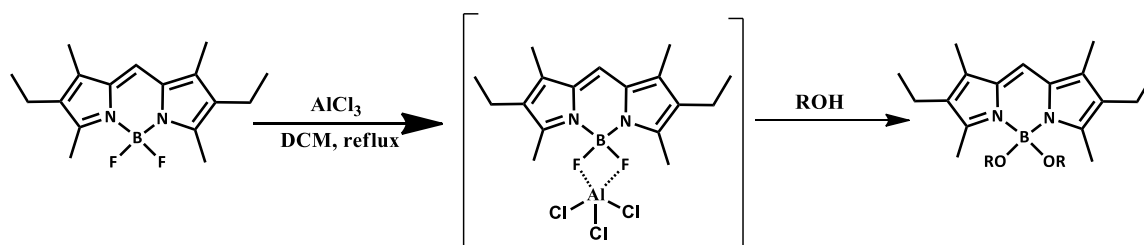
Among the different possibilities of functionalization of the BODIPY structures, the functionalization at the boron centre is one of the less investigated. The substitution of one or both fluorine atoms could allow the expansion of the chromophore by the inclusion of other moieties, functional groups, and modify its properties.<sup>1-6</sup>

In 1999, Burgess and co-workers reported the first oxygen substitution at the boron centre by intramolecular cyclization of 3,5-*ortho*-hydroxyphenyl groups.<sup>7</sup> Since then, this type of BODIPY molecules underwent a significant development.<sup>8-10</sup> Presently, BODIPY dyes having alkoxy or aryloxy substituents at boron centre (O-BODIPY) are typically obtained after activation of the BODIPY precursor with a Lewis acid ( $\text{AlCl}_3$  or  $\text{BCl}_3$ ).<sup>11,10</sup> Apart from a few exceptional cases, the O-BODIPYs present similar photophysical properties to their unfunctionalized fluorinated analogues.

This chapter explores a series of O-BODIPY dyes (fourth series (**4S-BDP**)) initially based on two molecules from **1S-BDP** (Chapter 2). This kind of functionalization was planned considering the quickness and proficiency of the synthetic method, general stability of O-BODIPY derivatives,<sup>12</sup> and the high probability to keep the excellent properties of the BODIPY structures described in the previous chapter.

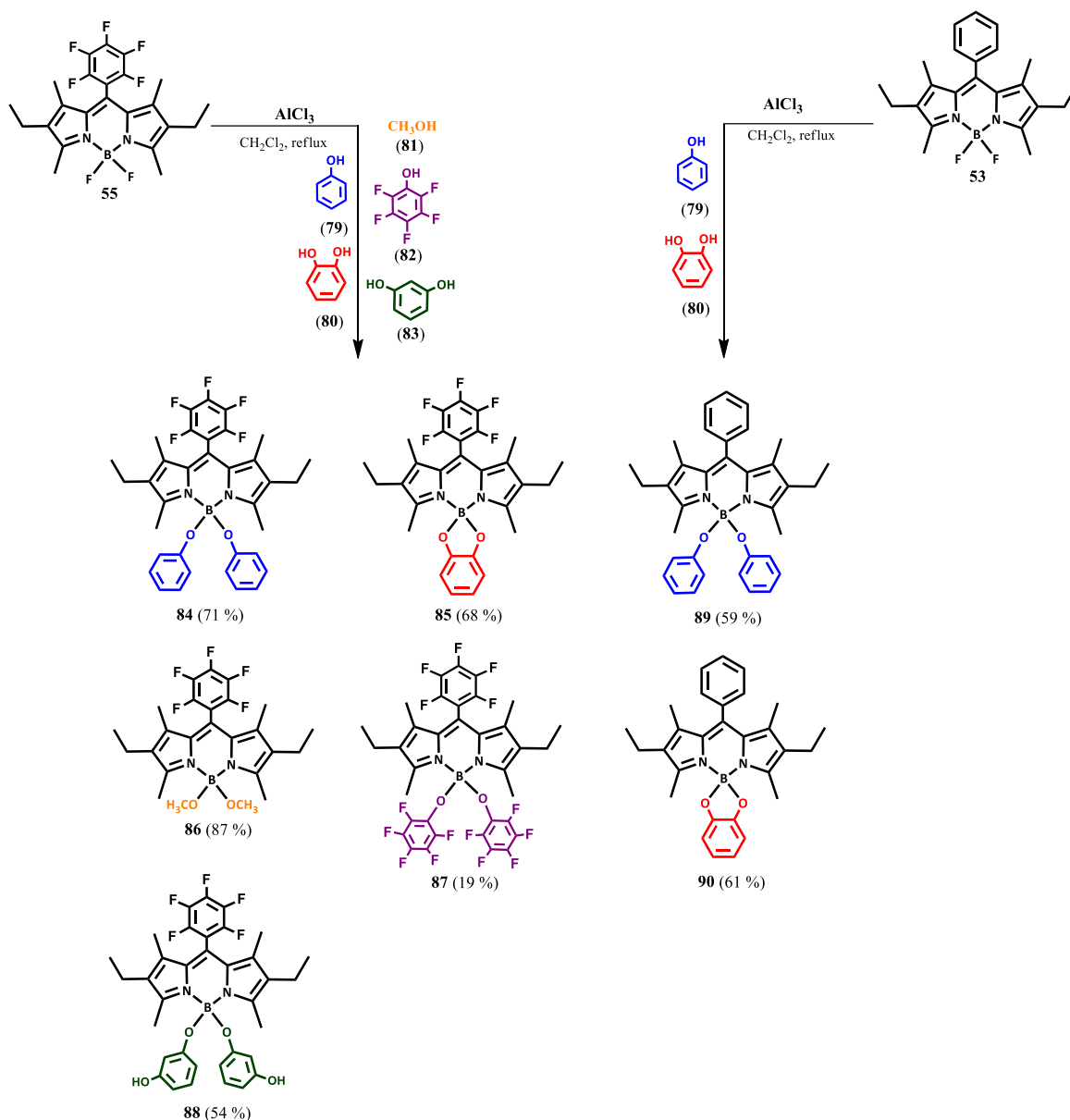
### 5.1. Synthesis and structural characterisation of the fourth series of BODIPY molecules (**4S-BDP**)

Using BODIPY **53** and **55** as starting compounds, a series of O-BODIPY dyes (**4S-BDP**) were prepared through a straightforward method for boron functionalization.<sup>11</sup> This method consists in the reaction of BODIPY with  $\text{AlCl}_3$ , followed by the addition of the selected alcohol (Scheme 5.1). Although the BODIPY intermediate has not been isolated, the importance of  $\text{AlCl}_3$  and its interaction with the fluorine atoms of the BODIPY were proved by NMR studies by Mély and co-workers.<sup>11</sup>



**Scheme 5.1.** The proposed mechanism for the formation of O-BODIPY dyes, using  $\text{AlCl}_3$  as catalyst, according to Mély and co-workers.<sup>11</sup>

Scheme 5.2 shows the synthesis and respective yields of the **4S-BDP**. Most of the BODIPYs (**84-88**) were prepared from the starting BODIPY **55**. However, two O-BODIPY derivatives (**89** and **90**) were also synthesised, through the reaction of **53** with phenol (**79**) or catechol (**80**).

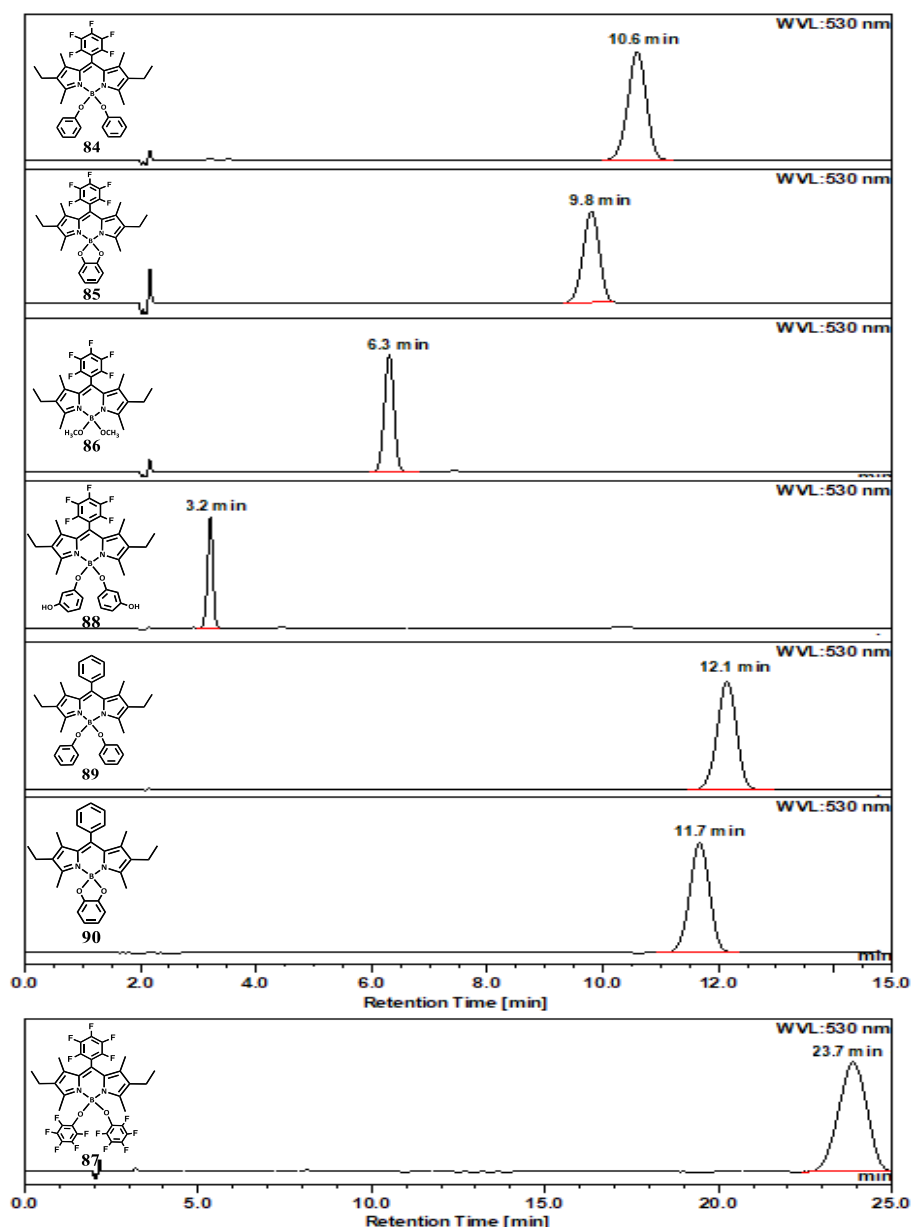


**Scheme 5.2.** General synthesis of **4S-BDP** and respective yields.

The preparation of BODIPYs **84-88** is justified by the positive influence on the photovoltaic response of the functionalizations of **55** (verified in Chapter 3 and Chapter 4), which demonstrated the potential of this framework upon well tailored structural modifications. BODIPY **89** and **90** were prepared from one of the most efficient BODIPY molecules of the first series (Chapter 2). The reaction took 20 minutes and was carried out

using two equivalents of  $\text{AlCl}_3$  and ten equivalents of the desired alcohol, leading to yields between 19 % and 87 %. In the synthesis of **86**, methanol was used as reagent and solvent.

Although compound **89** and **90** were already reported,<sup>13, 10</sup> to the best of our knowledge compounds **84-88** have not been published yet. The final **4S-BDP** products were isolated by silica gel column chromatography (dichloromethane or dichloromethane-THF (9:1) for **86** and **88**) and the purification efficiency was evaluated by HPLC (Figure 5.1).



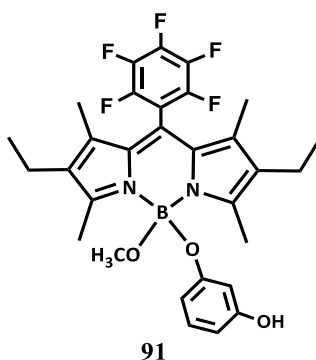
**Figure 5.1.** HPLC chromatograms obtained at 30 °C with acetonitrile:  $\text{H}_2\text{O}$  (8:2) as isocratic eluent with a volume of injection of 10  $\mu\text{L}$  and a flow rate of 0.8 ml/min.

All the chromatograms reveal a single peak that proves the efficient isolation of each **4S-BDP** compound. These peaks have higher or lower retention times according to the higher or lower hydrophilicity, thereby the BODIPY with alcohol groups has the lower



retention time and the highly fluorinated BODIPY (**87**) presents the peak at higher retention time.

Before the selection of THF as co-eluent in the column chromatography for purification of BODIPY **88**, we used methanol. However, in this case, a small amount of **86** (methoxide ligand) and **91** (Figure 5.2) were isolated along with **88**. This occurrence highlights the fact that methanol has replaced the resorcinol moiety, probably catalysed for some aluminium chloride that was still present in the sample matrix before the chromatography.



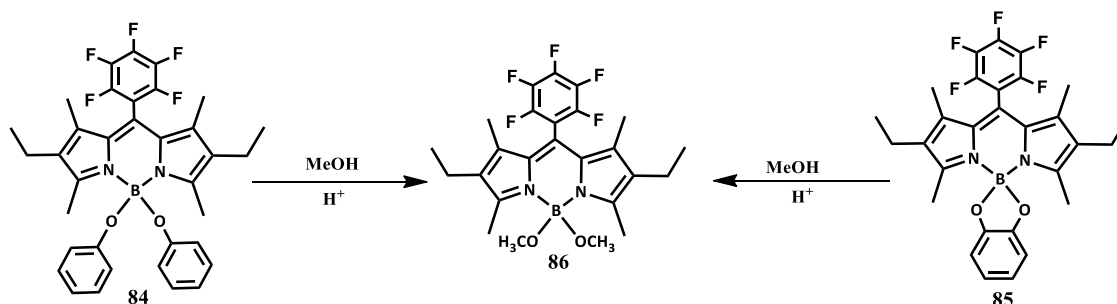
**Figure 5.2.** Structure of BODIPY **91**.

In 2013, Raymo and co-workers reported that the catecholate ligand of BODIPY **90** can be substituted by a pair of methoxide ligands in a solution of methanol with the aid of a photoacid generator.<sup>13</sup> Therefore, it was investigated the extent of modification of the **4S-BDP** structures when a methanol solution is used.

Three different solutions of BODIPY **84** and **85**, at  $1 \times 10^{-5}$  M, were prepared. The first solution was prepared using methanol with 1 equivalent of formic acid, the second solution was prepared only with methanol, and the third solution was prepared using acetonitrile with 1 equivalent of formic acid. After 2 minutes of stirring, it was possible to see that the methanol acidic solution was suffering changes since the initially non-fluorescence pink solution (for BODIPY **85**) was becoming fluorescent and yellow. Since the solution of BODIPY **84** is yellow the control for this BODIPY was only possible by TLC.

After 10 minutes all the solutions were controlled by HPLC, and both BODIPYs presented exactly the same features. In the methanol or in the acidic acetonitrile solution, none of the two dyes suffered any change. On the other hand, the HPLC chromatograms of the BODIPYs in methanol with formic acid confirmed a 100 % conversion of those BODIPYs into **86** (Scheme 5.3). The HPLC analyses were repeated after 24 hours and they

presented equal outcome. Later, the same study was carried out for BODIPY **55** and under no circumstances, it was converted into BODIPY **86**.

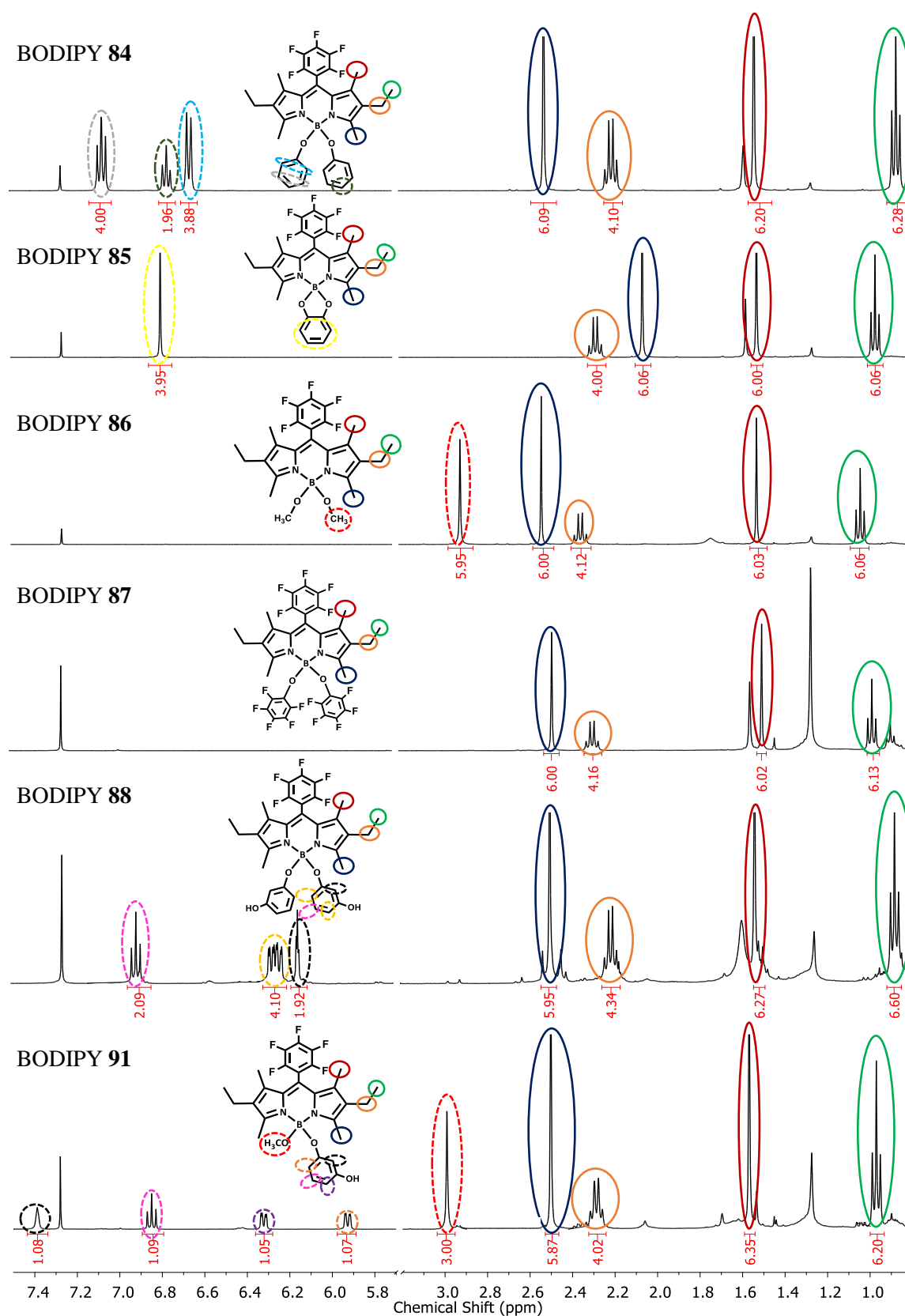


**Scheme 5.3.** Exchange of boron-ligand through treatment with methanol under acidic conditions.

Figure 5.3 shows the <sup>1</sup>H NMR spectrum of the *meso*-pentafluorophenyl BODIPY derivatives from **3S-BDP** with the identification of all signals (solid line to BODIPY's core and dashed line to O-B substitution groups). The spectra of the *meso*-phenyl derivatives (**89** and **90**) are very similar to their pentafluoro analogous (**84** and **85**) and are presented in the experimental section (Chapter 8) along with the high-resolution mass spectra of the components of this series.

While the majority of the structures does not present a meaningful variation of the core's signals, if compared with their predecessor (**55**). BODIPY **85** shows a considerable change in the chemical shift of the singlet assigned to the methyl groups at  $\alpha$ -position (blue solid line). This shift is associated with the orientation of the catecholate moiety that induces a shielding effect, increasing the protection of the hydrogen atoms.

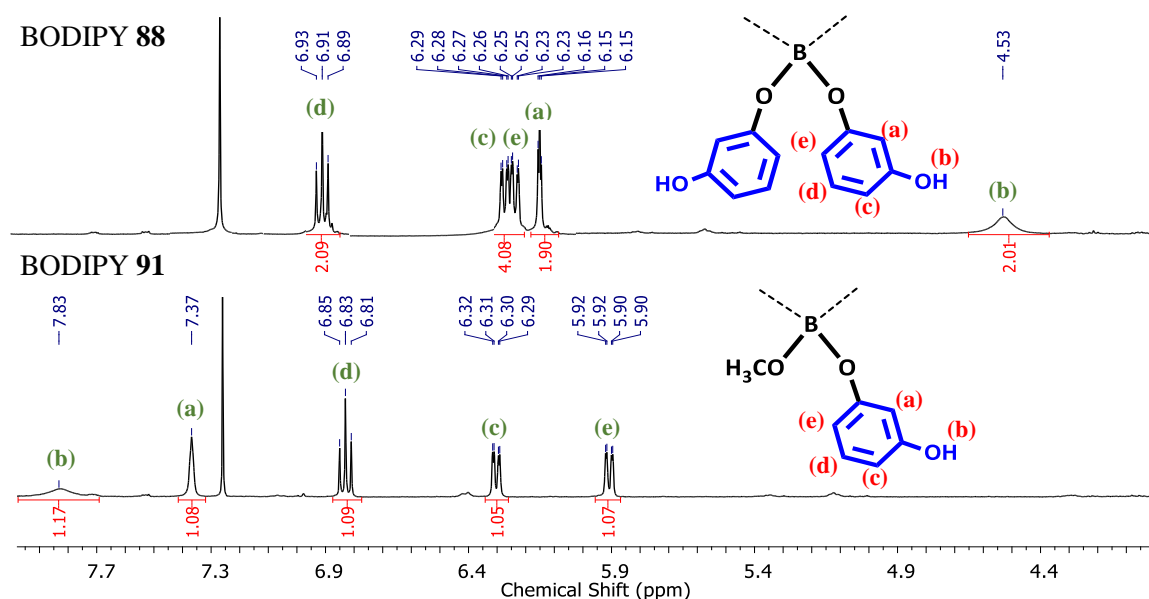
The other main differences in <sup>1</sup>H NMR spectrum are related to the O-B substituent groups. The *meta*, *para* and *ortho* protons from the phenoxy group of BODIPY **84** are respectively assigned to the triplets (7.07 ppm and 6.76 ppm) and doublet signal (6.66 ppm). The catecholate protons (**85**) are represented by a singlet at 6.8 ppm. The protons from the methoxy groups (**86** and **91**) are also represented by a singlet (2.9 ppm). BODIPY **87** does not show any extra signal, which makes its spectrum a replicate of that of BODIPY **55**.



**Figure 5.3.**  $^1\text{H}$  NMR spectra (400 MHz) of **84-88**, **91**, in  $\text{CDCl}_3$ .

BODIPYs **88** and **91** have a divergent chemical environment around the resorcinol derivative moieties. As shown in Figure 5.4, the  $^1\text{H}$  NMR spectrum of **88** shows the -OH

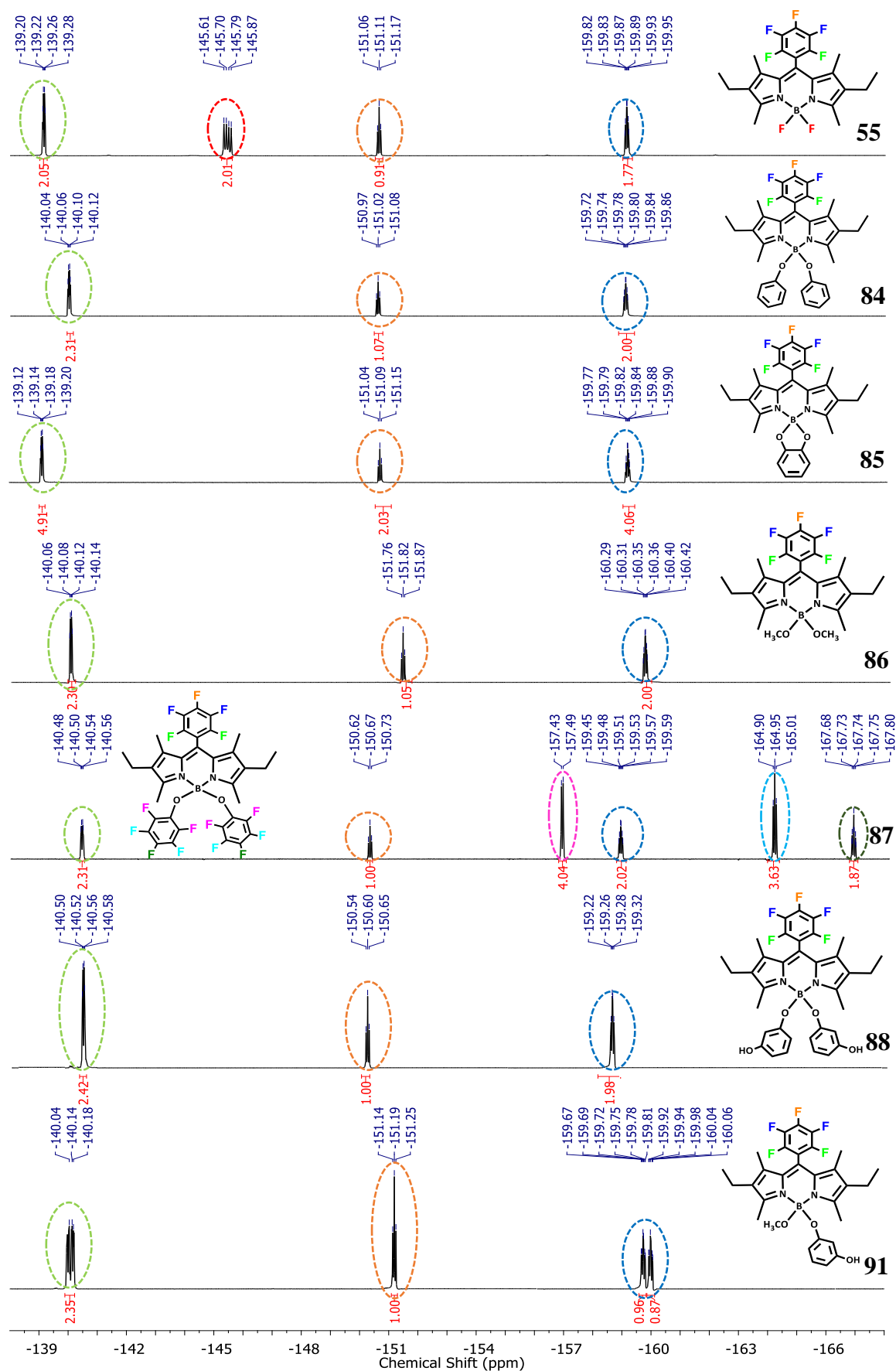
signal (b) at 4.53 ppm, while for **91** the signal for the same group is lying at 7.83 ppm. Another substantial difference between both spectra are related to the signal of protons (a), (d) and (e). For **88** the signal assigned to (a) is at 6.15 ppm and the doublet of doublets slightly overlapped, at 6.25, are associated to (c) and (e). BODIPY **91** presents the signal of (a) at higher chemical shifts (7.37), the doublet of doublets (c) and (e) much more separated and the signal of (e) at lower chemical shifts.



**Figure 5.4.** Expansion of the  $^1\text{H}$  NMR spectra (400 MHz) of **88** and **91**, in  $\text{CDCl}_3$ .

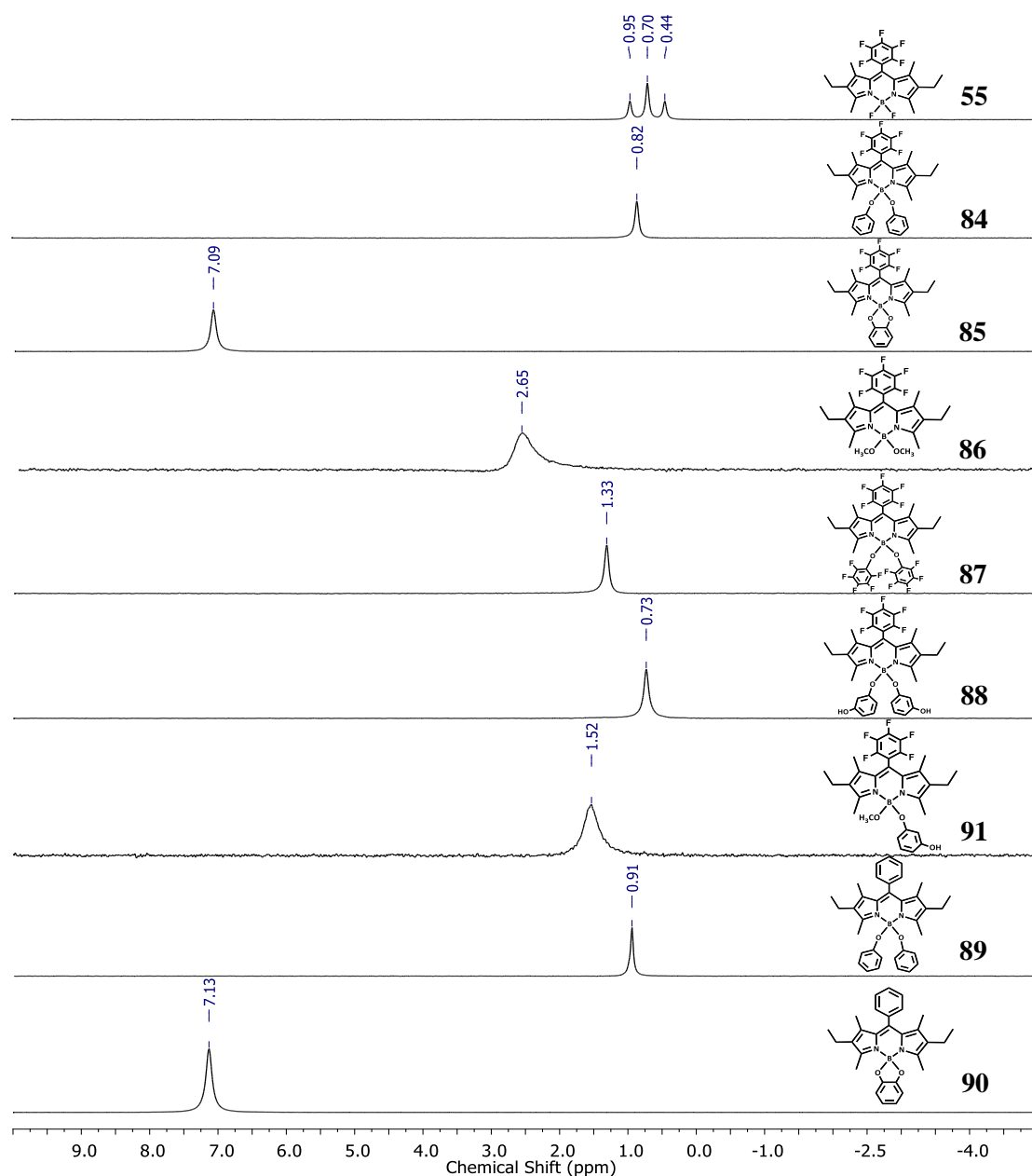
In Chapter 2, it was demonstrated, by X-ray diffraction and DFT studies, that the fluorine atoms at boron centre are perpendicular to BODIPY core. Since BODIPY core acts as a macrocyclic aromatic ring, the hydrogens that are in phase with it could receive some shielding due to the anisotropic field generated by the circulating  $\pi$ -electrons from the BODIPY core. In this light, the resorcinol derivative moieties of both compounds should have different axial orientation, where the (a) and (b) of **88** are more shielded than the same protons of **91**.

Figure 5.5 shows the  $^{19}\text{F}$  NMR spectra of all molecules from **4S-BDP** with fluorine atoms (**84-88** and **91**) and their precursor (**55**). With the exchange of boron ligands, there is one less signal to be detected in  $^{19}\text{F}$  NMR. Apart from the absent B-F signal, the dyes from **4S-BDP** have  $^{19}\text{F}$  NMR spectra similar to that of **55**. However, the spectrum of **87** has an extra doublet (-157.46 ppm), triplet (-164.95 ppm) and a triplet of the triplet (-167.74 ppm) assigned to the *ortho*, *meta* and *para* positions of the pentafluorophenoxy group, respectively. Due to the asymmetry of BODIPY **91**, the *ortho* and *meta* signals are both represented by two signals each, but they are almost completely overlapped.



**Figure 5.5.**  $^{19}\text{F}$  NMR spectra (376 MHz) of **84**–**88** and **91**, in  $\text{CDCl}_3$ .

As expected, the  $^{11}\text{B}$  NMR (Figure 5.6) shows that the substitution of both fluorine atoms by the aryloxy groups leads to the conversion of the typical triplet into a singlet.

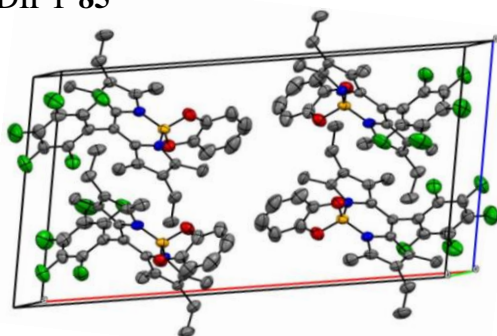
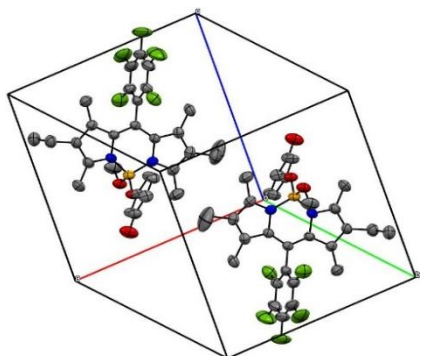


**Figure 5.6.**  $^{11}\text{B}$  NMR spectra (128 MHz) of **4S-BDP**, obtained in  $\text{CDCl}_3$ .

Through the analysis of Figure 5.6, it is possible to conclude that most of the compounds present similar spectra with a small deviation of the peaks. Only the BODIPY dyes with a catechol group present a large shift (around 6 ppm), which denotes a different electronic distribution in the BODIPY core.

### 5.1.1. X-ray diffraction studies

Suitable crystals for X-ray diffraction analysis were obtained for compound **85** and **91** by slow evaporation from a dichloromethane/hexane solution. The crystallographic unit cell and crystallographic data of these two new structures are depicted in Figure 5.7.

BODIPY **85**BODIPY **91**

Crystal data	<b>85</b>	<b>91</b>
Chemical formula	C <sub>29</sub> H <sub>26</sub> B F <sub>5</sub> N <sub>2</sub> O <sub>2</sub>	C <sub>30</sub> H <sub>30</sub> B F <sub>5</sub> N <sub>2</sub> O <sub>3</sub>
$M_r$	540.20	572.37
Crystal system, space group	monoclinic, $P2_1/c$	Triclinic, $P-1$
Temperature (K)	273	273
$a, b, c$ (Å)	21.6270(18), 9.8417(9), 22.2385(10)	11.646(5), 12.064(5), 12.416(5)
$\alpha, \beta, \gamma$ (°)	90.00(10), 100.055(2), 90.00	111.890(13), 93.694(14), 114.239(13)
$V$ (Å <sup>3</sup> )	2564.91	1426.35(10)
$Z$	4	2
Radiation type	Mo $K\alpha$	Mo $K\alpha$

**Figure 5.7.** Crystallographic unit cell and details of structure **85** and **91**.

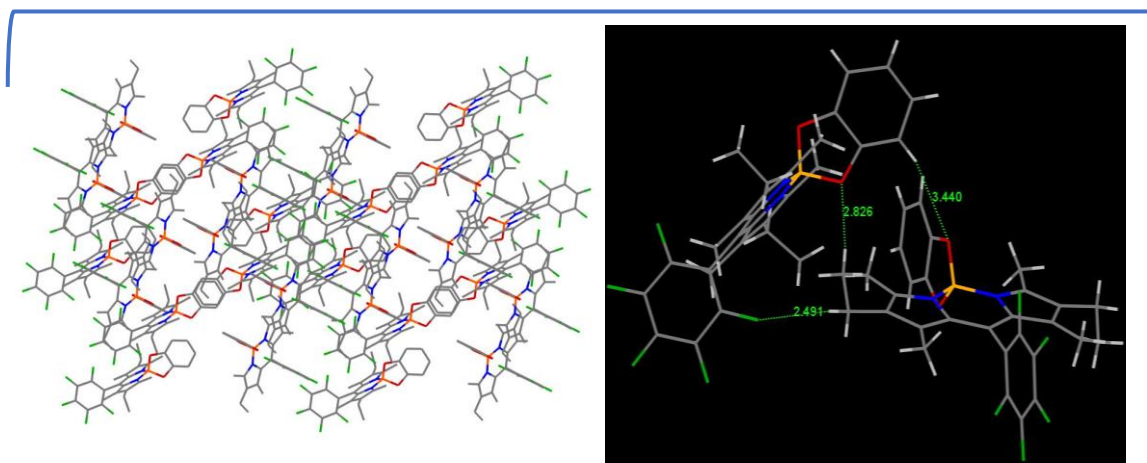
BODIPY **85** crystallises in a monoclinic crystal system (space group  $P2_1/c$ ) with a unit cell composed of four molecules, while BODIPY **91** crystallises in a triclinic crystal system (space group  $P1^-$ ) with unit cell composed of two molecules.

As shown in Figure 5.8, BODIPY **85** shows a more efficient packing than **91** since the catecholate does not expand to the axial space of the BODIPY core with the same amplitude than resorcinol derivative group do in **91**. The axial space occupied by these groups supports the premise that B–O BODIPY derivatives are not so prone to aggregation phenomena as B–F or B–C BODIPY compounds.<sup>12</sup>

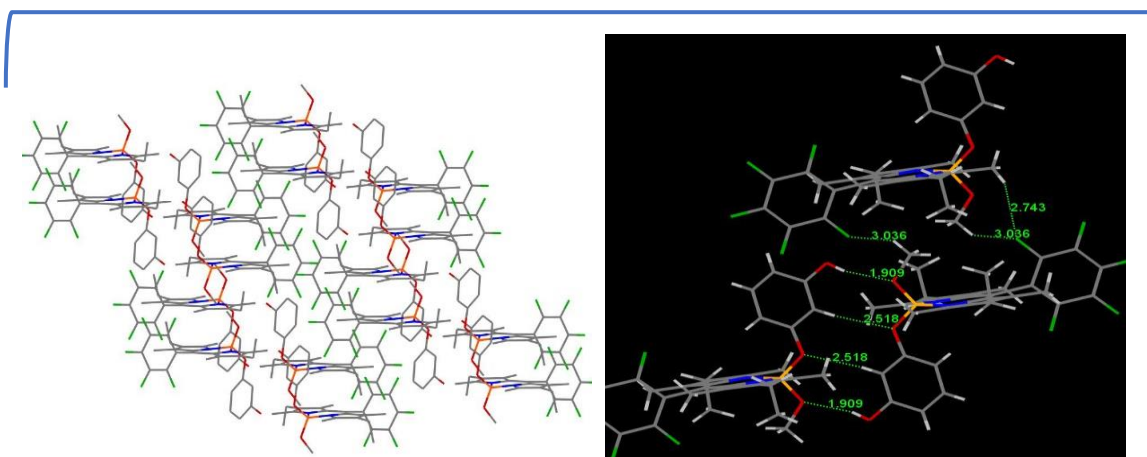
The packing of BODIPY **85** is dominated by short contacts. In Figure 5.8, it is possible to see the existence of interaction between the oxygen atom from catecholate and hydrogens from  $\beta$ -pyrrolic ethyl group ( $-\text{CH}_3$ ) with a bond distance of 2.83 Å and between

a fluorine atom from pentafluoro moiety and a hydrogen from  $\beta$ -pyrrolic ethyl group ( $-\text{CH}_2$ ), with a distance of 2.49 Å. Additionally, a weak intermolecular interaction should exist between the oxygen atom from catecholate and hydrogens from another catecholate (3.44 Å).

### BODIPY 85



### BODIPY 91



**Figure 5.8.** Crystal packing and main intermolecular interactions of BODIPY **85** and **91**.

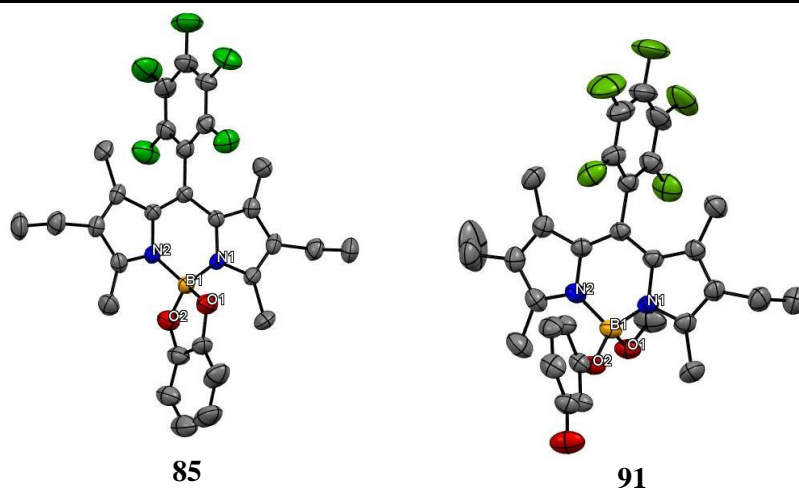
The crystal packing arrangement of **91** is dependent on hydrogen bonds, formed between the hydroxide groups with  $\text{O}-\text{H}\cdots\text{O}$  distances of 1.91 Å. Other short contacts, such as the interaction of the oxygen from methoxy group with a hydrogen from the resorcinol moiety (2.52 Å) and the fluorine atoms with hydrogens from  $\alpha$ -pyrrolic methyl group or from methoxy group (2.74 Å and 3.03 Å, respectively), can be identified as well in Figure 5.8.

From the data presented in Table 5.1, it is possible to verify the structural characteristics of **85** and **91**, such as the angle between the *meso*-group and the core and the



planarity of the structure. The geometry of the boron centre did not change with the modification of boron-ligands. Thus, the pentafluorophenyl group is almost perpendicular to the nearly planar BODIPY's core, the boron atom takes a somewhat distorted tetrahedral coordination and the B-N bond distances are similar.

**Table 5.1** Conformation of the ethyl groups, selected bond lengths and angles of the crystal's structures of **85** and **91**.



Conformation	<i>trans</i>	<i>cis</i>
$\Theta_{\text{core-meso}}$ ( $^{\circ}$ )	88.30	85.64
N1-B (Å); N2-B (Å)	1.536(5); 1.543(5)	1.561(3); 1.555(3)
B1-O1 (Å); B1-O2 (Å)	1.473(5); 1.489(5)	1.440(3); 1.440(3)
N1-B1-N2 ( $^{\circ}$ )	107.64	105.37
O1-B1-O2 ( $^{\circ}$ )	104.39	104.99
Boron planarity ( $^{\circ}$ )	179.32	174.44

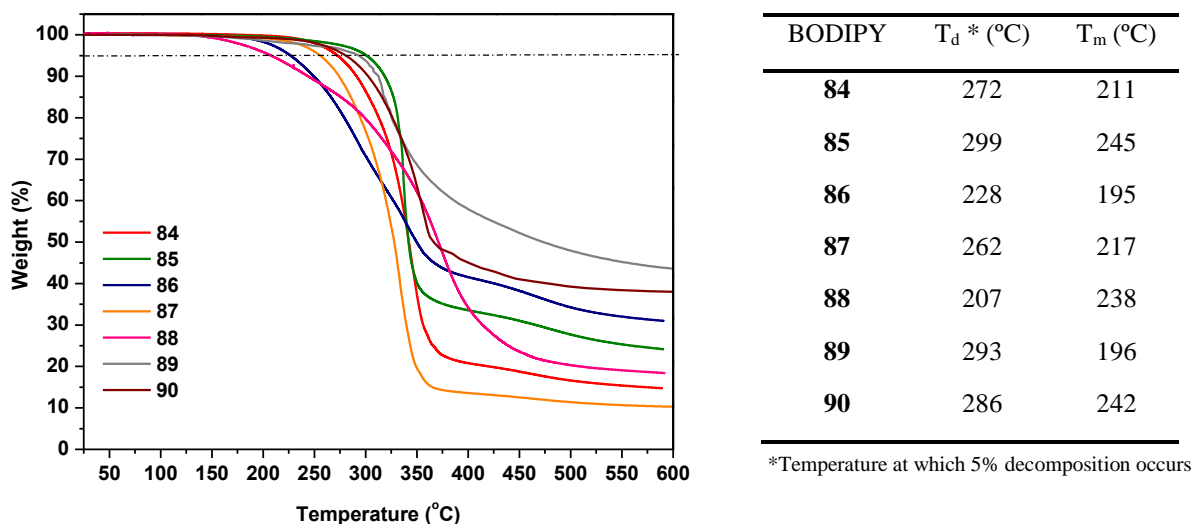
The X-ray diffraction of BODIPY **55**, reveals a *trans* conformation between the ethyl groups at the  $\beta$ -pyrrolic position. In the opposite way, the structure of **91** presents *cis* conformation of the ethyl groups and *trans* conformation between the ethyl groups and the resorcinol derivative.

## 5.2. Characterisation of the fourth series of BODIPY molecules (4S-BDP)

The entire series was characterised in terms of thermal behaviour, absorption and emission features and the electrochemical properties. Furthermore, we calculate the HOMO and LUMO energies upon the combination of absorption and electrochemical data and conclude about the changes that the alkoxy or aryloxy ligands have brought to the BODIPYs.

### 5.2.1. Thermal characterisation

Following the thermogravimetry analysis and the measurements of the melting temperatures (Figure 5.9), it can be concluded that this series of BODIPY dyes have in general higher melting points and better thermal stability than the generality of the compounds of the first series (**1S-BDP**).

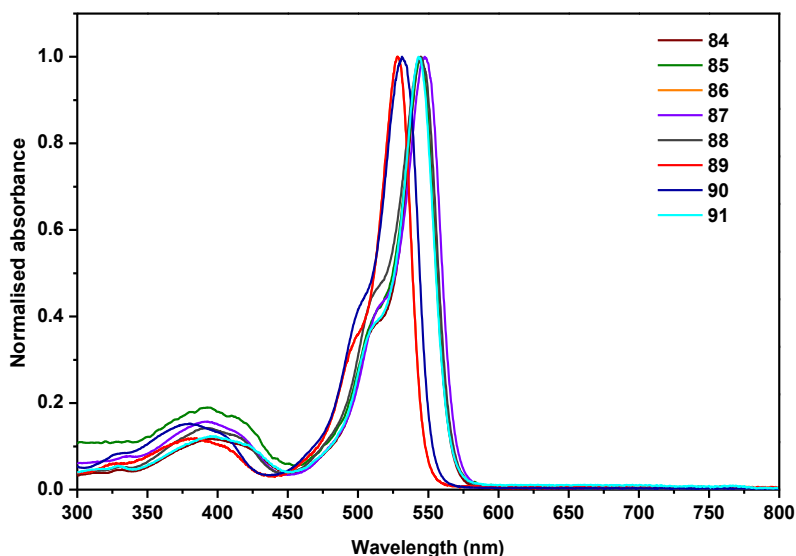


**Figure 5.9.** TGA traces of the BODIPY dyes recorded at a heating rate of 20 °C/min and a table with their melting temperatures and temperature at which 5 % of degradation occurs.

In the case of *meso*-pentafluorophenyl derivatives, the change of fluorine ligands to methoxy (compound **55** to compound **86**) does not significantly change the melting temperature (190 °C vs 195 °C) but achieves 5 % of decomposition at lower temperatures (256 °C vs 228 °C). With the use of aryloxy ligands, the BODIPY compounds melt at higher temperatures and, except for **88**, they need a higher temperature to degrade. This behaviour was also observed for the *meso*-phenyl derivatives (**89** and **90**).

### 5.2.2. Photophysical characterisation

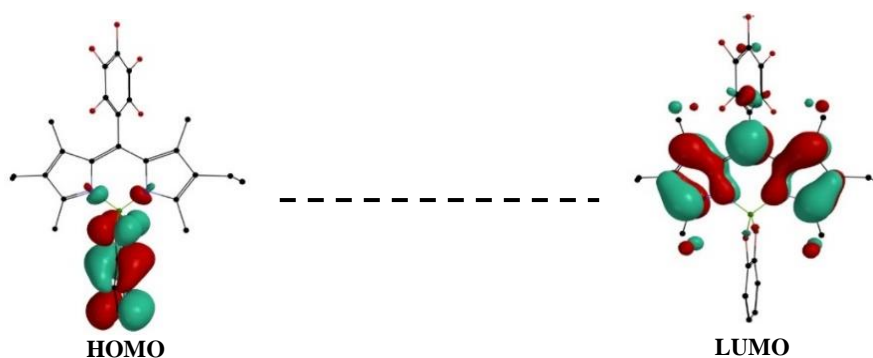
The photophysical properties of the **4S-BDP** were determined in chloroform solution and they are summarised in Table 5.2. The absorption spectra (Figure 5.10) show that all compounds exhibit the two absorption bands characteristic of the BODIPY, which are the S<sub>0</sub>→S<sub>2</sub> located around 390 nm, and the S<sub>0</sub>→S<sub>1</sub> transition at around 545 nm for pentafluorophenyl derivatives or 525 nm for phenyl derivatives. Therefore, the exchange of ligands has a negligible influence on the absorption spectra of the BODIPY dyes.



**Figure 5.10.** Normalised absorption spectra of **4S-BDP**, in chloroform.

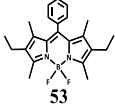
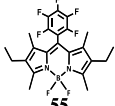
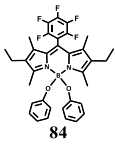
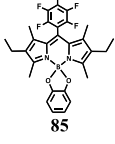
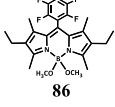
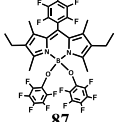
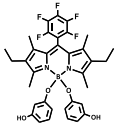
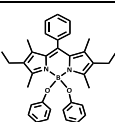
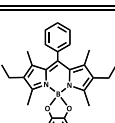
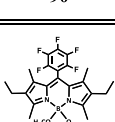
Compounds **85** and **90** are the only molecules that do not exhibit fluorescence in solution. Some works have already reported that the replacement of the two fluorine ligands with a catecholate suppresses fluorescence completely.<sup>13,14</sup> This fluorescence quenching is observed for **85** and **90**, and results from the electron transfer from the catecholate to BODIPY backbone, upon photoexcitation.<sup>13</sup>

Figure 5.11 shows the DFT the electronic density of both HOMO and LUMO of **85**. The HOMO orbital of **85** is lying at catechol and boron centre, instead of being delocalized over the BODIPY core as it happens with its predecessor (**53**). However, the LUMO orbitals have the electrons delocalised within the BODIPY core just like the generality of **1S-BDP**. This  $\pi$ -electrons delocalization extension over the different fraction of the molecules and the quenching of fluorescence indicates a photoinduced electron transfer (PET).



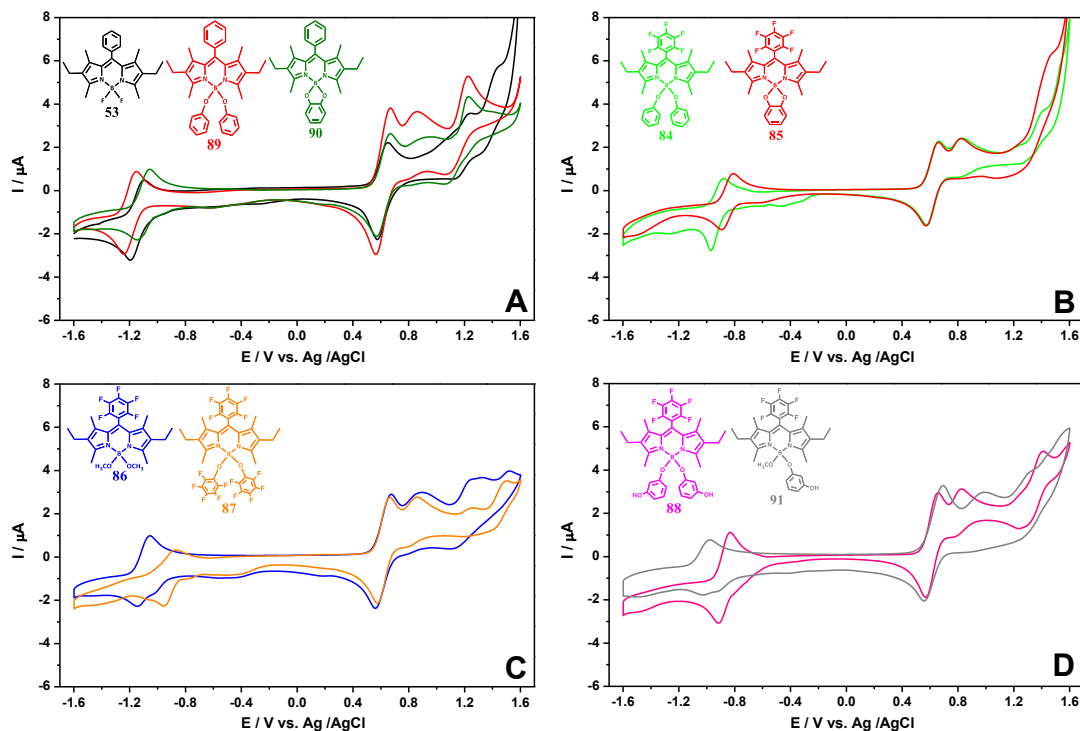
**Figure 5.11.** HOMO and LUMO of BODIPY **85**.

**Table 5.2.** Photophysical data of the **4S-BDP**, measured in chloroform solution.

BODIPY	$\lambda^{\text{abs}}$ (nm)	$\epsilon$ ( $\text{cm}^{-1} \text{M}^{-1}$ )	$\lambda^{\text{abs}}$ film (nm)	$\lambda^{\text{em}}$ (nm)	$\Phi_{\text{F}}$ (%)	SS ( $\text{cm}^{-1}$ )	$E_{\text{g}}^{\text{opt}}$ (eV)
	525	$6.8 \times 10^4$	548	538	98	460	2.28
	544	$5.9 \times 10^4$	551	558	98	461	2.19
	545	$6.1 \times 10^4$	553	559	81	460	2.20
	550	$8.1 \times 10^4$	562	-	-	-	2.17
	544	$4.0 \times 10^4$	554	560	100	525	2.21
	547	$4.6 \times 10^4$	555	560	96	424	2.18
	545	$5.9 \times 10^4$	554	559	68	460	2.19
	528	$6.1 \times 10^4$	549	539	93	387	2.27
	532	$7.4 \times 10^4$	552	-	-	-	2.25
	543	$6.5 \times 10^4$	553	558	72	495	2.19

### 5.2.3. Electrochemical characterisation

Considering the cyclic voltammograms (Figure 5.12) and the data summarised in Table 5.3, it is possible to observe that the substitution of fluorine atoms of the boron centre affects the redox potentials of the BODIPY molecules.



**Figure 5.12.** Cyclic voltammograms of **63**, **89** and **90** (A); **84** and **85** (B); **88** and **87** (C); **88** and **91** (D), in dichloroethane, containing 1 mM ferrocene/ferrocenium (Fc/Fc<sup>+</sup>) as internal standard, recorded at 50 mV/s.

It was already reported, for an O-BODIPY derivative with a catecholate ligand, a shift (390 mV) of the oxidation process to lower potential.<sup>15</sup> However, the cyclic voltammograms of the **4S-BDP** demonstrate that this behaviour is not specific for catecholate ligands since the voltammograms of **4S-BDP** compounds show large shifts in the oxidation potential (300 mV - 540 mV) when compared with the voltammograms of **53** or **55**. This feature is clear in Figure 5.12 (A) where the voltammograms of **53**, **89** and **90** are in the same plot, but through Table 5.3 it is possible to compare all the compounds. The deviations on the reduction process are much smaller or negligible.

These large differences in oxidation indicate that this new series has significant differences in the HOMO orbitals. As previously published for other O-BODIPY structures,<sup>13,15</sup> or demonstrated for **85** in Figure 5.11, the O-BODIPY molecules have the HOMO located primarily on the aryloxy ligand group, whereas BODIPY molecules from **1S-BDP** have the HOMO located on the BODIPY core.

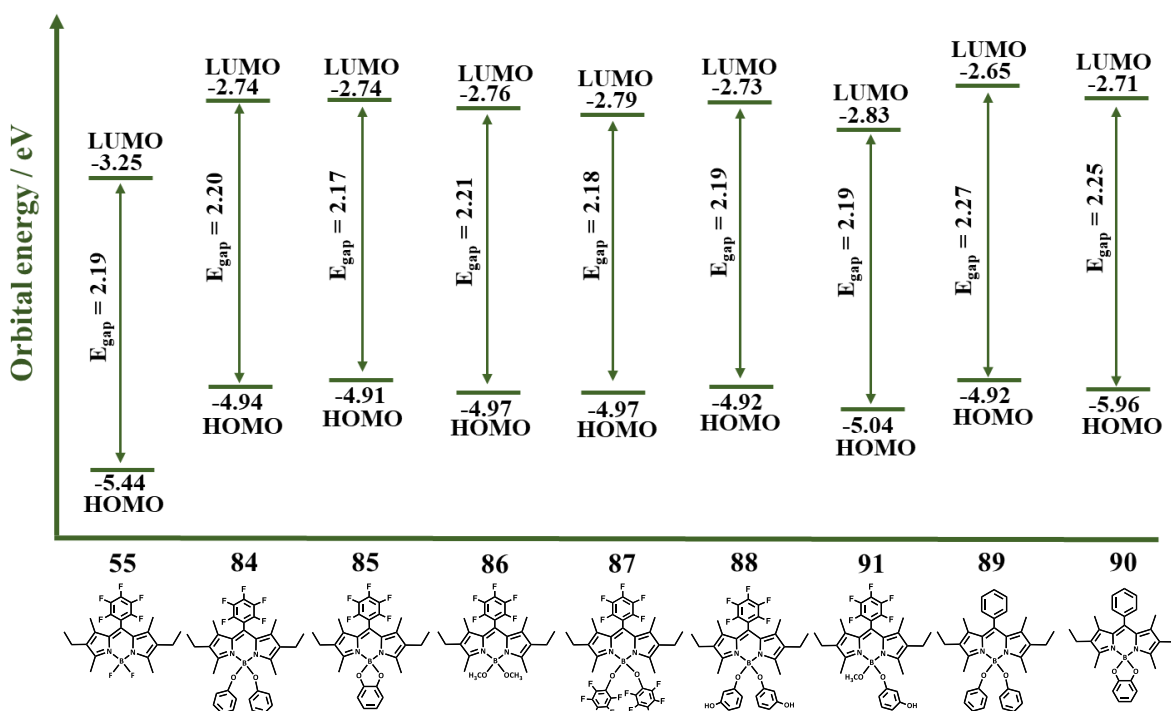
**Table 5.3.** Electrochemical properties of the **4S-BDP**.

Dyes	$E_{red}^1$ (V)	$E_{ox}^1$ (V)	$E_{ox}^2$ (V)	$E_{onset}^{ox1}$ (V)	$E_{HOMO}$ (eV) <sup>a</sup>	$E_g^{opt}$ (eV)	$E_{LUMO}$ (eV) <sup>b</sup>
<b>53</b>	-1.15	1.17	1.43	1.09	-5.28	2.28	-3.00
<b>55</b>	-0.97	1.35	1.53	1.21	-5.44	2.19	-3.25
<b>84</b>	-0.93	0.81	1.36	0.75	-4.94	2.20	-2.74
<b>85</b>	-0.85	0.81	1.40	0.72	-4.91	2.17	-2.74
<b>86</b>	-1.10	0.85	1.23	0.79	-4.97	2.21	-2.76
<b>87</b>	-0.91	0.83	1.23	0.79	-4.97	2.18	-2.79
<b>88</b>	-0.87	0.82	1.32	0.74	-4.92	2.19	-2.73
<b>89</b>	-1.20	0.83	1.15	0.74	-4.92	2.27	-2.65
<b>90</b>	-1.12	0.88	1.16	0.78	-4.96	2.25	-2.71
<b>91</b>	-0.99	0.95	1.27	0.86	-5.04	2.19	-2.83

<sup>a</sup>  $E_{HOMO} = [-(E_{onset}^{ox1} - E^{Fc/Fc+}) - 4.8]$  eV ; <sup>b</sup>  $E_{LUMO} = [E_{HOMO} + E_g^{opt}]$  eV.

Among the dyes from **4S-BDP**, there are small deviations between the pentafluorophenyl derivatives or between **89** and **90**. However it should be noted the lower shifts observed for **91**, and the reduction process of **86** at lower potentials which suggest that this structure is not so prone to stabilize a negative charge.

As Table 5.3 and Scheme 5.4 show, all the calculated HOMO and LUMO orbital energies lie above the corresponding levels of PC<sub>61</sub>BM (-3.70 eV and -6.10 eV) allowing the potential formation of type II heterojunction.

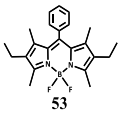
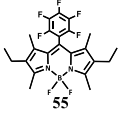
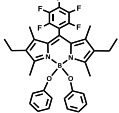
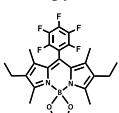
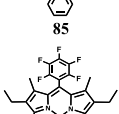
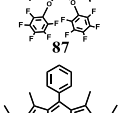
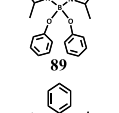
**Scheme 5.4.** HOMO and LUMO energies of BODIPY **55** and the **4S-BDP**.

### 5.3. Photovoltaic studies of the fourth series of BODIPY molecules (4S-BDP)

BODIPYs **84**, **85**, **87**, **89** and **90** were blended with PC<sub>61</sub>BM and tested in a bulk heterojunction OPVs. These were prepared as described in Chapter 2 for the OPVs based on compounds **53** and **55**. Thus, the structure of the OPV was based on: ITO/PEDOT:PSS/active layer/LiF/Al, and the BODIPY:PC<sub>61</sub>BM blends, on a weight ratio of 1:3, were spin-coated (1200-1300 rpm) from a chloroform solution.

As shown in Table 5.4, the overall efficiency of the OPVs based on the structures from the **4S-BDP** does not exceed those obtained by **53** and **55**.

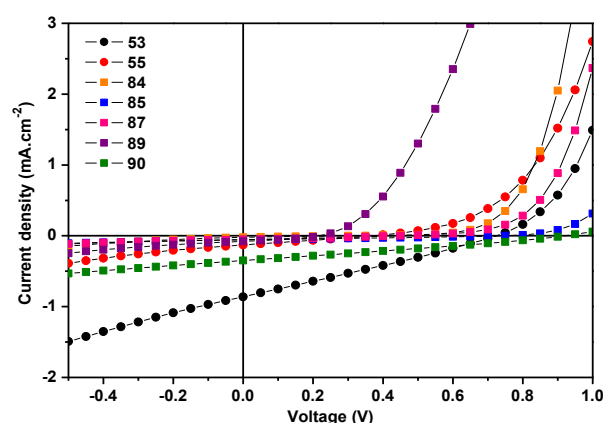
**Table 5.4.** Photovoltaic performance parameters of the BODIPY:PC<sub>61</sub>BM-based OPV cells, with the active layer prepared with a BODIPY:PC<sub>61</sub>BM weight ratio of 1:3 from a solution of chloroform at 15mg/ml, under AM 1.5G illumination at 84 mW/cm<sup>2</sup>.

Dye	Active layer thickness (nm)	Maximum						Average*			
		J <sub>sc</sub> (mA/cm <sup>2</sup> )	V <sub>oc</sub> (V)	FF	R <sub>SH</sub> (Ω.cm <sup>2</sup> )	R <sub>S</sub> (Ω.cm <sup>2</sup> )	PCE (%)	J <sub>sc</sub> (mA/cm <sup>2</sup> )	V <sub>oc</sub> (V)	FF	PCE (%)
 53	80	0.93	0.73	0.27	810	454	0.22	0.85	0.62	0.27	0.17
 55	77	0.13	0.37	0.27	2956	2321	0.02	0.11	0.37	0.27	0.01
 84	125	0.02	0.30	0.22	9429	20080	0.002	0.02	0.26	0.23	0.001
 85	118	0.06	0.75	0.28	13567	6684	0.02	0.06	0.66	0.31	0.01
 87	127	0.08	0.46	0.27	10452	6799	0.01	0.05	0.40	0.29	0.007
 89	114	0.08	0.22	0.36	4689	1087	0.01	0.07	0.21	0.35	0.006
 90	120	0.38	0.91	0.28	2542	1311	0.12	0.37	0.89	0.27	0.11

\*Average values calculated from at least 5 devices.

The exchange of ligands had a negative impact on the short-circuit current ( $J_{sc}$ ) of the cell and, consequently, caused a decrease in PCE. The variation of HOMO and LUMO energies could be an important factor for that, as well as the higher thicknesses of the active layers that may lead to higher electronic loss by charge recombination.

Noteworthy, OPVs based on the structures with catecholate revealed an impressive progression on their  $V_{oc}$ , if compared with their precursors. The OPVs based on **85** showed a raise from 0.37 volts to 0.75 volts and **90**-based OPVs a raise from 0.73 V to 0.91 V (Figure 5.13).



**Figure 5.13.** Current density-voltage characteristics of BODIPY:PC<sub>61</sub>BM-based OPVs, under AM 1.5G illumination at 84 mW.cm<sup>-2</sup>.

Since the energy levels of the molecular compounds with catecholate are roughly equivalent to those of other BODIPYs from **4S-BDP**, the improvement of the  $V_{oc}$  could be related to a better organization of the blend and better intermolecular contacts between the photoactive species within the layers.

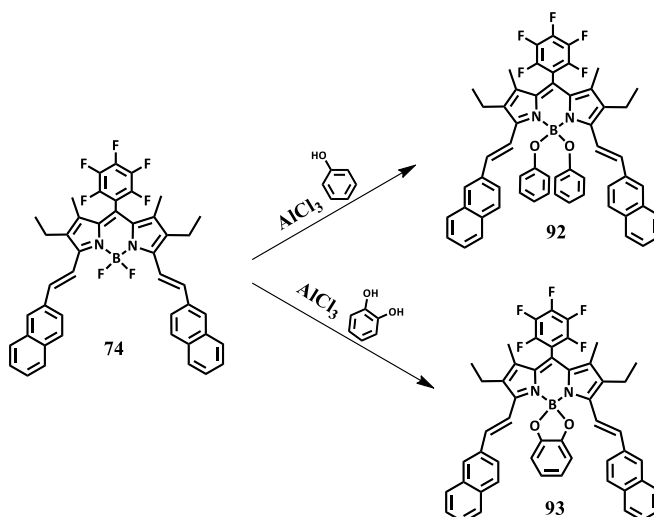
## 5.4 Functionalization of BODIPY 74

Prompted by the results obtained for the former O-BODIPYs, BODIPY **74** (presented in Chapter 4) was functionalized with a phenol and with a catechol, in order to check if the characteristic of the former BODIPYs would be reproduced in more complex structures and to evaluate the possibility of improvement of  $V_{oc}$  and PCE (1.00 V and 2.79 %).

### 5.4.1. Synthesis and structural characterisation of BODIPYs 92 and 93

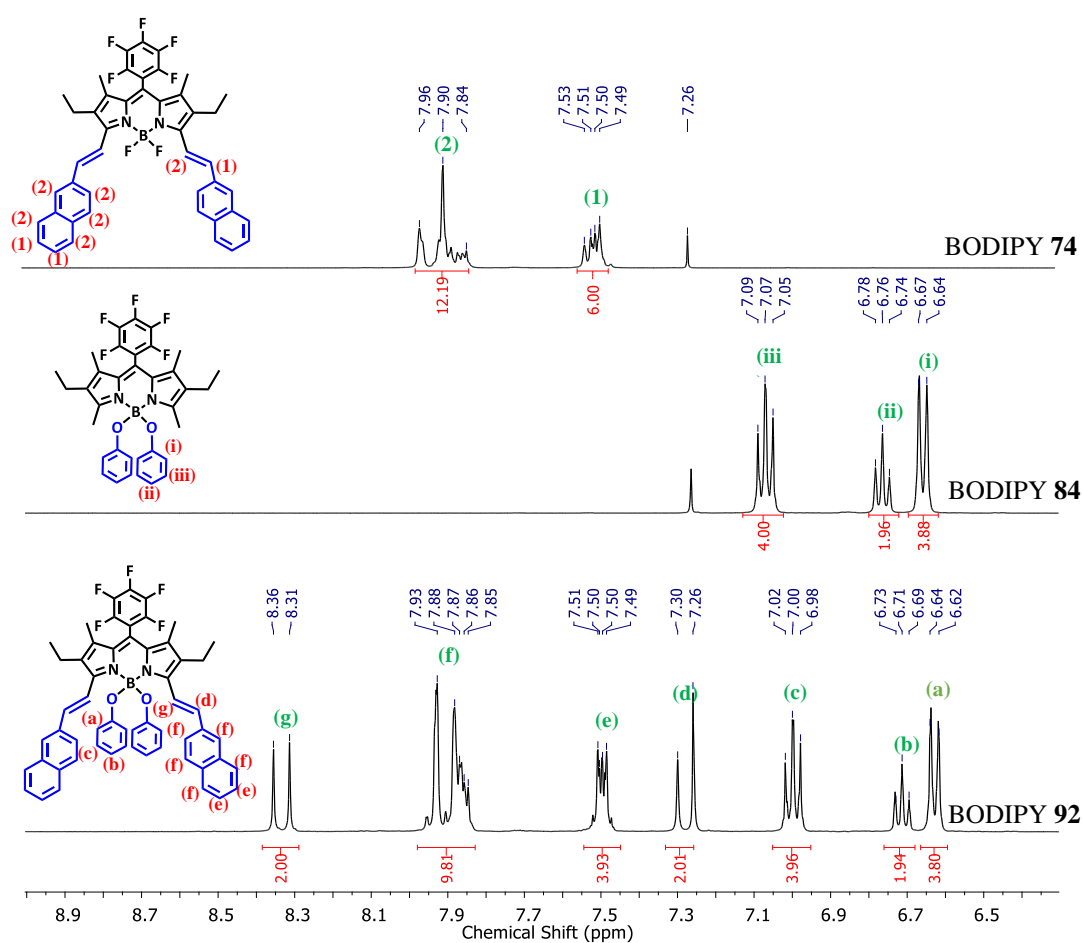
BODIPYs **92** and **93** were synthesised by refluxing a dichloromethane solution of **74** with two equivalents of AlCl<sub>3</sub>, and ten equivalents of phenol or catechol (Scheme 5.5). Yields of 59 % and 53 %, respectively, were obtained, and these new structures were confirmed by NMR and HRMS (all details in the experimental section (Chapter 8)).





**Scheme 5.5.** Synthesis of BODIPY **92** and **93**.

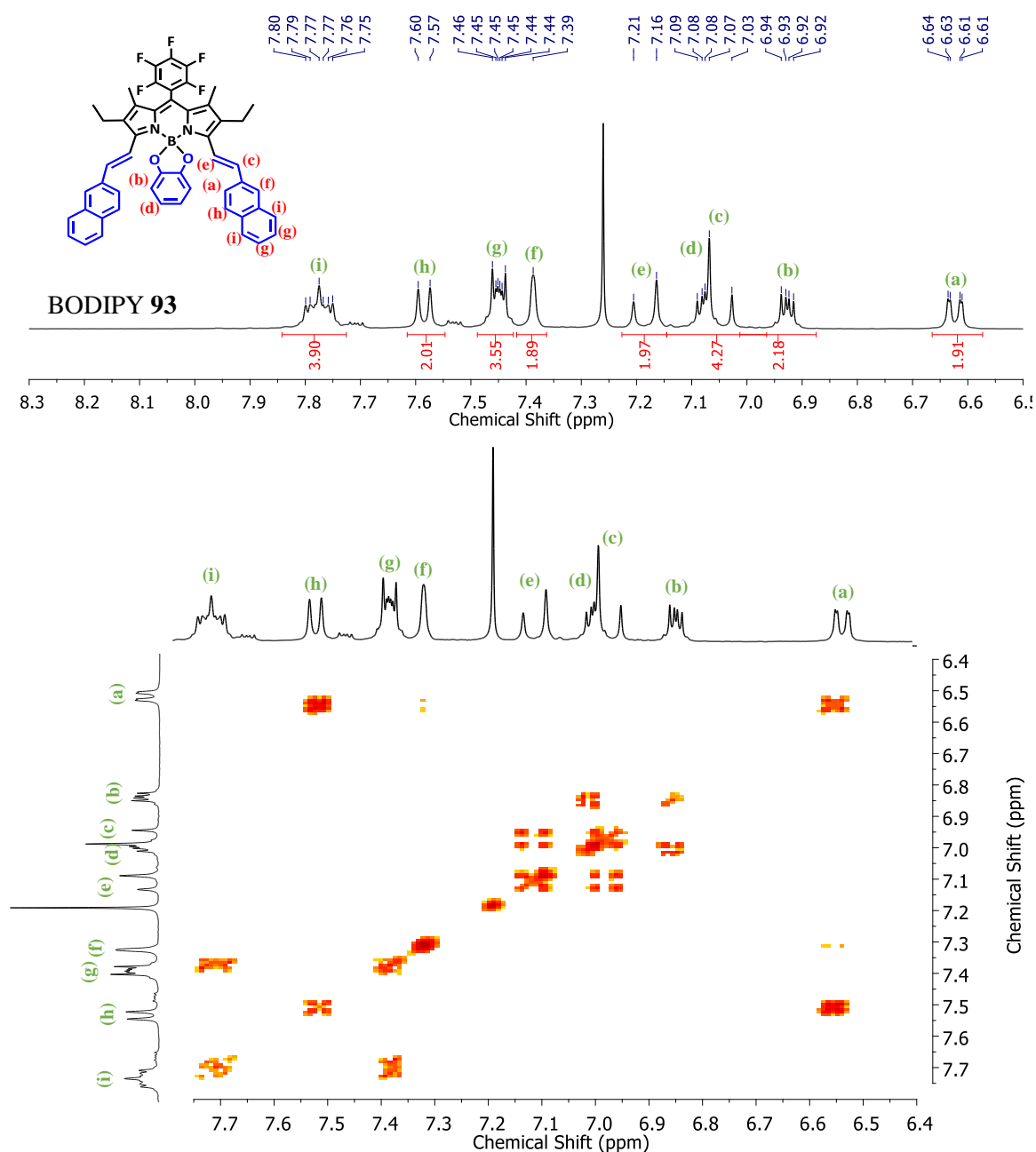
Upon analysis of the NMR spectra of BODIPY **92** and BODIPY **93** (Figure 5.14 and 5.15), it is possible to notice that some variations between themselves and between them and their precursor (**74**) are found.



**Figure 5.14.**  $^1\text{H}$  NMR spectra (400 MHz) of **74**, **84** and **92**, in  $\text{CDCl}_3$ .

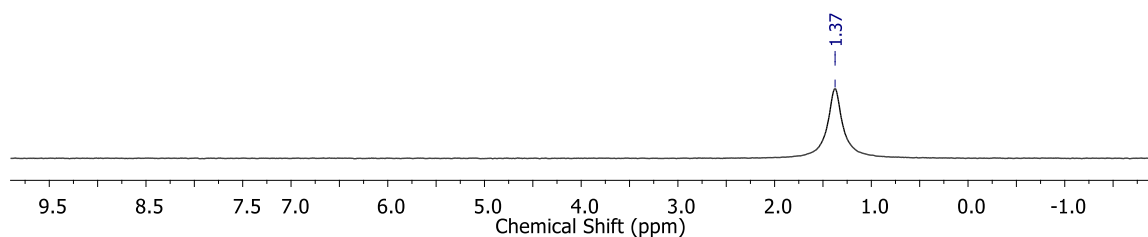
Compound **92** has a  $^1\text{H}$  NMR spectrum nearly identical to the sum of the spectra of **74** and **84**. The phenoxy ligands, that are bulkier than the fluorine atoms, induce shifts on the doublets assigned to the vicinal protons ((d) and (g)). On the other hand, the phenoxy or anthracenyl protons do not display any noteworthy variation.

The  $^1\text{H}$  NMR of **93** presents some deviations from the spectrum of **92**. The assignment of the proton signals was made after an analysis of the COSY spectrum that is also represented in Figure 5.15.



**Figure 5.15.**  $^1\text{H}$  NMR and COSY spectrum (400 MHz) of **93**, in  $\text{CDCl}_3$ .

Due to the orientation of catecholate, the vicinal protons ((c) and (e)) are more protected and, because of the vinyl groups, the protons of catecholate are now represented by two distinguished signals ((b) and (d)). The orientation of catecholate groups also increases the protection of the proton (a).

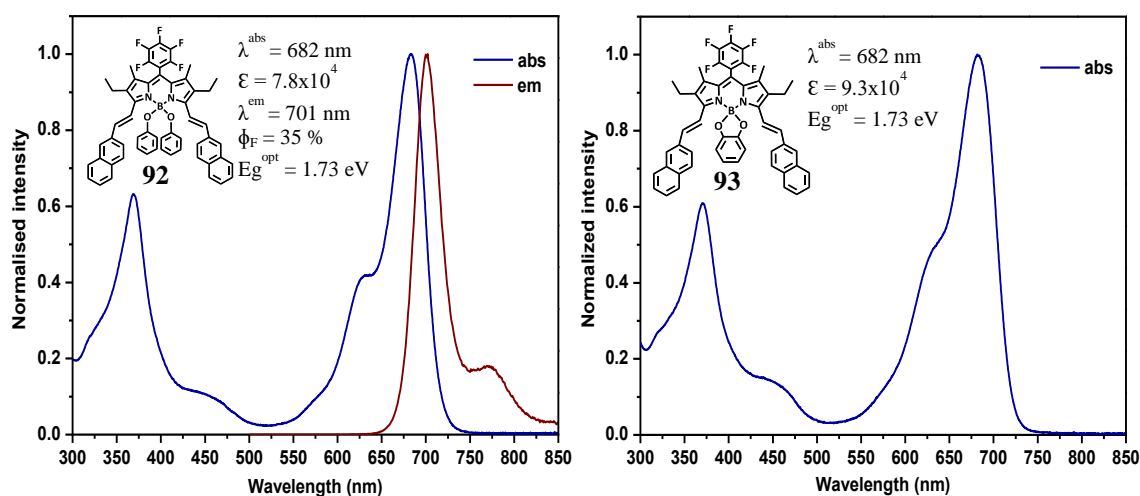


**Figure 5.16.**  $^{11}\text{B}$  NMR spectrum (128 MHz) of **93**, in  $\text{CDCl}_3$ .

The  $^{11}\text{B}$  NMR spectra (Figure 5.16) of **92** and **93** are exactly equal and the only signal is represented by a singlet (as observed for BODIPY **84**) at the same chemical shifts of the triplet signal obtained from **74**.

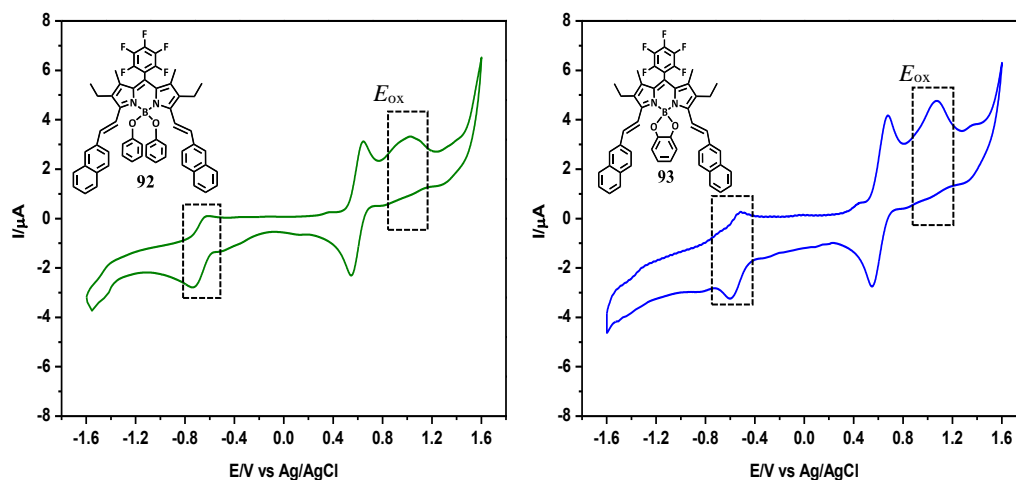
#### 5.4.2. Photophysical and electrochemical characterisation of BODIPYs **92** and **93**

As featured by the simple O-B BODIPY dyes (**85** and **90**), the fluorescence is strongly quenched when catecholate is used as ligand and the insertion of alcohol derivatives does not have any influence on the optical band gap. Therefore, the absorption characteristics (Figure 5.17) of BODIPY **74** are retained in these two new BODIPY molecules, but only compound **92** presents fluorescence.



**Figure 5.17.** Normalised absorption and emission spectra of **92** and **93** (the insets show some photophysical parameters).

The cyclic voltammograms of BODIPYs **92** and **93** are shown in Figure 5.18, and the electrochemical characteristics along with the experimental HOMO and LUMO energies of **74**, **92** and **93** are summarised in Table 5.5.



**Figure 5.18.** Cyclic voltammograms of 1 mM **92** and **93** in 0.1 M TBATFB in dichloroethane, using internal standard 1 mM Fc/Fc<sup>+</sup>, recorded at scan rate of 50 mV/s.

The cyclic voltammograms of BODIPYs **92** and **93** are similar to the voltammogram of BODIPY **74** (Chapter 4). Contrary to the others O-BODIPY dyes (**84-91**) there is not a significant difference between the oxidation potentials obtained for these two molecules (**92** and **93**) and their precursor (**74**), which is explained by the electronic delocalisation effect introduced by the vinyl naphthalene groups. As a consequence of their similar optical absorption and electrochemical properties, the HOMO and LUMO energies are very close.

**Table 5.5.** Electrochemical properties of BODIPYs **74**, **92** and **93**.

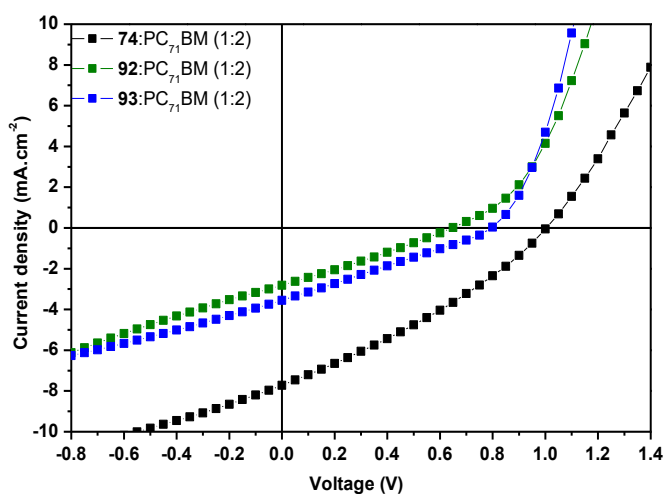
BODIPY	$E_{\text{red}}^1$ (V)	$E_{\text{ox}}^1$ (V)	$E_{\text{onset}}^{\text{ox}1}$ (V)	$E_{\text{HOMO}}$ (eV)	$E_{\text{g}}^{\text{opt}}$ (eV)	$E_{\text{LUMO}}$ (eV)
<b>74</b>	-0.59	1.03	0.89	-5.08	1.73	-3.35
<b>92</b>	-0.69	0.93	0.84	-5.03	1.73	-3.30
<b>93</b>	-0.58	0.95	0.88	-5.07	1.73	-3.34

<sup>a</sup>  $E_{\text{HOMO}} = [-(E_{\text{onset}}^{\text{ox}1} - E^{\text{Fc/Fc}^+}) - 4.8]$  eV ; <sup>b</sup>  $E_{\text{LUMO}} = [E_{\text{HOMO}} + E_{\text{g}}^{\text{opt}}]$  eV.

### 5.4.3. Photovoltaic studies of BODIPYs **92** and **93**

As described in the first part of this chapter, the use of phenoxy or catechol groups as boron-ligands has a contradictory effect on photovoltaic parameters. The phenoxy groups promoted a significant decrease of all photovoltaic performance parameters, but the BODIPY with catecholates (both **85** and **90**) led to OPVs with very high  $V_{OC}$  values. In light with these findings, BODIPYs **92** and **93** were planned to evaluate if this feature also occurs in systems with BODIPYs functionalized in the 3,5-positions and to check if it is possible to achieve even better results than those of the **74**-based OPV (PCE of 2.79 %). Thus, the OPVs based on **92** and **93** were prepared in the same way as the best system of **74**.

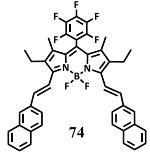
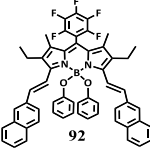
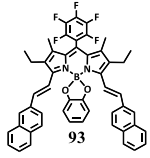
The photovoltaic parameters of the photovoltaic cells fabricated with **92** and **93** are presented in Table 5.6 and the best J-V characteristics of each system are shown in Figure 5.19. From these data, it is possible to conclude that the  $V_{OC}$  and the efficiency of the OPVs based on these two new structures are far behind those obtained for **74**:PC<sub>71</sub>BM OPVs. In view of the former results with phenoxy groups, the poorest results achieved by **92** are consistent with the expectations.



**Figure 5.19.** Current density-voltage characteristics of OPVs based on **67**: PC<sub>61</sub>BM, **67**: PC<sub>71</sub>BM, **70**: PC<sub>61</sub>BM and **70**:PC<sub>71</sub>BM, recorder under AM 1.5G illumination at 84 mW/cm<sup>2</sup>.

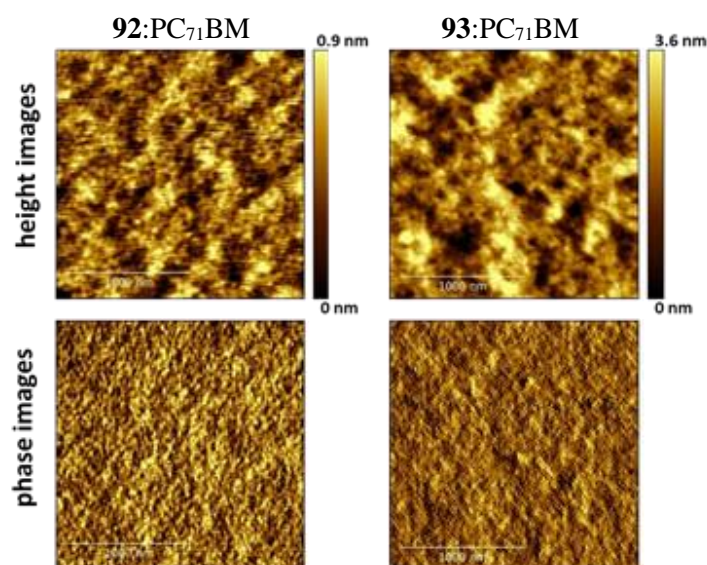
Despite the anticipated decrease of the  $J_{SC}$ , the drop of more than 0.2 V in  $V_{OC}$  and the lowering of FF of **93**-based OPV did not follow the tendency of the other BODIPYs with catecholates ligands. Since there is not a substantial difference in the molecular orbitals energy levels that justify the observed decrease of  $V_{OC}$ , and both systems used the same architecture of cell (equal work function electrode and interfacial layers), the reason for such an impact should be attributed to other  $V_{OC}$  influencing factors, such as recombination process, or details of the donor-acceptor interface.

**Table 5.6.** Photovoltaic performance parameters of the OPV cells, containing a ratio of 1:2 BODIPY to PC<sub>71</sub>BM acceptor photoactive layer prepared from a solution of chloroform at 15mg/ml, under AM 1.5G illumination at 84 mW/cm<sup>2</sup>.

Dye	Active layer thickness (nm)	Maximum				Average*			
		J <sub>sc</sub> (mA/cm <sup>2</sup> )	V <sub>oc</sub> (V)	FF	PCE (%)	J <sub>sc</sub> (mA/cm <sup>2</sup> )	V <sub>oc</sub> (V)	FF	PCE (%)
	87	7.52	1.00	0.31	2.79	7.04	0.96	0.32	2.57
	114	2.87	0.64	0.27	0.59	2.46	0.62	0.27	0.49
	108	3.55	0.79	0.27	0.90	3.21	0.79	0.27	0.82

\* Average values calculated from at least 6 devices.

When analysed by AFM (Figure 5.20), the films of **92:PC<sub>71</sub>BM** and **93:PC<sub>71</sub>BM** exhibited homogeneous surfaces with low surface roughness (0.58 nm and 0.76 nm, respectively), which is the general profile of the BODIPY:fullerene blends presented in this thesis. Although this analysis only gives information regarding the surface of the film, the lack of aggregates or grains gives a solid sign of good intermixing layer.

**Figure 5.20.** AFM height and phase images (2 $\mu$ m vs 2 $\mu$ m) of the **92:PC<sub>71</sub>BM** and **93:PC<sub>71</sub>BM** films.

## 5.5. Conclusions for Chapter 5

In this chapter, we described the synthesis and characterization of several new BODIPY molecules with different aryloxy groups bonded to boron (**4S-BDP**), and two new crystal structures were also reported.

The ligand change did not cause a disturbance on the absorption features. However, the structures with catecholate ligand showed a fluorescence quenching, attributed to a photoinduced electron transfer from the catecholate to BODIPY's core.

In general, OPVs based on the compounds from **4S-BDP** showed poor photovoltaic efficiencies. Despite the low  $J_{SC}$  and PCE, the OPVs based on BODIPY structures with catecholate groups (**85** and **90**) achieved high  $V_{OC}$ . Their  $V_{OC}$  increased by 0.38 V and 0.17 V, respectively, if compared with their precursors (**53** and **55**), reaching values of 0.75 V and 0.91 V.

Driven by the results obtained for BODIPY structures with catecholate groups, functionalizations of compound **74** (BODIPY-based OPV with the best  $V_{OC}$  and PCE) with phenol and catechol were done, and two more structures were produced (**92** and **93**). These two new structures kept the optoelectrical characteristics of their precursor (**74**). They were blended with PC<sub>71</sub>BM and tested exactly like **74**. However, both BODIPYs led to worst OPV performance results in all photovoltaic parameters. As obtained for the other O-BODIPYs, the aryloxy ligands induced a large decrease of  $J_{SC}$ , but, in this case, the BODIPY with catecholate revealed a lower  $V_{OC}$  as well.

## 5.6. References for Chapter 5

1. A. Harriman, G. Izzet, R. Ziessel, *Journal of the American Chemical Society*, **2006**, 128, 10868-10875.
2. E. Bodio, C. Goze, *Dyes and Pigments*, **2019**, 160, 700-710.
3. A. L. Nguyen, K. E. Griffin, Z. Zhou, F. R. Fronczek, K. M. Smith, M. G. H. Vicente, *New Journal of Chemistry*, **2018**, 42, 8241-8246.
4. P. Didier, G. Ulrich, Y. Mély, R. Ziessel, *Organic & Biomolecular Chemistry*, **2009**, 7, 3639-3642.
5. G. Zhang, M. Wang, F. R. Fronczek, K. M. Smith, M. G. H. Vicente, *Inorganic Chemistry*, **2018**, 57, 14493-14496.
6. A. L. Nguyen, F. R. Fronczek, K. M. Smith, M. G. H. Vicente, *Tetrahedron Letters*, **2015**, 56, 6348-6351.
7. H. Kim, A. Burghart, B. Welch, M. Reibenspies, J.; K. Burgess, *Chemical Communications*, **1999**, 1889-1890.
8. Y. Gabe, T. Ueno, Y. Urano, H. Kojima, T. Nagano, *Analytical and Bioanalytical Chemistry*, **2006**, 386, 621-626.
9. A. M. Courtis, S. A. Santos, Y. Guan, J. A. Hendricks, B. Ghosh, D. M. Szantai-Kis, S. A. Reis, J. V. Shah, R. Mazitschek, *Bioconjugate Chemistry*, **2014**, 25, 1043-1051.
10. T. Lundrigan, S. M. Crawford, T. S. Cameron, A. Thompson, *Chemical Communications*, **2012**, 48, 1003-1005.
11. C. Tahtaoui, C. Thomas, F. Rohmer, P. Klotz, G. Duportail, Y. Mély, D. Bonnet, M. Hibert, *The Journal of Organic Chemistry*, **2007**, 72, 269-272.
12. B. Brizet, C. Bernhard, Y. Volkova, Y. Rousselin; P. D. Harvey, C. Goze, F. Denat, *Organic & Biomolecular Chemistry*, **2013**, 11, 7729-7737.
13. S. Shaban, S. Swaminathan, E. Deniz, B. Captain, F. M. Raymo, *Organic Letters*, **2013**, 15, 3154-3157.
14. E. Deniz, M. Battal, J. Cusido, S. Sortino, F. M. Raymo, *Physical Chemistry Chemical Physics*, **2012**, 14, 10300-10307.
15. V. J. Richards, A. L. Gower, J. E. H. B. Smith, E. S. Davies, D. Lahaye, A. G. Slater, W. Lewis, A. J. Blake, N. R. Champness, D. L. Kays, *Chemical Communications*, **2012**, 48, 1751-1753.



## **CHAPTER 6. BODIPY-porphyrin dyads**

Tetrapyrrolic heterocycles have been the most studied pyrrolic compounds, with thousands of published reports in many fields, and, amongst all the pyrrole-based compounds, porphyrins are the most prominent.<sup>1-6</sup> The porphyrin's core offers large versatility for selective chemical derivatisation. Their stability, solubility, photophysical and electrochemical properties can be readily tuned depending on the peripheral substituents. Moreover, the extended  $\pi$ -conjugated systems of porphyrin molecules allow effective pathways to the transport of electrons.<sup>7</sup>

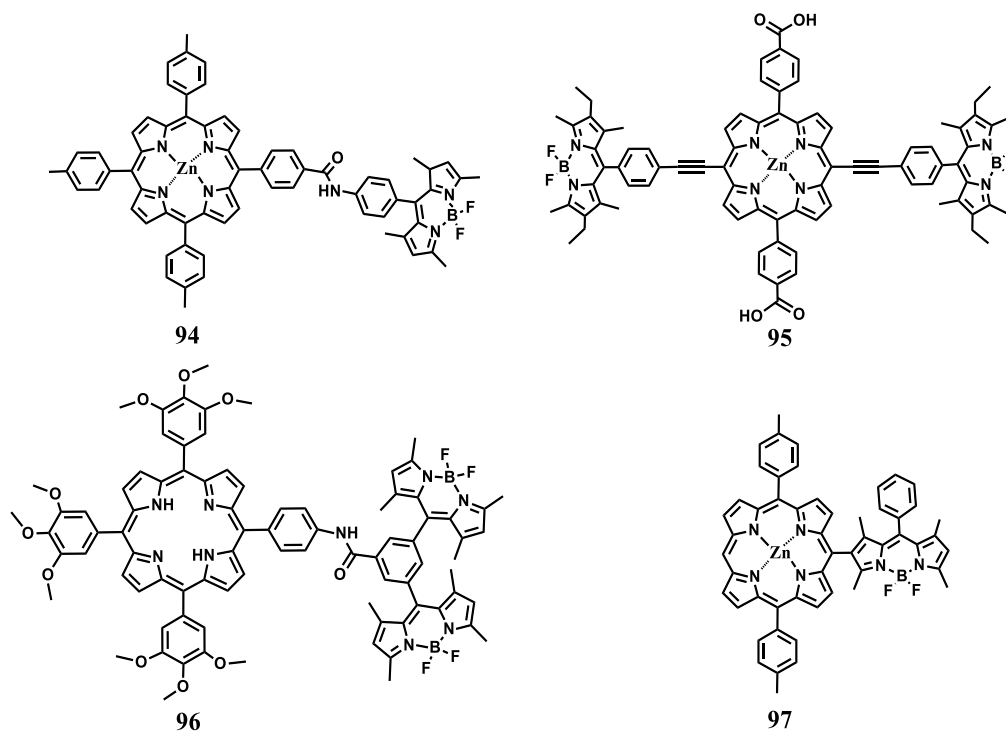
Chlorophyll (reduced porphyrin complexed with  $\text{Mg}^{2+}$ ) is a key element in the light-harvesting process of natural photosystems.<sup>8,9</sup> This biological process, ensures the critical roles of porphyrin in the conversion of light into energy and have inspired artificial light-harvesting systems like OPVs. Even though porphyrins exhibit many advantages for photovoltaic purposes, the reduced absorption in the high photon flux wavelengths (500 nm – 900 nm) is a limitation. In this way, the conjugation of porphyrins with BODIPY molecules is a very appealing combination. Among all the singular advantages, the porphyrins and BODIPY molecules have complementary light absorbing profiles. Therefore, conjugation of both molecules can increase the absorption over a broader range of visible light and improve their global light-harvesting efficiencies.

Probably due to the fact that BODIPYs' research has become more intense since the 90s, studies related to the conjugation of porphyrin (or metalloporphyrin) with BODIPY have started only twenty years ago. In 2003, Hecht *et al.*<sup>10,11</sup> linked one, two and four fluorescent BODIPY dyes with metal-free porphyrins by resorcin-4-arene linkers. Since then, various porphyrin-BODIPY conjugates have been reported to be used in different applications, such as photodynamic therapy,<sup>12</sup> light sources,<sup>13</sup> molecular electronics<sup>14</sup> and artificial photosynthetic systems (antenna systems).<sup>15</sup>

The study of the kinetic and thermodynamic aspects of energy transfer in BODIPY-porphyrin systems (dimer, trimer, tetramer, pentamer or even more complex models) has been attracting much attention. Both revision articles of Ravikanth *et al.*<sup>14</sup> and Coutsolelos *et al.*<sup>16</sup> make a righteous description of several ways to conjugate porphyrins with BODIPY compounds. Figure 6.1 shows some examples of BODIPY-porphyrin arrays presented in the literature (**94**,<sup>17</sup> **95**,<sup>18</sup> **96**,<sup>19</sup> **97**<sup>20</sup>).

The antenna reaction system consists of an energy-transfer cascade, that involves two or more fluorescent units directly attached by a spacer-group. In a dichromophoric system, one component acts as an energy donor and the other as energy acceptor. The energy-donor absorbs light and then transfers energy to the acceptor, which subsequently emits at a longer

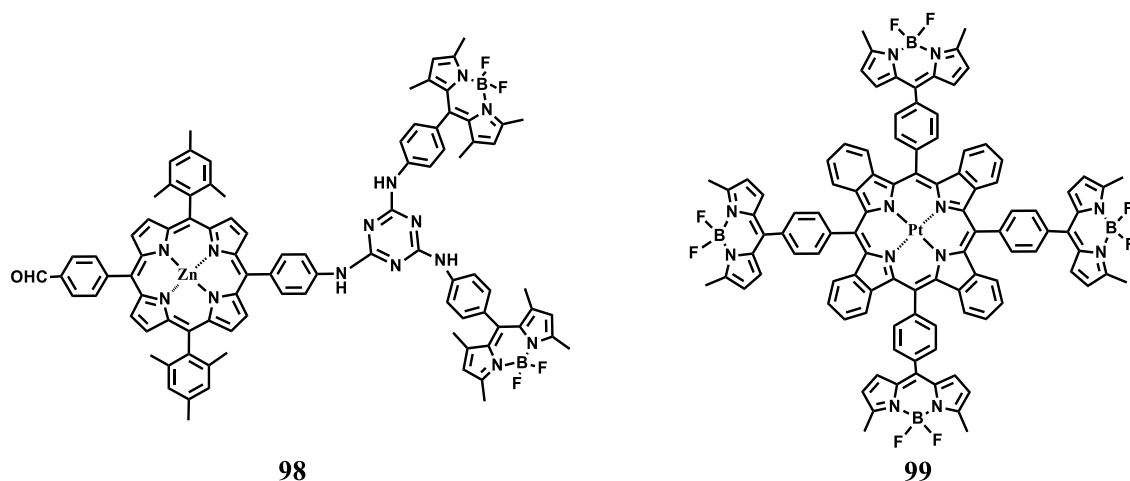
wavelength. The effectiveness of the energy-transfer process is dependent on the spectral overlap of the emission of the donor to the absorbance of the acceptor, the distance between components, the relative orientation of donor and acceptor, and the occurrence of other de-excitation modes such as nonradiative processes.<sup>21</sup>



**Figure 6.1.** Chemical structures of some BODIPY-porphyrin dyes from literature: **94**,<sup>17</sup> **95**,<sup>18</sup> **96**,<sup>19</sup> **97**.<sup>20</sup>

Among the BODIPY-porphyrin derivatives, BODIPY is generally the donor and the porphyrin the acceptor unit. This feature was proved by both steady-state and time-resolved emission studies, which demonstrated the occurrence of efficient singlet-singlet energy transfer from BODIPY to porphyrins, or metalloporphyrin, in a scale of tens of picoseconds.<sup>15, 17, 20, 22</sup>

Despite the studies of several antenna systems and some works concerning their application in DSSCs,<sup>15, 18</sup> the use of BODIPY-porphyrin arrays in OPVs is limited. In 2015, Sharma, Coutsolelos and co-workers,<sup>23</sup> developed a BODIPY-porphyrin trimer (**98**), where the single units were covalently attached via cyanuric chloride bridge. The trimer was tested in OPVs, upon blending with PC<sub>71</sub>BM, which exhibited respectable power conversion efficiencies, for a pyrrole-based OPV. Initially, the OPV system showed a power conversion efficiency of 3.48 % with short-circuit of 8.04 mA/cm<sup>2</sup>, open-circuit voltage of 0.94 V and fill factor of 0.46. Then the PCE result was improved up to 5.29 % with the addition of 4 % of pyridine to the active layer blend.



**Figure 6.2.** Structures of some BODIPY-porphyrin dyes (**98**<sup>23</sup> and **99**<sup>24</sup>) tested in OPVs.

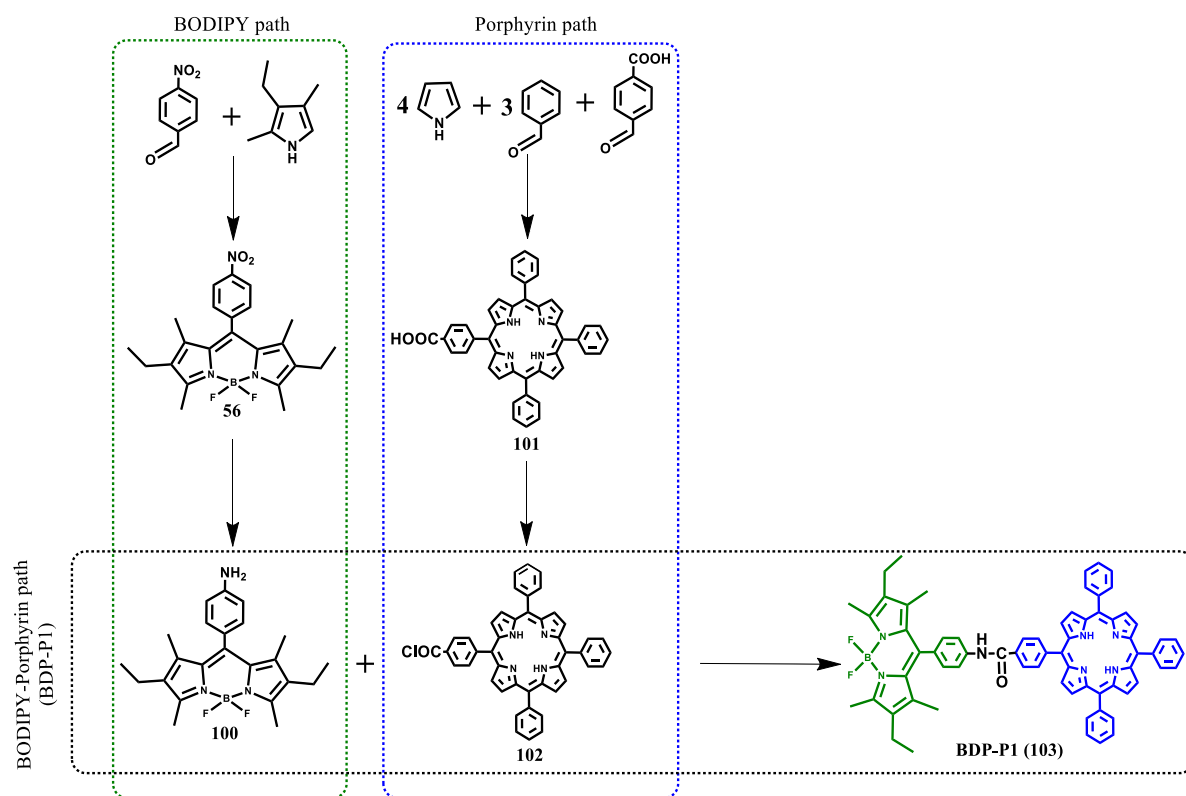
In the same year, Tompson and co-workers used a pentamer based on platinum tetrabenzoporphyrin bonded to the *meso*-position of four BODIPYs (**99**) in OPV studies.<sup>24</sup> The dye was tested in a lamellar biphasic active layer, with fullerene C<sub>60</sub> as acceptor species, and its photovoltaic response (1.42 % of PCE) overcame that of the devices based on either neat platinum porphyrin or neat BODIPY analogues.

## 6.1. Synthesis and structural characterisation of the BODIPY-porphyrin dyads

We aimed to synthesise BODIPY-porphyrin derivatives that could maximise the light absorption ability of the two chromophores and evaluate how the intramolecular energy transfer can influence the photovoltaic response. Therefore, three different BODIPY-porphyrin dyads (**BDP-P1**, **BDP-P2** and **BDP-P3**) were prepared and characterised.

### 6.1.1. Preparation of BDP-P1 (103)

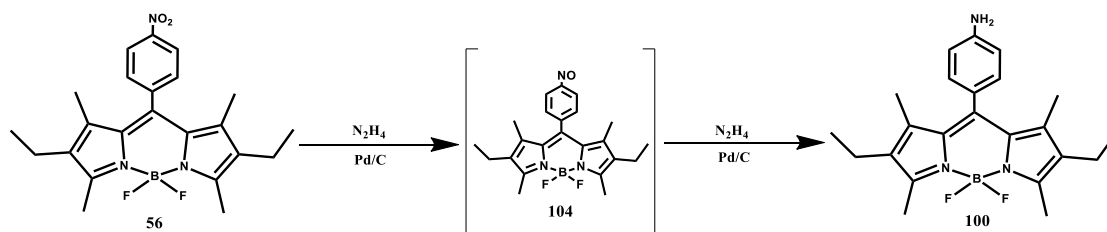
The synthesis of **BDP-P1** involved the coupling of a BODIPY, having an amino group at the *meso*-phenyl group (**100**), and a porphyrin carrying a carboxylic acid group (**101**), that was converted into acyl chloride (**102**) before the linkage. This multi-step procedure (Scheme 6.1) was inspired by the synthesis of the BODIPY-porphyrin compound presented by D'Souza and co-workers.<sup>17</sup>



**Scheme 6.1.** General steps for the preparation of **BDP-P1**.

### 6.1.1.1. Synthesis and characterisation of BODIPY 100

**BODIPY 100** was obtained through reduction of **56** (Scheme 6.2), using the procedure reported by Zhang and co-workers.<sup>25</sup> Despite the existence of other methods for the reduction of aromatic nitro derivatives to anilines, this approach proved to be quite efficient and smooth. The reduction reaction using tin chloride was also tested but being carried out under strongly acidic conditions severely decreases the final yield.

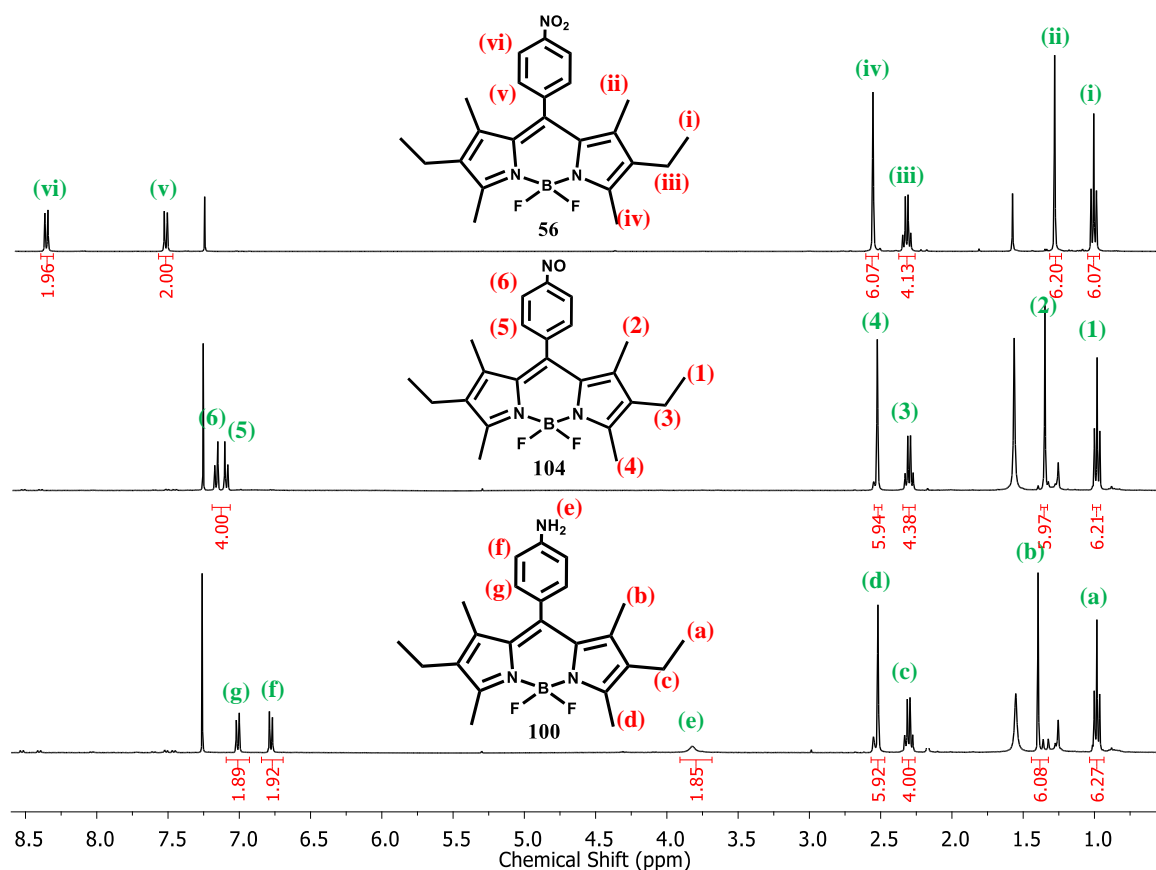


**Scheme 6.2.** Synthesis of **BODIPY 100**.

The progress of the synthesis was controlled by TLC. After 6 hours, the reaction stops evolving, resulting in a yield of 50 %. As proposed by Rozas and co-workers,<sup>26</sup> the first step of the reaction involves the formation of a nitroso intermediate (**104**) and the release of diazene and water. Then a second hydrazine molecule reacts with the nitroso derivative

to yield the BODIPY **100**. This premise agrees with the control that was being done and with the characterisation of the isolated products.

Compound **100** was characterised by NMR (Figure 6.3), and its purity was checked by HPLC-MS. The nitroso intermediate (**104**) was also characterised via  $^1\text{H}$  NMR,  $^{19}\text{F}$  NMR and confirmed by HRMS (found peak at 410.2210 m/z vs theoretical peak at 410.2215 m/z).

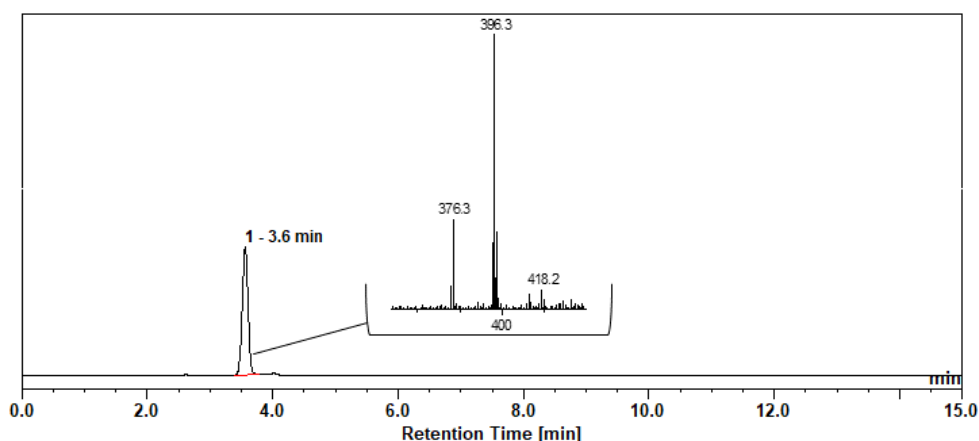


**Figure 6.3.**  $^1\text{H}$  NMR spectra (400MHz) of **56**, **104** and **100** in  $\text{CDCl}_3$ .

The main differences between **56**, **104** and **100**  $^1\text{H}$  NMR spectra are in the *ortho* and *meta* protons of the *meso*-substituted groups. Through the reduction of the nitro group to nitroso and then to amine, the acceptor character of the group is decreasing, and consequently, a movement to lower chemical shifts is observed.

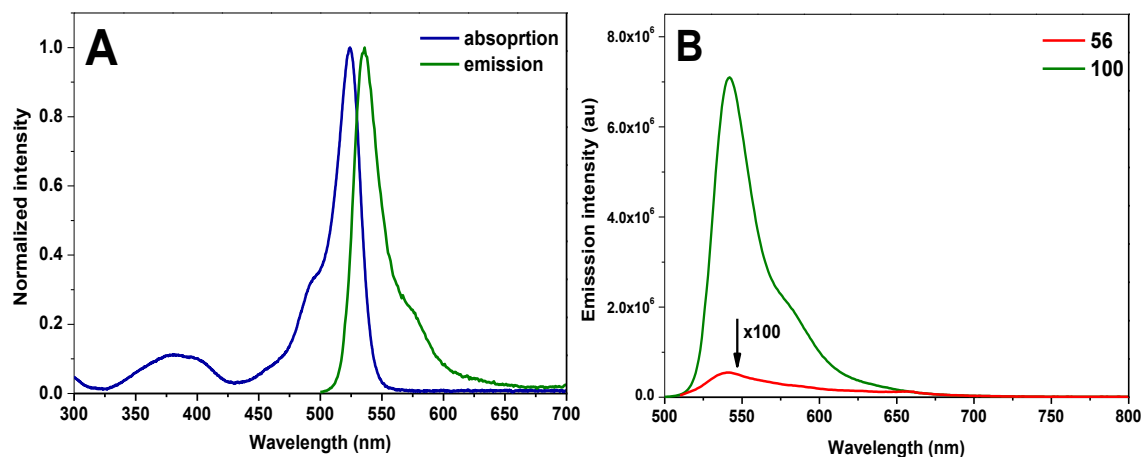
The  $^{19}\text{F}$  NMR spectra of the three BODIPY dyes is the same, with a signal (quartet) at the same chemical shift (145.7 ppm) with the same coupling constant (32.71 Hz).

The HPLC-MS (Figure 6.4) analysis confirmed that **100** was well isolated since only one peak at 3.6 min was obtained. The mass spectrum of the peak shows two intense signals corresponding to the molecular ion  $[\text{M} + \text{H}]^+$  at 396.3 m/z, and the ion resulting from the neutral loss of HF ( $[\text{M} + \text{H} - \text{HF}]^+$ ) at 376.3 m/z.



**Figure 6.4.** HPLC chromatogram obtained at 30 °C with acetonitrile: H<sub>2</sub>O (8:2) as isocratic eluent with a volume of injection of 10 μL and a flow rate of 0.8 ml/min, in a C18 RP column and a segment of the mass spectrum showing the [M + H]<sup>+</sup> and [M + H – HF]<sup>+</sup> ion peaks.

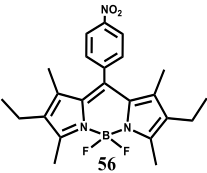
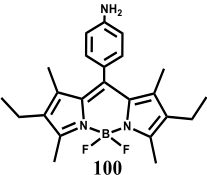
The absorption and emission spectra of **100** resemble that of **56**, as shown in Figure 6.5. Nevertheless, with the reduction (**56** to **100**), the absorption bands undergo a slight blue-shift (Table 6.1) and the Stokes shift increases. From Figure 6.5 (B) and Table 6.1, it is possible to notice that the main dissimilarity between the two dyes lies in the emission spectra since the NH<sub>2</sub> group induces a significant increase in the fluorescence quantum yield, Figure 6.5 (B).



**Figure 6.5.** (A) Normalised absorption and emission spectra of **100** in chloroform solution; (B) comparison of emission spectra of **56** and **100** in chloroform.

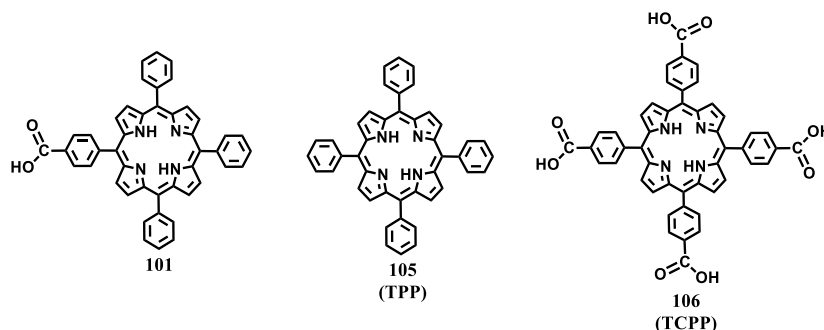
BODIPY **100** reveals an emission dependence on the polarity of the solvents. When measured in a chloroform solution, strong fluorescence is observed, but in acetonitrile, the fluorescence is quenched. This feature is related to a reductive photoinduced electron transfer process, previously reported for similar *p*-aminophenyl BODIPY derivatives.<sup>28, 29</sup>

**Table 6.1.** Photophysical properties of **56** and **100**.

Dye	Solvent	$\lambda^{\text{abs}}$ (nm)	$\epsilon$ ( $\text{cm}^{-1} \text{M}^{-1}$ )	$\lambda^{\text{em}}$ (nm)	$\Phi_{\text{F}}$	SS ( $\text{cm}^{-1}$ )	$E_{\text{g}}^{\text{opt}}$ (eV)
 56	acetonitrile	526	$7.8 \times 10^4$	534; 650	0.4%	285	2.27
	chloroform	530	$6.2 \times 10^4$	539	0.6%	315	2.25
 100	acetonitrile	519	$7.9 \times 10^4$	536	5.3%	611	2.29
	chloroform	527	$5.3 \times 10^4$	541	85%	491	2.26

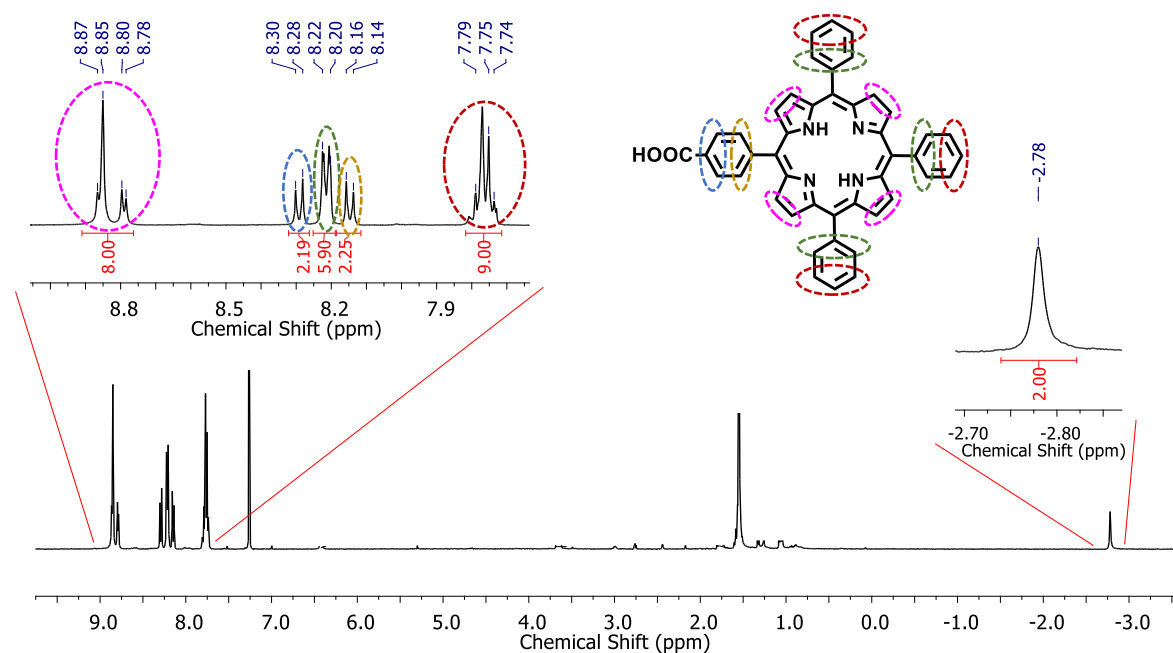
### 6.1.1.2. Synthesis and characterisation of compound **101**

Compound **101** was prepared through the condensation of pyrrole with benzaldehyde and 4-carboxybenzaldehyde in the presence of propionic acid and acetic anhydride. Despite the possibility of synthesis of the *meso*-dicarboxyphenyl and *meso*-tricarboxyphenyl porphyrins, only the porphyrins **101**, **105** (usually known as **TPP**) and **106** (usually known as **TCPP**) were isolated (Figure 6.6).

**Figure 6.6.** Structures of compound **101**, **105** (**TPP**) and **106** (**TCPP**).

The  $^1\text{H}$  NMR spectrum of **101** (Figure 6.7) shows the NH proton signals at negative chemical shifts (-2.78 ppm), which is characteristic for porphyrin molecules, due to the electric current around the macrocycles that makes the inner -NH hydrogens strongly protected. Regarding the  $\beta$ -pyrrolic and *meso*-phenyl hydrogens, the spectrum shows a multiplet corresponding to the six *meta*-hydrogens and three *para*-hydrogens (red circle). Between 7.60 and 8.80 ppm, the following signals are three doublets corresponding to the *ortho* and *meta*-hydrogens from the 4-carboxyphenyl group respectively, and the six *ortho*-hydrogens from the phenyl groups. The signal of the eight  $\beta$ -pyrrolic hydrogens is divided into two signals between 8.75 ppm and 9.00 ppm.

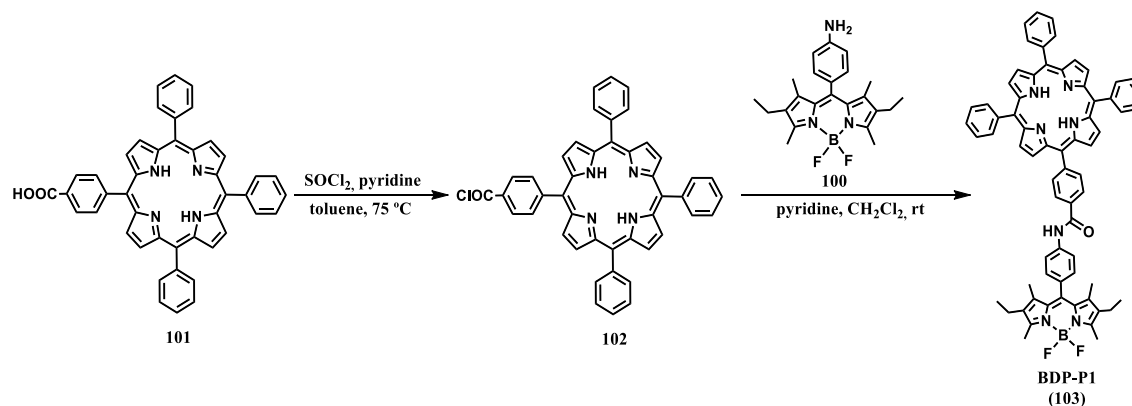




**Figure 6.7.**  $^1\text{H}$  NMR spectrum (400 MHz) of **101** in  $\text{CDCl}_3$  and the enlargement of the 7-9 ppm region.

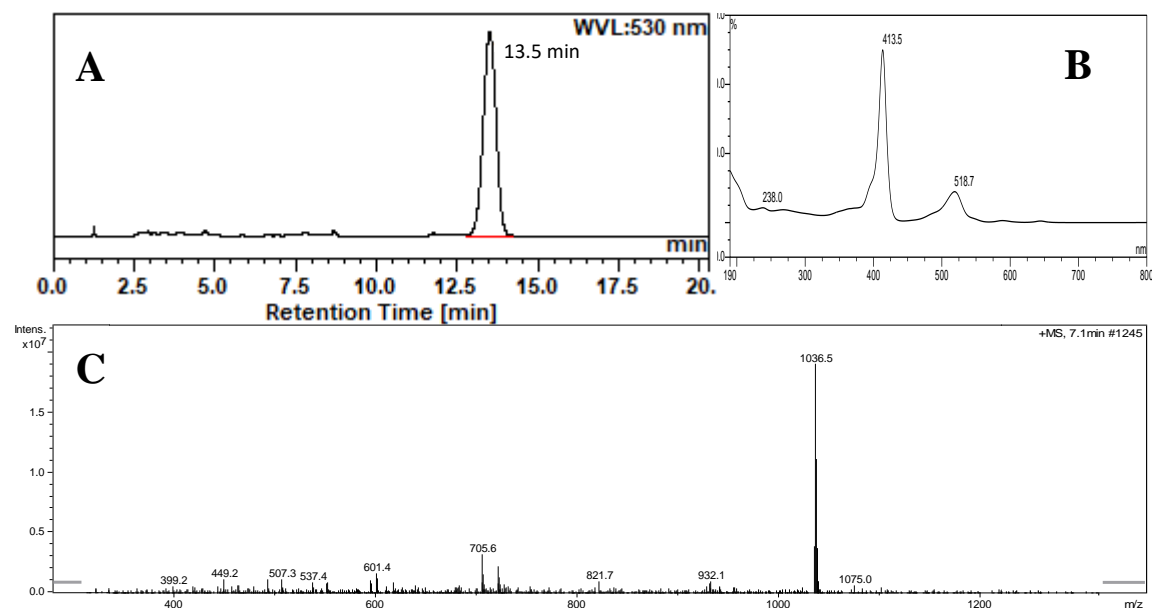
### 6.1.1.3. Synthesis and structural characterisation of BDP-P1 (103)

As shown in Scheme 6.3, **BDP-P1** was produced in a two steps reaction, where firstly, to increase the reactivity of porphyrin component, compound **101** was converted into **102** (conversion of the carboxylic acid into acyl chloride) by treatment with thionyl chloride, in THF solution, at  $75^\circ\text{C}$  in the presence of pyridine. After 1 hour all **101** had reacted and the solvent was evaporated. Then, the resulting dark green compound was redissolved in dry dichloromethane, and pyridine and **100** were added. The reaction mixture was allowed to stir at room temperature for 18 hours. The reaction of the acyl chloride porphyrin with the amino group of the BODIPY originated the **BDP-P1** (**103**) with 18 % of yield. **BDP-P1** was characterised by HPLC-MS, HRMS,  $^1\text{H}$  NMR,  $^{19}\text{F}$  NMR, which are all described in the experimental section (Chapter 8).



**Scheme 6.3.** Synthesis of **BDP-P1** (**103**).

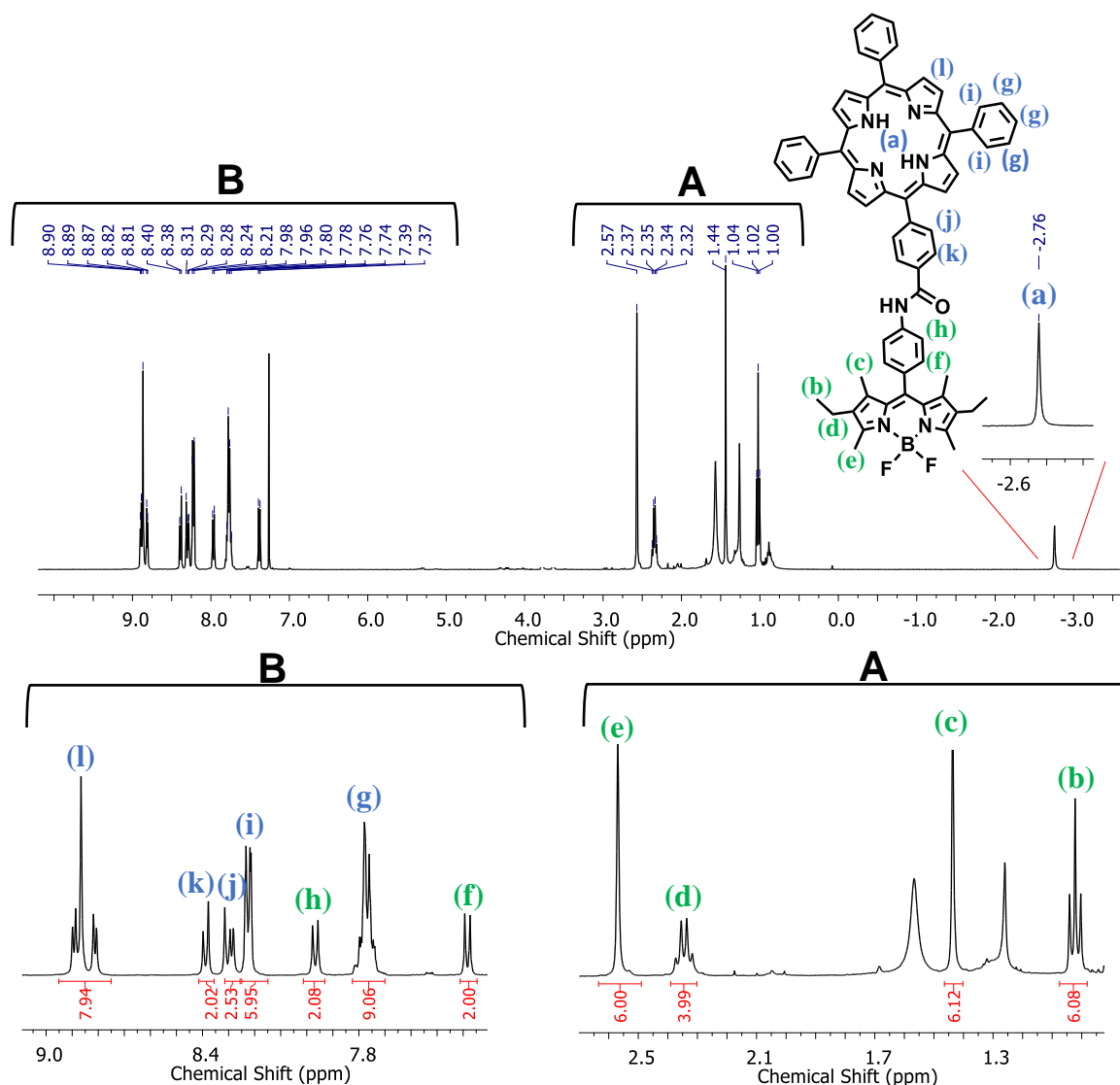
After the chromatographic purification, the isolated **BDP-P1** was analysed by HPLC-MS. As shown in Figure 6.8, the chromatogram of the sample presents a prominent peak at 13.5 min. The spectral data obtained by the diode-array detector shows the Soret band (the most characteristic band of porphyrins), at 413.5 nm, and the main band of BODIPY, at 518.7 nm. Using mass spectrometry, it was possible to detect a peak showing the expected mass of the molecular ion  $[M + H]^+$ , at 1036.5 m/z.



**Figure 6.8.** (A) HPLC chromatogram of **BDP-P1**, obtained at 30 °C with acetonitrile: H<sub>2</sub>O (9:1) as isocratic eluent with a volume of injection of 10 μL and a flow rate of 0.8 ml/min, in a C18 RP column; (B) Diode-array spectrum of the peak at 13.5 min; (C) Mass spectrum of the peak at 13.5 min.

All signals from the <sup>1</sup>H NMR spectrum of **BDP-P1** are presented and identified in Figure 6.8. Apart from the *ortho* and *meta*-hydrogens of BODIPY fraction ((f) and (h)) which moved to higher chemical shifts, the spectrum of **BDP-P1** presents tiny differences from the spectra of the individual moieties (**100** and **101**) presented in the Figures 6.3 and 6.7.

The <sup>19</sup>F NMR spectrum (experimental section (Chapter 8)) presents the usual quartet signal at -145.74 ppm referring to BODIPY's boron-fluorine coupling.



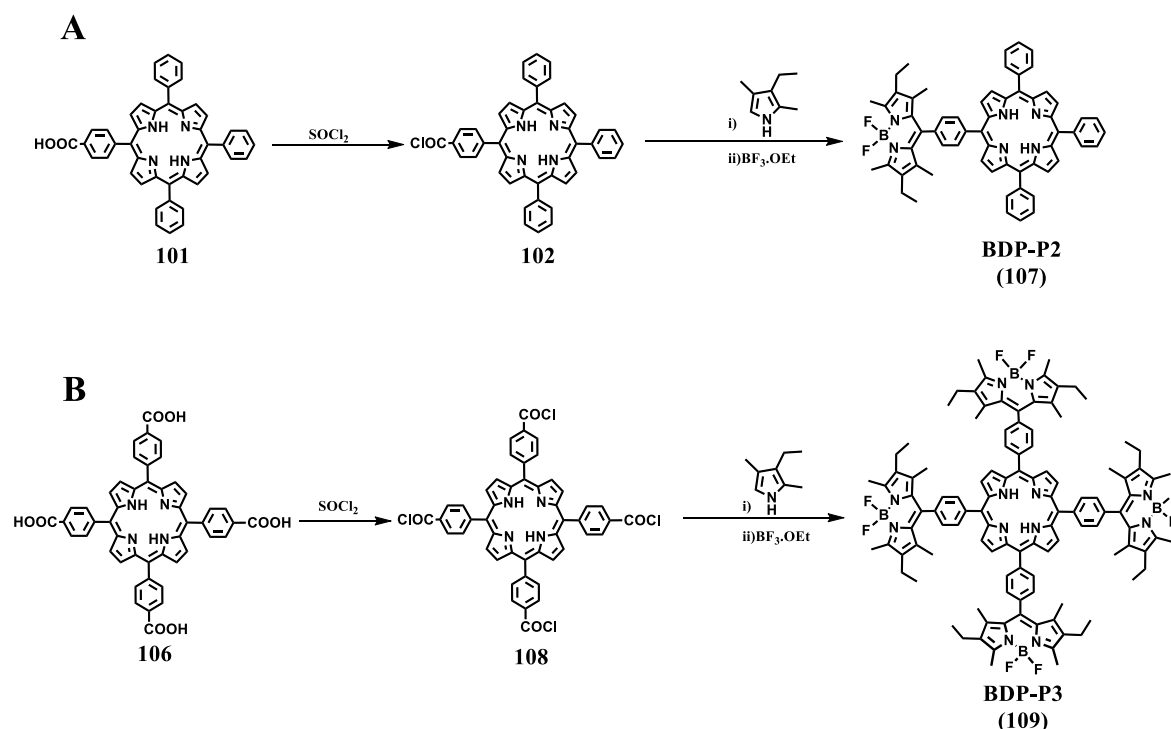
**Figure 6.9.** <sup>1</sup>H NMR (400 MHz) spectrum of **BDP-P1** in CDCl<sub>3</sub>, expansions (A and B).

### 6.1.2. Synthesis and structural characterisation of BDP-P2 (107) and BDP-P3 (109)

In general, BODIPY-porphyrin derivatives result from the connection of BODIPY dye(s) with porphyrin(s) moieties, individually prepared. However, there are a few examples of BODIPY-porphyrin conjugates using one of the compounds as starting material.<sup>25, 15, 30, 31</sup>

The use of a fragment of BODIPY or porphyrin to synthesise the other chromophore reduces the number of reaction steps. Moreover, the resulting dyads may have the BODIPY and porphyrin counterparts closer, and the electronic conjugation improved.<sup>30, 31</sup> To the best of our knowledge, all the published works that report this approach are based on the same principle: preparation of a structure with a formyl group, and then the condensation with pyrroles.

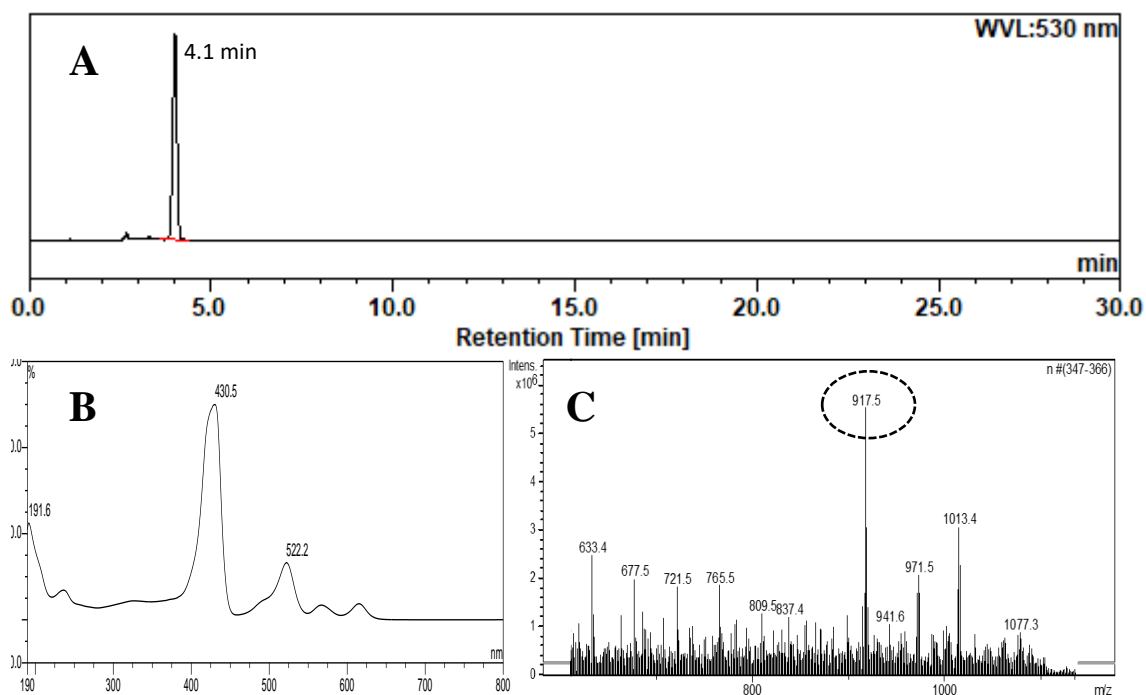
As shown in Scheme 6.4, we developed a different method to prepare two new structures: a dimer (**BDP-P2**) and a pentamer (**BDP-P3**). In this new approach, the formed *p*-acyl-phenyl-porphyrin (**102** or **108**) reacts with the  $\alpha$ -free pyrrole originating a dipyrromethene, which is complexed by boron trifluoride diethyl etherate, originating the dyads. After completion of the synthesis of both compounds, the reaction mixture was neutralised with carbonate solution and deionised water, to avoid the porphyrin dication contamination.



**Scheme 6.4.** Synthesis of **BDP-P2** (A) and **BDP-P3** (B).

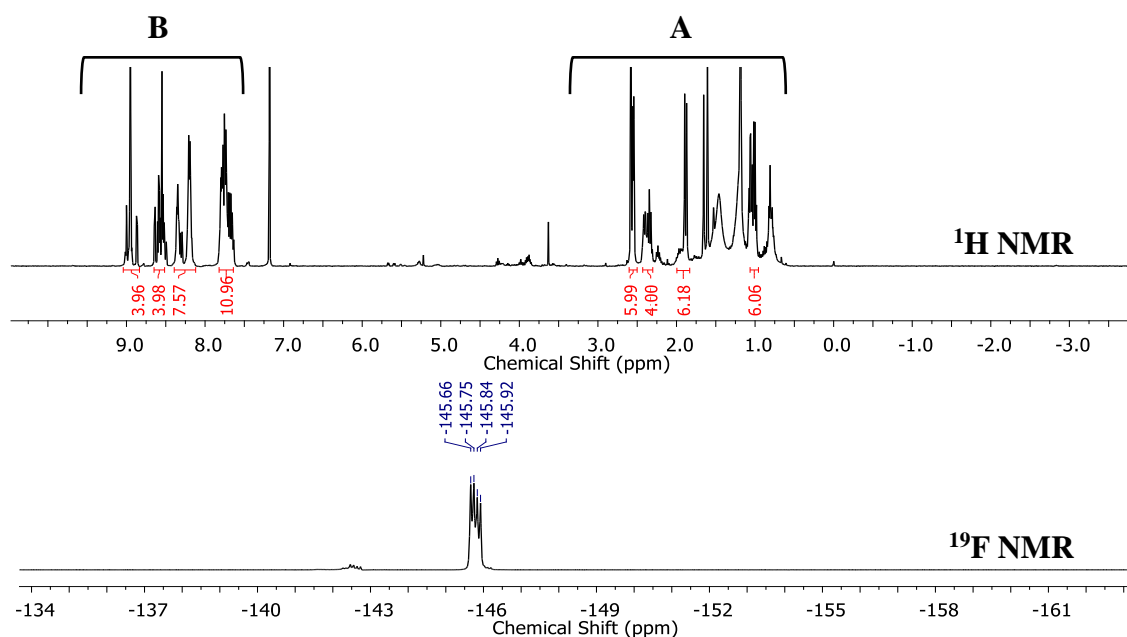
Through HPLC-DAD-MS (Figure 6.10), it was possible to identify a single peak assigned to BODIPY-porphyrin dimer (**BDP-P2**). The detected absorption profile is representative of this kind of dimers (main bands of both chromophores), and a mass of a molecular ion consistent with the mass of the positively charged structure  $[M + H]^+$  was detected in mass spectrometry. Later, the HRMS (shown in the experimental chapter (Chapter 8)) confirmed the peak of the molecular ion  $[M + H]^+$  of **BDP-P2** at 917.4306  $m/z$ , which is in agreement with the calculated mass (917.4314  $m/z$ ).

Porphyrins usually present low distortions in their macrocycle, which contributes to the appearance of the -NH hydrogen's NMR signals at negative chemical shifts. However, some tetrapyrrolic compounds present a significant shift (to less negative chemical shifts) in the -NH signal due to a high structural asymmetry and distortion.<sup>32-34</sup>



**Figure 6.10.** (A) HPLC chromatogram of **BDP-P2** obtained at 30 °C with acetonitrile asc eluent with a volume of injection of 10  $\mu$ L and a flow rate of 0.8 ml/min, in a C18 RP column; (B) Spectrum obtained by Diode-array peak; (C) Mass spectrum related to the HPLC peak.

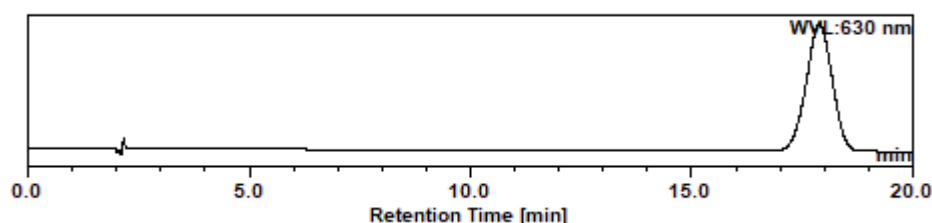
The absorption spectrum of **BDP-P2** obtained by HPLC-DAD shows a broadening of the Soret band (430 nm), that could arise from a distortion in the porphyrin core, a hypothesis that is supported by the non-appearance of the -NH signal at negative chemical shifts in the  $^1\text{H}$  NMR spectrum (Figure 6.11).



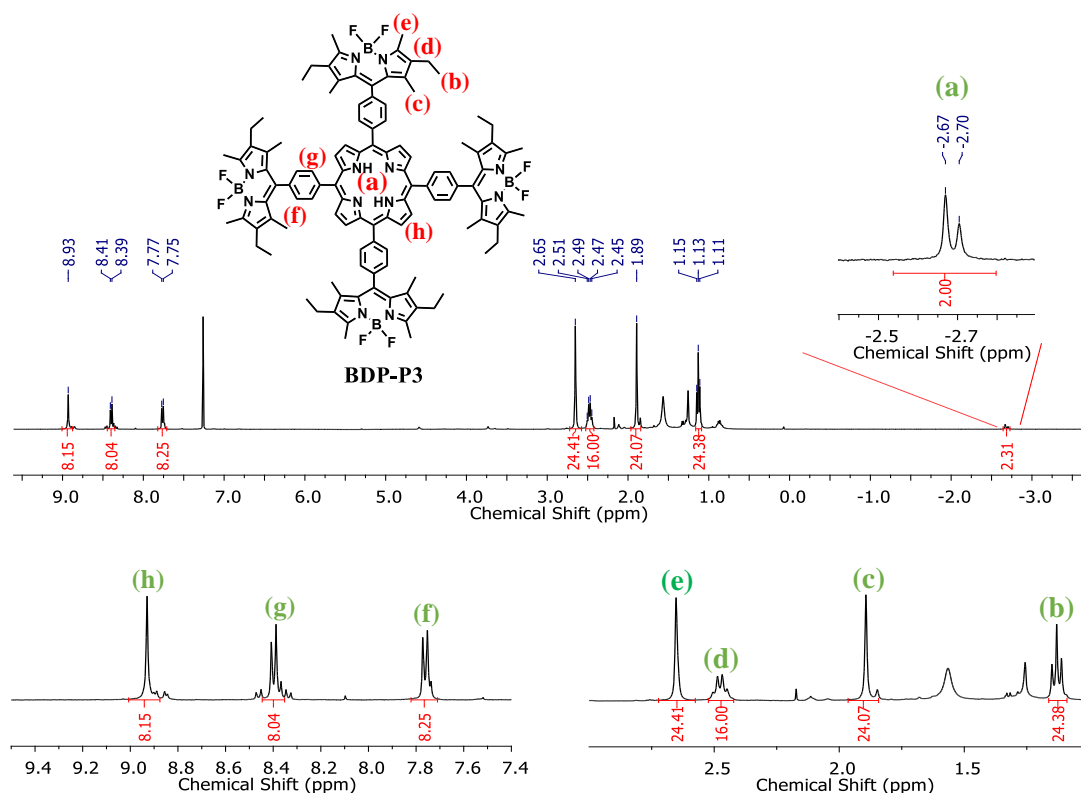
**Figure 6.11.**  $^1\text{H}$  NMR (400 MHz) with the identification of the BODIPY proton signals region (A) and phenyl and porphyrin proton signals region (B);  $^{19}\text{F}$  NMR (376 MHz) spectra of **BDP-P2**.

Despite the low definition of the spectrum, it was possible to identify the peaks assigned to BODIPY's hydrogens (A) and the signals associated with the hydrogens from the  $\beta$ -pyrrolic position of porphyrin and *meso*-phenyl groups (B). The  $^{19}\text{F}$  NMR spectrum only shows the quartet signal at -145.79 ppm, as observed for other BODIPY dyes from **1S-BDP**.

The **BDP-P3** synthesis proceeded as expected and none of any possible dimer, trimer or tetramer compounds, resulting from the incomplete reaction, were found. The HPLC chromatogram of **BDP-P3** (Figure 6.12), reveals a broad peak at higher retention times (17.9 min), but it was not possible to detect the exact mass of the protonated molecular ion (1839.95 m/z). Nevertheless, the  $^1\text{H}$  NMR and  $^{19}\text{F}$  NMR spectra, presented in Figure 6.13 and 6.14, provide solid evidence of **BDP-P3**'s structure.

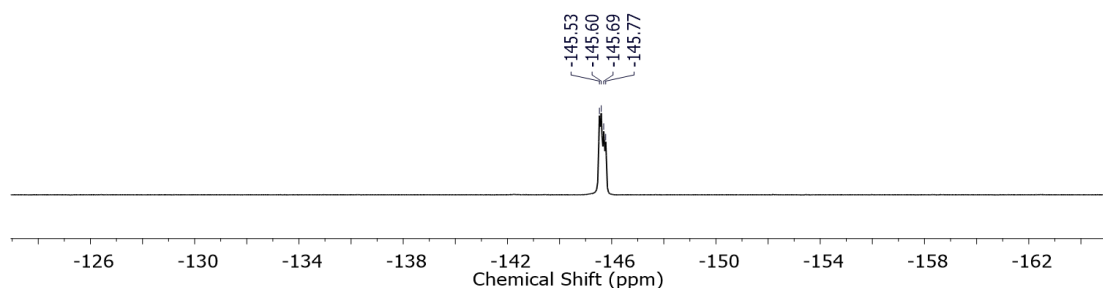


**Figure 6.12.** HPLC chromatogram of **BDP-P3**, obtained at 30 °C with acetonitrile as eluent, and a flow rate of 0.8 cm<sup>3</sup>/min, in a C18 RP column.



**Figure 6.13.**  $^1\text{H}$  NMR (400 MHz) spectrum of **BDP-P3** in  $\text{CDCl}_3$  and corresponding expansions.

In the  $^1\text{H}$  NMR spectrum, the signals of -NH protons,  $\beta$ -pyrrolic and phenyl protons confirm the structure of **BDP-P3**. The spectrum reveals a change in the -NH protons signal similar to some bacteriochlorins presented in the literature.<sup>33,35</sup> This change of profile indicates lower flatness of the tetrapyrrolic ring compared with ordinary porphyrins. The  $\beta$ -pyrrolic protons (h) are represented as a singlet at 8.93 ppm, and the protons of the phenyl moieties (g and f) are both characterised as doublets at 7.76 ppm and 8.39 ppm. The signals associated with BODIPY fraction are in line with the BODIPY **58** (structure without *meso*-substituted group) which is an indication of lower magnetic protection of the phenyl ring, probably related to a less perpendicular orientation to BODIPY's core.



**Figure 6.14.**  $^{19}\text{F}$  NMR (376 MHz) spectra of **BDP-P3**, in  $\text{CDCl}_3$ .

The  $^{19}\text{F}$  NMR spectrum shows the signal assigned to the fluorine atoms coupled to boron at 145 ppm, which is at the same chemical shifts as observed for the **BDP-P2** and the BODIPY molecules from **1S-BDP**.

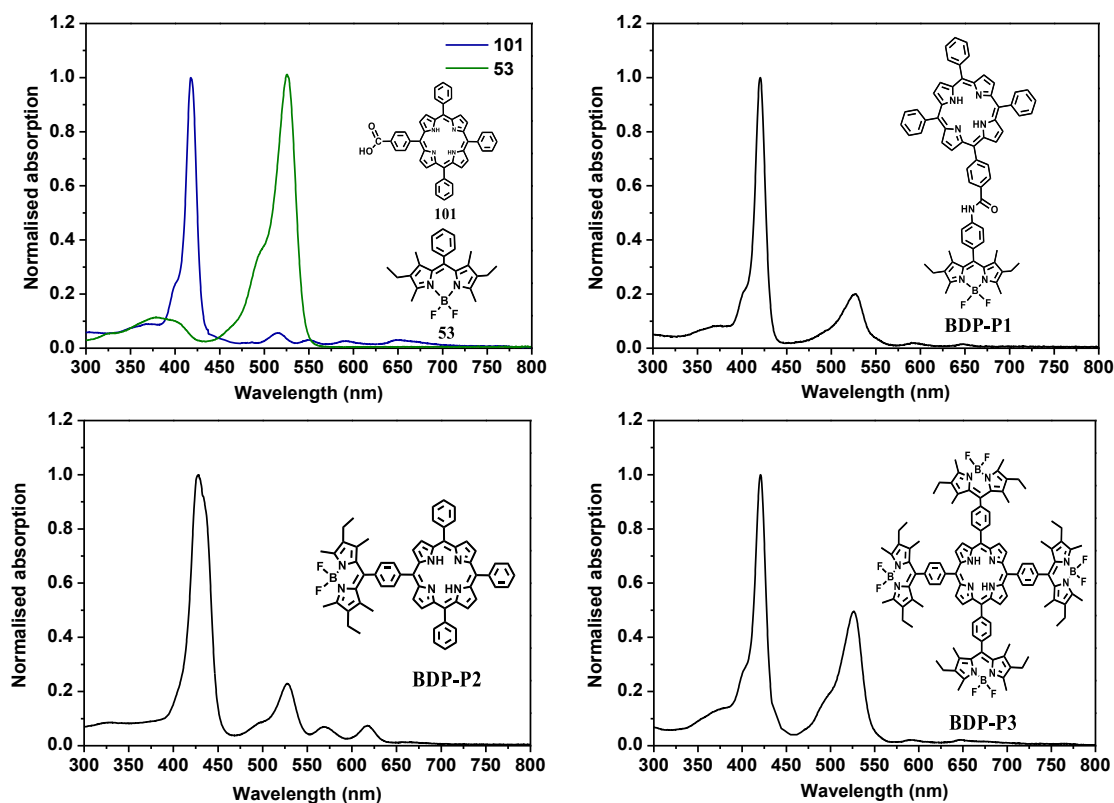
## 6.2. Photophysical characterisation of BDP-P1, BDP-P2 and BDP-P3

The absorption spectra of **53**, **101**, **BDP-P1 (103)**, **BDP-P2 (107)** and **BDP-P3 (109)** are presented in Figure 6.15 and their photophysical data are summarised in Table 6.2.

The absorption spectrum of **101** exhibits an intense band at 420 nm (Soret band), and four less intense bands (Q bands) in the 500-650 nm spectral region. The Soret band is due to the eighteen  $\pi$ -electron delocalisation through the tetrapyrrolic macrocyclic. The Q bands result from symmetry forbidden electronic transitions ( $S_0 \rightarrow S_1$ ) and are designated by IV, III, II, I.<sup>36</sup>

The absorption spectra of **BDP-P1**, **BDP-P2** and **BDP-P3** are nearly identical to the sum of the individual absorptions of porphyrin and BODIPY, indicating the existence of a low ground state coupling between the chromophores. The complementarity of absorption bands provides an opportunity to make a multichromophoric compound with a broad

absorption profile. Spectral data shown in Table 6.2 reveal that the  $\lambda_{\max}$  and  $\epsilon$  values of the BODIPY-porphyrin dyads are within the same range of the individual moieties.



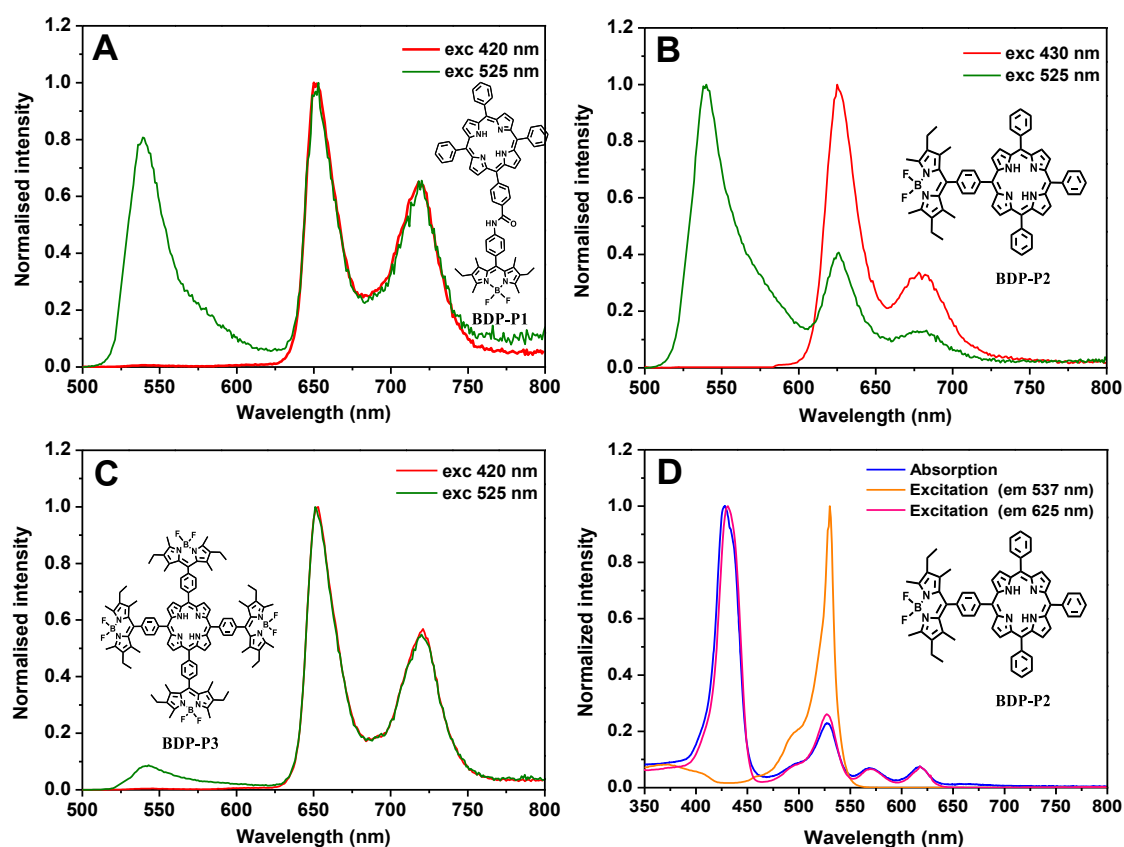
**Figure 6.15.** Normalised absorption spectra of BODIPYs **53**, **101**, **BDP-P1**, **BDP-P2** and **BDP-P3**, recorded in toluene solution.

Comparing the main bands of the dyads it is found that the ratio between the Soret and the BODIPY band (at 525 nm) is similar for **BDP-P1** and **BDP-P2** (0.27 and 0.24 respectively) and much lower for **BDP-P3** (0.52), which is expectable since the first two dyes have an equal number of BODIPY and porphyrin units and **BDP-P3** has four times more BODIPY units. The **BDP-P2** absorption spectrum shows a little broadening and shift of the Soret band, which can be explained by the distortion of the structure.

While **101** and **106** present two emission bands, BODIPY **53** has an intense fluorescence embodied by a band at 539 nm. The three BODIPY-porphyrin dyes have the same emission spectra profile (Figure 6.16 (A-C)). When the excitation was made at the Soret wavelength, only the emission bands of porphyrin appeared. On the other hand, when the excitation was made at 525 nm, within the BODIPY absorption band, the emission bands of both chromophores showed up. The emission band of BODIPY (around 540 nm) displayed a strong quenching, and the other two bands presented an enhancement, indicating that energy transfer from BODIPY to porphyrin moieties takes place.



Since the multichromophores did not reveal any new absorbance band or a major difference with respect to the sum of BODIPY or porphyrin individual absorption spectra, we conclude that there is no conjugation between donor and acceptor units. However, the quenching of BODIPY's fluorescence combined with the substantial overlap between the emission of BODIPY and the absorption of porphyrin (Q bands) suggests an intramolecular excited state energy transfer from BODIPY to the porphyrin.



**Figure 6.16.** Normalised emission spectra of **BDP-P1** (A), **BDP-P2** (B) and **BDP-P3** (C) (excitation wavelength at 420 nm and 525 nm); Absorption and excitation spectra (emission wavelength at 537 nm or 625 nm) of **BDP-P2** (D).

The excitation spectra of **BDP-P2**, shown in Figure 6.16 (D), gives another proof that there are no ground state interactions between the different units of the molecular array and there is an energy transfer from the BODIPY component to porphyrin fraction. When the excitation was recorded at BODIPY emission wavelength only the BODIPY spectrum was obtained, but when the excitation recorded at the lower energy emission (650 nm or 719 nm), a spectrum equivalent to the absorption spectra was found.

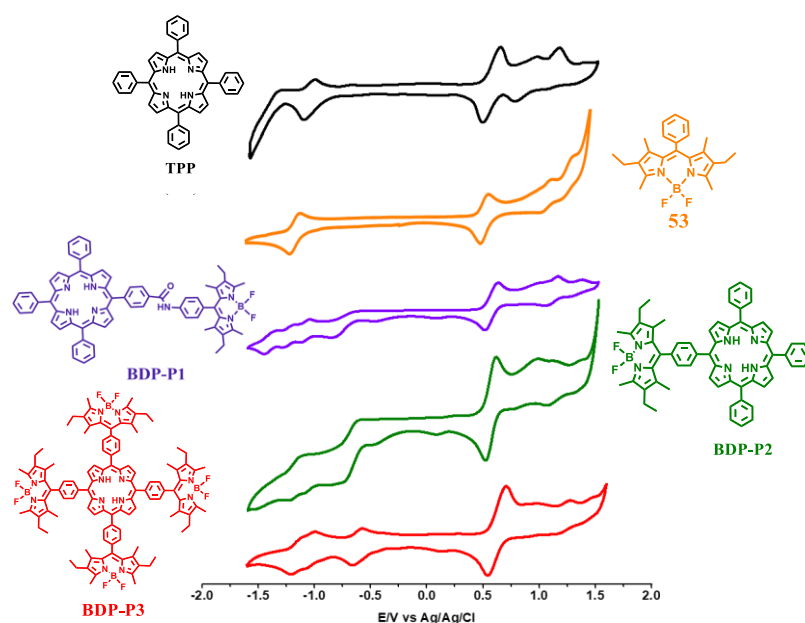
**Table 6.2.** Absorption and emission properties of **101**, **105**, **53**, **BDP-P1**, **BDP-P2** and **BDP-P3**, measured in toluene solutions.

Dye	Absorption bands $\lambda_{\max}$ (nm) ( $\epsilon$ [ $M^{-1}\cdot cm^{-1}$ ])						Emission band (nm)
	Soret	BODIPY	IV	III	II	I	
<b>101</b>	417 ( $3.2 \times 10^5$ )	-	515 ( $3.2 \times 10^4$ )	549 ( $1.6 \times 10^4$ )	588 ( $1.1 \times 10^4$ )	650 ( $9.7 \times 10^3$ )	647; 717
<b>106*</b>	418 ( $2.7 \times 10^5$ )	-	513 ( $2.7 \times 10^4$ )	548 ( $1.0 \times 10^3$ )	592 ( $9.6 \times 10^3$ )	649 ( $9.4 \times 10^3$ )	650; 715
<b>53</b>	-	525 ( $6.8 \times 10^4$ )	-	-	-	-	538
<b>BDP-P1</b> ( <b>103</b> )	420 ( $3.1 \times 10^5$ )	526 ( $6.1 \times 10^4$ )	-	-	592 ( $1.2 \times 10^4$ )	645 ( $1.1 \times 10^4$ )	539; 650; 719;
<b>BDP-P2</b> ( <b>107</b> )	428 ( $9.6 \times 10^4$ )	527 ( $2.9 \times 10^4$ )	-	-	569 ( $1.1 \times 10^4$ )	617 ( $1.2 \times 10^4$ )	537; 625; 678
<b>BDP-P3</b> ( <b>109</b> )	420 ( $2.4 \times 10^5$ )	525 ( $1.1 \times 10^5$ )	-	-	591 ( $2.1 \times 10^4$ )	649 ( $1.0 \times 10^4$ )	540; 651; 720

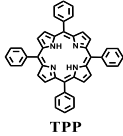
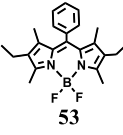
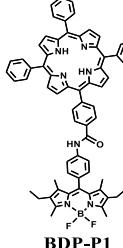
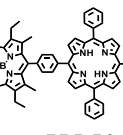
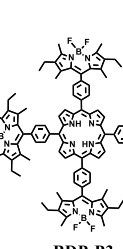
\*Measured in THF solution.

### 6.3. Electrochemical characterisation of BDP-P1, BDP-P2 and BDP-P3

The cyclic voltammograms of **TPP** (**105**) and of the BODIPYs **53**, **BDP-P1**, **BDP-P2** and **BDP-P3** are shown in Figure 6.17, and the corresponding redox potential data are summarised in Table 6.3. **TPP** was chosen instead of porphyrin **101** or **106** due to its good solubility in the majority of organic solvents, which is an essential requirement for the further photovoltaic application.

**Figure 6.17.** Cyclic voltammograms of **TPP**, **53**, **BDP-P1**, **BDP-P2** and **BDP-P3** in dichloroethane solution, in the presence of 1 mM ferrocene/ferrocenium ( $Fc/Fc^+$ ) as internal standard, recorded at 50 mV/s in deoxygenated solution ( $N_2$ ).

**Table 6.3.** Electrochemical properties of **TPP**, **53**, **BDP-P1**, **BDP-P2** and **BDP-P3**.

Dye	Reduction (V)				Oxidation (V)			$E_{\text{HOMO}}$ (eV) <sup>a</sup>	$E_{\text{LUMO}}$ (eV) <sup>b</sup>
	$E^1$ (onset)	$E^2$	$E^3$	$E^4$	$E^1$ (onset)	$E^2$	$E^3$		
 <b>TPP</b>	-0.68 (-0.83)	-1.06	-	-	0.93 (0.89)	1.19	1.44	-5.08	-3.36
 <b>53</b>	-1.15 (-1.07)	-	-	-	1.17 (1.09)	1.43	-	-5.28	-3.12
 <b>BDP-P1</b>	-0.75 (-0.63)	-1.08	-1.23	1.41	0.95 (0.86)	1.18	1.39	-5.05	-3.56
 <b>BDP-P2</b>	-0.69 (-0.54)	-1.07	-1.18	-	0.93 (0.83)	1.15	1.39	-5.02	-3.65
 <b>BDP-P3</b>	-0.62 (-0.49)	-1.03	-1.18	-	0.95 (0.89)	1.22	1.42	-5.08	-3.70

<sup>a</sup> $E_{\text{HOMO}} = [-(E_{\text{onset}}^{\text{ox1}} - E^{\text{Fc}/\text{Fc}^+}) - 4.8]$  eV;

<sup>b</sup> $E_{\text{HOMO}} = [-(E_{\text{onset}}^{\text{red1}} - E^{\text{Fc}/\text{Fc}^+}) - 4.8]$  eV.

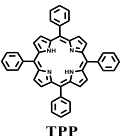
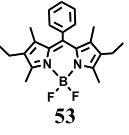
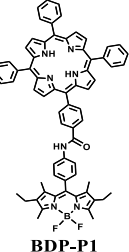
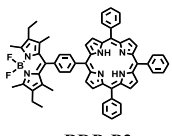
The cyclic voltammograms show that there is no significant difference between the three BODIPY-porphyrin structures, and the redox potential values are close to the corresponding potentials of the reference compounds (**TPP** and **53**).

For the three BODIPY-porphyrin molecules, three oxidation processes are detected. On the reduction side, four processes are observed for **BDP-P1**, and three processes are detected for **BDP-P2** and **BDP-P3**. Though the comparison of the BODIPY-porphyrin voltammograms with the individual porphyrin and BODIPY voltammograms, it is possible to attribute the first and second reduction processes to the reduction of porphyrin and the third reduction process to the reduction of BODIPY fraction.

#### 6.4. Photovoltaic studies of BDP-P1 and BDP-P2

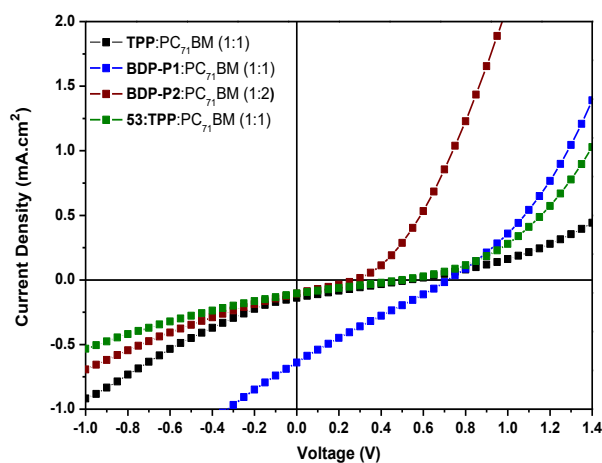
**BDP-P1** and **BDP-P2** were tested as electron-donor molecules in BHJ-OPVs, blended with PC<sub>71</sub>BM. The cell architecture was the same as that used in former chapters (ITO/PEDOT:PSS/BODIPY-porphyrin:PC<sub>71</sub>BM/Ca/Al) and the active layer blend was prepared from a solution of chloroform at 15mg/ml solids concentration. Besides the photovoltaic studies of **BDP-P1** and **BDP-P2**, **TPP** and a system with **TPP** and **53** were tested as well. Table 6.4 compiles all the photovoltaic parameters resulting from these preliminary tests, and the best I-V curves are represented in Figure 6.18.

**Table 6.4.** Photovoltaic performance parameters of OPV cells from a solution of chloroform at 15mg/ml, under AM 1.5G illumination at 84 mW/cm<sup>2</sup>.

Dye	Ratio (Dye/PC <sub>71</sub> BM)	Active layer thickness (nm)	Maximum			
			J <sub>sc</sub> (mA/cm <sup>2</sup> )	V <sub>oc</sub> (V)	FF	PCE (%)
 TPP	1:1	132	0.14	0.53	0.24	0.02
 53	1:3	80	0.93	0.73	0.27	0.22
 BDP-P1	2:1	85	0.56	0.50	0.25	0.07
	1:1	89	0.64	0.72	0.24	0.111
	1:2	105	0.51	0.71	0.25	0.09
 BDP-P2	1:1	112	0.08	0.32	0.27	0.007
	1:2	146	0.10	0.28	0.28	0.009
	1:3	152	0.09	0.21	0.25	0.005
<b>TPP + 53</b>	1:1	101	0.10	0.50	0.25	0.013

The most favourable weight ratios for **BDP-P1**:PC<sub>71</sub>BM and **BDP-P2**:PC<sub>71</sub>BM were found to be 1:1 and 1:2, respectively. None of the BODIPY-porphyrin systems showed better photovoltaic results than the OPVs based on the reference BODIPY (**53**:PC<sub>71</sub>BM). The devices based on **TPP**, **BDP-P2** and the ternary system showed poor PCE values. This is the result of lower current values and a considerable drop in V<sub>oc</sub>. On the other hand, **BDP-P1**-

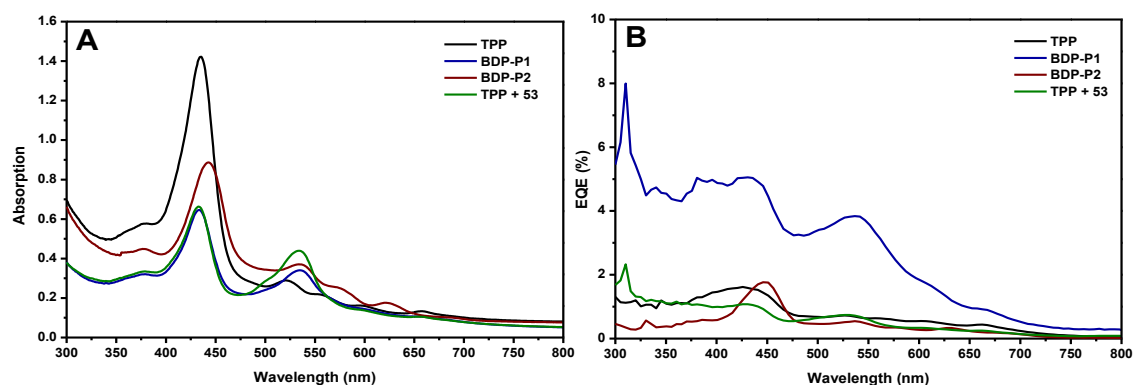
based OPVs presented 10 times better efficiency than its analogous, since  $J_{SC}$  was not so unfavourable and the  $V_{OC}$  values were in line with those obtained for the BODIPY-based OPVs explored in the previous chapters.



**Figure 6.18.** Current density-voltage characteristics of the best case of each OPV system presented in Table 6.4.

The weak photovoltaic results achieved for **TPP** shows that the inclusion of this porphyrin moiety may have a detrimental effect on the overall efficiency of the dyads-based OPV systems. Notwithstanding, the **BDP-P1**-based OPV showed results somewhat similar to those achieved in Chapter 2 with simple BODIPY dyes, and better than some of the styryl functionalized BODIPYs tested in chapter 3.

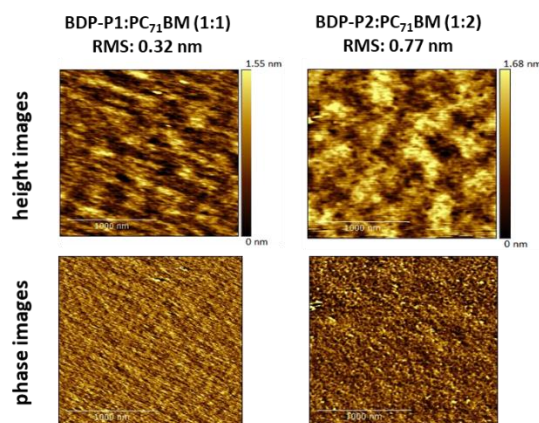
Figure 6.19 shows the absorption spectra of the active layers and the external quantum efficiencies (EQE) of the best OPVs based on **TPP:PC<sub>71</sub>BM (1:1)**, **BDP-P1:PC<sub>71</sub>BM (1:1)**, **BDP-P2: PC<sub>71</sub>BM (1:2)** and **53:TPP:PC<sub>71</sub>BM (1:1)**. The absorption spectra of the films are very similar to the solution absorption spectra (Figure 6.15). Due to the low current density, the EQE response is not high, but the profile is similar to the corresponding absorption spectra of the films. The EQE results for **BDP-P1: PC<sub>71</sub>BM** are consistent with its larger  $J_{SC}$ .



**Figure 6.19.** (A) Absorption spectra (films) of the best cases presented in Table 4.4; (B) EQE spectrum of the best cases presented in Table 6.4.

### 6.4.1. Surface morphology of the active layers

The blends of **BDP-P1**:PC<sub>71</sub>BM (1:1) and **BDP-P2**: PC<sub>71</sub>BM (1:2) were analysed by AFM and, as observed for other BODIPY-based OPV blends, the images of the surfaces rule out the possibility of unfavourable morphology. The measurements indicate smooth surfaces and no significant phase domains.



**Figure 6.20.** AFM height images (top) and phase images (bottom) (2 $\mu$ m vs 2 $\mu$ m) of the **BDP-P1**:PC<sub>71</sub>BM (1:1) and **BDP-P2**: PC<sub>71</sub>BM (1:2) blends.

## 6.5. Conclusions for Chapter 6

In this chapter, it was explored the synthesis and photovoltaic application of three structures based on BODIPY-porphyrin dyads. **BDP-P2** and **BDP-P3** were synthesised through a pathway that has not been reported so far for this sort of dyads.

Photophysical studies showed that there is no conjugation between both chromophore moieties. However, from the quenching of the fluorescence and excitation spectra, it is possible to conclude that there is energy transfer from BODIPY to the porphyrin moiety.

OPVs based on **BDP-P2** revealed poor efficiency, but the photovoltaic response of **BDP-P1** is comparable to those obtained for dyes of the **1S-BDP** series. Only preliminary studies were carried out, and these show that dyads are different from the BODIPY structures tested in the remaining of this thesis. Thus, we believe that PCE could still be improved, by optimisation of the active layer blend, in terms of morphology and charge transport upon addition of additives or changing the contact layers. The tests with **TPP** prove that this porphyrin is a poor performing active compound to be applied as electron-donor material since its OPVs achieved some of the worst results in this thesis. Considering that, **BDP-P1** reveals some potential and should be object of more research in the future.

## 6.6. References for Chapter 6

1. A. Kadhim, L. K. McKenzie, H. E. Bryant, L. J. Twyman, *Molecular Pharmaceutics* **2019**, 16, 1132-1139.
2. S. Bouramtane, L. Bretin, A. Pinon, D. Leger, B. Liagre, L. Richard, F. Bregier, V. Sol, Chaleix, V. *Carbohydrate Polymers*, **2019**, 213, 168-175.
3. K.Prakash, V. Sudhakar, M. Sankar, K. Krishnamoorthy, *Dyes and Pigments*, **2019**, 160, 386-394.
4. L. Y. Wang, H. H. Li, J. C. Deng, D. R. Cao, *Current Organic Chemistry*, **2013**, 17, 3078-3091.
5. J. L. S. Milani, A. M. Meireles, B. N.Cabral, W. D. Bezerra, F. T. Martins, D. C. D. Martins, R. P. das Chagas, *Journal of CO<sub>2</sub> Utilization* **2019**, 30, 100-106.
6. L. J. Zhu, J. Wang, T. G. Reng, C. Y Li. D. C. Guo, C. C. Guo, *Journal of Physical Organic Chemistry*, **2010**, 23, 190-194.
7. L. R. Milgrom, *The Colours of Life: An Introduction to the Chemistry of Porphyrins and Related Compounds*; Oxford University Press, ISBN: 0198553803, Oxford, **1997**, 191-242.
8. A. Melis, *Plant Science*, **2009**, 177, 272-280.
9. Sujatha, B. In *Plant Biology and Biotechnology: Plant Diversity, Organization, Function and Improvement*, Springer, ISBN: 9788132222859, New Delhi, **2015**, 569-591.
10. V. A. Azov, P. J. Skinner, Y. Yamakoshi, P. Seiler, V. Gramlich, F. Diederich, *Helvetica Chimica Acta*, **2003**, 86, 3648-3670.
11. V. A. Azov, F. Diederich, Y. Lill, B. Hecht, *Helvetica Chimica Acta*, **2003**, 86, 2149-2155.
12. T. Zhang, R. Lan, L. Gong, B. Wu, Y. Wang, D. W. J. Kwong, W. K. Wong, K.-L. Wong, Xing, D. *ChemBioChem*, **2015**, 16, 2357-2364.
13. M. D. Weber, V. Nikolaou, J. E. Wittmann, A. Nikolaou, P. A. Angaridis, G. Charalambidis, C. Stangel, A. Kahnt, A. G. Coutsolelos, R. D. Costa, *Chemical Communications*, **2016**, 52, 1602-1605.
14. T. K. Khan, M. Bröring, S. Mathur, M. Ravikanth, *Coordination Chemistry Reviews*, **2013**, 257, 2348-2387.
15. F. Li, S. I. Yang, Y. Ciringh, J. Seth, C. H. Martin, D. L. Singh, D. Kim, R. R. Birge, D. F. Bocian, D. Holten, J. S Lindsey, *Journal of the American Chemical Society*, **1998**, 120, 10001-10017.
16. K. Ladomenou, V. Nikolaou, G. Charalambidis, A. Charisiadis, A. G. Coutsolelos, *Comptes Rendus Chimie*, **2017**, 20, 314-322.
17. E. Maligaspe, T. Kumpulainen, N. K. Subbaiyan, M. E. Zandler, H. Lemmetyinen, N. V. Tkachenko, F. D'Souza, *Physical Chemistry Chemical Physics*, **2010**, 12, 7434-7444.
18. C. Stangel, K. Ladomenou, G. Charalambidis, M. K. Panda, T. Lazarides, A. G. Coutsolelos, *European Journal of Inorganic Chemistry*, **2013**, 2013, 1275-1286.
19. A. N. Kursunlu, *RSC Advances*, **2014**, 4, 47690-47696.
20. Q. Q. Hu, Y. Z. Zhu, S. C. Zhang, Y. Z. Tong, J. Y. Zheng, *Dalton Transactions*, **2015**, 44, 15523-15530.
21. Y. Chen, L. Wan, X. Yu, W. Li, Y. Bian, J. Jiang, *Organic Letters*, **2011**, 13, 5774-5777.
22. C. Berney, G. Danuser, *Biophysical journal*, **2003**, 84, 3992-4010.

23. G. N. Lim, E. Maligaspe, M. E. Zandler, F. D'Souza, *Chemistry – A European Journal*, **2014**, 20, 17089-17099.
24. G. D. Sharma, S. A. Siddiqui, A. Nikiforou, G. E. Zervaki, I. Georgakaki, K. Ladomenou, A. G. Coutsolelos, *Journal of Materials Chemistry C*, **2015**, 3, 6209-6217.
25. P. Erwin, S. M. Conron, J. H. Golden, K. Allen, M. E. Thompson, *Chemistry of Materials*, **2015**, 27, 5386-5392.
26. M. L. Li, H. Wang, X. Zhang, H. S. Zhang, *Spectrochimica Acta Part a-Molecular and Biomolecular Spectroscopy*, **2004**, 60, 987-993.
27. E. Diez-Cecilia, B. Kelly, I. Rozas, *Tetrahedron Letters*, **2011**, 52, 6702-6704.
28. A. Cui, X. Peng, J. Fan, X. Chen, Y. Wu, B. Guo, *Journal of Photochemistry and Photobiology A: Chemistry*, **2007**, 186, 85-92.
29. Z. H. Pan, G. G. Luo, J. W. Zhou, J. X. Xia, K. Fang, R. B. Wu, *Dalton Transactions*, **2014**, 43, 8499-8507.
30. C. Jiao, L. Zhu, J. Wu, *Chemistry – A European Journal*, **2011**, 17, 6610-6614.
31. K. Tan, L. Jaquinod, R. Paolesse, S. Nardis, C. Di Natale, A. Di Carlo, L. Prodi, M. Montalti, N. Zaccheroni, K. M Smith, *Tetrahedron*, **2004**, 60, 1099-1106.
32. Y. Yu, T. Furuyama, J. Tang, Z.-Y. Wu, J. Z. Chen, N. Kobayashi, J.-L Zhang, *Inorganic Chemistry Frontiers*, **2015**, 2, 671-677.
33. J. Almeida, A. Aguiar, A. Leite, A. M. N. Silva, L. Cunha-Silva, B. de Castro, M. Rangel, G. Barone, A. C. Tomé, A. M. G. Silva, *Organic Chemistry Frontiers*, **2017**, 4, 534-544.
34. S. Singh, A. Aggarwal, S. Thompson, J. P. C. Tomé, X. Zhu, D. Samaroo, M. Vinodu, R. Gao, C. M. Drain, *Bioconjugate Chemistry*, **2010**, 21, 2136-2146.
35. A. Aguiar, A. Leite, A. M. N. Silva, A. C. Tomé, L. Cunha-Silva, B. de Castro, M. Rangel, A. M. G. Silva, *Organic & Biomolecular Chemistry*, **2015**, 13, 7131-7135.
36. M. R. Dayer, A. A. Moosavi-Movahedi, M. S. Dayer, *Protein Pept Lett*, **2010**, 17, 473-9.



## **CHAPTER 7. Final remarks and future perspectives**

This PhD thesis reports the synthesis of a library of BODIPY structures with suitable characteristics to be applied in organic photovoltaic cells. Four different sets of BODIPY molecules and three BODIPY-porphyrin dyads were synthesised. Most of the compounds show very good solubility, high thermal stability, favourable photophysical properties, proper HOMO and LUMO energies, which made these dyes very suitable to be applied in OPVs. Throughout the PhD work, 26 different BODIPY molecules were blended with PC<sub>61</sub>BM or PC<sub>71</sub>BM and tested as electron-donor in BHJ-OPVs.

The first series (**1S-BDP**) is composed of simple *meso*-aryl substituted BODIPY molecules that are originated from the  $\alpha$ -free-pyrrole condensation with aromatic aldehydes. The stability, photophysical and redox characteristics make these dyes very appealing to be applied as electron-donor materials. Additionally, two new crystal structures were obtained by X-ray diffraction. We demonstrated that the appearance of the *meso*-free BODIPY by-product in the synthesis of *meso*-substituted BODIPY molecules results from the reaction of the  $\alpha$ -free-pyrrole with the halogenated solvent. We also showed that dihalogenated reagents like  $\alpha,\alpha$ -dichlorotoluene or  $\alpha,\alpha$ -dibromotoluene can be used to synthesise the *meso*-phenyl-substituted BODIPY (**53**), which is a new non-acidic alternative to the synthesis of BODIPY derivatives.

Encouraged by the suitable characteristics and photovoltaic performance of **1S-BDP** dyes, some of those BODIPY dyes were functionalized via Knoevenagel condensation originating a series of styryl BODIPY molecules (**2S-BDP**). This second series includes some new structures with interesting photophysical and redox properties due to the enhancement of the  $\pi$ -electron delocalisation. The OPVs based in some of these structures revealed a remarkable improvement in their efficiencies regarding the **1S-BDP**.

Taking the BODIPY from **2S-BDP** with the best photovoltaic response, as reference, we built the third series of BODIPY molecules (**3S-BDP**) exploring its backbone (*meso*-pentafluorophenyl BODIPY) with several vinyl groups (phenyl, naphthalenyl, anthracenyl and N-ethyl-carbazolyl). **3S-BDP** dyes showed excellent thermal stability, strong spectral coverage, deep HOMO energy levels and good miscibility with PC<sub>61</sub>BM and PC<sub>71</sub>BM. With the increase of aromaticity of styryl groups, the shifting of absorbance to higher wavelengths was attained, and the band gap was reduced (to 1.62 eV). The insertion of two N-ethyl-3-vinylcarbazole units improved significantly the short-circuit current leading to efficiencies around 2.4 %. The BODIPY with two vinylnaphthalene units achieved a maximum PCE of 2.79 % when blended with PC<sub>71</sub>BM, and its V<sub>OC</sub> value (1.00 V) is amongst the best ever reported in OPVs.

The fourth series (**4S-BDP**) is composed of several BODIPY dyes with various aryloxy groups bonded to boron. In addition to several new molecules, two new crystal structures are also reported. The functionalization at the boron centre does not change the absorption feature of the molecule but causes some changes on the redox potentials. The molecules with catecholate ligands showed an improvement in  $V_{OC}$  when blended with PC<sub>61</sub>BM.

Additionally, we explored BODIPY-porphyrin dyad systems. A new route of synthesis was developed, and three new structures were obtained. The photophysical characterisation confirmed energy transfer from BODIPY to porphyrin moiety but further optimisations must be done to reach a definitive conclusion about the photovoltaic potential of this system.

This thesis reports some structures that overcame the barrier of 1 % PCE and most OPVs had high  $V_{OC}$  values which attest the suitability of the dyes for BHJ-OPVs. AFM measurements showed very smooth surfaces and no aggregate formation, indicating a good intermixing of the two active layer materials (BODIPY and fullerene).

In the near future, it will be important to study the charge transport characteristics and the OPVs stability in order to better understand the full potential of the BODIPY small molecules. The results here reported are very encouraging and demonstrate that BODIPY dyes can be good photovoltaic materials if carefully planned and tailored. Further chemical derivatization leading to the incorporation of high hole conduction donor units, and device optimisation upon addition of additives or changing the contact layers can lead to higher  $J_{sc}$  and FF, and consequently better photovoltaic efficiencies.

In summary, this thesis brings pertinent conclusions about the structure, properties and photovoltaic application of the BODIPY class. The diversity and versatility of the presented compounds, as well as the vast photovoltaic screening, will undoubtedly be relevant for future photovoltaic works.

This page intentionally left blank

**CHAPTER 8. Experimental procedures and  
supplementary information**

## 8.1. Reagents and Solvents

Reagents and solvents were obtained from Sigma-Aldrich, VWR, Acros Organics or Fluka and used without further purification. Solvents for synthesis were distilled and dried through standard literature methods. Only solvents with 99.5 % or above of purity grade were used in the photovoltaic studies. Analytical thin layer chromatography (TLC) was performed on Merck silica gel plates with F-254 indicator. Visualization was accomplished by a twin wavelength ultraviolet lamp (254 and 365 nm). Silica gel column chromatography was carried out using silica gel (230-400 mesh) from Fluka or Acros Organics. Preparative thin layer chromatography was performed using 20 x 20 cm glass plates and silica gel 60G from Fluka.

## 8.2 Instrumentation

### 8.2.1. Nuclear magnetic resonance spectroscopy

$^1\text{H}$ ,  $^{13}\text{C}$ ,  $^{11}\text{B}$  and  $^{19}\text{F}$  NMR spectra were acquired in a Bruker AVANCE III NMR (running at 400 MHz for proton, 100 MHz for carbon, 128 MHz for boron, and 376 MHz for fluorine) with  $\text{CDCl}_3$  as solvent. The solvent protons were used as internal standards. The coupling constants were calculated using the chemical shifts with three decimal places.

### 8.2.2. High performance liquid chromatography

High-performance liquid chromatography (HPLC) analyses were performed using a Dionex Ultimate 3000 system equipped with an auto-injector and an Hichrom 5 C18 column (15 cm x 5 mm x 4.6 mm). The experiments were performed at 30 °C using an ultimate 3000 diode array detector.

### 8.2.3. Mass spectrometry

Mass spectra were obtained from an ion trap MS: Amazon SL, Bruker Daltonics spectrometer coupled to the HPLC, using electronic spray ionization (ESI).

The high-resolution ESI positive mode mass spectra were obtained on a QqTOF Impact IITM mass spectrometer (Bruker Daltonics) operating in the high-resolution mode. Samples were analysed by flow injection analysis (FIA) using an isocratic gradient 30 A:70 B of 0.1% formic acid in water (A) and 0.1% of formic acid in acetonitrile (B), at a flow rate of  $10 \mu\text{Lmin}^{-1}$  over 15 min. The TOF analyser was calibrated in the  $m/z$  range 100-1500 using an internal calibration standard (Tune-mix solution) which was supplied by Agilent.

The full scan mass spectra were acquired over a mass range of 100-1350 m/z at a rate of 1 Hz.

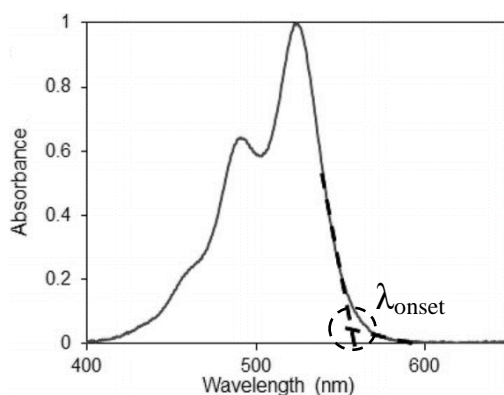
#### 8.2.4. X-ray crystallography

The single-crystal X-ray acquisition experiments were done by Professor Manuela Ramos from Center for Physics of the University of Coimbra. Single-crystal X-ray diffraction studies were carried out on a Bruker APEX II diffractometer using the MoK $\alpha$  radiation. Data reduction was performed with SMART and SAINT software.<sup>1</sup> Lorenz and polarization corrections were applied. A multi-scan absorption correction was applied using SADABS.<sup>2</sup> The structure was solved by direct methods using SHELXS-97 program and refined on F2s by full-matrix least-squares with SHELXL-97 program.<sup>3</sup> Anisotropic displacement parameters for non-hydrogen atoms were applied. The hydrogen atoms were placed at calculated positions and refined with isotropic parameters as riding atoms.

#### 8.2.5. Absorption spectroscopy

Electronic absorption spectra were recorded on an Ocean Optics USB4000-UV-VIS spectrophotometer, Jasco V-530 double-beam UV/Vis spectrometer, or in a Cecil 7200 spectrophotometer using 1 cm path length quartz cells. Thin films were prepared by spin-coating of solutions of the compounds in chloroform solution (15 mg/ml) onto quartz substrates at 1300 rpm for 45 seconds.

The optical band gap ( $E_{g}^{opt}$ ) was calculated by Equation 8.1, where the  $\lambda_{onset}$  is obtained from the energy onset of the absorption at lower energies as represented in Figure 8.1.



$$E_{g}^{opt} = \frac{1240}{\lambda_{onset}} \quad \text{Equation 8.1}$$

**Figure 8.1.** Estimation of the  $\lambda_{onset}$  through the absorption spectrum, adapted from Warner and co-workers.<sup>4</sup>

### 8.2.6. Emission spectroscopy

Steady-state fluorescence studies were carried out using a Horiba-Jobin-Yvon SPEX Fluorolog 3-22 spectrometer. Fluorescence spectra were made by using optically dilute solutions.

Fluorescence quantum yields were calculated by a comparative method (Equation 8.2) using rhodamine 6G ( $\phi_F$  (470 – 555 nm) = 0.88 in ethanol) and cresyl violet  $\phi_F$  ((510 – 655 nm) = 0.51 in ethanol) as reference.<sup>5</sup>

$$\frac{\phi_{sample}}{\phi_{reference}} = \frac{area_{sample}}{area_{reference}} \times \frac{Abs_{reference}}{Abs_{sample}} \times \frac{n_{sample}^2}{n_{reference}^2} \quad \text{Equation 8.2}$$

### 8.2.7. Thermal gravimetric analysis (TGA)

Thermogravimetric analyses (TGA) were conducted under a dry nitrogen gas flow at a heating rate of 20 °C min<sup>-1</sup> on a Parkin-Elmer STA 6000 instrument.

### 8.2.8. Differential scanning calorimetry (DSC)

Differential scanning calorimetry analyses were conducted on Netzsch DSC 200F3 instrument. The samples were hermetically sealed in aluminium pans, and an empty pan was used as reference.

### 8.2.9. Cyclic voltammetry

Cyclic voltammetric (CV) measurements were carried out with a computer controlled Ivium Compact Stat, in a one-compartment three electrode system consisting of a glassy carbon electrode (GCE) (geometric area 0.00785 cm<sup>2</sup>) working electrode, a platinum wire as counter electrode and an Ag/AgCl (3 M KCl) as reference electrode at a scan rate of 50 mV/s. The supporting electrolyte was tetrabutylammonium tetrafluoroborate (TBATFB, 0.1 M) in anhydrous dichloroethane (CH<sub>2</sub>Cl<sub>2</sub>). CV experiments were carried out using 1 mM concentrations of each BODIPY studied.

### 8.2.10. DFT calculations

The computational studies were performed by Professor Luís Alcácer from Instituto de Telecomunicações. The HOMO/LUMO calculations were performed with the basis set



split valence, increased with polarization function type (d) 6-31G\*, using the SPARTAN v.10 software package (Spartan, Wave Function Inc. USA).

### 8.2.11. AFM measurements

AFM studies were performed on a Nano Observer from Concept Scientific Instruments (LesUlis, France), operating in noncontact mode, with cantilevers having a resonance frequency between 200 and 400 kHz and silicon probes with tip radius smaller than 10 nm.

### 8.3. Photovoltaic device preparation and I-V measurements

The photovoltaic devices were prepared on glass substrates coated with 100 nm thick indium-tin oxide (ITO), cleaned under ultrasounds with distilled water and a non-ionic detergent (Derquim Im 02 neutral phosphate free) followed by washing with distilled water, acetone and isopropyl alcohol. The ITO surface was then treated with UV-oxygen plasma for 3 min prior to depositing, by spin coating, a 40 nm layer of poly (3,4-ethylenedioxythiophene):polystyrene sulfonic acid (PEDOT:PSS), which was then dried on a hot plate at 125 °C for 10 min. The solutions of the blends were spin-coated (1300 rpm, 60 s) on top of the PEDOT:PSS in air. Following the spin coating of the active blends, LiF (0.6 nm) or Ca (20 nm) with Al (80 nm) were thermally evaporated on top, under a base pressure of  $10^{-6}$  mbar, defining a device area of 0.24 cm<sup>2</sup>. The current-voltage curves of the photovoltaic cells were measured under inert atmosphere (N<sub>2</sub>) using a Keithley 2400 Source-Meter unit. The curves under illumination were measured with a solar simulator with simulated AM1.5G illumination at 82-100 mW/cm<sup>2</sup> (Oriel Sol 3A, 69920, Newport). At least 8 devices of each series were prepared. The light intensity of the solar simulator was verified using a calibrated solar cell. External quantum efficiency (EQE) spectra were obtained under short-circuit conditions, using a homemade system with a halogen lamp as light source coupled to a monochromator. Its intensity at each wavelength was determined using a calibrated photodiode. The short-circuit current was measured with a Keithley 2400 Source-Meter.

## 8.4. Synthetic procedures and supplementary information

### 8.4.1. Chapter 2

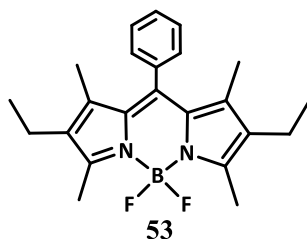
#### 8.4.1.1. General procedures for the synthesis of the first series of the 1S-BDP

3-Ethyl-2,5-dimethyl-pyrrole (0.75 ml, 5.5 mmol) and 2.75 mmol of the corresponding aldehyde (benzaldehyde, 4-formylbenzoic acid, pentafluorobenzaldehyde, 4-nitrobenzaldehyde and 9-anthracenecarboxyaldehyde for **53**, **54**, **55**, **56**, **57** respectively) were added to dried, freshly distilled dichloromethane (50 mL) and the solution was stirred for 10 min under nitrogen atmosphere. Then, a catalytic amount of trifluoroacetic acid was added and the mixture was stirred overnight, at room temperature. After that, 2,3-dichloro-5,6-dicyanobenzoquinone (1 eq.) was added to the reaction mixture, and was stirred 2 hours, under N<sub>2</sub> atmosphere, at room temperature. Then N,N-diisopropylethylamine (12 eq.) and BF<sub>3</sub>.Et<sub>2</sub>O (17 eq.) were added to the reaction mixture, and it was left under an inert atmosphere, for 6 hours. After that, the reaction mixture was washed successively with water (30 mL) and brine (30 mL). The layers were separated, and the organic layer was dried with anhydrous sodium sulfate and concentrated under reduced pressure.

BODIPY **58**, was found as a by-product of the **53-57** syntheses. However, **58** can also be synthesized using the same protocol but with halogenated reagent like iodomethane instead of the aldehyde, as is described in Table 2.2 (Chapter 2). Compounds **61** and **62** were also found as by-products on the reaction synthesis of **55**.

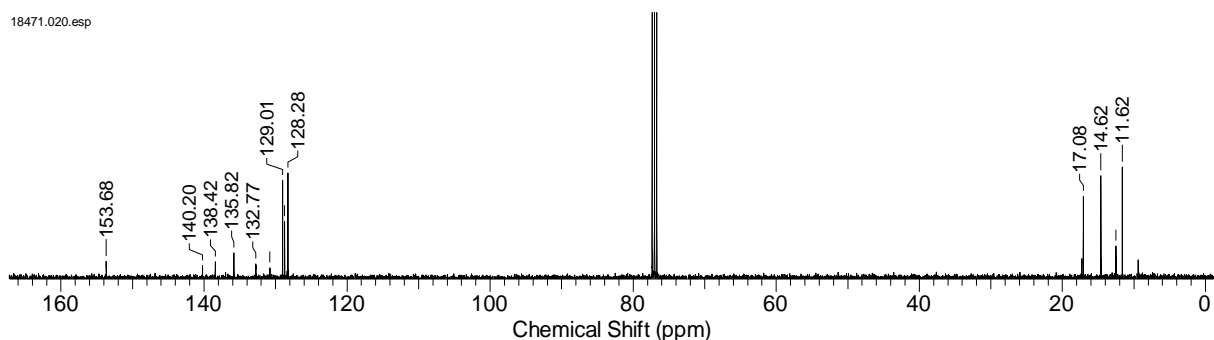
The compounds were isolated by column chromatography on silica gel using CH<sub>2</sub>Cl<sub>2</sub>:hexane (1:1). Preparative thin layer chromatography was necessary to separate **58** from **53** or **57**.

#### 8-(phenyl)-1,3,5,7-tetramethyl-2,6-diethyl-4,4-difluoro-4-bora-3a,4a-diaza-s-indacene (**53**)

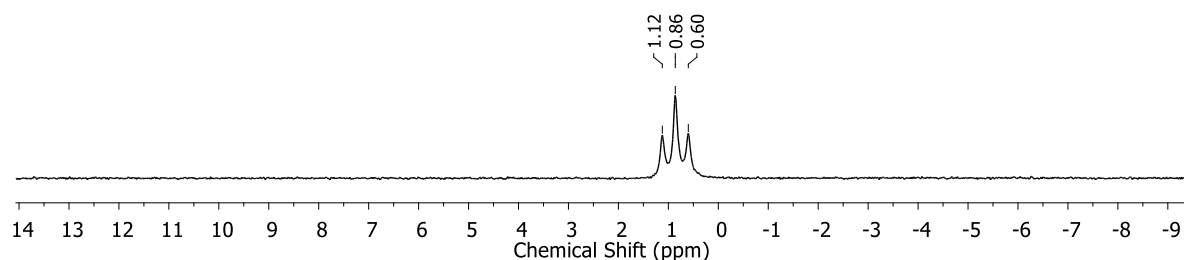


<sup>1</sup>H NMR (400 MHz, CDCl<sub>3</sub>) δ (ppm): 7.49 – 7.45 (m; 3H); 7.30 – 7.26 (m; 2H); 2.53 (s, 6H), 2.30 (q, J = 7.6 Hz, 4H), 1.26 (s, 6H), 0.98 (t, J = 7.6 Hz, 6H); <sup>13</sup>C NMR (100 MHz, CDCl<sub>3</sub>): 153.68; 140.20; 138.42; 135.81 ; 132.77; 130.79; 129.01; 128.73; 128.28;

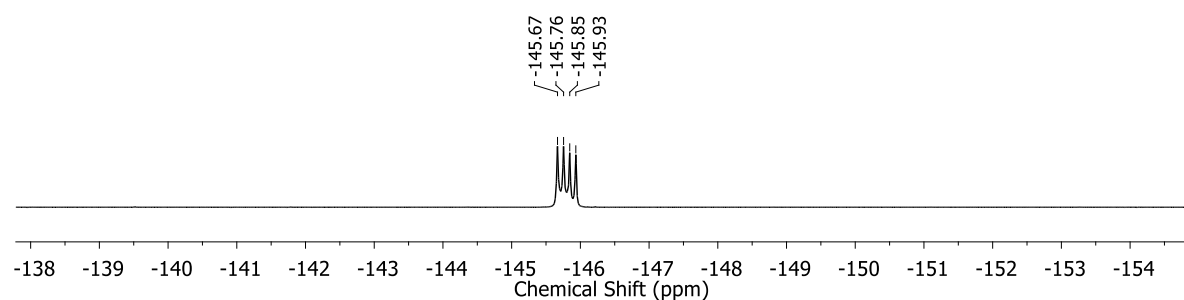
17.08; 14.62; 12.50; 11.62;  $^{11}\text{B}$  NMR (128 MHz,  $\text{CDCl}_3$ )  $\delta$  (ppm): 0.86 (t,  $J = 33.28$  Hz);  $^{19}\text{F}$  NMR (376 MHz,  $\text{CDCl}_3$ )  $\delta$  (ppm): -145.80 (q,  $J = 33.46$  Hz, 2F); HRMS  $m/z$   $[\text{M}+\text{H}]^+$  calculated for  $\text{C}_{23}\text{H}_{28}\text{BF}_2\text{N}_2^+$ : 381.2308; Found: 381.2312



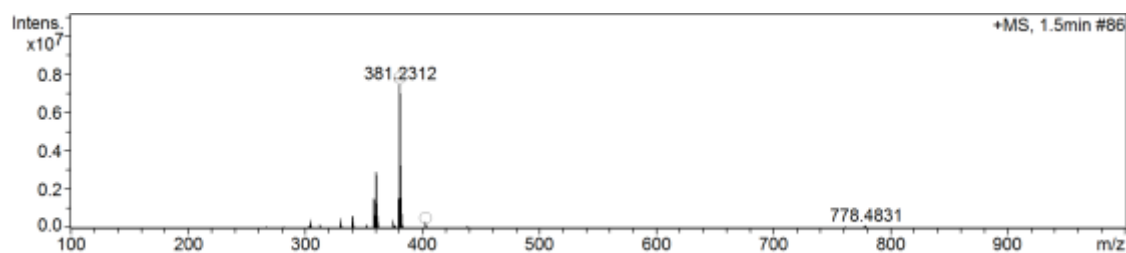
**Figure 8.2.**  $^{13}\text{C}$  NMR spectrum of **53** (100 MHz,  $\text{CDCl}_3$ ).



**Figure 8.3.**  $^{11}\text{B}$  NMR spectrum of **53** (128 MHz,  $\text{CDCl}_3$ ).

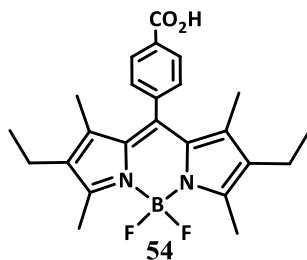


**Figure 8.4.**  $^{19}\text{F}$  NMR spectrum of **53** (376 MHz,  $\text{CDCl}_3$ ).

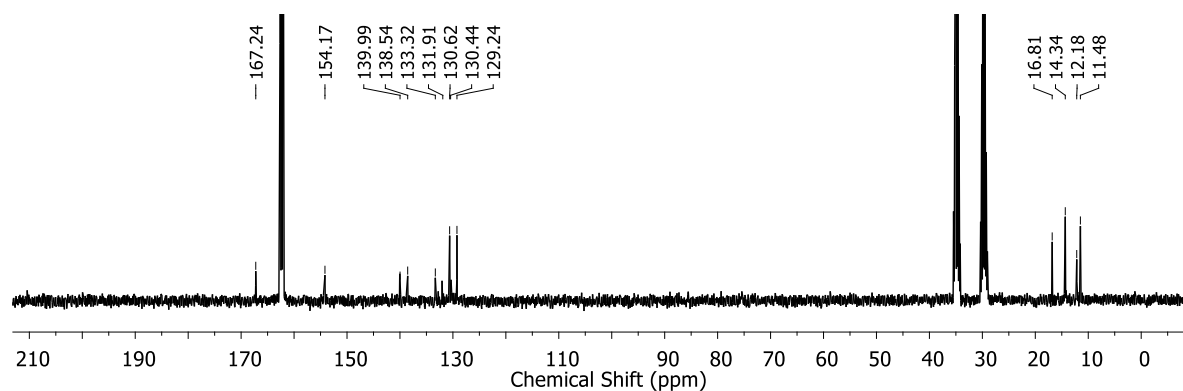


**Figure 8.5.** High resolution mass spectrum (positive mode) of **53**.

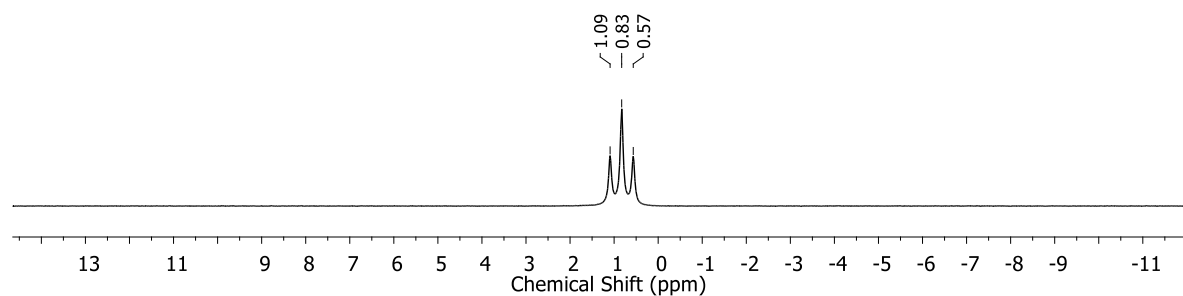
**8-(4-Formylphenyl)-1,3,5,7-tetramethyl-2,6-diethyl-4,4-difluoro-4-bora-3a,4a-diaza-s-indacene (54)**



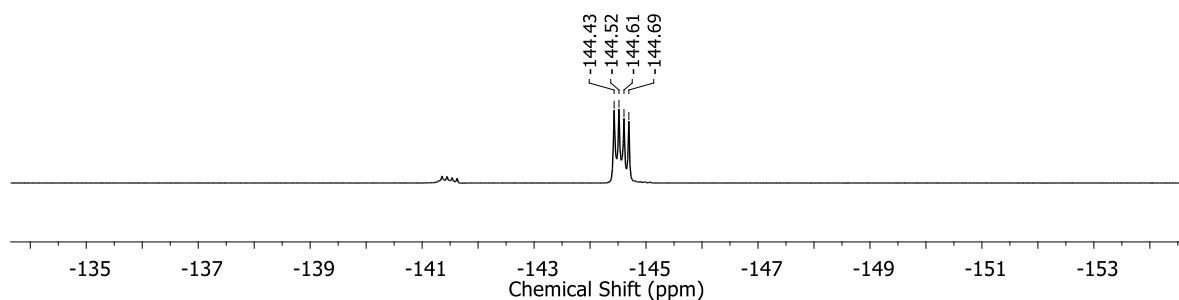
**$^1\text{H}$  NMR (400 MHz,  $\text{CDCl}_3$ )  $\delta$  (ppm):** 8.25 (d;  $J = 8.4$  Hz, 2H); 7.45 (d;  $J = 8.4$  Hz, 2H); 2.54 (s, 6H), 2.37 (q,  $J = 7.6$  Hz, 2F), 1.27 (s, 6H), 0.99 (t,  $J = 7.6$  Hz, 6H);  **$^{13}\text{C}$  NMR (100 MHz,  $\text{DCON}(\text{CD}_3)_2$ )  $\delta$  (ppm):** 167.24; 154.17; 139.99; 138.55; 133.32; 132.05; 130.62; 129.24; 16.81; 14.34; 12.18; 11.49;  **$^{11}\text{B}$  NMR (128 MHz,  $\text{CDCl}_3$ )  $\delta$  (ppm):** 0.83 (t,  $J = 33.66\text{Hz}$ );  **$^{19}\text{F}$  NMR (376 MHz,  $\text{CDCl}_3$ )  $\delta$  (ppm):** -146.30 (q,  $J = 32.71\text{Hz}$  2F); **HRMS  $m/z$   $[\text{M}+\text{H}]^+$  calculated for  $\text{C}_{24}\text{H}_{28}\text{BF}_2\text{N}_2\text{O}_2^+$ :** 425.2206; **Found:** 425.2205;



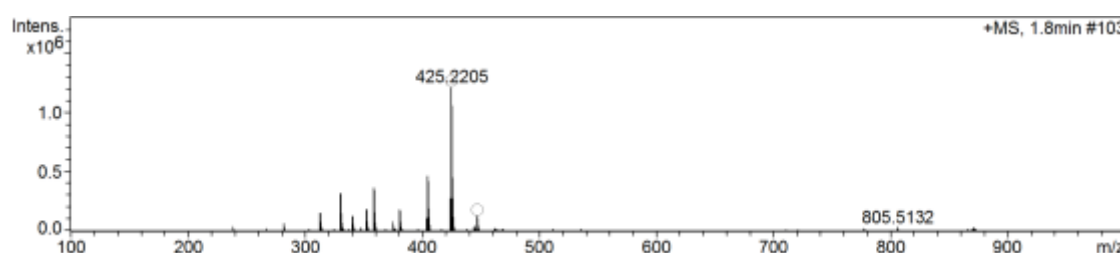
**Figure 8.6.**  $^{13}\text{C}$  NMR spectrum of **54** (100 MHz,  $\text{DCON}(\text{CD}_3)_2$ ).



**Figure 8.7.**  $^{11}\text{B}$  NMR spectrum of **54** (128 MHz,  $\text{CDCl}_3$ ).

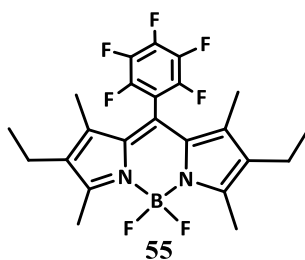


**Figure 8.8.**  $^{19}\text{F}$  NMR spectrum of **54** (376 MHz,  $\text{CDCl}_3$ ).



**Figure 8.9.** High resolution mass spectrum (positive mode) of **54**.

**8-(pentafluorophenyl)-1,3,5,7-tetramethyl-2,6-diethyl-4,4-difluoro-4-bora-3a,4a-diaza-s-indacene (55)**



$^1\text{H}$  NMR (400 MHz,  $\text{CDCl}_3$ )  $\delta$  (ppm): 2.54 (s, 6H), 2.33 (q,  $J = 7.6$  Hz, 4H), 1.51 (s, 6H), 1.02 (t,  $J = 7.6$  Hz, 6H);  $^{13}\text{C}$  NMR (100 MHz,  $\text{CDCl}_3$ )  $\delta$  (ppm): 156.15; 144.2 (d,  $J = 250.52$  Hz); 141.94 (d,  $J = 262$  Hz); 138.19 (d,  $J = 257.86$  Hz); 136.58 ; 133.91; 130.36; 121.16; 110.32 (td,  $J = 19.44, 4.03$  Hz); 17.09; 14.54; 12.74 (t,  $J = 2.57$  Hz); 10.85;  $^{11}\text{B}$  NMR (128 MHz,  $\text{CDCl}_3$ )  $\delta$  (ppm): 0.70 (t,  $J = 32.13$  Hz);  $^{19}\text{F}$  NMR (376 MHz,  $\text{CDCl}_3$ )  $\delta$  (ppm): -139.23 (dd,  $J = 21.81, 6.39$  Hz, 2F), -145.74 (q,  $J = 32.71$  Hz, 2F), -151.11 (t,  $J = 20.61$  Hz, 1F), -159.89 (td,  $J = 21.06, 6.77$  Hz, 2F); HRMS  $m/z$   $[\text{M}+\text{H}]^+$  calculated for  $\text{C}_{23}\text{H}_{22}\text{BF}_7\text{N}_2^+$ : 471.1842; Found: 471.1842.

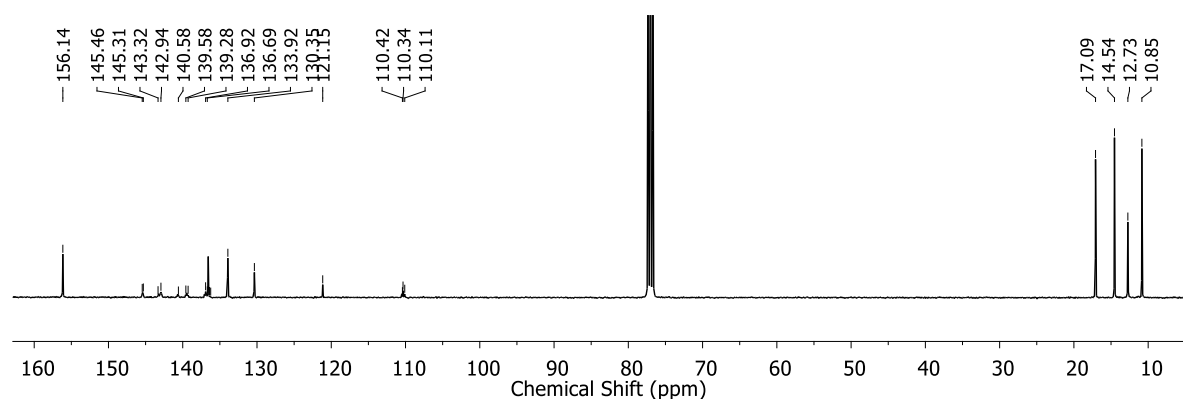


Figure 8.10.  $^{13}\text{C}$  NMR spectrum of **55** (100 MHz,  $\text{CDCl}_3$ ).

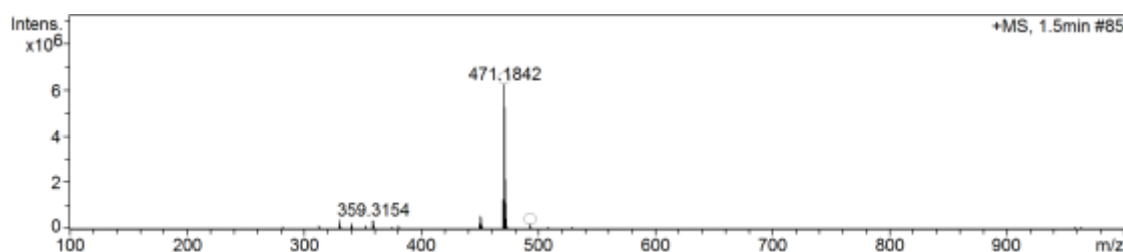
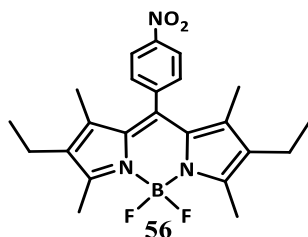
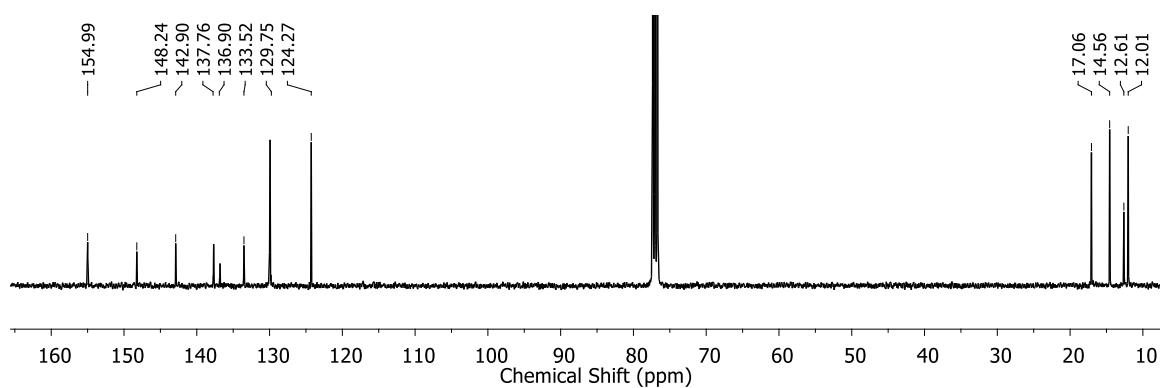


Figure 8.11. High resolution mass spectrum (positive mode) of **55**.

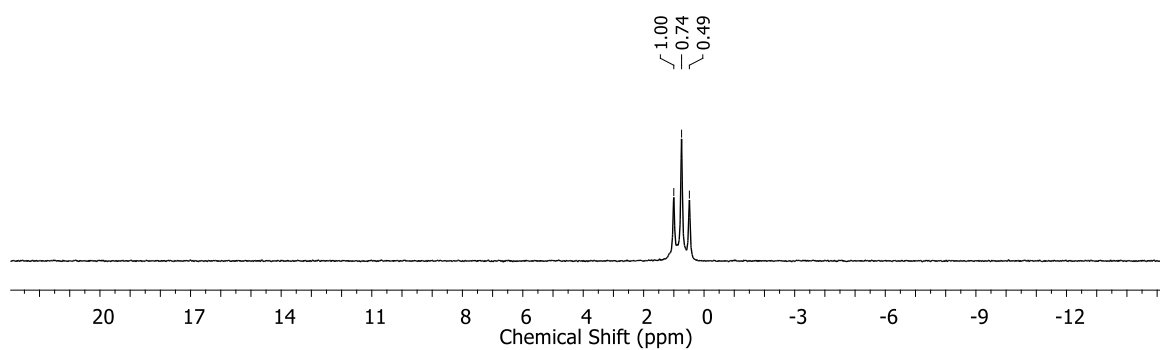
**8-(4-nitrophenyl)-1,3,5,7-tetramethyl-2,6-diethyl-4,4-difluoro-4-bora-3a,4a-diaza-s-indacene (**56**)**



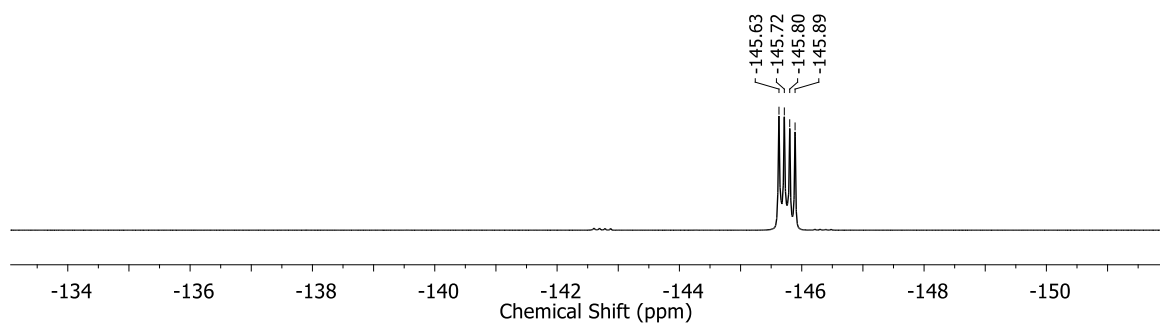
$^1\text{H}$  NMR (400 MHz,  $\text{CDCl}_3$ )  $\delta$  (ppm): 8.37 (d,  $J = 8.8$  Hz, 2H); 7.53 (d,  $J = 8.8$  Hz, 2H); 2.54 (s, 6H), 2.30 (q,  $J = 7.6$  Hz, 4H), 1.26 (s, 6H), 0.98 (t,  $J = 7.6$  Hz, 6H);  $^{13}\text{C}$  NMR (100 MHz,  $\text{CDCl}_3$ )  $\delta$  (ppm): 155.00; 148.24 ; 142.90; 137.68; 136.81; 133.52; 129.93; 124.97; 17.08; 14.57; 12.62; 12.01;  $^{11}\text{B}$  NMR (128 MHz,  $\text{CDCl}_3$ )  $\delta$  (ppm): 0.74 (t,  $J = 32.51$  Hz);  $^{19}\text{F}$  NMR (376 MHz,  $\text{CDCl}_3$ )  $\delta$  (ppm): -145.76 (q,  $J = 32.71$  Hz, 2F); HRMS  $m/z$   $[\text{M}+\text{H}]^+$  calculated for  $\text{C}_{23}\text{H}_{27}\text{BF}_2\text{N}_3\text{O}_2^+$ : 426.2159; Found: 426.2162.



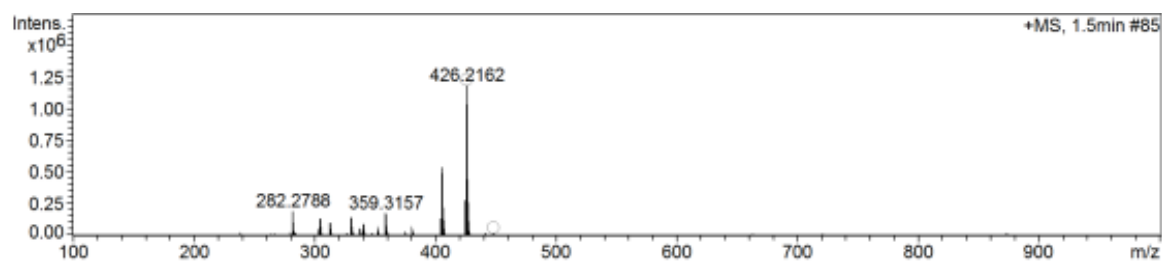
**Figure 8.12.**  $^{13}\text{C}$  NMR spectrum of **56** (100 MHz,  $\text{CDCl}_3$ ).



**Figure 8.13.**  $^{11}\text{B}$  NMR spectrum of **56** (128 MHz,  $\text{CDCl}_3$ ).

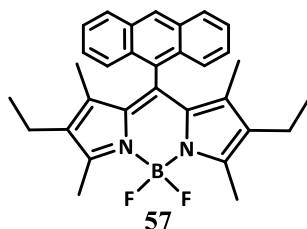


**Figure 8.14.**  $^{19}\text{F}$  NMR spectrum of **56** (376 MHz,  $\text{CDCl}_3$ ).

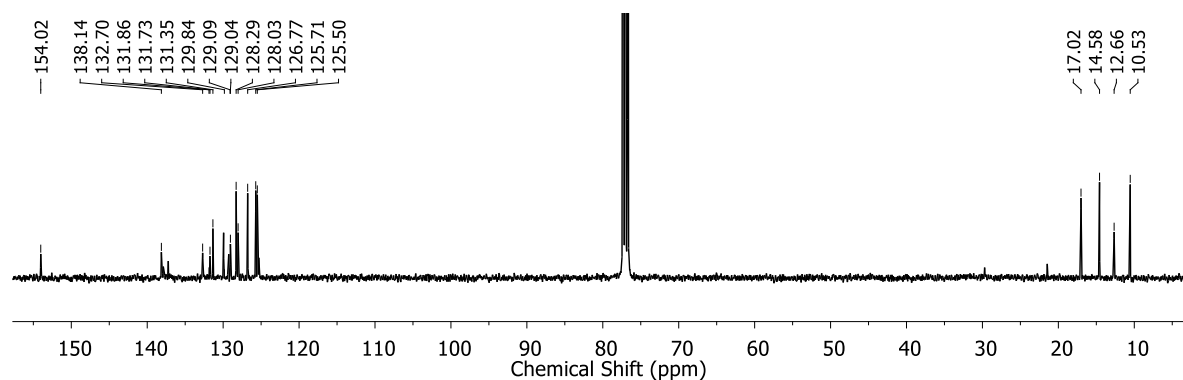


**Figure 8.15.** High resolution mass spectrum (positive mode) of **56**.

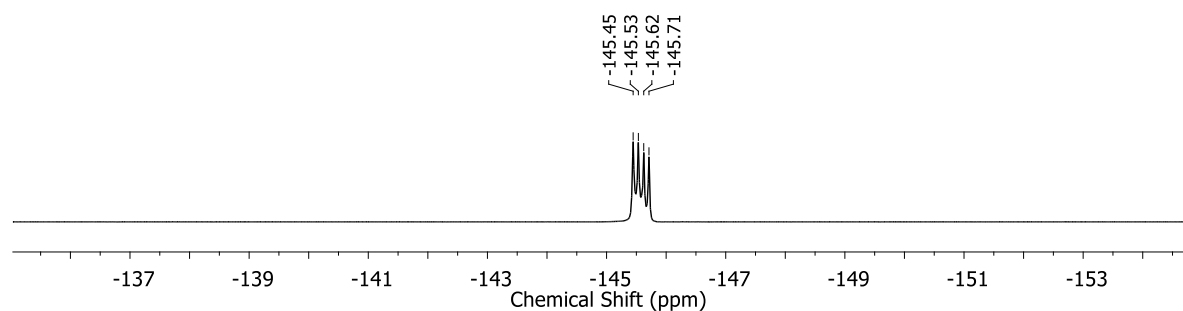
**8-(anthracenyl)-1,3,5,7-tetramethyl-2,6-diethyl-4,4-difluoro-4-bora-3a,4a-diaza-s-indacene (57)**



**$^1\text{H}$  NMR (400 MHz,  $\text{CDCl}_3$ )  $\delta$  (ppm):** 8.56 (s, 1H); 8.03 (d,  $J = 8.4$  Hz, 2H); 7.93 (d,  $J = 8.8$  Hz, 2H); 7.45 (m, 4H); 6.94 (s, 1H); 2.60 (s, 6H), 2.18 (q,  $J = 8$  Hz, 4H), 0.89 (t,  $J = 8$  Hz, 6H) 0.55 (s, 6H);  **$^{13}\text{C}$  NMR (100 MHz,  $\text{CDCl}_3$ )  $\delta$  (ppm):** 154.02; 138.14; 132.70; 131.86; 131.73; 131.35; 129.84; 129.09; 129.04; 128.29; 128.03; 126.77; 125.71; 125.51; 17.02; 14.58; 12.66; 10.54;  **$^{11}\text{B}$  NMR (128 MHz,  $\text{CDCl}_3$ )  $\delta$  (ppm):** 1.09 (t,  $J = 33.39$  Hz);  **$^{19}\text{F}$  NMR (376 MHz,  $\text{CDCl}_3$ )  $\delta$  (ppm):** -145.57 (q,  $J = 33.09$  Hz, 2F); **HRMS  $m/z$   $[\text{M}+\text{H}]^+$  calculated for  $\text{C}_{31}\text{H}_{32}\text{BF}_2\text{N}_2^+$ :** 481.2621; **Found:** 481.2624.

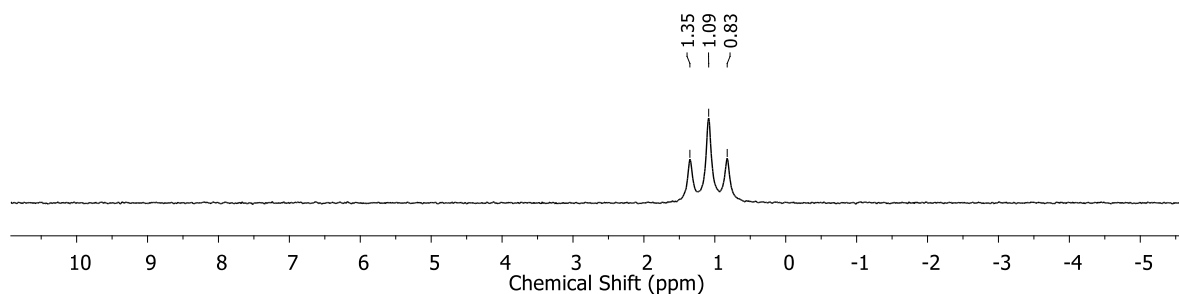


**Figure 8.16.**  $^{13}\text{C}$  NMR spectrum of **57** (100 MHz,  $\text{CDCl}_3$ ).

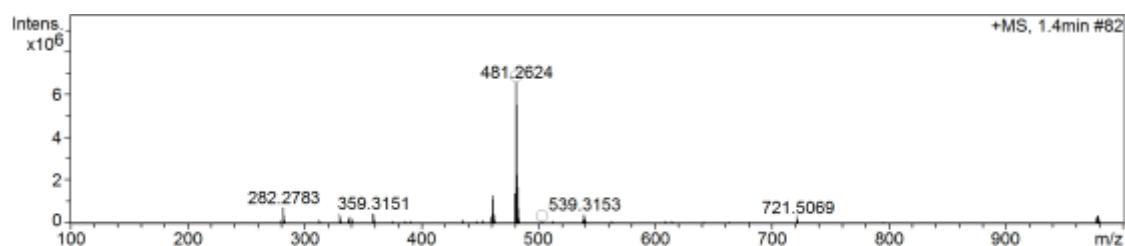


**Figure 8.17.**  $^{19}\text{F}$  NMR spectrum of **57** (376 MHz,  $\text{CDCl}_3$ ).



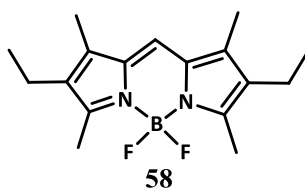


**Figure 8.18.**  $^{11}\text{B}$  NMR spectrum of **57** (128 MHz,  $\text{CDCl}_3$ ).

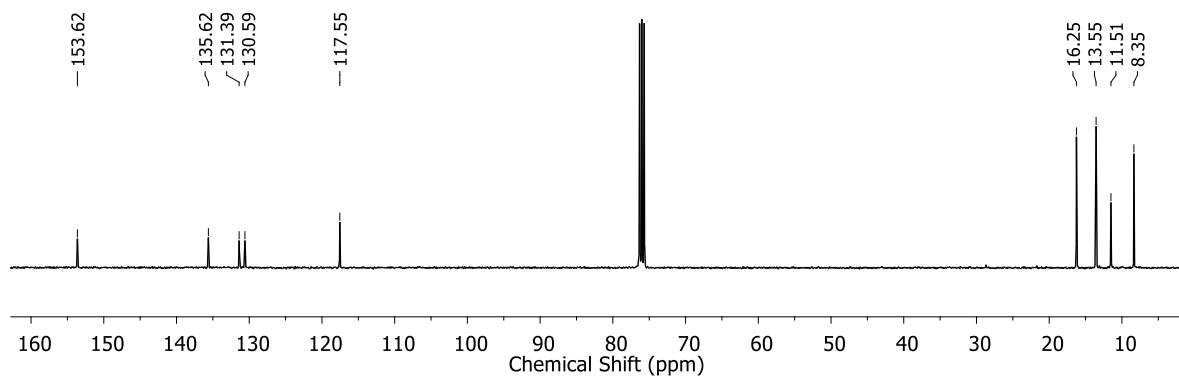


**Figure 8.19.** High resolution mass spectrum (positive mode) of **57**.

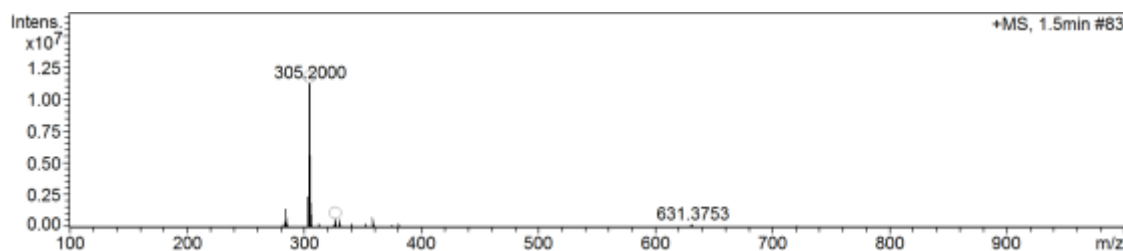
**8-H-1,3,5,7-tetramethyl-2,6-diethyl-4,4-difluoro-4-bora-3a,4a-diaza-s-indacene (58)**



$^1\text{H}$  NMR (400 MHz,  $\text{CDCl}_3$ )  $\delta$  (ppm): 6.94 (s; 1H); 2.49 (s, 6H), 2.37(q,  $J = 7.6$  Hz, 4H), 2.16(s, 6H), 1.06 (t,  $J = 7.6$  Hz, 6H);  $^{13}\text{C}$  NMR (100 MHz,  $\text{CDCl}_3$ )  $\delta$  (ppm): 153.63; 135.62 ; 131.40; 130.60; 117.55; 16.26; 13.56; 11.51 (t,  $J = 2.20$  Hz); 8.35;  $^{11}\text{B}$  NMR (128 MHz,  $\text{CDCl}_3$ )  $\delta$  (ppm): 0.74 (t,  $J = 33.54$  Hz);  $^{19}\text{F}$  NMR (376 MHz,  $\text{CDCl}_3$ )  $\delta$  (ppm): -146.31 (q,  $J = 33.84$  Hz, 2F); HRMS  $m/z$   $[\text{M}+\text{H}]^+$  calculated for  $\text{C}_{17}\text{H}_{24}\text{BF}_2\text{N}_2^+$ : 305.1995; Found: 305.2000.

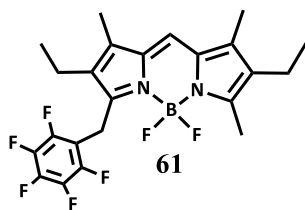


**Figure 8.20.**  $^{13}\text{C}$  NMR spectrum of **58** (100 MHz,  $\text{CDCl}_3$ ).



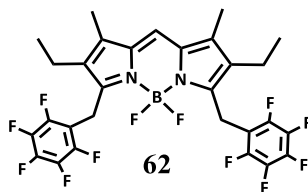
**Figure 8.21.** High resolution mass spectrum (positive mode) of **58**.

**8-H-3-(pentafluorobenzyl)-1,5,7-trimethyl-2,6-diethyl-4,4-difluoro-4-bora-3a,4a-diaza-s-indacene (60)**



$^1\text{H NMR}$  (400 MHz,  $\text{CDCl}_3$ )  $\delta$  (ppm): 7.00 (s; 1H); 4.33 (s, 2H), 2.57 (q,  $J = 7.6$  Hz, 2H), 2.49 (s, 3H), 2.38 (q,  $J = 7.6$  Hz, 2H), 2.18 (s, 3H), 1.79 (s, 3H), 1.14 (t,  $J = 7.6$  Hz, 3H); 1.05 (t,  $J = 7.6$  Hz, 3H);  $^{19}\text{F NMR}$  (376 MHz,  $\text{CDCl}_3$ )  $\delta$  (ppm): -141.54 (d,  $J = 20.4$  Hz 2F) 144.56 (q,  $J = 33.84$  Hz, 2F) 157.06 (t,  $J = 21.06$  Hz, 1F), -163.62 (td,  $J = 21.81, 7.14$  Hz, 2F); **ESI-MS**  $m/z$   $[\text{M}+\text{H}]^+$  calculated for  $\text{C}_{23}\text{H}_{23}\text{BF}_7\text{N}_2^+$ : 471.2; **Found:** 471.1 and 451.1 (-HF).

**8-H-3,5-(di(pentafluorobenzyl))-1,7-tetramethyl-2,6-diethyl-4,4-difluoro-4-bora-3a,4a-diaza-s-indacene (61)**



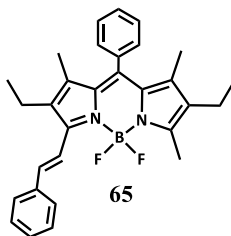
$^1\text{H NMR}$  (400 MHz,  $\text{CDCl}_3$ )  $\delta$  (ppm): 7.06 (s; 1H); 4.29 (s, 4H), 2.59 (q,  $J = 7.6$  Hz, 4H), 1.83 (s, 6H), 1.15 (t,  $J = 7.6$  Hz, 6H);  $^{19}\text{F NMR}$  (376 MHz,  $\text{CDCl}_3$ )  $\delta$  (ppm): -141.38 (m, 4F), 143.27 (q,  $J = 33.84$  Hz, 2F), 156.81 (t,  $J = 21.06$  Hz, 2F), -163.00 (td,  $J = 21.43, 7.52$  Hz, 2F); **ESI-MS**  $m/z$   $[\text{M}+\text{H}]^+$  calculated for  $\text{C}_{29}\text{H}_{21}\text{BF}_{12}\text{N}_2^+$ : 637.2; **Found:** 637.1 and 617.1 (-HF).

## 8.4.2. Chapter 3

### 8.4.2.1. General procedures for the synthesis of BODIPY **65** and **66**

BODIPY **53** (250 mg; 0.66 mmol), and 0.70 ml of benzaldehyde (6.9 mmol) were dissolved in 20 ml of toluene and refluxed in a mixture with 16 mg of *p*-TsOH.H<sub>2</sub>O (0.01mmol), 1 mL of piperidine (10 mmol) and 0.50 g of 4A molecular sieves for 40 hours. Then the mixture was washed with water for several times, the organic phase was evaporated, and purified by column chromatography on silica gel eluting with DCM-hexane (1:1). BODIPY **65** (3%) was obtained as magenta solid and BODIPY **66** (11%) was obtained as blue solid.

#### 8-phenyl-1,7,3-trimethyl-5-[(phenyl)styryl]-2,6-diethyl-4,4-difluoro-4-bora-3a,4a-diaza-s-indacene (**65**).



<sup>1</sup>H NMR (400 MHz, CDCl<sub>3</sub>) δ (ppm): 7.73 (d, J = 16.80 Hz, 1H), 7.59 (d, J = 7.20 Hz, 2H), 7.58-7.43 (m, 3H), 7.37 (t, J = 7.6 Hz, 2H), 7.32 – 7.26 (m, 3H), 7.19 (d, J = 16.80 Hz, 1H), 2.66-2.56 (m, 5H), 2.31 (q, J = 7.6 Hz, 2H), 1.35-1.25 (m, 6H), 1.15 (t, J = 7.6 Hz, 3H), 0.99 (t, J = 7.6 Hz, 3H); <sup>19</sup>F NMR (376 MHz, CDCl<sub>3</sub>) δ (ppm): -142.37 (q, J = 33.46 Hz, 2F); HRMS m/z [M+H]<sup>+</sup> calculated for C<sub>30</sub>H<sub>32</sub>BF<sub>2</sub>N<sub>2</sub><sup>+</sup>: 469.2627; Found: 469.2624.

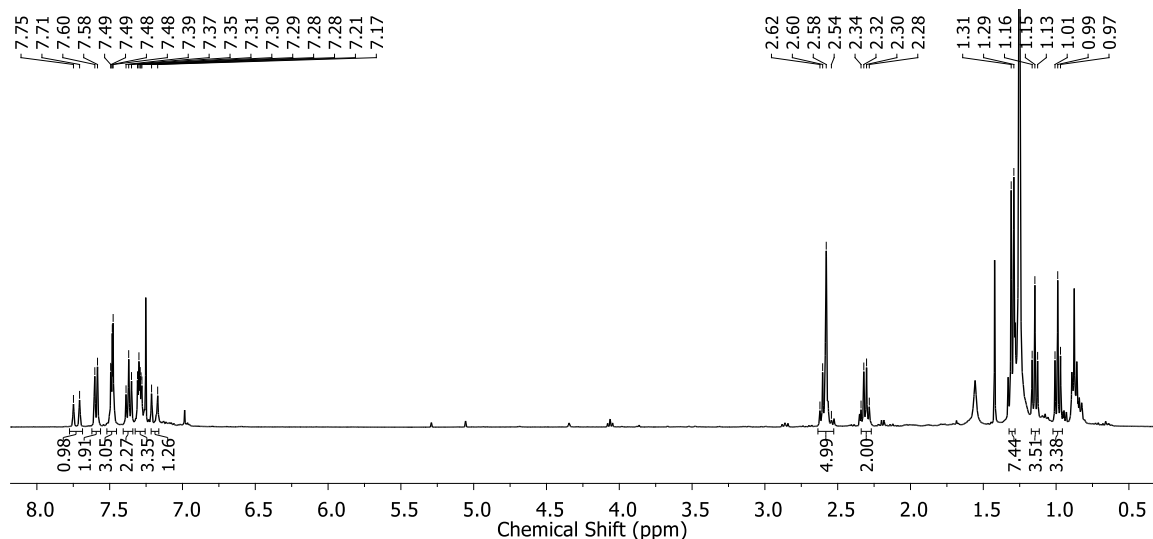
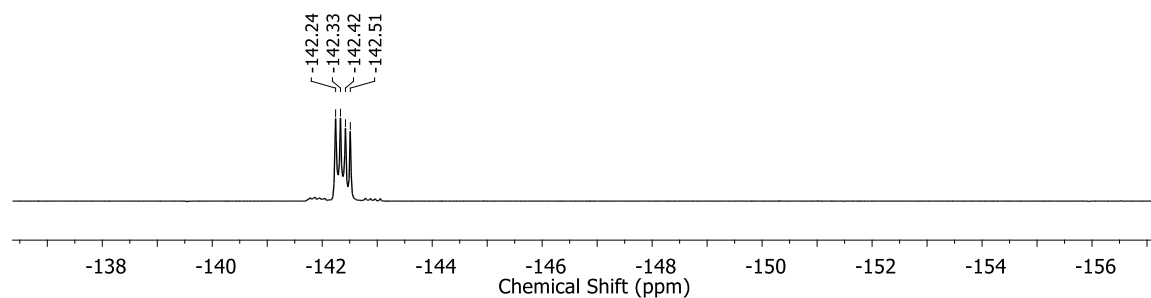
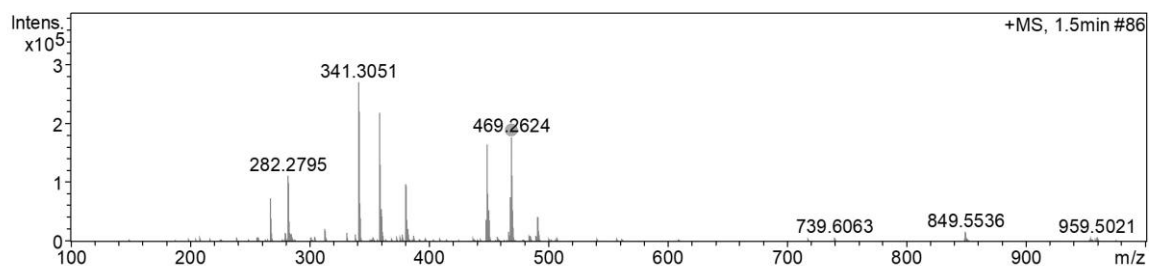


Figure 8.22. <sup>1</sup>H NMR spectrum of **65** (400 MHz, CDCl<sub>3</sub>).

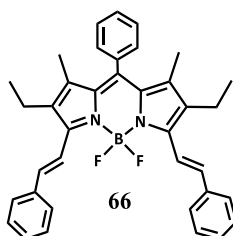


**Figure 8.23.**  $^{19}\text{F}$  NMR spectrum of **65** (376 MHz,  $\text{CDCl}_3$ ).

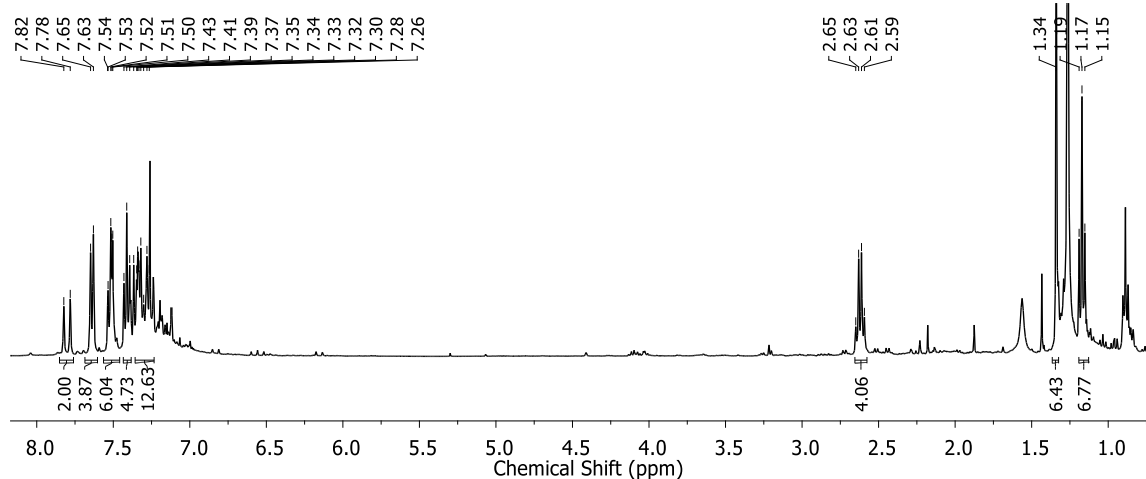


**Figure 8.24.** High resolution mass spectrum (positive mode) of **65**.

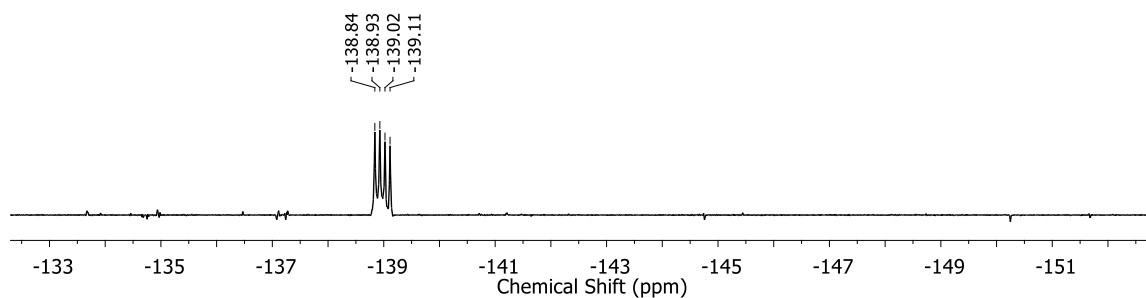
**8-phenyl-1,7-dimethyl-3,5-di-[(phenyl)styryl]-2,6-diethyl-4,4-difluoro-4-bora-3a,4a-diaza-s-indacene (**66**)**



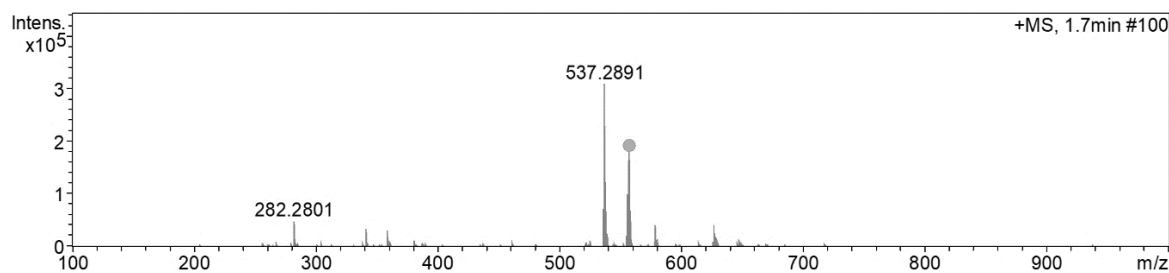
$^1\text{H}$  NMR (400 MHz,  $\text{CDCl}_3$ )  $\delta$  (ppm): 7.80 (d,  $J = 16.80$  Hz, 2H), 7.64 (d,  $J = 7.20$  Hz, 4H), 7.57-7.47 (m, 6H), 7.41 (t,  $J = 7.2$  Hz, 2H), 7.38–7.22 (m, 5H), 2.62 (q,  $J = 7.6$  Hz, 4H), 1.34 (s, 6H), 1.17 (t,  $J = 7.6$  Hz, 6H);  $^{19}\text{F}$  NMR (376 MHz,  $\text{CDCl}_3$ )  $\delta$  (ppm): -138.98 (q,  $J = 33.84$  Hz, 2F); HRMS  $m/z$   $[\text{M}+\text{H}]^+$  calculated for  $\text{C}_{37}\text{H}_{36}\text{BF}_2\text{N}_2^+$ : 557.2934; Found: 557.2945.



**Figure 8.25.**  $^1\text{H}$  NMR spectrum of **66** (400 MHz,  $\text{CDCl}_3$ ).



**Figure 8.26.**  $^{19}\text{F}$  NMR spectrum of **66** (376 MHz,  $\text{CDCl}_3$ ).

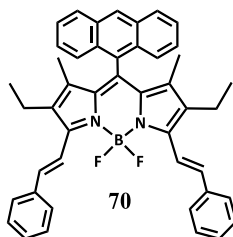


**Figure 8.27.** High resolution mass spectrum (positive mode) of **66**.

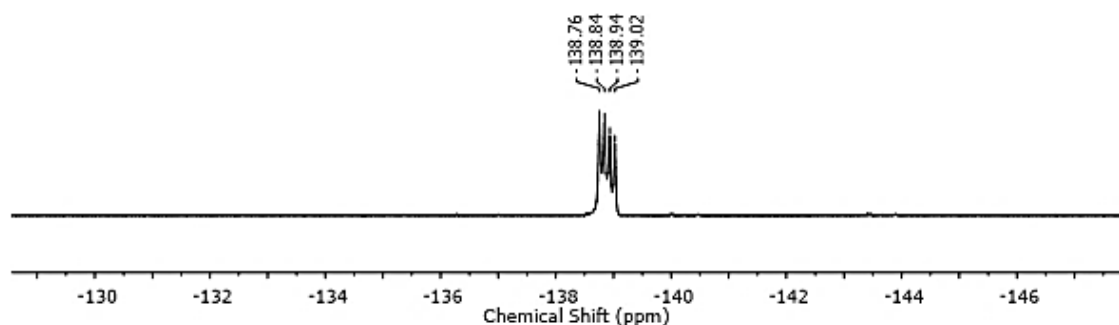
#### 8.4.2.2. General procedures for the synthesis of BODIPY **70**

BODIPY **57** (150 mg; 0.30 mmol), and 0.30 ml of benzaldehyde (3.0 mmol) were dissolved into 15 ml of toluene and refluxed with 12 mg of *p*-TsOH.H<sub>2</sub>O (0.008mmol), 0.5 mL of piperidine (51 mmol) and 0.50 g of 4A molecular sieves for 40 hours. Then the mixture was washed with water for several times, the organic phase was evaporated and purified by column chromatography on silica gel eluting with DCM-hexane (1:1). BODIPY **70** (9%) was obtained as blue solid.

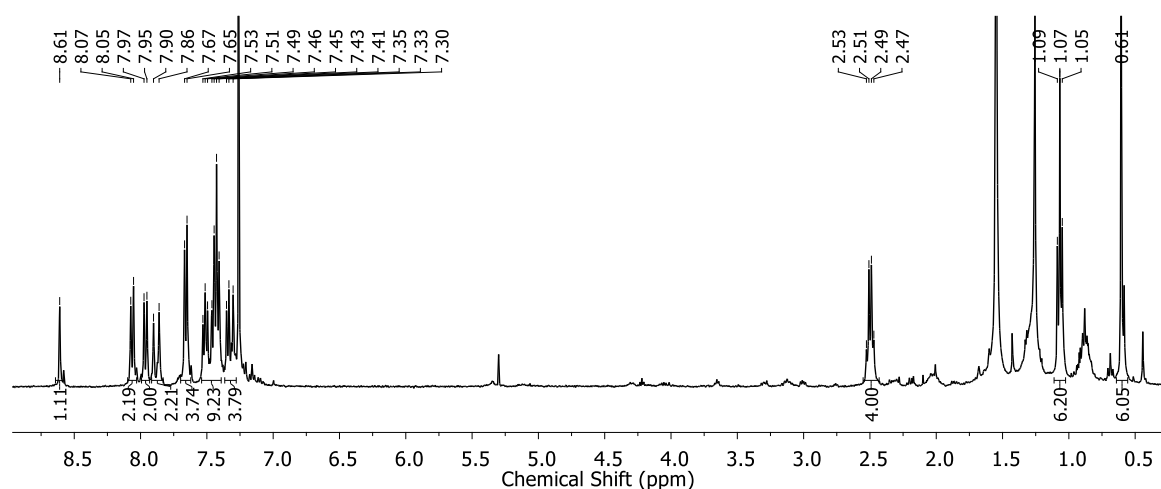
**8-anthracenyl-1,7-dimethyl-3,5-di-[(phenyl)styryl]-2,6-diethyl-4,4-difluoro-4-bora-3a,4a-diaza-s-indacene (70)**



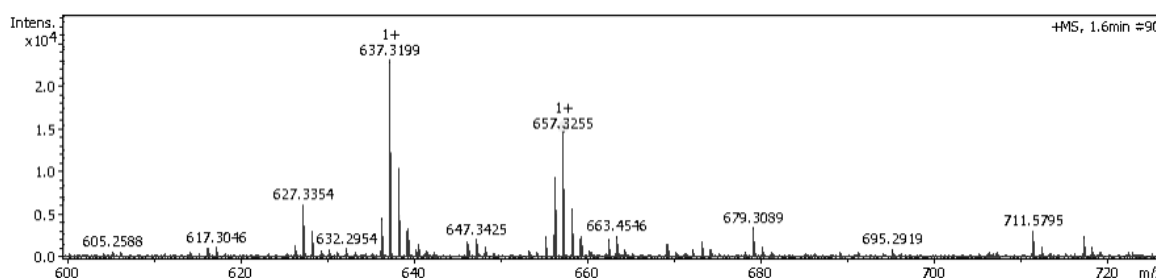
$^1\text{H}$  NMR (400 MHz,  $\text{CDCl}_3$ )  $\delta$  (ppm): 8.61 (s, 1H), 8.06 (d,  $J = 8.40$  Hz, 2H), 7.96 (d,  $J = 8.8$  Hz, 2H), 7.88 (d,  $J = 16.8$  Hz, 2H), 7.66 (d,  $J = 7.2$  Hz, 4H), 7.72-7.37 (m, 8H), 7.37-7.26 (m, 4H), 2.50 (q,  $J = 7.6$  Hz, 4H), 1.07 (t,  $J = 7.6$  Hz, 6H), 0.61 (s, 6H);  $^{19}\text{F}$  NMR (376 MHz,  $\text{CDCl}_3$ )  $\delta$  (ppm): -138.89 (q,  $J = 33.46$  Hz, 2F); HRMS  $m/z$   $[\text{M}+\text{H}]^+$  calculated for  $\text{C}_{45}\text{H}_{40}\text{BF}_2\text{N}_2^+$ : 657.3253; Found: 657.3255.



**Figure 8.28.**  $^{19}\text{F}$  NMR spectrum of 70 (376 MHz,  $\text{CDCl}_3$ ).



**Figure 8.29.**  $^1\text{H}$  NMR spectrum of 70 (400 MHz,  $\text{CDCl}_3$ ).

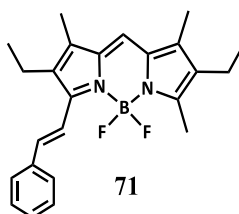


**Figure 8.30.** High resolution mass spectrum (positive mode) of **70**.

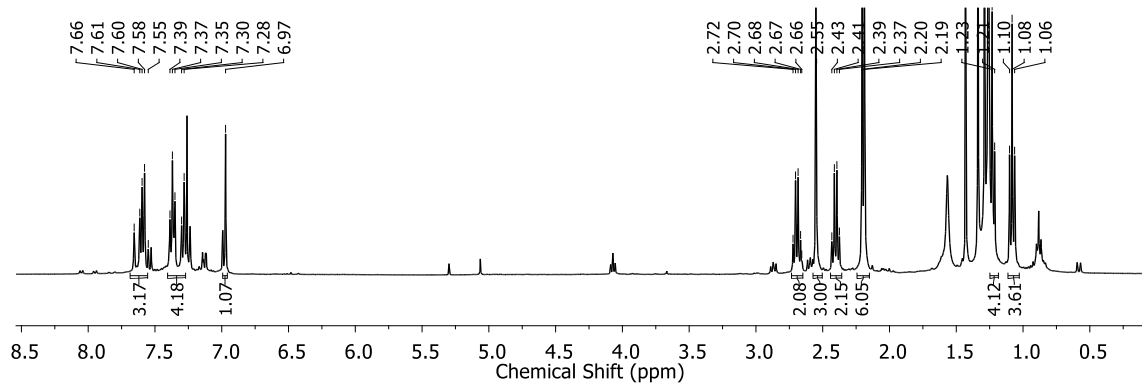
#### 8.4.2.3. General procedures for the synthesis of BODIPY **71** and **72**

BODIPY **58** (150 mg; 0.50mmol), and 0.50 ml of benzaldehyde (5.0 mmol) were dissolved into 15 ml of toluene and refluxed with 13 mg of *p*-TsOH.H<sub>2</sub>O (0.009mmol), 0.5 mL of piperidine (51 mmol) and 0.50 g of 4A molecular sieves for 40 hours. Then the mixture was washed with water for several times, the organic phase was evaporated, and purified by column chromatography on silica gel eluting with DCM-hexane (1:1). BODIPY **71** (4%) was obtained as magenta solid and BODIPY **72** (14%) was obtained as blue solid.

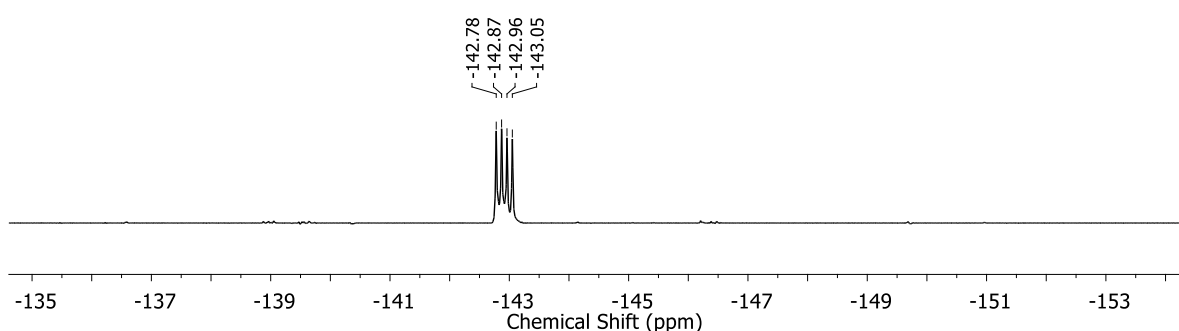
#### 1,7,3-trimethyl-5-[(phenyl)styryl]-2,6-diethyl-4,4-difluoro-4-bora-3a,4a-diaza-s-indacene (**71**)



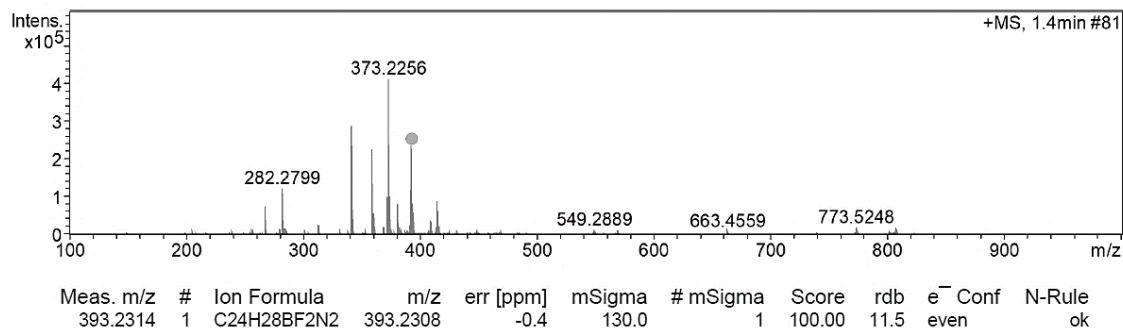
<sup>1</sup>H NMR (400 MHz, CDCl<sub>3</sub>) δ (ppm): 7.63 (d, J = 16.80 Hz, 1H), 7.53 (d, J = 7.6 Hz, 2H), 7.40-7.32 (m, 4H), 6.97 (s, 1H), 2.69 (q, J = 7.6 Hz, 2H), 2.55 (s, 3H), 2.40 (q, J = 7.6 Hz, 2H), 2.21-2.18 (m, 6H), 1.08(t, J = 7.6 Hz, 6H); <sup>11</sup>B NMR (128 MHz, CDCl<sub>3</sub>) δ (ppm): 0.89 (t, J = 33.82 Hz); <sup>19</sup>F NMR (376 MHz, CDCl<sub>3</sub>) δ (ppm): -142.92 (q, J = 34.21 Hz, 2F); HRMS m/z [M+H]<sup>+</sup> calculated for C<sub>24</sub>H<sub>28</sub>BF<sub>2</sub>N<sub>2</sub><sup>+</sup>: 393.2308; Found: 393.2314.



**Figure 8.31.**  $^1\text{H}$  NMR spectrum of **71** (400 MHz,  $\text{CDCl}_3$ ).

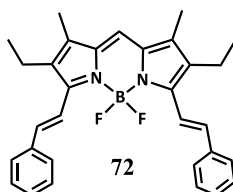


**Figure 8.32.**  $^{19}\text{F}$  NMR spectrum of **71** (376 MHz,  $\text{CDCl}_3$ ).



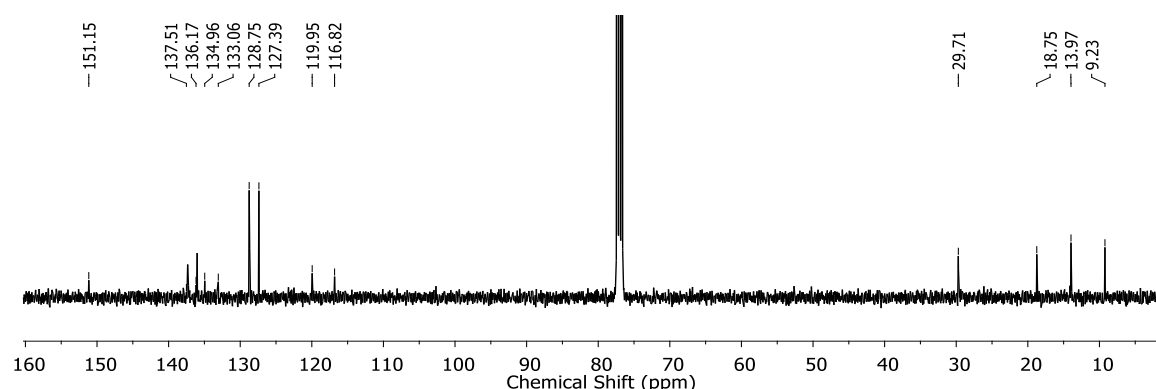
**Figure 8.33.** High resolution mass spectrum (positive mode) of **71**.

**1,7-dimethyl-3,5-di-[(phenyl)styryl]-2,6-diethyl-4,4-difluoro-4-bora-3a,4a-diaza-s-indacene (**72**)**

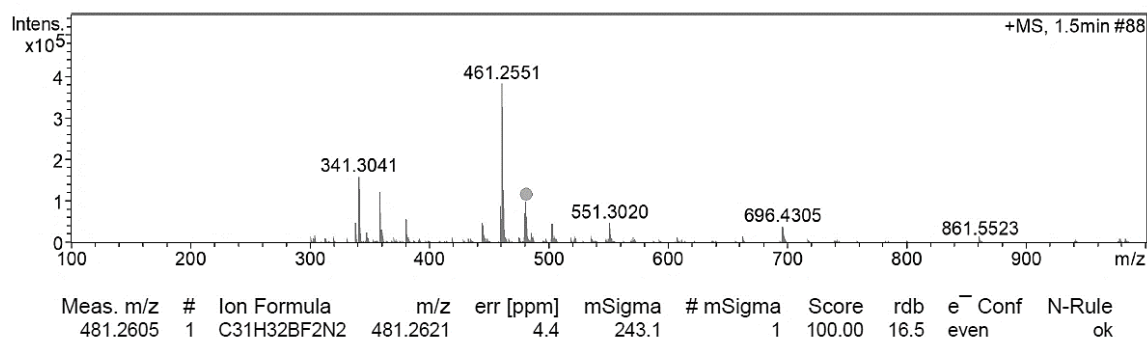




**$^1\text{H}$  NMR (400 MHz,  $\text{CDCl}_3$ )  $\delta$  (ppm):** 7.70 (d,  $J = 16.80$  Hz, 2H), 7.62 (d,  $J = 7.6$  Hz, 4H), 7.40 (t,  $J = 7.6$  Hz, 4H), 7.35-7.28 (m, 4H), 6.98 (s, 1H) 2.71 (q,  $J = 7.6$  Hz, 4H), 2.23 (s, 6H), 1.25 (m, 6H);  **$^{11}\text{B}$  NMR (128 MHz,  $\text{CDCl}_3$ )  $\delta$  (ppm):** 0.89 (t,  $J = 33.3$  Hz);  **$^{13}\text{C}$  NMR (100 MHz,  $\text{CDCl}_3$ )  $\delta$  (ppm):** 151.15, 137.51, 136.16, 134.96, 133.06, 128.75, 127.39, 119.95, 116.82, 29.82, 18.75, 13.97, 9.23;  **$^{11}\text{B}$  NMR (128 MHz,  $\text{CDCl}_3$ )  $\delta$  (ppm):** 1.09 (t,  $J = 33.28$  Hz);  **$^{19}\text{F}$  NMR (376 MHz,  $\text{CDCl}_3$ )  $\delta$  (ppm):** -139.52 (q,  $J = 33.84$  Hz, 2F). **HRMS  $m/z$   $[\text{M}+\text{H}]^+$  calculated for  $\text{C}_{24}\text{H}_{28}\text{BF}_2\text{N}_2^+$ :** 481.2621; **Found:** 481.2605.



**Figure 8.34.**  $^{13}\text{C}$  NMR spectrum of **72** (100 MHz,  $\text{CDCl}_3$ ).



**Figure 8.35.** High resolution mass spectrum (positive mode) of **72**.

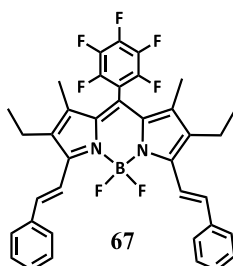
### 8.4.3. Chapter 4

#### 8.4.3.1. General procedures for the synthesis of BODIPY **67**, **74**, **76**, **78**

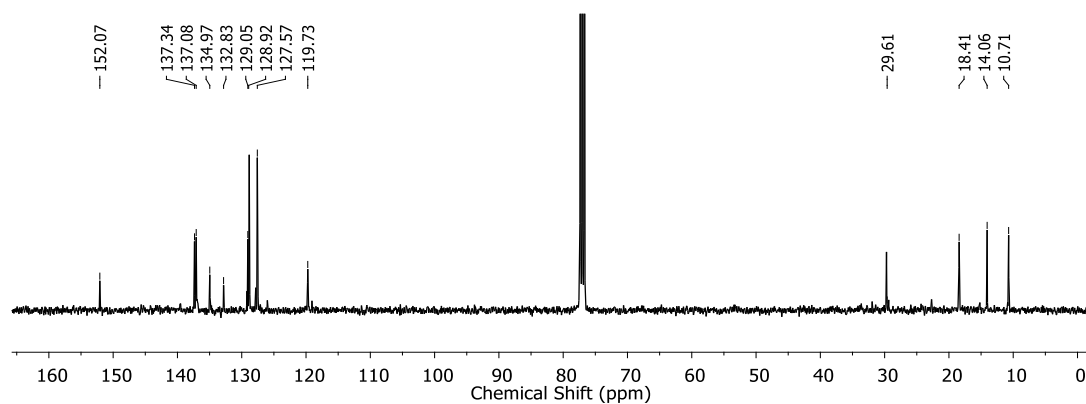
BODIPY **55** (250 mg; 0.54 mmol), 12.5 mg of p-TsOH.H<sub>2</sub>O, 10 equivalents of the respective aldehyde (benzaldehyde for **67**, 2-naphthaldehyde for **74**, 9-anthracenecarboxaldehyde for **76** and N-ethylcarbazole-3-carboxaldehyde for **78**) and 0.50 g of 4A molecular sieves were added to a 50 mL round-bottom flask with 20 ml of degassed and dried toluene. Then 0.25 mL of piperidine were added and the mixture was refluxed for 2 hours. Then, the mixture was washed with water for several times, the organic solvent was

removed under vacuum, and the obtained solid was purified by column chromatography on silica gel eluting with dichloromethane-hexane (v/v 1:1) and preparative TLC using dichloromethane-hexane (v/v 4:6). **67** (31 % yield), **74** (36 % yield), **76** (19 % yield) were obtained as dark-blue solid and **78** (72% yield) as dark-green solid.

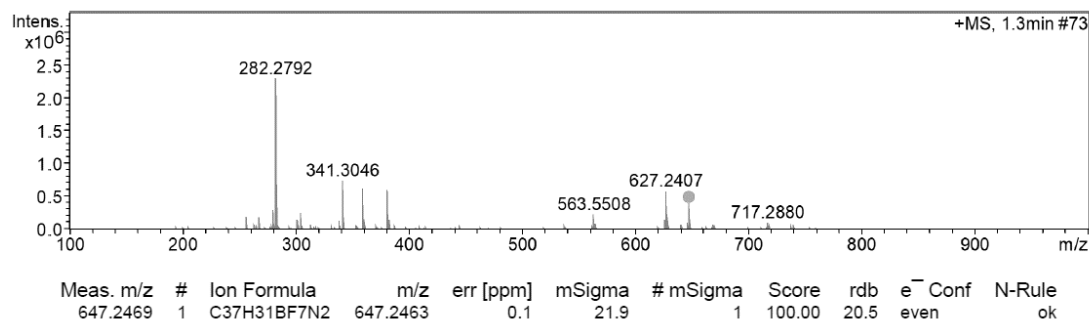
**8-(pentafluorophenyl)-1,7-dimethyl-3,5-di-[(phenyl)styryl]-2,6-diethyl-4,4-difluoro-bora-3a,4a-diaza-s-indacene (67)**



$^1\text{H NMR}$  (400 MHz,  $\text{CDCl}_3$ )  $\delta$  (ppm): 7.78 (d,  $J = 16.8$  Hz, 2H), 7.64 (d,  $J = 7.6$  Hz, 4H), 7.42 (t,  $J = 7.6$  Hz, 4H), 7.36 – 7.26 (m, 4H), 2.66 (q,  $J = 7.6$  Hz, 4H), 1.58 (s, 6H) 1.21 (t,  $J = 7.6$  Hz, 6H);  $^{13}\text{C NMR}$  (100 MHz,  $\text{CDCl}_3$ )  $\delta$  (ppm): 152.07; 137.34; 137.08; 134.97; 132.83; 129.05; 128.84; 127.92; 127.57; 119.73; 29.61; 18.41; 14.06; 10.71;  $^{11}\text{B NMR}$  (128 MHz,  $\text{CDCl}_3$ )  $\delta$  (ppm): 1.14 (t,  $J = 33.28$  Hz);  $^{19}\text{F NMR}$  (376 MHz,  $\text{CDCl}_3$ )  $\delta$  (ppm): -138.71 (dd,  $J = 7.52, 22.56$  Hz 2F), -138.98 (q,  $J = 33.84$  Hz, 2F), -150.79 (t,  $J = 22.56$  Hz, 1F), -159.71 (td,  $J = 7.52, 22.56$  Hz 2F); HRMS  $m/z$   $[\text{M}+\text{H}]^+$  calculated for  $\text{C}_{37}\text{H}_{30}\text{BF}_7\text{N}_2^+$ : 647.2463; Found: 647.2469.

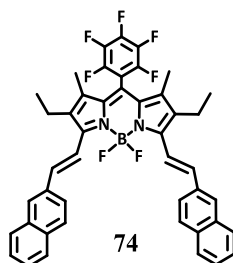


**Figure 8.36.**  $^{13}\text{C NMR}$  spectrum of **67** (100 MHz,  $\text{CDCl}_3$ ).

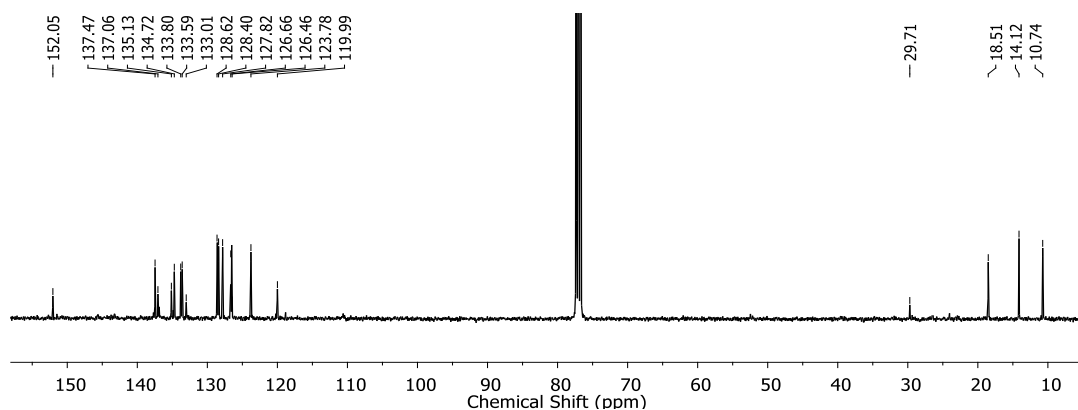


**Figure 8.37.** High resolution mass spectrum (positive mode) of **67**.

**8-(pentafluorophenyl)-1,7-dimethyl-3,5-di-[(naphthalen-2-yl)vinyl]-2,6-diethyl-4,4-difluoro-4-bora-3a,4a-diaza-s-indacene (**74**)**



**<sup>1</sup>H NMR (400 MHz, CDCl<sub>3</sub>) δ (ppm):** 8.00 – 7.80 (m, 12 H), 7.56 – 7.46 (m, 6H), 2.72 (q, J = 7.6 Hz, 4H), 1.60 (s, 6H) 1.27 (t, J = 7.6 Hz, 6H); **<sup>13</sup>C NMR (CDCl<sub>3</sub>) δ (ppm):** 152.05; 137.47; 137.06; 135.13; 134.72; 133.80; 133.59; 133.01; 128.62; 128.40; 127.82; 126.66; 126.53; 123.78; 119.99; 29.71; 18.51; 14.12; 10.74; **<sup>11</sup>B NMR (128 MHz, CDCl<sub>3</sub>) δ (ppm):** 1.16 (t, J = 33.28 Hz); **<sup>19</sup>F NMR (376 MHz, CDCl<sub>3</sub>) δ (ppm):** -138.36 – -139.31 (m, 4F), 150.76 (t, J = 22.56 Hz, 1F), 159.69 (td, 22.56 Hz, 2F); **HRMS m/z [M+H]<sup>+</sup> calculated for C<sub>45</sub>H<sub>34</sub>BF<sub>7</sub>N<sub>2</sub><sup>+</sup>: 747.2776 ; Found: 747.2763.**



**Figure 8.38.** <sup>13</sup>C NMR spectrum of **74** (100 MHz, CDCl<sub>3</sub>).

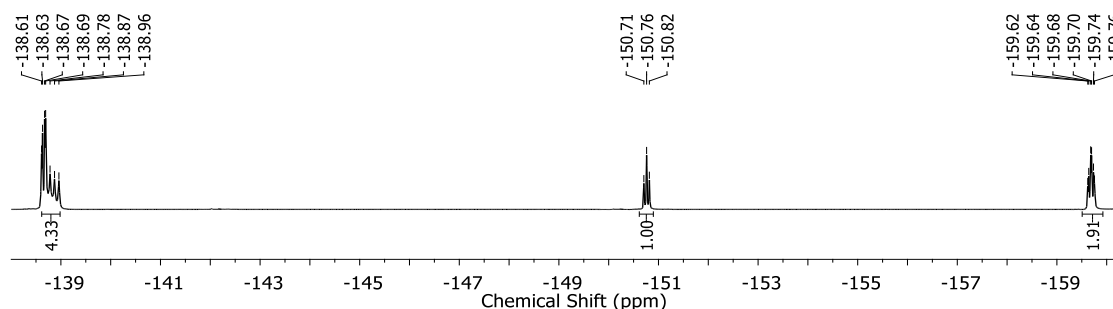


Figure 8.39.  $^{19}\text{F}$  NMR spectrum of **74** (376 MHz,  $\text{CDCl}_3$ ).

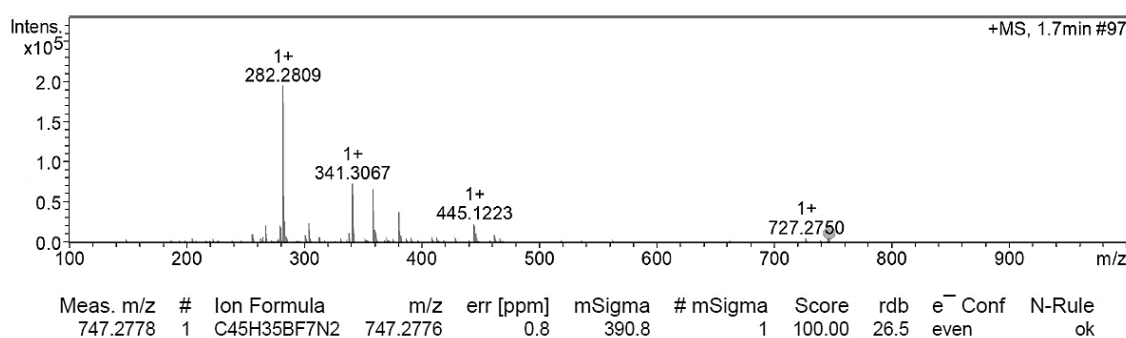
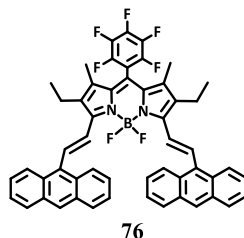
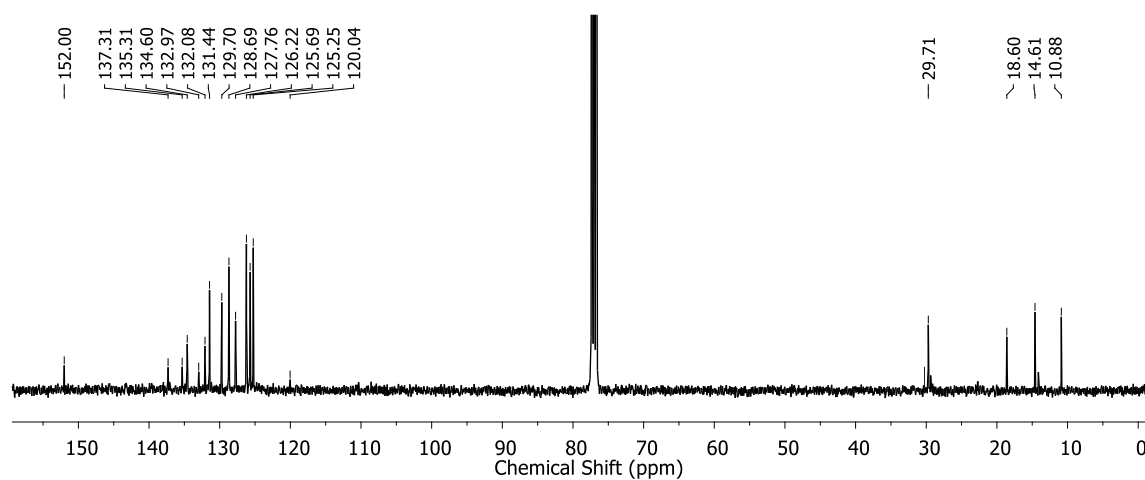


Figure 8.40. High resolution mass spectrum (positive mode) of **74**.

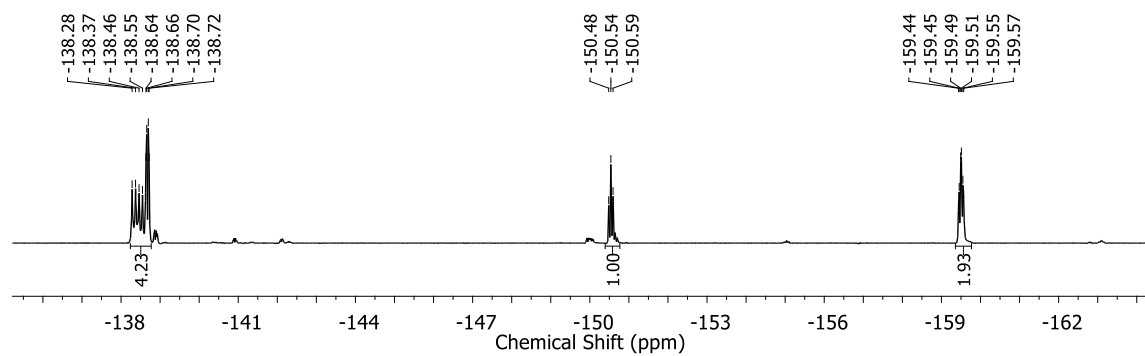
**8-(pentafluorophenyl)-1,7-dimethyl-3,5-di-[(anthracen-9-yl)vinyl]-2,6-diethyl-4,4-difluoro-4-bora-3a,4a-diaza-s-indacene (**76**)**



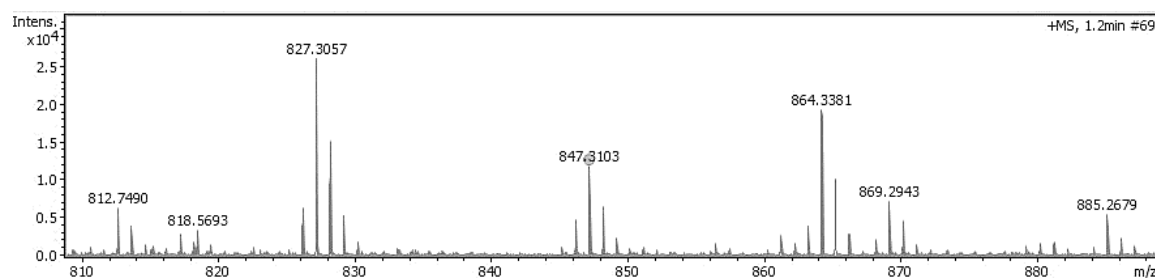
$^1\text{H}$  NMR (400 MHz,  $\text{CDCl}_3$ )  $\delta$  (ppm): 8.43 (d,  $J = 8.80$  Hz, 4H), 8.38 (s, 2H), 8.28 (d,  $J = 17.2$  Hz, 2H), 7.96 (d,  $J = 8.00$  Hz, 4H), 7.56 (d,  $J = 17.2$  Hz, 2H), 7.43 – 7.32 (m, 8H), 2.83 (q,  $J = 7.6$  Hz, 4H), 1.68 (s, 6H), 1.33 (t,  $J = 7.6$  Hz, 6H);  $^{13}\text{C}$  NMR ( $\text{CDCl}_3$ )  $\delta$  (ppm): 152.00, 137.31, 135.31, 134.60, 132.97, 132.08, 131.44, 129.70, 128.69, 127.76, 126.22, 125.69, 125.25, 120.04, 29.71, 18.60, 14.61, 10.89;  $^{11}\text{B}$  NMR (128 MHz,  $\text{CDCl}_3$ )  $\delta$  (ppm): 1.27 (t,  $J = 33.28$  Hz);  $^{19}\text{F}$  NMR (376 MHz,  $\text{CDCl}_3$ )  $\delta$  (ppm): -138.42 (q,  $J = 33.84$  Hz, 2F), -138.68 (dd,  $J = 7.52, 22.56$  Hz 2F), -150.54 (t,  $J = 22.56$  Hz, 1F), -159.50 (td,  $J = 7.52, 22.56$  Hz 2F); HRMS  $m/z$   $[\text{M}+\text{H}]^+$  calculated for  $\text{C}_{53}\text{H}_{38}\text{BF}_7\text{N}_2^+$ : 847.3089; Found: 847.3102.



**Figure 8.41.**  $^{13}\text{C}$  NMR spectrum of **76** (100 MHz,  $\text{CDCl}_3$ ).

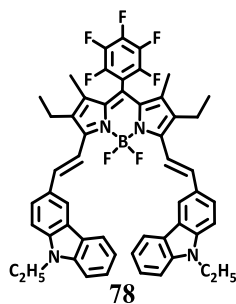


**Figure 8.42.**  $^{19}\text{F}$  NMR spectrum of **76** (376 MHz,  $\text{CDCl}_3$ ).

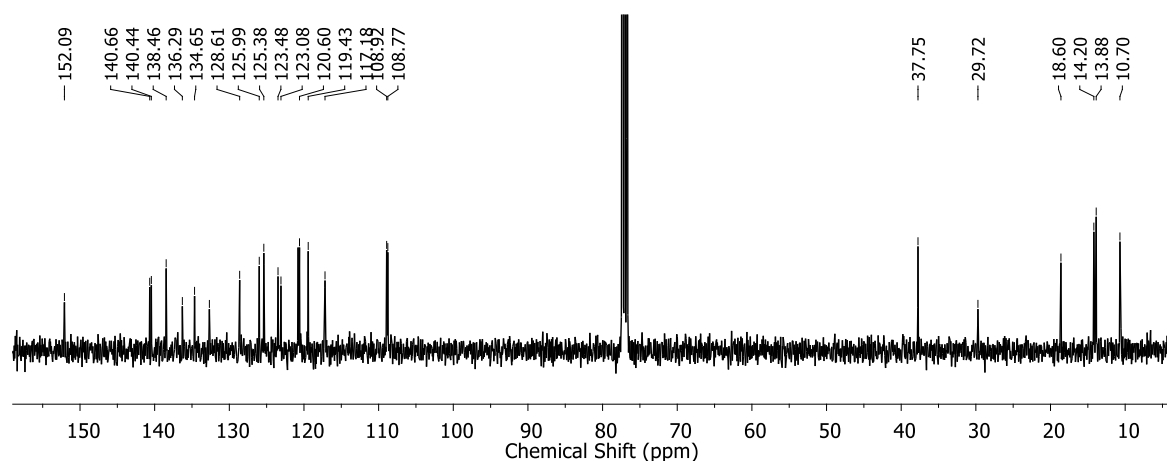


**Figure 8.43.** High resolution mass spectrum (positive mode) of **76**.

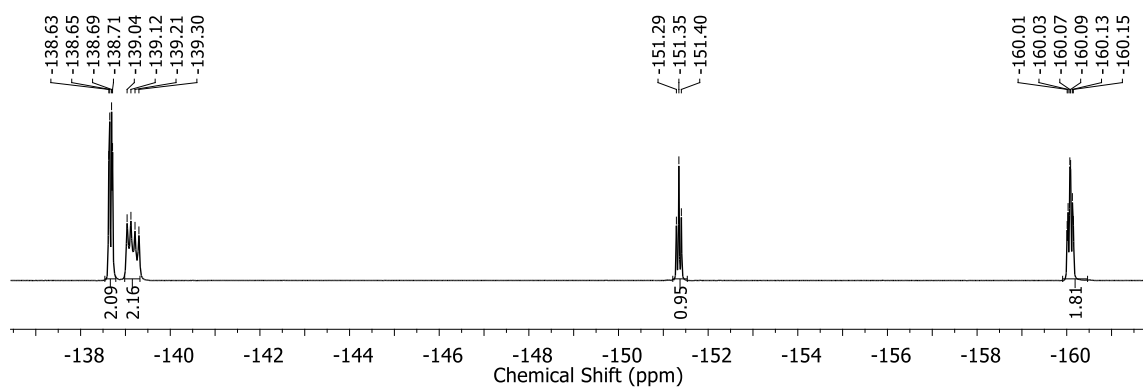
**8-(pentafluorophenyl)-1,7-dimethyl-3,5-di-[(9-ethyl-carbazol-3-yl)vinyl]-2,6-diethyl-4,4-difluoro-4-bora-3a,4a-diaza-s-indacene (78)**



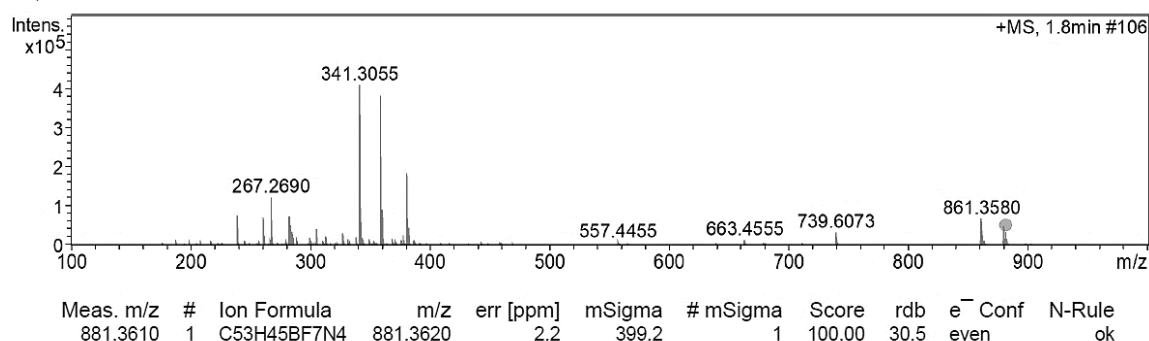
**$^1\text{H}$  NMR (400 MHz,  $\text{CDCl}_3$ )  $\delta$  (ppm):** 8.31 (s, 2H), 8.19 (d,  $J = 7.6$  Hz, 2H), 7.96–7.80 (m, 4H), 7.57 (d,  $J = 16.40$  Hz, 2H), 7.50 (t,  $J = 7.20$  Hz, 2H), 7.43 (d,  $J = 7.20$  Hz, 4H), 7.30 – 7.20 (m, 2H), 4.39 (q,  $J = 7.2$  Hz, 4H), 2.74 (q,  $J = 7.6$  Hz, 4H), 1.6 (s, 6H), 1.46 (t,  $J = 7.2$  Hz, 6H), 1.29 (t,  $J = 7.6$  Hz, 6H);  **$^{13}\text{C}$  NMR ( $\text{CDCl}_3$ )  $\delta$  (ppm):** 152.09, 140.66, 138.46, 136.29, 134.65, 132.67, 132.67, 128.61, 125.99, 125.38, 123.48, 123.08, 120.73 (d, 25 Hz), 119.43, 117.18, 108.85 (d, 14 Hz), 37.75, 29.72, 18.60, 14.04 (d, 32 Hz), 10.70;  **$^{11}\text{B}$  NMR (128 MHz,  $\text{CDCl}_3$ )  $\delta$  (ppm):** 1.38 (t,  $J = 33.28$  Hz);  **$^{19}\text{F}$  NMR (376 MHz,  $\text{CDCl}_3$ )  $\delta$  (ppm):** -138.67 (dd,  $J = 7.52, 22.56$  Hz 2F), -139.26 (q,  $J = 33.84$  Hz, 2F), -151.35 (t,  $J = 22.56$  Hz, 1F), -160.08 (td,  $J = 7.52, 22.56$  Hz 2F); **HRMS  $m/z$   $[\text{M}+\text{H}]^+$  calculated for  $\text{C}_{53}\text{H}_{45}\text{BF}_7\text{N}_4^+$ :** 881.3620; **Found:** 881.3610.



**Figure 8.44.**  $^{13}\text{C}$  NMR spectrum of **78** (100 MHz,  $\text{CDCl}_3$ ).



**Figure 8.45.**  $^{19}\text{F}$  NMR spectrum of **78** (376 MHz,  $\text{CDCl}_3$ ).

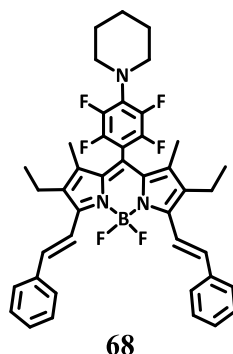


**Figure 8.46.** High resolution mass spectrum (positive mode) of **78**.

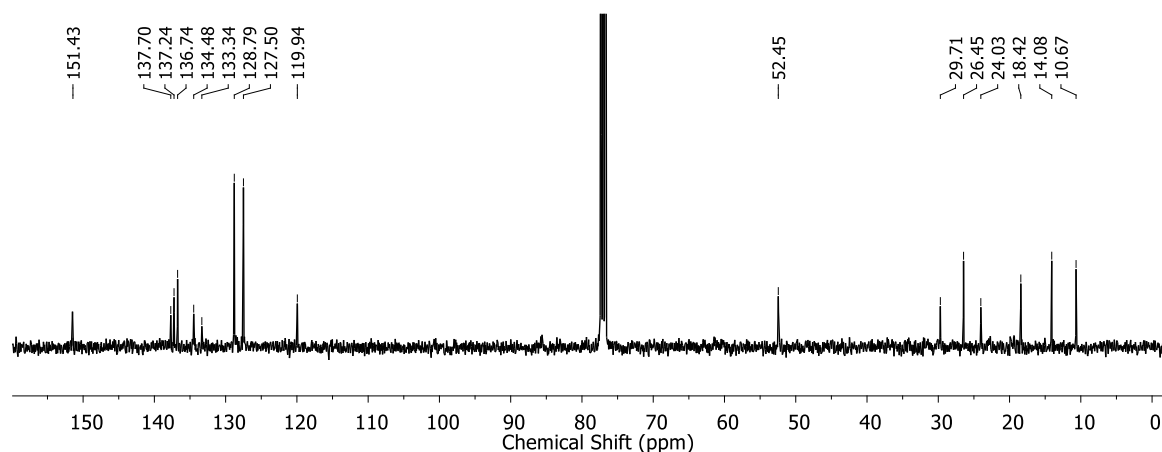
#### 8.4.3.2. General procedures for the synthesis of BODIPY **68**, **75**, **77**

BODIPY **55** (100 mg; 0.22 mmol), 5 mg of p-TsOH.H<sub>2</sub>O, 10 equivalents of the respective aldehyde (benzaldehyde for **68**, 2-naphthaldehyde for **75**, 9-anthracenecarboxaldehyde for **77**) and 0.50 g of 4A molecular sieves were added to a 50 mL round-bottom flask with 10 ml of degassed and dried toluene. Then 1 mL of piperidine was added and the mixture was refluxed. After 24 hours, the mixture was washed with water for several times, the organic phase solvent was removed under vacuum, and the obtained solid was purified by column chromatography on silica gel eluting with DCM-hexane (v/v 1:1). **68** (34 % yield), **74** (24 % yield), **76** (14 % yield) were obtained as dark-blue solids.

**8-((2,3,5,6-tetrafluoro-4-(piperidin-1-yl)phenyl)-1,7-dimethyl-3,5-di-[(phenyl)styryl]-2,6-diethyl-4,4-difluoro-4-bora-3a,4a-diaza-s-indacene (68)**



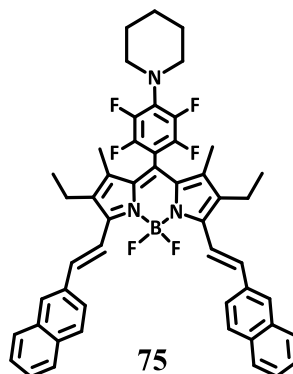
**<sup>1</sup>H NMR (400 MHz, CDCl<sub>3</sub>)**  $\delta$  (ppm): 7.78 (d, *J* = 16.8 Hz, 2H), 7.65 (d, *J* = 8 Hz, 4H), 7.41 (t, *J* = 8 Hz, 4H), 7.37 – 7.26 (m, 4H), 3.38 – 3.28 (m, 4H), 2.66 (q, *J* = 7.6 Hz, 4H), 1.79-1.63 (m, 6H), 1.62 (s, 6H) 1.21 (t, *J* = 7.6 Hz, 6H); **<sup>13</sup>C NMR (100 MHz, CDCl<sub>3</sub>)**  $\delta$  (ppm): 151.43, 137.69, 137.24, 136.74, 134.48, 133.34, 128.84, 127.50, 119.94, 52.45, 29.71, 26.46, 24.03, 18.42, 14.08, 10.67; **<sup>11</sup>B NMR (128 MHz, CDCl<sub>3</sub>)**  $\delta$  (ppm): 1.14 (t, *J* = 33.28 Hz); **<sup>19</sup>F NMR (376 MHz, CDCl<sub>3</sub>)**  $\delta$  (ppm): -138.86 (q, *J* = 33.84 Hz, 2F), -142.10 (dd, *J* = 7.52, 22.56 Hz 2F), -150.18 (dd, *J* = 7.52, 22.56 Hz 2F); **Anal Calculated for C<sub>42</sub>H<sub>40</sub>BF<sub>6</sub>N<sub>3</sub>**: C, 70.89; H, 5.67; N, 5.91; **Found**: C, 70.89; H, 6.89; N, 5.81.



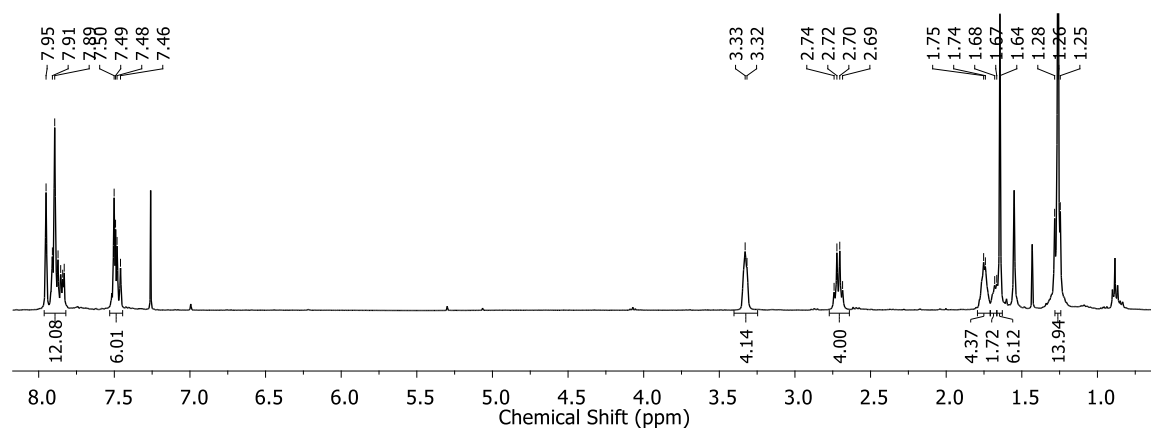
**Figure 8.47.** <sup>13</sup>C NMR spectrum of **68** (100 MHz, CDCl<sub>3</sub>).



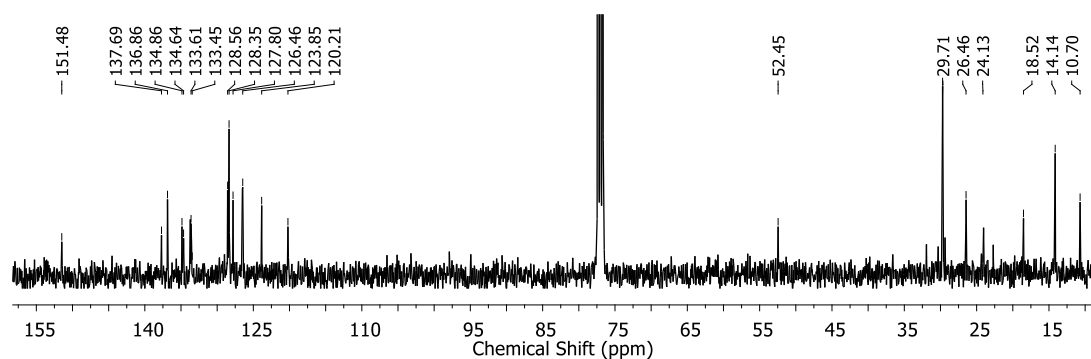
**8-((2,3,5,6-tetrafluoro-4-(piperidin-1-yl)phenyl)-1,7-dimethyl-3,5-di-[(naphthalen-2-yl)vinyl]-2,6-diethyl-4,4-difluoro-4-bora-3a,4a-diaza-s-indacene (75)**



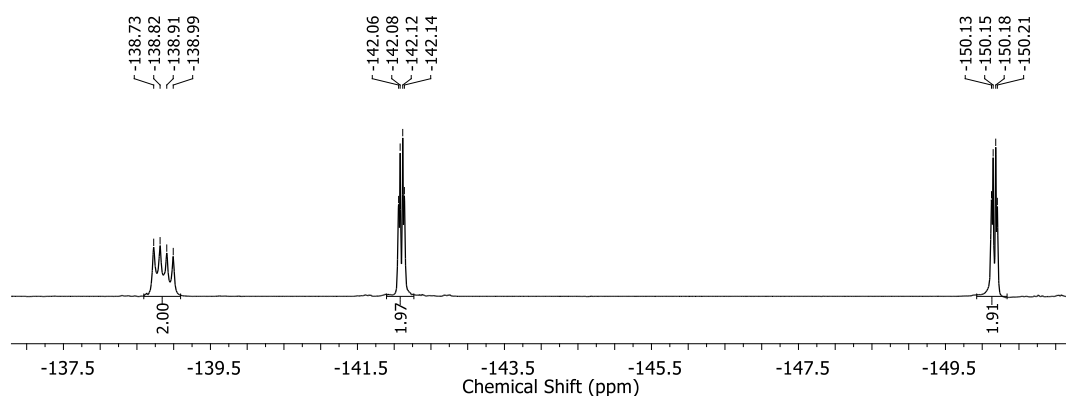
$^1\text{H NMR}$  (400 MHz,  $\text{CDCl}_3$ )  $\delta$  (ppm): 7.98 – 7.82 (m, 12H), 7.55 – 7.43 (m, 6H), 3.37 – 2.27 (m, 4H), 2.71 (q,  $J = 7.6$  Hz, 4H), 1.80 – 1.70 (m, 4H), 1.70 – 1.66 (m, 2H), 1.64 (s, 6H) 1.30 – 1.24 (m, 6H);  $^{13}\text{C NMR}$  ( $\text{CDCl}_3$ )  $\delta$  (ppm): 151.48, 137.69, 136.87, 134.87, 133.72, 133.62, 128.55, 128.36, 127.80, 126.52, 123.85, 120.21, 52.51, 29.71, 26.47, 24.04, 18.52, 14.14, 10.70.  $^{11}\text{B NMR}$  (128 MHz,  $\text{CDCl}_3$ )  $\delta$  (ppm): 1.16 (t,  $J = 33.28$  Hz);  $^{19}\text{F NMR}$  (376 MHz,  $\text{CDCl}_3$ )  $\delta$  (ppm): -138.97 (q,  $J = 33.84$  Hz, 2F), -142.10 (dd,  $J = 7.52, 22.56$  Hz 2F), -150.16 (dd,  $J = 7.52, 22.56$  Hz 2F) Anal Calculated for  $\text{C}_{50}\text{H}_{44}\text{BF}_6\text{N}_3$ : C, 73.98; H, 5.46; N, 5.18; Found: C, 73.87; H, 5.62; N, 4.98.



**Figure 8.48.**  $^1\text{H NMR}$  spectrum of **75** (400MHz,  $\text{CDCl}_3$ ).

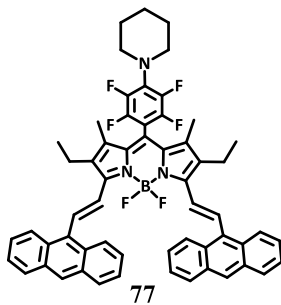


**Figure 8.49.**  $^{13}\text{C}$  NMR spectrum of **75** (100 MHz,  $\text{CDCl}_3$ ).



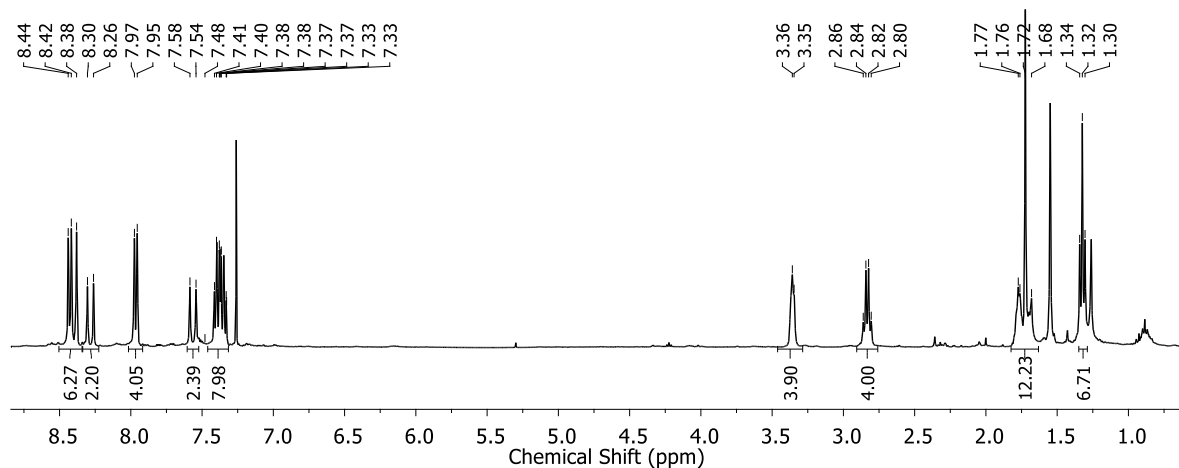
**Figure 8.50.**  $^{19}\text{F}$  NMR spectrum of **75** (376 MHz,  $\text{CDCl}_3$ ).

**8-((2,3,5,6-tetrafluoro-4-(piperidin-1-yl)phenyl)-1,7-dimethyl-3,5-di-[(anthracen-9-yl)vinyl]-2,6-diethyl-4,4-difluoro-4-bora-3a,4a-diaza-s-indacene (**76**)**

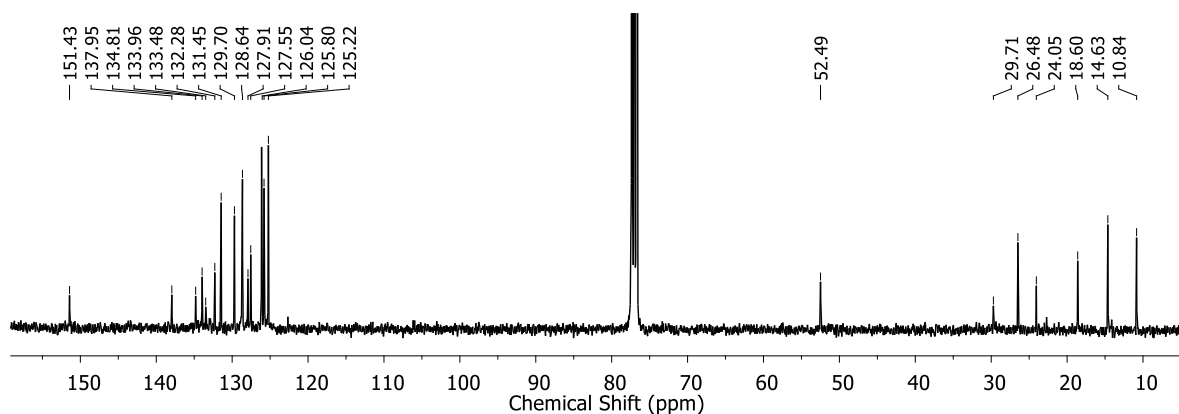


$^1\text{H}$  NMR (400 MHz,  $\text{CDCl}_3$ )  $\delta$  (ppm): 8.43 (d,  $J = 8.40$  Hz, 4H), 8.38 (s, 2H), 8.28 (d,  $J = 17.20$  Hz, 2H), 7.96 (d,  $J = 8.00$  Hz, 4H), 7.56 (d,  $J = 17.20$  Hz, 2H), 7.45 – 7.30 (m, 8H), 3.45 – 3.30 (m, H), 2.83 (q,  $J = 7.6$  Hz, 4H), 1.84 – 1.62 (m, H), 1.33 (t,  $J = 7.6$  Hz, 6H);  $^{13}\text{C}$  NMR ( $\text{CDCl}_3$ )  $\delta$  (ppm): 151.43, 137.95, 134.81, 133.96, 133.48, 132.28, 131.45, 129.70, 128.64, 127.91, 127.55, 126.04, 125.80, 125.22, 52.49, 29.71, 26.48, 24.05, 18.60, 14.63, 10.84.  $^{11}\text{B}$  NMR (128 MHz,  $\text{CDCl}_3$ )  $\delta$  (ppm): 1.27 (t,  $J = 33.28$  Hz);  $^{19}\text{F}$  NMR (376 MHz,  $\text{CDCl}_3$ )  $\delta$  (ppm): -138.45 (q,  $J = 33.84$  Hz, 2F), -142.11 (dd,  $J = 7.52, 22.56$  Hz 2F),

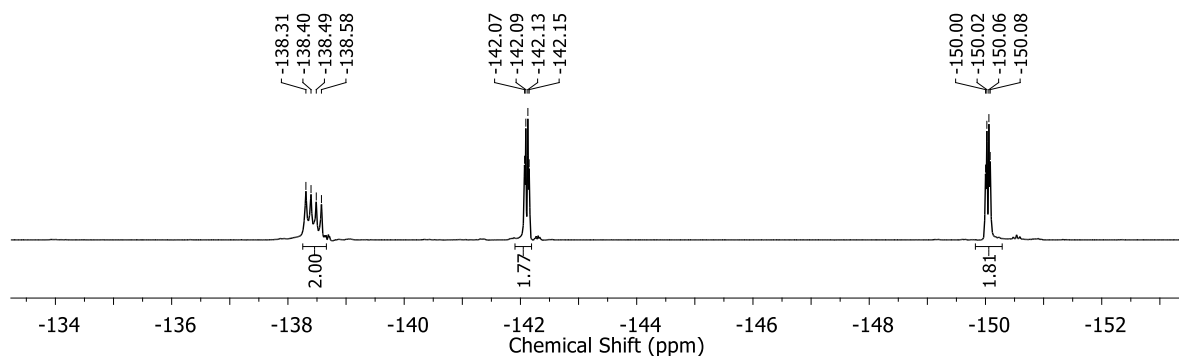
-150.04 (dd,  $J = 7.52, 22.56$  Hz 2F) **Anal Calculated for  $C_{58}H_{48}BF_6N_3$** : C, 76.40; H, 5.31; N, 4.61; **Found**: C, 76.32; H, 5.62; N, 4.42.



**Figure 8.51.**  $^1\text{H}$  NMR spectrum of **77** (400 MHz,  $\text{CDCl}_3$ ).



**Figure 8.52.**  $^{13}\text{C}$  NMR spectrum of **77** (100 MHz,  $\text{CDCl}_3$ ).

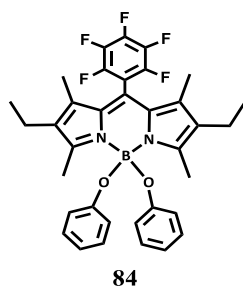


**Figure 8.53.**  $^{19}\text{F}$  NMR spectrum of **77** (376 MHz,  $\text{CDCl}_3$ ).

## 8.4.5. Chapter 5

## 8.4.4.1. General procedures for the synthesis of 4S-BDP (84-90)

Into a solution of **53** or **55** in dry dichloromethane was added 5 equivalents of aluminium trichloride, and the mixture was refluxed for 10 min under a nitrogen atmosphere. Then, 5 equivalents of the respective alcohol reagent (phenol for **84** and **89**, catechol for **85** and **90**, methanol for **86**, pentafluorophenol for **87** and resorcinol for **88**) was added to the purple solution, and the resulting mixture was stirred for 20 min. After that, the reaction mixture was washed successively with water (30 mL) and brine (30 mL). The layers were separated, the organic layer was dried with anhydrous sodium sulfate and concentrated under reduced pressure. The crude product was purified by silica gel column chromatography using a mixture of dichloromethane and hexane (1 : 1) as eluent.

**8-(pentafluorophenyl)-1,3,5,7-tetramethyl-2,6-diethyl-4,4-diphenoxy-4-bora-3a,4a-diaza-s-indacene (84)**


$^1\text{H}$  NMR (400 MHz,  $\text{CDCl}_3$ )  $\delta$  (ppm): (t,  $J = 7.2$  Hz, 4H), 6.76 (t,  $J = 7.2$  Hz, 2H), 6.65 (d,  $J = 8.8$  Hz, 4H), 2.52 (s, 6H), 2.18(q,  $J = 7.6$  Hz, 4H), 1.53 (s, 6H), 0.86 (t,  $J = 7.6$  Hz, 6H);  $^{13}\text{C}$  NMR (100 MHz,  $\text{CDCl}_3$ )  $\delta$  (ppm): 157.01, 156.48, 136.34, 134.50, 130.97, 129.10, 119.50, 118.40, 17.08, 14.47, 13.05, 11.02;  $^{11}\text{B}$  NMR (128 MHz,  $\text{CDCl}_3$ )  $\delta$  (ppm): 0.82 (s);  $^{19}\text{F}$  NMR (376 MHz,  $\text{CDCl}_3$ )  $\delta$  (ppm): -140.08 (dd,  $J = 22.56, 7.52$  Hz, 2F), -151.02 (t,  $J = 21.06$  Hz, 1F), -159.79 (td,  $J = 21.06, 7.52$  Hz, 2F); HRMS  $m/z$   $[\text{M}+\text{H}]^+$  calculated for  $\text{C}_{35}\text{H}_{33}\text{BF}_5\text{N}_2\text{O}_2^+$ : 619.2550; Found: 619.2550.

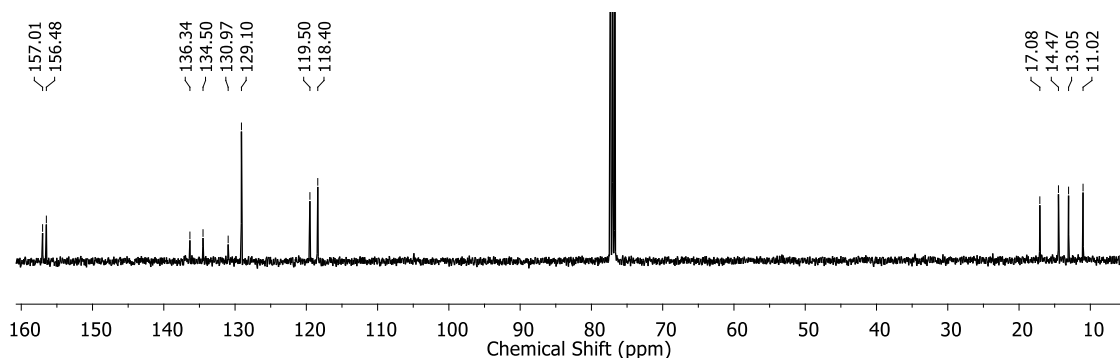


Figure 8.54.  $^{13}\text{C}$  NMR spectrum of **84** (100 MHz,  $\text{CDCl}_3$ ).

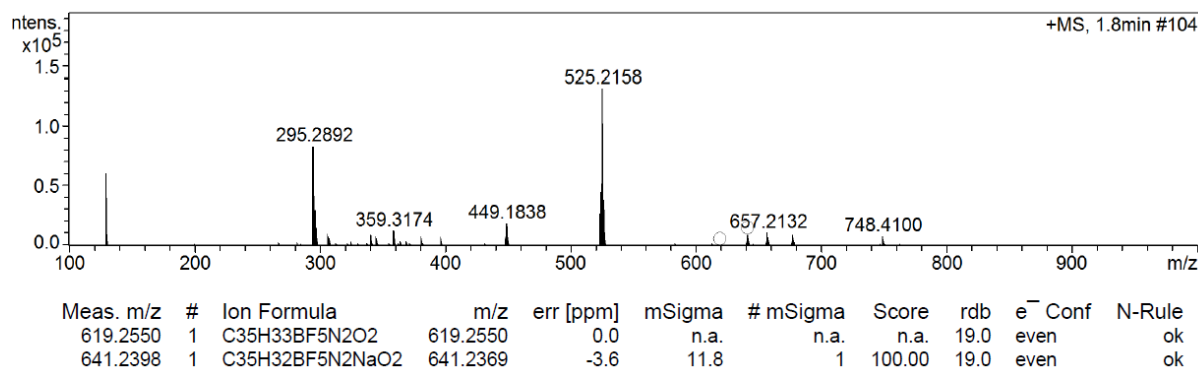
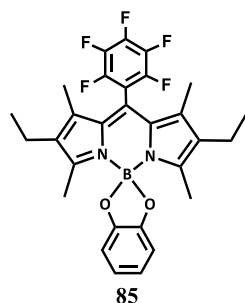


Figure 8.55. High resolution mass spectrum (positive mode) of **84**.

**8-(pentafluorophenyl)-1,3,5,7-tetramethyl-2,6-diethyl-4-benzo(dioxaborole)-4-bora-3a,4a-diaza-s-indacene (85)**



<sup>1</sup>H NMR (400 MHz, CDCl<sub>3</sub>) δ (ppm): 6.79 (s, 4H), 2.27 (q, J = 7.6 Hz, 4H), 2.05 (s, 6H), 1.51 (s, 6H), 0.96 (t, J = 7.6 Hz, 6H); <sup>13</sup>C NMR (100 MHz, CDCl<sub>3</sub>) δ (ppm): 157.92, 151.69, 137.30, 134.57, 131.05, 121.12, 119.54, 108.85, 17.10, 14.53, 12.93, 10.98; <sup>11</sup>B NMR (128 MHz, CDCl<sub>3</sub>) δ (ppm): 7.09 (s); <sup>19</sup>F NMR (376 MHz, CDCl<sub>3</sub>) δ (ppm): -139.16 (dd, J = 22.18, 7.14 Hz, 2F), -151.09 (t, J = 21.06 Hz, 1F), -159.84 (td, J = 21.06, 7.14 Hz, 2F); HRMS m/z [M+H]<sup>+</sup> calculated for C<sub>29</sub>H<sub>27</sub>BF<sub>5</sub>N<sub>2</sub>O<sub>2</sub><sup>+</sup>: 541.2080; Found: 541.2081.

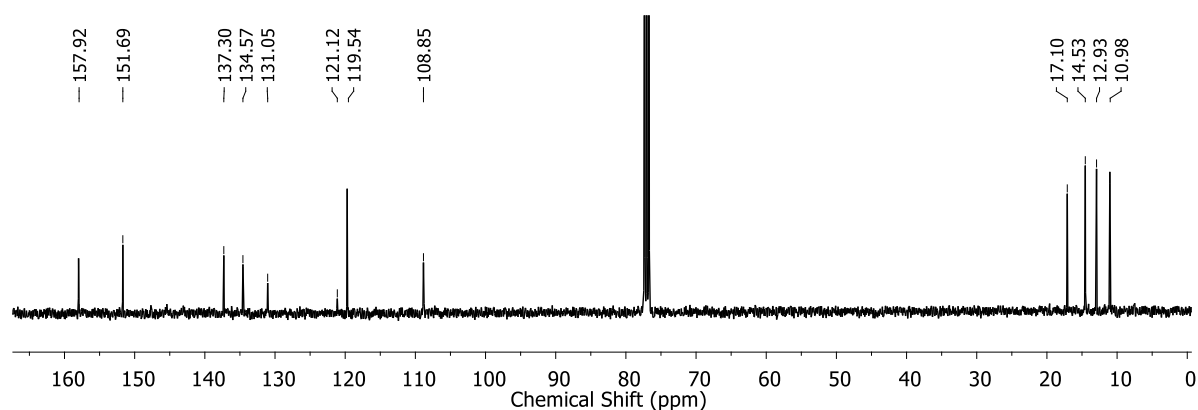
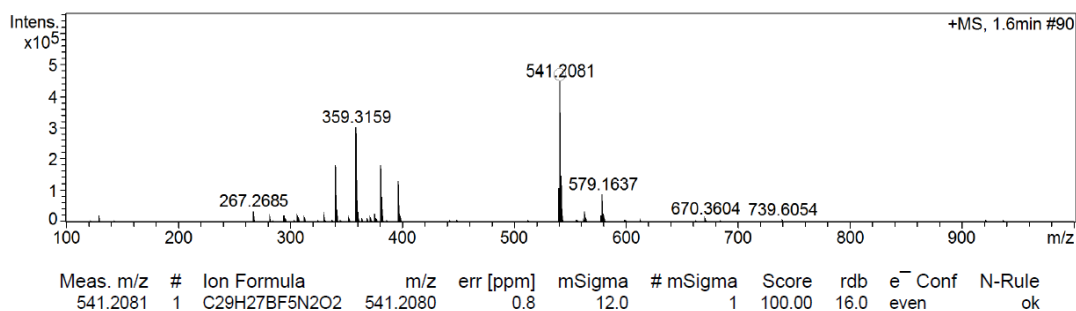
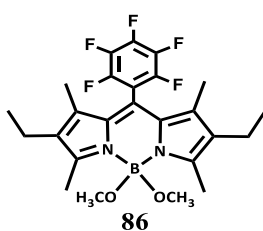


Figure 8.56. <sup>13</sup>C NMR spectrum of **85** (100 MHz, CDCl<sub>3</sub>).

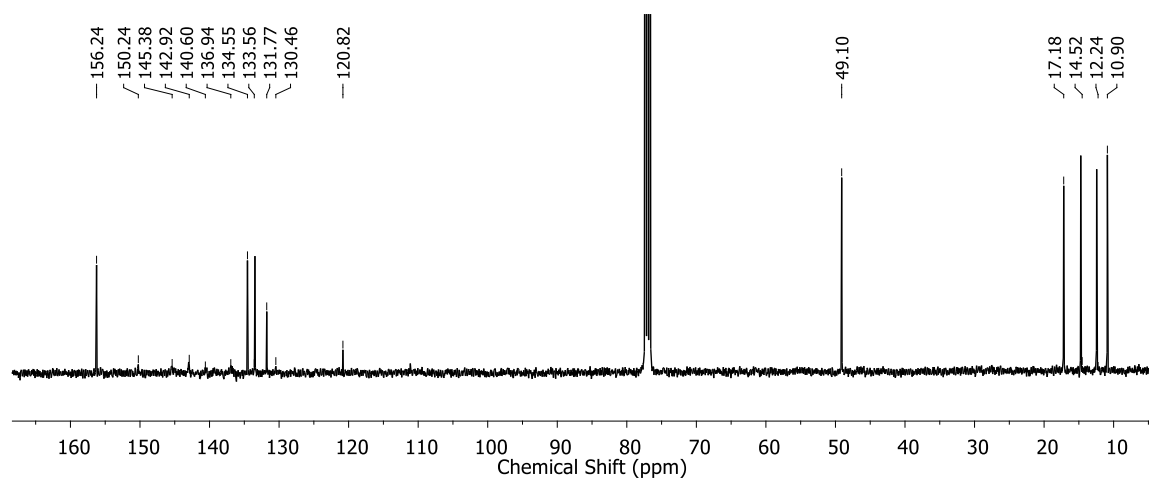


**Figure 8.57.** High resolution mass spectrum (positive mode) of **85**.

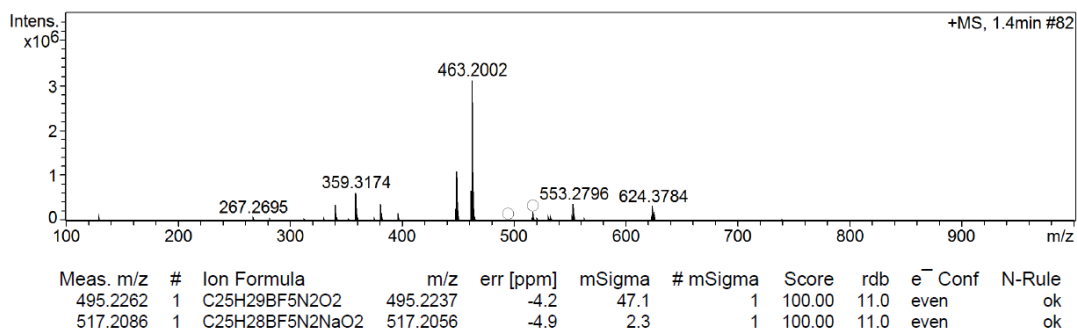
**8-(pentafluorophenyl)-1,3,5,7-tetramethyl-2,6-diethyl-4,4-dimethoxy-4-bora-3a,4a-diaza-s-indacene (86)**



**<sup>1</sup>H NMR (400 MHz, CDCl<sub>3</sub>) δ (ppm):** 2.91 (s, 6H), 2.53 (s, 6H), 2.32 (q, J = 7.6 Hz, 4H), 1.51 (s, 6H), 1.02 (t, J = 7.6 Hz, 6H); **<sup>13</sup>C NMR (100 MHz, CDCl<sub>3</sub>) δ (ppm):** 156.24, 150.24, 145.38, 142.92, 140.60, 136.94, 134.55, 133.56, 131.77, 130.46, 120.82, 49.10, 17.18, 14.52, 12.24, 10.90; **<sup>11</sup>B NMR (128 MHz, CDCl<sub>3</sub>) δ (ppm):** 2.65 (br); **<sup>19</sup>F NMR (376 MHz, CDCl<sub>3</sub>) δ (ppm):** -140.10 (dd, J = 22.94, 7.52 Hz, 2F), -151.82 (t, J = 20.68 Hz, 1F), -160.36 (td, J = 21.06, 7.52 Hz, 2F); **HRMS m/z [M+H]<sup>+</sup> calculated for C<sub>25</sub>H<sub>29</sub>BF<sub>5</sub>N<sub>2</sub>O<sub>2</sub><sup>+</sup>:** 495.2237; **Found:** 495.2262.

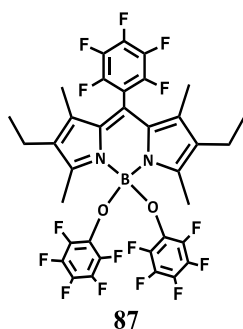


**Figure 8.58.** <sup>13</sup>C NMR spectrum of **86** (100 MHz, CDCl<sub>3</sub>).



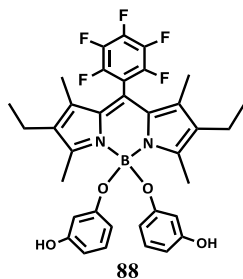
**Figure 8.59.** High resolution mass spectrum (positive mode) of **86**.

**8-(pentafluorophenyl)-1,3,5,7-tetramethyl-2,6-diethyl-4,4-bis(pentafluorophenoxy)-4-bora-3a,4a-diaza-s-indacene (87)**



**<sup>1</sup>H NMR (400 MHz, CDCl<sub>3</sub>) δ (ppm):** 2.49 (s, 6H), 2.29 (q, J = 7.6 Hz, 4H), 1.49 (s, 6H), 0.97 (t, J = 7.6 Hz, 6H); **<sup>11</sup>B NMR (128 MHz, CDCl<sub>3</sub>) δ (ppm):** 1.33 (s); **<sup>19</sup>F NMR (376 MHz, CDCl<sub>3</sub>) δ (ppm):** -140.52 (dd, J = 22.56, 7.52 Hz, 2F), -150.67 (t, J = 20.68 Hz, 1F), -157.46 (d, J = 22.18 Hz, 4F) -159.52 (td, J = 21.06, 8.27 Hz, 2F), -164.95 (t, J = 20.68 Hz, 4F), -167.74 (tt, J = 22.56, 3.76 Hz, 2F).

**8-(pentafluorophenyl)-1,3,5,7-tetramethyl-2,6-diethyl-4,4-bis(3-hydroxyphenoxy)-4-bora-3a,4a-diaza-s-indacene (88).**



**<sup>1</sup>H NMR (400 MHz, CDCl<sub>3</sub>) δ (ppm):** 6.91(t, J = 8 Hz, 2H), 6.26 (dd, J = 8, 4 Hz, 4H), 6.15 (t, J = 4 Hz, 2H), 4.53 (br, 2H), 2.50 (s, 6H), 2.21 (q, J = 7.6 Hz, 4H), 1.53 (s, 6H), 0.88 (t, J = 7.6 Hz, 6H); **<sup>13</sup>C NMR (100 MHz, CDCl<sub>3</sub>) δ (ppm):** 157.61, 157.20, 157.01, 156.39, 136.52, 134.68, 130.89, 130.32, 129.81, 120.86, 110.95, 107.80, 106.81, 105.69,

17.11, 14.48, 13.04, 11.01;  $^{11}\text{B}$  NMR (128 MHz,  $\text{CDCl}_3$ )  $\delta$  (ppm): 0.73 (s);  $^{19}\text{F}$  NMR (376 MHz,  $\text{CDCl}_3$ )  $\delta$  (ppm): -140.54 (dd,  $J = 22.56, 7.14$  Hz, 2F), -150.60 (t,  $J = 20.68$  Hz, 1F), -159.26 (td,  $J = 21.06, 7.52$  Hz, 2F).

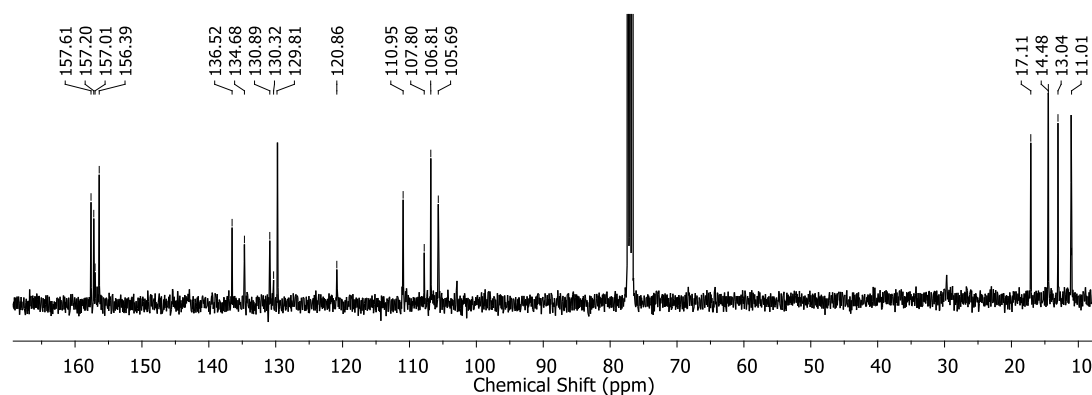
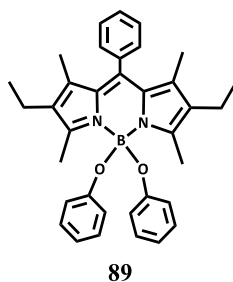


Figure 8.60.  $^{13}\text{C}$  NMR spectrum of **88** (100 MHz,  $\text{CDCl}_3$ ).

### 8-(phenyl)-1,3,5,7-tetramethyl-2,6-diethyl-4,4-diphenoxy-4-bora-3a,4a-diaza-s-indacene (**89**)



$^1\text{H}$  NMR (400 MHz,  $\text{CDCl}_3$ )  $\delta$  (ppm): 7.60-7.45 (m, 3H), 7.33-7.10 (m, 2H), 7.10 (t,  $J = 7.2$  Hz, 4H), 6.80 (t,  $J = 7.2$  Hz, 2H), 6.65 (d,  $J = 7.6$  Hz, 4H), 2.54 (s, 6H), 2.20 (q,  $J = 7.6$  Hz, 4H), 1.29 (s, 6H), 0.87 (t,  $J = 7.6$  Hz, 6H);  $^{13}\text{C}$  NMR (100 MHz,  $\text{CDCl}_3$ )  $\delta$  (ppm): 156.88, 154.48, 138.13, 136.06, 133.28, 131.38, 128.95, 128.37, 119.35, 118.79, 17.16, 14.58, 12.80, 11.77;  $^{11}\text{B}$  NMR (128 MHz,  $\text{CDCl}_3$ )  $\delta$  (ppm): 0.91 (s); HRMS  $m/z$   $[\text{M}+\text{H}]^+$  calculated for  $\text{C}_{35}\text{H}_{38}\text{BN}_2\text{O}_2^+$ : 529.3021; Found: 529.3020.

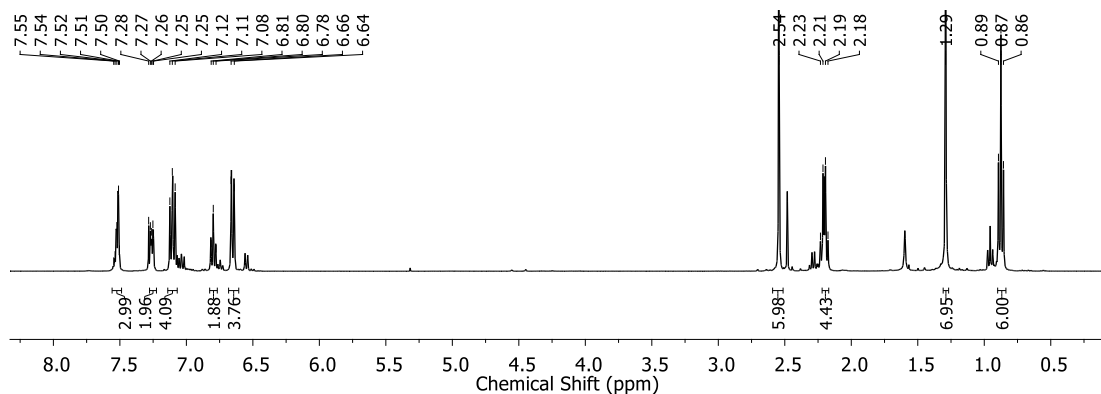
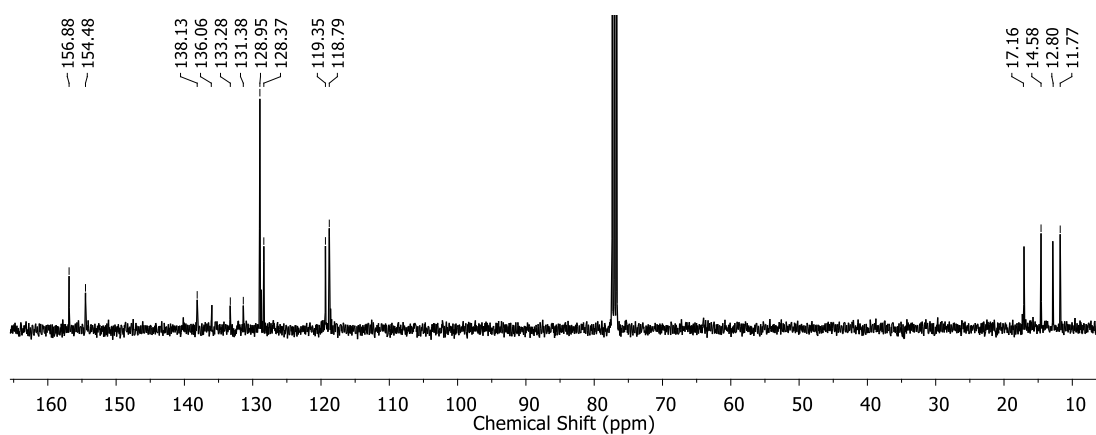
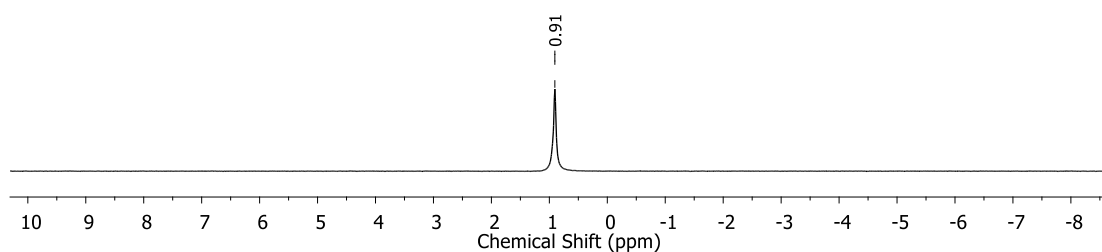


Figure 8.61.  $^1\text{H}$  NMR spectrum of **89** (400 MHz,  $\text{CDCl}_3$ ).

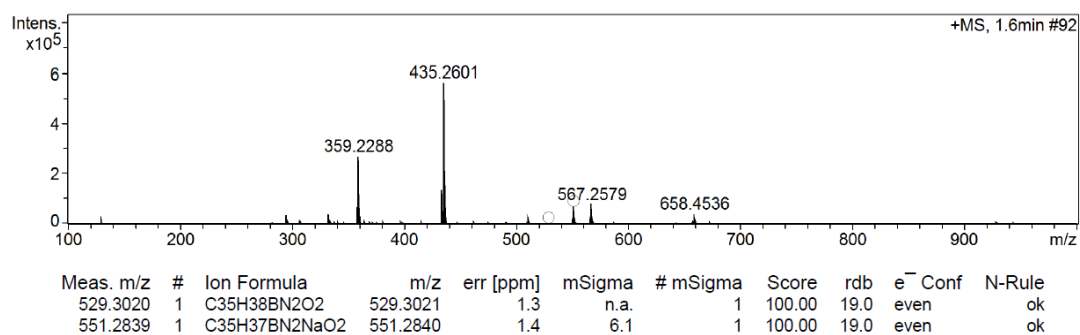




**Figure 8.62.**  $^{13}\text{C}$  NMR spectrum of **89** (100 MHz,  $\text{CDCl}_3$ ).

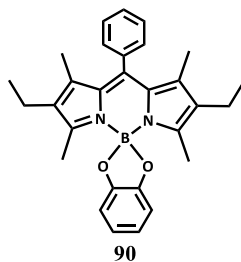


**Figure 8.63.**  $^{11}\text{B}$  NMR spectrum of **89** (128 MHz,  $\text{CDCl}_3$ ).

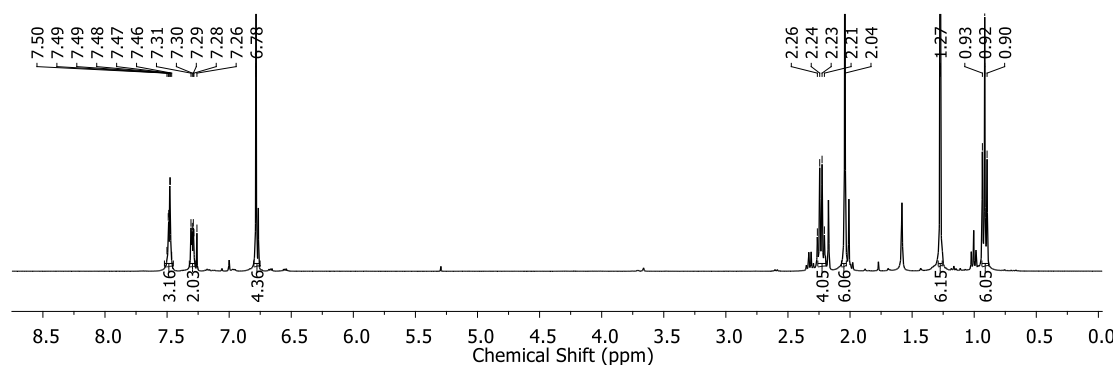


**Figure 8.64.** High resolution mass spectrum (positive mode) of **89**.

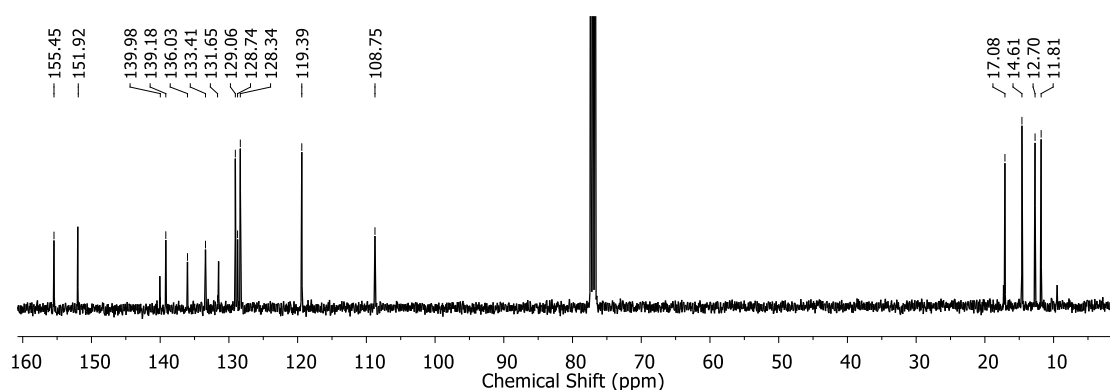
**8-(phenyl)-1,3,5,7-tetramethyl-2,6-diethyl-4-benzo(dioxaborole)-4-bora-3a,4a-diaza-s-indacene (90)**



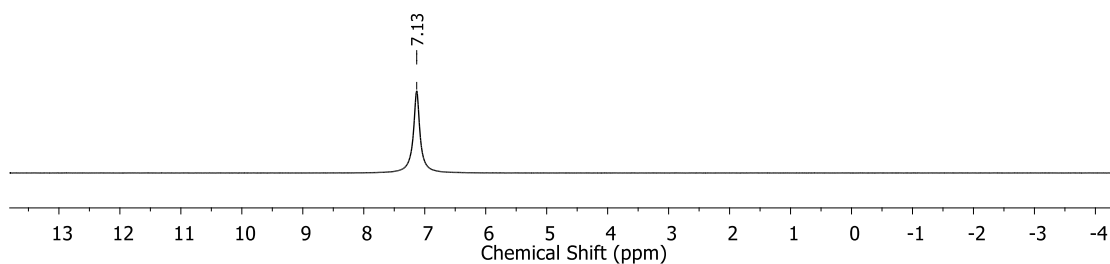
**$^1\text{H}$  NMR (400 MHz,  $\text{CDCl}_3$ )  $\delta$  (ppm):** 7.55-7.40 (m, 3H), 7.30-7.16 (m, 2H), 6.78 (s, 4H), 2.23 (q,  $J = 7.6$  Hz, 4H), 2.04 (s, 6H), 1.27 (s, 6H), 0.92 (t,  $J = 7.6$  Hz, 6H);  **$^{13}\text{C}$  NMR (100 MHz,  $\text{CDCl}_3$ )  $\delta$  (ppm):** 155.45, 151.92, 139.98, 139.18, 136.03, 133.41, 131.65, 129.06, 128.74, 128.34, 119.39, 108.75, 17.08, 14.61, 12.70, 11.81;  **$^{11}\text{B}$  NMR (128 MHz,  $\text{CDCl}_3$ )  $\delta$  (ppm):** 7.13 (s); **HRMS  $m/z$   $[\text{M}+\text{H}]^+$  calculated for  $\text{C}_{29}\text{H}_{32}\text{BN}_2\text{O}_2^+$ :** 451.2551; **Found:** 451.2553.



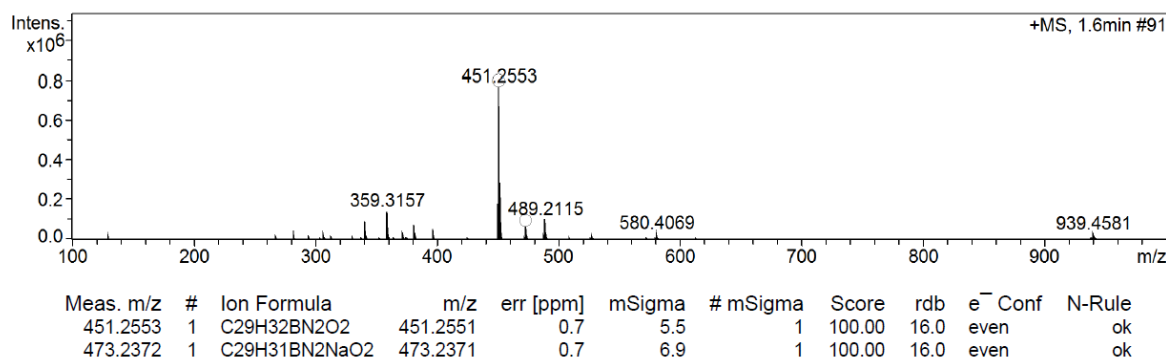
**Figure 8.65.**  $^1\text{H}$  NMR spectrum of **90** (400 MHz,  $\text{CDCl}_3$ )



**Figure 8.66.**  $^{13}\text{C}$  NMR spectrum of **90** (100 MHz,  $\text{CDCl}_3$ ).

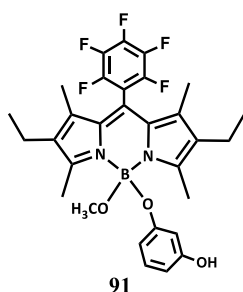


**Figure 8.67.**  $^{11}\text{B}$  NMR spectrum of **90** (128 MHz,  $\text{CDCl}_3$ ).



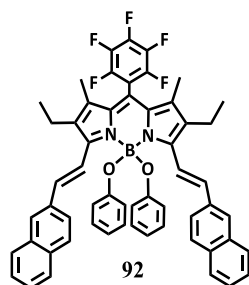
**Figure 8.68.** High resolution mass spectrum (positive mode) of **90**.

**8-(pentafluorophenyl)-1,3,5,7-tetramethyl-2,6-diethyl-4-(3-hydroxyphenoxy)-4-methoxy-4-bora-3a,4a-diaza-s-indacene (**91**)**



**<sup>1</sup>H NMR (400 MHz, CDCl<sub>3</sub>) δ (ppm):** 7.28 (br, 1H), 7.37 (s, 1H), 6.83 (t, J = 8 Hz, 1H), 6.31 (dd, J = 6.4, 1.6 Hz, 1H), 5.91 (dd, J = 6.4, 1.6 Hz, 1H), 2.97 (s, 3H), 2.48 (s, 6H), 2.26 (q, J = 7.6 Hz, 4H), 1.55 (s, 6H), 0.95 (t, J = 7.6 Hz, 6H); **<sup>11</sup>B NMR (128 MHz, CDCl<sub>3</sub>) δ (ppm):** 1.52 (br); **<sup>19</sup>F NMR (376 MHz, CDCl<sub>3</sub>) δ (ppm):** -140.00 (dd, J = 24.06, 7.52 Hz, 1F), -140.16 (dd, J = 24.06, 7.52 Hz, 1F), -151.19 (t, J = 20.68 Hz, 1F), -159.74 (td, J = 21.81, 8.27 Hz, 1F), -159.99 (td, J = 21.81, 8.65 Hz, 1F).

**8-(pentafluorophenyl)-1,7-dimethyl-3,5-di-[(naphthalen-2-yl)vinyl]-2,6-diethyl-4,4-diphenoxy -4-bora-3a,4a-diaza-s-indacene (**92**)**



**<sup>1</sup>H NMR (400 MHz, CDCl<sub>3</sub>) δ (ppm):** 8.33 (d, J = 16.8 Hz, 2H), 8.02 – 7.80 (m, 10 H), 7.58 – 7.44 (m, 4H), 7.28 (d, J = 16 Hz, 2H), 6.63 (t, J = 7.2 Hz, 4H), 6.71 (t, J = 7.2 Hz,

2H), 6.63 (d,  $J = 9.2$  Hz, 4H), 2.61 (q,  $J = 7.6$  Hz, 4H), 1.58 (s, 6H) 1.14 (t,  $J = 7.6$  Hz, 6H);  $^{13}\text{C}$  NMR ( $\text{CDCl}_3$ )  $\delta$  (ppm): 156.56, 152.47, 136.62, 136.45, 135.22 (d, 17 Hz), 133.65 (d, 10 Hz), 128.98, 127.82, 126.45 (d, 7 Hz), 122.33, 119.62, 119.15, 18.52, 14.13, 10.84;  $^{11}\text{B}$  NMR (128 MHz,  $\text{CDCl}_3$ )  $\delta$  (ppm): 1.37 (s,  $J = 33.28$  Hz);  $^{19}\text{F}$  NMR (376 MHz,  $\text{CDCl}_3$ )  $\delta$  (ppm): -139.36 (dd,  $J = 22.94, 7.52$  Hz, 2F), -150.94 (t,  $J = 21.06$  Hz, 1F), -159.81 (td,  $J = 22.6, 7.52$  Hz, 2F); HRMS  $m/z$   $[\text{M}+\text{H}]^+$  calculated for  $\text{C}_{57}\text{H}_{45}\text{BF}_5\text{N}_2\text{O}_2^+$ : 895.3489; Found: 895.3496.

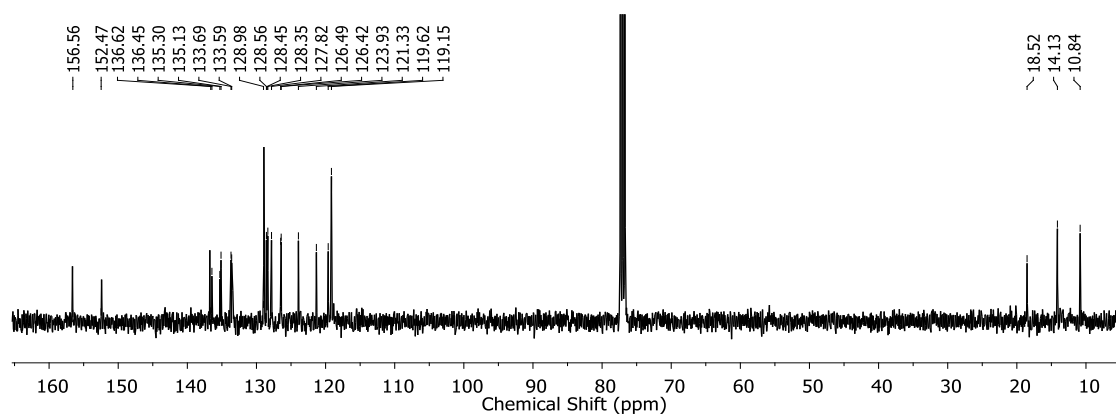


Figure 8.69.  $^{13}\text{C}$  NMR spectrum of **92** (100 MHz,  $\text{CDCl}_3$ )

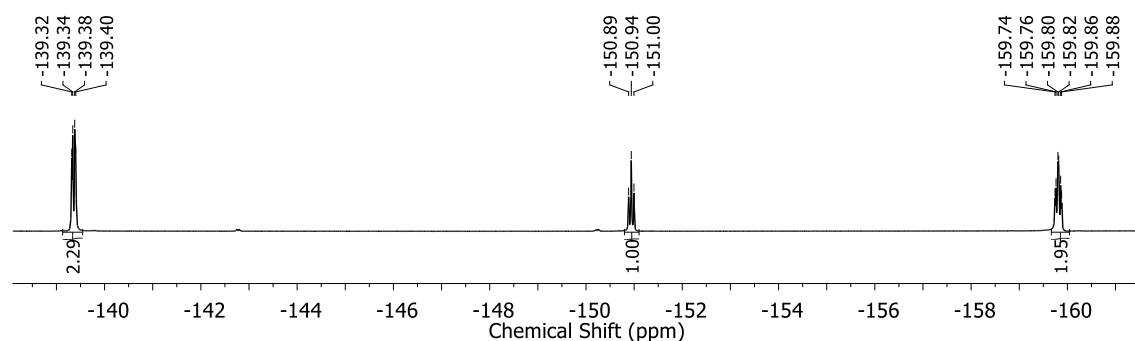


Figure 8.70.  $^{19}\text{F}$  NMR spectrum of **92** (376 MHz,  $\text{CDCl}_3$ ).

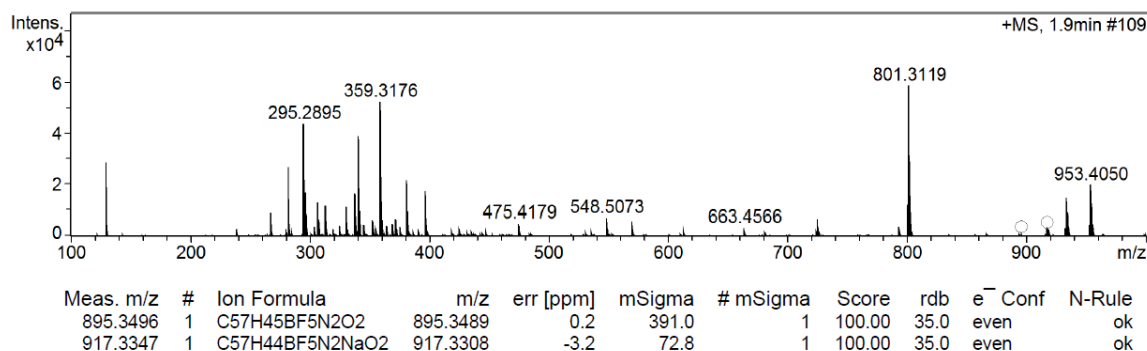
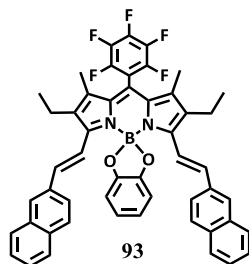
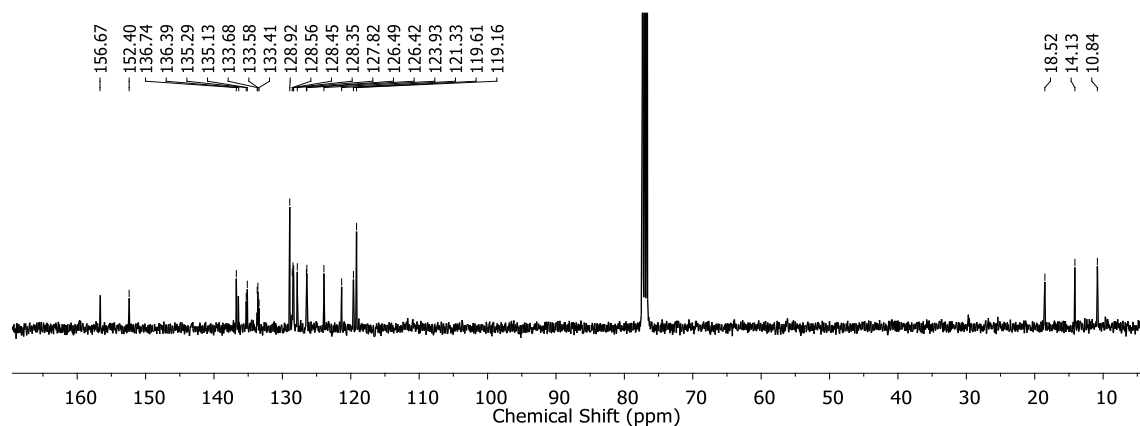


Figure 8.71. High resolution mass spectrum (positive mode) of **92**.

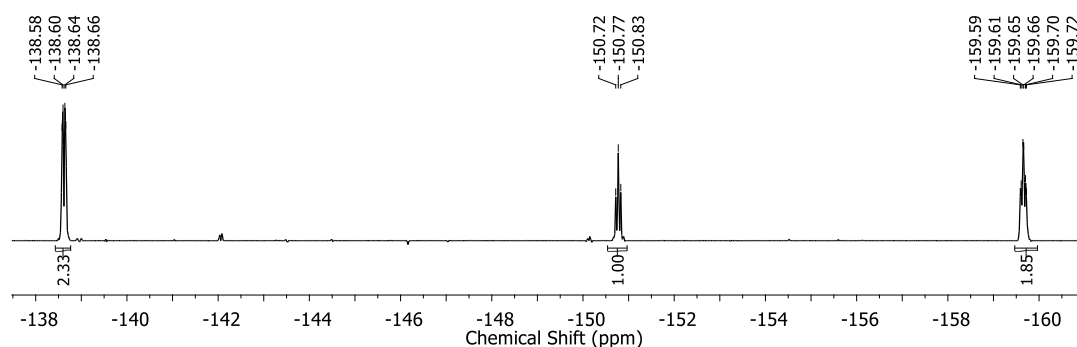
**8-(pentafluorophenyl)-1,7-dimethyl-3,5-di-[(naphthalen-2-yl)vinyl]-2,6-diethyl-4-benzo(dioxaborole)-4-bora-3a,4a-diaza-s-indacene (93).**



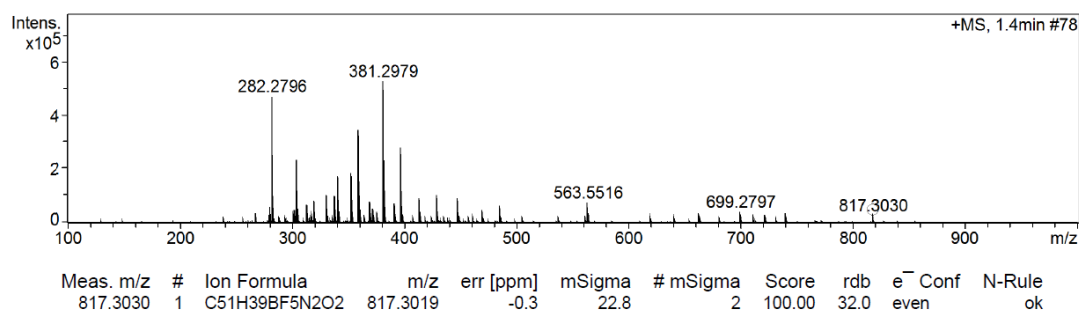
$^1\text{H}$  NMR (400 MHz,  $\text{CDCl}_3$ )  $\delta$  (ppm): 7.84 – 7.72 (m, 4 H), 7.58 (d,  $J = 8.4$  Hz, 2H), 7.49 – 7.42 (m, 4 H), 7.39 (s, 2H), 7.18 (d,  $J = 16.4$  Hz, 2H), 7.12 – 7.00 (m, 4H), 6.96 – 6.89 (m, 2H), 6.62 (dd,  $J = 8.8, 1.6$  Hz, 2H), 2.65 (q,  $J = 7.6$  Hz, 4H), 1.55 (s, 6H) 1.25–1.18 (m, 6H);  $^{13}\text{C}$  NMR ( $\text{CDCl}_3$ )  $\delta$  (ppm): 156.67, 152.40, 136.74, 136.39, 135.21 (d, 16 Hz), 133.78 (d, 10 Hz), 133.41, 128.92, 128.45 (t, 10 Hz), 126.46 (d, 8 Hz), 123.93, 121.33, 119.16, 18.52, 14.13, 10.84;  $^{11}\text{B}$  NMR (128 MHz,  $\text{CDCl}_3$ )  $\delta$  (ppm): 1.37 (s,  $J = 33.28$  Hz);  $^{19}\text{F}$  NMR (376 MHz,  $\text{CDCl}_3$ )  $\delta$  (ppm): -138.62 (dd,  $J = 22.94, 7.52$  Hz, 2F), -150.77 (t,  $J = 21.06$  Hz, 1F), -159.66 (td,  $J = 21.06, 7.52$  Hz, 2F). HRMS  $m/z$   $[\text{M}+\text{H}]^+$  calculated for  $\text{C}_{51}\text{H}_{39}\text{BF}_5\text{N}_2\text{O}_2^+$ : 817.3019; Found: 817.3030.



**Figure 8.72.**  $^{13}\text{C}$  NMR spectrum of **93** (100 MHz,  $\text{CDCl}_3$ ).



**Figure 8.73.**  $^{19}\text{F}$  NMR spectrum of **93** (376 MHz,  $\text{CDCl}_3$ ).



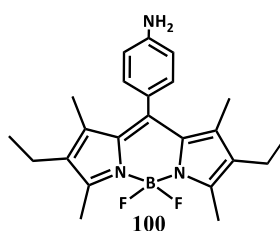
**Figure 8.74.** High resolution mass spectrum (positive mode) of **93**.

## 8.4.5. Chapter 6

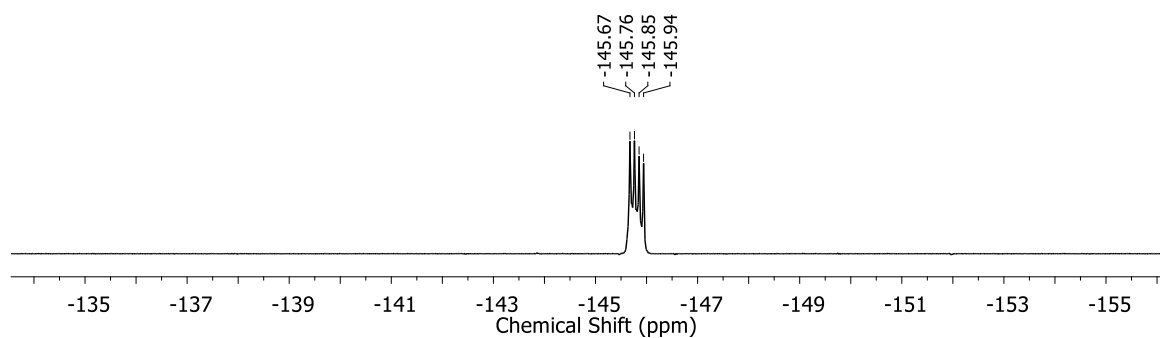
### 8.4.5.1. General procedures for the synthesis of BODIPY **100** and **104**

Into a solution of BODIPY **56** (250 mg (0.59 mmol)) THF (20 ml), were added 20 equivalents of hydrazine and 50 mg of 10 % Pd/C and left stirring at reflux temperature. After 1 hour of reaction, the amount of **104** is much more relevant than **100** ( 55 % vs 6 % respectively), however after 6 hours the yield of **100** was around 50 %, and the yield of **104** was around 2%. When the reaction is stopped (after 1 or 6 hours), the aqueous mixture is washed with water and extracted with dichloromethane, and then evaporated. The compounds were isolated by preparative thin layer chromatography using dichloromethane as eluent.

### 8-(4-aminophenyl)-1,3,5,7-tetramethyl-2,6-diethyl-4,4-difluoro-4-bora-3a,4a-diaza-s-indacene (**100**)

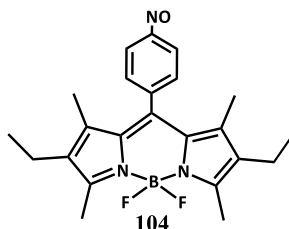


<sup>1</sup>H NMR (400 MHz, CDCl<sub>3</sub>) δ (ppm): 7.01 (d, J = 8.4 Hz, 2H); 6.78 (d, J = 8.4 Hz, 2H); 2.53 (s, 6H), 2.30 (q, J = 7.6 Hz, 4H), 1.40 (s, 6H), 0.98 (t, J = 7.6 Hz, 6H); <sup>19</sup>F NMR (376 MHz, CDCl<sub>3</sub>) δ (ppm): -145.80 (q, J = 32.71 Hz, 2F); MS m/z [M+H]<sup>+</sup> calculated for C<sub>23</sub>H<sub>29</sub>BF<sub>2</sub>N<sub>3</sub><sup>+</sup>: 396.23; Found: 396.3 and 376.3 ([M+H -HF]<sup>+</sup>);

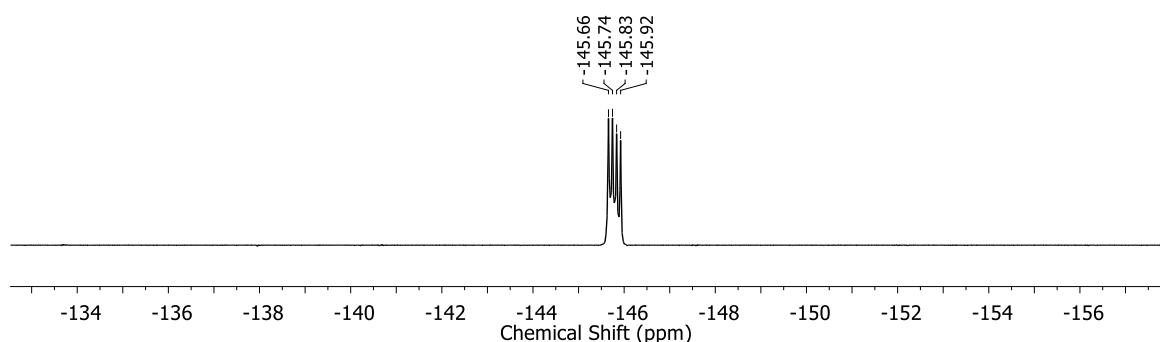


**Figure 8.75.**  $^{19}\text{F}$  NMR spectrum of **100** (376 MHz,  $\text{CDCl}_3$ ).

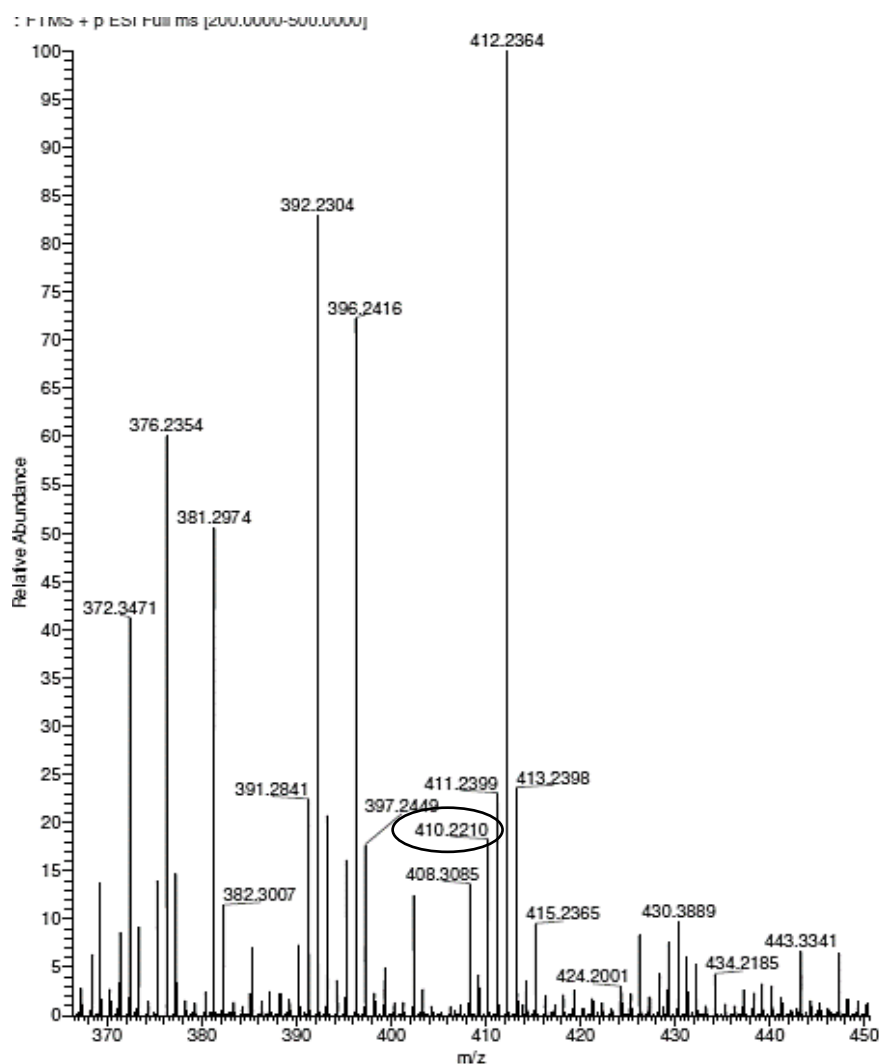
**8-(4-nitrosophenyl)-1,3,5,7-tetramethyl-2,6-diethyl-4,4-difluoro-4-bora-3a,4a-diaza-s-indacene (104)**



$^1\text{H}$  NMR (400 MHz,  $\text{CDCl}_3$ )  $\delta$  (ppm): 7.16 (d,  $J = 8.4$  Hz, 2H); 7.10 (d,  $J = 8.4$  Hz, 2H); 2.52 (s, 6H), 2.30 (q,  $J = 7.6$  Hz, 4H), 1.35 (s, 6H), 0.98 (t,  $J = 7.6$  Hz, 6H);  $^{19}\text{F}$  NMR (376 MHz,  $\text{CDCl}_3$ )  $\delta$  (ppm): -145.79 (q,  $J = 32.71$  Hz, 2F); HRMS  $m/z$   $[\text{M}+\text{H}]^+$  calculated for  $\text{C}_{23}\text{H}_{27}\text{BF}_2\text{N}_3\text{O}^+$ : 410.2210; Found: 410.2210.



**Figure 8.76.**  $^{19}\text{F}$  NMR spectrum of **104** (376 MHz,  $\text{CDCl}_3$ ).



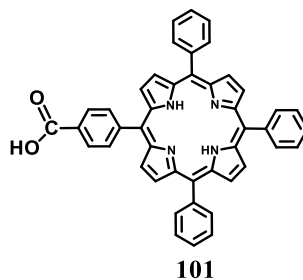
**Figure 8.77.** High resolution ESI positive mode mass spectrum of **104**.

#### 8.4.5.2. General procedures for the synthesis of porphyrin **101**, **104** and **105**

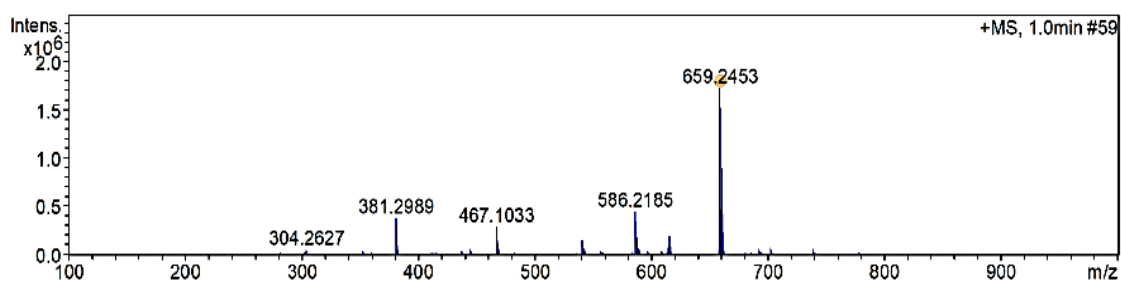
To 80 ml of propionic acid and 20 ml of anhydride acetic was added 1.5 ml of benzaldehyde and 2.3 g of 4-carboxybenzaldehyde. The mixture was heated to 120 ° C, and then 2 ml of pyrrole was added dropwise. After 2 hours, the reaction mixture was poured in water and left at air overnight. Then, the precipitate was filtrated, refluxed in water around 30 min. After that, the residue was filtered and washed with water again. Finally, the solid residue was dissolved with dichloromethane and purified by silica gel column chromatography (dichloromethane as eluent). After the chromatographic process, **101** was isolated with (8 % of yields), but it was also possible to isolate **104** (1 %) and **105** (2%).

Compounds **104** and **105** were also synthesized by the same method but using only one aldehyde reagent (benzaldehyde (for **104**) or 4-carboxybenzaldehyde (for **105**)). These two compounds can easily precipitate/crystalize.

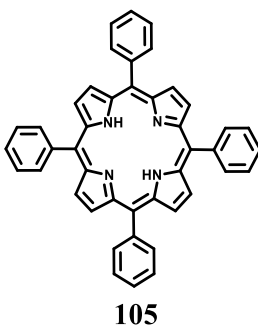


**5-(4-carboxyphenyl)-10,15,20-(triphenyl)porphyrin (101)**

$^1\text{H NMR}$  (400 MHz,  $\text{CDCl}_3$ )  $\delta$  (ppm): 8.29 – 8.75 (m, 8H), 8.29 (d,  $J = 8.4$  Hz, 2H), 8.21 (d,  $J = 7.6$  Hz, 6H), 8.15 (d,  $J = 8.0$  Hz, 2H), 7.85 – 7.71 (m, 9H), -2.78 (br, 2H); **HRMS**  $m/z$   $[\text{M}+\text{H}]^+$  calculated for  $\text{C}_{45}\text{H}_{30}\text{N}_4\text{O}_2^+$ : 659.2442; **Found**: 659.2453.



**Figure 8.78.** High resolution mass spectrum (positive mode) of **101**.

**5,10,15,20-(tetraphenyl)porphyrin (105)**

$^1\text{H NMR}$  (400 MHz,  $\text{CDCl}_3$ )  $\delta$  (ppm): 8.86 (s, 8H), 8.31 – 8.15 (m, 8H), 7.89 – 7.68 (m, 12H), -2.75 (s, 2H).

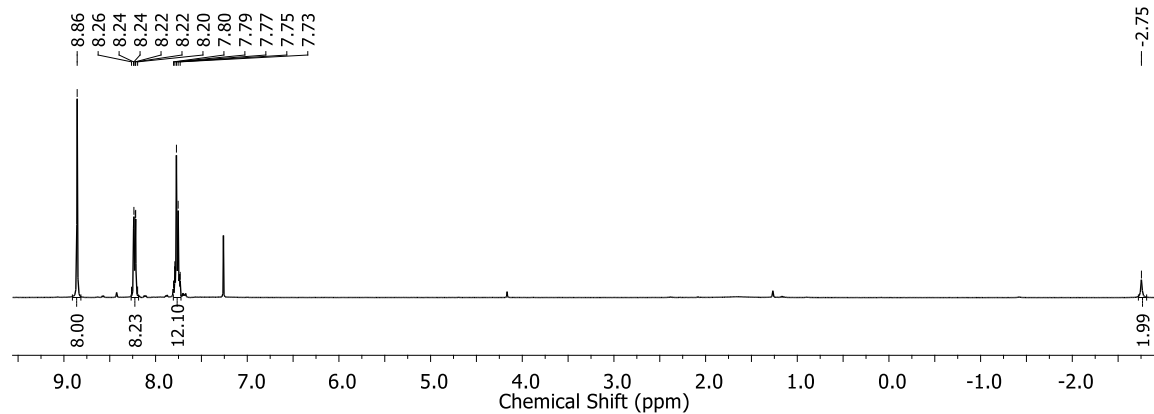
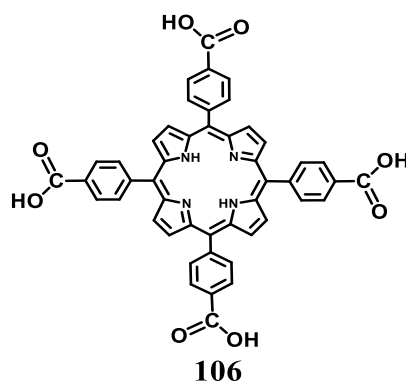


Figure 8.79.  $^1\text{H}$  NMR spectrum of **105** (400 MHz,  $\text{CDCl}_3$ ).

**5,10,15,20-tetra(4-carboxyphenyl)porphyrin (106)**



$^1\text{H}$  NMR (400 MHz,  $\text{CDCl}_3$ )  $\delta$  (ppm): 9.16 (s, 8H), 8.76 – 8.58 (m, 16H), -2.58 (s, 2H).

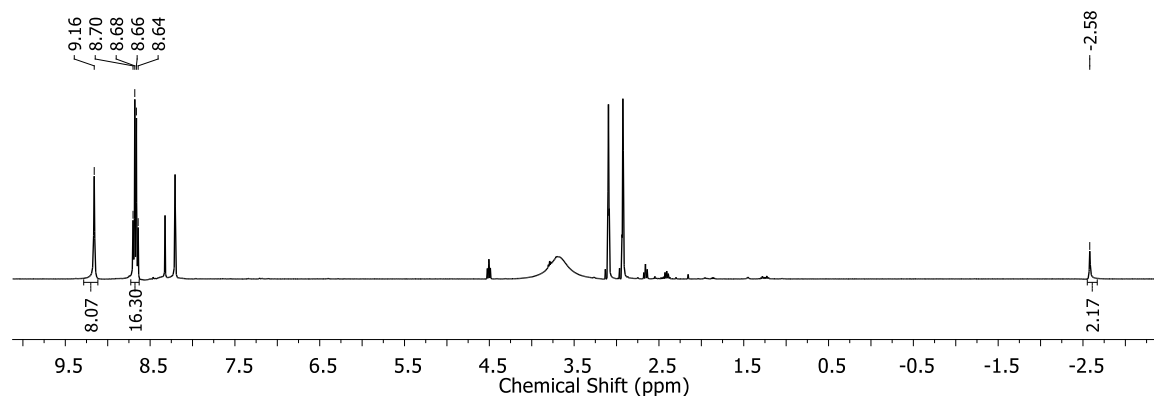
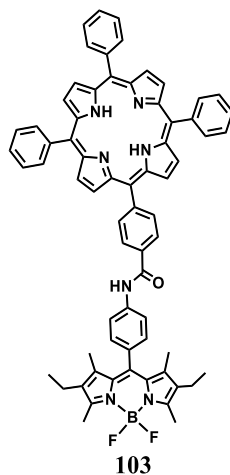


Figure 8.80.  $^1\text{H}$  NMR spectrum of **106** (400 MHz,  $\text{CDCl}_3$ ).

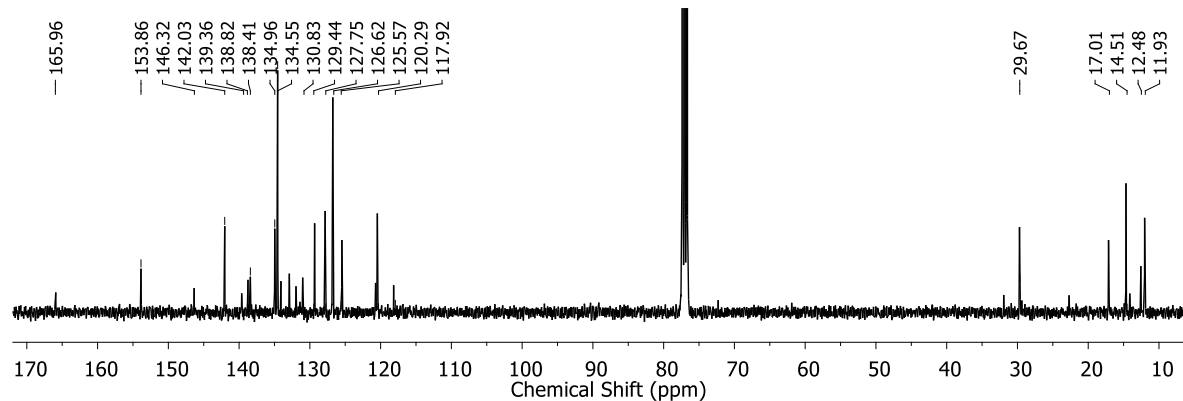
### 8.4.5.3. General procedures for the synthesis of BDP-P1 (103)

Porphyrin **101** (150 mg, 0.23 mmol) was taken in dry toluene (20 mL), with THF as co-solvent (5ml), then thionyl chloride (0.34 mL, 4.6 mmol) and pyridine (0.34 mL) were added and the reaction mixture was heated to 110 °C under inert atmosphere for 3 hours. After cooling, the solvent was evaporated and the resulting compound was dissolved in dry toluene (50 mL), followed by the addition of 0.4 ml of pyridine and 30 mg of **100** (0.08 mmol). The reaction was allowed to stir at room temperature for 18 h. Then the reaction mixture was washed with water, brine, and the organic layer evaporated. The crude compound was purified by preparative thin layer chromatography with dichloromethane:hexane (8:2) and **103** was obtained as red solid with 18 % of yield.

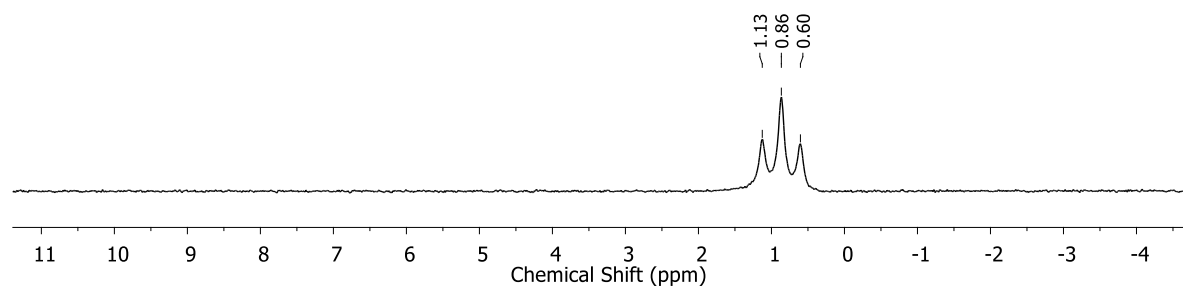
#### 5,10,15-phenyl-20-(4-((1,3,5,7-tetramethyl-2,6-diethyl-4,4-difluoro-4-bora-3a,4a-diaza-s-indacene)-8-phenyl-4-carbamoyl)phenyl)-porphyrin (BDP-P1 (103))



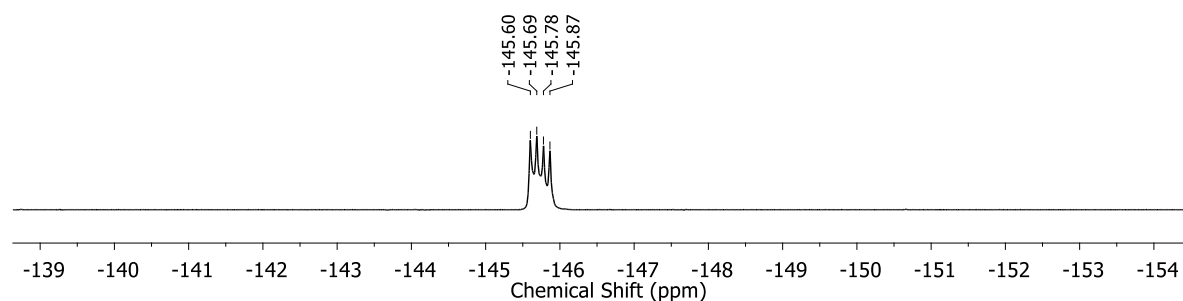
$^1\text{H NMR}$  (400 MHz,  $\text{CDCl}_3$ )  $\delta$  (ppm): 8.96 – 8.76 (m, 8H), 8.39 (d,  $J = 8$  Hz, 2H), 8.30 (d,  $J = 8.0$  Hz, 2H); 8.25 – 8.19 (m, 6H), 7.97 (d,  $J = 8.4$  Hz, 2H), 7.85 – 7.68 (m, 9H), 7.38 (d,  $J = 8.4$  Hz, 2H); 2.57 (s, 6H), 2.34 (q,  $J = 7.6$  Hz, 4H), 1.44 (s, 6H), 1.02 (t,  $J = 7.6$  Hz, 6H);  $^{13}\text{C NMR}$  ( $\text{CDCl}_3$ )  $\delta$  (ppm): 165.96, 153.86, 146.32, 142.03, 139.36, 138.82, 138.41, 134.96, 134.55, 130.83, 129.44, 127.75, 126.62, 1125.57, 120.29, 117.92, 29.67, 17.01, 14.51, 12.48, 11.93;  $^{11}\text{B NMR}$  (128 MHz,  $\text{CDCl}_3$ )  $\delta$  (ppm): 0.86 (t,  $J = 33.41$  Hz);  $^{19}\text{F NMR}$  (376 MHz,  $\text{CDCl}_3$ )  $\delta$  (ppm): -145.74 (q,  $J = 33.84$  Hz, 2F) MS  $m/z$   $[\text{M}+\text{H}]^+$  calculated for  $\text{C}_{68}\text{H}_{57}\text{BF}_2\text{N}_7\text{O}^+$ : 1036.4685; Found: 1036.5; HRMS  $m/z$   $[\text{M}]^-$  calculated for  $\text{C}_{68}\text{H}_{55}\text{BF}_2\text{N}_7\text{O}^-$ : 1034.4529; Found: 1034.4546.



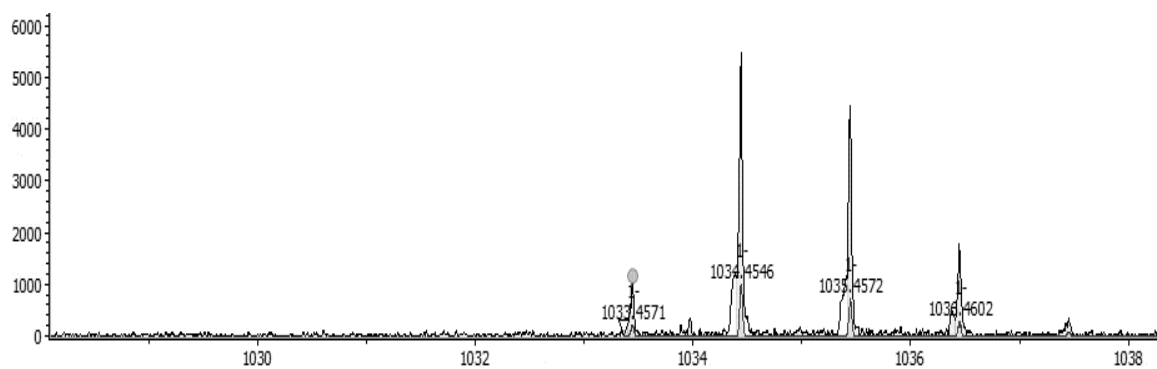
**Figure 8.81.**  $^{13}\text{C}$  NMR spectrum of **103** (100 MHz,  $\text{CDCl}_3$ ).



**Figure 8.82.**  $^{11}\text{B}$  NMR spectrum of **103** (128 MHz,  $\text{CDCl}_3$ ).



**Figure 8.83.**  $^{19}\text{F}$  NMR spectrum of **103** (376 MHz,  $\text{CDCl}_3$ ).

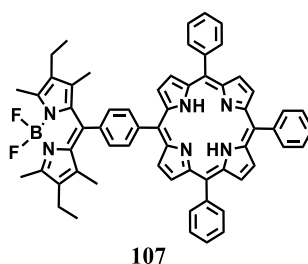


**Figure 8.84.** High resolution mass spectrum (negative mode) of **103**

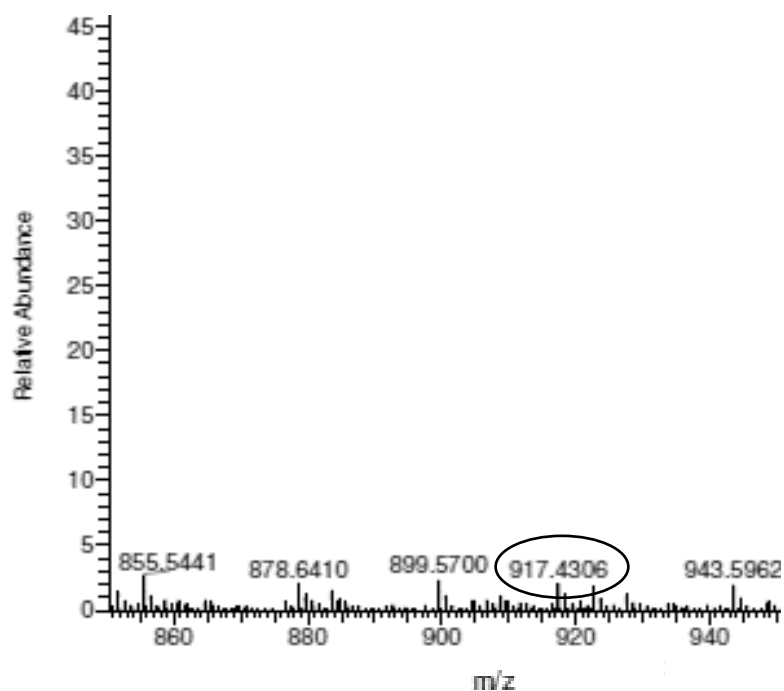
#### 8.4.5.4. General procedures for the synthesis of BDP-P2 (107)

Porphyrin **101** (150 mg, 0.23 mmol) was taken in dry toluene (20 mL), with THF as co-solvent (5ml), then thionyl chloride (0.34 mL, 4.6 mmol) and pyridine (0.34 mL) were added and the reaction mixture was heated to 110 °C under inert atmosphere for 3 hours. After cooling, the solvent was evaporated, and the resulting compound was dissolved in dry dichloromethane (100 mL). Then, 10 equivalents of 3-ethyl-2,5-dimethyl-pyrrole and a catalytic amount of TFA were added and the reaction was kept under nitrogen atmosphere for 16 hours. After that, 0.5 ml of N,N-diisopropylethylamine and 0.5 ml of BF<sub>3</sub>.Et<sub>2</sub>O were added to the reaction mixture, and the reaction was stirred under inert atmosphere, for 6 hours. Then, the reaction mixture was washed successively with water (30 mL) and brine (30 mL). The layers were separated, the organic layer was dried with anhydrous sodium sulfate and concentrated under reduced pressure. The crude was purified by column chromatography on silica gel with dichloromethane:hexane (60:40) as eluent. The compound was obtained with 6 % of yield.

#### 5,10,15-phenyl-20-(4-((1,3,5,7-tetramethyl-2,6-diethyl-4,4-difluoro-4-bora-3a,4a-diaza-s-indacene)-8-phenyl)-porphyrin (BDP-P2 (107))



<sup>1</sup>H NMR (400 MHz, CDCl<sub>3</sub>) δ (ppm): 9.12 – 9.00 (m, 4H), 8.75 – 8.55 (m, 4H), 8.48 – 8.21 (m, 8H), 7.92 – 7.70 (m, 11H), 2.73 – 2.57 (m, 6H), 2.41 (q, J = 7.6 Hz, 4H), 1.99 – 1.91 (m, 6H), 1.15 – 1.05 (m, 6H); <sup>19</sup>F NMR (376 MHz, CDCl<sub>3</sub>) δ (ppm): -145.79 (q, J = 33.84 Hz, 2F) MS m/z [M+H]<sup>+</sup> calculated for C<sub>61</sub>H<sub>52</sub>N<sub>6</sub>BF<sub>2</sub><sup>+</sup>: 917.4309; Found: 917.4306.

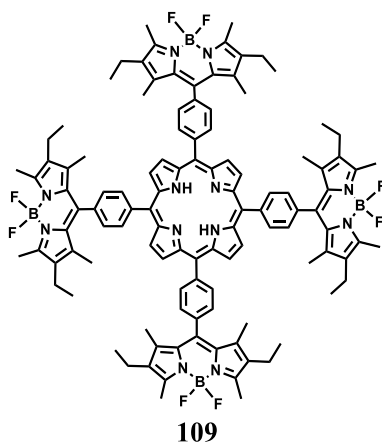


**Figure 8.85.** High resolution mass spectrum (positive mode) spectrum of **107**.

#### 8.4.5.5. General procedures for the synthesis of BDP-P3 (**109**)

Porphyrin **106** (200 mg, 0.25 mmol) was taken in dry toluene (20 mL), with THF as co-solvent (5ml), then thionyl chloride (1.5 mL, 20 mmol) and pyridine (1.5 mL) were added and the reaction mixture was heated to 110 °C under inert atmosphere for 3 hours. After cooling, the solvent was evaporated, and the resulting compound was dissolved in dry dichloromethane (100 mL). Then, 40 equivalents of 3-ethyl-2,5-dimethyl-pyrrole and a catalytic amount of TFA were added and the reaction was stirring under nitrogen atmosphere for 16 hours. After that, 2 ml of N,N-diisopropylethylamine and 2 ml of BF<sub>3</sub>.Et<sub>2</sub>O were added to the reaction mixture, and it was stirred under inert atmosphere, for 6 hours. Then, the reaction mixture was washed successively with water (30 mL) and brine (30 mL). The layers were separated, and the organic layer was dried with anhydrous sodium sulfate. Then, it was concentrated under reduced pressure and the crude was purified by column chromatography on silica gel with dichloromethane:hexane (60:40) as eluent. The compound was obtained with 1 % of yield.

**5,10,15,20-(4-((1,3,5,7-tetramethyl-2,6-diethyl-4,4-difluoro-4-bora-3a,4a-diaza-s-indacene)-8-phenyl)-porphyrin (BDP-P3 (109))**



**<sup>1</sup>H NMR (400 MHz, CDCl<sub>3</sub>) δ (ppm):** 8.93 (s, 8H), 8.39 (d, J = 8 Hz, 8H), 8.39 (d, J = 8 Hz, 8H), 2.65 (s, 24 H), 2.34 (q, J = 7.6 Hz, 16H), 1.89 (s, 24H), 1.31 (t, J = 7.6 Hz, 6H); **<sup>19</sup>F NMR (376 MHz, CDCl<sub>3</sub>) δ (ppm):** -145.65 (m, 2F).

### 8.5. References for Chapter 8

1. SAINT Plus Data Reduction and Correction Program va, Bruker AXS: Madison, Wisconsin, **2003**.
2. G.M. Sheldrick S, University of Gottingen, Germany, **1996**.
3. Sheldrick G. Crystal structure refinement with SHELXL. Acta Crystallographica Section C. **2015**; 71, 3-8.
4. A. N. Jordan, S. Das, N. Siraj, S. L. de Rooy, M. Li, B. El-Zahab, L. Chandler, G. A. Baker and I. M. Warner, Nanoscale, **2012**, 4, 5031-5038.
5. J. Olmsted, The Journal of Physical Chemistry, **1979**, 83, 2581-2584.